Project Acronym:

SOUNDPET (INTEGRATED/0918/0008)

MRI-guided Focused ultraSOUND system for cancer in PETs (dogs and cats)

Deliverable number: 2.8

Title: Publication in a scientific journal

Prepared by:

Anastasia Antoniou (CUT, Limassol, Cyprus)
Antria Filippou (CUT, Limassol, Cyprus)
Christakis Damianou (CUT, Limassol, Cyprus)

Date: 13/07/2023

Table of Contents

Executive summary

This deliverable presents the Journal papers that were submitted or published during the third reporting period of the SOUNDPET project. The research papers covered multiple topics related to Focused Ultrasound (FUS) including but not limited to the MRI monitoring of thermal lesions, the development of an advanced software and dedicated gel phantoms, as well as the FUS ablation of naturally occuring mammary tumors in pets. Causion was given to avoid disclosure of the SOUNDPET system's features and components prior to the relevant patent application.

Table 1 lists the title and journal for all papers submitted/published during the relevant reporting period, along with the date of initial submission/publication. It is noted that some of the research work carried out under the SOUNDPET project was a synergy with other projects running at the same time. It is also clarified that some of the papers published during the 3rd reporting period of the project were submitted during the previous one, and thus, they can also be found in the relevant deliverable (Del. 2.6). The proof of paper submisison and the published papers can be found in the Appendix (in the order they appear in Table 1). Note that for accepted papers (not available online yet) the submitted revised manuscript is provided.

A paper regarding the MRI compatible FUS robotic system, which was developed and optimized during the project, entitled "Robotic device for Magnetic Resonance Imaging guided Focused Ultrasound treatment of abdominal targets" was prepared by the team and will be submitted after the relevant patent application is filed since it includes confidential data, i.e., detailed description of the system's components and features, that should not be disclosed currently so as to not compromise the possibility of obtaining a patent. The relevant manuscript and Figures are presented at the end of Appendix.

Table 1: List of papers submitted/published during the 3rd reporting period of the project.

#	Title	Journal	Date
Submitted during the 3rd reporting period			
1	Estimation of PRF coefficient in agar based phantoms	Ultrasonics	03/01/2023
2	MRI monitoring of thermal lesions produced by focused ultrasound	Medical Physics	01/05/2023
3	MR thermometry of Focused Ultrasound using a preclinical FUS robotic system at 3 T	Physica Medica	1st revision 22/05/2023
4	Advanced software for MRgFUS treatment planning	Computer Methods and Programs in Biomedicine	1st revision 03/07/2023
5	Workflow of a preclinical robotic MRI-guided FUS body system	Physica Medica	05/07/2023
6	MRI compatibility testing of commercial HIFU transducers	Physica Medica	03/07/2023
Published during the 3rd reporting period			
7	Preclinical robotic device for magnetic resonance imaging guided focussed ultrasound	Medical Robotics and Computer Assisted Surgery	28/09/ 2022
8	Challenges regarding MR compatibility of an MRgFUS robotic system	Journal of Magnetic Resonance	18/10/2022
9	Simple, inexpensive, and ergonomic phantom for quality assurance control of MRI guided Focused Ultrasound systems	Journal of Ultrasound	04/11/2022
10	Characterization of a fat tissue mimicking material for high intensity focused ultrasound applications	Journal of Ultrasound	21/11/2022
11	Robotic device for transcranial focused ultrasound applications in small animal models	Medical Robotics and Computer Assisted Surgery	17/12/2022
12	Development of an US, MRI, and CT imaging compatible realistic mouse phantom for thermal ablation and focused ultrasound evaluation	Ultrasonics	23/02/2023
13	Treatment of mammary cancer with Focused Ultrasound: A pilot study in canine and feline patients	Ultrasonics	10/03/2023
14	Tumor phantom model for MRI guided Focused Ultrasound ablation studies	Medical Physics	25/05/2023
15	Feasibility of ultrasonic heating through skull phantom using single-element transducer	Journal of Medical Ultrasound	Accepted 31/03/2023
16	FUS-mediated Blood-brain barrier disruption for delivering anti-Aβ antibodies in 5XFAD Alzheimer's disease mice	Journal of Ultrasound	Accepted 28/06/2023
17	Focused Ultrasound heating in brain tissue/skull phantoms with 1-MHz single element transducer	Journal of Ultrasound	Accepted 09/07/2023
18	High Quality Agar and Polyacrylamide Tumour Mimicking Phantom Models for MR-guided Focused Ultrasound Applications	Journal of Medical Ultrasound	Accepted 13/07/2023
To be submitted when patent application is filed			
19	Robotic device for Magnetic Resonance Imaging guided Focused Ultrasound treatment of abdominal targets	Medical Robotics and Computer Assisted Surgery	-

Appendix: Proof of papers submission & Published papers

Ultrasonics

Estimation of the Proton Resonance Frequency coefficient in agar-based phantoms

--Manuscript Draft--

Manuscript Number:	ULTRAS-D-23-00005
Article Type:	Research Paper
Section/Category:	High intensity focused ultrasound, HIFU
Keywords:	thermometry; ultrasound; agar; phantoms; MRI; silicon dioxide
Corresponding Author:	Christakis Damianou Cyprus University of Technology Limassol, Cyprus
First Author:	Antria Filippou
Order of Authors:	Antria Filippou
	Nikolas Evripidou
	Andreas Georgiou
	Anastasia Nikolaou
	Christakis Damianou
Abstract:	Background Agar-based phantoms imitate human tissue properties, thus are popular in High intensity focused ultrasound (HIFU) studies, with Magnetic resonance imaging (MRI) preferred for guidance since it provides temperature monitoring by proton resonance frequency shift (PRF) magnetic resonance (MR) thermometry. MR thermometry monitoring depends on several factors, thus, herein, the PRF coefficient of agar-based phantoms was estimated. Methods Seven phantoms were developed with varied agar (2, 4, or 6% w/v) or constant agar (6% w/v) and varied silicon dioxide concentrations (2, 4, 6, or 8% w/v) to assess the effect of the varied concentration on the PRF coefficient. Each phantom was sonicated using varied acoustical power (18-42 W) for a sonication time of 30 s in both a laboratory setting and inside a 3 T MRI scanner. PRF coefficient was estimated for each phantom by fitting linear trends between phase shift acquired using gradient pulse-sequence and thermocouple-based temperature changes. Results For all phantoms, linear regression (R2=0.8581-0.957) demonstrated a proportional dependency of phase shift with temperature change induced by the sonications, resulting in PRF coefficients between -0.0184 to -0.0384 ppm/oC for the various phantom recipes taken. Inverse linear dependencies of the PRF coefficient were observed with increased agar. With silicon dioxide concentrations, the dependence was linear. For all phantoms and sonications, calibrated PRF coefficients resulted in lower, by 1.6 to 4.1-fold, temperature changes compared to values calculated using a literature PRF coefficient. Conclusions Phantoms developed with a 4% or 6% w/v agar concentration or doped with 2% w/v silicon dioxide best resemble tissue PRF coefficients and should be preferred in future HIFU validation studies, while the estimated PRF coefficients can be employed, resulting in accurate MR thermometry monitoring and enhanced evaluation of HIFU protocols.
Suggested Reviewers:	Leonidas Georgiou

	Leonidas.Georgiou@goc.com.cy Related to and experienced in the field.
	Costas Pattichis pattichi@cs.ucy.ac.cy Related to and experienced in the field.
	Chrit Moonen C.Moonen@umcutrecht.nl Related to and experienced in the field

- Estimation of the proton resonance frequency (PRF) coefficient in agar-based phantoms
- Seven phantoms developed with varied agar or silicon dioxide to assess effect on PRF
- PRF coefficients estimated from linear trends between phase shift and temperature changes
- PRF coefficients for all phantoms were between -0.0184 to -0.0384 ppm/^{o}C
- Linear dependencies of the PRF coefficient were found with increased agar and silica

Estimation of the Proton Resonance Frequency coefficient in agar-based phantoms

Antria Filippou[a1], Nikolas Evripidou[a2], Andreas Georgiou[a3], Anastasia Nikolaou[a4], Christakis Damianou[a*]

[a] Cyprus University of Technology, Department of Electrical Engineering, Computer Engineering, and Informatics, Limassol, Cyprus.

Emails: [1]ap.filippou@edu.cut.ac.cy
[2]nk.evripidou@edu.cut.ac.cy
[3]andreas-georgiou1@outlook.com
[4]ann.nikolaou@edu.cut.ac.cy

***For correspondence contact:**
Christakis Damianou,
Cyprus University of Technology,
Department of Electrical Engineering, Computer Engineering, and Informatics,
30 Archbishop Kyprianou Street,
3036 Limassol,
CYPRUS
Email: christakis.damianou@cut.ac.cy
Tel.: 0035725002039
Fax: 0035725002849

ABSTRACT

Background: Agar-based phantoms imitate human tissue properties, thus are popular in High intensity focused ultrasound (HIFU) studies, with Magnetic resonance imaging (MRI) preferred for guidance since it provides temperature monitoring by proton resonance frequency shift (PRF) magnetic resonance (MR) thermometry. MR thermometry monitoring depends on several factors, thus, herein, the PRF coefficient of agar-based phantoms was estimated.

Methods: Seven phantoms were developed with varied agar (2, 4, or 6 % w/v) or constant agar (6 % w/v) and varied silicon dioxide concentrations (2, 4, 6, or 8 % w/v) to assess the effect of the varied concentration on the PRF coefficient. Each phantom was sonicated using varied acoustical power (18-42 W) for a sonication time of 30 s in both a laboratory setting and inside a 3 T MRI scanner. PRF coefficient was estimated for each phantom by fitting linear trends between phase shift acquired using gradient pulse-sequence and thermocouple-based temperature changes.

Results: For all phantoms, linear regression (R^2=0.8581-0.957) demonstrated a proportional dependency of phase shift with temperature change induced by the sonications, resulting in PRF coefficients between -0.0184 to -0.0384 ppm/^{o}C for the various phantom recipes taken. Inverse linear dependencies of the PRF coefficient were observed with increased agar. With silicon dioxide concentrations, the dependence was linear. For all phantoms and sonications, calibrated PRF coefficients resulted in lower, by 1.6 to 4.1-fold, temperature changes compared to values calculated using a literature PRF coefficient.

Conclusions: Phantoms developed with a 4 % or 6 % w/v agar concentration or doped with 2 % w/v silicon dioxide best resemble tissue PRF coefficients and should be preferred in future HIFU validation studies, while the estimated PRF coefficients can be employed, resulting in accurate MR thermometry monitoring and enhanced evaluation of HIFU protocols.

KEYWORDS: thermometry, ultrasound, agar, phantoms, MRI, silicon dioxide

1. INTRODUCTION

Phantoms developed with tissue mimicking materials possess a pivotal role in the medical field in that they can be tailored to accurately mimic specific properties of human tissue, thus serving as a tool in the evaluation of existing and emerging diagnostic and therapeutic medical systems [1]–[2]. Phantoms were initially introduced in the 1960s for calibrating diagnostic ultrasound (US) systems [3], and have thenceforth been abundantly developed with specific inclusion materials in homogeneous or anthropomorphic forms, in both research and commercial states, resembling specific biological tissues and tailored to certain medical applications [2]–[3]. In this regard, phantoms enable accurate and cost-effective quality assurance, quality control and efficacy validation of preclinical or clinical systems, minimising the need for animal and human subjects [2], [4]. Consequently, the ever-increasing development of novel therapeutic High Intensity Focused Ultrasound (HIFU) systems and applications [5] has been associated with an increased development of phantoms dedicated for use with HIFU validation studies [2].

Phantoms tailored for HIFU feasibility studies should ideally emulate human tissue acoustic and thermal properties [6] as well as possess tissue-like properties encountered in Magnetic Resonance Imaging (MRI) [7]. Remarkably, the Onda Corporation (Sunnyvale, California, USA) company possesses a monopoly on the only commercially available phantom particularly suited for HIFU applications [2]. Although this phantom is manufactured with a polyacrylamide (PAA) gelling agent that provides transparency, and locally turns opaque upon exposure to specific temperature thresholds [2], it possesses fixed acoustic and thermal properties [2]. Contrary, in-house developed water-based phantoms for HIFU applications can be fabricated with appropriate additives that individually adjust certain properties [8]–[10], thus specifically emulating the tissue of interest. PAA is considered a favoured gelling agent for developing phantoms for HIFU applications since it possesses a high melting temperature

[11] and results in transparent phantoms [8]–[9], [12]–[13] that permit visual assessment of the efficacy of the HIFU system under investigation. Nevertheless, PAA phantoms are toxic during the fabrication process [8], with the developed phantoms exhibiting limited lifetime if not properly stored [14]. Gelatin is another gelling agent preferred in custom development of phantoms, with additional inclusions employed to appropriately adjust specific phantom properties [15]–[17]. Nevertheless, although gelatin-based phantoms are manufactured in an easy and cost-effective manner [16], their employment in HIFU exposures is only subjected to application of low acoustic power [16], accounting for the low melting temperature of gelatin [4].

Contrary, agar is considered the most popular material for custom fabrication of phantoms dedicated to thermal therapies and HIFU applications since it is non-toxic and possesses a high temperature melting point [4]. Silicon dioxide [18], and evaporated milk [19] are often used as additional ingredients to increase the acoustic attenuation [18] and absorption of the developed phantoms [19], respectively. Increased concentrations of agar, silicon dioxide, and evaporated milk can independently enhance the acoustic properties of the agar-based phantoms to soft tissue levels [19], while simultaneously adjusting the magnetic properties [20] of these phantoms. Moreover, these materials can adjust the thermal properties of agar-based hydrogels, thus mimicking soft tissue [6], while addition of alcohols was recently reported in this sense for adjusting the thermal properties to fat tissue levels [21]. Given the popularity of agar, many studies have concentrated around the development of agar-based phantoms dedicated to HIFU feasibility studies [22]–[24], with silicon dioxide and evaporated milk in appropriate concentrations reported for the development of anthropomorphic breast [23] and head [22] phantoms exhibiting tissue-like properties [22]–[23], intended for evaluation of breast-specific HIFU systems [23] and HIFU brain applications [22], respectively.

HIFU systems and therapeutic protocols are normally guided by either US or MRI systems that provide visual monitoring of the procedure [5]. MRI is preferred as a guidance modality since it exhibits higher tissue image resolution than US [25] and enables utilisation of MRI thermometry tools for monitoring the temperature of the tissue [26]. Most MRI thermometry tools employed for monitoring MRI guided focused ultrasound (MRgFUS) procedures, are based on the temperature-dependent proton resonance frequency shift (PRF) technique [26]–[27], that is in turn related to tissue temperature-induced changes observed in the hydrogen bonds [26]–[27]. Specifically, increased tissue temperatures arising during HIFU or other thermal exposures, result in reduced proton resonance frequency and increased electron screening that ultimately induce a phase shift in the detected MRI signal [26]–[27]. Therefore, PRF-based magnetic resonance (MR) thermometry provides quantitative temperature mapping by relating phase measurements of MR images acquired prior to and throughout thermal procedures, to tissue temperature changes [26]–[27]. Notably, these temperature and phase changes are further related to the magnetic field strength, the acquisition parameters of the MR imaging sequence and the PRF temperature change tissue coefficient [26]–[27]. The PRF tissue coefficient describes the linear temperature dependence of the proton resonance frequency and is normally taken as a standard value of -0.010 ppm/^{o}C [27]. Nevertheless, calibration experiments are sometimes performed to accurately derive the PRF coefficient of the tissue under investigation and utilise the calibrated value in MR thermometry temperature monitoring. Similar methods are often employed for calibrating the PRF coefficient, wherein the investigated tissue is thermally heated, and the value is quantitatively acquired from linear relationships arising between temperature and phase difference measurements [28]–[38].

The PRF coefficient is generally considered independent of tissue type following ex-vivo animal tissue calibrations over a 20-80 ^{o}C temperature range [28]. Excised rabbit and

porcine kidney, brain, liver, and muscle tissues heated with a water bath over this temperature range within a 1.5 T MRI scanner, with temperature measurements simultaneously acquired using fibre-optic probes, resulted in PRF coefficients in the range of -0.010 to -0.0105 ppm/°C, calculated from the slopes of linear relations between the temperature measurements and the phase shifts of MR images acquired at every 1 °C temperature change [28]. Contrary, analogous temperature and phase measurements acquired at a 7 T MRI scanner during *in vivo* microwave heating of rabbit muscle tissues resulted in a lower calibrated PRF coefficient of -0.00976 ppm/°C [29], similar to the corresponding PRF coefficient (-0.009 ppm/°C) of *in vivo* porcine muscle tissue as measured at 0.5 T during radiofrequency heating [30]. Notably, *in vivo* focused ultrasound heating of rabbit muscle tissue over a temperature range of 37-60 °C inside a 1.5 T scanner reported an even lower PRF coefficient of -0.007 ppm/°C [31], while similar temperature sensitivities were reported for *in vivo* rabbit brain tissues at 1.5 T following laser (-0.0088 ppm/°C) [32] and microwave heating (-0.008 ppm/°C) [33] over corresponding temperature ranges. Accordingly, *in vivo* radiofrequency heating of canine brain and muscle tissues over hyperthermic temperatures resulted in similar temperature sensitivities between the two tissue types, with the PRF coefficients calibrated at -0.00695 ppm/°C and -0.00674 ppm/°C, respectively [34]. Further inconsistencies in the calibrated PRF coefficients were reported for other *in vivo* studies in canine brain [35], and rabbit muscle [36] and brain [37], [38] tissues possibly attributed to physiological tissue differences and discrepancies in the experimental calibration procedure [28], while some deviations from linearity between the PRF shift and the temperature change have also been reported [39].

Contrary to tissues, agar-based phantoms offer excellent linear thermal response of the PRF shift, thus making them suitable tools for employment with the PRF method [39] which is considered the most accurate temperature monitoring modality in agar-based phantoms [40]. Nevertheless, PRF coefficient dependencies have been described with magnetic susceptibility

changes attributed to the orientation and spatial distribution of thermal heating relative to the magnetic field, resulting in up to 30 % deviations in MR-thermometry based temperature measurements [41]. Experimental studies performed for water-bath heated 2 % agar-based phantoms within a 1.5 T clinical MRI scanner, revealed PRF coefficients of -0.0094 ppm/^{o}C and ranging between -0.0055 to -0.0130 ppm/^{o}C for thermal heating distribution in planes parallel and perpendicular relative to the magnetic field orientation, respectively [41]. Accordingly, PRF calibrations of 2 % agar-based phantoms doped with black ink during laser heating, with the heating source aligned parallel to the main magnetic field and temperatures concurrently acquired with fibre-optic probes, resulted in PRF coefficients decreasing from -0.0104 ppm/^{o}C to -0.0084 ppm/^{o}C for a 2-fold increase in the slice thickness of the imaging sequence, attributable to volume averaging effects in the phase measurements arising with the increased slice thickness [42].

Olsrud et al. [39] developed 2 % agar-based phantoms doped with nickel nitrate that were heated to temperatures in the 25-80 ^{o}C range by means of a water bath, while being scanned within a 1.5 T MRI scanner. From the simultaneous phase difference and thermocouple-based temperature change measurements, the authors [39] reported an average PRF coefficient of -0.0085 ppm/^{o}C. Similar utilisation of a water bath [28] and microwave applicators [29] for heating agar-based phantoms having the corresponding agar concentration (2 %) inside 1.5 T [28] and 7 T [29] scanners, resulted in PRF coefficients between -0.01 to -0.0105 ppm/^{o}C [28] and -0.00977 ppm/^{o}C [29], respectively. Recently, Wang [43] performed agar-phantom-based PRF coefficient calibrations for executing MR thermometry calculations at 7 T, wherein MRI-compatible thermocouples were inserted within a hollow annular 1 % agar-based phantom, while hot water was introduced within the hollow area to increase the temperature of the phantom. A value of -0.0095 ppm/^{o}C was reported for the PRF coefficient of the phantom from a typical linear relationship fitted between phase shifts and temperature

changes arising from MR images and concurrent thermocouple measurements acquired during heating, respectively [43]. Accordingly, PRF coefficient measurements were reported for muscle-like PAA phantoms from a linear trend existing between sensor-based temperature change measurements in the range of 20-55 ºC and phase shifts of images acquired at 1.5 T during microwave heating, wherein values of -0.008 ppm/ºC and -0.0091 ppm/ºC were reported using a clinical MRI scanner and spectroscopic techniques for imaging, respectively [44]. In another study [45], employment of a 1.5 T scanner for imaging and fibre-optic probes for temperature measurements during laser heating of another acrylamide phantom doped with bovine serum albumin (BSA), resulted in an identical PRF coefficient of -0.0088 ppm/ºC. Lochhead et al. [46] utilised a previously developed PAA-based phantom doped with BSA protein [10] to calibrate it for MRgFUS studies and examine its PRF temperature dependencies. Simultaneous sensor-based temperature measurements and MR images at 1.5 T were acquired during focused ultrasound heating of the phantom and were related to the PRF equation, resulting in an average PRF coefficient of -0.0095 ppm/ºC [46]. Appropriately, PRF coefficients at -0.0104 ppm/ºC [47] and -0.0123 ppm/ºC [48] were reported for oil-in-gelatin phantoms from phase shifts at 1.5 T and temperature measurements acquired with single [47] and multiple [48] temperature sensors, respectively, being similar to the PRF coefficient of a 1.5 % agar-based phantom (-0.011 ppm/ºC) as calculated for radiofrequency heating at 0.5 T [30].

Considering that accurate PRF MR thermometry temperature calculations are dependent on the PRF coefficient [41], [48], PRF coefficient calibrations of several agar-based phantoms were executed in the present study, following the vast development and use in HIFU validation studies [18]–[24]. The phantoms were developed with varied concentrations of agar or silicon dioxide to assess the effect of the varying concentrations on the calibrated PRF coefficient. A series of identical HIFU exposures were executed on the agar-based phantoms

within a 3 T clinical MRI environment and in a laboratory setting. Given the excellent linear thermal response agar-based phantoms exhibit with the PRF technique [39], the PRF coefficient of each phantom was estimated through linear relationships taken between temperature and phase shift measurements acquired from the laboratory and MRI HIFU exposures, respectively. Subsequently, MR thermometry calculations were performed for the HIFU exposures to assess the effect of the calibrated PRF coefficients on the temperature measurements.

2. MATERIALS AND METHODS

2.1 Agar-based phantoms

Initially, three agar-based phantoms were developed with varied % weight per volume (w/v) concentrations of agar (101614, Merck KGgA, Darmstadt, Germany) to examine any dependency of the PRF temperature coefficient with the agar concentration. In this regard, the agar-based phantoms were individually developed with 2, 4, or 6 % w/v agar concentrations following the fabrication procedure previously mentioned by Drakos et al. [19]. Briefly, 510 ml of pure, deionised and degassed water were steadily heated by means of a glass beaker that was accommodated on a magnetic hotplate (SBS A160, Steinberg Systems, Hamburg, Germany). A magnetic stir-bar immersed in the water volume, interacted with the magnetic hotplate (SBS A160, Steinberg Systems) and provided continuous stirring of the water throughout heating. The appropriate % w/v agar concentration (2, 4 or 6) was grinded into a fine powder that was added in the water when its temperature, as recorded with a digital thermometer (HH806AU, Omega Engineering, Connecticut, USA) reached 50 ^{o}C. Thereafter, the agar-water solution was continuously heated while concurrently being magnetically stirred until the temperature of the solution exceeded 85 ^{o}C, whereupon the heating function of the magnetic hotplate (SBS A160, Steinberg Systems) was switched off and the solution was allowed to cool to approximately 50 ^{o}C while undergoing continuous magnetic stirring.

Subsequently, the solution was poured into 3D-printed (FD270, Stratasys, Minnesota, USA) cuboid molds with dimensions of 80 mm (w) × 90 mm (l) × 70 mm (h) and was allowed to solidify within a refrigerator.

Thereafter, four agar-based phantoms doped with silicon dioxide (Sigma-Aldrich, Missouri, USA) were developed with a constant 6 % w/v concentration of agar and varied % w/v silicon dioxide concentration (2, 4, 6, or 8 % w/v) to investigate any effect of the increased silicon dioxide concentration on the PRF temperature coefficient. Notably, the four phantoms were fabricated following the abovementioned preparation process utilising identical water volumes and heating temperature thresholds, with the development process only differing in the addition of silicon dioxide in the agar-water solution. Silicon dioxide was appropriately added with the correct concentration (2, 4, 6, or 8 % w/v) in the solution, within a short timeframe following the addition of agar (6 % w/v). The agar-based silicon dioxide doped solutions were individually poured in the aforementioned 3D-printed molds (FD270, Stratasys) and were placed in the refrigerator to undergo jellification. Notably, before experimental studies, the seven phantoms were removed from the molds and were allowed to reach ambient temperature.

2.2 Features of robotic system for MRgFUS ablations

An MRgFUS robotic system was selected from a range of existing robotic systems developed for preclinical MRgFUS applications [49]–[55]. Remarkably, the existing robotic systems have all been fabricated with MRI-compatible materials enabling proper operation within clinical MRI scanners and uninfluenced MR imaging for monitoring sonications [49]–[55]. Specifically, the selected MRgFUS robotic system [49] was fabricated with Acrylonitrile Styrene Acrylate (ASA) thermoplastic using a 3D-printer (FD270, Stratasys) and provides mechanical computer-controlled linear motion in three axes (X, Y, and Z). Notably, MRI-compatible piezoelectric motors (USR60-S3N, Shinsei Kogyo Corporation, Tokyo Japan)

coupled to linear optical encoders (US Digital, Vancouver, Washington, USA) are employed to initiate and precisely control linear motion, respectively [49]. Motion is transferred to a single-element concave transducer with a diameter of 50 mm operating at a frequency of 2.75 MHz and focusing at 65 mm, that frontally extends from the positioning mechanisms to a water-filled container. It is worth mentioning that the water-filled container is fitted with an opening, thus allowing ultrasonic beam to be transmitted from the transducer to the targeted subject, through the deionised and degassed water medium.

2.3 Control software for HIFU exposures

The MRgFUS robotic system interfaces with an in-house software developed in C# (Visual Studio, Microsoft Corporation, Washington, USA) that controls the parameters of the HIFU exposures. Specifically, the operating frequency of the transducer, the amount of power delivered, and the sonication time can be arranged through suitable commands. Additionally, the developed software allows interfacing with clinical MRI scanners for MR image transfer, thus enabling treatment monitoring through MR thermometry tools based on the PRF method [26]–[27].

2.4 HIFU exposures within an MRI environment

The MRgFUS robotic system was accommodated on the table of a 3 T clinical MRI scanner (Magnetom Vida, Siemens Healthineers, Erlangen, Germany) as shown in Figure 1. The phantoms were individually accommodated on the acoustic opening of the robotic system via a rigid 3D-printed (FD270, Stratasys) ASA phantom holder. The 3D-printed ASA phantom holder provided support of each phantom at the centre of the acoustic opening so that ultrasonic beam directly propagated from the transducer to the centre of the agar-based phantom. Similarly, a rigid ASA structure was accommodated on the MRI table, surrounding the robotic system, providing support to a multi-channel body MR imaging coil (Body18, Siemens Healthineers) on top of the agar-based phantom. The transducer was connected to an amplifier

(AG1016, T & C Power Conversion, Rochester, NY, USA) and to the in-house developed software that was in turn interfaced with the MRI scanner for MR image acquisition.

Identical single-point sonications were individually executed on each of the seven agar-based phantoms. Each phantom was sonicated by applying varied acoustic power of 18, 24, 30, 36, and 42 W for a constant sonication time of 30 s at a focal depth of 25 mm. During the five individual sonications, MRI scans of each of the seven agar-based phantoms were performed in the coronal plane using the MR imaging body coil (Body18, Siemens Healthineers) and a Fast low angle shot (FLASH) sequence with the following acquisition parameters: Repetition time (TR) = 25 ms, Echo time (TE) = 10 ms, Field of View (FOV) = 280 × 280 mm^2, Slice thickness = 5 mm, Acquisition matrix = 96 × 96, Number of excitations (NEX) = 1, Echo train length (ETL) = 1, Flip angle = 30°, and Pixel bandwidth = 240 Hz/pixel. Notably, for each of the seven phantoms, three FLASH scans were performed before each individual HIFU exposure at varied acoustical power for acquisition of three reference images. Acquisition of images prior to each HIFU exposure was necessary for imaging the phantoms at baseline temperatures, while the number of reference images acquired (3) was essential to adjust for any irregularities of the FLASH pulse-sequence. Correspondingly, FLASH images throughout the HIFU exposures were acquired at timeframes of 2.4 s for a total imaging time of 60 s, corresponding to 30 s sonication time and 30 s cooling time after the elapsed sonication time.

2.5 HIFU exposures in the laboratory environment

Following the HIFU exposures within the MRI environment, equivalent benchtop ultrasonic protocols were performed with the MRgFUS robotic system on the seven phantoms inside the laboratory setting. In this regard, each of the phantoms were individually accommodated in the acoustic opening of the robotic system, through the 3D-printed (FD270, Stratasys) ASA phantom holder, in an equivalent manner to the experimental setting configuration within the MRI environment. It is worth noting that the ASA phantom supporting

structure, apart from providing rigid support to the phantom at the centre of the acoustic opening, additionally permitted accurate insertion of thermocouples at every 5 mm within the phantom, in a plane perpendicular to the propagation of the ultrasonic beam, through small circular apertures vertically existing on the 3D-printed (FD270, Stratasys) structure.

The five sonication protocols defined by the varied acoustic power (18, 24, 30, 36, and 42 W) for the sonication time of 30 s at a focal depth of 25 mm were equivalently executed on the seven agar-based and agar-based doped with silicon dioxide phantoms. In this regard, a 100 μm thick thermocouple (5SRTC-TT-K-30-36, type K insulated beaded wire, Omega Engineering) was individually inserted within each of the seven agar-based phantoms at a 25 mm depth. The tip of the thermocouple was carefully inserted at the centre of the phantom to directly measure the temperature at the focal point. The temperature induced resulting each ultrasonic exposure was recorded by the thermocouple and the digital thermometer (HH806AU, Omega Engineering) with a temporal resolution of 1 s. Accommodation of the phantoms on the 3D-printed ASA structure ensured that benchtop sonications on each of the phantoms were executed at the exact location where exposures within the MRI environment were performed. In this regard, experimental measurements acquired within the two environments (laboratory, and MRI) could be comparable.

2.6 PRF temperature change coefficient

2.6.1 Acquisition of phase image

The coronal magnitude and phase images of each of the seven agar-based phantoms acquired using the FLASH sequence before (reference images) and during the varied HIFU exposures (ablation images) were loaded into a Digital Imaging and Communication in Medicine (DICOM) software (MicroDicom, MicroDicom Ltd., Sofia, Bulgaria) for post-processing. On the individual phase FLASH images of each phantom, circular regions of interest (ROIs) with a diameter of 3 mm were set. The ROIs were arranged on all images

(reference and ablation) at the corresponding location of the focal spot, as visualised on the magnitude images acquired throughout the HIFU exposures, while the diameter of the ROIs (3 mm) was chosen after considerations related to the width of the focal beam. Consequently, for phase images the average signal intensity (SI) within the ROI was measured with the MicroDicom (MicroDicom Ltd.) software for the three reference images acquired before heating, as well as for the image acquired at the maximum ablation temperature during exposures. The SI measurements of the reference and ablation phase images were converted to radians within the range of 0 to 2π, by utilizing the minimum and maximum image pixel values as defined by the acquired DICOM image (minimum and maximum image pixel values of 0 and 4095, respectively), thus resulting in phase values for the reference and ablation phase images.

2.6.2 PRF temperature change coefficient calculations

Ultimately, calculations were performed to measure the temperature change coefficient (α) of each phantom developed with either varied agar or silicon dioxide concentrations, using the PRF method [26]–[27]. With the PRF technique, temperature changes (ΔT) within the tissue arising during exposure to thermal heating induce a shift in the proton resonance frequency that is consequently observed as a phase difference ($\Delta\varphi$) in MR images acquired before and throughout HIFU exposures. The PRF technique relates these temperature changes to the phase difference through the following equation:

$$\Delta T = \frac{\varphi(T)-\varphi(T_o)}{\alpha.\gamma.B_0.TE} \quad (1)$$

where $\varphi(T)$ and $\varphi(T_o)$ are the phase of images acquired before (baseline tissue temperature) and during HIFU exposure (ablation temperature), respectively, γ is the gyromagnetic ratio, B_0 is the local magnetic field strength and TE is the echo time of the employed MR imaging sequence.

In this regard, for temperature change coefficient (α) calculations, Equation 1 was rearranged into the following format, where all variables have their abovementioned meanings:

$$a = \frac{\Delta\varphi}{\Delta T.\gamma.B_0.TE} \quad (2)$$

For each of the five individual HIFU sonications executed on each of the seven agar-based phantoms, the phase difference ($\Delta\varphi$) was calculated from the phase measurements that were performed on the FLASH phase reference and ablation images acquired for the HIFU exposures performed within the MRI environment. It is worth stating that the phase difference was calculated by taking the absolute difference between the phase values of the ablation image and the average value of the individual phases of the three reference images. Accordingly, for each of the five sonications executed on each developed phantom, the corresponding phase difference value was related to the maximum temperature change as recorded with the thermocouple during benchtop sonications performed in the laboratory setting. Consequently, graphical plots of the temperature change against the phase difference values, as calculated for each of the sonications executed at varied applied acoustic power, were individually generated for the seven phantoms. Eventually, regression analysis was performed and the PRF coefficient of each fabricated phantom was calculated by fitting the inverse of the slope of the regression analysis (i.e. $\Delta\varphi/\Delta T$) in Equation 2. Concerning the three remaining variables of the equation, the gyromagnetic ratio of the water proton γ was taken as 42.58 MHz/T, the magnetic field strength B_0 was set at 3 T, while a TE of 10 ms was utilised arising from the acquisition parameters of the employed FLASH sequence.

2.7 MR thermometry temperature measurements

Following calculations for the PRF coefficients of the seven agar-based phantoms, MR thermometry temperature estimations were executed based on the PRF technique [26]–[27] using the aforementioned in-house control software. The coronal FLASH images of the various agar-based phantoms acquired in the course of sonications executed at varied acoustic power

(18, 24, 30, 36, and 42 W) for a constant sonication time (30 s) within the 3 T MRI scanner (Magnetom Vida, Siemens Healthineers), were processed by the in-house software to derive the temperature increase induced as a result of each individual sonication executed on each of the seven phantoms. The FLASH images of each phantom were processed by the software, and temperatures induced resulting each sonication at varied acoustic power were calculated in a particular ROI within each phantom using PRF-based MR thermometry and Equation 1. Notably, for consistency and accuracy purposes, the ROI at which temperatures were estimated, was set in each phantom with an identical size (diameter of 3 mm) at the corresponding locations where phase measurements for the PRF coefficient calibrations were executed. Initially, for each phantom, temperatures within the specific ROIs resulting each sonication executed at varied acoustical power were calculated utilising the corresponding calibrated PRF coefficient. Subsequently, MR thermometry temperature estimations were additionally executed for each phantom and sonication, utilising a PRF coefficient of -0.0094 ppm/^{o}C that is typically reported in literature for MR thermometry estimations in in-house gel phantoms [41], [56]–[57] and is employed as a default value for the PRF coefficient by the in-house developed software. MR thermometry data, specifically colour-coded thermal maps and timeseries plots of the temperature at the specified ROI were generated for each sonication and phantom using the calibrated and default values of the PRF coefficients to assess the effect of the calibrated coefficient on temperature measurements. It is worth stating that the colour-coded thermal maps generated for each phantom and sonication were overlapped on the corresponding magnitude scans of the phantom, thus presenting the extent of thermal heating throughout the phantom during sonications.

3. RESULTS

3.1 Acquisition of phase image

Post-processing of FLASH phase images of each of the seven phantoms acquired before heating and at maximum ablation temperatures for sonications at the varied acoustical power resulted in phase measurements in the range of [0, 2π] as indicatively shown in Table 1 for the varied sonications executed on the 2 % w/v agar-based phantom. For the corresponding phantom, phase differences (Δφ) between 0.449-1.671 radians were induced at varied acoustical power of 18-42 W as calculated by averaging the individual phase measurements of the three reference images and subtracting from the corresponding phase value of the maximum temperature ablation image.

3.2 PRF temperature change coefficient calculations

Phase shift measurements as derived from phase images of each of the seven agar-based phantoms acquired during sonications at varied acoustic power within the MRI environment were correlated with the maximum thermocouple measured temperature changes. Figure 2A and Figure 2B show characteristic graphical plots of a linear response of the temperature change with the phase shift at various sonication protocols executed on an agar-based phantom (6 % w/v agar) and on the corresponding agar-based phantom doped with silicon dioxide (6 % w/v agar and 6 % w/v silicon dioxide). Following least-squares linear regression analysis between the temperature changes and phase difference values resulting the five sonications individually performed on each phantom, the PRF coefficient was estimated for the three agar-based phantoms and the four agar-based phantoms doped with silicon dioxide as shown in Table 2 and Table 3, respectively.

Figure 3A shows the effect of the varied agar concentration (2, 4, and 6 % w/v) on the calibrated PRF coefficient of the three agar-based phantoms. Following linear regression analysis (R^2=0.683), an inverse proportional effect on the PRF coefficient was observed with an increased concentration of agar. Accordingly, the effect of the varied concentration of silicon dioxide (2, 4, 6, or 8 % w/v) on the calibrated PRF coefficient of the four agar-based

phantoms (6 % w/v) doped with silicon dioxide is shown in Figure 3B. The calibrated PRF coefficient (-0.0184 ppm/^{o}C) of the purely agar-based phantom developed with the corresponding agar concentration (6 % w/v) without silicon dioxide (0 % w/v) is also included in Figure 3B for comparison purposes. After least-squares linear regression fit with a Pearson correlation coefficient (R^2) of 0.729, a proportional relation was observed between the PRF coefficient with an increased concentration of silicon dioxide.

3.3 MR thermometry temperature measurements

MR thermometry data produced for each phantom and sonication using either the respective calibrated or default PRF coefficients, were generated every 2.4 s for the duration of the exposures, equivalent to the temporal resolution of the FLASH sequence. Figure 4A shows typical thermal maps generated in the coronal plane (perpendicular to the ultrasonic beam propagation) at the end of sonications (sonication time of 30 s) executed with a low acoustic power (24 W) on an agar-based phantom (4 % w/v) using the corresponding calibrated PRF coefficient (-0.0166 ppm/^{o}C) of the specific phantom. At the ROI specified within the agar-based phantom (4 % w/v) a maximum temperature of about 45 ^{o}C was recorded utilising the calibrated PRF coefficient of the phantom as shown in Figure 4B. Accordingly, Figure 5A shows the respective coronal thermal maps of the same agar-based phantom (4 % w/v) generated at the identical timepoint for the equivalent ultrasonic protocols (acoustic power of 24 W for sonication time of 30 s at a 25 mm focal depth) by employing the default value of the PRF coefficient. Figure 5B shows a maximum temperature of approximately 51 ^{o}C achieved at the corresponding ROI within the agar-based phantom (4 % w/v) resulting sonications, as generated with MR thermometry based on the default value of the PRF coefficient. Table 4 and Table 5 show the temperature changes, from a reference temperature of 37 ^{o}C, derived with MR thermometry using either the corresponding calibrated or default PRF coefficients, resulting the different ultrasonic protocols performed on the three agar-based phantoms

developed with varied agar concentrations and the four agar-based phantoms (6 % w/v) having varied concentrations of silicon dioxide, respectively. Generally, for the seven phantoms, irrespective of varied agar or silicon dioxide concentrations or the varied applied acoustical power, thermometry-based temperature change estimations based on the corresponding calibrated PRF coefficients were lower compared to equivalent temperature changes estimated utilising the default PRF coefficient.

4. DISCUSSION

In this study, the PRF temperature coefficient of several agar-based phantoms was calibrated following a series of HIFU sonications executed within a laboratory setting and inside a clinical 3 T MRI environment. Particularly, the HIFU exposures were controlled with an in-house software that also provides PRF MR thermometry monitoring, and were executed with an MRgFUS robotic system [49] integrated with a single-element concave transducer operating at 2.75 MHz, that was chosen from a range of previously developed devices dedicated to preclinical MRgFUS studies [49]–[55]. Agar was preferred as a gelling agent for the development of phantoms employed herein, following its popularity in the fabrication process of phantoms dedicated to HIFU feasibility studies attributed to its ability to withstand the high temperatures induced by exposures [4] and accurately mimicking specific human tissues upon employment of additional inclusions [18]–[19]. In this regard, seven phantoms were fabricated in the present study with varied agar (2, 4, and 6 % w/v) and silicon dioxide (2, 4, 6, and 8 % w/v) concentrations following previous studies that revealed that appropriate concentrations of these materials result in phantoms that accurately mimic the acoustic, thermal [6], [19], [22]–[23] and magnetic [20] properties of certain biological tissues. While previous studies have primarily focused on the independent effect of the varied agar and silicon dioxide concentrations on the acoustic [6], [19] and magnetic [20] properties of the developed phantoms, the current study investigated the effect of the varied concentrations of the phantom

448 inclusions on the PRF temperature coefficient, and thus the temperature dependence of the
449 phase shifts of the MR signal.

450 In this regard, the PRF coefficient of each phantom fabricated with varied agar or
451 silicon dioxide concentrations was calibrated utilising a method that has repeatedly been
452 reported in the literature, wherein the parameter is calculated based on the PRF technique [26]–
453 [27], from linear relations between phase and temperature changes induced resulting thermal
454 exposure of the investigated tissue within an MRI environment [28]–[38]. Specifically, a series
455 of sonications executed at varied acoustic power (18-42 W) were comparably performed on
456 each of the fabricated phantoms within the 3T MRI, while concurrently being scanned with a
457 FLASH sequence. Phase shifts resulting each varied ultrasonic protocol executed on each of
458 the different phantoms were derived in a plane perpendicular to the ultrasonic beam
459 propagation (coronal plane) after careful post-processing of the acquired MRI scans. Contrary
460 to most literature studies [28]–[31], [42]–[48] that interstitially insert temperature sensors in
461 the investigated material during MRI-based thermal heating of the targeted subject for
462 simultaneous acquisition of temperatures and phase shifts, in the current study thermocouple-
463 based temperature change measurements were acquired in a plane perpendicular to the
464 propagation of the beam from identical benchtop ultrasonic sonications that were executed on
465 each of the various phantoms inside the laboratory setting. This approach was followed to
466 prevent artifacts inadvertently arising on the MR images due to thermocouple presence within
467 the phantom that could potentially impact phase shift measurements. Nevertheless, providing
468 that the developed agar-based phantoms exhibit excellent thermal repeatability [6] and that
469 special structures were employed allowing ablation of each phantom at corresponding locations
470 during benchtop and MRI-based sonications, temperature changes derived in the laboratory
471 setting were comparable to phase shifts arising from the MR images for each sonication and
472 phantom. Consequently, increased phase shifts were calculated resulting sonications at

increased acoustic power that in turn induced increased temperatures within either of the developed agar-based phantoms, thus being in accordance with previous studies performed in different magnetic field strength scanners where a proportional dependency of phase shift with temperature change was observed [30], [39], [41], [43]. Specifically, for the agar-based phantom developed with a 2 % w/v agar concentration, increased phase shifts in the range of 0.449-1.671 radians were observed for increased temperature changes in the range of 19.1-50.5 ^{o}C induced resulting sonications at increased varied acoustic power (18-42 W). Notably, phase shifts recorded in the present study were similar to phase shift measurements reported over corresponding temperature changes for other agar-based phantoms having approximately similar (1.5 % w/v) agar concentrations in a lower magnetic field strength scanner [30], thus corroborating the accuracy of the phase and temperature change measurements executed herein.

Consequently, for either the agar-based (2, 4, or 6 % w/v agar) or agar-based (6 % w/v) doped with silicon dioxide (2, 4, 6, or 8 % w/v silicon dioxide) phantoms, least-squares linear regression confirmed a proportional dependency of the phase shift with the temperature change induced resulting the varied ultrasonic protocols comparably executed on each of the phantoms. Upon validating a linear phase and temperature change dependency (R^2=0.8581-0.957) for each of the phantoms employed herein, being in agreement with similar trends reported in the literature [39]–[48], the PRF coefficient was individually calibrated for each phantom. Particularly, for the phantoms fabricated with varied agar concentrations (2, 4 or 6 % w/v) PRF coefficients in the range of -0.0184 to -0.0384 ppm/^{o}C were reported, decreasing with an increased concentration of agar. Accordingly, PRF coefficients between -0.0194 to -0.0352 ppm/^{o}C were calibrated for the agar-based phantoms (6 % w/v) developed with varied concentrations of silicon dioxide (2, 4, 6, or 8 % w/v), generally increasing with an increased silicon dioxide concentration. In this regard, by following linear regression analysis, an inverse

498 linear dependency of the PRF coefficient was observed with an increased concentration of agar,
499 decreasing by -0.005 ppm/ ^{o}C for a unit increase in the % w/v agar concentration. Nevertheless,
500 the effect on the PRF coefficient for agar concentrations above 6 % w/v was not investigated
501 since these would result in extremely stiff phantoms that would not mechanically resemble
502 human tissue [19]. In this regard, the 6 % w/v agar concentration was chosen for development
503 of phantoms doped with varied concentrations of silicon dioxide (2, 4, 6, or 8 % w/v) where
504 contrary, a proportional linear effect on the PRF coefficient was observed with an increased
505 concentration of silicon dioxide. Approximately a 5 % increase in the PRF coefficient was
506 observed for addition of 2 % w/v silicon dioxide in the phantom compared to the corresponding
507 value of the PRF coefficient of the purely agar-based phantom (6 % w/v agar), with further
508 increases observed for increased silicon dioxide concentrations thereafter. Specifically, it was
509 perceived that a unit increase in the % w/v concentration of silicon dioxide induced a -0.0019
510 ppm/ ^{o}C increase in the PRF coefficient.

511 Upon calibrating the PRF coefficient of each of the seven phantoms, the in-house
512 control software was employed for offline PRF-based MR thermometry [26]–[27] of the varied
513 ultrasonic exposures. Particularly, for each varied ultrasonic protocol executed on each
514 phantom, colour-coded thermal maps and timeseries temperature plots were successfully
515 generated showing the extent of thermal heating throughout the phantom (through overlay of
516 the thermal map on the corresponding magnitude scans) and the temperature increase at the
517 focal spot (specific ROI within the phantom), respectively. Notably, MR thermometry data for
518 the individual sonications executed on each phantom were effectively generated by employing
519 the corresponding calibrated PRF coefficient of the phantom as well as a default PRF
520 coefficient value (-0.0094 ppm/^{o}C) that is typically used by the in-house software for MR
521 thermometry calculations, to assess the effect of the PRF coefficient on the MR thermometry-
522 based temperature measurements. Inherently, for either phantoms developed with varied agar

(2, 4, or 6 % w/v) or silicon dioxide (2, 4, 6, or 8 % w/v) concentrations, lower temperature changes were produced by employing the corresponding calibrated PRF coefficients compared to data derived with the default PRF coefficient value. Specifically, for the three phantoms having varied agar concentrations (2, 4, or 6 % w/v), temperature changes in the range of 1.6-13.8 ºC were derived using the calibrated PRF coefficients, indicating a 1.6-fold to 4.1-fold decrease relative to temperature elevations (6.4-26.1 ºC) arising with the default PRF coefficient. Similarly, a 2-fold to 3.8-fold increase in the temperature changes (18.6-34.7 ºC) was observed in the four phantoms developed with varied concentrations of silicon dioxide (2, 4, 6, or 8 % w/v) using the default PRF coefficient, compared to corresponding MR thermometry-based temperature changes (5-14.8 ºC) derived utilising the calibrated PRF coefficients, thus indicating the effect of the PRF coefficient on the MR thermometry temperature calculations.

Generally, the PRF coefficients as calculated in the present study for the three agar-based phantoms developed with varied agar concentrations (-0.0184 to -0.0384 ppm/ºC) and the four agar-based (6 % w/v) phantoms doped with varied concentrations of silicon dioxide (-0.0194 to -0.0352 ppm/ºC) were slightly higher than calibrated PRF coefficients reported in the literature for other phantoms developed with an agar base [28]–[29], [39], [41]–[43] or using alternative gelling agents [45]–[48]. Nevertheless, PRF coefficient calibrations have shown to be dependent on the parameters of the employed MR pulse sequence [28], [42], thus potentially explaining any deviations observed in the calibrated coefficients of the present study from similar studies found in the literature [28]–[29], [39], [41]–[43], [45]–[48]. Given the increased employment of agar-based phantoms doped with silicon dioxide in HIFU validation studies [18]–[20], [22]–[23] and based on the present results, phantoms developed with a 4 % or 6 % w/v concentration of agar, or doped with a 2 % w/v concentration of silicon dioxide best approximate the PRF coefficient of pure water [58] and of several animal tissues

[28]–[30], [35]–[38] and should therefore be considered in future MRgFUS validation studies as tissue mimicking materials since other concentrations of gel inclusions than the abovementioned, result in phantoms with a PRF coefficient that extremely deviates from corresponding tissue coefficients [28]–[30], [35]–[38]. Furthermore, PRF coefficients as calibrated for each of the seven phantoms in the present study could be utilised in PRF-based MR thermometry calculations during evaluation studies of future MRgFUS systems, resulting in a more accurate MR thermometry monitoring of the temperature increase, therefore providing enhanced insights on the actual efficacy of the developed system.

LIST OF FIGURE AND TABLE CAPTIONS

Figure 1: Experimental set-up with the robotic system accommodated on the table of a clinical MRI scanner and an agar-based phantom positioned on the acoustic opening of the robotic system and an MR imaging coil employed for image acquisition.

Figure 2: Temperature change versus phase difference as calculated for sonications executed on agar-based phantoms with a 2.75 MHz transducer using varied acoustical power for a sonication time of 30 s at 25 mm focal depth. Graphical plots for sonications executed on A) a 6 % w/v agar-based phantom, and B) a 6 % w/v agar-based phantom doped with silicon dioxide (6 % w/v).

Figure 3: A) PRF temperature coefficients of three agar-based phantoms developed with varied agar concentrations (2, 4, and 6 % w/v), and B) PRF temperature coefficients of five agar-based phantoms (6 % w/v agar) doped with varied silicon dioxide concentrations (0, 2, 4, 6, and 8 % w/v).

Figure 4: A) Coronal thermal maps acquired at the end of sonications (acoustic power of 24 W for 30 s at 25 mm focal depth) on an agar-based phantom (4 % w/v) as calculated using the calibrated PRF coefficient of the phantom, and B) Timeseries temperature increase at the focal spot in the agar-based phantom (4 % w/v) during sonications (acoustic power of 24 W for 30 s at 25 mm focal depth) as calculated using the calibrated PRF coefficient of the phantom.

Figure 5: A) Coronal thermal maps acquired at the end of sonications (acoustic power of 24 W for 30 s at 25 mm focal depth) on an agar-based phantom (4 % w/v) as calculated using the default PRF coefficient, and B) Timeseries temperature increase at the focal spot in the agar-based phantom (4 % w/v) during sonications (acoustic power of 24 W for 30 s at 25 mm focal depth) as calculated using the default PRF coefficient.

Table 1: Phase measurements calculated from FLASH phase images of a 2 % w/v agar-based phantom acquired prior to and during sonications with a 2.75 MHz transducer using varied acoustical power for a sonication time of 30 s at 25 mm focal depth.

Table 2: PRF temperature coefficient of agar-based phantoms having varied concentrations of agar as calibrated from linear regression fits between temperature change and phase differences resulting sonications executed with a 2.75 MHz transducer at varied acoustical power for a sonication time of 30 s at 25 mm focal depth.

Table 3: PRF temperature coefficient of agar-based phantoms doped with varied concentrations of silicon dioxide as calibrated from linear regression fits between temperature change and phase differences resulting sonications executed with a 2.75 MHz transducer at varied acoustical power for a sonication time of 30 s at 25 mm focal depth.

Table 4: Temperature changes achieved resulting sonications executed with a 2.75 MHz transducer on agar-based phantoms having varied agar concentrations using varied acoustical power for a sonication time of 30 s at 25 mm focal depth as calculated with PRF MR thermometry by utilising calibrated or default PRF coefficients of each phantom.

Table 5: Temperature changes achieved resulting sonications executed with a 2.75 MHz transducer on agar-based phantoms doped with varied concentrations of silicon dioxide using varied acoustical power for a sonication time of 30 s at 25 mm focal depth as calculated with PRF MR thermometry by utilising calibrated or default PRF coefficients of each phantom.

ACKNOWLEDGMENTS

The study has been co-funded by the European Structural & Investment Funds (ESIF) and the Republic of Cyprus through the Research and Innovation Foundation (RIF) under the projects SOUNDPET (INTEGRATED/0918/0008), FUSROBOT (ENTERPRISES/0618/0016), and FUSVET (SEED/1221/0080).

REFERENCES

[1] A. T. Mobashsher and A. M. Abbosh, "Artificial human phantoms: Human proxy in testing microwave apparatuses that have electromagnetic interaction with the human body," *IEEE Microw Mag*, vol. 16, no. 6, 2015, doi: 10.1109/MMM.2015.2419772.

[2] C. K. McGarry *et al.*, "Tissue mimicking materials for imaging and therapy phantoms: A review," *Physics in Medicine and Biology*, vol. 65, no. 23. 2020. doi: 10.1088/1361-6560/abbd17.

[3] M. O. Culjat, D. Goldenberg, P. Tewari, and R. S. Singh, "A review of tissue substitutes for ultrasound imaging," *Ultrasound Med Biol*, vol. 36, no. 6, pp. 861–873, 2010, doi: 10.1016/j.ultrasmedbio.2010.02.012.

[4] A. Dabbagh, B. J. J. Abdullah, C. Ramasindarum, and N. H. Abu Kasim, "Tissue-mimicking gel phantoms for thermal therapy studies," *Ultrason Imaging*, vol. 36, no. 4, 2014, doi: 10.1177/0161734614526372.

[5] F. Siedek *et al.*, "Magnetic Resonance-Guided High-Intensity Focused Ultrasound (MR-HIFU): Technical Background and Overview of Current Clinical Applications (Part 1),"

RoFo Fortschritte auf dem Gebiet der Rontgenstrahlen und der Bildgebenden Verfahren, vol. 191, no. 6. 2019. doi: 10.1055/a-0817-5645.

[6] G. Menikou and C. Damianou, "Acoustic and thermal characterization of agar based phantoms used for evaluating focused ultrasound exposures," *J Ther Ultrasound*, vol. 5, no. 1, pp. 1–14, 2017, doi: 10.1186/s40349-017-0093-z.

[7] A. Antoniou and C. Damianou, "MR relaxation properties of tissue-mimicking phantoms," *Ultrasonics*, vol. 119, 2022, doi: 10.1016/j.ultras.2021.106600.

[8] C. Lafon *et al.*, "Gel phantom for use in high-intensity focused ultrasound dosimetry," *Ultrasound Med Biol*, vol. 31, no. 10, pp. 1383–1389, 2005, doi: 10.1016/j.ultrasmedbio.2005.06.004.

[9] A. Eranki, A. S. Mikhail, A. H. Negussie, P. S. Katti, B. J. Wood, and A. Partanen, "Tissue-mimicking thermochromic phantom for characterization of HIFU devices and applications," *International Journal of Hyperthermia*, vol. 36, no. 1, 2019, doi: 10.1080/02656736.2019.1605458.

[10] M. McDonald, S. Lochhead, R. Chopra, and M. J. Bronskill, "Multi-modality tissue-mimicking phantom for thermal therapy," *Phys Med Biol*, vol. 49, no. 13, 2004, doi: 10.1088/0031-9155/49/13/001.

[11] M. N. Iizuka, M. D. Sherar, and I. A. Vitkin, "Optical phantom materials for near infrared laser photocoagulation studies," *Lasers Surg Med*, vol. 25, no. 2, 1999, doi: 10.1002/(SICI)1096-9101(1999)25:2<159::AID-LSM10>3.0.CO;2-V.

[12] K. Takegami, Y. Kaneko, T. Watanabe, T. Maruyama, Y. Matsumoto, and H. Nagawa, "Polyacrylamide gel containing egg white as new model for irradiation experiments using focused ultrasound," *Ultrasound Med Biol*, vol. 30, no. 10, 2004, doi: 10.1016/j.ultrasmedbio.2004.07.016.

[13] M. J. Choi, S. R. Guntur, K. I. L. Lee, D. G. Paeng, and A. Coleman, "A Tissue Mimicking Polyacrylamide Hydrogel Phantom for Visualizing Thermal Lesions Generated by High Intensity Focused Ultrasound," *Ultrasound Med Biol*, vol. 39, no. 3, 2013, doi: 10.1016/j.ultrasmedbio.2012.10.002.

[14] M. G. Bini, A. Ignesti, L. Millanta, R. Olmi, N. Rubino, and R. Vanni, "The Polyacrylamide as a Phantom Material for Electromagnetic Hyperthermia Studies," *IEEE Trans Biomed Eng*, vol. BME-31, no. 3, 1984, doi: 10.1109/TBME.1984.325271.

[15] E. L. Madsen, G. R. Frank, T. A. Krouskop, T. Varghese, F. Kallel, and J. Ophir, "Tissue-mimicking oil-in-gelatin dispersions for use in heterogeneous elastography phantoms," *Ultrason Imaging*, vol. 25, no. 1, 2003, doi: 10.1177/016173460302500102.

[16] A. I. Farrer *et al.*, "Characterization and evaluation of tissue-mimicking gelatin phantoms for use with MRgFUS," *J Ther Ultrasound*, vol. 3, no. 1, 2015, doi: 10.1186/s40349-015-0030-y.

[17] L. W. Hofstetter *et al.*, "Development and characterization of a tissue mimicking psyllium husk gelatin phantom for ultrasound and magnetic resonance imaging," *International Journal of Hyperthermia*, vol. 37, no. 1, 2020, doi: 10.1080/02656736.2020.1739345.

[18] A. Partanen, C. Mougenot, and T. Vaara, "Feasibility of agar-silica phantoms in quality assurance of MRgHIFU," in *AIP Conference Proceedings*, 2009, vol. 1113. doi: 10.1063/1.3131434.

[19] T. Drakos *et al.*, "Ultrasonic attenuation of an agar, silicon dioxide, and evaporated milk gel phantom," *J Med Ultrasound*, vol. 29, no. 4, pp. 239–249, 2021.

[20] A. Antoniou *et al.*, "MR relaxation times of agar- based tissue- mimicking phantoms," *J Appl Clin Med Phys*, vol. 23, no. 5, May 2022, doi: 10.1002/acm2.13533.

[21] A. Filippou, I. Louca, and C. Damianou, “Characterization of a fat tissue mimicking material for high intensity focused ultrasound applications,” *J Ultrasound*, Nov. 2022, doi: 10.1007/s40477-022-00746-4.

[22] G. Menikou, T. Dadakova, M. Pavlina, M. Bock, and C. Damianou, “MRI compatible head phantom for ultrasound surgery,” *Ultrasonics*, vol. 57, no. C, pp. 144–152, 2015, doi: 10.1016/j.ultras.2014.11.004.

[23] G. Menikou, M. Yiannakou, C. Yiallouras, C. Ioannides, and C. Damianou, “MRI-compatible breast/rib phantom for evaluating ultrasonic thermal exposures,” *International Journal of Medical Robotics and Computer Assisted Surgery*, vol. 14, no. 1, pp. 1–12, 2018, doi: 10.1002/rcs.1849.

[24] T. Drakos, M. Giannakou, G. Menikou, G. Constantinides, and C. Damianou, “Characterization of a soft tissue-mimicking agar/wood powder material for MRgFUS applications,” *Ultrasonics*, vol. 113, 2021, doi: 10.1016/j.ultras.2021.106357.

[25] C. G. Hernando, L. Esteban, T. Cañas, E. van den Brule, and M. Pastrana, “The role of magnetic resonance imaging in oncology,” *Clinical and Translational Oncology*, vol. 12, no. 9. 2010. doi: 10.1007/s12094-010-0565-x.

[26] V. Rieke and K. B. Pauly, “MR Thermometry,” *Journal of Magnetic Resonance Imaging*, vol. 27, pp. 376–390, 2008.

[27] H. Odéen and D. L. Parker, “Magnetic resonance thermometry and its biological applications – Physical principles and practical considerations,” *Progress in Nuclear Magnetic Resonance Spectroscopy*, vol. 110. 2019. doi: 10.1016/j.pnmrs.2019.01.003.

[28] R. D. Peters, R. S. Hinks, and R. M. Henkelman, “Ex vivo tissue-type independence in proton-resonance frequency shift MR thermometry,” *Magn Reson Med*, vol. 40, no. 3, 1998, doi: 10.1002/mrm.1910400316.

[29] K. Demura *et al.*, "An Easy-to-Use Microwave Hyperthermia System Combined with Spatially Resolved MR Temperature Maps: Phantom and Animal Studies," *Journal of Surgical Research*, vol. 135, no. 1, 2006, doi: 10.1016/j.jss.2006.02.016.

[30] R. M. Botnar, P. Steiner, B. Dubno, P. Erhart, G. K. von Schulthess, and J. F. Debatin, "Temperature quantification using the proton frequency shift technique: In vitro and in vivo validation in an open 0.5 Tesla interventional MR scanner during RF ablation," *Journal of Magnetic Resonance Imaging*, vol. 13, no. 3, 2001, doi: 10.1002/jmri.1063.

[31] R. v. Mulkern, A. H. Chung, F. A. Jolesz, and K. Hynynen, "Temperature monitoring of ultrasonically heated muscle with RARE chemical shift imaging," *Med Phys*, vol. 24, no. 12, 1997, doi: 10.1118/1.598103.

[32] M. D. Sherar *et al.*, "Comparison of thermal damage calculated using magnetic resonance thermometry, with magnetic resonance imaging post-treatment and histology, after interstitial microwave thermal therapy of rabbit brain," *Phys Med Biol*, vol. 45, no. 12, 2000, doi: 10.1088/0031-9155/45/12/304.

[33] J. A. Moriarty *et al.*, "MRI monitoring of interstitial microwave-induced heating and thermal lesions in rabbit brain in vivo," *Journal of Magnetic Resonance Imaging*, vol. 8, no. 1, 1998, doi: 10.1002/jmri.1880080125.

[34] J. R. MacFall, D. M. Prescott, H. C. Charles, and T. v. Samulski, "1H MRI phase thermometry in vivo in canine brain, muscle, and tumor tissue," *Med Phys*, vol. 23, no. 10, 1996, doi: 10.1118/1.597760.

[35] A. Muacevic *et al.*, "Image guided interstitial laser thermotherapy: A canine model evaluated by magnetic resonance imaging and quantitative autoradiography," *Acta Neurochir (Wien)*, vol. 147, no. 2, 2005, doi: 10.1007/s00701-004-0409-y.

738 [36] A. H. Chung, F. A. Jolesz, and K. Hynynen, “Thermal dosimetry of a focused ultrasound
739 beam in vivo by magnetic resonance imaging,” *Med Phys*, vol. 26, no. 9, 1999, doi:
740 10.1118/1.598707.
741 [37] L. Chen, J. P. Wansapura, G. Heit, and K. Butts, “Study of laser ablation in the in vivo
742 rabbit brain with MR thermometry,” *Journal of Magnetic Resonance Imaging*, vol. 16,
743 no. 2, 2002, doi: 10.1002/jmri.10152.
744 [38] N. Vykhodtseva, V. Sorrentino, F. A. Jolesz, R. T. Bronson, and K. Hynynen, “MRI
745 detection of the thermal effects of focused ultrasound on the brain,” *Ultrasound Med*
746 *Biol*, vol. 26, no. 5, 2000, doi: 10.1016/S0301-5629(00)00216-7.
747 [39] J. Olsrud *et al.*, “MRI thermometry in phantoms by use of the proton resonance
748 frequency shift method: Application to interstitial laser thermotherapy,” *Phys Med Biol*,
749 vol. 43, no. 9, 1998, doi: 10.1088/0031-9155/43/9/012.
750 [40] J. de Poorter, C. de Wagter, Y. de Deene, C. Thomsen, F. Ståhlberg, and E. Achten,
751 “The Proton-Resonance-Frequency-Shift Method Compared with Molecular Diffusion
752 for Quantitative Measurement of Two-Dimensional Time-Dependent Temperature
753 Distribution in a Phantom,” *J Magn Reson B*, vol. 103, no. 3, 1994, doi:
754 10.1006/jmrb.1994.1035.
755 [41] R. D. Peters, R. S. Hinks, and R. M. Henkelman, “Heat-source orientation and geometry
756 dependence in proton-resonance frequency shift magnetic resonance thermometry,”
757 *Magn Reson Med*, vol. 41, no. 5, 1999, doi: 10.1002/(SICI)1522-
758 2594(199905)41:5<909::AID-MRM9>3.0.CO;2-N.
759 [42] R. D. Peters *et al.*, “Magnetic resonance thermometry for predicting thermal damage:
760 An application of interstitial laser coagulation in an in vivo canine prostate model,”
761 *Magn Reson Med*, vol. 44, no. 6, 2000, doi: 10.1002/1522-
762 2594(200012)44:6<873::AID-MRM8>3.0.CO;2-X.

763 [43] P. Wang, “Evaluation of MR thermometry with proton resonance frequency method at
764 7T,” *Quant Imaging Med Surg*, vol. 7, no. 2, 2017, doi: 10.21037/qims.2017.03.05.
765 [44] I. A. Vitkin *et al.*, “Magnetic resonance imaging of temperature changes during
766 interstitial microwave heating: A phantom study,” *Med Phys*, vol. 24, no. 2, 1997, doi:
767 10.1118/1.598096.
768 [45] B. Bazrafshan *et al.*, “Temperature imaging of laser-induced thermotherapy (LITT) by
769 MRI: Evaluation of different sequences in phantom,” *Lasers Med Sci*, vol. 29, no. 1,
770 2014, doi: 10.1007/s10103-013-1306-5.
771 [46] S. Lochhead, D. Bradwell, R. Chopra, and M. J. Bronskill, “A gel phantom for the
772 calibration of MR-guided ultrasound thermal therapy,” in *Proceedings - IEEE*
773 *Ultrasonics Symposium*, 2004, vol. 2. doi: 10.1109/ultsym.2004.1418082.
774 [47] Y. Yuan *et al.*, “A heterogeneous human tissue mimicking phantom for RF heating and
775 MRI thermal monitoring verification,” *Phys Med Biol*, vol. 57, no. 7, 2012, doi:
776 10.1088/0031-9155/57/7/2021.
777 [48] M. R. Tarasek *et al.*, “Validation of MR thermometry: Method for temperature probe
778 sensor registration accuracy in head and neck phantoms,” *International Journal of*
779 *Hyperthermia*, vol. 30, no. 2, 2014, doi: 10.3109/02656736.2014.887794.
780 [49] M. Giannakou, A. Antoniou, and C. Damianou, “Preclinical robotic device for magnetic
781 resonance imaging guided focussed ultrasound,” *The International Journal of Medical*
782 *Robotics and Computer Assisted Surgery*, Oct. 2022, doi: 10.1002/rcs.2466.
783 [50] T. Drakos *et al.*, “MRI-Guided Focused Ultrasound Robotic System for Preclinical use,”
784 *Journal of Veterinary Medicine and Animal Sciences*, vol. 4, no. 1, 2020.
785 [51] T. Drakos, M. Giannakou, G. Menikou, and C. Damianou, “Magnetic Resonance
786 Imaging–Guided Focused Ultrasound Positioning System for Preclinical Studies in

Small Animals," *Journal of Ultrasound in Medicine*, vol. 40, no. 7, 2021, doi: 10.1002/jum.15514.

[52] K. Spanoudes, N. Evripidou, M. Giannakou, T. Drakos, G. Menikou, and C. Damianou, "A high intensity focused ultrasound system for veterinary oncology applications," *J Med Ultrasound*, vol. 29, no. 3, 2021, doi: 10.4103/JMU.JMU_130_20.

[53] M. Giannakou *et al.*, "Magnetic resonance image–guided focused ultrasound robotic system for transrectal prostate cancer therapy," *International Journal of Medical Robotics and Computer Assisted Surgery*, vol. 17, no. 3, 2021, doi: 10.1002/rcs.2237.

[54] A. Antoniou, M. Giannakou, N. Evripidou, S. Stratis, S. Pichardo, and C. Damianou, "Robotic system for top to bottom MRgFUS therapy of multiple cancer types," *International Journal of Medical Robotics and Computer Assisted Surgery*, vol. 18, no. 2, 2022, doi: 10.1002/rcs.2364.

[55] M. Giannakou, G. Menikou, K. Ioannides, and C. Damianou, "Magnetic resonance-image-guided focused ultrasound robotic system with four computer-controlled axes with endorectal access designed for prostate cancer focal therapy," *Digit Med*, vol. 6, pp. 32–43, 2020, doi: 10.4103/digm.digm.

[56] J. A. de Zwart, F. C. Vimeux, C. Delalande, P. Canioni, and C. T. W. Moonen, "Fast lipid-suppressed MR temperature mapping with echo-shifted gradient- echo imaging and spectral-spatial excitation," *Magn Reson Med*, vol. 42, no. 1, 1999, doi: 10.1002/(SICI)1522-2594(199907)42:1<53::AID-MRM9>3.0.CO;2-S.

[57] C. Bing *et al.*, "Drift correction for accurate PRF-shift MR thermometry during mild hyperthermia treatments with MR-HIFU," *International Journal of Hyperthermia*, vol. 32, no. 6, 2016, doi: 10.1080/02656736.2016.1179799.

[58] J. C. Hlndman, "Proton resonance shift of water in the gas and liquid states," *J Chem Phys*, vol. 44, no. 12, 1966, doi: 10.1063/1.1726676.

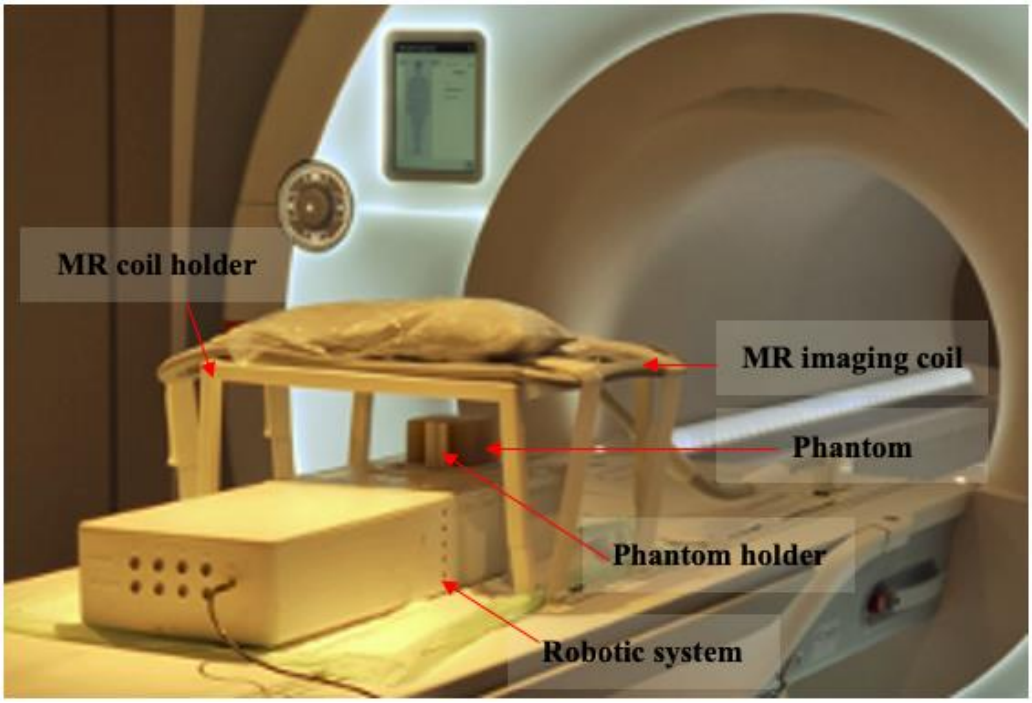

Figure 1

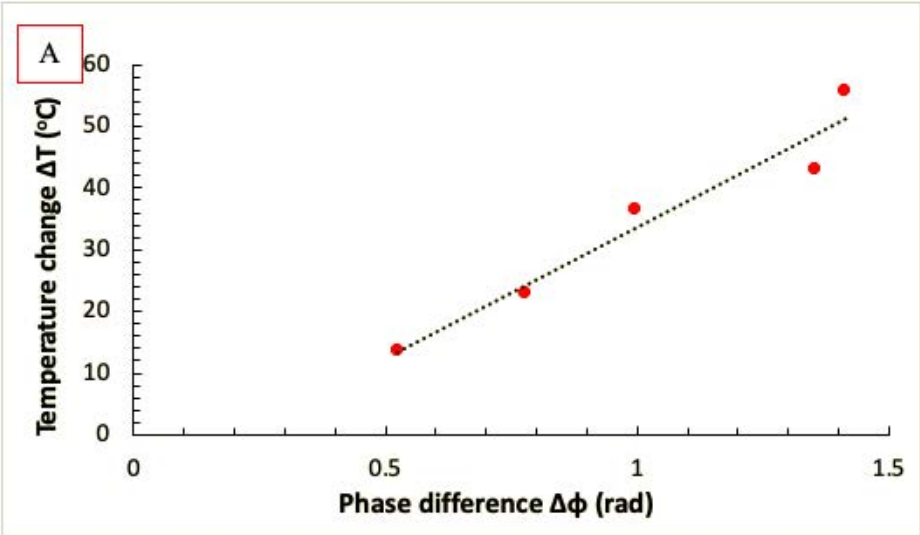
A
Temperature change ΔT (°C)
60
50
40
30
20
10
0
0
0.5
1
1.5
Phase difference Δϕ (rad)

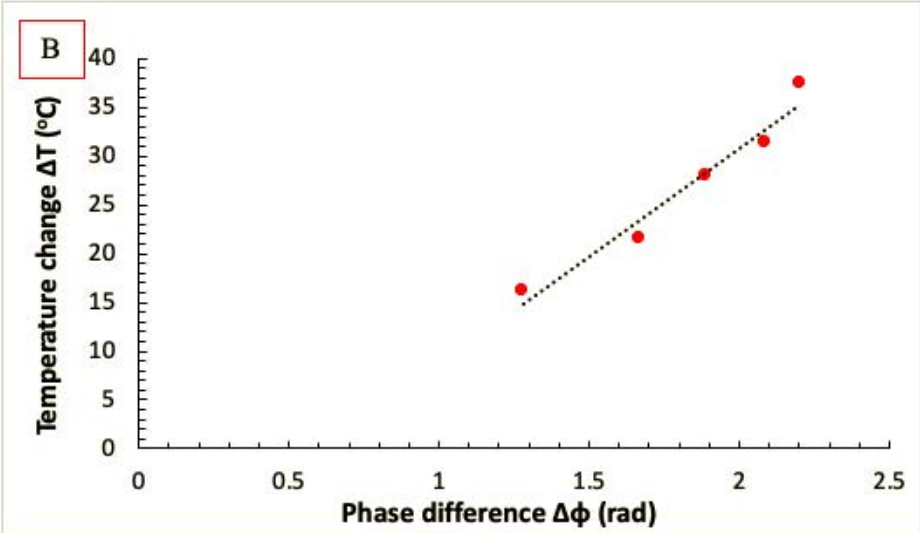
B
Temperature change ΔT (°C)
40
35
30
25
20
15
10
5
0
0
0.5
1
1.5
2
2.5
Phase difference Δϕ (rad)

Figure 2

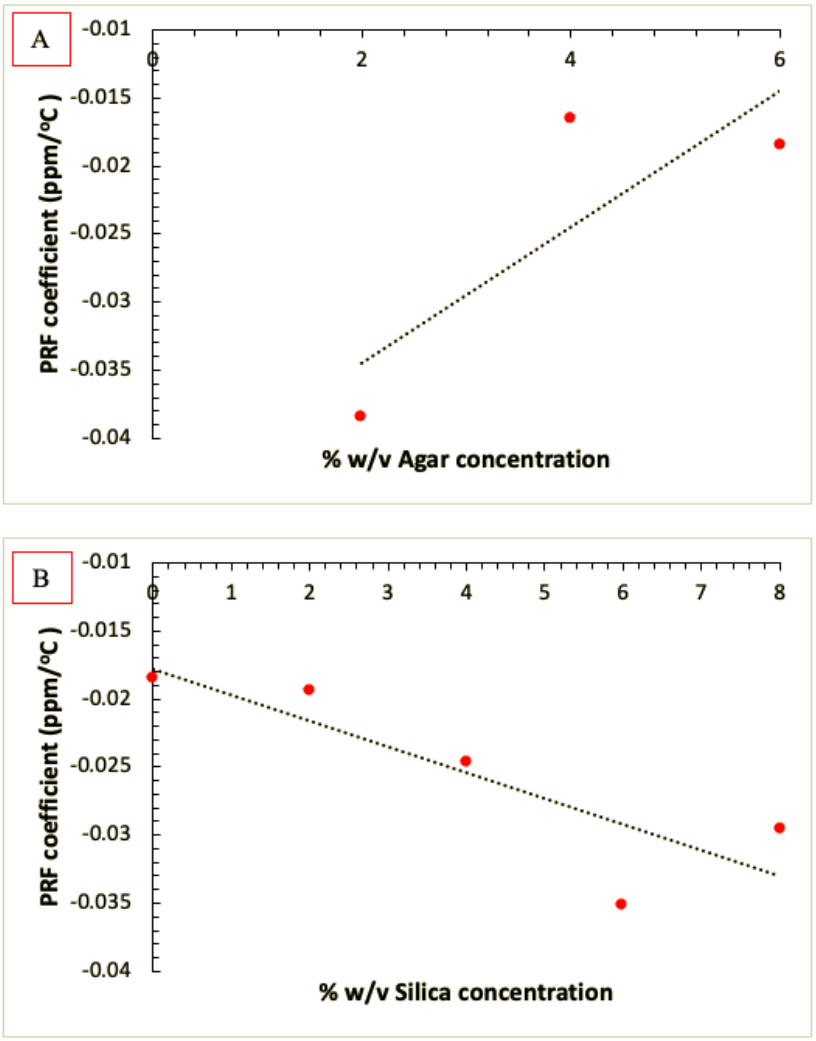

Figure 3

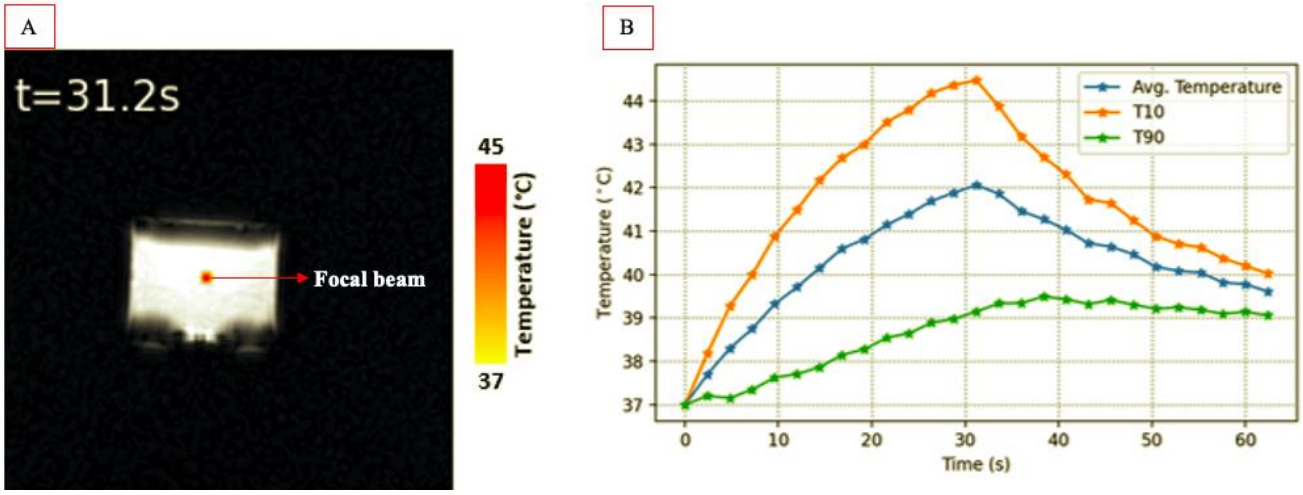

Figure 4

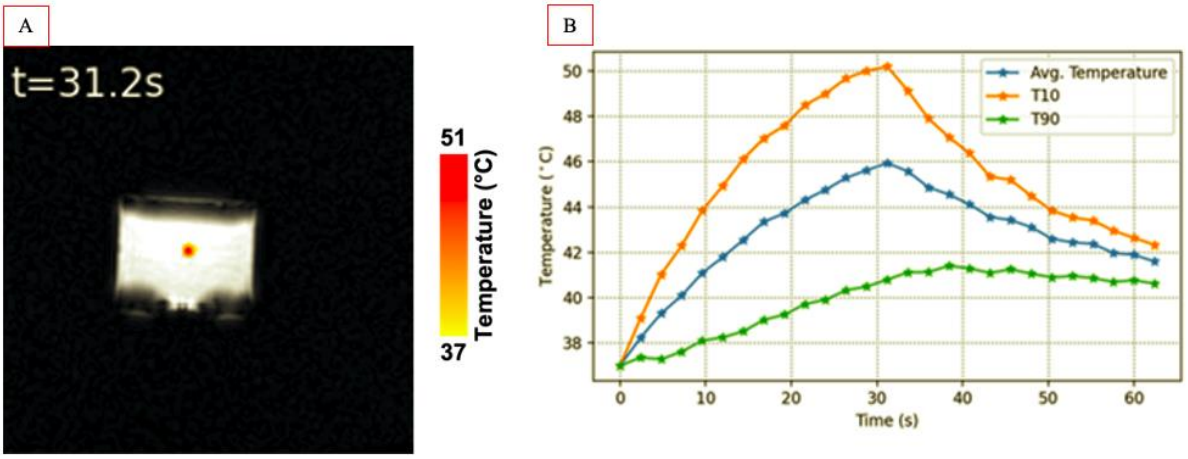

Figure 5

Table 1

Acoustic power (W)	Phase (radians)		
	Reference image (average of 3)	*Maximum temperature ablation image*	*Phase difference Δφ (radians)*
18	4.09621743	3.647162753	0.449
24	3.91772075	3.240558576	0.677
30	3.76326231	2.657503529	1.106
36	3.5883458	1.96550925	1.623
42	3.38683379	1.715409322	1.671

Table 2

Agar content (% w/v)	Linear regression	Pearson correlation coefficient (R^2)	PRF temperature coefficient (ppm/^oC)
2	y = 20.38x + 12.835	0.8622	-0.0384
4	y = 47.199x – 7.5436	0.8775	-0.0166
6	y = 42.533x – 8.8483	0.9445	-0.0184

Table 3

Agar = 6 % w/v, Silica content (% w/v)	Linear regression	Pearson correlation coefficient (R^2)	PRF temperature coefficient (ppm/^{o}C)
2	y = 40.342x – 40.105	0.8581	-0.0194
4	y = 31.705x – 23.783	0.945	-0.0247
6	y = 22.26x – 13.753	0.957	-0.0352
8	y = 26.543x – 22.164	0.9468	-0.0295

Table 4

Phantom (% w/v agar)	Acoustic power (W)	Maximum ΔT with estimated PRF coefficient (ºC)	Maximum ΔT with default PRF coefficient (ºC)	Difference (ΔT with default PRF/ΔT with estimated PRF)
2	18	1.6	6.4	4
	24	2.5	10.1	4
	30	4.1	16.7	4.1
	36	5.8	21.6	3.7
	42	6.4	26.1	4.1
4	18	5.4	9.5	1.76
	24	7.5	13.2	1.76
	30	9.7	17.1	1.76
	36	12.3	20.2	1.64
	42	13.8	24.4	1.77
6	18	4.3	8.5	1.98
	24	5.9	11.7	1.98
	30	8.2	15.9	1.94
	36	10.4	20.5	1.97
	42	11.4	22.3	1.96

Table 5

Agar = 6 % w/v, Silica content (% w/v)	Acoustic power (W)	Maximum ΔT with calibrated PRF coefficient (°C)	Maximum ΔT with default PRF coefficient (°C)	Difference (ΔT with default PRF/ΔT with estimated PRF)
2	18	10.2	21.1	2.07
	24	12	24.9	2.08
	30	13.7	28	2.04
	36	14.8	30.7	2.07
	42	14.2	29.3	2.06
4	18	7.9	20.7	2.62
	24	9.4	24.8	2.64
	30	10.7	28	2.62
	36	11.4	29.9	2.62
	42	12.3	32.4	2.63
6	18	5	18.6	3.72
	24	6.7	25	3.73
	30	7.7	28.6	3.71
	36	8.2	31	3.78
	42	8.5	32.3	3.8
8	18	6.6	20.6	3.12
	24	8.8	27.8	3.16
	30	10.1	31.6	3.13
	36	10.9	34.2	3.14
	42	11.1	34.7	3.13

MRI monitoring of thermal lesions produced by focused ultrasound

Anastasia Antoniou[a], Nikolas Evripidou[a], Anastasia Nikolaou[a], Andreas Georgiou[a], Marinos Giannakou[a], Antreas Chrysanthou[b], Leonidas Georgiou[b], Cleanthis Ioannides[b], Christakis Damianou[a]*

[a] Department of Electrical Engineering, Computer Engineering, and Informatics, Cyprus University of Technology, Limassol, Cyprus

[b] Department of Interventional Radiology, German Oncology Center, Limassol, Cyprus

Running title: MRI monitoring of thermal lesions

* For correspondence contact:
Prof. Christakis Damianou,
Department of Electrical Engineering, Computer Engineering, and Informatics,
Cyprus University of Technology, 30 Archbishop Kyprianou Street, 3036 Limassol, Cyprus,
E-mail: christakis.damianou@cut.ac.cy
Tel: 0035725002039
Fax: 0035725002849

ABSTRACT

Background: T1-Weighted (T1-W) and T2-Weighted (T2-W) Fast Spin Echo (FSE) sequences were widely employed for the post-sonication assessment of lesions produced by Focused Ultrasound (FUS).

Purpose: The main goal of the study was to find the Magnetic Resonance Imaging (MRI) parameters that optimize contrast between tissue and thermal lesions produced by FUS on T1-W and T2-W FSE images, so that intraprocedural monitoring of lesion progression is feasible.

Methods: FUS sonications were performed in ex-vivo porcine tissue using a single-element FUS transducer of 2.6 MHz in 1.5 and 3 T MRI scanners. The difference in the relaxation times, as well as the impact of critical MRI parameters on the resultant contrast to noise ratio (CNR), between coagulated and normal tissue was assessed. Discrete and overlapping lesions were inflicted in tissue with simultaneous acquisition of T2-W FSE images.

Results: FUS lesions are characterized by lower relaxation times than intact porcine tissue. CNR values above 80 were deemed sufficient for proper lesion visualization. For T1-W FSE imaging, Repetition time (TR) values close to 1500 ms were considered optimum for obtaining sufficiently high CNR (>80) at the minimum time cost. Echo time (TE) values close to 50 ms offered the maximum lesion contrast in T2-W FSE imaging. For both T1-W and T2-W imaging, an ETL value of 60 was considered ideal by balancing CNR and acquisition time. Monitoring of acute FUS lesions during grid sonications was performed successfully. Lesions appeared as hypointense spots with excellent contrast from the surrounding tissue.

Conclusions: Overall, MRI monitoring of SI changes during FUS sonication in grid patterns using optimized sequence parameters can provide useful information about lesion progression and the success of ablation.

KEYWORDS: lesion, Ultrasound, monitoring, MRI, porcine, contrast

1. INTRODUCTION

In the last decades, the adoption of thermal ablation modalities has been rapid, enabling safe and efficient delivery of thermal energy to deep-seated body targets.[1,2] This is achieved in a minimally invasive manner with the use of radiofrequency ablation (RFA), microwave ablation (MWA), and Laser interstitial thermal therapy (LITT), or in a non-invasive manner using thermal Focused Ultrasound (FUS).[1,2] While these modalities have been characterized by remarkable developments, such as the introduction of image guidance and robotics,[3,4] the establishment of methods for monitoring ablation lesions has fallen behind.

The superior performance of Magnetic Resonance Imaging (MRI) over other imaging modalities in the acquisition of high resolution anatomical images with excellent contrast among soft tissues and its ability to monitor tissue temperature non-invasively contributed to developing safe and efficient thermal ablation applications that were more easily adopted into clinical practice.[5,6] Nowadays, there exists a wide range of MRI contrast mechanisms for post-sonication lesion assessment and temperature estimation methods, among which MR thermometry based on the Proton Resonance Frequency Shift (PRFS) method is predominantly utilized for the intraprocedural monitoring of ablation therapy.[7,8]

In the case of thermal FUS, ultrasonic waves are strongly concentrated resulting in a focal point in the order of a few mm, thus rapidly raising the local tissue temperature to ablative levels without harming nearby tissues.[9] Since the ROI is typically in the order of centimeters, multiple adjacent lesions should be produced to ablate the full ROI volume. Accordingly, remote navigation of the FUS transducer is required for thermal applications in the MRI setting and is achieved with the use of MRI-compatible robotics.[4,10–17]

As early as the 1990s, T2-Weighted (T2-W) MR sequences were proven to provide excellent contrast between FUS lesions and the surrounding intact tissue in excised and *in-vivo* animal tissue,[18–20] and they are still considered among the standard methods for determining the extent of ablation lesions. In the same period, Hynynen et al.[21] reported that the size of lesions inflicted in rabbit thigh muscle as visualized on T2-W images matched well the size estimated after tissue excision by caliper measurements and Hematoxylin and Eosin examination. Another important observation made was that contrast-enhanced T2-W Fast spin echo (FSE) imaging showed signal enhancement only in normal tissue and not in lesions.[21] This phenomenon was also reported a few years later for rabbit skeletal muscle,[22] rabbit brain,[23] and synovial tissue[24] and is considered to be attributed to vascular disruption.

Contrast-enhanced T1-Weighted (T1-W) FSE imaging also allowed accurate lesion assessment following FUS ablation in rabbit skeletal muscle[22] and brain,[25] synovial tissue,[24] as well as in the clinical setting,[26] where the predicted size was well correlated with the histological lesion size. While both T2-W FSE and contrast-enhanced T1-W FSE sequences are currently considered as gold standard for assessing the extent of FUS damage, it seems that in early studies, T1-W FSE sequences were more frequently employed for MR thermometry rather than lesion assessment due to the superior T2-W FSE contrast between intact and damaged tissues reported in numerous studies at the time.[27] Later, it was clarified that the selection of proper sequence in terms of optimizing lesion contrast and delineation highly depends on the specific tissue characteristics. This has been demonstrated in a study by Damianou et al.,[28] who performed FUS ablations below and above the boiling level in freshly excised lamb and *in-vivo* rabbit tissue. Both T1-W and T2-W FSE imaging were suggested by authors for accurately visualizing ablation lesions in the kidney and liver, whereas for boiling lesions, the T2-W sequence was considered optimal. T1-W FSE imaging was proposed as the optimal sequence for detecting brain lesions of either kind. This was supported by another study where T2-W FSE images showed higher anatomical resolution in the brain compared to T1-W FSE images, but the latter ones offered better contrast between lesion and brain tissue.[29]

Lesion discrimination can be further optimized by selecting proper imaging parameters. For these two basic sequences; T1-W and T2-W FSE, the effect of the repetition time (TR) and echo time (TE) on the resultant contrast to noise ratio (CNR) was investigated in excised lamb brain, with authors suggesting the use of TR values above 500 ms and TE values in the range of 40 to 60 ms for optimized contrast.[29] Another example is a study concerning MR characterization of acute RFA lesions,[30] where TI relaxation times in the range of 500 to 600 ms were deemed to offer adequate visualization of RFA-induced lesions on Late gadolinium enhancement (LGE) images.

Intraoperative monitoring of thermal ablation procedures is critical in deciding whether heating should be continued or modified depending on the desired therapeutic outcome. Lesion monitoring is typically carried out utilizing thermosensitive sequences that allow precise monitoring of temperature evolution for controlled coagulative necrosis.[7, 31] There is though a limited literature on the intraprocedural monitoring of signal and contrast changes in the region of interest (ROI) and how these correlate with histological tissue damage and lesion formation.

Bremer et al.[32] investigated the efficacy of non-enhanced MRI to accurately monitor lesion size during LITT in pig liver compared to histological size assessment. For this purpose, T1-W turbo fast low-angle shot (FLASH) images were acquired at 1-minute interval, revealing a stable reduction in the standardized signal intensity (SI) in the center and periphery of the lesion during LITT, which was partially recovered throughout the cooling period. Furthermore, the SI in the lesion center was found to decrease with increasing deposited laser energy. The employed sequence highly overestimated the lesion size both during and immediately after ablation, whereas after tissue cooling, the visualized damaged area was more accurately associated with the real necrotic area, most probably owing to the absence of temperature-dependent SI fluctuations.[32]

Vergara et al.[33] developed a novel system for navigating electrophysiology catheters to ablate atrial tissue under real-time guidance in a 3T MR scanner with the assistance of dedicated MR sequences,[33] whose performance was tested in pigs. Multiple T2-W Half Fourier single-shot turbo spin-echo (HASTE) scans were taken during RFA in the myocardium allowing visualization of lesion progression over time. Tissue enhancement observed during and a few minutes after sonication was associated with heat-induced tissue edema and injury, simultaneously providing evidence of lesion creation, which was then confirmed by LGE imaging. As discussed by authors, the specific sequence tends to overstate the size of the lesion during tissue coagulation by displaying the surrounding edema.[33]

Another study in the content of electrophysiology aimed to establish MRI techniques for intraprocedural lesion visualization. In a study,[34] catheter RFA of myocardial tissues was performed in minipigs. The performance of several MR sequences, including nonenhanced T2-W and contrast-enhanced T1-W gradient echo, T2-W turbo spin echo (TSE), and FLASH sequences, was tested in terms of acute lesion assessment. The authors proposed non-enhanced T2-W imaging techniques as beneficial for intraprocedural lesion monitoring because they can be used repeatedly without delays related to the administration of contrast agents. Notably, T2-W images revealed a constant lesion size for the first few hours after RFA.[34]

Clinical results on intraprocedural lesion monitoring during MWA of liver malignancies under MRI guidance in a 1.5 T scanner were reported by Lin et al.[35] Specifically, a series of T2-W fat-suppressed fast-recovery FSE images were acquired every 35 s during ablation to monitor tissue effects, with the results showing a gradual SI decrease in the tumor.

In the context of FUS applications, T1-W and T2-W FSE imaging was mostly employed before ablation for ROI definition and treatment planning and post-ablation for assessing FUS-induced tissue damage.[8,28,29] Furthermore, they were employed in numerous studies involving the use of tissue mimicking phantoms and freshly excised animal tissue in the effort to investigate the effect of acoustic energy and grid parameters in the formation of discrete and overlapping lesions, as well as how the selected imaging parameters affect lesion visualization.[28,29] Despite the widespread use of these imaging sequences in MRI-guided FUS (MRgFUS) studies, their performance was not well investigated in the context of intraoperative lesion monitoring, which may refer to visualization and/or quantification of progressive changes in the SI of the exposed ROI over time and also to real-time monitoring of lesions' formation according to the desired pattern.

Although intraoperative T1-W and T2-W MRI were proven less effective in predicting the therapeutic outcome in terms of the final size of thermal lesions and the extent of tissue necrosis,[36] such monitoring could be beneficial in providing early indication of successful tissue ablation and whether the location of inflicted lesions coincides with the planned ablation patterns. It may also reveal other useful information, such as off-target heat accumulation or insufficient target heating, which are likely to contribute in optimizing the therapeutic outcome and preventing adverse events by enabling intraprocedural alteration of the treatment parameters.

The main goal of the current study was to provide insights on the topic of intraoperative lesion monitoring by presenting indicative results of a series of MRI-guided ablation experiments carried out in freshly excised pork tissue. Multiple sonications in sequential patterns were planned on a custom-made dedicated software and executed by an MRI-compatible robotic system featuring a single element spherically FUS transducer with a central frequency of 2.6 MHz.[37] The T1 and T2 relaxation times of the pork tissue and coagulation lesion were estimated in a 3 T MRI scanner. The impact of critical imaging parameters on the resultant CNR between coagulated and intact tissue was then investigated to optimize lesion discrimination on T1-W and T2-W FSE images. Both discrete and overlapping lesions were inflicted in pork tissue samples with simultaneous acquisition of T2-W images at a specific rate to enable visualization of the heated area and assessment of lesion progression with time. Following MRI assessment, the tissue was dissected to confirm successful lesion formation and assess how it is correlated with the CNR changes observed intraoperatively, as well as to obtain quantitative information of the real extent of tissue damage by caliper measurements.

2. MATERIALS AND METHODS

The present study was carried out in *ex-vivo* porcine tissue. No human or animal participants were involved. Therefore, no informed consents or ethical approval were necessary.

2.1 FUS ablation of *ex-vivo* porcine tissue

FUS was generated by a spherically focused ultrasonic transducer (Piezo Hannas Tech Co. Ltd, Wuhan, China) with a nominal frequency of 2.6 MHz, a diameter of 50 mm, a radius of curvature of 65 mm, and an acoustic efficiency of 30 %, which was utilized over the course of all experiments. The transducer was mounted on an MRI-compatible computer-controlled positioning system with 4 degrees of freedom (DOF) driven by piezoelectric motors, which was detailed described elsewhere,[37] and was supplied by an RF amplifier (AG1016, AG Series Amplifier, T & C Power Conversion, Inc., Rochester, US).

All the experiments were carried out in a General Electric (GE) 1.5 T MRI scanner (GE Signa HD16, GE Healthcare, Chicago, Illinois, United States), as well as in a Siemens 3 T scanner (Magnetom Vida, Siemens Healthineers, Erlangen, Germany). As shown in the photo of Figure 1a, the FUS positioning system was seated on the MRI table and connected to the electronic driving system placed outside of the room through shielded cables. The top cover of the device includes an acoustic opening above the working space of the FUS transducer, to which the porcine tissue sample was fixed. The distance between the bottom surface of the tissue sample and transducer was adjusted at 35 mm resulting in a focal depth of 30 mm. Degassed, deionized water was poured inside the container until it reached the bottom surface of the tissue sample to achieve efficient ultrasonic coupling. Multichannel body coils (12-channel body coil, Signa 1.5T, GE Healthcare Coils, Aurora, Ohio, USA and 18-channel body coil, Siemens Healthineers) were utilized for image acquisition. In each case, the coil was attached to a rigid plastic structure at some distance from the tissue surface to improve the signal by preventing tissue vibrations due to FUS from being transferred to the coil.[38] Figure 1b is an axial T2-W FSE image of the setup showing the concept of tissue sample placement above the FUS transducer and through-water ultrasonic coupling. The imaging parameters were as follows: Repetition time (TR) = 2500 ms, Echo time (TE) = 90 ms, Flip angle (FA) = 90º, Echo train length (ETL) = 60, Pixel Bandwidth (pBW) = 0.50 Hz/pixel, Number of averages (NEX) = 2, matrix size = 192×128, and Field of view (FOV) = 260×260×10 mm^3.

A treatment planning/monitoring software was interfaced with the amplifier and electronic driving system enabling remote control of the motion and ultrasonic parameters. The

transducer's location was registered relative to the target location based on images obtained at the level of the porcine tissue sample and transducer as illustrated in the graphic of Figure 1c. Specifically, the user segments the transducer (lower image) and the center of the transducer is fused in the tissue image (upper image). Then, the position of the transducer relative to the tissue is easily found

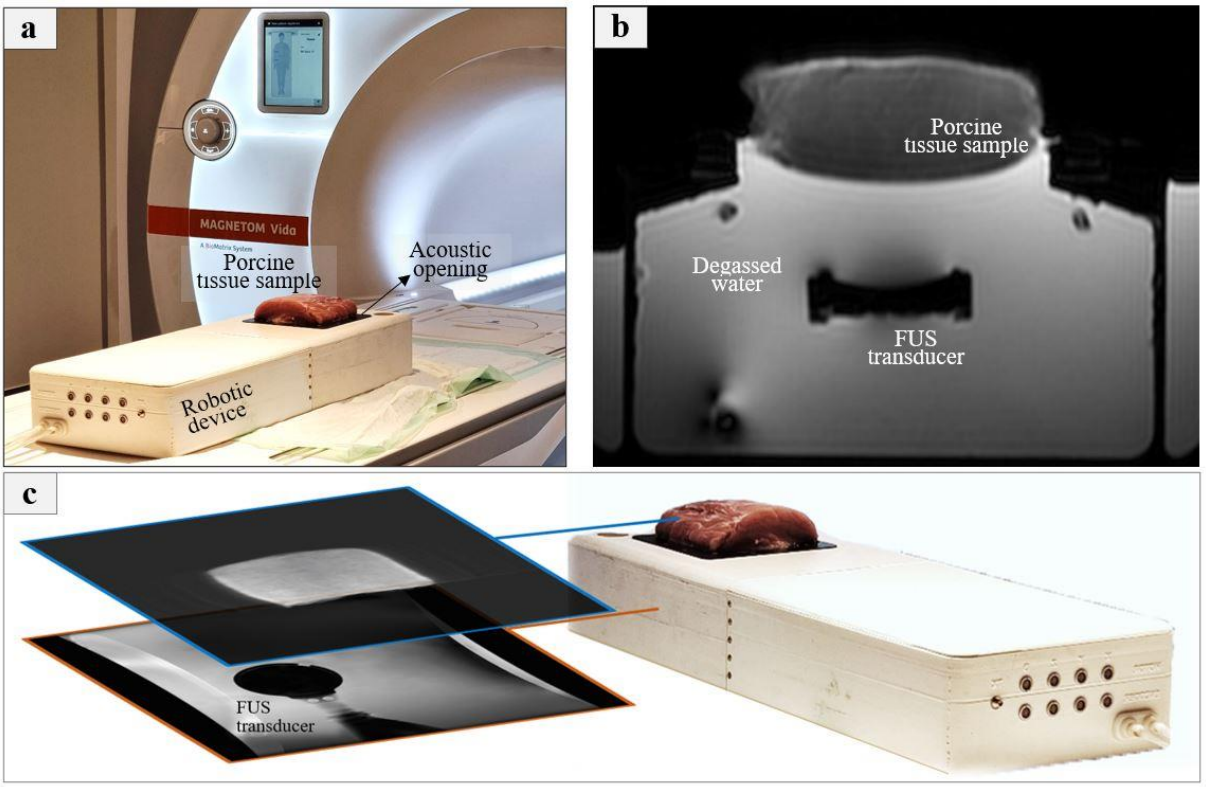

Figure 1: (a) The robotic device positioned on the MRI table with the piece of raw porcine meat mounted on the acoustic opening for ablation experiments in the MRI setting. (b) Axial T2-W FSE image (TR = 2500 ms, TE = 90 ms, FA = 90º, ETL = 60, pBW = 0.50 Hz/pixel, NEX = 2, matrix size = 192×128, and FOV = 260×260×10 mm^3) of the setup showing the concept of tissue sample placement above the FUS transducer. (c) The concept of registering the transducer location relative to the tissue sample by acquiring parallel coronal images at the level of the tissue and transducer.

2.2 Estimation of MR relaxation times of lesion and normal porcine tissue

The difference in relaxation times between coagulated and intact porcine tissue was investigated in the 3 T scanner. A piece of raw porcine meat received a single sonication at electrical power of 225 W (corresponding to an acoustic power of nearly 68 W) for 120 s at a focal depth of 30 mm, which resulted in a well-defined lesion. For T1 relaxation time measurements, images of the tissue sample with the inflicted lesion were acquired using a

Gradient Echo (GRE) sequence with variable FA. Circular ROIs were defined in the inflicted lesion and surrounding intact tissue. The mean SI measured in each ROI was plotted as a function of FA and the data were fitted to the following formula:[39]

$$\mathrm{M_z} = \mathrm{M_{0z}}\left(\frac{1-\mathrm{e}^{-\frac{\mathrm{TR}}{\mathrm{T1}}}}{1-\cos a\ \mathrm{e}^{-\frac{\mathrm{TR}}{\mathrm{T1}}}}\right)\sin a \quad (1)$$

where $\mathrm{M_z}$ is the longitudinal magnetization, $\mathrm{M_{0z}}$ is the magnetization at thermal equilibrium, a is the excitation flip angle (herein referred to as FA), TR is the repetition time, and T1 is the longitudinal relaxation time. The imaging parameters were as follows: TR = 15 ms, TE = 2.3 ms, pBW = 275 Hz/pixel, Matrix size = 256×256, FOV = 160×160×5 mm^3, NEX = 1, ETL = 1, and FA values ranging from 5º to 26 º (step of 3º).

Images were then acquired using a T2-W SE sequence at variable TE for T2 relaxation time mapping. For each ROI, the mean SI was plotted as a function of TE. Following regression analysis, an exponential trendline was fitted to the plotted data to calculate the T2 relaxation time based on the following exponential function:[40]

$$M_{xy} = M_o e^{-\frac{TE}{T_2}} \quad (2)$$

describing the recovery of the transverse magnetization M_{xy} following the RF pulse to its initial maximum value of M_o. For image acquisition, the following parameters were employed: TR = 2000 ms, FA = 180º, ETL = 10, pBW = 202 Hz/pixel, Matrix size = 192×192, FOV = 220×220×5 mm^3, NEX = 1, and TE values ranging from 10 to 110 ms (step of 10 ms).

2.3 Effect of MR parameters on CNR between lesion and normal porcine tissue

In this experimental part, the contrast between the lesion (68 W acoustic power for 120 s) and surrounding intact tissue was calculated as a function of critical MR parameters in the Siemens 3T MRI scanner for optimizing lesion contrast and detectability on FSE sequences; alternatively referred to as TSE by Siemens.

The effect of TE and ETL on the CNR was explored for the T2-W FSE sequence. Specifically, the ETL was varied from 6 to 129 with a TE equal to 51 ms and the TE was varied from 10 to 154 ms for a contrast ETL of 60 while in both cases the TR was set at 2000 ms. For the T1-W FSE sequence, variable ETL of 6 to 129 at a constant TR of 2000 ms and variable TR values of 700 to 2500 ms at a constant ETL of 60 were tested using a TE of 10 ms. In all cases, the rest imaging parameters were as follows: FA = 180º, and pBW = 150 Hz/pixel, matrix size =

256×256, and FOV = 280×280×5 mm^3. For comparison purposes measurements of the CNR between coagulated and intact porcine tissue as a function of TE were also conducted in the GE 1.5 T MRI scanner (TE = 10 – 150 ms, TR = 2000 ms, FA = 90º, ETL = 12, pBW = 81.4 Hz/pixel, matrix size = 224×192, and FOV = 260×260×4 mm^3).

For both sequences, the changes in CNR with varying matrix size and NEX were investigated. Different matrix sizes of 64×64, 96×96, 128×128, 256×256, and 512×512 were tested using a constant NEX of 1. The NEX was varied from 1 to 4 for a contrast matrix size of 256×256. The rest imaging parameters of the T1-W FSE sequence were as follows: TE = 10 ms, TR = 1500 ms, ETL = 60, FA = 180º, pBW = 150 Hz/pixel, and FOV = 280×280×5 mm^3. For T2-W FSE imaging, the TE value was changed to 51 ms and the TR value to 2000 ms.

Circular ROIs of 3 mm in diameter were initially defined for the lesion, normal tissue, and background noise. These ROIs were consistently placed at the same anterior-posterior location to eliminate signal difference due to the drop of signal as one moves further away from the coil. For the CNR estimation, the following formula was used:[41]

$$CNR = \frac{SI_{intact\ tissue} - SI_{lesion}}{\sigma_{noise}} \quad (3)$$

The SI was measured as the mean value in the corresponding ROI and the σ_{noise} as the standard deviation from a ROI placed in air/background noise, where the noise was assumed to follow a gaussian distribution.

2.4 Lesion monitoring during grid ablation in *ex-vivo* porcine tissue

The transducer's location relative to the target was registered in the MRI coordinates and different sonication patterns were planned on the relevant software as described previously. The sonication patterns were executed by the FUS robotic system under MRI monitoring of lesion formation. Specifically, an image was acquired immediately after each individual sonication to visualize lesion progression in discrete and overlapping patterns.

Regarding experiments in the 1.5 T MRI scanner, grid sonications with different spatial step were performed, where an electrical power of 180 W (acoustical power of 54 W) was applied to each individual grid spot for a total duration of 120 s. T2-W FSE images were acquired using TR = 2000 ms, TE = 59 ms, FA = 90º, ETL =60, pBW = 27.1 Hertz/pixel, matrix size = 224×192, and FOV = 260×260×6 mm^3. The time delay between successive sonications was set at 60 s to minimize pre-focal heating.[42]

Accordingly, in the 3 T scanner, T2-W FSE images were obtained with TR = 2500 ms, TE = 48 ms, ETL = 60, FA = 180º, pBW = 50 Hz/pixel, matrix size = 256×256, and FOV = 200×200×10 mm^3. Various sonications patterns were tested using a specific electric power of 150 W (acoustic power of 60 W) while the sonication time and spatial step were varied. Again a 60-s cooling time was left between sonications. Post-ablation, the tissue samples were dissected to visualize and quantify the extent of necrosis in planes parallel and perpendicular to the FUS beam direction.

3. RESULTS

3.1 Characterization of MR relaxation times of lesion and normal porcine tissue

The lesion was found to possess a mean longitudinal relaxation time T1 of 738 ± 46 ms, whereas a larger T1 value of 1158 ± 58 ms was estimated for the normal porcine tissue (3T). Regarding the transverse relaxation time T2, mean values of 43 ± 3 and 50 ± 2 ms were calculated for the lesion and normal tissue, respectively. As expected, the FUS lesion is characterized by lower relaxation times than the intact tissue, which is considered to be attributed to changes in the water content of coagulated tissue. The difference in these properties between coagulated and intact tissue allowed assessment of lesion formation by T1-W and T2-W FSE imaging.

3.2 Effect of MR parameters on CNR between lesion and normal porcine tissue

Figure 2 shows the T1-W FSE CNR between lesion (created using 68 W acoustic power and 120 s sonication time) and surrounding intact porcine tissue as well as the ratio of the CNR to the acquisition time plotted against the ETL and TR. ETL values up to 60 provided CNR higher than 80 allowing proper lesion discrimination (Figure 2a). ETL values in the range of 35 to 60 resulted in the highest CNR/acquisition time. Considering the importance of minimizing imaging time, an ETL value around 60 was considered optimum.

As seen in the graph of Figure 2b, the CNR/acquisition time reached its maximum value and remained almost constant for TR values in the range of 1500 to 2000 while the CNR was increased from 90 to 120. Although the TR of 2500 ms may be considered ideal in terms maximizing contrast, one should alternatively select a value close to 1500 that still provides good CNR (>80) at the minimum time cost possible.

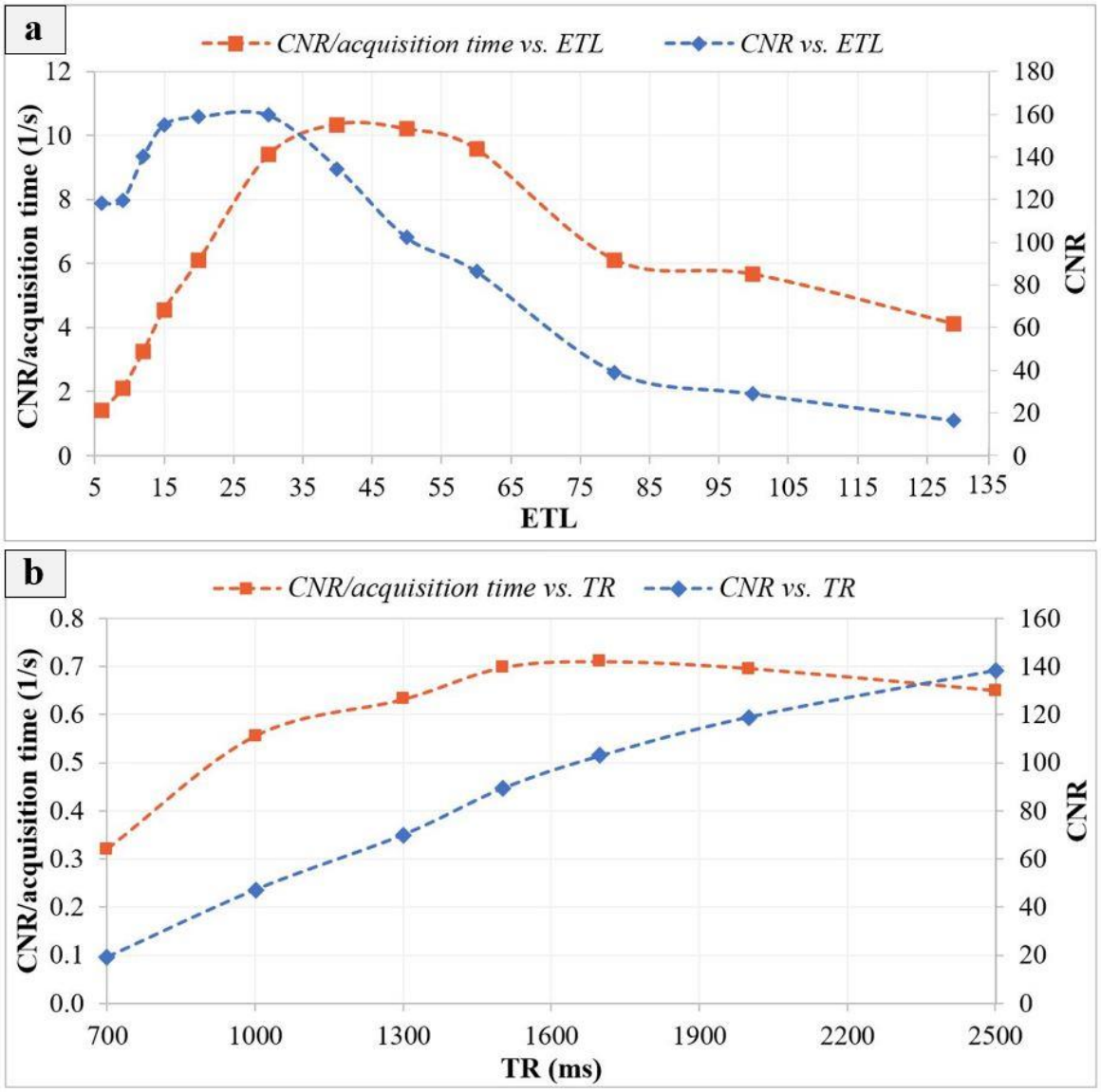

Figure 2: (a) Plots of the CNR between lesion and normal tissue and CNR/acquisition time of T1-W FSE images (TR = 2000 ms, TE = 10 ms, FA = 180º, pBW = 150 Hz/pixel, matrix size = 256×256, and FOV = 280×280×5 mm^3) versus ETL (6 – 129) at 3 T. (b) Plots of the CNR between lesion and normal tissue and CNR/acquisition time of T1-W FSE images (ETL = 60, TE = 10 ms, FA = 180º, pBW = 150 Hz/pixel, matrix size = 256×256, and FOV = 280×280×5 mm^3) versus TR (700 - 2500 ms) at 3 T.

The corresponding results of the ETL and TE effect on lesion contrast of T2-W FSE images are shown in Figure 3. From Figure 3a, it is observed that ETL values around 90 resulted in the highest values of CNR/acquisition time but in a very poor CNR (< 80), which made lesion detectability difficult. On the contrary, values in the range of 25 to 60 offered both sufficiently high CNR (>80) and CNR/acquisition time, with the ETL of 60 considered the ideal in terms of minimizing the acquisition time.

In Figure 3b, the trend of CNR vs. TE increases until the TE of 50 ms and then gradually decreases, clearly suggesting the TE value of 50 ms as optimum for maximizing CNR. Note that the acquisition time is not considered in that case since it is not affected by TE. The corresponding plot for evaluation at 1.5 T shows a quite similar trend but with a lower increase rate in the TE range of 20 to 90 ms and remarkably smaller CNR values.

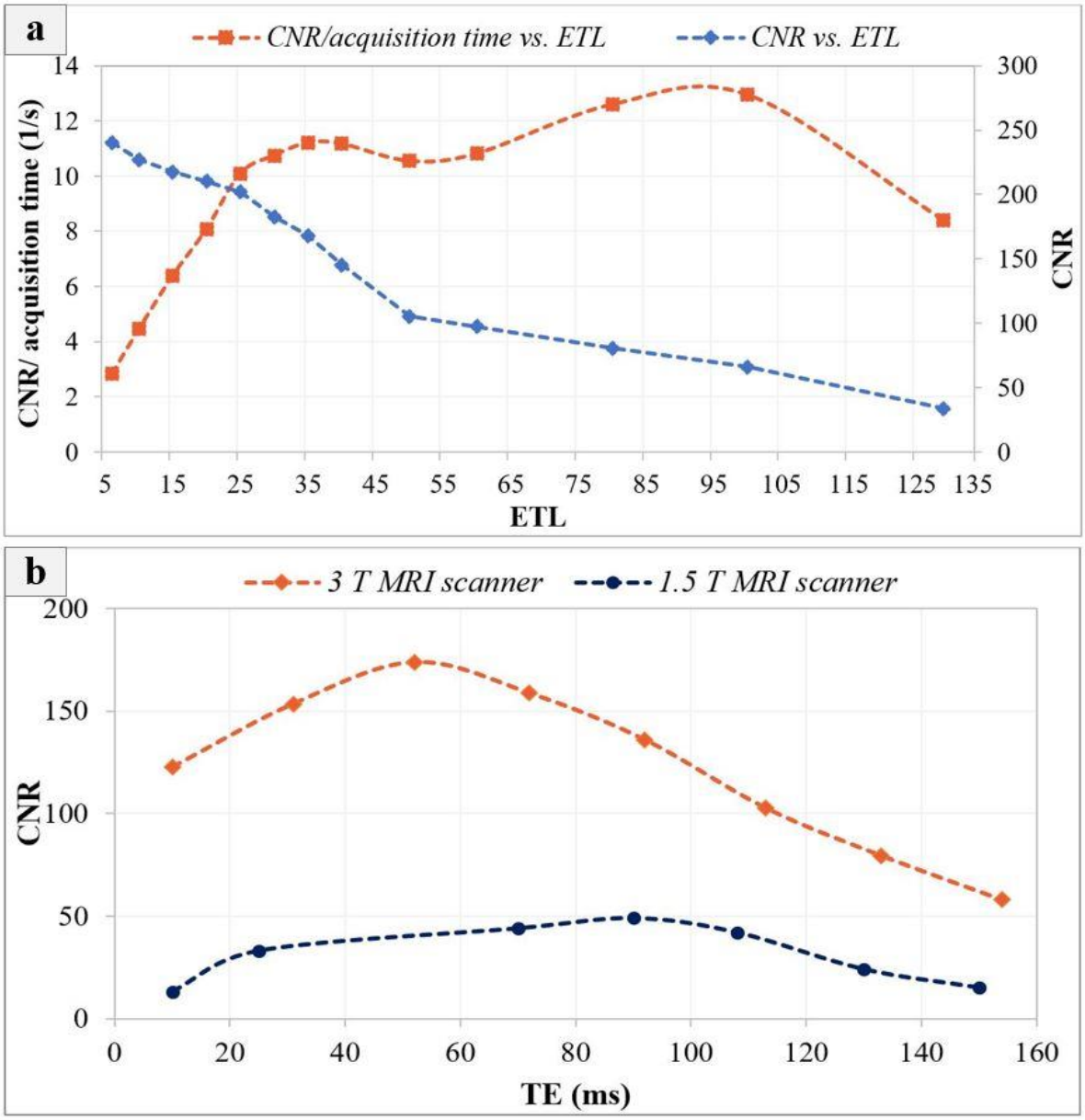

Figure 3: (a) Plots of the CNR between lesion and normal tissue and CNR/acquisition time of T2-W FSE images (TR = 2000 ms, TE = 51 ms, FA = 180º, pBW = 150 Hz/pixel, matrix size = 256×256, and FOV = 280×280×5 mm^3) versus ETL (6 – 129) at 3 T. (b) Plots of the CNR between lesion and normal tissue of T2-W FSE images (TR = 2000 ms, ETL = 60, FA = 180º, pBW = 150 Hz/pixel, matrix size = 256×256, and FOV = 280×280×5 mm^3) versus TE (10 - 154 ms) at 1.5 T and 3 T.

The graphs of Figure 4 show the changes in the CNR and CNR/acquisition time of T2-W FSE images as a function of NEX. The minimum NEX of 1 offered CNR much higher than the minimum suggested value of 80, and thus, the use of a larger NEX is unnecessary provided that it results in longer acquisition times. Similar results were obtained for the T1-W FSE imaging suggesting the NEX of 1 as the optimum.

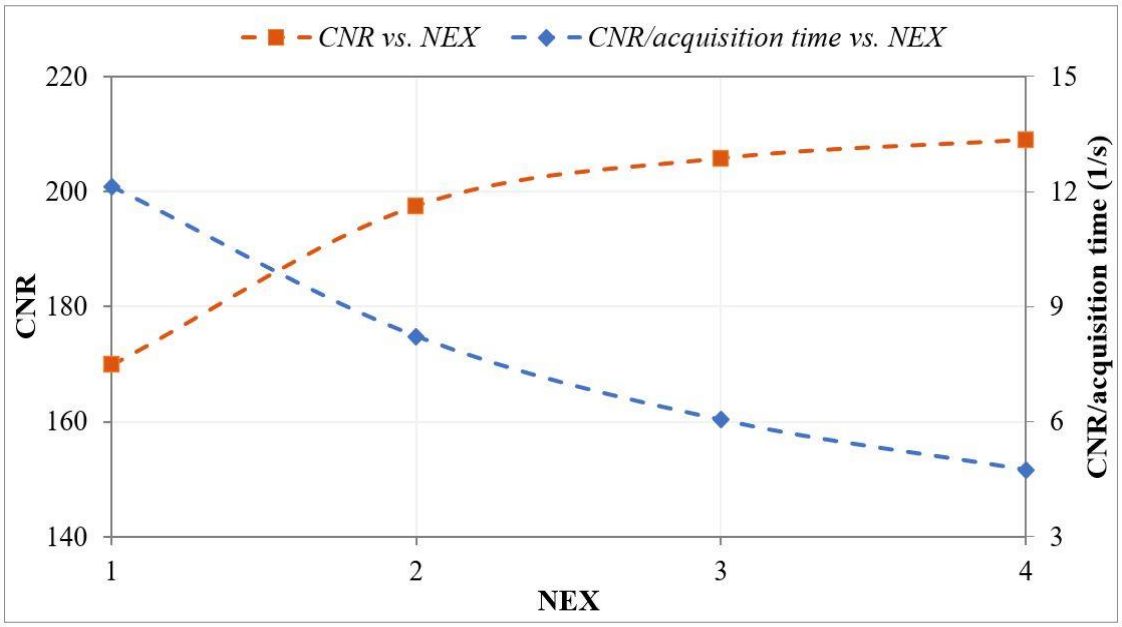

Figure 4: Plots of the CNR between lesion and normal tissue and CNR/acquisition time of T2-W FSE images (TR = 2000 ms, TE = 51 ms, FA = 180°, pBW = 150 Hz/pixel, matrix size = 256×256, and FOV = 280×280×5 mm^3) versus NEX (1 – 4) at 3 T.

Finally, concerning the effect of the matrix size, the CNR decreased from about 740 to 95 with increasing matrix size from 64×64 to 512×512 for the T1-W FSE imaging, whereas the CNR in T2-W images decreased from 880 to 140. The smallest matrix size is preferred in terms of minimizing the acquisition time, but it provided poor resolution. On the contrary, the biggest matrix size provided excellent resolution and sufficiently high CNR (>80), but at the cost of increased acquisition time. By balancing the parameters of CNR and imaging time, the use of a 256×256 matrix size is proposed.

The MR parameters suggested by the current study for optimizing the CNR between FUS lesions and surrounding tissue on T1-W and T2-W FSE images also considering the importance of minimizing the acquisition time are summarized in Table 1.

340 **Table 1**: Summary of the suggested MR parameters for optimizing CNR between lesion and
341 tissue at the minimum time cost for the specific parameters employed in the study (3 T).

MR parameter	T1-W FSE	T2-W FSE
TR (ms)	1500	2000
TE (ms)	10	50
ETL	60	60
NEX	1	1
pBW (Hz/pixel)	150	150
Matrix size	256×256	256×256
FOV (mm^2)	280×280	280×280
Slice thickness (mm)	5	5

342

343 **3.3 Lesion monitoring during grid ablation in *ex-vivo* porcine tissue**

344 An indicative example of lesion monitoring in the 1.5 T MRI scanner is shown in Figure 5.
345 Figure 5a shows a series of T2-W FSE images acquired during ablation in a 3x3 pattern with a
346 special step of 10 mm, where the coagulated regions appear as spots of reduced SI. The
347 acoustical power of 54 W applied for 120 s was sufficient to induce well-defined easily
348 detectable lesions. Note that the lesion created at the reference location of the transducer is
349 visible on the left side of all images. Note also that a circular area of reduced intensity appears
350 immediately after the first sonication (#1) but not in the next images, thus revealing heat
351 accumulation in the ROI but no evidence of lesion formation. Figure 5b is a cross section photo
352 of the meat at 10 mm from the sonicated surface. In contrast to the MRI images, all 9 lesions
353 were visible. Tissue was also dissected vertically to visualize the extent of necrosis in a plane
354 parallel to the beam direction. Again, all 9 lesions were visible extending 29 to 32 mm from
355 the tissue top surface as shown in Figures 5c to 5e.

356 Typical results obtained in the 3T MRI scanner are presented by Figures 6 to 8. All lesions
357 were formed using acoustic power of 60 W. Figure 6 shows T2-W FSE images of the porcine
358 tissue sample sonicated in a 2×3 grid with varying step of 10 or 15 mm and sonication duration
359 of 10 to 60 s, revealing the effect of sonication time on the resultant lesion size and distance
360 between adjacent lesions. The T2-W FSE images of Figure 7 show the lesion progression for
361 a 3x3 grid with a 10-mm step, where each spot was sonicated for 40 s. With the specific
362 parameters, discrete lesions were inflicted in tissue. The T2-W FSE image of Figure 8a shows
363 the overlapping lesion created by reducing the step to 5 mm while keeping the rest parameters

identical. Figure 8b is a photo of a (horizontal) cross-section of the tissue sample at 10 mm from the top surface, revealing a rectangular necrotic area of about 20×20 mm^2.

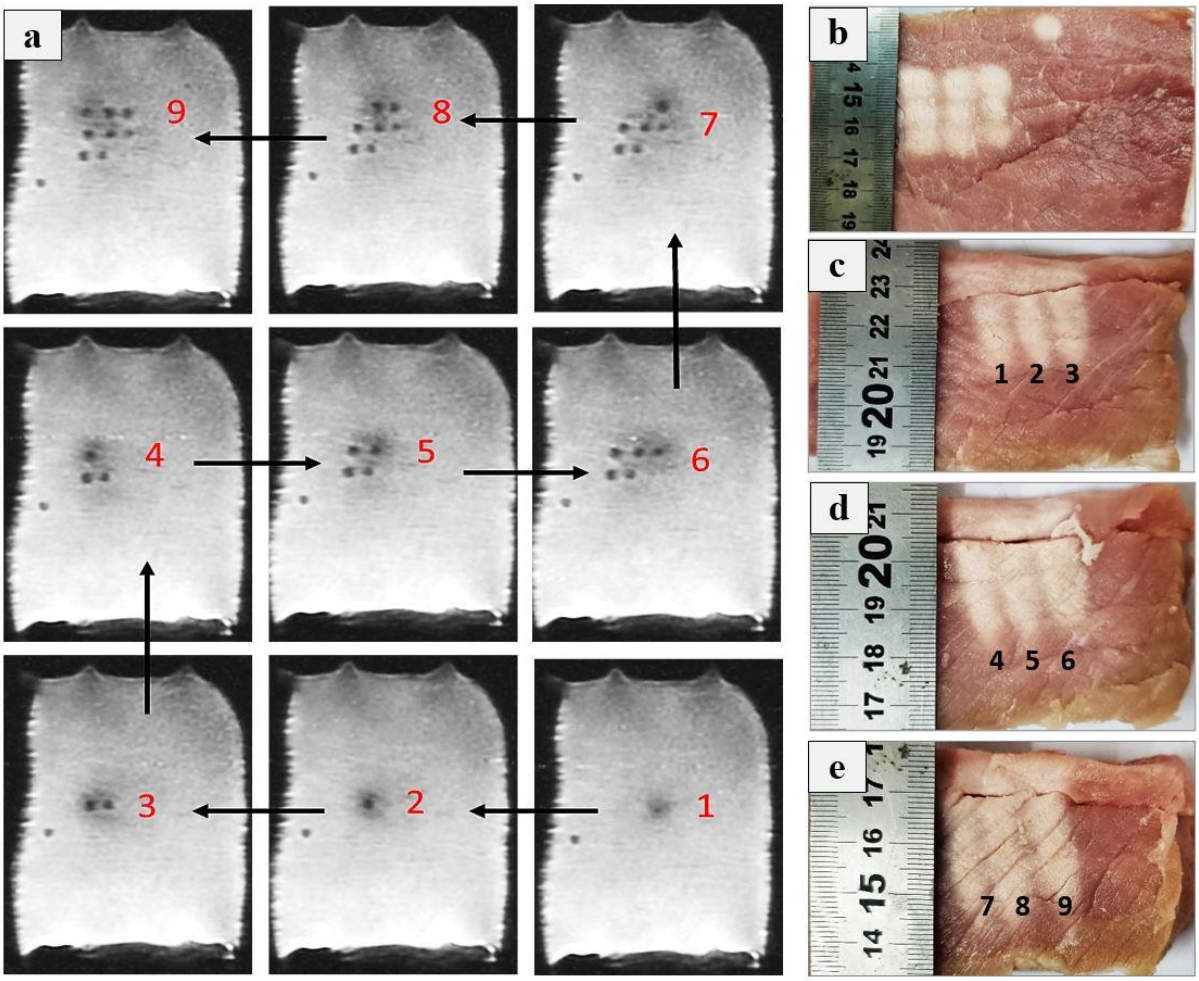

Figure 5: (a) 2D Coronal T2-W FSE images (TR = 2000 ms, TE = 59 ms, FA = 90º, ETL =60, pBW = 27.10 Hertz/pixel, matrix size = 224×192, FOV = 260×260×6 mm^3, and NEX =2) acquired during ablation in a 3×3 pattern (acoustical power of 54 W for 120, 10-mm step, 60-s delay) in the 1.5 T MRI scanner. (b) The meat sliced (horizontally) at 10 mm from the sonicated side showing the formed lesions and the reference point lesion. (c)-(e) Photos of the tissue sliced vertically to assess the extent of necrosis in a plane parallel to the ultrasonic beam propagation: Lesions 1 to 3 had a length of 29 mm, lesions 4 to 6 a length of 30 mm, and lesions 7 to 9 a length of 32 mm.

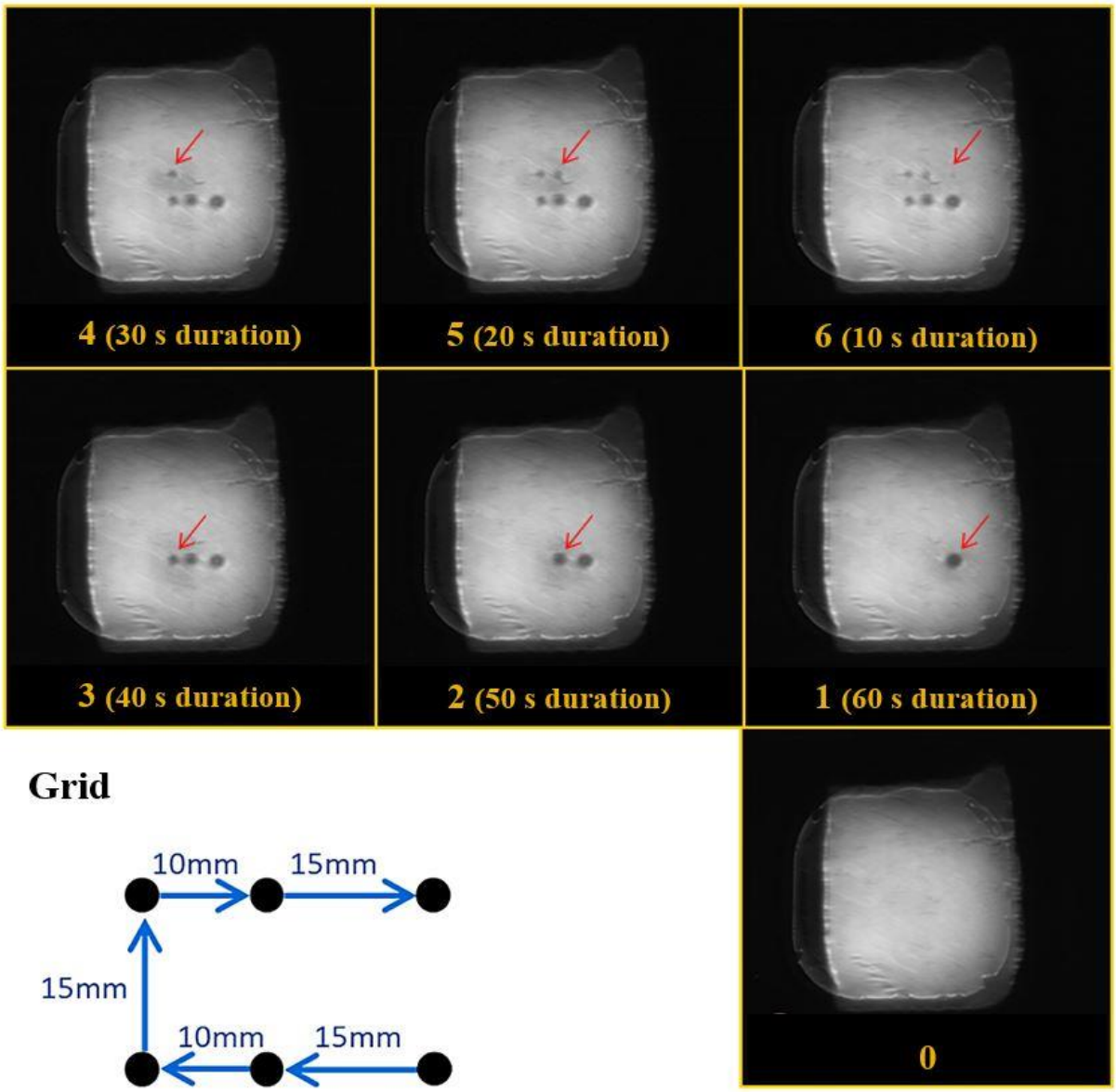

Figure 6: 2D Coronal T2-W FSE images (TR = 2500 ms, TE = 48 ms, FA = 180º, ETL = 60, PB = 50 Hz/pixel, matrix size = 256×256, and FOV = 200×200×10 mm^3) acquired during sonication in a 2×3 grid (acoustic power of 60 W) using varying sonication time and spatial step in the 3 T MRI scanner. The sonication pattern is presented on the left bottom corner.

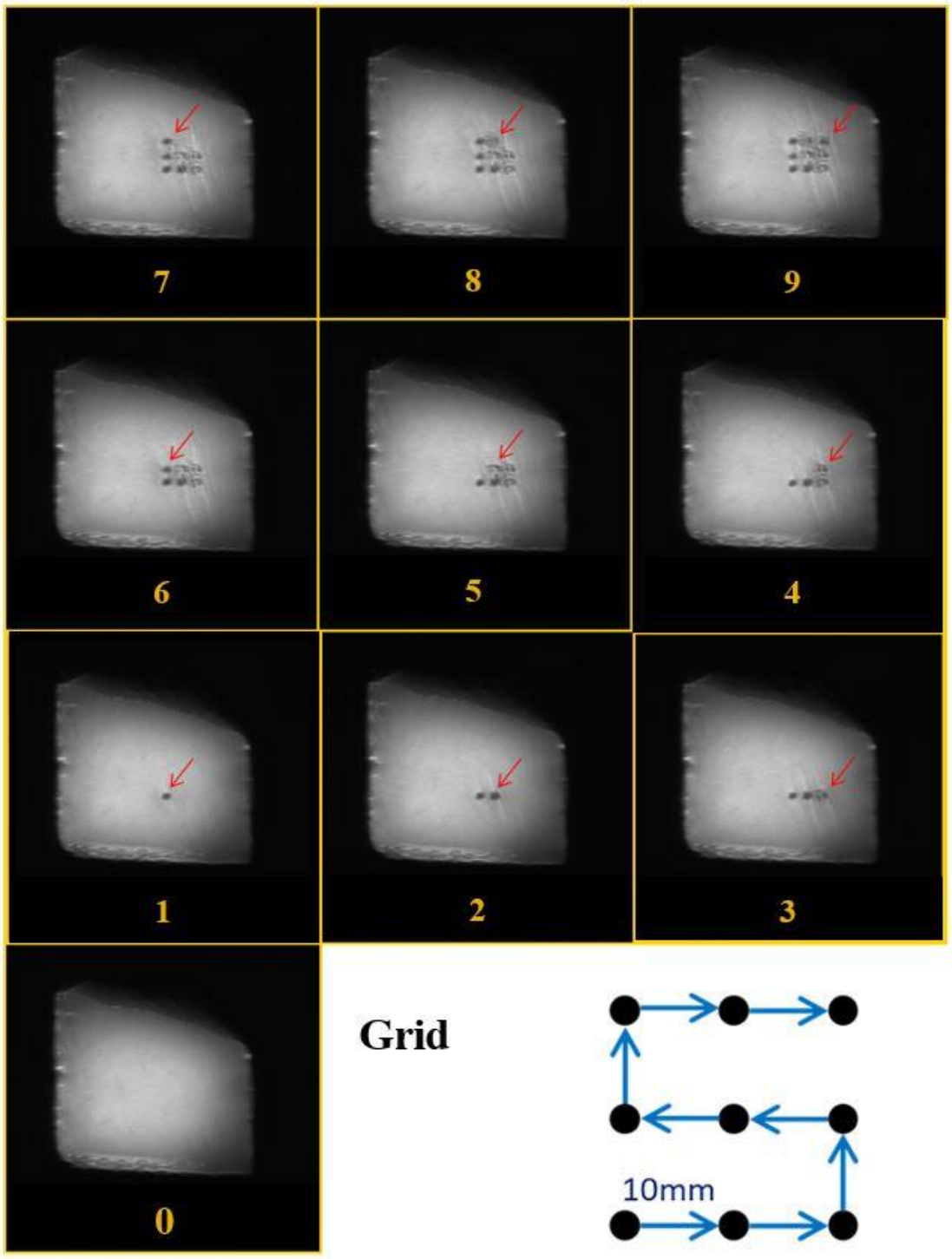

Figure 7: 2D Coronal T2-W FSE images (TR = 2500 ms, TE = 48 ms, FA = 180º, ETL = 60, PB = 50 Hz/pixel, matrix size = 256×256, and FOV = 200×200×10 mm^3) acquired during sonication in a 3×3 grid (acoustic power of 60 W for 40 s) with a spatial step of 10 mm (time delay of 60 s) in the 3 T MRI scanner. The sonication pattern is presented on the right bottom corner.

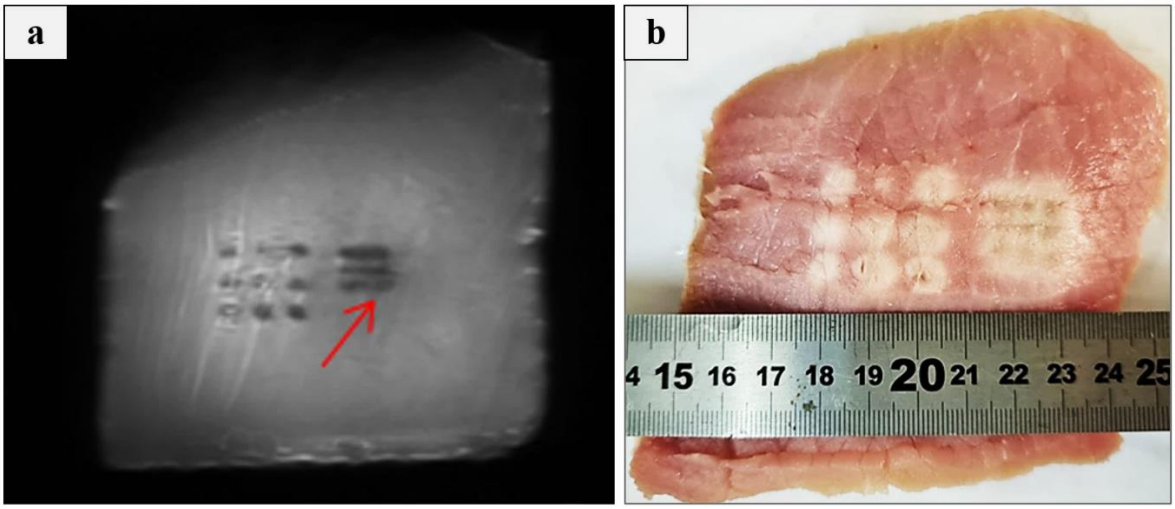

Figure 8: (a) 2D Coronal T2-W FSE image (TR = 2500 ms, TE = 48 ms, FA = 180º, ETL = 60, PB = 50 Hz/pixel, matrix size = 256×256, and FOV = 200×200×10 mm^3) acquired after sonication in a 3×3 grid (acoustic power of 60 W for 40 s) with a spatial step of 5 mm (time delay of 60 s) in the 3 T MRI scanner. The red arrow indicates the formed overlapping lesion. The discrete lesion created with the 10-mm step is also visible on the left side. (b) Photo of the tissue sample cut horizontally at 10 mm from the sonicated surface.

4. DISCUSSION

The present study provides parameter optimization on MRI monitoring of lesions produced by high intensity FUS using T1-W and T2-W FSE sequences. Such sequences were widely employed for post-sonication lesion assessment, but not for intraprocedural monitoring of lesion progression during multiple ablations in grid patterns. A series of experiments were carried out in freshly excised porcine tissue to provide insights on this topic.

The contrast in T1-W and T2-W FSE images arises from the variation in the longitudinal (T1) and transverse (T2) relaxation times among tissues.[31] It has been previously demonstrated that the relaxation times of FUS lesions and thus the contrast between healthy tissue and FUS lesions are strongly affected by the specific host tissue characteristic.[43–45] Herein, the FUS lesions were found as expected to possess lower T1 and T2 values than the surrounding non-sonicated porcine tissue at 3 T. This is consistent with what has been found in another study by Hadjisavvas et al.,[43] where lower T1 and T2 values were estimated for thermal lesions in *in-vivo* rabbit kidney, liver, heart, and brain compared to the corresponding host tissue. Contrary to these findings, Eranki et al.[44] report that FUS lesions inflicted in *ex-vivo* porcine liver, kidney, and cardiac muscle tissues appeared hyperintense in T2-W images with T2 values

noticeably greater than the adjacent, untreated tissue.[44] However, this appears to be a case of cavitation lesions as confirmed by previous research showing that thermal lesions produced by FUS appear hypointense in T2-W FSE images, whereas hyperintensity is associated with tissue boiling.[28] Opposite behavior is observed in the case of T1-W FSE imaging.[28] Therefore, the hypointense appearance of lesions on T2-W FSE images in the current study provides clear evidence of lesion creation by thermal mechanisms.

The study findings further suggest that the difference in MR relaxation properties between damaged and intact porcine tissue allows excellent lesion discrimination using T1-W and T2-W FSE sequences, provided that appropriate imaging parameters are employed. In this regard, a series of scans with varying parameters were performed to assess how the contrast between ablated and normal tissue is affected. For this purpose, a piece of porcine meat was sonicated using the 2.6 MHz FUS transducer using 68 W acoustic power for 120 s. The ETL, TE, and TR were the sequence parameters tested in terms of the CNR and acquisition time. Overall, higher CNR was achieved with the T2-W FSE sequence. It was thus concluded that T2-W FSE imaging is preferred for lesion monitoring in dead tissue, whereas in the case of live animals T1-W imaging may be preferred due to the use of contrast agents.

CNR values above 80 were deemed sufficient for ease detectability and proper visualization of FUS lesions. With the T1-W FSE sequence, CNR values above 80 were achieved for ETL values of up to 60 (Figure 2a), with the value of 60 offering sufficiently high CNR at the minimum time cost (9 s). Therefore, considering both parameters, an ETL of 60 is suggested as the optimum.

The corresponding results on the effect of TR (Figure 2b) reveal that the ratio of CNR to the acquisition time in T1-W FSE imaging begins to increase with increasing TR up to 1500 ms, and then becomes almost flat while at TR longer than 2000 ms it begins to decrease again. On the contrary, the CNR gradually increases from 20 to 140 as TR increases from 700 to 2500 ms, attributing to the increase in the SI difference between lesion and tissue. Notably, this trend is expected to be reversed as the TR is getting longer and the SI of lesion and tissue is reaching its maximum value. Generally, while TR values close to 2500 ms may be considered ideal in terms of maximizing contrast, a value close to 1500 ms constitutes a wiser option in the case of intraoperative monitoring of lesion progression since it still provides good CNR (>80) at smaller acquisition time.

Regarding T2-W FSE imaging, the results (Figure 3a) confirm that the use of longer ETL causes CNR decrease. Nevertheless, when the CNR is divided by the acquisition time an increasing trend is observed owing to that the acquisition time and ETL are inversely proportional. By choosing an ETL value in the range of 25 to 60 acceptable CNR (>80) is achieved at a reasonable acquisition time (< 20 s). Further increasing the ETL to reduce the time may result in poor contrast making lesion discrimination difficult or infeasible. Again, the ETL of 60 was deemed ideal for minimizing the acquisition time.

Concerning the effect of TE, the trend of CNR versus TE (Figure 3b) begins to increase until it reaches its maximum value of about 170 at TE close to 50 ms and then gradually decreases. Since the imaging time is not affected by the chosen TE, it was concluded that the TE of 50 ms is ideal for lesion monitoring by T2-W FSE imaging and was adopted in follow up experiments. Interestingly, TE values around 50 ms can be considered appropriate for imaging at 1.5 T as well. However, as expected, superior contrast was observed in the 3 T scanner, with almost 4-fold increase in the CNR at the TE of 50 ms. This result ties well with previous studies wherein authors have suggested the use of TE values between 40 and 50 ms to maximize the contrast of thermal lesions on T2-W FSE images following *in-vivo* rabbit experiments.[43]

Finally, the effect of the matrix size and NEX on the CNR was investigated using the optimized TR, TE, and ETL values. For both sequences, the minimum NEX of 1 provided excellent CNR and was considered optimum in terms of minimizing the acquisition time. As expected, increasing matrix size resulted in a better resolution and CNR drop simultaneously increasing the imaging time. The matrix size of 256×256 was deemed optimum providing both good CNR (>80) and CNR/acquisition time.

The feasibility of monitoring lesion progression during grid sonications was assessed at both 1.5 T and 3 T using T2-W FSE sequences. The FUS transducer was navigated by a positioning system in the horizontal plane to sonicate porcine tissue samples in grid patterns with varying ultrasonic and grid parameters. Navigation was initiated by registering the transducer's location relative to the target in the MRI coordinates and sonicating the meat at the reference location of the transducer. Lesion formation at the reference point was confirmed by T2-W FSE imaging providing evidence of efficient ultrasonic coupling. The sonication pattern was then executed with intraprocedural acquisition of T2-W FSE images that enabled assessment of lesions progression over time. The lesions appeared as circular black spots with excellent contrast from the surrounding tissue. Notably, immediately after sonication, the tissue surrounding these

black spots appeared as a less hypointense area indicating heat accumulation around the coagulated tissue, which returned to its normal intensity during tissue cooling through heat dissipation mechanisms (Figures 5 and 6). Note also that circular focal beams constitute evidence of lesion formation by thermal mechanisms while in the case of boiling lesions the beam was shown to be distorted.[28]

An interesting observation made during lesion monitoring in the 1.5 T MRI scanner (Figure 5) is that while only 8 out of the 9 sonicated spots showed clear evidence of lesion formation on the series of T2-W FSE images, 9 well-defined lesions were visualized following tissue dissection. In fact, a circular hypo-enhanced area was observed immediately after the first sonication revealing heat accumulation in the relevant ROI, but it was not present in the next acquisitions (Figure 5a). Tissue dissection revealed that the lesion had been shifted from the tissue surface and could only be detected if a deeper slice had been selected. It was also observed that the length of the formed lesions varied from 29 to 32 mm, most probably attributed to heat dissipation from previously sonicated spots (Figures 5c-5e).

The excellent lesion contrast from the surrounding hyperintense background also allowed assessment of the lesion size depending on the applied acoustic energy. In Figure 6, the spots of a 2x3 grid were sequentially exposed at similar acoustic power while the sonication time was decreased from 60 to 10 s resulting in lesions of decreasing diameter, with the last one receiving the lowest energy being barely visible. Furthermore, by varying the spatial step between sequential sonications the distance between adjacent lesions on the T2-W FSE images was varied accordingly.

Lesion progression in both discrete and overlapping patterns was successfully monitored in the 3 T MRI scanner. When the grid spacing was reduced from 10 to 5 mm, while keeping the sonication parameters (acoustic power of 60 W, sonication time of 40 s) and time delay (60 s) constant, overlapping lesions were created (Figure 8). In that case, the acquired images revealed a well-defined square area of reduced intensity (Figure 8a) that coincided well with the planned sonication pattern and actual overlapping lesion observed on tissue (Figure 8b).

5. CONCLUSIONS

Overall, the current study provides insights on the topic of FUS lesion progression monitoring by T1-W and T2-W FSE imaging through a series of ablation experiments in *ex-vivo* porcine tissue. The study findings confirmed that lesion discrimination on T1-W and T2-W FSE images highly depends on the selected MRI parameters while the imaging time should also be

507 considered in the context of intraprocedural lesion monitoring. Thereby, critical MR
508 parameters, i.e., TE, TR, and ETL, should be optimized by balancing between the CNR and
509 acquisition time. In this regard, the use of CNR values above 80 was set as the criterion for
510 proper lesion visualization. Also considering the need to minimize the acquisition time, a TR
511 close to 1500 ms is suggested for T1-W FSE imaging. A TE close to 50 ms was considered
512 optimum for T2-W FSE imaging. For both sequences, an ETL of 60 was proven ideal. During
513 sonications in discrete and overlapping patterns, acute FUS lesions were visualized as spots of
514 reduced intensity on T2-W FSE images with excellent contrast from the surrounding intact
515 tissue. It was demonstrated that multiple images should be acquired at varying depth in tissue
516 to avoid non-detectability of shifted lesions, which constitutes a common phenomenon
517 attributing to tissue inhomogeneities and/or the presence of bubbles that disturb the propagation
518 of ultrasonic waves.

519

520 **REFERENCES**

521 1. Knavel EM, Brace CL. Tumor ablation: Common modalities and general practices. *Tech*
522 *Vasc Interv Radiol*. 2013;16(4):192-200. doi:10.1053/j.tvir.2013.08.002
523 2. Mellal I, Oukaira A, Kengene E, Lakhssassi A. Thermal Therapy Modalities for Cancer
524 Treatment: A Review and Future Perspectives. *Int J Appl Sci - Res Rev*. 2017;04(02):1-
525 11. doi:10.21767/2394-9988.100064
526 3. Tinguely P, Paolucci I, Ruiter SJS, et al. Stereotactic and Robotic Minimally Invasive
527 Thermal Ablation of Malignant Liver Tumors: A Systematic Review and Meta-
528 Analysis. *Front Oncol*. 2021;11. doi:10.3389/fonc.2021.713685
529 4. Yiallouras C, Damianou C. Review of MRI positioning devices for guiding focused
530 ultrasound systems. *Int J Med Robot Comput Assist Surg*. 2015;11:247-255.
531 doi:10.1002/rcs.1601.
532 5. Mortele KJ, Silverman SG, Cantisani V, Tuncali K, Shankar S, VanSonnenberg E.
533 Magnetic Resonance Imaging Guidance for Tumor Ablation. In: VanSonnenberg E,
534 McMullen WN, Solbiati L, Livraghi T, MÃ¼eller PR, Silverman SG, eds. *Tumor*
535 *Ablation: Principles and Practise*. New York, NY: Springer; 2005:148-166.
536 doi:https://doi.org/10.1007/0-387-28674-8_12
537 6. Lee EJ, Fomenko A, Lozano AM. Magnetic resonance-guided focused ultrasound:
538 Current status and future perspectives in thermal ablation and blood-brain barrier
539 opening. *J Korean Neurosurg Soc*. 2019;62(1):10-26. doi:10.3340/jkns.2018.0180
540 7. Zhu M, Sun Z, Ng CK. Image-guided thermal ablation with MR-based thermometry.
541 *Quant Imaging Med Surg*. 2017;7(3):356–368. doi:10.21037/qims.2017.06.06
542 8. Fite BZ, Wang J, Ghanouni P, Ferrara KW. A Review of Imaging Methods to Assess
543 Ultrasound-Mediated Ablation. *BME Front*. 2022;2022:1-17.
544 doi:10.34133/2022/9758652
545 9. Izadifar Z, Izadifar Z, Chapman D, Babyn P. An Introduction to High Intensity Focused
546 Ultrasound: Systematic Review on Principles, Devices, and Clinical Applications. *J Clin*
547 *Med*. 2020;9(2):460. doi:10.3390/jcm9020460
548 10. Antoniou A, Giannakou M, Evripidou N, et al. Robotic system for magnetic resonance
549 guided focused ultrasound ablation of abdominal cancer. *Int J Med Robot Comput Assist*
550 *Surg*. 2021;17(5). doi:10.1002/rcs.2299
551 11. Antoniou A, Giannakou M, Evripidou N, Stratis S, Pichardo S, Damianou C. Robotic
552 system for top to bottom MRgFUS therapy of multiple cancer types. *Int J Med Robot*

Comput Assist Surg. 2022. doi:10.1002/rcs.2364

12. Epaminonda E, Drakos T, Kalogirou C, Theodoulou M, Yiallouras C, Damianou C. MRI guided focused ultrasound robotic system for the treatment of gynaecological tumors. *Int J Med Robot Comput Assist Surg*. 2016;12:46-52. doi:10.1002/rcs.1653
13. Giannakou M, Yiallouras C, Menikou G, Ioannides C, Damianou C. MRI-guided frameless biopsy robotic system with the inclusion of unfocused ultrasound transducer for brain cancer ablation. *Int J Med Robot Comput Assist Surg*. 2019;15(1):1-9. doi:10.1002/rcs.1951
14. Menikou G, Yiallouras C, Yiannakou M, Damianou C. MRI-guided focused ultrasound robotic system for the treatment of bone cancer. *Int J Med Robot Comput Assist Surg*. 2017;13(1):1-11. doi:10.1002/rcs.1753
15. Yiannakou M, Menikou G, Yiallouras C, Ioannides C, Damianou C. MRI guided focused ultrasound robotic system for animal experiments. *Int J Med Robot Comput Assist Surg*. 2017;13(4):e1804. doi:10.1002/rcs.1804
16. Antoniou A, Giannakou M, Georgiou E, Kleopa KA, Damianou C. Robotic device for transcranial focussed ultrasound applications in small animal models. *Int J Med Robot Comput Assist Surg*. 2022:1-11. doi:10.1002/rcs.2447
17. Giannakou M, Antoniou A, Damianou C. Preclinical robotic device for magnetic resonance imaging guided focussed ultrasound. *Int J Med Robot Comput Assist Surg*. 2022:1-10. doi:10.1002/rcs.2466
18. Cline HE, Schenck JF, Watkins RD, Hynynen K, Jolesz FA. Magnetic resonance-guided thermal surgery. *Magn Reson Med*. 1993;30(1):98-106. doi:10.1002/mrm.1910300115
19. Hynynen K, Freund W, Cline H, et al. A clinical, noninvasive, MR imaging-monitored ultrasound surgery method. *RadioGraphics*. 1996;16(1):185-195. doi:10.1148/radiographics.16.1.185
20. Hynynen K, Darkazanli A, Unger E, Schenck J. MRI-guided noninvasive ultrasound surgery. *Med Phys*. 1993;20(1):107-115. doi:10.1118/1.597093
21. Schenck JF, Hynynen K, Unger E, Darkazanli A, Damianou CA. The Usefulness of a Contrast Agent and Gradient–Recalled Acquisition in a Steady–State Imaging Sequence for Magnetic Resonance Imaging–Guided Noninvasive Ultrasound Surgery. *Investig Radiol*. 1994;29(10):897-903. doi:10.1097/00004424-199410000-00006
22. Chung AH, Jolesz FA, Hynynen K. Thermal dosimetry of a focused ultrasound beam in vivo by magnetic resonance imaging. *Med Phys*. 1999;26(9):2017-2026. doi:10.1118/1.598707

587 23. Chen L, Bouley D, Yuh E, D'Arceuil H, Butts K. Study of focused ultrasound tissue
588 damage using MRI and histology. *J Magn Reson Imaging*. 1999;10(2):146-153.
589 doi:10.1002/(sici)1522-2586(199908)10:2<146::aid-jmri6>3.0.co;2-c
590 24. Foldes K, Hynynen K, Shortkroff S, et al. Magnetic Resonance Imaging-guided Focused
591 Ultrasound Synovectomy. *Scand J Rheumatol*. 1999;28(4):233-237.
592 doi:10.1080/03009749950155607
593 25. Vykhodtseva N, Sorrentino V, Jolesz FA, Bronson RT, Hynynen K. MRI detection of
594 the thermal effects of focused ultrasound on the brain. *Ultrasound Med Biol*.
595 2000;26(5):871-880. doi:10.1016/S0301-5629(00)00216-7
596 26. Curiel L, Souchon R, Rouviere O, Gelet A, Chapelon J. Elastography for the follow-up
597 of high-intensity focused ultrasound prostate cancer treatment: Initial comparison with
598 MRI. *Ultrasound Med Biol*. 2005;31(11):1461–1468.
599 doi:10.1016/j.ultrasmedbio.2005.06.013
600 27. Rivens I, Shaw A, Civale J, Morris H. Treatment monitoring and thermometry for
601 therapeutic focused ultrasound. *Int J Hyperth*. 2007;23(2):121-139.
602 doi:10.1080/02656730701207842
603 28. Damianou C, Ioannides K, Hadjisavvas V, et al. MRI monitoring of lesions created at
604 temperature below the boiling point and of lesions created above the boiling point using
605 high intensity focused ultrasound. *J Biomed Sci Eng*. 2010;03(08):763-775.
606 doi:10.4236/jbise.2010.38102
607 29. Damianou C, Ioannides K, Hadjisavvas V, Mylonas N, Couppis A, Iosif D. In vitro and
608 in vivo brain ablation created by high-intensity focused ultrasound and monitored by
609 MRI. *IEEE Trans Ultrason Ferroelectr Freq Control*. 2009;56(6):1189-1198.
610 doi:10.1109/TUFFC.2009.1160
611 30. Celik H, Ramanan V, Barry J, et al. Intrinsic contrast for characterization of acute
612 radiofrequency ablation lesions. *Circ Arrhythmia Electrophysiol*. 2014;7(4):718-727.
613 doi:10.1161/CIRCEP.113.001163
614 31. Rieke V, Pauly KB. MR Thermometry. *J Magn Reson Imaging*. 2008;27(2):376-390.
615 doi:10.1002/jmri.21265.MR
616 32. Bremer C, Kreft G, Filler T, Reimer P. Accuracy of non-enhanced MRI to monitor
617 histological lesion size during laser-induced interstitial thermotherapy. *Eur Radiol*.
618 2002;12(1):237-244. doi:10.1007/s003300101118
619 33. Vergara GR, Vijayakumar S, Kholmovski EG, et al. Real-time magnetic resonance
620 imagingguided radiofrequency atrial ablation and visualization of lesion formation at 3

Tesla. *Hear Rhythm*. 2011;8(2):295-303. doi:10.1016/j.hrthm.2010.10.032

34. Nordbeck P, Hiller KH, Fidler F, et al. Feasibility of contrast-enhanced and nonenhanced MRI for intraprocedural and postprocedural lesion visualization in interventional electrophysiology : Animal studies and early delineation of isthmus ablation lesions in patients with typical atrial flutter. *Circ Cardiovasc Imaging*. 2011;4(3):282-294. doi:10.1161/CIRCIMAGING.110.957670
35. Lin Z, Chen J, Yan Y, Chen J, Li Y. Microwave ablation of hepatic malignant tumors using 1.5T MRI guidance and monitoring: feasibility and preliminary clinical experience. *Int J Hyperth*. 2019;36(1):1216-1222. doi:10.1080/02656736.2019.1690166
36. Allen SP, Prada F, Xu Z, et al. A preclinical study of diffusion-weighted MRI contrast as an early indicator of thermal ablation. *Magn Reson Med*. 2021;85(4):2145-2159. doi:10.1002/mrm.28537
37. Drakos T, Giannakou M, Menikou G, et al. MRI-Guided Focused Ultrasound Robotic System for Preclinical use. *J Vet Med Anim Sci*. 2021;4(1):1-11.
38. Antoniou A, Georgiou L, Evripidou N, Ioannides C, Damianou C. Challenges regarding MR compatibility of an MRgFUS robotic system. *J Magn Reson*. 2022;344:107317. doi:10.1016/j.jmr.2022.107317
39. Liberman G, Louzoun Y, Ben Bashat D. T1 Mapping using variable flip angle SPGR data with flip angle correction. *J Magn Reson Imaging*. 2014;40(1):171-180. doi:10.1002/jmri.24373
40. Bojorquez JZ, Bricq S, Acquitter C, Brunotte F, Walker PM, Lalande A. What are normal relaxation times of tissues at 3 T? *Magn Reson Imaging*. 2017;35(2017):69-80. doi:10.1016/j.mri.2016.08.021
41. Hendrick RE. Signal, Noise, Signal-to-Noise, and Contrast-to-Noise Ratios. In: *Breast MRI: Fundamentals and Technical Aspects*. New York, NY: Springer New York; 2008:107-110. doi:10.1007/978-0-387-73507-8_7
42. Filippou A, Drakos T, Giannakou M, Evripidou N, Damianou C. Experimental evaluation of the near-field and far-field heating of focused ultrasound using the thermal dose concept. *Ultrasonics*. 2021;116:106513. doi:10.1016/j.ultras.2021.106513
43. Hadjisavvas V, Ioannides K, Komodromos M, Mylonas N, Damianou C. Evaluation of the contrast between tissues and thermal lesions in rabbit in vivo produced by high intensity focused ultrasound using fast spin echo MRI sequences. *J Biomed Sci Eng*. 2010;4(1):51-61. doi:10.4236/jbise.2011.41007

44. Eranki A, Farr N, Partanen A, et al. Mechanical Fractionation of Tissues using Microsecond-Long HIFU Pulses on a Clinical MR-HIFU System. *Int J Hyperth*. 2019;34(8):1213-1224. doi:10.1080/02656736.2018.1438672

45. Kholmovski E, Ranjan R, Angel N, Marrouche NF. T2* -weighted MRI technique for visualization of RF ablation lesions. *J Cardiovasc Magn Reson*. 2016;18(Suppl 1):2-4. doi:10.1186/1532-429X-18-S1-O128

LIST OF FIGURE CAPTIONS

Figure 1: (a) The robotic device positioned on the MRI table with the piece of raw porcine meat mounted on the acoustic opening for ablation experiments in the MRI setting. (b) Axial T2-W FSE image (TR = 2500 ms, TE = 90 ms, FA = 90º, ETL = 60, pBW = 0.50 Hz/pixel, NEX = 2, matrix size = 192×128, and FOV = 260×260×10 mm^3) of the setup showing the concept of tissue sample placement above the FUS transducer. (c) The concept of registering the transducer location relative to the tissue sample by acquiring parallel coronal images at the level of the tissue and transducer.

Figure 2: (a) Plots of the CNR between lesion and normal tissue and CNR/acquisition time of T1-W FSE images (TR = 2000 ms, TE = 10 ms, FA = 180º, pBW = 150 Hz/pixel, matrix size = 256×256, and FOV = 280×280×5 mm^3) versus ETL (6 – 129) at 3 T. (b) Plots of the CNR between lesion and normal tissue and CNR/acquisition time of T1-W FSE images (ETL = 60, TE = 10 ms, FA = 180º, pBW = 150 Hz/pixel, matrix size = 256×256, and FOV = 280×280×5 mm^3) versus TR (700 - 2500 ms) at 3 T.

Figure 3: (a) Plots of the CNR between lesion and normal tissue and CNR/acquisition time of T2-W FSE images (TR = 2000 ms, TE = 51 ms, FA = 180º, pBW = 150 Hz/pixel, matrix size = 256×256, and FOV = 280×280×5 mm^3) versus ETL (6 – 129) at 3 T. (b) Plots of the CNR between lesion and normal tissue of T2-W FSE images (TR = 2000 ms, ETL = 60, FA = 180º, pBW = 150 Hz/pixel, matrix size = 256×256, and FOV = 280×280×5 mm^3) versus TE (10 - 154 ms) at 1.5 T and 3 T.

Figure 4: Plots of the CNR between lesion and normal tissue and CNR/acquisition time of T2-W FSE images (TR = 2000 ms, TE = 51 ms, FA = 180º, pBW = 150 Hz/pixel, matrix size = 256×256, and FOV = 280×280×5 mm^3) versus NEX (1 – 4) at 3 T.

Figure 5: (a) 2D Coronal T2-W FSE images (TR = 2000 ms, TE = 59 ms, FA = 90º, ETL =60, pBW = 27.10 Hertz/pixel, matrix size = 224×192, FOV = 260×260×6 mm^3, and NEX =2) acquired during ablation in a 3×3 pattern (acoustical power of 54 W for 120, 10-mm step, 60-s delay) in the 1.5 T MRI scanner. (b) The meat sliced (horizontally) at 10 mm from the sonicated side showing the formed lesions and the reference point lesion. (c)-(e) Photos of the tissue sliced vertically to assess the extent of necrosis in a plane parallel to the ultrasonic beam propagation: Lesions 1 to 3 had a length of 29 mm, lesions 4 to 6 a length of 30 mm, and lesions 7 to 9 a length of 32 mm.

694 **Figure 6**: 2D Coronal T2-W FSE images (TR = 2500 ms, TE = 48 ms, FA = 180º, ETL = 60,
695 PB = 50 Hz/pixel, matrix size = 256×256, and FOV = 200×200×10 mm^3) acquired during
696 sonication in a 2×3 grid (acoustic power of 60 W) using varying sonication time and spatial
697 step in the 3 T MRI scanner. The sonication pattern is presented on the left bottom corner.

698 **Figure 7**: 2D Coronal T2-W FSE images (TR = 2500 ms, TE = 48 ms, FA = 180º, ETL = 60,
699 PB = 50 Hz/pixel, matrix size = 256×256, and FOV = 200×200×10 mm^3) acquired during
700 sonication in a 3×3 grid (acoustic power of 60 W for 40 s) with a spatial step of 10 mm (time
701 delay of 60 s) in the 3 T MRI scanner. The sonication pattern is presented on the right bottom
702 corner.

703 **Figure 8**: (a) 2D Coronal T2-W FSE image (TR = 2500 ms, TE = 48 ms, FA = 180º, ETL =
704 60, PB = 50 Hz/pixel, matrix size = 256×256, and FOV = 200×200×10 mm^3) acquired after
705 sonication in a 3×3 grid (acoustic power of 60 W for 40 s) with a spatial step of 5 mm (time
706 delay of 60 s) in the 3 T MRI scanner. The red arrow indicates the formed overlapping lesion.
707 The discrete lesion created with the 10-mm step is also visible on the left side. (b) Photo of the
708 tissue sample cut horizontally at 10 mm from the sonicated surface.

709

ACKNOWLEDGMENTS

The project was funded by the Research and Innovation Foundation of Cyprus. The robotic device used for the purposes of the study was developed under the project FUSROBOT (ENTERPRISES/0618/0016), whereas the reported experiments were carried out under the project SOUNDPET (INTEGRATED/0918/0008) and FUSVET (SEED/1221/0080).

CONFLICT OF INTERESTS

Authors declare NO conflict of interest.

Magnetic Resonance thermometry of Focused Ultrasound (FUS) using a preclinical FUS robotic system at 3 T

Antria Filippou[a], Nikolas Evripidou[a], Andreas Georgiou[a], Leonidas Georgiou[b], Antreas Chrysanthou[b], Cleanthis Ioannides[b], Christakis Damianou[a*]

[a] Cyprus University of Technology, Department of Electrical Engineering, Computer Engineering, and Informatics, Limassol, Cyprus.
[b] German Oncology Centre, Department of Interventional Radiology, Limassol, Cyprus.

Authors' emails: ap.filippou@edu.cut.ac.cy, nk.evripidou@edu.cut.ac.cy, andreas-georgiou1@outlook.com, Leonidas.Georgiou@goc.com.cy, Antreas.Chrysanthou@goc.com.cy, Cleanthis.Ioannides@goc.com.cy

***For correspondence contact:**
Christakis Damianou,
Cyprus University of Technology,
Electrical Engineering Department,
30 Archbishop Kyprianou Str.,
3036 Limassol,
CYPRUS
Email: christakis.damianou@cut.ac.cy
Tel.: 0035725002039
Fax: 0035725002849

ABSTRACT

Purpose: High Intensity Focused Ultrasound (HIFU) therapies are often performed within Magnetic Resonance Imaging (MRI) systems providing thermometry-based temperature monitoring. In this study, the temporal and spatial resolution of MRI thermometry was assessed for HIFU sonications executed using a preclinical system on agar based phantoms at 1.5 T and 3 T MRI scanners, using the Proton Resonance Frequency Shift (PRF) technique.

Methods: Sonications were executed at 1.5 T and 3 T to assess the HIFU system and observe variations in MR thermometry temperature measurements. MR-thermometry was assessed at 3 T, for identical HIFU sonications on three 6 % w/v agar based phantoms doped with varied concentrations of silica and evaporated milk, and for sonications executed at varied acoustic power of 1.5-45 W. Moreover, echo time (TE) values of 5-20 ms were used to assess the effect on the signal to noise ratio (SNR) and temperature change sensitivity.

Results: Clearer thermal maps with a 2.5-fold higher temporal resolution were produced for sonications at 3 T compared to 1.5 T, despite employment of similar thermometry sequences. At 3 T, temperature changes between 41-50 ^{o}C were recorded for the three phantoms produced with varied silica and evaporated milk, with the addition of 2 % w/v silica resulting in a 20 % increase in temperature change. The lowest acoustic power that produced reliable beam detection within a voxel was 1.5 W. A TE of 10 ms resulted in the highest temperature sensitivity with adequate SNR.

Conclusions: MR thermometry performed at 3 T achieved short temporal resolution with spatial temperature dependencies exhibited with the sonication and imaging parameters. The present data could be used in preclinical MRgFUS feasibility studies to enhance MR thermometry.

KEYWORDS: Thermometry, MRI, agar, ultrasound

1. INTRODUCTION

Since its introduction 7 decades ago [1], high intensity focused ultrasound (HIFU) has been extensively explored in almost every human tissue, emerging as a noninvasive clinical surgical tool for a wide range of oncological and non-oncological applications [2,3]. HIFU therapeutic techniques employ ultrasound waves that locally focus within tissue to raise its temperature to hyperthermic or ablative levels [2], with the procedures typically guided by ultrasound (US) or Magnetic Resonance Imaging (MRI) systems that provide treatment monitoring [3]. MRI guidance offers superior performance than US guided systems since it provides increased image spatial resolution [4] and enables real time noninvasive quantitative monitoring of the tissue temperature increase through Magnetic Resonance (MR) thermometry techniques [5]. MR thermometry is a potent temperature monitoring tool utilising various temperature dependent methods such as the proton resonance frequency shift (PRF), proton density, T_1 relaxation time mapping, T_2 relaxation time mapping, apparent diffusion coefficient and magnetization transfer [6].

Among the various techniques, the PRF is considered the gold standard and the only clinically available method for monitoring temperature evolution in MRI guided focused ultrasound (MRgFUS) applications [7], since it is aqueous tissue type independent and offers a proportional correlation with temperature over a large temperature range [5]. The technique is based on the temperature dependence of the hydrogen bonds that at increased tissue temperatures result in increased electron screening and ultimately decreased proton resonance frequency [5,6]. These resonant frequency changes induce a phase shift in MRI images, which PRF utilises to provide HIFU induced temperature changes in the form of thermal mapping, by subtracting the phases of MR images acquired prior and throughout HIFU heating [5,6]. PRF is usually employed for MR thermometry in MRI scanners with field strengths between 1 T

[12] and 3 T [13], and is typically implemented with Gradient echo (GRE) sequences that provide simple and relatively high temperature sensitivities [5]. However, more rapid sequences such as Echo planar imaging (EPI), segmented EPI or single shot EPI (ss-EPI) can be employed to rapidly generate MR thermometry data [12,14,15], albeit with these sequences negatively impacting the quality of acquired images, thus affecting temperature estimations [12,16].

Notably, the type of imaging sequence when used with similar acquisition parameters, does not seem to affect the image signal to noise ratio (SNR) in either 1.5 T or 3 T scanners [12], with increased SNR and PRF sensitivity observed at both field strengths at echo times (TE) closer to the T2* relaxation times of the tissue under investigation [12,17,18], and for flip angles similar to the Ernst angle [18]. Moreover, SNR dependencies with the sampling bandwidth have been reported at 3 T, with a low bandwidth resulting in high SNR however, with possible presence of off-resonance artifacts [20]. Nevertheless, recently, multiecho spiral [20] and multislice [17] thermometry sequences were reported to result in enhanced and faster MR thermometry, with decreased artifacts and better resolution compared to conventional sequences, thus suited for monitoring *in vivo* HIFU sonications at 3 T [17,20].

Lately, an increased number of MRgFUS studies are performed within a higher field scanner (3 T) since the increased magnetic field strength leads to higher temperature sensitivity [6], increased measurement accuracy and smaller temperature variations compared to 1.5 T scanners [12]. Although the PRF is considered the preferred method for MR thermometry monitoring in HIFU tissue ablations, the technique has been reported as inferior for *in vivo* pulsed [23] or hyperthermic [24] MRgFUS procedures executed inside 3 T MRI scanners since it underestimates temperatures and requires factor [23] and phase [24] corrections, respectively, to yield accurate temperatures. However, recently, a graphical interface was developed for real time PRF MR thermometry for hyperthermic HIFU prostate applications [25], with feasibility

studies executed in phantoms inside a 3 T scanner generating, temperature maps with a minimal temperature error (0.5 ^{o}C) [25]. Notably, lately, photogrammetry has also been reported as a potential technique for quality control of hyperthermic treatments, offering quantitative pre-treatment monitoring of the applied thermal dose [26].

Notwithstanding its high accuracy, PRF is sensitive to magnetic field changes and organ motion [6], with MRgFUS studies at 3 T also demonstrating temperature artifacts and errors arising due to magnetic susceptibility differences induced by injection of MRI contrast agents [28]. Subsequently, several techniques such as two step filters [27], multibaseline [29], or referenceless algorithms [30–32] have been successfully employed and validated in 3 T scanners for compensation of artifacts present [27,29–32]. Nevertheless, in phantom experiments executed in both a 1.5 T and 3 T scanners, referenceless thermometry has been reported as inferior at 3 T for adjusting magnetic field changes [32]. Notably, *in vivo* studies [29,31] executed at 3 T have shown that respiration induced noise in PRF MR thermometry can be decreased by applying motion compensation multibaseline algorithms [29] or by using rapid segmented interleaved EPI sequences for successfully monitoring HIFU treatments of moving organs.

Moreover, although PRF is preferred because of its aqueous tissue independency [35], employment of the technique for temperature monitoring in fat tissues poses significant difficulties [35] attributed to absence of hydrogen bonds [8]. In such manner, fat suppression techniques are usually employed [14,19,36] to account for temperature estimation errors attributed to phase difference modifications related to lipid presence [35] and magnetic field susceptibilities arising during HIFU fat ablation [37,38]. Nevertheless, several techniques combining PRF and T1 or T2 mapping have been examined for performing MR thermometry for fat at high field scanners [7]. Diakite et al. [39] developed a hybrid PRF-T1 mapping sequence to provide concurrent temperature imaging of aqueous and fat tissues in a 3D plane,

with feasibility studies executed at 3 T on excised tissue providing high SNR temperature maps of aqueous and fat tissues, thus indicating potential clinical applications of the technique [39].

As abovementioned, PRF calculates temperature changes by utilising differences in the phase of the acquired MRI images [5,6]. Noteworthy, the phase of the images represents a single rotation of the MRI signal, characterized by both amplitude and direction taking values between $-\pi$ and π [40]. In this regard, signal rotations outside of this 2π range are wrapped around to gain values in the constrained range, thus making the real phase values indistinguishable [40]. Subsequently, unwrapping algorithms [41–43] need to be employed on matrix voxels of the acquired wrapped phase images to uncover the correct phase value, thus resulting in accurate estimations of the induced temperature change. Notably, Kim et al. [44] developed a programme for generating PRF MR thermometry data, wherein the phase difference is not directly calculated from phase values, but is rather determined by subtracting complex numbers, thus sparing the need for unwrapping algorithms. Accurate temperatures were acquired with the programme for HIFU sonications executed *ex vivo* in a 3 T scanner for an SPGR sequence [44].

Considering the increasing development of novel MRgFUS systems [49] and the recent improvements in MR thermometry techniques for monitoring temperature evolution during therapeutic procedures [7], ~~In~~ in this study the PRF technique was employed for assessing the sensitivity, temporal and spatial resolution of MR thermometry monitoring during HIFU sonications executed with a preclinical MRgFUS robotic system [50] on agar based phantoms doped with silica [51–55]. PRF based MR thermometry data for temperature monitoring of the HIFU sonications were generated using an inhouse software developed in C# (Visual Studio, Microsoft Corporation, Washington, USA) that executes thermometry with scripts written in Python (Python Software Foundation, Delaware, USA). HIFU sonications were executed within two clinical MRI scanners of varied magnetic field strength, namely 1.5 T and 3 T, to

assess the performance of the preclinical MRgFUS robotic system [50] within the different MRI environments and examine any variations in thermometry mapping arising from the varied magnetic field strength. Moreover, dependencies of the temporal and spatial resolution of MR thermometry temperature measurements with the HIFU sonication parameters and MR sequence acquisition parameters were examined for a series of sonications executed at 3 T, evaluating the system and optimising thermometry sequences at the higher magnetic field scanner.

2. MATERIALS AND METHODS

2.1 PRF MR thermometry calculations

MR thermometry data were generated using the widely used PRF technique [5,6] that relates the temperature changes (ΔT) that influence the precession frequency of protons to the phase shift (Δφ) observed in the MRI signal. The phase shift is calculated from the phase of MR images of the tissue under treatment, acquired at baseline temperatures before heating, and at specific time intervals during HIFU heating. Typically, more than one reference images are acquired at baseline temperatures before heating, to account for pulse sequence variability. The temperature change (ΔT) from baseline is then calculated from the cumulative phase difference of the images acquired before and during heating using the following Equation 1:

$$\Delta T = \frac{\varphi(T) - \varphi(T_o)}{\gamma . \alpha . B_o . TE} \quad (1)$$

where $\varphi(T)$ is the phase of the image acquired during heating, $\varphi(T_o)$ is the phase difference of the reference images acquired at baseline temperature, γ is the gyromagnetic ratio, α is the PRF temperature change tissue coefficient, B_o is the local magnetic field strength and TE is the echo time of the MR imaging sequence. The PRF temperature change coefficient is a tissue constant taking values in the -0.007 to -0.011 ppm/^{o}C range [6]. For the purposes of MR thermometry data calculated and presented herein, the PRF temperature change tissue coefficient was set at -0.01 ppm/^{o}C.

2.1.2 MRgFUS software with MR thermometry monitoring capabilities

An inhouse user friendly software written in the C# (Visual Studio, Microsoft Corporation) language was implemented for generating PRF based MR thermometry data. The software controls the motion and sonication parameters of various preclinical MRgFUS robotic systems equipped with single element focused transducers developed for specific applications [50,56–61]. In a typical experimental setting within the MRI environment, the software interfaces with the robotic system, and navigates the ultrasonic transducer along predetermined trajectories. Specifically, transducer navigation is performed according to User commands that determine the size of the sonication trajectory (single point or grid operation), the spatial resolution of the transducer's navigation (grid spatial step) as well as the time delay amidst consecutive sonications. Moreover, the sonication parameters of the treatment are appropriately adjusted through User commands relating to the transducer's operating frequency, the applied power as well as the sonication time. The software additionally offers MRI interfacing capabilities, enabling direct acquisition of MR images from clinical MRI scanners, therefore allowing treatment planning and HIFU treatment monitoring using MR thermometry.

MR thermometry data for HIFU treatments with the software are generated based on the PRF technique. During interfacing with a clinical scanner, two types of MRI images, specifically magnitude and phase images of the subject undergoing MRgFUS sonications, are exported from the MRI scanner to the developed software using a script written in the Python language (Python Software Foundation, Delaware, USA) and a series of Python libraries (Proteus MRI-HIFU Software Development Suite). The flowchart of the PRF based MR thermometry calculations executed by the software is shown in Figure 1. The software directly retrieves and reads the reference magnitude and phase images of the subject, acquired at baseline temperatures before HIFU heating. The reference magnitude image of the tissue is

then displayed by the software on the available graphical user interface (GUI). Notably, the region of interest (ROI) where the focal spot is located, and where ultimately MR thermometry calculations are performed, is automatically generated by the software, and is overlapped as a small red point on the displayed magnitude image of the subject. Nevertheless, the software allows the User to manually adjust the location of the ROI appropriately. Concurrently, the magnitude and phase images of the subject, acquired during the HIFU ablations are retrieved and read by the software using the Python script (Python Software Foundation). Upon retrieval of both the reference and ablation images, the phase difference between the two types of images is calculated, followed by application of certain unwrapping algorithms that adjust for the wrapped around phases and retrieve the actual rotation of the phase signal [40]. The unwrapped phase differences are followed by application of intrascan transient phase offset correction on the calculated phase difference. Thereafter, the induced temperature shift is calculated in a pixel by pixel approach on the defined ROI, using the PRF method and Equation 1. Advantageously, the other three variables (local magnetic field strength, α PRF coefficient, and TE) required for MR thermometry calculations have already been acquired by the software. Specifically, the temperature tissue coefficient α is commanded by the User through the GUI of the software alongside other variables that affect MR thermometry calculations (i.e., baseline temperature of subject and number of reference images acquired). Regarding the TE and magnetic field strength values, these data are automatically acquired by the software from the reference magnitude images of the subject. After the calculations, a colour coded thermal map of the temperature, and a timeseries temperature graph are demonstrated by the software, therefore enabling PRF based MR thermometry monitoring of the sonications executed within the corresponding ROI.

Notably, the colour coded thermal map is also overlapped on the equivalent ROI on the magnitude image of the subject, thus permitting for visual depiction of the location and extent

of thermal heating relative to the spatial anatomy of the subject. Furthermore, the generated MR thermometry data are saved and automatically updated throughout the procedure upon acquisition of new MRI images. In this regard, the time resolution at which MR thermometry data are generated is determined and limited by the temporal resolution of the MR sequence employed for imaging the HIFU sonications. Figure 2 shows an indicative example of the MR thermometry monitoring provided by the software, with MR thermometry data generated for sonications executed on agar based phantoms [51–55] that are habitually employed in MRgFUS studies [62]. The colour coded thermal map, the thermal map overlapped on the magnitude image of the phantom and the time series tissue temperature graph are calculated and presented on the GUI, next to the treatment planning image, therefore allowing PRF based MR thermometry monitoring.

2.2 MR thermometry for MRgFUS sonications

2.2.1 MRgFUS robotic system

A previously developed MRgFUS robotic system [50] was implemented for executing HIFU sonications on agar based phantoms doped with silica [51–55] within a clinical MRI environment as shown in Figure 3. Materials utilised in the development of the robotic system were particularly chosen to result in an MRI compatible system, allowing unrestricted and safe operation within the MRI environment [50]. In this regard, the system was 3D printed (FD270, Stratasys, Minnesota, USA) using only Acrylonitrile Styrene Acrylate (ASA) thermoplastic. The robotic system is integrated with a single element spherically focused transducer that is navigated to a specified location through computer controlled positioning mechanisms that allow motion in 3 stages (X, Y, and Z) that is actuated by piezoelectric motors (USR60-S3N, Shinsei Kogyo Corp., Tokyo, Japan) and accurately controlled by optical encoders (US Digital, Vancouver, Washington, USA). The transducer is extended from the mechanical positioning stages to a container filled with deionised and degassed water. An acoustic window opening

on the water container allows placement of the target on top of the transducer and the degassed water, resulting in acoustic coupling and thus unrestricted propagation of the ultrasonic beam to the targeted area. The positioning mechanisms and the water container are housed in an ASA enclosure that allows placement within the table of clinical MRI scanner. In this study, an inhouse developed ultrasonic transducer operating at a frequency of 2.6 MHz, having a diameter of 50 mm, and focusing beam at 65 mm was integrated in the robotic system.

The robotic system was placed on the table of either a 1.5 T (Signa HDxt 16x, GE Healthcare, Chicago, Illinois, USA) or 3 T (Magnetom Vida, Siemens Healthineers, Erlangen, Germany) clinical MRI scanner. The agar based phantom, developed with appropriate concentrations of inclusion materials, was accommodated on the acoustic opening of the robotic system as indicatively shown in Figure 3 for the 3 T scanner (Magnetom Vida, Siemens Healthineers). A 3D printed (FD270, Stratasys) ASA structure was positioned around the robotic system to allow support of the MR coil employed for imaging the executed sonication protocols. The robotic system was connected through cables to an inhouse developed electronic system that controls the motion of the motors, while the transducer was connected to an RF amplifier (AG1016, T & C Power Conversion, Rochester, NY, USA) for powering purposes. It is worth stating that the electronic system, software, and RF amplifier were located within the MRI control room.

2.2.2 Agar based tissue mimicking materials

Agar based phantoms were developed and utilised as targets during sonications since they exhibit a high melting point [62] that can withstand the temperatures normally induced by high intensity sonications. In this study, agar based phantoms were produced following a preparation procedure mentioned in the literature [51] and utilising certain inclusion materials that in specific concentrations can precisely mimic acoustic and thermal properties of human tissues [51,53–55] as well as producing a human tissue like MRI signal [52]. In this regard,

agar (10164, Merck KGaA, Darmstadt, Germany) and silica (Sigma-Aldrich, Missouri, USA) powders, as well as liquid evaporated milk (Nounou, Friesland Campina, Marousi, Greece) were employed in specific percent (%) weight per volume (w/v) or volume per volume (v/v) concentrations, respectively, following the preparation procedure mentioned by Drakos et al. [51]. The tissue mimicking materials were developed in a 3D printed (FD270, Stratasys) mold with dimensions 90 mm (w) × 160 mm (l) × 100 mm (h), thus allowing support of the rectangular agar based phantom on the acoustic window of the robot.

2.2.3 MR thermometry for sonications at 1.5 T and 3 T

A Fast Spoiled Gradient Echo (FSPGR) sequence with the following parameters: Repetition time (TR) = 20 ms, Echo time (TE) = 10 ms, Field of View (FOV) = 28 × 28 cm^2, Slice thickness = 10 mm, Acquisition Matrix = 128 × 128, Number of Excitations (NEX) = 2, Echo train length (ETL) = 1, and Flip angle = 35º, was employed along with a General Purpose Flex (GPFLEX) surface coil (GPFLEX, Signa 1.5 T receiver only, GE Healthcare) for MR imaging the agar based phantoms during sonications within the 1.5 T MRI scanner (Signa HDxt 16x, GE Healthcare; 33 mT/m maximum gradient amplitude, 120 T/m/ms slew rate, 100 % duty cycle, 0.02 ppm homogeneity over a 20 cm diametrical spherical volume). Notably, the FSPGR sequence with the abovementioned acquisition parameters induced a specific absorption rate (SAR) of 1.771 W/kg within the agar based phantoms during MR image acquisition.

Accordingly, MRI scans of the agar based phantoms during sonications implemented within the 3 T scanner (Magnetom Vida, Siemens Healthineers; 45 mT/m maximum gradient amplitude, 200 T/m/ms slew rate, 100 % duty cycle, 0.04 ppm homogeneity over a 20 cm diametrical spherical volume) were executed using a Fast low angle shot (FLASH) sequence, which is similar to the FSPGR sequence employed for imaging inside the 1.5 T MRI scanner (Signa HDxt 16x, GE Healthcare). The agar based phantoms were imaged using a body coil

(Body18, Siemens Healthineers) and the FLASH sequence that was used with comparable acquisition parameters (TR = 20 ms, TE = 10 ms, FOV: 28×28 cm^2, Slice thickness = 10 mm, Acquisition matrix = 128 × 128, NEX = 1, ETL = 1, and Flip angle = 35°) as the FSPGR sequence. Correspondingly, agar-based phantoms received a SAR of 0.6877 W/kg during the FLASH imaging performed inside the 3 T MRI scanner.

PRF based MR thermometry calculations for sonications within the 1.5 T and 3 T scanners were executed using FSPGR and FLASH images acquired in both coronal and axial planes, that were respectively loaded into the developed MRgFUS control and MR monitoring software. For both field strengths (1.5 T and 3 T) and imaging planes (coronal and axial), the time series temperature plots and colour coded thermal maps as overlayed on the corresponding magnitude images of the agar based phantom were extracted from the software.

2.4 MR thermometry for sonications at 3 T

2.4.1 SNR dependence and MR thermometry sensitivity with varied TE values

A series of equivalent sonications were executed on the agar based phantom that was scanned in the coronal plane using the FLASH pulse sequence with the abovementioned acquisition parameters. Regarding the TE value of the FLASH sequence, scans were performed with varied TE values of 5, 10, 15, and 20 ms to assess the effect of the TE on the SNR of the acquired images, and ultimately the effect on the temperature changes measured with PRF MR thermometry.

For each FLASH image acquired with a varied TE value, SNR estimations were implemented by measuring the average signal intensity of the image in two specific ROIs set inside the agar based phantom and the air background, respectively, and using the following equation:

$$SNR = \frac{SI_{phantom}}{\sigma_{noise}} \quad (2)$$

where $SI_{phantom}$ represents the average signal intensity of the ROI set within the agar based phantom, while σ_{noise} indicates the standard deviation of the signal intensity measurements of the ROI set in the air background. Noteworthy, noise in the air background was assumed to follow a Gaussian distribution.

2.4.2 MR thermometry for sonications on agar based phantoms with varied inclusions

MR thermometry data were generated for monitoring single sonications executed on three agar based phantoms developed with different compositions of the 3 inclusion materials (agar, silica, and evaporated milk). For development of the three phantoms, the composition of agar remained constant at 6 % w/v with the % composition of additional inclusions varying. In this regard, a 6 % w/v agar phantom, a 6 % w/v agar, 2 % w/v silica phantom, and a 6 % w/v agar, 2 % w/v silica, 30 % v/v evaporated milk phantom were developed and used as sonication targets. It is worth mentioning that the three phantoms were developed in a manner that enabled simultaneous accommodation of all three phantoms on the acoustic opening of the system.

3. RESULTS

3.1 MR thermometry for sonications at 1.5 T and 3 T

PRF based MR thermometry was performed for identical sonication protocols (acoustic power of 60 W for 60 s at a focal depth of 40 mm) executed on an agar based phantom (6 % w/v agar) inside the two MRI scanners of different magnetic field strength. MR thermometry for the single sonications executed within the 1.5 T MRI scanner (Signa HDxt 16x, GE Healthcare) generated thermal maps with a temporal resolution of 6.6 s using the FSPGR sequence. Accordingly, sonications performed on the same agar based phantom (6 % w/v agar) using an identical ultrasonic protocol (acoustic power of 60 W for 60 s) within the 3 T MRI scanner (Magnetom Vida, Siemens Healthineers) and imaged with a FLASH sequence with identical acquisition parameters as the corresponding FSPGR sequence at 1.5 T, resulted in thermal maps generated in time intervals of 2.6 s during sonications. Figure 4A and Figure 4B

show the coronal thermal maps of the agar based phantom produced at specific times throughout the sonications implemented within the 1.5 T and 3 T scanners, respectively. The evolution of heating during sonications is observed at specific ROIs within the agar based phantom through the overlay of the colour coded thermal map on the respective magnitude image of the agar based phantom as acquired at either of the two MRI scanners of varied magnetic field strength. Regarding sonications executed at the higher field scanner (3 T), maximum temperatures (T10 percentile) of 47.8 ^{o}C were recorded within the agar based phantom at the focus, in a plane perpendicular to the beam (coronal plane) as shown in the temperature evolution timeseries graph in Figure 5. Figure 6A and Figure 6B show the thermal maps produced in an axial plane (parallel to the ultrasonic beam propagation) at different timepoints during sonications, as generated with MR thermometry for equivalent sonications (acoustic power of 60 W for 60 s) at 1.5 T and 3 T, respectively. Correspondingly, the advancement of thermal heating during exposure, as well as the diffusion of heating after the elapsed sonication time are noticeable within the agar based phantom at both 1.5 T and 3 T scanners.

3.2 MR thermometry at 3 T

3.2.1 MR thermometry for assessing effect of acoustic power on temperature change

MR images acquired during single sonications performed on a 6 % w/v agar, 2 % w/v silica phantom utilising varied acoustic power (1.5, 3, 6, 9, 15, 30, and 45 W) for a constant sonication time of 60 s at equivalent focal depths (45 mm) were processed with MR thermometry to assess the effect of the varied acoustic power on the MR thermometry calculated temperature change. Figure 7A shows the maximum temperature change, from a baseline of 37 ^{o}C, induced resulting application of varied acoustic power (1.5, 3, 6, 9, 15, 30, and 45 W). Following linear regression ($R^2 = 0.9811$), a proportional dependency between the induced temperature change and the applied acoustic power was discovered as shown in Figure

7A. Accordingly, Figure 7B shows thermal maps acquired at different timepoints during sonications executed at an acoustical power of 1.5 W. Thermal heating at the focal spot was clearly visible on the thermal maps as shown in Figure 7B.

3.2.2 SNR dependence and MR thermometry sensitivity with varied TE values

Figure 8A shows a bar chart of the SNR calculated from FLASH images acquired with varied TE values (5, 10, 15, and 20 ms) during sonications executed on the agar based phantom doped with silica (6 % w/v agar, 2 % w/v silica) using a constant sonication protocol (acoustic power of 45 W for a sonication time of 30 s at a focal depth of 35 mm). Generally, a decreased SNR was observed with increased TE values. Accordingly, Figure 8B shows the effect of the varied TE (5, 10, 15, and 20 ms) used for imaging on the temperature changes (from a baseline temperature of 37 ^{o}C) measured with MR thermometry in the coronal plane (perpendicular to the ultrasonic beam). Advantageously, among the varied TE values, the largest temperature change of 23 ^{o}C was recorded with MR thermometry at the focal point within the agar based phantom for sonications imaged with a TE of 10 ms.

3.2.3 MR thermometry for sonications on agar based phantoms with varied inclusions

Identical sonication protocols (acoustic power of 45 W for sonication time of 60 s at a focal depth of 45 mm) individually implemented on the 3 agar based phantoms developed with varied inclusions, generated thermal maps at specific time intervals during sonications. Thermal maps generated in a coronal plane are indicatively shown in Figure 9A at different timepoints during sonications performed on the agar based phantom doped with silicon dioxide (6 % w/v agar, 2 % w/v silica), showing the amount of thermal heating gradually induced at the focal spot within the phantom. The acoustic power of 45 W applied for a sonication time of 60 s on the 6 % w/v agar, 2 % w/v silica phantom was sufficient to induce T90 percentile, average, and T10 percentile temperatures of 70 ^{o}C, 79 ^{o}C and 86 ^{o}C, respectively, as shown in the timeseries temperature graph of the sonications in Figure 9B. Correspondingly,

temperatures induced on the remaining two agar based phantoms resulting analogous sonications, were sufficiently high as shown in Table 1. The maximum temperatures (T10 percentile) for the 3 phantoms induced by application of the constant ultrasonic protocol ranged between 78-87 ºC, therefore indicating maximum temperature changes between 41-50 ºC from the baseline temperature of 37 ºC.

3.2.4 MR thermometry for grid sonications on an agar based phantom

The FLASH images acquired in a coronal plane during sonications (acoustic power of 60 W for a sonication time of 60 s at a 45 mm focal depth) in a 3 × 3 grid operation with a 10 mm spatial step executed on the agar based phantom (6 % w/v agar, 2 % w/v silica) provided real time monitoring of the location of the thermal heating at each of the nine sonication points of the specified grid (3 × 3) as shown in Figure 10. The accumulation of thermal heating at each sonication point was visualised as a small black spot on the acquired magnitude images presented for each of the 9 sonications at approximately the end of each sonication time (60 s). Accordingly, MR thermometry for the grid sonications executed on the 6 % w/v agar, 2 % w/v silica phantom, produced sufficiently rapid thermal maps, resulting in a 2.6 s temporal resolution. Figure 11 shows the coronal thermal maps generated for each of the 9 sonication points of the specified grid operation (3 × 3) at roughly towards the end of each 60 s sonication time (limited by the temporal resolution). Overlap of the thermal maps on the magnitude images of the agar based phantom clearly indicate increased thermal heating accumulated at the respective grid sonication point, show the extent of the diffusion of thermal heating throughout the agar based phantom as well as the heating remaining from previous sonications.

4. DISCUSSION

In the present study, the sensitivity of MR thermometry based on the extensively employed PRF technique [5,6], was assessed for a series of HIFU sonications executed on agar based phantoms within a clinical 3 T MRI scanner using a previously developed robotic system

[50] equipped with a 2.6 MHz single element focused transducer, dedicated to preclinical MRgFUS studies [50,56–61]. Nevertheless, a small number of sonications were also executed within a 1.5 T MRI, to assess the sensitivity of the MR thermometry temperature mapping in the lower field clinical scanner. Furthermore, the quality of MR thermometry between the two clinical scanners was assessed through comparable ultrasonic exposures. The agar based phantoms employed herein, were specifically chosen since they have previously shown to mimic the acoustic and thermal properties of human tissues [51,53–55] as well as exhibiting a human tissue like MRI signal [52]. Notably, HIFU sonications were controlled with an inhouse developed software that allowed interfacing with the MRI for image acquisition, enabling temperature monitoring and thermal mapping of the HIFU sonications using PRF based MR thermometry.

Initially, comparable sonications were executed on an agar based phantom within the two clinical MRI scanners of varied magnetic field strength (1.5 and 3 T) to assess the performance of the system and compare the quality and sensitivity of MR thermometry based temperature mapping between the two scanners. Although the two scanners were from different vendors and some differences between scanner parameters, other than field strength, existed (i.e., maximum gradient amplitude, homogeneity, and slew rate), the effect of these parameters on the generated PRF thermal mapping was not investigated. The quality of MR thermometry mapping between the two scanners was rather investigated herein based solely on magnetic field strength differences, with the impact of other MRI hardware parameters on the quality of MR thermometry possibly explored in future studies. MR thermometry was efficiently employed for temperature monitoring, resulting in generation of colour coded thermal maps at specific time intervals during the ultrasonic exposures. Notably, thermal maps as generated at 1.5 T had a 2.5-fold lower temporal resolution (6.6 s) compared to the results at 3 T (2.6 s), despite employment of similar imaging sequences with comparable acquisition parameters

(NEX was increased by one unit at 1.5 T). Furthermore, the thermal maps generated in a coronal plane at the higher magnetic field strength scanner (3 T), as overlayed on the magnitude images of the agar based phantom, were characterised by an increased image quality with decreased artifacts (presence of grey shadows within the agar based phantom) compared to the corresponding maps produced at 1.5 T. Accordingly, axial thermal maps of the sonications at 3 T exhibited similar increased image quality than the corresponding maps at 1.5 T. Nevertheless, despite inherent similarities between the two imaging sequences, the ultrafast gradient echo sequence (FSPGR) that was utilised at 1.5 T differs in the sense that a 180^{o} inversion pulse is initially utilised before data acquisition, while the spoiled gradient echo sequence (FLASH) that was employed at the 3 T scanner applies a spoiler gradient prior to acquisition of new data, thus minimising remaining transverse magnetization and reducing image artifacts [63]. Additionally, the FSPGR sequence employed at 1.5 T induced a significantly higher SAR (1.771 W/kg) within the agar based phantoms compared to the FLASH sequence utilised for imaging at the 3 T scanner, indicating approximately a 2.5-fold increased electromagnetic energy absorbed by phantoms during imaging at the lower field strength MRI scanner (1.5 T). Nevertheless, at both MRI scanners of varied magnetic field strength, sufficiently high temperatures were recorded with MR thermometry thus indicating the efficacy of the monitoring method and the accuracy of the calculations.

Upon validating that MR thermometry at 3 T results in higher quality thermal mapping, a series of sonications were exclusively executed within the higher magnetic field clinical scanner (3 T), to assess the effect of various experimental parameters (sonication target, sonication parameters, or image acquisition parameters) on the MR thermometry temperature measurements. In this regard, the effect of applied acoustic power on the temperature change as measured with PRF based MR thermometry was initially examined for a series of sonications of constant exposure (sonication time of 60 s), wherein by linear regression, a

proportional relationship was observed. Particularly, temperature changes in the range of 2.3-49 ^{o}C were recorded for varied applied acoustic power between 1.5-45 W, resulting in a 1.14 increase in temperature change for a unit increase in the applied acoustic power. Furthermore, acquired thermal maps indicated that thermal heating within the agar based phantom, was detectable at the lowest applied acoustic power of 1.5 W, thus providing insights on the lowest acoustic power that can provide reliable detection of the ultrasonic beam within a single image voxel with volume of $2.18 \times 2.18 \times 10$ mm^3. It is worth stating that the lowest acoustic power for optimal beam detection as established herein, is only valid for the employed sonication target (agar based phantom) and the current transducer, since heat transfer at the focal spot is dependent on several tissue parameters, the mode of the exposure, and the structural characteristics of the focused transducer [2]. Nevertheless, although the proposed acoustic power is conservative in this regard, current values could be potentially used in preclinical MRgFUS studies executed on agar based phantoms using transducers of similar characteristics, to help provide reliable visualisation of the beam on MR imaging during sonications that induce temperature increases below permanent damage thresholds.

More importantly, the effect of the scanning parameters of the FLASH imaging sequence, and specifically the echo time, on the SNR of the magnitude images and ultimately its effect on the thermometry based temperature measurements was successfully assessed. Standard SNR calculations performed for a series of comparable MR images acquired during identical ultrasonic exposures using varied TE values in the range of 5-20 ms (5 ms step) revealed a negative effect of the increased TE on the image SNR and therefore on the quality of the acquired image. Specifically, a TE of 5 ms exhibited an SNR of 127.7 ± 20.8 that decreased by almost 85 % to an SNR value of 18.4 ± 3.1 for a 4-fold increase in the TE (20 ms). Appropriately, for the varied TE values examined (5, 10, 15, and 20 ms) temperature changes between 12-23 ^{o}C were recorded, with the highest temperature change measured at the

TE of 10 ms. Notably, for a TE at 5 ms, temperature changes of 16 ºC were recorded, despite this TE value exhibiting the highest image quality in terms of SNR. Contrary, the TE of 20 ms resulted in a temperature change of only 12 ºC, in accordance to presenting with the lowest SNR and thus the most inferior image quality. In this regard, the increased spatial resolution of the MR thermometry based temperature measurements with the increased TE values employed for image acquisition observed in the present study, are in accordance to similar temperature resolution dependencies with the acquisition parameters reported for other types of sequences (EPI) for MRgFUS sonications at 3 T [19]. Nevertheless, although SNR calculations in the present study were executed using a standard approach, the employed method of using image and background ROIs has been reported to result in significantly inaccurate SNR calculations [64]. In this manner, retrospective SNR calculations executed in this study for images acquired at varied TE values (5, 10, 15, and 20 ms) might be over or underestimated by approximately 34 % [64]. However, since background noise was homogeneously distributed in images acquired at varied TE values, similar inaccuracies in the calculated SNR values for images acquired at each TE value would be expected, thus still making inherent the effect of the varied TE on the SNR of magnitude FLASH images.

Moreover, the effect of the varied inclusion materials (agar, silica, evaporated milk) employed for development of three agar based phantoms (used as a sonication target) on the MR thermometry measurements was examined. Silica and evaporated milk were utilised as additional inclusions since they have previously shown to enhance the scattering [51] or absorption [65] properties of the developed phantoms, respectively, therefore independently adjusting the acoustic properties of the phantom [51]. Application of a constant ultrasonic protocol (acoustic power of 45 W for a sonication time of 60 s) on the three phantoms sufficiently induced high temperature increases from baseline, in the range of 41-50 ºC. Inherently, addition of silica in a 2 % w/v concentration presented approximately 20 % higher

temperature increases (49-50 ^{o}C) compared to the purely agar based phantom (6 % w/v) (41 ^{o}C). These findings suggest that addition of silica enhances absorption of acoustic energy, resulting in higher temperatures for identical ultrasonic protocols compared to phantoms developed merely with agar that do not seem to absorb a significant amount of ultrasonic energy. That said, Menikou et al. [54] also demonstrated that addition of silica in agar based phantoms results in absorption based ultrasonic attenuation mechanisms that are reflected as increased temperatures recorded within the agar based phantoms during ultrasonic exposures. In this context, results presented herein, replicate the findings of the study previously presented by Menikou et al. [54], thus further validating the accuracy of the MR thermometry calculations performed herein.

Sonications executed in a grid manner, confirmed the accurate navigation of the transducer in predetermined trajectories commanded by the inhouse developed software, evidenced by the equally spaced thermal heating spots that were visualised as a small black circular area on the corresponding predefined sonication point on the magnitude FLASH images of the agar based phantom acquired during exposures. Moreover, thermal maps of the grid operation generated with MR thermometry, indicated that temperatures close to 100 ^{o}C were consistently produced resulting sonications at each of the grid sonication points. Nevertheless, thermal maps as overlapped on the magnitude images of the agar based phantom revealed that thermal heating at each of the predefined sonication points remained until subsequent sonications, thus contributing to the overall accumulation of thermal heating within the targeted trajectory during exposures. As a result, the high temperatures that were consistently produced, were sufficient to create demarcated circular lesions (visualised as white spots) at each of the nine sonication points, indicating that the temperatures induced by sonications surpassed the temperature threshold of the melting point of agar [66].

Overall, successful MR thermometry monitoring, using an inhouse developed software, was achieved in the present study for HIFU sonications performed within a clinical 3 T scanner, with the MR thermometry data generated with a short temporal resolution (~2.6 s). In this regard, the temperature resolution could be further enhanced in future experiments through employment of EPI sequences that are known to result in more rapid imaging and thus thermal mapping [12,14]. Moreover, while thermometry data indicated successful performance of the MRgFUS system within both MRI environments, increased quality of acquired images was observed at 3 T compared to similar sonications performed at 1.5 T. Future studies could quantitatively examine the change in temperature accuracy of MR thermometry measurements between the two varied magnetic field strengths to determine whether higher accuracies are achieved at the higher field scanner for the sequences and experimental settings employed in the present study, as previously demonstrated in the literature for other types of sequences and MRgFUS systems [12]. In this sense, associations between image quality and temperature measurement accuracies between the two varied field strength scanner could be derived. Nevertheless, the FLASH sequence employed herein for MR image acquisition, was optimized in terms of TE for optimal SNR and temperature sensitivity. It is worth stating, that although optimal SNR is often achieved when the echo time is in the same range as the T2* relaxation times of the tissue under investigation [18], and considering that T2* relaxation times of these agar based phantoms were recently measured between 18.5-21.7 ms at 3 T [67], a TE of 10 ms was considered optimal herein to achieve sufficiently high image quality. Consequently, although image acquisition parameters are well optimised for clinical PRF MR thermometry [18], results presented herein are conservative in the sense that they are optimised for the currently employed experimental setup. Nevertheless, acquisition parameters as suggested in this study could be proven useful for use in MR thermometry during future preclinical MRgFUS studies executed on agar based phantoms, reducing time needed for optimisation of

the thermometry sequence. Moreover, insightful observations were derived relating to the dependency of the spatial resolution of temperature with the HIFU sonication parameters (acoustic power) and the inclusions of the agar based phantoms used as sonication targets. Results presented herein demonstrated the sensitivity, spatial and temporal resolution of MR thermometry monitoring using the PRF technique at 3 T for HIFU sonications on agar based phantoms. In this sense, the present data could be used in future preclinical MRgFUS feasibility studies executed on agar based phantoms to enhance MR thermometry techniques for optimal monitoring and evaluation of novel MRgFUS systems.

LIST OF FIGURE AND TABLE CAPTIONS

Figure 1: Flowchart of the PRF based MR thermometry calculations.

Figure 2: Screenshot of the inhouse software providing MR thermometry monitoring.

Figure 3: Experimental setup with the robotic system accommodated on the table of the 3 T MRI scanner and the agar based phantom positioned on the acoustic opening of the system.

Figure 4: Coronal thermal maps of the agar based phantom obtained during sonications with a 2.6 MHz transducer (Diameter = 50 mm, Radius of curvature = 65 mm) at acoustic power of 60 W for a sonication time of 60 s at 40 mm focal depth. Colour coded temperature increase observed within the phantom at different timepoints for sonications A) inside a 1.5 T scanner, and B) inside a 3 T scanner.

Figure 5: Temperature evolution observed within the agar based phantom in coronal plane during sonications with a 2.6 MHz transducer (Diameter = 50 mm, Radius of curvature = 65 mm) at acoustic power of 60 W for a sonication time of 60 s at 40 mm focal depth inside a 3 T scanner.

Figure 6: Axial thermal maps of the agar based phantom obtained during sonications with a 2.6 MHz transducer (Diameter = 50 mm, Radius of curvature = 65 mm) at acoustic power of 60 W for a sonication time of 60 s at 40 mm focal depth. Colour coded temperature increase observed within the phantom at different timepoints for sonications A) inside a 1.5 T scanner, and B) inside a 3 T scanner.

Figure 7: A) Temperature changes observed within an agar based phantom for sonications executed with different values of acoustic power (1.5 W, 3 W, 6 W, 9 W, 15 W, 30 W, 45 W) for a constant sonication time of 60 s using the 2.6 MHz transducer (Diameter = 50 mm, Radius of curvature = 65 mm) at a focal depth of 45 mm inside a 3 T scanner, and B) Coronal thermal maps of the agar based phantom obtained at different timepoints during sonications at the acoustic power of 1.5 W.

Figure 8: A) Bar chart of signal to noise ratio (SNR) for four FLASH scans acquired with different TE values. The error bars indicate standard error across images within a scan, and B) Maximum temperature change measured in coronal plane for different TE values as a result of sonications executed on the agar based phantom using the 2.6 MHz transducer (Diameter = 50 mm, Radius of curvature = 65 mm) at acoustic power of 45 W for a sonication time of 30 s at 35 mm focal depth inside a 3 T scanner.

Figure 9: A) Coronal thermal maps of the agar based phantom (6 % w/v agar, 2 % w/v silica) acquired at different timepoints during sonications with a 2.6 MHz transducer (Diameter = 50 mm, Radius of curvature = 65 mm) at acoustic power of 45 W for a sonication time of 60 s at 45 mm focal depth inside a 3 T scanner, and B) Timeseries temperature graph of the sonications.

Figure 10: Coronal magnitude images of the agar based phantom obtained during a series of sonications with a 2.6 MHz transducer (Diameter = 50 mm, Radius of curvature = 65 mm) in a 3×3 grid (10 mm distance between successive points) using an acoustic power of 45 W for a sonication time of 60 s at 45 mm focal depth inside a 3 T scanner. Red arrows indicate thermal heating. Images acquired at the end of sonications at A) 1st grid point, B) 2nd grid point, C) 3rd grid point, D) 4th grid point, E) 5th grid point, F) 6th grid point, G) 7th grid point, H) 8th grid point, and I) 9th grid point.

Figure 11: Coronal thermal maps of an agar based phantom acquired during sonications with a 2.6 MHz transducer (Diameter = 50 mm, Radius of curvature = 65 mm) in a 3×3 grid with a 10 mm step using an acoustic power of 45 W for a sonication time of 60 s at 45 mm focal depth inside a 3 T scanner. Maps acquired at the end of sonications at A) 1st grid point, B) 2nd grid point, C) 3rd grid point, D) 4th grid point, E) 5th grid point, F) 6th grid point, G) 7th grid point, H) 8th grid point, and I) 9th grid point.

Table 1: Temperature change recorded within three different agar based phantoms during sonications with a 2.6 MHz transducer (Diameter = 50 mm, Radius of curvature = 65 mm) at acoustic power of 45 W for a sonication time of 60 s at 45 mm focal depth inside a 3 T scanner.

Table 1

Phantom	Maximum Temperature (°C)	Maximum ΔT (°C)
6 % w/v agar	78	41
6 % w/v agar, 2 % w/v silica	86	49
6 % w/v agar, 2 % w/v silica, 30 % v/v milk	87	50

ACKNOWLEDGMENTS

The authors would like to express their gratitude to Samuel Pichardo for providing the Python libraries (Proteus MRI-HIFU Software Development Suite) for MR thermometry calculations. The study has been co-funded by the European Structural & Investment Funds (ESIF) and the Republic of Cyprus through the Research and Innovation Foundation (RIF) under the projects SOUNDPET (INTEGRATED/0918/0008).

DECLARATION OF INTEREST STATEMENT

All authors declare no conflicts of interest.

REFERENCES

[1] FRY WJ, MOSBERG WH, BARNARD JW, FRY FJ. Production of focal destructive lesions in the central nervous system with ultrasound. J Neurosurg 1954;11. https://doi.org/10.3171/jns.1954.11.5.0471.

[2] ter Haar G. HIFU tissue ablation: Concept and devices. Adv Exp Med Biol, vol. 880, 2016. https://doi.org/10.1007/978-3-319-22536-4_1.

[3] Siedek F, Yeo SY, Heijman E, Grinstein O, Bratke G, Heneweer C, et al. Magnetic Resonance-Guided High-Intensity Focused Ultrasound (MR-HIFU): Technical Background and Overview of Current Clinical Applications (Part 1). RoFo Fortschritte Auf Dem Gebiet Der Rontgenstrahlen Und Der Bildgebenden Verfahren 2019;191:522–30. https://doi.org/10.1055/a-0817-5645.

[4] Hernando CG, Esteban L, Cañas T, van den Brule E, Pastrana M. The role of magnetic resonance imaging in oncology. Clinical and Translational Oncology 2010;12:606–13. https://doi.org/10.1007/s12094-010-0565-x.

[5] Rieke V, Pauly KB. MR Thermometry. Journal of Magnetic Resonance Imaging 2008;27:376–90.

[6] Odéen H, Parker DL. Magnetic resonance thermometry and its biological applications – Physical principles and practical considerations. Prog Nucl Magn Reson Spectrosc 2019;110:34–61. https://doi.org/10.1016/j.pnmrs.2019.01.003.

[7] Kuroda K. MR techniques for guiding high-intensity focused ultrasound (HIFU) treatments. Journal of Magnetic Resonance Imaging 2018;47. https://doi.org/10.1002/jmri.25770.

[8] Hindman JC. Proton resonance shift of water in the gas and liquid states. J Chem Phys 1966;44. https://doi.org/10.1063/1.1726676.

[9] Ishihara Y, Calderon A, Watanabe H, Okamoto K, Suzuki Y, Kuroda K, et al. A precise and fast temperature mapping using water proton chemical shift. Magn Reson Med 1995;34. https://doi.org/10.1002/mrm.1910340606.

[10] Poorter J de. Noninvasive MRI thermometry with the proton resonance frequency method: Study of susceptibility effects. Magn Reson Med 1995;34. https://doi.org/10.1002/mrm.1910340313.

[11] Poorter J de, Wagter C de, Deene Y de, Thomsen C, Ståhlberg F, Achten E. Noninvasive MRI Thermometry with the Proton Resonance Frequency (PRF) Method: In Vivo Results in Human Muscle. Magn Reson Med 1995;33. https://doi.org/10.1002/mrm.1910330111.

[12] Kickhefel A, Roland J, Weiss C, Schick F. Accuracy of real-time MR temperature mapping in the brain: A comparison of fast sequences. Physica Medica 2010;26. https://doi.org/10.1016/j.ejmp.2009.11.006.

[13] Wang P. Evaluation of MR thermometry with proton resonance frequency method at 7T. Quant Imaging Med Surg 2017;7. https://doi.org/10.21037/qims.2017.03.05.

[14] Weidensteiner C, Quesson B, Caire-Gana B, Kerioui N, Rullier A, Trillaud H, et al. Real-time MR temperature mapping of rabbit liver in vivo during thermal ablation. Magn Reson Med 2003;50. https://doi.org/10.1002/mrm.10521.

[15] Stafford RJ, Price RE, Diederich CJ, Kangasniemi M, Olsson LE, Hazle JD. Interleaved echo-planar imaging for fast multiplanar magnetic resonance temperature imaging of ultrasound thermal ablation therapy. Journal of Magnetic Resonance Imaging 2004;20. https://doi.org/10.1002/jmri.20157.

[16] Yuan J, Mei C-S, Panych LP, McDannold NJ, Madore B. Towards fast and accurate temperature mapping with proton resonance frequency-based MR thermometry. Quant Imaging Med Surg 2012;2. https://doi.org/10.3978/j.issn.2223-4292.2012.01.06.

[17] Marx M, Plata J, Pauly KB. Toward volumetric MR thermometry with the MASTER sequence. IEEE Trans Med Imaging 2015;34. https://doi.org/10.1109/TMI.2014.2349912.

[18] Chung AH, Hynynen K, Colucci V, Oshio K, Cline HE, Jolesz FA. Optimization of spoiled gradient-echo phase imaging for in vivo localization of a focused ultrasound beam. Magn Reson Med 1996;36. https://doi.org/10.1002/mrm.1910360513.

[19] Ramsay E, Mougenot C, Köhler M, Bronskill M, Klotz L, Haider MA, et al. MR thermometry in the human prostate gland at 3.0T for transurethral ultrasound therapy. Journal of Magnetic Resonance Imaging 2013;38. https://doi.org/10.1002/jmri.24063.

[20] Marx M, Butts Pauly K. Improved MRI thermometry with multiple-echo spirals. Magn Reson Med 2016;76. https://doi.org/10.1002/mrm.25914.

[21] Chopra R, Colquhoun A, Burtnyk M, N'djin WA, Kobelevskiy I, Boyes A, et al. MR imaging-controlled transurethral ultrasound therapy for conformal treatment of prostate tissue: Initial feasibility in humans. Radiology 2012;265. https://doi.org/10.1148/radiol.12112263.

[22] Bronskill M. MRI-controlled transurethral ultrasound therapy for localised prostate cancer 2010;26:804–21. https://doi.org/10.3109/02656736.2010.503670.

[23] O'Neill BE, Karmonik C, Sassaroli E, Li KC. Estimation of thermal dose from MR thermometry during application of nonablative pulsed high intensity focused ultrasound. Journal of Magnetic Resonance Imaging 2012;35. https://doi.org/10.1002/jmri.23526.

[24] Bing C, Staruch RM, Tillander M, Köhler MO, Mougenot C, Ylihautala M, et al. Drift correction for accurate PRF-shift MR thermometry during mild hyperthermia treatments with MR-HIFU. International Journal of Hyperthermia 2016;32. https://doi.org/10.1080/02656736.2016.1179799.

[25] Ozhinsky E, Salgaonkar VA, Diederich CJ, Rieke V. MR thermometry-guided ultrasound hyperthermia of user-defined regions using the ExAblate prostate ablation array. J Ther Ultrasound 2018;6:1–10. https://doi.org/10.1186/s40349-018-0115-5.

[26] Drizdal T, Paulides MM, Sumser K, Vrba D, Malena L, Vrba J, et al. Application of photogrammetry reconstruction for hyperthermia quality control measurements. Physica Medica 2022;101. https://doi.org/10.1016/j.ejmp.2022.08.008.

[27] Schmitt A, Mougenot C, Chopra R. Spatiotemporal filtering of MR-temperature artifacts arising from bowel motion during transurethral MR-HIFU. Med Phys 2014;41. https://doi.org/10.1118/1.4897382.

[28] Hijnen NM, Elevelt A, Pikkemaat J, Bos C, Bartels LW, Grüll H. The magnetic susceptibility effect of gadolinium-based contrast agents on PRFS-based MR thermometry during thermal interventions. J Ther Ultrasound 2013;1. https://doi.org/10.1186/2050-5736-1-8.

[29] Pichardo S, Köhler M, Lee J, Hynnyen K. In vivo optimisation study for multi-baseline MR-based thermometry in the context of hyperthermia using MR-guided high intensity focused ultrasound for head and neck applications. International Journal of Hyperthermia 2014;30. https://doi.org/10.3109/02656736.2014.981299.

[30] Salomir R, Viallon M, Kickhefel A, Roland J, Morel DR, Petrusca L, et al. Reference-free PRFS MR-thermometry using near-harmonic 2-D reconstruction of the background phase. IEEE Trans Med Imaging 2012;31. https://doi.org/10.1109/TMI.2011.2168421.

[31] Holbrook AB, Santos JM, Kaye E, Rieke V, Pauly KB. Real-time MR thermometry for monitoring HIFU ablations of the liver. Magn Reson Med 2010;63. https://doi.org/10.1002/mrm.22206.

[32] Ferrer CJ, Bartels LW, van der Velden TA, Grüll H, Heijman E, Moonen CTW, et al. Field drift correction of proton resonance frequency shift temperature mapping with

multichannel fast alternating nonselective free induction decay readouts. Magn Reson Med 2020;83. https://doi.org/10.1002/mrm.27985.

[33] Grissom WA, Rieke V, Holbrook AB, Medan Y, Lustig M, Santos J, et al. Hybrid referenceless and multibaseline subtraction MR thermometry for monitoring thermal therapies in moving organs. Med Phys 2010;37. https://doi.org/10.1118/1.3475943.

[34] Odéen H, Todd N, Diakite M, Minalga E, Payne A, Parker DL. Sampling strategies for subsampled segmented EPI PRF thermometry in MR guided high intensity focused ultrasound. Med Phys 2014;41. https://doi.org/10.1118/1.4892171.

[35] Rieke V. MR Thermometry. In: Kahn T, Busse H, editors. Interventional Magnetic Resonance Imaging, Berlin, Heidelberg: Springer; 2011, p. 271–88. https://doi.org/10.1007/174_2011_478.

[36] de Zwart JA, Vimeux FC, Delalande C, Canioni P, Moonen CTW. Fast lipid-suppressed MR temperature mapping with echo-shifted gradient- echo imaging and spectral-spatial excitation. Magn Reson Med 1999;42. https://doi.org/10.1002/(SICI)1522-2594(199907)42:1<53::AID-MRM9>3.0.CO;2-S.

[37] Baron P, Deckers R, de Greef M, Merckel LG, Bakker CJG, Bouwman JG, et al. Correction of proton resonance frequency shift MR-thermometry errors caused by heat-induced magnetic susceptibility changes during high intensity focused ultrasound ablations in tissues containing fat. Magn Reson Med 2014;72. https://doi.org/10.1002/mrm.25063.

[38] Baron P, Deckers R, Bouwman JG, Bakker CJG, de Greef M, Viergever MA, et al. Influence of water and fat heterogeneity on fat-referenced MR thermometry. Magn Reson Med 2016;75. https://doi.org/10.1002/mrm.25727.

[39] Diakite M, Odéen H, Todd N, Payne A, Parker DL. Toward real-time temperature monitoring in fat and aqueous tissue during magnetic resonance-guided high-intensity

focused ultrasound using a three-dimensional proton resonance frequency T1 method. Magn Reson Med 2014;72. https://doi.org/10.1002/mrm.24900.

[40] Chavez S, Xiang QS, An L. Understanding phase maps in MRI: A new cutline phase unwrapping method. IEEE Trans Med Imaging 2002;21. https://doi.org/10.1109/TMI.2002.803106.

[41] Domínguez-Guzmán G, Castillo-Mixcóatl J, Beltrán-Pérez G, Muñoz-Aguirre S. Itoh algorithm to unwrap 2D phase. Seventh Symposium Optics in Industry, vol. 7499, 2009. https://doi.org/10.1117/12.851057.

[42] Itoh K. Analysis of the phase unwrapping algorithm. Appl Opt 1982;21. https://doi.org/10.1364/ao.21.002470.

[43] Herráez MA, Burton DR, Lalor MJ, Gdeisat MA. Fast two-dimensional phase-unwrapping algorithm based on sorting by reliability following a noncontinuous path. Appl Opt 2002;41. https://doi.org/10.1364/ao.41.007437.

[44] Kim EJ, Jeong K, Oh SJ, Kim D, Park EH, Lee YH, et al. MR thermometry analysis program for laser- or high-intensity focused ultrasound (HIFU)-induced heating at a clinical MR scanner. Journal of the Korean Physical Society 2014;65. https://doi.org/10.3938/jkps.65.2126.

[45] Todd N, Vyas U, de Bever J, Payne A, Parker DL. Reconstruction of fully three-dimensional high spatial and temporal resolution MR temperature maps for retrospective applications. Magn Reson Med 2012;67:724–30. https://doi.org/10.1002/mrm.23055.

[46] Todd N, Prakash J, Odéen H, de Bever J, Payne A, Yalavarthy P, et al. Toward real-time availability of 3D temperature maps created with temporally constrained reconstruction. Magn Reson Med 2014;71. https://doi.org/10.1002/mrm.24783.

[47] Jiang R, Jia S, Qiao Y, Chen Q, Wen J, Liang D, et al. Real-time volumetric MR thermometry using 3D echo-shifted sequence under an open source reconstruction platform. Magn Reson Imaging 2020;70. https://doi.org/10.1016/j.mri.2020.04.001.

[48] Gaur P, Grissom WA. Accelerated MRI thermometry by direct estimation of temperature from undersampled k-space data. Magn Reson Med 2015;73. https://doi.org/10.1002/mrm.25327.

[49] Yiallouras C, Damianou C. Review of MRI positioning devices for guiding focused ultrasound systems. International Journal of Medical Robotics and Computer Assisted Surgery 2015:247–55. https://doi.org/10.1002/rcs.

[50] Giannakou M, Antoniou A, Damianou C. Preclinical robotic device for magnetic resonance imaging guided focussed ultrasound. The International Journal of Medical Robotics and Computer Assisted Surgery 2022. https://doi.org/10.1002/rcs.2466.

[51] Drakos T, Antoniou A, Evripidou N, Alecou T, Giannakou M, Menikou G, et al. Ultrasonic attenuation of an agar, silicon dioxide, and evaporated milk gel phantom. J Med Ultrasound 2021;29:239–49.

[52] Antoniou A, Georgiou L, Christodoulou T, Panayiotou N, Ioannides C, Zamboglou N, et al. MR relaxation times of agar-based tissue-mimicking phantoms. J Appl Clin Med Phys 2022;23. https://doi.org/10.1002/acm2.13533.

[53] Menikou G, Yiannakou M, Yiallouras C, Ioannides C, Damianou C. MRI-compatible breast/rib phantom for evaluating ultrasonic thermal exposures. International Journal of Medical Robotics and Computer Assisted Surgery 2018;14:1–12. https://doi.org/10.1002/rcs.1849.

[54] Menikou G, Dadakova T, Pavlina M, Bock M, Damianou C. MRI compatible head phantom for ultrasound surgery. Ultrasonics 2015;57:144–52. https://doi.org/10.1016/j.ultras.2014.11.004.

[55] Menikou G, Damianou C. Acoustic and thermal characterization of agar based phantoms used for evaluating focused ultrasound exposures. J Ther Ultrasound 2017;5:1–14. https://doi.org/10.1186/s40349-017-0093-z.

[56] Drakos T, Giannakou M, Menikou G, Filippou A, Evripidou N, Spanoudes K, et al. MRI-Guided Focused Ultrasound Robotic System for Preclinical use. Journal of Veterinary Medicine and Animal Sciences 2020;4.

[57] Drakos T, Giannakou M, Menikou G, Damianou C. Magnetic Resonance Imaging–Guided Focused Ultrasound Positioning System for Preclinical Studies in Small Animals. Journal of Ultrasound in Medicine 2021;40. https://doi.org/10.1002/jum.15514.

[58] Spanoudes K, Evripidou N, Giannakou M, Drakos T, Menikou G, Damianou C. A high intensity focused ultrasound system for veterinary oncology applications. J Med Ultrasound 2021;29. https://doi.org/10.4103/JMU.JMU_130_20.

[59] Giannakou M, Drakos T, Menikou G, Evripidou N, Filippou A, Spanoudes K, et al. Magnetic resonance image–guided focused ultrasound robotic system for transrectal prostate cancer therapy. International Journal of Medical Robotics and Computer Assisted Surgery 2021;17. https://doi.org/10.1002/rcs.2237.

[60] Antoniou A, Giannakou M, Evripidou N, Stratis S, Pichardo S, Damianou C. Robotic system for top to bottom MRgFUS therapy of multiple cancer types. International Journal of Medical Robotics and Computer Assisted Surgery 2022;18:e2364. https://doi.org/10.1002/rcs.2364.

[61] Giannakou M, Menikou G, Ioannides K, Damianou C. Magnetic resonance-image-guided focused ultrasound robotic system with four computer-controlled axes with endorectal access designed for prostate cancer focal therapy. Digit Med 2020;6:32–43. https://doi.org/10.4103/digm.digm.

[62] Antoniou A, Damianou C. MR relaxation properties of tissue-mimicking phantoms. Ultrasonics 2022;119. https://doi.org/10.1016/j.ultras.2021.106600.

[63] Wood ML, Silver M, Runge VM. Optimization of spoiler gradients in flash MRI. Magn Reson Imaging 1987;5. https://doi.org/10.1016/0730-725X(87)90379-1.

[64] Dietrich O, Raya JG, Reeder SB, Reiser MF, Schoenberg SO. Measurement of signal-to-noise ratios in MR images: Influence of multichannel coils, parallel imaging, and reconstruction filters. Journal of Magnetic Resonance Imaging 2007;26. https://doi.org/10.1002/jmri.20969.

[65] Drakos T, Giannakou M, Menikou G, Ioannides C, Damianou C. An improved method to estimate ultrasonic absorption in agar-based gel phantom using thermocouples and MR thermometry. Ultrasonics 2020;103:106089. https://doi.org/10.1016/j.ultras.2020.106089.

[66] Ortega R, Téllez A, Leija L, Vera A. Measurement of ultrasonic properties of muscle and blood biological phantoms. Phys Procedia 2010;3:627–34. https://doi.org/10.1016/j.phpro.2010.01.079.

[67] Antoniou A, Evripidou N, Georgiou L, Chrysanthou A, Ioannides C, Damianou C. Tumor phantom model for MRI guided Focused Ultrasound ablation studies. Med Phys 2023.


Read MRI reference magnitude and phase images
Display magnitude reference image on GUI
Region of interest (ROI) where focal spot is generated is automatically overlapped on the magnitude reference image
Location of the ROI can be manually adjusted
Read MRI ablation magnitude and phase reference images
Calculate phase difference
Apply phase unwrapping algorithms
TE and B are automatically acquired from the MRI magnitude reference image
Apply intra-scan transient offset corrections
The User sets the α PRF coefficient, the baseline temperature and the number of reference images
Calculate temperature shift in a pixel-by-pixel approach using the PRF method
Display color-coded thermal map, time-series temperature graph and overlayed thermal map on magnitude image

Figure 1

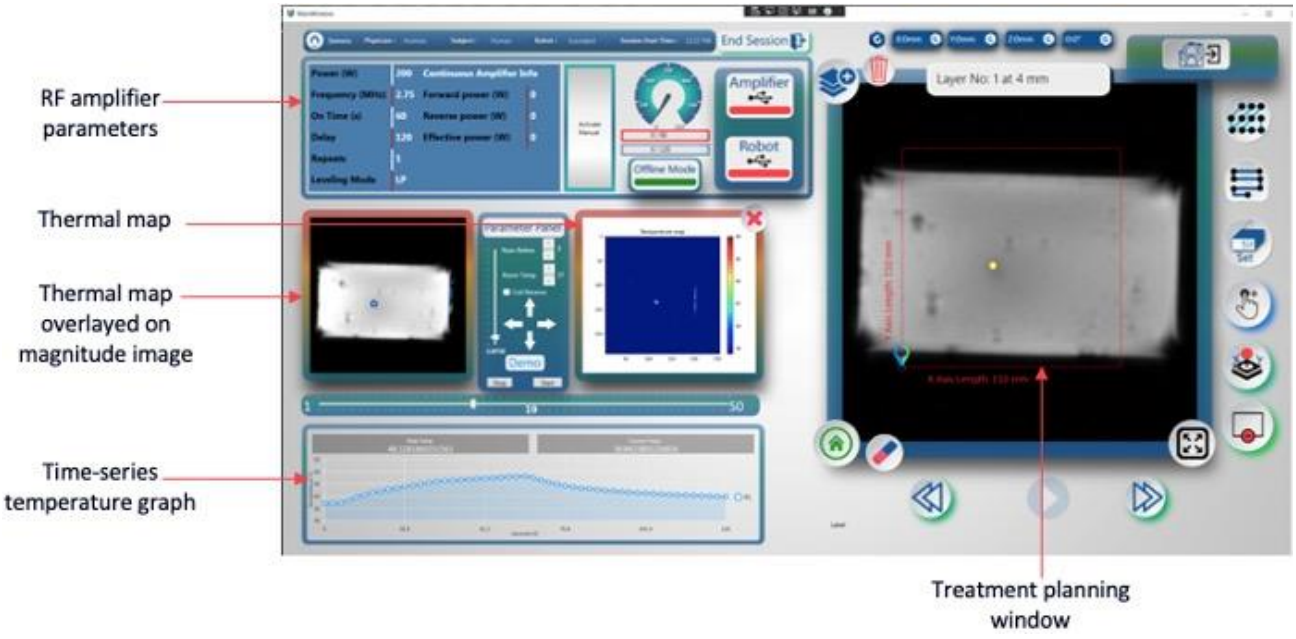
RF amplifier parameters
Thermal map
Thermal map overlayed on magnitude image
Time-series temperature graph
End Session
Amplifier
Robot
Offline Mode
Layer No: 1 at 4 mm
Parameter Panel
Demo
Treatment planning window

Figure 2

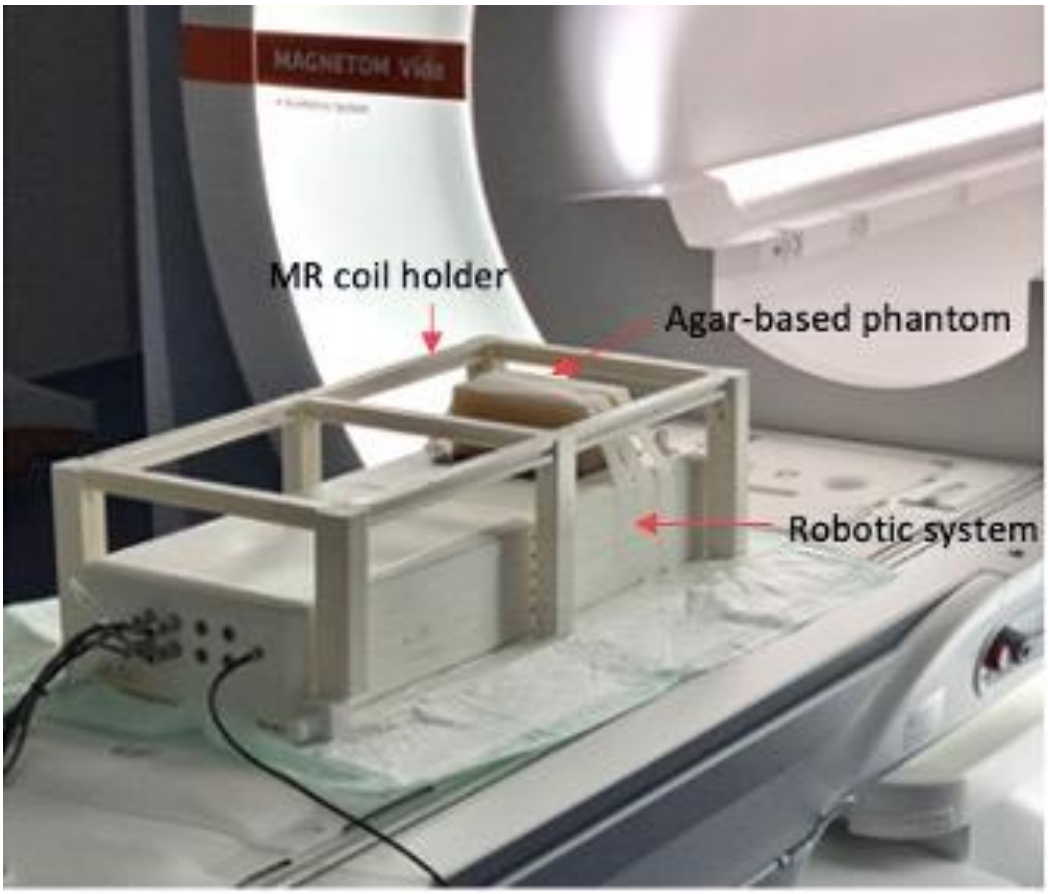
MAGNETOM Vida
MR coil holder
Agar-based phantom
Robotic system

Figure 3

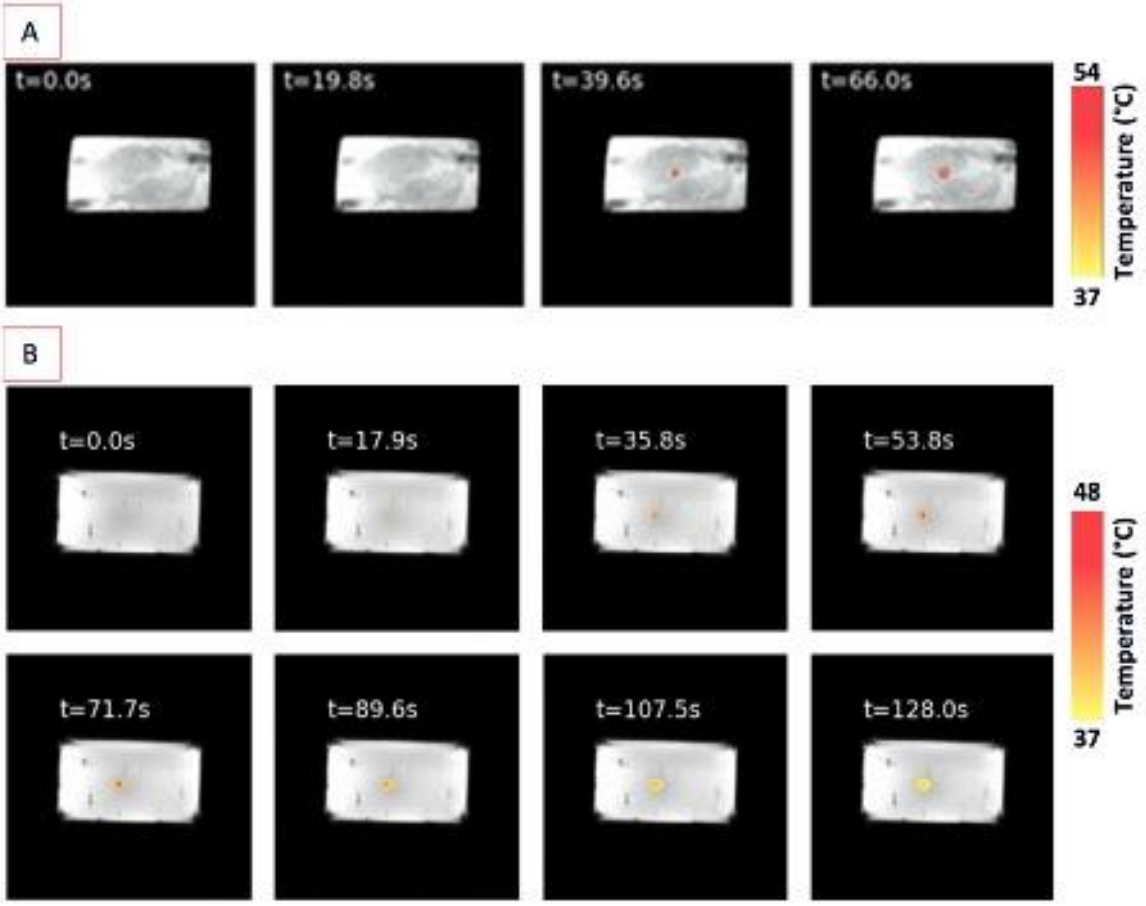
A
t=0.0s
t=19.8s
t=39.6s
t=66.0s
54
Temperature (°C)
37
B
t=0.0s
t=17.9s
t=35.8s
t=53.8s
48
Temperature (°C)
37
t=71.7s
t=89.6s
t=107.5s
t=128.0s

Figure 4

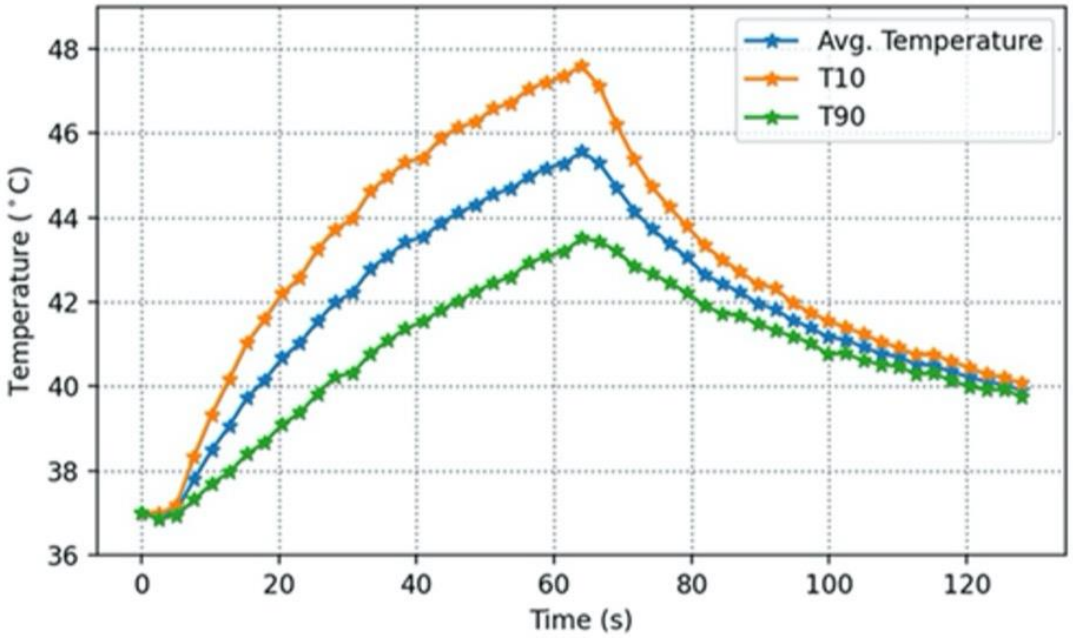
Avg. Temperature
T10
T90
Temperature (°C)
Time (s)
48
46
44
42
40
38
36
0
20
40
60
80
100
120

Figure 5

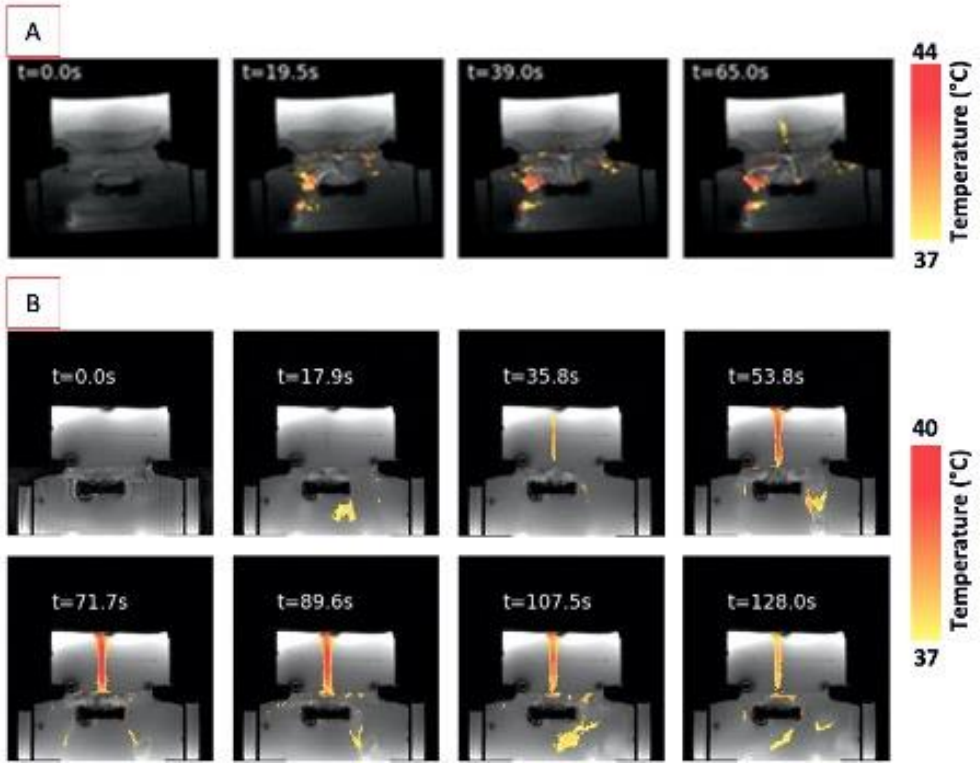
A
t=0.0s
t=19.5s
t=39.0s
t=65.0s
44
Temperature (°C)
37
B
t=0.0s
t=17.9s
t=35.8s
t=53.8s
40
Temperature (°C)
37
t=71.7s
t=89.6s
t=107.5s
t=128.0s

Figure 6

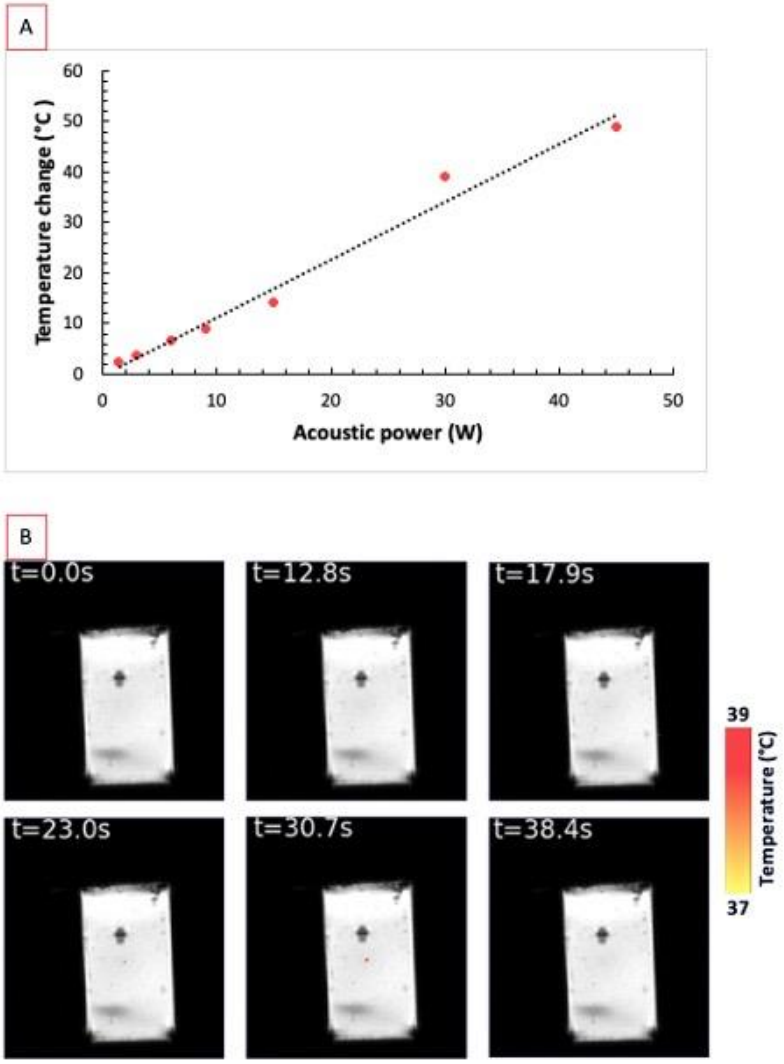
A
Temperature change (°C)
Acoustic power (W)
0
10
20
30
40
50
60
B
t=0.0s
t=12.8s
t=17.9s
t=23.0s
t=30.7s
t=38.4s
39
37
Temperature (°C)

Figure 7

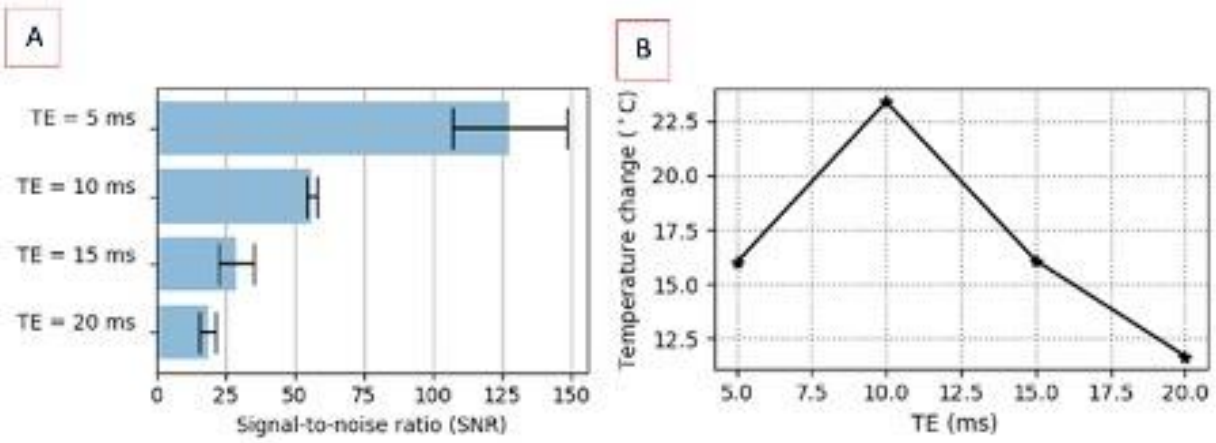
A
TE = 5 ms
TE = 10 ms
TE = 15 ms
TE = 20 ms
0
25
50
75
100
125
150
Signal-to-noise ratio (SNR)
B
Temperature change (°C)
22.5
20.0
17.5
15.0
12.5
5.0
7.5
10.0
12.5
15.0
17.5
20.0
TE (ms)

Figure 8

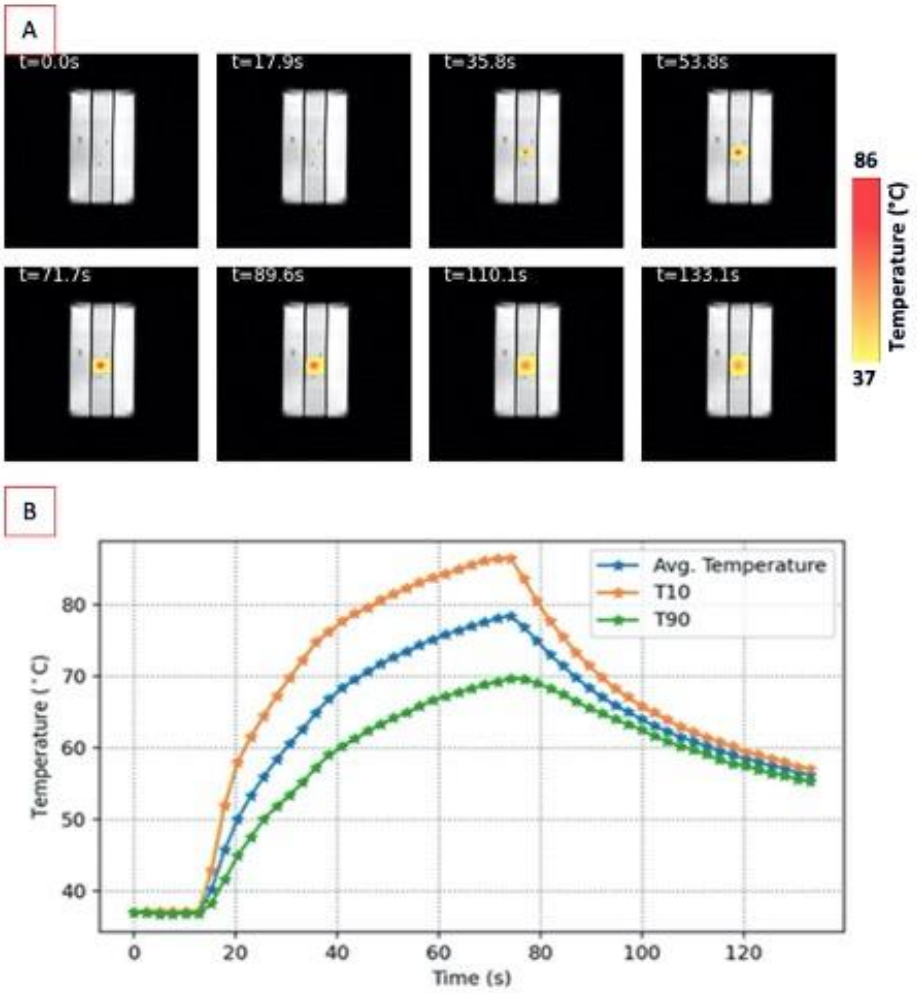
A
t=0.0s
t=17.9s
t=35.8s
t=53.8s
t=71.7s
t=89.6s
t=110.1s
t=133.1s
86
Temperature (°C)
37
B
Avg. Temperature
T10
T90
Temperature (°C)
Time (s)
40
50
60
70
80
0
20
40
60
80
100
120

Figure 9

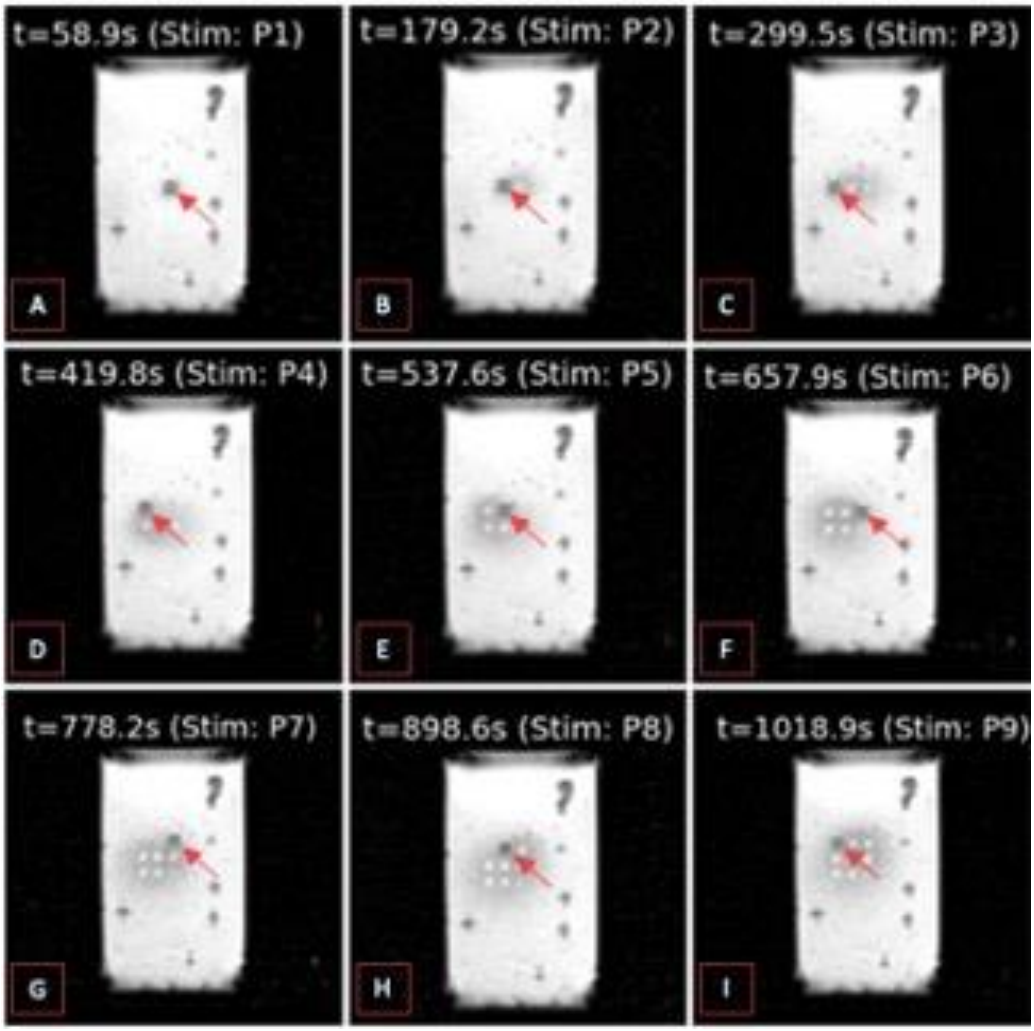
t=58.9s (Stim: P1)
A
t=179.2s (Stim: P2)
B
t=299.5s (Stim: P3)
C
t=419.8s (Stim: P4)
D
t=537.6s (Stim: P5)
E
t=657.9s (Stim: P6)
F
t=778.2s (Stim: P7)
G
t=898.6s (Stim: P8)
H
t=1018.9s (Stim: P9)
I

Figure 10

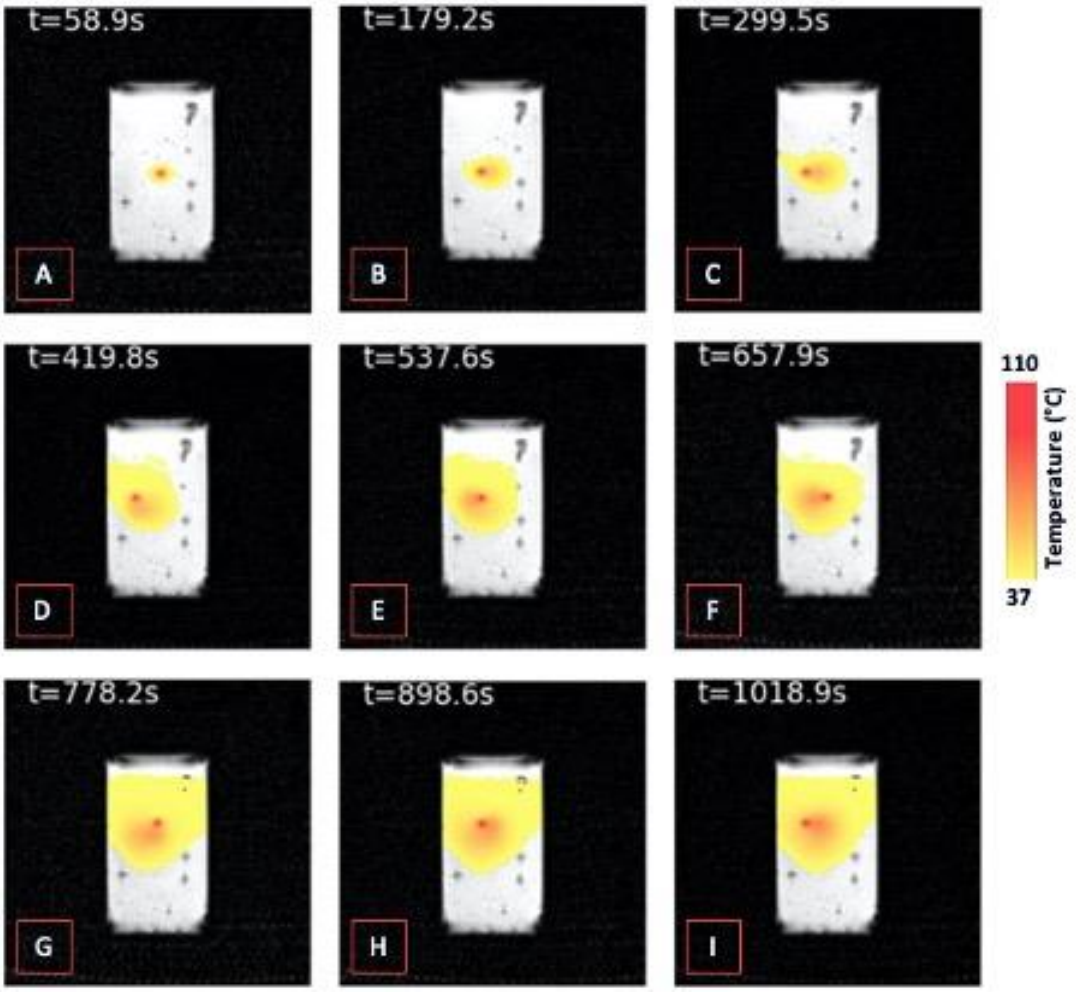
t=58.9s
A
t=179.2s
B
t=299.5s
C
t=419.8s
D
t=537.6s
E
t=657.9s
F
t=778.2s
G
t=898.6s
H
t=1018.9s
I
110
Temperature (°C)
37

Figure 11

Advanced software for MRgFUS treatment planning

Antria Filippou[a1], Andreas Georgiou[a2], Anastasia Nikolaou[a3], Nikolas Evripidou[a4], Christakis Damianou[a*]

[a] Cyprus University of Technology, Department of Electrical Engineering, Computer Engineering, and Informatics, Limassol, Cyprus.

Emails: [1]ap.filippou@edu.cut.ac.cy

[2]andreas-georgiou1@outlook.com

[3]ann.nikolaou@edu.cut.ac.cy

[4]nk.evripidou@edu.cut.ac.cy

***For correspondence contact:**

Christakis Damianou,

Cyprus University of Technology,

Electrical Engineering Department,

30 Archbishop Kyprianou Str.,

3036 Limassol, CYPRUS

Email: christakis.damianou@cut.ac.cy

Tel.: 0035725002039

Fax: 0035725002849

ABSTRACT

Background and Objectives: Herein, a user-friendly software platform for 3-dimensional Focused Ultrasound treatment planning based on Magnetic Resonance Imaging (MRI) images is presented.

Methods: The software directly retrieves and loads MRI images. Various design tools can be used on the MRI images to define the treatment area and the sonication parameters. Based on the treatment plan, the software controls the robotic motion and motion pattern of Magnetic Resonance guided Focused Ultrasound (MRgFUS) robotic systems for executing the treatment planning procedure. Real-time treatment monitoring is achieved through MRI images and thermometry. The software's functionality and performance were evaluated in both laboratory and MRI environments. Different treatment plans were designed on MRI images and sonications were executed on agar-based phantoms and polymer films.

Results: Magnetic Resonance (MR) thermometry maps were acquired in the agar-based phantoms. Exceptional agreement was observed between the software-planned treatment area and the lesions produced on the polymer films.

Conclusions: The developed software was successfully integrated with the MRI and robotic system controls for performing accurate treatment planning and real-time monitoring during sonications. The software provides an extremely user-friendly interface, while in the future it could be enhanced by providing dynamic modulation of the ultrasonic parameters during the treatment process.

KEYWORDS: software, MRgFUS, HIFU, treatment planning

1. INTRODUCTION

High Intensity Focused Ultrasound (HIFU) was first proposed as a therapeutic modality 80 years ago [1], and has since been examined as a non-invasive therapy for various applications [2]. HIFU uses pulsed or continuous ultrasonic waves that focus within a millimetre-sized area in biological tissue to induce various thermal and mechanical effects on the targeted tissue without affecting intervening or nearby organs [2]. These effects cause a significant increase in tissue temperature that instantaneously leads to coagulative necrosis of the tissue [2]. Due to significant advantages, HIFU has gained a prominent role as a non-invasive treatment for various oncological diseases and neurological applications [3].

HIFU therapeutic procedures are performed with systems generally guided by either conventional Ultrasound (US) or Magnetic Resonance Imaging (MRI), offering visualization of tissue anatomy and monitoring during the targeted treatment [4]. While US guidance offers the benefits of cost-effectiveness [5], MRI is increasingly preferred since it provides enhanced spatial tissue anatomy [6] and near real-time monitoring of the temperature increase through the employment of Magnetic Resonance (MR) thermometry, resulting in accurate feedback of tissue ablation [7]. Notably, clinically available US-guided or MRI-guided focused ultrasound (MRgFUS) systems are integrated with a user-friendly system control and treatment planning and monitoring software [3] that incorporates essential functionalities for safe execution of the targeted treatment. The main treatment planning and monitoring functionalities of software platforms of commercially available systems are listed in Table 1. Generally, these software platforms provide manual user-defined treatment planning on pre-operative images directly acquired with the employed guidance modality (US or MRI), automatic segmentation and overlay of the sonication area on the image according to the user-planned region of interest (ROI), transducer localization and system control for sonications of the ROI according to the

75 treatment plan, monitoring and possible adjustment of the plan during treatment, as well as the
76 ability of post-operative image acquisition for evaluating the extent of the ablation [8].

			Main Features	
Software	**Company**	**Imaging Modality**	***Treatment Planning***	***Treatment Safety and Monitoring***
JC-HIFU software	HAIFU (China)	US	• User defines treatment area margins on US images [9] • Treatment planning on multiple treatment area US images acquired based on User-defined slice spacing [9] • Choice between linear or dot treatment mode [9] • Ultrasonic parameters defined for both linear and	• Dot mode: Varied ultrasonic parameters can be commanded for individual ablation points [9] • Transducer localization through focal point overlay on US images [11], [12] • Focal point overlayed as yellow oval for executed sonications [11] • Subsequent sonications shown through focus image overlay as green oval [12]

			dot treatment modes [9], [10] • Linear mode: Length and direction of linear ablation zone specified [9] • Dot mode: Space between ablation zones defined to create voxel ablation areas [9] • Manual delineation of treatment and sensitive areas [13], [14] • Treatment area automatically segmented in multiple treatment units [13], [14] • User decision-making for treatment unit inclusion in treatment plan on individual basis [14]	
ECHOPULSE system software	Theraclion (France)	US		• Power for first treatment unit adjusted until production of hyperechoic marks (HEM) on US images [13], [14] • Automatic treatment of remaining units executed with HEM-producing power [14] • Ultrasonic parameters can be adjusted anytime during treatment [14]

			• Constant sonication time and cooling period commanded for all treatment units [13]	
			• Transducer registration with MR tracking coils [15] • Manual definition of sonication ROI and areas at risk on MRI images [16]–[19] • Supports import of CT images to adjust for beam aberrations due to intervening bone structures [20] • Predefined treatment protocols based on anatomy and size of target organ [18] • 3D treatment plan automatically generated [19]	• Colour-coded sonication safety status of segmented sonication points [21] • Manual modification of acoustic energy, sonication duration and acoustic power [16], [18], [21] • Automatic adjustment of sonication parameters upon cavitation presence [22] • Ultrasonic beam simulated on images [17], [18], [21] • MR thermometry generated temperature graph of each sonication [17], [23]
ExAblate systems software	Insightec (Israel)	MRI		

				• Areas marked with blue colour once sonicated with necrotic level temperatures [21] • Colour-coded sonication status overlayed on image [24], [27] • Non-sonicated points overlayed with green colour [24] • Sonicated points overlayed with yellow colour [27] • MR thermometry-based temperature feedback of focal point, near and far-field regions [26] • Manual adjustment of sonication parameters during treatment [26] • Colour-coded MR thermometry temperature and thermal dose values overlayed on MRI images [28]
Sonalleve system software	Profound (Canada)	MRI	• Manual choice of ellipsoidal treatment area [24] • User definition of oval sonication points of varied diameters [25], [26] • Set sonication durations for sonication points of varied diameters [24] • Varied acoustic power and frequency can be assigned for each sonication point [26]	

				• Closed-feedback temperature algorithm accounts for adjacent sonication heating [28], [31]
TULSA-PRO system software			• Target area boundary manually defined [28], [29] • Transducer registration achieved using fiducial markers [30]	• Ultrasound intensity, frequency and delivery rate dynamically adjusted to exceed necrotic temperatures [28], [31] • Colour-coded MR thermometry temperature and thermal dose maps superimposed on MRI images [31]
Thermoguide software	Image Guided Therapy (Pessac, France)	MRI	• 3D rectangular treatment trajectories [32] • Transducer registered with 3D-printed guide employed on transducer and alignment of simulated transducer	• Real-time monitoring with MR thermometry temperature maps [34] • Thermal dose maps generated post-sonications [34]

	with the guide as shown on MRI images [33] • Manual definition of sonication points on MRI images [32] • Sonication points can also be defined by inserting coordinates [32] • Mechanical and electronic transducer steering can be combined [32], [33] • Frequency, sonication duration, power, amplitude and time between sonications can be commanded [32] • Electronic steering: focal depth, number of trajectory repetitions and time between repetitions

	can be commanded
	[32]

Table 1: Treatment planning and monitoring features of software platforms of commercial systems.

Typically, since US-guided HIFU systems incorporate the ultrasonic equipment required for acquisition of treatment planning and monitoring US images [2], [13], [35], the integrated software incorporate treatment planning and monitoring functionalities in either single [14], [35] or multiple [9] platforms. The clinical US-guided JC-HIFU system (HAIFU, Chongqing, China) that offers treatment of liver, kidney, and breast tumours [2] is integrated with several monitors, one featuring software for treatment planning, transducer position control and ultrasonic parameters control, and one dedicated to treatment monitoring using US images [9]. Contrary, the US-guided ECHOPULSE system (Theraclion, Paris, France) utilised for clinical treatment of benign thyroid [13] and breast nodules [14], [35] is integrated with a treatment planning software that incorporates essential functionalities in a single interactive touch screen interface [13], [35].

Comparably, software platforms of commercial MRgFUS systems communicate with MRI scanners for image acquisition and display, with the various MRgFUS systems compatible with scanners from specific MRI manufacturers [36]. Insightec (Haifa, Israel) is considered the major manufacturer of commercial MRgFUS systems [3], with the various ExAblate systems (Insightec) approved for clinical treatment of prostate cancer, uterine fibroids and bone metastases as well as for neurological applications [3]. The ExAblate systems (Insightec) are integrated with a software platform that incorporates essential functionalities required for MRgFUS treatment planning [8]. Notably, different software platforms with similar functionalities exist for exclusive use with each of the commercial ExAblate systems (Insightec). The ExAblate software platforms (Insightec) communicate with MRI scanners for

image acquisition and display, and through multiple graphical user interface (GUI) buttons guide the physician through the treatment planning process [16], while during treatment, the real-time temperature increase of sonications is controlled using MR thermometry and visualized with a graph [17], [23]. Similarly, Profound (Toronto, Canada) manufactures the commercially available Sonalleve system offering clinical MRgFUS treatment of uterine fibroids [24], [37] and pain palliation for bone metastases [25], [27] and the TULSA-PRO system for MRgFUS treatment of prostate cancer [28], [29], [38]. Correspondingly, each system is integrated with a user-friendly treatment planning software with all basic functionalities, offering communication with the MRI, manual definition of the sonication ROI on the MRI image, generation and overlay of the treatment plan on the image, control of the system for performing ablation, and treatment monitoring with MR thermometry [24], [25], [28], [29]. Interestingly, besides production of MR thermometry maps during treatment [31], [37], both software platforms perform thermal dose calculations [39] that are colour-coded and superimposed on the image after individual sonications [31], [37].

The increasing employment of MRgFUS for clinical applications has led to the development of a significant amount of preclinically developed MRgFUS robotic systems [32], [40]–[47]. Software platforms of commercial MRgFUS systems are considered expensive for preclinical studies, and although many choose an in-house developed software [40]–[48], some perform such studies based on the commercial third-party Thermoguide software (Image Guided Therapy, Pessac, France) [32], [33]. Thermoguide (Image Guided Therapy) offers the ability to plan 3-dimensional rectangular treatment trajectories [32] and achieves real-time treatment monitoring using MR temperature maps, with thermal dose maps additionally generated post-sonications [34].

Characteristic is the development of the first and sole preclinical software, the TRANS-FUSIMO, that accounts for organ motion during MRgFUS treatment of abdominal targets

[49]–[52]. The TRANS-FUSIMO software communicates with MRI scanners by General Electric (Chicago, Illinois, USA) and controls the ExAblate Body system (Insightec) [49], [52] for efficient energy delivery [50], adjusting the beam for organ motion [49]. The software comprises multiple tabbed pages for setting treatment parameters for the various sonication types [52], while treatment planning on MRI images initially includes user-definition of organ locations followed by planning of the treatment trajectory, and automatic simulation and overlay of organ motion on the treatment planning trajectory on the MRI image [51]. Previously, our group developed a software written in C # (Microsoft Corporation, Washington, USA) for controlling preclinical MRgFUS robotic systems [48]. This software provides basic functionalities of MRgFUS treatment such as communication with the MRI for image retrieval, treatment using mechanical motion according to user-defined rectangular grid trajectories, and monitoring using MR thermometry [48]. Lately, this software has been enhanced to allow treatment planning to be performed on MRI images using user-defined non-uniform sonication areas with specific algorithms achieving full coverage of the segmented ROI [53]. Nevertheless, the interface is slightly complex, with the various functionalities (treatment planning, ultrasound control, MR thermometry) initiated from numerous tabbed pages [48].

In the present study, an in-house software was developed for controlling several MRgFUS robotic systems dedicated to specific therapies, previously developed by our group [40]–[45]. These systems [40]–[45] are integrated with a single element spherically focused transducer and offer movement in up to 4 computer-controlled axes (X, Y, Z, Θ). The software controls several functionalities (robotic motion, motion pattern, sonication parameters) of the robotic systems and translates these for active treatment planning and therapy using preoperative MRI images. The software interfaces with the MRI so that Digital Imaging and Communications in Medicine (DICOM) images can be directly retrieved from the scanner. The

DICOM images are used by the software for treatment planning purposes as well as for monitoring during the HIFU treatment through MR thermometry [7]. The software was merely based on the previously reported software [48] and was mainly developed using the C # language (Microsoft Corporation), with some parallel scripts developed in the Python language (Python Software Foundation, Wilmington, Delaware, USA), offering additional functionalities. Moreover, software development has progressed from the Windows platform (Microsoft Corporation) [48] to the Windows Presentation Foundation (WPF) platform (Microsoft Corporation) to result in a modern, more ergonomic and user-friendly GUI offering rapid execution of commands and flexibility for future expansions. Table 2 lists the main treatment planning and monitoring functionalities supported by the in-house developed software.

Main Features	
Treatment Planning	***Treatment Safety and Monitoring***
• Digital transducer registration • User delineates sonication area on MRI images • Choice between single point, grid pattern and non-uniform sonication trajectories • Step size between sonication points defined • Type of transducer motion path commanded • Sonication parameters defined • Choice between pulsed or continuous mode • Continuous mode: power, frequency, sonication period, and time between sonications commanded • Pulsed mode: power, frequency, pulse time, time between pulses, pulse count and sonication time are set	• Colour-coded sonication point status overlayed on image • Transducer localized through dynamic digital marker overlay on MRI image • MR thermometry-based temperature graph of each sonication point • Colour-coded MR thermometry temperature map of each sonication point

Table 2: Treatment planning and monitoring features of the developed software.

2. MATERIALS AND METHODS

2.1 Software development

Figure 1 shows the flowchart of the treatment planning procedure using the developed MRgFUS software. To initiate the treatment planning procedure, the software performs a robot positioning process by aligning the transducer integrated within the system to the origin of the robotic axes, thus offering targeted treatment according to the user-selected MRgFUS robotic system. The software was developed in a manner to offer treatment planning in layers, resulting

in planning and therapy in the 3-dimensional space. A pre-operative DICOM image (acquired with the MRI at a slice location set at the level of the targeted area), which corresponds to a single layer, is selected for treatment planning purposes. The user specifies the Z-position of the layer which is then interpreted into the corresponding height on the Z-axis of the robotic system for executing HIFU exposures on that specific height. In this sense, treatment in the 3-dimensional space can be performed through the creation of multiple layers with numerous Z-positions. On each layer, the user defines the sonication area and the configuration for robotic motion (grid pattern, step size) as well as the sorting type of the sonication points. Finally, the amplifier (sonication) parameters (power, frequency, sonication time, time between sonications) are selected, resulting in execution of the treatment plan according to the designated sonication and motion parameters. Notably, the software provides a choice between continuous or pulsed ultrasound signals for respectively employing the thermal or mechanical effects of ultrasound, according to the desired therapeutic application. Specifically, continuous signals can be employed to achieve thermal tissue ablation, while the pulsed mode can be commanded to exploit the non-thermal effects of HIFU that are usually applied to attain targeted drug delivery locally within tissue and HIFU-mediated disruption of the Blood Brain Barrier (BBB) [54].

Figure 2 shows the GUI of the developed MRgFUS software, with all buttons required for the treatment planning procedure. A single layer is created utilising the respective “create layer” button (Figure 2). A DICOM image of an agar-based phantom has been selected and loaded into the software for treatment planning purposes. The user can navigate the DICOM image using the image “zoom/pan” tool shown in Figure 2. Accordingly, the user has the option to create or delete layers (buttons in Figure 2) so as to generate treatment plans on various layers, resulting in treatment in the 3-dimensional space.

2.2 Treatment planning procedure using the software GUI

The different elements of the software GUI as shown in Figure 2, can be utilised for execution of the treatment planning procedure as undermentioned.

2.2.1 Robot panel

Through the robot panel, the software provides the opportunity to the user for easy integration of new robotic systems resulting in quick adaptability and interchangeability between several MRgFUS robotic devices dedicated to specific therapies [40]–[45]. For addition of new robotic systems, the user specifies the degrees of freedom and the motion range on each axis. During initial software launch, all available robotic systems are listed on the panel through illustrative images, with the user selecting the desired robotic system for MRgFUS treatment. The software receives all motion parameters of the user-selected robotic system (degrees of freedom and motion range on each axis), thus offering accurate treatment of the targeted area. The motion range on each robotic axis designates the available treatment area that is presented with a dashed red boundary on the DICOM image as shown in Figure 2.

2.2.2 Home menu

The treatment planning process is initiated by the home menu, by performing the robot positioning procedure according to the user-defined DICOM image. For this purpose, a DICOM image of the single-element focused transducer as integrated at the origin of the axes within the robotic device is employed. The software automatically produces a yellow circle with the specified diameter of the transducer. By overlapping the yellow circle on the circumference of the transducer on the DICOM image (creation of two concentric circles) a marker appears at the centre of the active element of the transducer as shown in Figure 3. The marker is then displayed on the preoperative DICOM image employed for treatment planning, accurately depicting the location of the transducer within the available treatment area as shown in Figure 2. In this regard, this procedure allows for accurate positioning of the transducer and translation of its actual position during treatment. Consequently, robotic motion of the

transducer can be automatically initiated after selection of the sonication area. Nevertheless, a functionality of manual motion control has also been integrated in the software (see relevant button in Figure 2) allowing manual control of the motion of the robotic system in up to 4 degrees of freedom (X, Y, Z, Θ).

2.2.3 Sonication area selection

The user manually defines the sonication area on the preoperative DICOM image through a choice of three different sonication area design tools ("single point", "grid pattern", and "non-uniform" area). The selected sonication area can be easily deleted ("sonication area deletion" button shown in Figure 2) and redefined prior to the treatment process. Single or multiple sonication points can be defined with the "single point" tool at various locations within the available treatment area, resulting in treatment of several randomly selected points. Accordingly, a grid pattern sonication area can be easily selected ("grid pattern" tool), with the user specifying the size of the sonication area and the step size on each axis (X, Y) that defines the motion resolution of the robotic system. Particularly, according to the treatment strategy, small step sizes can be commanded to create overlapping areas of ablation, while larger step sizes can be utilised to create discrete cigar-shaped necrotic areas. Correspondingly, a non-uniform area can be sonicated after selecting the appropriate design tool ("non-uniform" area) and creating the ROI as a freehand trajectory on the image. Notably, for sonicating the non-uniform area, movement of the robotic system is performed according to a path planning algorithm previously described for full coverage of a ROI [53]. Similarly, the motion resolution is indicated by the user who commands the step size for motion in the X and Y axes.

2.2.4 Sorting type selection

Upon definition of the sonication area, the software provides the choice of selecting the sorting type of the sonication points and thus the motion path of the transducer. Nevertheless, sorting type selection is available merely for the grid pattern and non-uniform sonication areas.

Noteworthy, for visiting sonication points that were randomly defined with the "single point" design tool, an algorithm was integrated into the software, allowing motion of the robotic system according to the order in which the single points were first arranged on the DICOM image and following a Zig-Zag motion pattern. For sonication areas designed with the "grid pattern" or "non-uniform" tools, motion of the robotic system during treatment is performed according to a user-defined arrangement of the sonication points and following predetermined motion algorithms. In this regard, the user decides between a sequential, spiral, or Zig-Zag arrangement of the sonication points with motion of the robotic system initiated accordingly. The designated sonication area is displayed on the DICOM image within the available treatment area and with the initial location of the transducer at the origin of the robotic axes indicated with the marker. Figure 4 shows a representative example of a 5×5 grid pattern sonication area with a 10 mm step size as displayed on the preoperative DICOM image as well as the sorting type selection for visiting the sonication points.

2.2.5 Amplifier settings panel

The respective section of the GUI sets the amplifier parameters that control the power output of the ultrasonic transducer. It is worth mentioning that the software automatically connects to the amplifier during launch, through Universal Serial Bus (USB) interfaces. Upon selection of the sonication area and the sorting type of the sonication points, the user specifies the type of the ultrasound signal (continuous or pulsed) and the respective amplifier parameters on a simple pop-up panel as shown in Figure 5, for execution of the treatment procedure. The choice of the continuous signal appears as a default upon launch of the pop-up panel, where the user specifies the power, frequency, sonication time (on time), and time between sonications (delay). However, the user can switch to a pulsed signal by clicking on the relevant button, and defining the respective parameters (% power1, % power2, frequency, pulse time, time between pulses, pulse count, and sonication time) for executing a treatment procedure that

283 employs the mechanical effects of ultrasound. During the treatment procedure, the amplifier
284 parameters (forward, reverse, and effective power) can be continuously monitored through the
285 amplifier settings monitoring panel shown in Figure 5.

286 **2.2.6 Treatment planning process**

287 The treatment process can be easily implemented from the treatment planning
288 procedure control (Figure 5). During the process, the user can start, stop or pause the treatment
289 process on the existing layer (designed on the DICOM image) as well as easily navigate
290 between created layers for performing treatment in the 3-dimensional space. A functionality
291 for active monitoring of the sonications during the treatment process was integrated in the
292 software. In this regard, during a sonication cycle (sonication of a single point of the sonication
293 area) the sonication points displayed on the DICOM image are colour-coded according to their
294 sonication status as shown in the timing diagram in Figure 6. Points that have not been
295 sonicated are shown with a blue colour that changes to green when the transducer reaches the
296 corresponding sonication point. Throughout the sonication time (time-on of the amplifier) the
297 point appears with a yellow colour that instantly changes to red after the end of the sonication
298 (time-off of the amplifier). During the time-off period (user-defined delay time) the transducer
299 progressively moves to the next sonication point, while concurrently the time required for this
300 robotic motion (robot movement delay) is calculated and deducted from the time-off period.
301 Thereby, on the next sonication point, the transducer is deactivated for a total time that does
302 not exceed the user-defined delay time. Notably, the transducer marker shows the actual
303 position of the transducer relative to the treatment planning DICOM image. Correspondingly,
304 during treatment, the marker is shown on the point of the sonication area subjected to
305 sonication, with its position continuously changing according to the user-defined sonication
306 path. Figure 7 shows an indicative example of the colour-coded sonication monitoring during
307 a treatment procedure of a user-defined 5×5 grid pattern sonication area with a 10 mm step

size. Figure 7 additionally shows the transducer marker translating the actual position of the transducer relative to the points of the sonication area.

More importantly, a feature has been integrated in the software allowing the automatic return of the transducer to the origin of the robotic axes after completion of the treatment procedure. Throughout the manuscript, this feature is referred to as the "Homing" procedure. The origin of the robotic axes of the system (lower-left corner of the World Frame Map of the robotic device) acts as the reference point for the transducer through a sensor, resulting in accurate feedback on the position of the transducer. Figure 8 shows the reference point diagram of the "Homing" functionality that was integrated in the developed software. Implementation of this functionality allows robotic motion in any consequent treatment procedures to be initiated from the origin of the axes resulting in accurate positioning prior to treatment.

2.2.7 DICOM monitoring panel

During the treatment procedure, high-resolution DICOM images of each sonication point are acquired by the MRI scanner and directly retrieved from the DICOM monitoring panel providing imaging of the sonication points. It is worth stating that DICOM images of each sonication point are acquired at the corresponding slice location as the pre-operative image employed for treatment planning, thus providing imaging at the level of the targeted area. The DICOM monitoring panel was developed in the Python language (Python Software Foundation) in a software script that runs parallel to the main treatment planning software. For each sonication point, high-resolution images are acquired by the MRI scanner throughout the time delay allowed between sonications, resulting in real-time visualization and monitoring of the ablation effects on each individual point. Consequently, as a prerequisite for multiple sonications, the user-defined time delay needs to exceed the scan time required by the MRI for image capture.

2.2.8 MR thermometry panel

The main treatment planning software communicates with the MRI scanner through a separate script programmed with the Python language (Python Software Foundation) for near real-time temperature monitoring during treatment using MR thermometry [7]. Throughout the treatment procedure, DICOM images of the treatment area are acquired, and the MR thermometry monitoring panel demonstrates a graph and a colour-coded thermal map indicating the temperature at the ROI that is defined as the point undergoing sonication. Figure 9 shows the flowchart of the parallel execution of the MR thermometry monitoring script and the main treatment planning software. The user defines the thermometry parameters (ROI, T tolerance value, baseline temperature, coil polarity) essential for temperature calculations. Interestingly, the T tolerance value is a decimal number that defines the signal-to-noise ratio (SNR) limit and therefore affects temperature calculations. Initially, the acquired DICOM images and the ROI are received by the MR thermometry script and the temperature data and thermal maps are calculated using the proton resonance frequency (PRF) shift method [7]. The temperature data and thermal maps of the ROI are displayed on the panel and automatically saved, with the ROI repeatedly updated for each sonication point during the treatment procedure. ROI updates occur since the initial robot positioning procedure translates the position of the transducer relative to the sonication area overlapped on the DICOM image. At 100 ms intervals, the thermometry script examines whether new DICOM images have been acquired by the MRI or the thermometry parameters have changed, whereupon new thermometry data are calculated. Graphs and thermal maps are automatically updated for each sonication point, throughout the sonication and time delay (i.e., cooling periods) periods, offering near real-time monitoring during treatment resulting in increased safety. The MR thermometry script automatically terminates upon sonication of the last point within the user-defined sonication area. Specifically, the script is terminated after the end of the cooling period

of the last sonication point, providing the user with temperature feedback for a specified interval after the end of the last exposure.

2.3 Evaluation of the functionality of the software

2.3.1 MRgFUS robotic system

A robotic system developed for preclinical applications of MRgFUS studies [40] was employed to evaluate the accuracy and functionality of the in-house developed software. The robotic system was developed using an industrial 3D printer (FDM400, Stratasys, Minnesota, USA) and Acrylonitrile Butadiene Styrene (ABS) material. The manufacturing materials were specifically selected to provide MR compatibility for safe and accurate operation within the MRI environment [40]. The robotic device provides motion in 4 computer-controlled axes (X, Y, Z, Θ) that is actuated by piezoelectric motors (USR30-S3, Shinsei Kogyo Corp., Tokyo, Japan) and controlled with optical encoders (US Digital, Vancouver, Washington, USA). The robotic mechanisms provide motion to a single element-focused ultrasonic transducer that is extended through an arm from the mechanisms to a separate water-filled section. For the purposes of this study, the robotic system was integrated with a transducer having a frequency of 2.75 MHz, a diameter of 50 mm, and a radius of curvature of 65 mm. The robotic mechanisms and water-filled sections are integrated within a compact enclosure that can be placed within the table of the MRI scanner. An acoustic window on the enclosure of the water-filled section allows propagation of ultrasonic beam from the transducer to the target, resulting in a bottom-to-top approach to treatment. For motion control purposes, an in-house developed electronic system with an Arduino microcontroller (Arduino, New York, USA) was employed. The developed software communicates with the electronic driving system through USB interfaces. Correspondingly, the transducer was connected to an amplifier (AG1016, T & C Power Conversion, Rochester, NY, USA) for powering purposes.

2.3.2 Tissue mimicking materials

DICOM images of tissue-mimicking materials were utilised by the software for treatment planning purposes in both MRI and laboratory environments. The software automatically executed the sonication protocols according to the treatment plans with sonications performed on agar-based phantoms [55]–[58] and polymer Polyvinyl Chloride (PVC) films. Sonication protocols within the MRI environment were executed on an agar-based phantom containing 6 % weight per volume agar (10164, Merck KGaA, Darmstadt, Germany) known to possess similar acoustic properties with specific human tissues [55]–[58]. Accordingly, sonication protocols in the laboratory environment were executed on thin PVC films (0.7 mm thickness, Fortus FDM400mc print plate, Stratasys) that were previously shown to result in deformation of the film and lesioning upon exposure to HIFU [53], [59], and have thus lately emerged as inexpensive materials for quality control of MRgFUS hardware and software [60].

2.3.3 Evaluation in MRI and MR thermometry

The robotic system was placed in a clinical 3 T MRI scanner (Magneton Vida, Siemens Healthineers, Erlangen, Germany) with the agar-based phantom positioned on the acoustic window of the robotic system to evaluate proper communication between the software and the MRI scanner. The electronic system, amplifier, and software (installed on PC) were placed outside of the main scanning room and inside the control room where they were connected to the robotic system through a cable panel. The water section of the robotic system was filled with deionized and degassed water for coupling purposes. A body coil (Body 18, Siemens Healthineers, Germany) and a 2D Fast Low Angle Shot (FLASH) sequence were utilised for MRI imaging. The 2D FLASH sequence had a 2.6 s temporal resolution utilising the following parameters: Repetition Time (TR)=20 ms, Echo Time (TE)=10 ms, Acquisition Matrix=256×256, Field of View (FOV)=28×28 cm^2, Flip Angle (FA)=35°, Number of Excitations (NEX)=1, slice thickness=10 mm. The software was employed to perform treatment planning according to the acquired 2D FLASH image of the phantom using the

407 "single point" design tool. A single point was defined on the image and robotic movement was
408 automatically executed to that location. A single sonication at the defined location was
409 performed using a moderate acoustical power of 50 W for a sonication time of 60 s at a focal
410 depth of 30 mm. The DICOM images acquired during sonications were utilised by the software
411 for MR thermometry purposes and production of the colour-coded temperature map indicating
412 the induced temperature.

413 **2.3.4 Evaluation of the software on PVC films**

414 In the laboratory environment, the PVC films were correspondingly positioned on the
415 acoustic window of the robotic device at a distance of 60 mm from the active element of the
416 transducer. Similarly, degassed water was added in the water section to the level of the PVC
417 film interface, thus acting as the coupling medium. Noteworthy, correct water level acts as a
418 main principle for the formation of white lesions on the PVC films since this is attributed
419 mainly due to reflection effects observed between the PVC film-air interface [53]. MRI images
420 of the agar-based phantom acquired as abovementioned, were inserted in the software for
421 treatment planning purposes. The various treatment planning design tools of the software were
422 employed for designing different treatment plans and sonication areas on the images.
423 Sonications on each point of the planned sonication areas were executed at an acoustical power
424 of 6 W for a sonication time of 5 s and using a 30 s delay time between successive sonications.
425 These sonication parameters were utilised after iterative experiments performed in a previous
426 study [60], wherein the optimal parameters for lesion formation on the plastic films and the
427 impact of the employed parameters on the dimensions of the formed lesions were investigated.
428 Based on previous results, where an energy of 36 J (power of 6 W for 6 s duration) resulted in
429 the formation of lesions having approximately a 5 mm diameter [60], the acoustic power of 6
430 W was chosen with a sonication time of 5 s to result in white lesions with a relatively small
431 diameter (~3-4 mm). Notably, the sonication time of 5 s was selected following

experimentation with varied sonication durations, while the time delay of 30 s was chosen to allow for adequate cooling of the PVC films between exposures. Visual evaluation of the accuracy of the in-house software was performed through a comparison between the user-defined treatment plan and the lesions formed on the PVC films as a result of the sonications.

Initially, seven single points were randomly selected by the user on the image by using the "single point" design tool. Prior to the treatment process, a single sonication was executed at the reference point of the transducer to evaluate proper movement of the transducer and the accuracy of the robotic motion. The transducer covered the planned sonication area following the Zig-Zag motion algorithm. The accuracy of robotic motion was evaluated through a digital caliper (ROHS NORM 2002/95/EC) employed for measuring the distances between the lesions formed on the film and comparing with the corresponding distances of the software. The "single point" design tool was additionally utilised for designing a multiple-point sonication area whose points form the abbreviation "CUT" (Cyprus University of Technology). Movement of the transducer along the planned trajectory was performed to evaluate appropriate communication between the software and the robotic device.

Thereafter, the "grid pattern" tool was employed for designing a cuboid 10×10 grid pattern sonication area on the DICOM image with a defined step size of 1 mm. Sonication of the points was performed following a sequential motion of the transducer with each spot sonicated with an acoustical power of 6 W and a sonication time of 5 s. Finally, a non-uniform sonication area was designed on the image using the "non-uniform" design tool. Each sonication point of the area was visited using a 4 mm step size. Notably, the two commanded step sizes were selected following the results of a previous study [53] that revealed that step sizes greater than 2 mm were required to create discrete lesions on the PVC films. In this sense, considering the herein use of a lower acoustic energy (~ 30 J) compared to the previous study

[53], the step sizes of 1 mm and 4 mm were conservatively chosen for creating overlapping and discrete lesions, respectively.

3. RESULTS

Proper communication between the developed software and the MRI scanner was evidenced from the MRI experiments. Appropriately, real-time loading of the DICOM images of the agar-based phantom to the software was accomplished, while proper functioning of the MR thermometry panel was attained. Figure 10 shows an indicative example of the colour-coded MR thermal map produced by the software on axial and coronal planes, as a result of the single sonication executed on the agar-based phantom. A temperature change of approximately 46 ^{o}C was recorded, indicating sufficient heating of the agar-based phantom and accurate near real-time monitoring of the induced temperature. Subsequently, the acquired MRI images of the phantom were utilised for assessing the accuracy and functionality of the software through treatment plans designed with the various design tools and with sonications executed on PVC films. Figure 11 shows the seven-random-point sonication area planned through the software and the representative lesions formed on the PVC film as a result of the sonications. Table 3 shows the distances between the sonication points as measured with the caliper and the corresponding distances from the software as shown in Figure 11. Accurate robotic motion was confirmed, as evidenced by the caliper-measured and software-measured distances between the sonication points. Figure 12 shows the multiple point sonication area forming the abbreviation "CUT" and the corresponding lesions formed on the PVC film after exposure at the set ultrasonic parameters (acoustical power of 6 W for sonication time of 5 s). Appropriately, extreme similarities between the user-defined area and the film lesions were observed, indicating proper communication between the software and the robotic system as well as the ability of the software in covering non-linear areas. Employment of the "grid pattern" design tool for sonication of a 10×10 grid area with the use of a 1 mm step size was proven adequate

for the formation of overlapping lesions as shown in Figure 13. Similarly, the employment of the "non-uniform" design tool for sonication of an irregularly shaped area and the use of a 4 mm step size between successive sonication points resulted in the formation of discrete lesions as shown in Figure 14. Once again, an exceptional agreement was observed between the non-uniform sonication area planned using the software and the lesions formed on the PVC films.

Distance number	Software measured distance between sonication points (mm)	Caliper measured distance between sonication points (mm)
1	18.6	18.5
2	16.5	16.5
3	14.3	14.3
4	17.0	17.0
5	21.1	20.3
6	20.6	20.5

Table 3: Distances between the seven random sonication points as measured from the lesions formed on the film compared to the corresponding software distances.

4. DISCUSSION

In this study, a software platform was developed for controlling several preclinical robotic systems previously developed for various MRgFUS applications that offer motion in up to 4 computer-controlled axes (X, Y, Z, Θ) [40]–[45]. The software was developed with the main objective to interface with the MRI so as to provide control of the robotic motion and the ultrasonic exposures, based on treatment planning executed on preoperative MRI images. Furthermore, near real-time monitoring of the temperature during the targeted treatments can be achieved using both MR thermometry maps and temperature graphs. The software utilises the loaded medical MRI images for user-defined treatment planning achieved by employing

various tools. Through the interface, the various tools can be employed to design the treatment area ("single point", "grid-pattern", "non-uniform") on the MRI image and define the sonication parameters. The user inputs are then interpreted by the software for executing robotic motion according to the sonication points segmented from the defined treatment trajectory. Notably, the software manipulates the loaded treatment planning MRI image as a single layer that is correlated with a user-defined distance on the Z-axis of the robotic system, thereby providing the ability to execute 3-dimensional treatment planning and therapy through the creation of multiple layers (multiple images acquired at different slice locations).

Notably, although the current software was merely based on an existing software [48], this provides substantially added functionalities and an extremely user-friendly and more ergonomic environment. Specifically, all treatment planning and therapy monitoring procedures of the developed software have been integrated in a single panel, resulting in an improved interface and faster execution of commands compared to the previous version where the various functionalities were initiated from multiple tabbed pages [48]. Evidently, compared to the previous software [48] the current software has been enhanced, providing active treatment planning overlapped on a medical MRI image, possibility of 3-dimensional treatment planning, accurate location of the transducer before and after treatment relative to the defined treatment area, automatic return of the transducer to the origin of the axes, active monitoring of the sonication status of each point overlayed on the image, as well as near real-time monitoring of the ablation effects and induced temperature through MRI images and PRF-based MR thermometry.

The software was mainly evaluated for its functionality using one of the preclinical MRgFUS robotic systems [40] and with treatment planning performed on MRI images of an agar-based phantom [55]–[58]. The planned treatment protocols were executed through sonications performed either on an agar-based phantom [55]–[58] or thin PVC films. The latter

has lately emerged as a cost-effective tissue-mimicking material for quality control purposes of MRgFUS systems [53], [59], [60] because of its ability to form white lesions when subjected to HIFU sonications that reach temperatures greater than 55 ºC [53]. Specifically, the software was assessed for successful and accurate communication with the MRI scanner, robotic system, motion control system and amplifier, without any problems. Introduction of the robotic system within the MRI scanner and connection to the software, resulted in successful communication between the software and the MRI scanner. The software directly and successfully retrieved the acquired DICOM images from the MRI scanner, while colour-coded thermal maps were properly and rapidly calculated providing near real-time (~2.6 s) temperature monitoring during a single sonication executed at an acoustic power of 50 W for a sonication time of 60 s. Notably, with the software, thermal maps are automatically calculated during treatment (sonication and cooling periods) only upon acquisition of new MRI images. Therefore the time required for their production is dependent on the scan time of the employed MRI sequence that in turn is known to be affected by the sequence parameters [61]. Furthermore, while the agar-based phantom employed for sonications emulates human tissue-like properties [55]–[58], it differs from biological tissue in the sense that it does not possess a blood perfusion environment. Previous studies executed on similar agar-based phantoms revealed an immediate decrease in temperature after the elapsed sonication duration [56], [57], while contrary, blood perfusion in tissue might still induce temperature increases after the end of the irradiation [62]. Nevertheless, since the software also calculates and presents thermometry data throughout the user-defined time delay, accurate temperature feedback of the targeted area and any possible tissue temperature increase after irradiation would be provided during an *in-vivo* treatment procedure.

Next, a bench-top evaluation of the software was performed with treatment planning implemented on MRI images using the various treatment area design tools (“single point”,

547 “grid pattern”, “non-uniform”) and with sonications executed on the PVC films using constant
548 ultrasonic parameters (acoustic power of 6 W for a 5 s sonication time). The ultrasonic
549 parameters were sufficient to produce white lesions as a result of the sonications. Visual
550 assessment of the results proved the accuracy of the treatment planning procedure with the
551 developed software, since no differences were observed between the software planned
552 treatment trajectory and the lesions formed on the PVC films. Accordingly, an excellent match
553 was observed in caliper-measured distances and software-measured distances between points
554 of a planned seven-point treatment trajectory. As a result, effective communication between
555 the software and motion control system as well as accuracy of robotic motion were evidenced.
556 Additionally, effective and accurate treatment planning in non-linear, non-uniform areas was
557 performed with the software. A step of 1 mm was proven adequate to form overlapping lesions
558 after treatment planning in a grid pattern sonication area. Appropriately, the step of 4 mm was
559 suitable to create well-demarcated uniform discrete lesions after treatment planning performed
560 following a non-uniform trajectory.

561 Although effective and accurate execution of the treatment trajectory with the software
562 was evidenced through sonications executed on PVC films, this study is limited in the sense
563 that the properties of the employed PVC films significantly differ from those of human tissues
564 [60]. In tissue, thermal diffusion effects are naturally observed, that significantly affect
565 temperature increases throughout a HIFU treatment resulting in a non-uniform ablation of the
566 targeted area, with smaller lesions often created during initial sonications and larger lesions
567 formed towards the end of a therapeutic procedure executed with constant sonication
568 parameters [63], [64]. Consequently, adjustment of sonication parameters throughout the
569 treatment is considered essential to achieve a uniform ablation of tissue [63], [64]. Herein,
570 uniform discrete lesions formed on the employed PVC films after treatment planning with the
571 non-uniform design tool, suggest minimal thermal diffusion effects. Moreover, sonications on

572 the PVC films were executed with constant ultrasonic parameters, a condition that is often not
573 employed in the clinical setting [8]. Nevertheless, PVC films were employed for visually
574 assessing accurate execution of the treatment trajectory and effective software communication
575 with motion control systems, since these represent the most inexpensive tool for quality control
576 [60], while constant sonication parameters were applied to observe consistent software
577 communication with the amplifier.

578 Generally, the developed software integrates essential functionalities of MRgFUS
579 treatments such as treatment planning, transducer registration and localization, direct
580 acquisition of MRI images and temperature monitoring. Thereby, it is equivalent to the
581 commercial software platforms integrated with the ExAblate (Insightec) [16]–[18], [21], [23],
582 Sonalleve (Profound Medical) [24]–[27], [37] and TULSA-PRO (Profound Medical) [28],
583 [29], [31], [38] MRgFUS systems as well as the third-party Thermoguide (Image Guided
584 Therapy) software [32], [33]. The treatment area designed with the developed software is
585 overlaid on the loaded medical image, thus being in accordance with the treatment planning
586 process executed using commercial software of US-guided [11], [35] or MRgFUS systems
587 [21], [24], [29], [31]. Furthermore, temperature monitoring during sonications is achieved in
588 near real-time by visualizing MR thermometry maps and temperature graphs as already
589 followed in other commercial [17], [23], [31], [37] and preclinical software [46], [47].
590 Additionally, the colour-coded sonication status (blue, green, orange and red) of the sonication
591 points as overlayed on the image during treatment, follows a similar approach to the colour-
592 coded sonication status provided by the Sonalleve software (Profound Medical) [24], [27].
593 However, compared to the Sonalleve software (Profound Medical), the current software utilises
594 an additional colour status (orange) during the actual sonication, thus alerting the user of the
595 active sonication of the corresponding sonication point.

Nevertheless, additional significant features and functionalities of the software described in this study suggest a somewhat improved platform over other commercial or preclinical software developed for MRgFUS applications. Generally, some of the preclinical [47], [52], [65] or commercial software [32] have a complex user interface. Evidently, the overall layout of the developed software integrating all functionalities in a single panel, offers a substantially better and more user-friendly interface which consists mainly of buttons and graphical representations that easily guide the user throughout the treatment planning procedure. Moreover, while some of the commercial software platforms communicate with MRI scanners from specific manufacturers since the hardware controlled is only compatible with vendor-specific scanners [36], the proposed software includes a modular code for communicating with MRI scanners. In this sense, communication with MRI scanners from different manufacturers is supported, allowing the software to achieve communication tailored to the corresponding MRI hardware employed for treatment guidance and monitoring. Noteworthy is also the ability provided by the current software of designing a non-uniform sonication area with the sonication points segmented according to a user-defined step size and sonicated following a motion algorithm for full coverage of the treatment area [53]. Inevitably, the current software is improved compared to the Sonalleve (Profound Medical) and Thermoguide (Image Guided Therapy) software that allow only the choice of an ellipsoidal [24] and rectangular treatment area [32] respectively. Additionally, the proposed software provides the user with the ability to command essential sonication parameters required for execution of the treatment protocol as already followed in the commercial Sonalleve (Profound) [24], [26] and Thermoguide (Image Guided Therapy) [32] software platforms**.** Nevertheless, contrary to the Sonalleve (Profound) software that permits only the choice of power and frequency for the segmented sonication points [26], and assigns set sonication durations based on the diameter of the sonication points [24], the developed software enables

621 the command of all sonication parameters (power, sonication time, and frequency). In this
622 sense, with the proposed software, the user has the potential to accurately control the delivery
623 of ultrasonic energy to achieve optimal ablation of the targeted tissue.

624 Moreover, in the developed software, notable is the novel functionality of the robot
625 positioning procedure that interprets the actual position of the transducer relative to the planned
626 sonication trajectory, through a digital transducer marker overlayed on the MRI image.
627 Currently, registration of the transducer on the treatment planning MRI images with some of
628 the preclinical [65] or commercial [30] MRgFUS software is achieved through the use of
629 fiducial markers [30], [65]. Consequently, the digital registration of the transducer relative to
630 the active sonication area on a single reference frame (medical image) as provided by the
631 software developed herein, could have a significant impact in any future clinical software
632 employment, providing accurate transducer localization without the requirement of fiducial
633 markers. Evidently, in this manner, the developed software is comparable to the digital
634 transducer registration and localization provided by the commercial ExAblate (Insightec) [15],
635 [17], [23] and Thermoguide (Image Guided Therapy) [33] software platforms. Furthermore,
636 the added software feature of selecting the arrangement of the sonication points for
637 preoperative planning of grid pattern or non-uniform sonication areas, evidently allows motion
638 of the transducer by exploiting the most common motion algorithms (sequential, spiral)
639 followed during MRgFUS treatments [66]–[68]. Hence, the software provides the ability to
640 appropriately select a motion trajectory and an adequate time delay, ultimately leading to a
641 reduction of the excess heating in the near and far-field regions during HIFU sonications [69].

642 Eventually, additional motion algorithms [70] can be introduced in the software,
643 ultimately providing the user with more options for the sorting of sonication points and the
644 order in which these should be sonicated. Notably, with the software, monitoring of the extent
645 of the ablation is performed for each individual sonication point during the time delay allowed

between successive sonications. Contrary, such images with commercial software such as the ExAblate (Insightec, Israel), are acquired after the end of all sonications [18], [23]. In this regard, the software is better at providing point-by-point feedback on the ablation extent, resulting in increased safety during treatments. However, currently the software is limited in the sense that an empirical time delay between sonications is commanded by the user to allow sufficient time for the MRI scan. Therefore, this software feature could be enhanced in the future through dynamic recognition of the time required for the MRI scan and its integration in the user inputs.

Moreover, although the software provides quasi-real-time monitoring of the temperature increase during treatment using the PRF shift thermometry method as followed in every commercial [17], [23], [31], [37] and preclinical software [46], [47] platforms, the employed technique suffers some limitations that affect temperature estimations [71]. Specifically, the PRF technique is known to be susceptible to interscan organ motion and magnetic field frequency shifts [72], it underestimates temperatures in hyperthermic [73] or pulsed [74] MRgFUS applications, presents difficulties in fat tissue temperature measurements [75], while also being inadequate for executing temperature measurements on skin [76]. Consequently, to achieve accurate temperature monitoring with the proposed software, MRI imaging of fat-tissues should be performed with fat-suppression techniques [77], [78], while referenceless algorithms [71], [76], [79] could be integrated in the software to compensate for temperature artifacts arising from magnetic field drift changes. Specifically, the software could be enhanced with a referenceless algorithm similar to the Radial Basis Function (RBF) method proposed by Agnello et al. [71] and Militello et al. [76] which was reported to effectively compensate frequency shift artifacts and record similar temperatures as the PRF technique contrary to other polynomial referenceless algorithms that overestimated sonication induced temperatures.

Furthermore, the software could be further improved through the integration of dynamic modulation of the ultrasonic parameters during treatments, so as to account for thermal diffusion effects that affect temperature increase and uniform lesion formation [63], [80]. In this regard, treatment will be achieved with the use of a treatment planning software that dynamically determines the impact of the sonication on the planned trajectory, an approach already integrated in the commercial TULSA-PRO (Profound Medical) [28] software, as well as in the preclinical open-source software developed by Poorman et al. [46]. Moreover, the software could be additionally enhanced through integration of real-time thermal dose calculations [39] during sonications executed on each location of the treatment trajectory, as already described in developed preclinical MRgFUS software [46], [47], [65], thus being more comparable to a number of the commercial software [31], [34], [37]. Consequently, thermal dose calculations could be combined with additional functionalities such as incorporation of a colour-coded status of the segmented sonication points once sonicated with ablative level temperatures and an indication of the extent of the necrotic regions, similar to what is currently followed with the commercial ExAblate software (Insightec) [21]. Furthermore, the software could be enhanced to account for organ motion as already reported by the preclinical TRANS-FUSIMO software [49]–[52], thus compensating for treatment time and energy lost due to organ motion. Additional improvements could also consider the inclusion and delineation of sensitive areas and structures at risk in the treatment planning procedure and the incorporation of safety distances and sonication safety status as followed in the commercial ECHOPULSE (Theraclion) [13], [14] and ExAblate (Insightec) [21] software platforms, respectively.

Overall, the proposed software integrates basic functionalities tailored to providing a complete and efficient workflow for planning, executing, and monitoring MRgFUS therapeutic procedures performed with various robotic systems developed by our group for different applications [40]–[45]. In this sense, the developed software platform can be exploited with

696 the corresponding hardware [40]–[45] to facilitate preclinical research that advances the field
697 of MRgFUS, while concurrently providing researchers with essential information for
698 developing in-house software platforms with similar functionalities for use with their own
699 MRgFUS systems, given that commercial software platforms are expensive for preclinical
700 studies. Future studies entailing *in-vivo* normal and tumorous tissues, where thermal diffusion
701 effects would be present, could be performed to further assess the ability of the software in
702 accurately executing treatment plans. In this sense, better assessment of the functionality of the
703 various treatment area design tools would be performed in real-case scenarios, while different
704 sonication parameters could be employed to observe their effect on the efficient ablation of the
705 segmented area and the duration of the treatment. Treatment protocols would be selected
706 following simulations that predict the size of lesions based on the bioheat transfer equation
707 [64], while cooling periods could be appropriately commanded between sonications to
708 adequately reduce near and far-field heating, concurrently adjusting for minimal treatment
709 durations [69]. Continuous monitoring with MR thermometry will provide accurate
710 temperature feedback of the targeted area during treatments, allowing operators to assess the
711 production of ablative level temperatures. Inherently, sonication protocols that produce
712 temperatures greater than 60 ^{o}C for more that 1 s which are known to produce nearly
713 instantaneous coagulative necrosis of tumour cells [81], could be determined to elucidate
714 parameters that efficiently and safely ablate *in-vivo* tumorous tissue.
715
716
717
718
719
720

ACKNOWLEDGMENTS

This work was funded by the Research & Innovation Foundation of Cyprus under the Project SOUNDPET (INTEGRATED/0918/0008).

AUTHORS CONTRIBUTION

Antria Filippou contributed to drafting of the manuscript.

Andreas Georgiou contributed to the development of the software.

Anastasia Nikolaou contributed to the evaluation of the developed software.

Nikolas Evripidou contributed to the development of the software.

Christakis Damianou supervised the development and evaluation of the software as well as the drafting of the manuscript.

CONFLICTS OF INTEREST STATEMENT

All authors have no competing interests to declare.

ETHICS APPROVAL

Not applicable.

LIST OF FIGURE LEGENDS

Figure 1: Flowchart of the treatment planning process with the MRgFUS software.

Figure 2: Graphical user interface of the developed MRgFUS software.

Figure 3: Screenshot of the software showing the "Robot positioning" procedure on an acquired DICOM image of the focused transducer.

Figure 4: Screenshot of the software showing the user-defined sonication area (5×5 grid pattern with a 10 mm step) and the sorting type selection of the sonication points.

Figure 5: Graphical user interface of the MRgFUS software indicating the setting of the amplifier parameters for execution of the treatment planning procedure.

Figure 6: Timing diagram of the sonication cycle.

Figure 7: Treatment planning procedure during the execution of a 5×5 grid pattern sonication area with a 10 mm motion step. (A) Treatment planning has not started, (B) Transducer sonicates first grid point, (C) Transducer has sonicated the first point and is at the second point idling, and (D) Transducer has sonicated several points of the grid.

Figure 8: Schematic reference point diagram of the "Homing" procedure integrated in the software.

Figure 9: Flowchart of the MR thermometry process.

Figure 10: MR thermal map acquired during sonications executed on an agar-based phantom using an acoustical power of 50 W for a sonication time of 60 s at a focal depth of 30 mm. (A) Axial plane, and (B) Coronal plane.

Figure 11: (A) Sonication path of seven random points as planned through the MRgFUS software, and (B) Lesions formed on the PVC film after execution of the treatment path planning using an acoustical power of 6 W for a sonication time of 5 s.

Figure 12: (A) Non-linear sonication path as planned using the MRgFUS software, and (B) Lesions formed on the PVC film after exposure at acoustical power of 6 W for a sonication time of 5 s.

Figure 13: (A) The 10×10 grid sonication path planned using the MRgFUS software, and (B) Overlapping lesions formed on the PVC film after exposure at an acoustical power of 6 W for a sonication time of 5 s and movement of the transducer in a 10×10 grid with a 1 mm step.

Figure 14: (A) The non-uniform grid sonication path planned using the MRgFUS software, and (B) Non-uniform area of lesions formed on the PVC film after exposure at an acoustical power of 6 W for a sonication time of 5 s and movement of the transducer with a 4 mm step.

REFERENCES

[1] J. G. Lynn, R. L. Zwemer, A. J. Chick, and A. E. Miller, "A new method for the generation and use of focused ultrasound in experimental biology," *J. Gen. Physiol.*, vol. 26, no. 2, 1942, doi: 10.1085/jgp.26.2.179.

[2] Z. Izadifar, Z. Izadifar, D. Chapman, and P. Babyn, "An Introduction to High Intensity Focused Ultrasound: Systematic Review on Principles, Devices, and Clinical Applications," *J. Clin. Med.*, vol. 9, no. 2, p. 460, 2020, doi: 10.3390/jcm9020460.

[3] F. Siedek *et al.*, "Magnetic Resonance-Guided High-Intensity Focused Ultrasound (MR-HIFU): Technical Background and Overview of Current Clinical Applications (Part 1)," *RoFo Fortschritte auf dem Gebiet der Rontgenstrahlen und der Bildgebenden Verfahren*, vol. 191, no. 6. pp. 522–530, 2019, doi: 10.1055/a-0817-5645.

[4] G. ter Haar, "HIFU tissue ablation: Concept and devices," in *Advances in Experimental Medicine and Biology*, vol. 880, 2016.

[5] I. Rivens, A. Shaw, J. Civale, and H. Morris, "Treatment monitoring and thermometry for therapeutic focused ultrasound," *Int. J. Hyperth.*, vol. 23, no. 2, 2007, doi: 10.1080/02656730701207842.

[6] Y. H. Hsiao, S. J. Kuo, H. Der Tsai, M. C. Chou, and G. P. Yeh, "Clinical application of high-intensity focused ultrasound in cancer therapy," *Journal of Cancer*, vol. 7, no. 3. 2016, doi: 10.7150/jca.13906.

[7] K. Kuroda, "MR techniques for guiding high-intensity focused ultrasound (HIFU) treatments," *Journal of Magnetic Resonance Imaging*, vol. 47, no. 2. 2018, doi: 10.1002/jmri.25770.

[8] A. J. Loeve *et al.*, "Workflow and intervention times of MR-guided focused ultrasound - Predicting the impact of new techniques," *J. Biomed. Inform.*, vol. 60, 2016, doi: 10.1016/j.jbi.2016.01.001.

[9] I. A. Shehata, “Treatment with high intensity focused ultrasound: Secrets revealed,” *European Journal of Radiology*, vol. 81, no. 3. 2012, doi: 10.1016/j.ejrad.2011.01.047.

[10] S. E. Jung, S. H. Cho, J. H. Jang, and J. Y. Han, “High-intensity focused ultrasound ablation in hepatic and pancreatic cancer: Complications,” *Abdom. Imaging*, vol. 36, no. 2, 2011, doi: 10.1007/s00261-010-9628-2.

[11] M. Rossi, C. Raspanti, E. Mazza, I. Menchi, A. R. De Gaudio, and R. Naspetti, “High-intensity focused ultrasound provides palliation for liver metastasis causing gastric outlet obstruction: Case report,” *J. Ther. Ultrasound*, vol. 1, no. 1, 2013, doi: 10.1186/2050-5736-1-9.

[12] F. Lü, W. Huang, and D. G. Benditt, “A feasibility study of noninvasive ablation of ventricular tachycardia using high-intensity focused ultrasound,” *J. Cardiovasc. Electrophysiol.*, vol. 29, no. 5, 2018, doi: 10.1111/jce.13459.

[13] B. H. H. Lang, C. K. H. Wong, E. P. M. Ma, Y. C. Woo, and K. W. H. Chiu, “A propensity-matched analysis of clinical outcomes between open thyroid lobectomy and high-intensity focused ultrasound (HIFU) ablation of benign thyroid nodules,” *Surg. (United States)*, vol. 165, no. 1, pp. 85–91, 2019, doi: 10.1016/j.surg.2018.05.080.

[14] D. R. Brenin, J. Patrie, J. Nguyen, and C. M. Rochman, “Treatment of Breast Fibroadenoma with Ultrasound-Guided High-Intensity Focused Ultrasound Ablation: A Feasibility Study,” *J. Breast Imaging*, vol. 1, no. 4, 2019, doi: 10.1093/jbi/wbz050.

[15] A. B. Holbrook, P. Ghanouni, J. M. Santos, C. Dumoulin, Y. Medan, and K. B. Pauly, “Respiration based steering for high intensity focused ultrasound liver ablation,” *Magn. Reson. Med.*, vol. 71, no. 2, 2014, doi: 10.1002/mrm.24695.

[16] A. Napoli *et al.*, “MR imaging-guided focused ultrasound for treatment of bone metastasis,” *Radiographics*, vol. 33, no. 6, 2013, doi: 10.1148/rg.336125162.

[17] M. Izumi *et al.*, “MR-guided focused ultrasound for the novel and innovative

management of osteoarthritic knee pain," *BMC Musculoskelet. Disord.*, vol. 14, 2013, doi: 10.1186/1471-2474-14-267.

[18] S. Dababou *et al.*, "High-intensity focused ultrasound for pain management in patients with cancer," *Radiographics*, vol. 38, no. 2, 2018, doi: 10.1148/rg.2018170129.

[19] A. Iannessi, J. Doyen, A. Leysalle, and A. Thyss, "Magnetic resonance guided focalised ultrasound thermo-ablation: A promising oncologic local therapy," *Diagn. Interv. Imaging*, vol. 95, no. 3, 2014, doi: 10.1016/j.diii.2013.09.003.

[20] N. Lipsman, T. G. Mainprize, M. L. Schwartz, K. Hynynen, and A. M. Lozano, "Intracranial Applications of Magnetic Resonance-guided Focused Ultrasound," *Neurotherapeutics*, vol. 11, no. 3. 2014, doi: 10.1007/s13311-014-0281-2.

[21] B. J. J. Abdullah *et al.*, "Magnetic resonance-guided focused ultrasound surgery (MRgFUS) treatment for uterine fibroids," *Biomed. Imaging Interv. J.*, vol. 6, no. 2, 2010, doi: 10.2349/biij.6.2.e15.

[22] S. K. Wu, C. L. Tsai, Y. Huang, and K. Hynynen, "Focused ultrasound and microbubbles-mediated drug delivery to brain tumor," *Pharmaceutics*, vol. 13, no. 1. 2021, doi: 10.3390/pharmaceutics13010015.

[23] B. Joo *et al.*, "Pain palliation in patients with bone metastases using magnetic resonance-guided focused ultrasound with conformal bone system: A preliminary report," *Yonsei Med. J.*, vol. 56, no. 2, 2015, doi: 10.3349/ymj.2015.56.2.503.

[24] S. L. Giles, G. Imseeh, I. Rivens, G. R. Ter Haar, A. Taylor, and N. M. DeSouza, "MR guided high intensity focused ultrasound (MRgHIFU) for treating recurrent gynaecological tumours: A pilot feasibility study," *Br. J. Radiol.*, vol. 92, no. 1098, 2019, doi: 10.1259/bjr.20181037.

[25] M. Huisman *et al.*, "Feasibility of volumetric MRI-guided high intensity focused ultrasound (MR-HIFU) for painful bone metastases," *J. Ther. Ultrasound*, vol. 2, no. 1,

pp. 1–10, 2014, doi: 10.1186/2050-5736-2-16.

[26] A. M. Venkatesan *et al.*, “Magnetic resonance imaging-guided volumetric ablation of symptomatic leiomyomata: Correlation of imaging with histology,” *J. Vasc. Interv. Radiol.*, vol. 23, no. 6, 2012, doi: 10.1016/j.jvir.2012.02.015.

[27] A. Waspe *et al.*, “Magnetic resonance guided focused ultrasound for noninvasive pain therapy of osteoid osteoma in children,” *J. Ther. Ultrasound*, vol. 3, no. S1, 2015, doi: 10.1186/2050-5736-3-s1-o48.

[28] M. Mueller-wolf, M. Röthke, B. Hadaschik, S. Pahernik, J. Chin, and J. Relle, “Transurethral MR-Thermometry Guided Ultrasound Ablation of the Prostate – The Heidelberg Experience During Phase I of the TULSA-PRO Device Trial,” no. 66, pp. 130–137, 2016.

[29] J. L. Chin *et al.*, “Magnetic Resonance Imaging – Guided Transurethral Ultrasound Ablation of Prostate Tissue in Patients with Localized Prostate Cancer : A Prospective Phase 1 Clinical Trial,” *Eur. Urol.*, vol. 70, no. 3, pp. 447–455, 2016, doi: 10.1016/j.eururo.2015.12.029.

[30] E. Ramsay *et al.*, “Evaluation of Focal Ablation of Magnetic Resonance Imaging Defined Prostate Cancer Using Magnetic Resonance Imaging Controlled Transurethral Ultrasound Therapy with Prostatectomy as the Reference Standard,” *J. Urol.*, vol. 197, no. 1, 2017, doi: 10.1016/j.juro.2016.06.100.

[31] D. Bonekamp *et al.*, “Twelve-month prostate volume reduction after MRI-guided transurethral ultrasound ablation of the prostate,” *Eur. Radiol.*, vol. 29, no. 1, 2019, doi: 10.1007/s00330-018-5584-y.

[32] R. Magnin *et al.*, “Magnetic resonance-guided motorized transcranial ultrasound system for blood-brain barrier permeabilization along arbitrary trajectories in rodents,” *J. Ther. Ultrasound*, vol. 3, no. 1, 2015, doi: 10.1186/s40349-015-0044-5.

[33] J. O. Szablowski and M. Harb, “Focused ultrasound induced blood-brain barrier opening for targeting brain structures and evaluating chemogenetic neuromodulation,” *J. Vis. Exp.*, vol. 2020, no. 166, 2020, doi: 10.3791/61352.

[34] B. Z. Fite *et al.*, “Magnetic resonance imaging assessment of effective ablated volume following high intensity focused ultrasound,” *PLoS One*, vol. 10, no. 3, 2015, doi: 10.1371/journal.pone.0120037.

[35] R. Kovatcheva, J. N. Guglielmina, M. Abehsera, L. Boulanger, N. Laurent, and E. Poncelet, “Ultrasound-guided high-intensity focused ultrasound treatment of breast fibroadenoma-a multicenter experience,” *J. Ther. Ultrasound*, vol. 3, no. 1, 2015, doi: 10.1186/s40349-014-0022-3.

[36] C. Yiallouras and C. Damianou, “Review of MRI positioning devices for guiding focused ultrasound systems,” *Int. J. Med. Robot. Comput. Assist. Surg.*, no. 11, pp. 247–255, 2015, doi: 10.1002/rcs.

[37] S. Giles *et al.*, “Magnetic Resonance Guided High Intensity Focused Ultrasound (MrgHIFU) for Treating Recurrent Gynaecological Tumours: Effect of Pre-Focal Tissue Characteristic on Target Heating,” *J. Imaging Interv. Radiol.*, vol. 3, no. 1, 2020.

[38] L. Klotz *et al.*, “Magnetic Resonance Imaging-Guided Transurethral Ultrasound Ablation of Prostate Cancer,” *J. Urol.*, vol. 205, no. 3, pp. 769–779, Mar. 2021, doi: 10.1097/JU.0000000000001362.

[39] S. A. Sapareto and W. C. Dewey, “Thermal dose determination in cancer therapy,” *Int. J. Radiat. Oncol. Biol. Phys.*, vol. 10, no. 6, pp. 787–800, 1984, doi: 10.1016/0360-3016(84)90379-1.

[40] T. Drakos *et al.*, “MRI-Guided Focused Ultrasound Robotic System for Preclinical use,” *J. Vet. Med. Anim. Sci.*, vol. 4, no. 1, 2020.

[41] T. Drakos, M. Giannakou, G. Menikou, and C. Damianou, “Magnetic Resonance

Imaging–Guided Focused Ultrasound Positioning System for Preclinical Studies in Small Animals," *J. Ultrasound Med.*, vol. 40, no. 7, 2021, doi: 10.1002/jum.15514.

[42] K. Spanoudes, N. Evripidou, M. Giannakou, T. Drakos, G. Menikou, and C. Damianou, "A high intensity focused ultrasound system for veterinary oncology applications," *J. Med. Ultrasound*, vol. 29, no. 3, 2021, doi: 10.4103/JMU.JMU_130_20.

[43] M. Giannakou *et al.*, "Magnetic resonance image–guided focused ultrasound robotic system for transrectal prostate cancer therapy," *Int. J. Med. Robot. Comput. Assist. Surg.*, vol. 17, no. 3, 2021, doi: 10.1002/rcs.2237.

[44] A. Antoniou, M. Giannakou, N. Evripidou, S. Stratis, S. Pichardo, and C. Damianou, "Robotic system for top to bottom MRgFUS therapy of multiple cancer types," *Int. J. Med. Robot. Comput. Assist. Surg.*, vol. 18, no. 2, p. e2364, 2022, doi: 10.1002/rcs.2364.

[45] M. Giannakou, G. Menikou, K. Ioannides, and C. Damianou, "Magnetic resonance-image-guided focused ultrasound robotic system with four computer-controlled axes with endorectal access designed for prostate cancer focal therapy," *Digit. Med.*, vol. 6, pp. 32–43, 2020, doi: 10.4103/digm.digm.

[46] M. E. Poorman *et al.*, "Open-source, small-animal magnetic resonance-guided focused ultrasound system," *J. Ther. Ultrasound*, vol. 4, no. 1, 2016, doi: 10.1186/s40349-016-0066-7.

[47] L. W. Kuo, G. C. Dong, C. C. Pan, S. F. Chen, and G. S. Chen, "An MRI-Guided Ring High-Intensity Focused Ultrasound System for Noninvasive Breast Ablation," *IEEE Trans. Ultrason. Ferroelectr. Freq. Control*, vol. 67, no. 9, 2020, doi: 10.1109/TUFFC.2020.2992764.

[48] C. Yiallouras, G. Menikou, M. Yiannakou, and C. Damianou, "Software that controls a magnetic resonance imaging compatible robotic system for guiding high-intensity focused ultrasound therapy," *Digit. Med.*, vol. 3, no. 3, 2017, doi:

941 10.4103/digm.digm_19_17.
942 [49] M. Schwenke *et al.*, “An integrated model-based software for FUS in moving abdominal
943 organs,” *Int. J. Hyperth.*, vol. 31, no. 3, 2015, doi: 10.3109/02656736.2014.1002817.
944 [50] S. Mihcin, J. Strehlow, D. Demedts, M. Schwenke, Y. Levy, and A. Melzer, “Evidence-
945 based cross validation for acoustic power transmission for a novel treatment system,”
946 *Minim. Invasive Ther. Allied Technol.*, vol. 26, no. 3, 2017, doi:
947 10.1080/13645706.2016.1273836.
948 [51] M. Schwenke *et al.*, “A focused ultrasound treatment system for moving targets (part I):
949 Generic system design and in-silico first-stage evaluation,” *J. Ther. Ultrasound*, vol. 5,
950 no. 1, 2017, doi: 10.1186/s40349-017-0098-7.
951 [52] S. Mihcin *et al.*, “Methodology on quantification of sonication duration for safe
952 application of MR guided focused ultrasound for liver tumour ablation,” *Comput.
953 Methods Programs Biomed.*, vol. 152, 2017, doi: 10.1016/j.cmpb.2017.09.006.
954 [53] A. Antoniou, A. Georgiou, N. Evripidou, and C. Damianou, “Full coverage path
955 planning algorithm for MRgFUS therapy,” *Int. J. Med. Robot. Comput. Assist. Surg.*,
956 2022, doi: 10.1002/rcs.2389.
957 [54] J. W. Jenne, T. Preusser, and M. Günther, “High-intensity focused ultrasound:
958 Principles, therapy guidance, simulations and applications,” *Z. Med. Phys.*, vol. 22, no.
959 4, pp. 311–322, Dec. 2012, doi: 10.1016/j.zemedi.2012.07.001.
960 [55] T. Drakos *et al.*, “Ultrasonic attenuation of an agar, silicon dioxide, and evaporated milk
961 gel phantom,” *J. Med. Ultrasound*, vol. 29, no. 4, pp. 239–249, 2021.
962 [56] G. Menikou, T. Dadakova, M. Pavlina, M. Bock, and C. Damianou, “MRI compatible
963 head phantom for ultrasound surgery,” *Ultrasonics*, vol. 57, no. C, pp. 144–152, 2015,
964 doi: 10.1016/j.ultras.2014.11.004.
965 [57] G. Menikou, M. Yiannakou, C. Yiallouras, C. Ioannides, and C. Damianou, “MRI-

compatible breast/rib phantom for evaluating ultrasonic thermal exposures," *Int. J. Med. Robot. Comput. Assist. Surg.*, vol. 14, no. 1, pp. 1–12, 2018, doi: 10.1002/rcs.1849.

[58] G. Menikou and C. Damianou, "Acoustic and thermal characterization of agar based phantoms used for evaluating focused ultrasound exposures," *J. Ther. Ultrasound*, vol. 5, no. 1, pp. 1–14, 2017, doi: 10.1186/s40349-017-0093-z.

[59] A. Antoniou *et al.*, "Simple methods to test the accuracy of MRgFUS robotic systems," *Int. J. Med. Robot. Comput. Assist. Surg.*, vol. 17, no. 4, 2021, doi: 10.1002/rcs.2287.

[60] A. Antoniou and C. Damianou, "Simple, inexpensive, and ergonomic phantom for quality assurance control of MRI guided Focused Ultrasound systems," *J. Ultrasound*, 2022, doi: 10.1007/s40477-022-00740-w.

[61] H. Lu, L. M. Nagae-Poetscher, X. Golay, D. Lin, M. Pomper, and P. C. M. Van Zijl, "Routine clinical brain MRI sequences for use at 3.0 tesla," *J. Magn. Reson. Imaging*, vol. 22, no. 1, 2005, doi: 10.1002/jmri.20356.

[62] P. Namakshenas and A. Mojra, "Microstructure-based non-Fourier heat transfer modeling of HIFU treatment for thyroid cancer," *Comput. Methods Programs Biomed.*, vol. 197, 2020, doi: 10.1016/j.cmpb.2020.105698.

[63] Y. Zhou, S. G. Kargl, and J. H. Hwang, "The Effect of the Scanning Pathway in High-Intensity Focused Ultrasound Therapy on Lesion Production," *Ultrasound Med. Biol.*, vol. 37, no. 9, 2011, doi: 10.1016/j.ultrasmedbio.2011.05.848.

[64] L. Curiel, F. Chavrier, B. Gignoux, S. Pichardo, S. Chesnais, and J. Y. Chapelon, "Experimental evaluation of lesion prediction modelling in the presence of cavitation bubbles: Intended for high-intensity focused ultrasound prostate treatment," *Med. Biol. Eng. Comput.*, vol. 42, no. 1, pp. 44–54, 2004, doi: 10.1007/BF02351010.

[65] Y. Qiao *et al.*, "MARFit: An Integrated Software for Real-Time MR Guided Focused Ultrasound Neuromodulation System," *IEEE Trans. Neural Syst. Rehabil. Eng.*, vol. 30,

2022, doi: 10.1109/TNSRE.2022.3146286.

[66] C. Yiallouras, N. Mylonas, and C. Damianou, “MRI-compatible positioning device for guiding a focused ultrasound system for transrectal treatment of prostate cancer,” *Int. J. Comput. Assist. Radiol. Surg.*, vol. 9, no. 4, pp. 745–753, 2014, doi: 10.1007/s11548-013-0964-x.

[67] K. Hynynen *et al.*, “MR imaging-guided focused ultrasound surgery of fibroadenomas in the breast: a feasibility study,” *Radiology*, vol. 219, no. 176–185, 2001.

[68] R. Salomir *et al.*, “Local hyperthermia with MR-guided focused ultrasound: Spiral trajectory of the focal point optimized for temperature uniformity in the target region,” *J. Magn. Reson. Imaging*, vol. 12, no. 4, pp. 571–583, 2000, doi: 10.1002/1522-2586(200010)12:4<571::AID-JMRI9>3.0.CO;2-2.

[69] A. Filippou, T. Drakos, M. Giannakou, N. Evripidou, and C. Damianou, “Experimental evaluation of the near-field and far-field heating of focused ultrasound using the thermal dose concept,” *Ultrasonics*, vol. 116, 2021, doi: 10.1016/j.ultras.2021.106513.

[70] M. Yiannakou, M. Trimikliniotis, C. Yiallouras, and C. Damianou, “Evaluation of focused ultrasound algorithms: Issues for reducing pre-focal heating and treatment time,” *Ultrasonics*, vol. 65, pp. 145–153, 2016, doi: 10.1016/j.ultras.2015.10.007.

[71] L. Agnello, C. Militello, C. Gagliardo, and S. Vitabile, “Radial basis function interpolation for referenceless thermometry enhancement,” *Smart Innov. Syst. Technol.*, vol. 37, 2015, doi: 10.1007/978-3-319-18164-6_19.

[72] H. Odéen and D. L. Parker, “Magnetic resonance thermometry and its biological applications – Physical principles and practical considerations,” *Prog. Nucl. Magn. Reson. Spectrosc.*, vol. 110, pp. 34–61, 2019, doi: 10.1016/j.pnmrs.2019.01.003.

[73] C. Bing *et al.*, “Drift correction for accurate PRF-shift MR thermometry during mild hyperthermia treatments with MR-HIFU,” *Int. J. Hyperth.*, vol. 32, no. 6, 2016, doi:

10.1080/02656736.2016.1179799.

[74] B. E. O'Neill, C. Karmonik, E. Sassaroli, and K. C. Li, "Estimation of thermal dose from MR thermometry during application of nonablative pulsed high intensity focused ultrasound," *J. Magn. Reson. Imaging*, vol. 35, no. 5, 2012, doi: 10.1002/jmri.23526.

[75] J. C. Hindman, "Proton resonance shift of water in the gas and liquid states," *J. Chem. Phys.*, vol. 44, no. 12, 1966, doi: 10.1063/1.1726676.

[76] C. Militello *et al.*, "A computational study on temperature variations in mrgfus treatments using prf thermometry techniques and optical probes," *J. Imaging*, vol. 7, no. 4, 2021, doi: 10.3390/jimaging7040063.

[77] E. Ramsay *et al.*, "MR thermometry in the human prostate gland at 3.0T for transurethral ultrasound therapy," *J. Magn. Reson. Imaging*, vol. 38, no. 6, 2013, doi: 10.1002/jmri.24063.

[78] J. A. De Zwart, F. C. Vimeux, C. Delalande, P. Canioni, and C. T. W. Moonen, "Fast lipid-suppressed MR temperature mapping with echo-shifted gradient- echo imaging and spectral-spatial excitation," *Magn. Reson. Med.*, vol. 42, no. 1, 1999, doi: 10.1002/(SICI)1522-2594(199907)42:1<53::AID-MRM9>3.0.CO;2-S.

[79] C. J. Ferrer *et al.*, "Field drift correction of proton resonance frequency shift temperature mapping with multichannel fast alternating nonselective free induction decay readouts," *Magn. Reson. Med.*, vol. 83, no. 3, 2020, doi: 10.1002/mrm.27985.

[80] X. Zou, S. Qian, Q. Tan, and H. Dong, "Formation of thermal lesions in tissue and its optimal control during HIFU scanning therapy," *Symmetry (Basel).*, vol. 12, no. 9, 2020, doi: 10.3390/SYM12091386.

[81] Y.-F. Zhou, "High intensity focused ultrasound in clinical tumor ablation," *World J. Clin. Oncol.*, vol. 2, no. 1, p. 8, 2011, doi: 10.5306/wjco.v2.i1.8.

1041

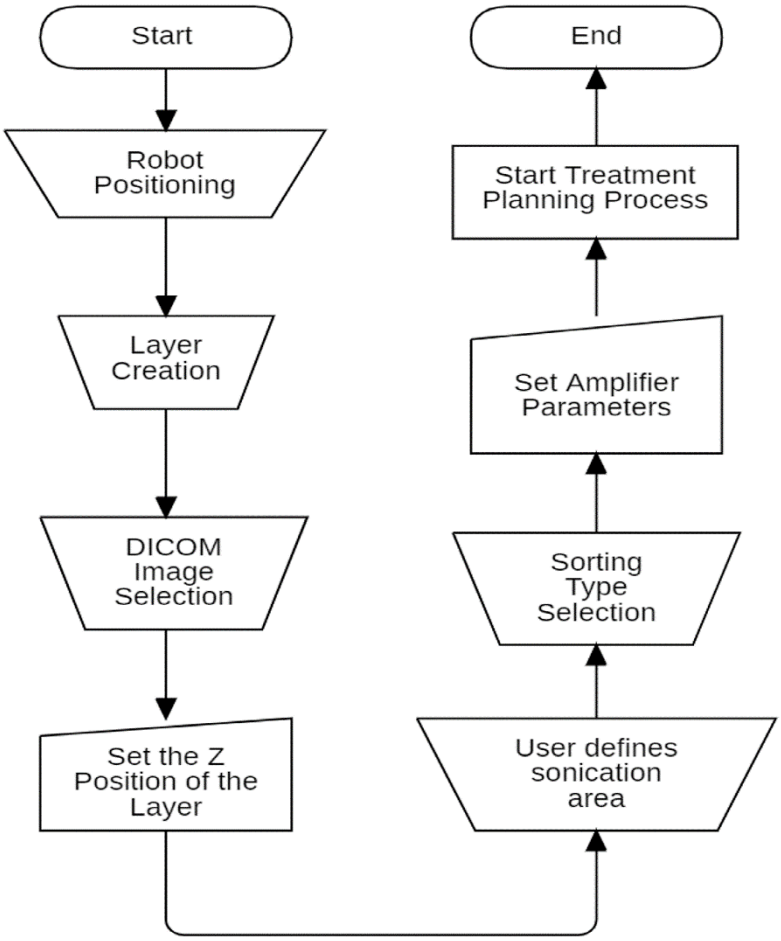

1042

1043 Figure 1

1044

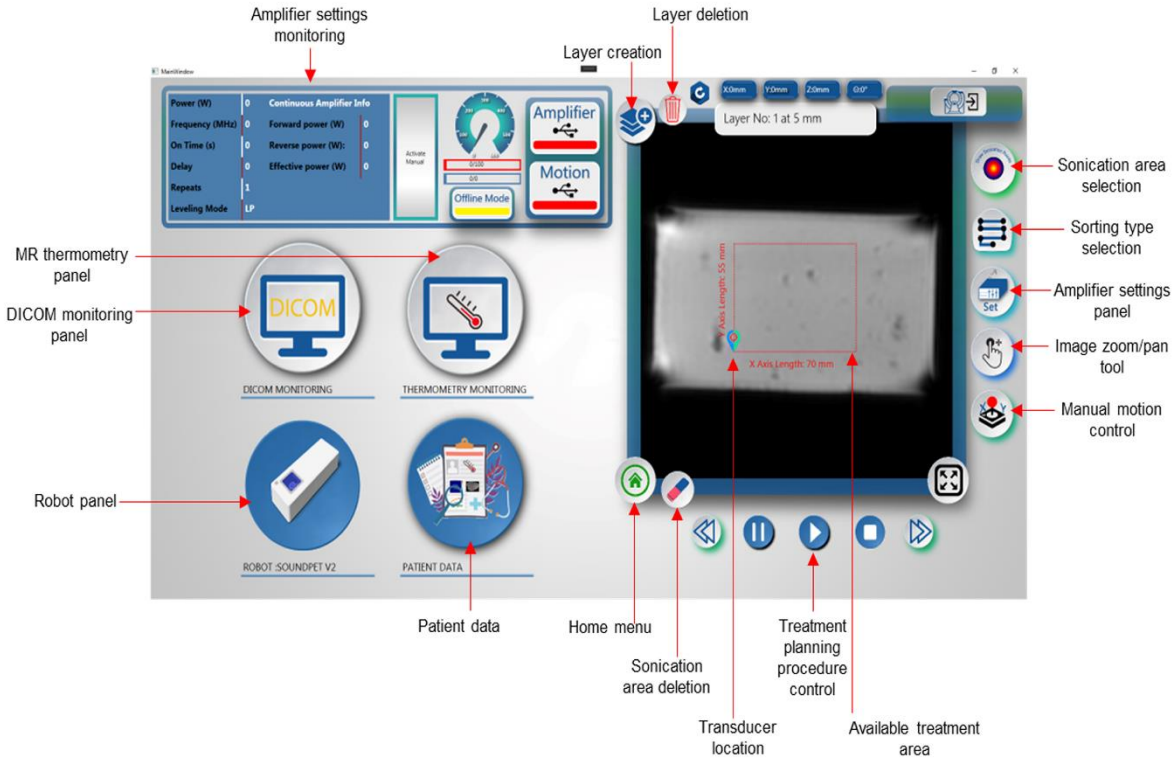
Amplifier settings monitoring
Layer deletion
Layer creation
Sonication area selection
Sorting type selection
Amplifier settings panel
Image zoom/pan tool
Manual motion control
MR thermometry panel
DICOM monitoring panel
Robot panel
Patient data
Home menu
Sonication area deletion
Transducer location
Treatment planning procedure control
Available treatment area
Layer No: 1 at 5 mm
Amplifier
Motion
Offline Mode
DICOM
DICOM MONITORING
THERMOMETRY MONITORING
ROBOT :SOUNDPET V2
PATIENT DATA

Figure 2

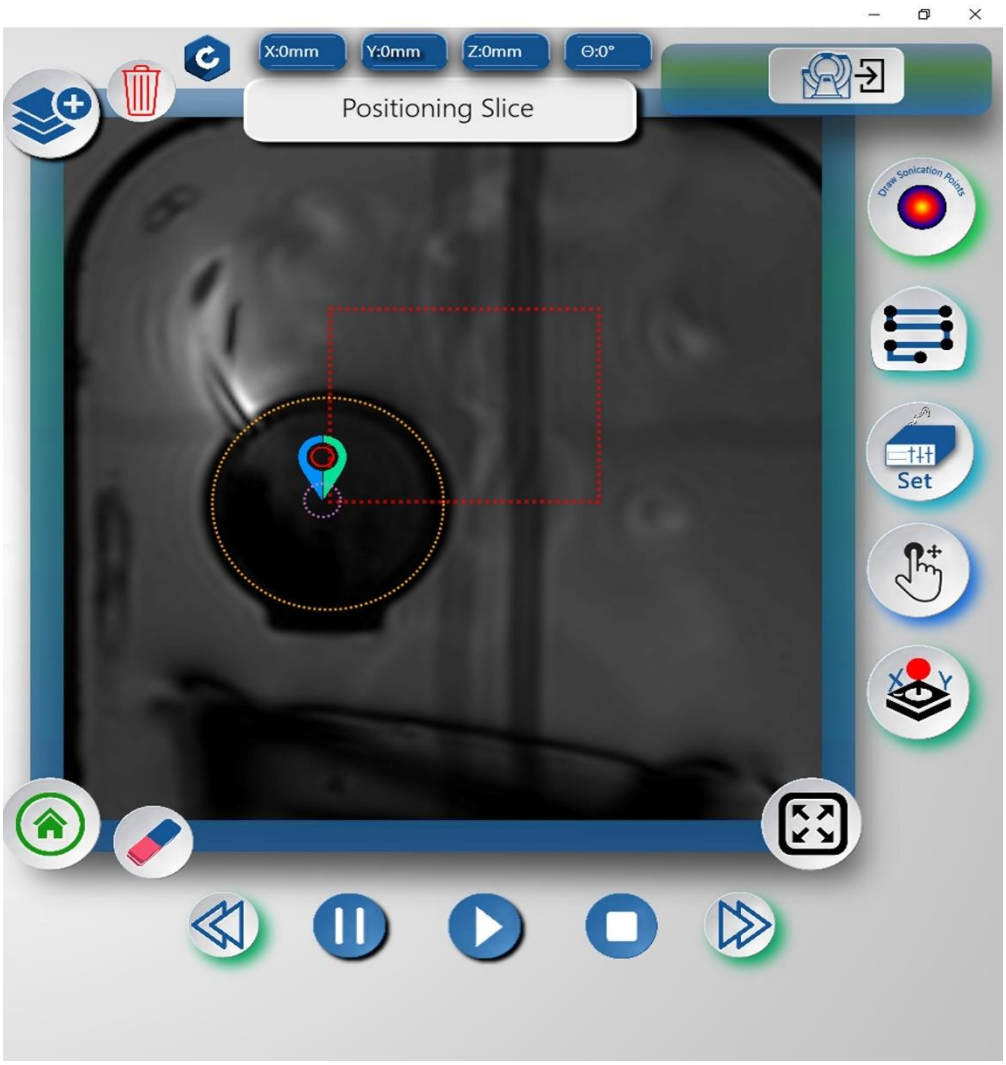
X:0mm
Y:0mm
Z:0mm
Θ:0°
Positioning Slice
Draw Sonication Points
Set

Figure 3

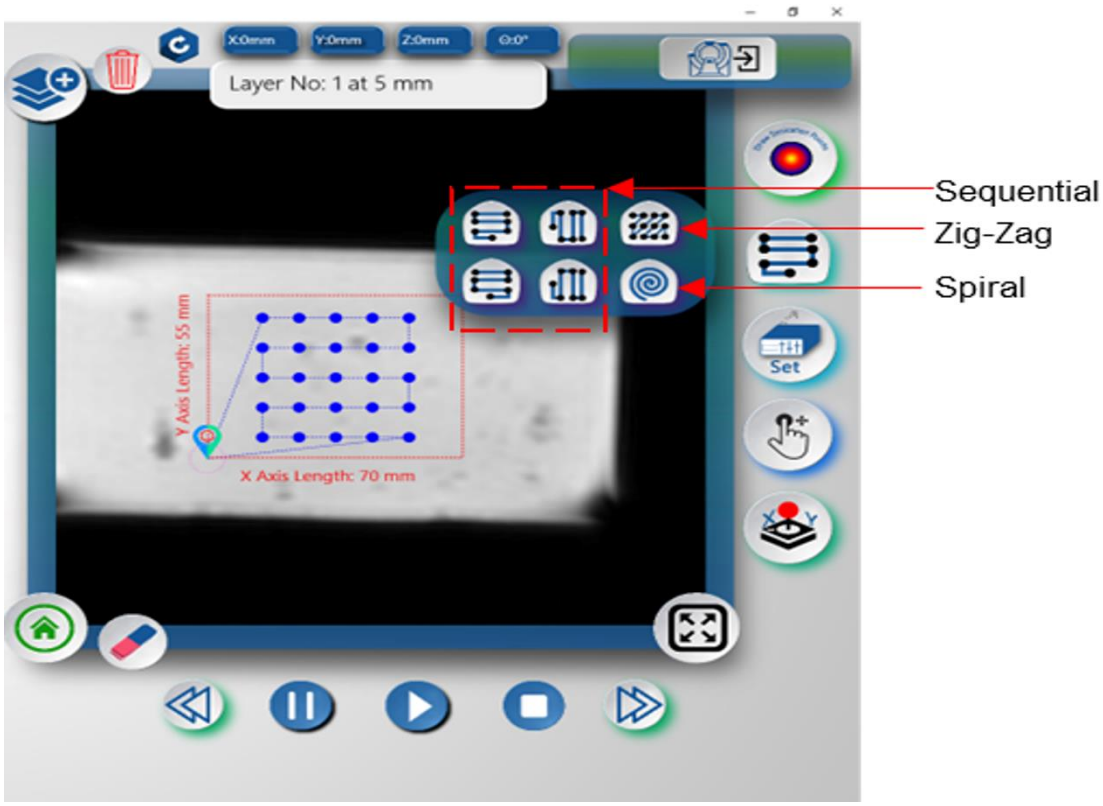
Layer No: 1 at 5 mm
Sequential
Zig-Zag
Spiral
Set
Y Axis Length: 55 mm
X Axis Length: 70 mm

Figure 4


Amplifier settings monitoring panel
Amplifier settings pop-up panel
Power (W)
Frequency (MHz)
On Time (s)
Delay
Repeats
Leveling Mode
Continuous Amplifier Info
Forward power (W)
Reverse power (W):
Effective power (W)
Amplifier
Motion
Offline Mode
DICOM
DICOM MONITORING
THERMOMETRY MONITORING
ROBOT :SOUNDPET V2
PATIENT DATA
Layer No: 1 at 5 mm
Amplifier Settings
Power (W) :
Frequency (MHz) :
On Time(s) :
Delay :
Repeats :
Leveling Mode :
Set
Treatment planning procedure control

Figure 5

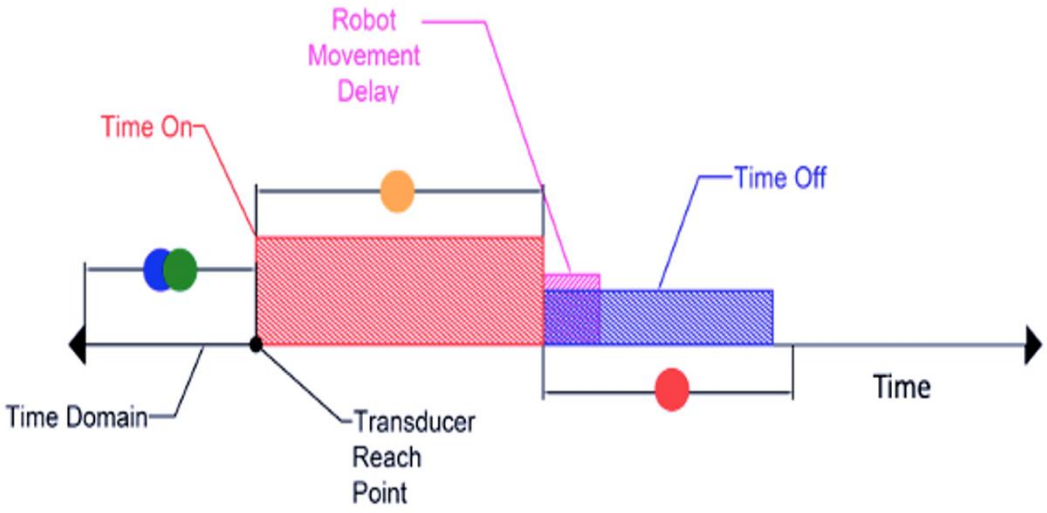

1059

1060 Figure 6

1061

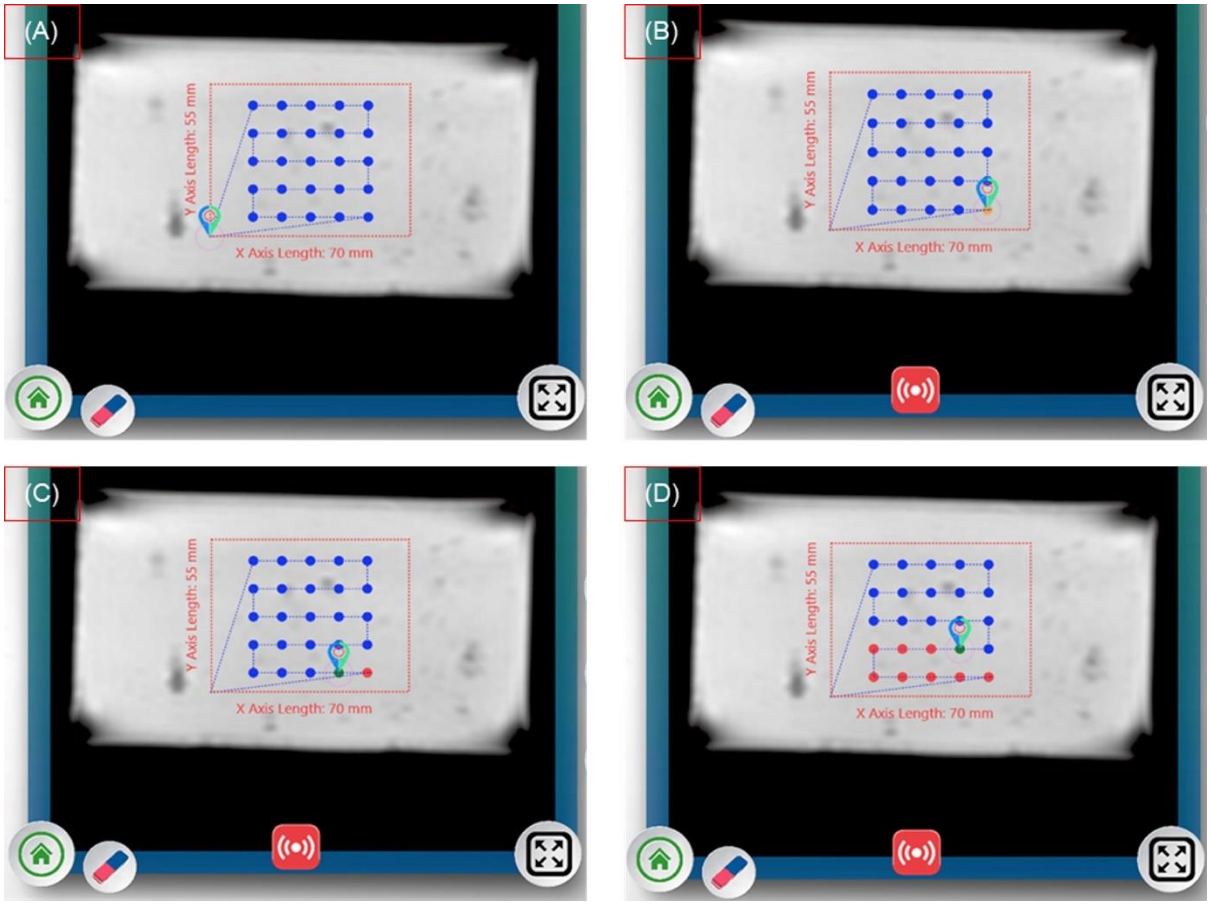
(A)
Y Axis Length: 55 mm
X Axis Length: 70 mm
(B)
Y Axis Length: 55 mm
X Axis Length: 70 mm
(C)
Y Axis Length: 55 mm
X Axis Length: 70 mm
(D)
Y Axis Length: 55 mm
X Axis Length: 70 mm

Figure 7

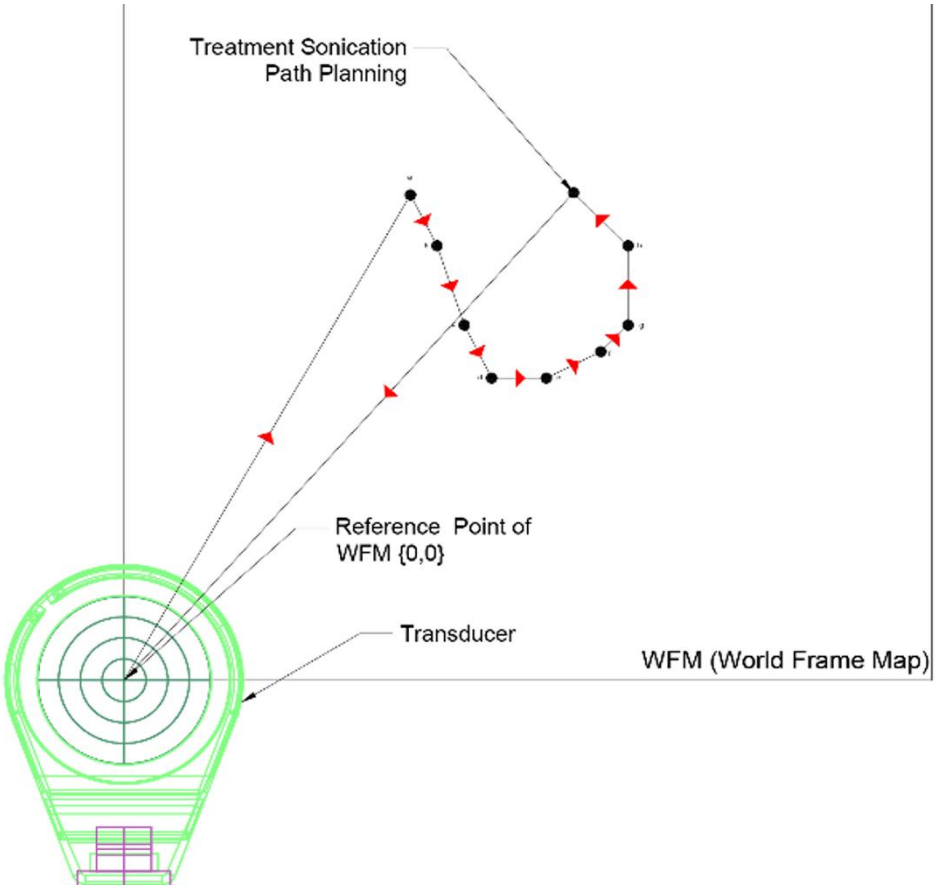
Treatment Sonication
Path Planning
Reference Point of
WFM {0,0}
Transducer
WFM (World Frame Map)

Figure 8

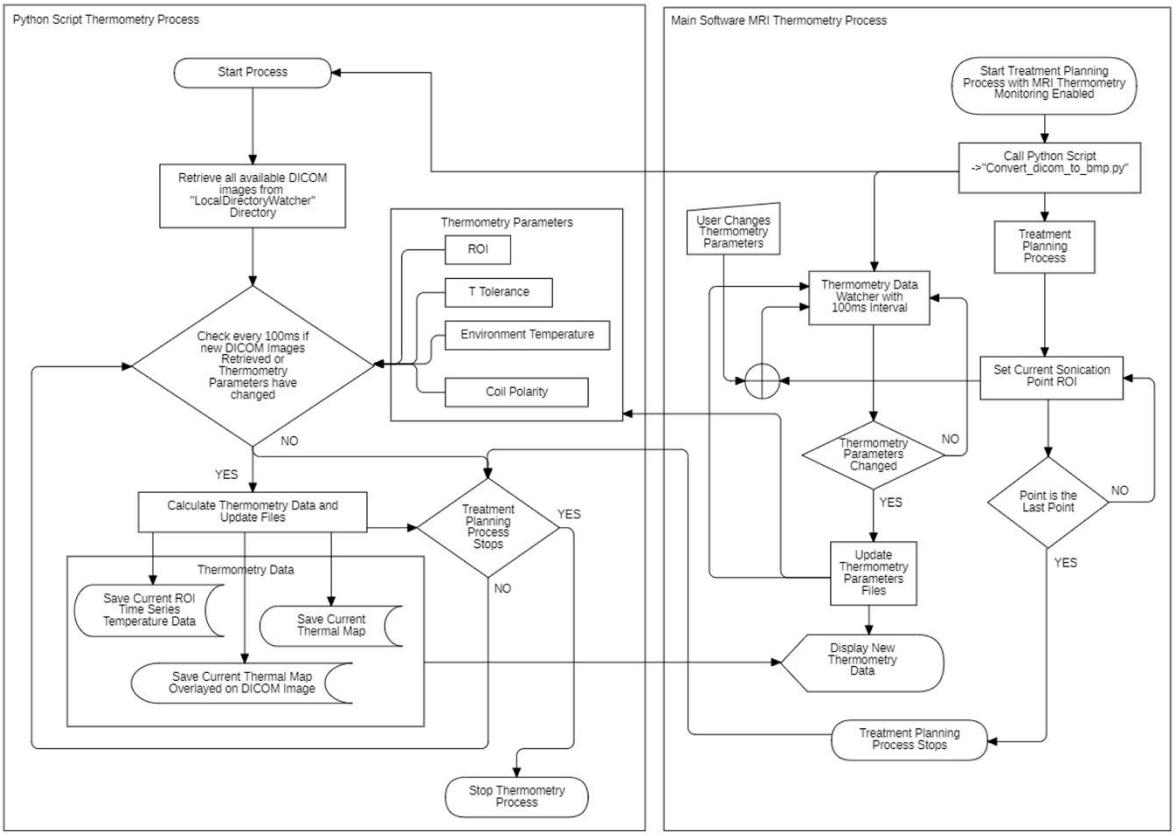
Python Script Thermometry Process
Start Process
Retrieve all available DICOM images from "LocalDirectoryWatcher" Directory
Thermometry Parameters
ROI
T Tolerance
Environment Temperature
Coil Polarity
Check every 100ms if new DICOM Images Retrieved or Thermometry Parameters have changed
NO
YES
Calculate Thermometry Data and Update Files
Treatment Planning Process Stops
YES
NO
Thermometry Data
Save Current ROI Time Series Temperature Data
Save Current Thermal Map
Save Current Thermal Map Overlayed on DICOM Image
Stop Thermometry Process
Main Software MRI Thermometry Process
Start Treatment Planning Process with MRI Thermometry Monitoring Enabled
Call Python Script ->"Convert_dicom_to_bmp.py"
User Changes Thermometry Parameters
Treatment Planning Process
Thermometry Data Watcher with 100ms Interval
Set Current Sonication Point ROI
Thermometry Parameters Changed
NO
YES
Point is the Last Point
NO
YES
Update Thermometry Parameters Files
Display New Thermometry Data
Treatment Planning Process Stops

Figure 9

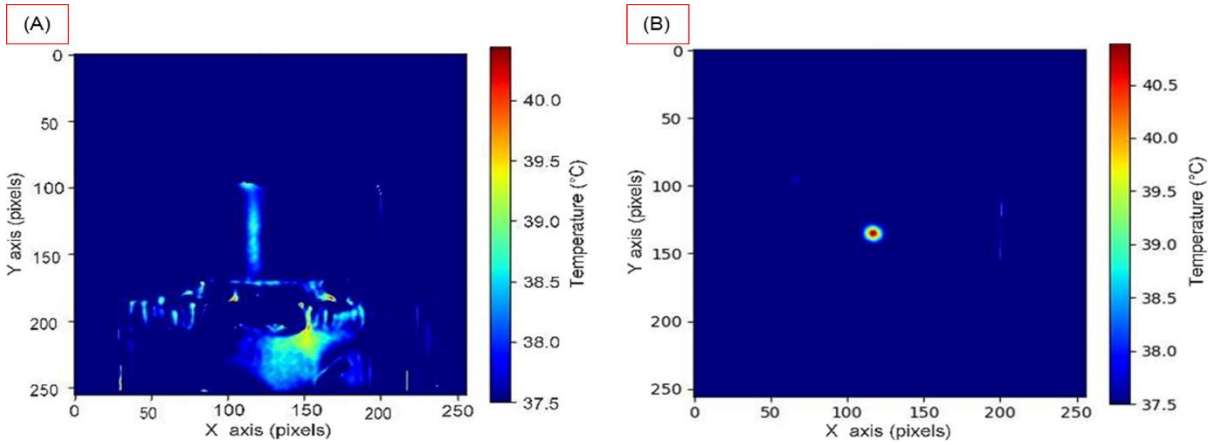

1071

1072 Figure 10

1073

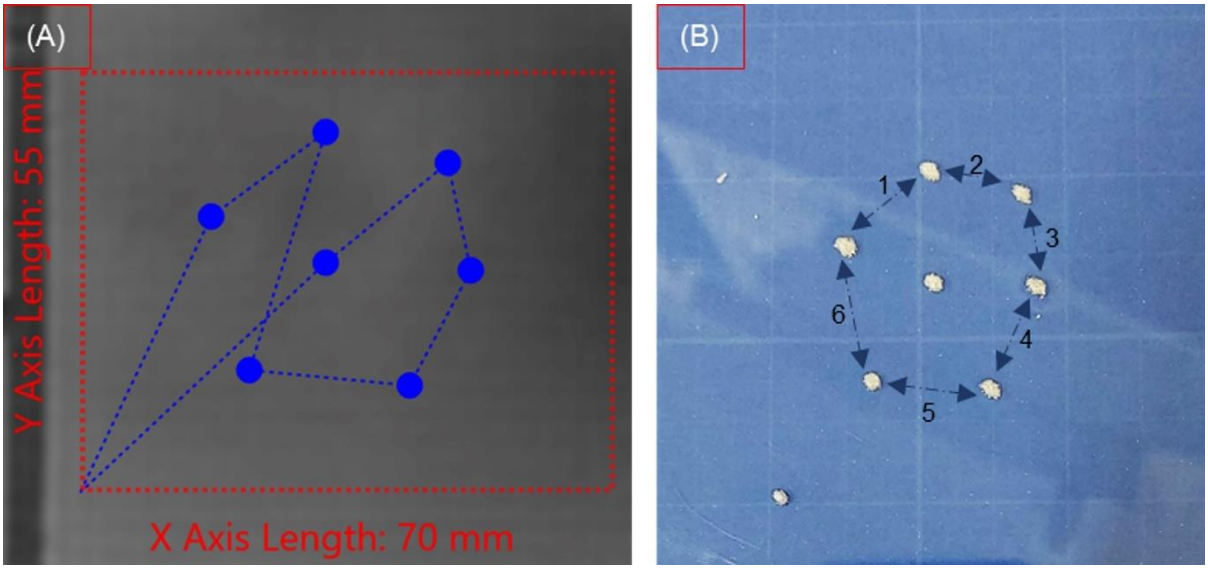

Figure 11

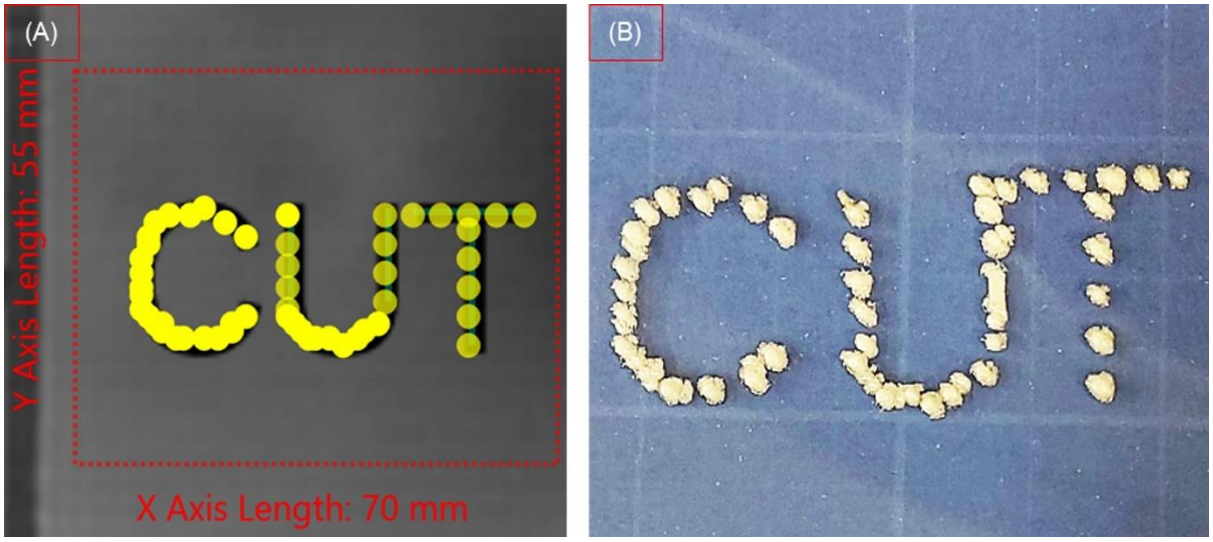

Figure 12

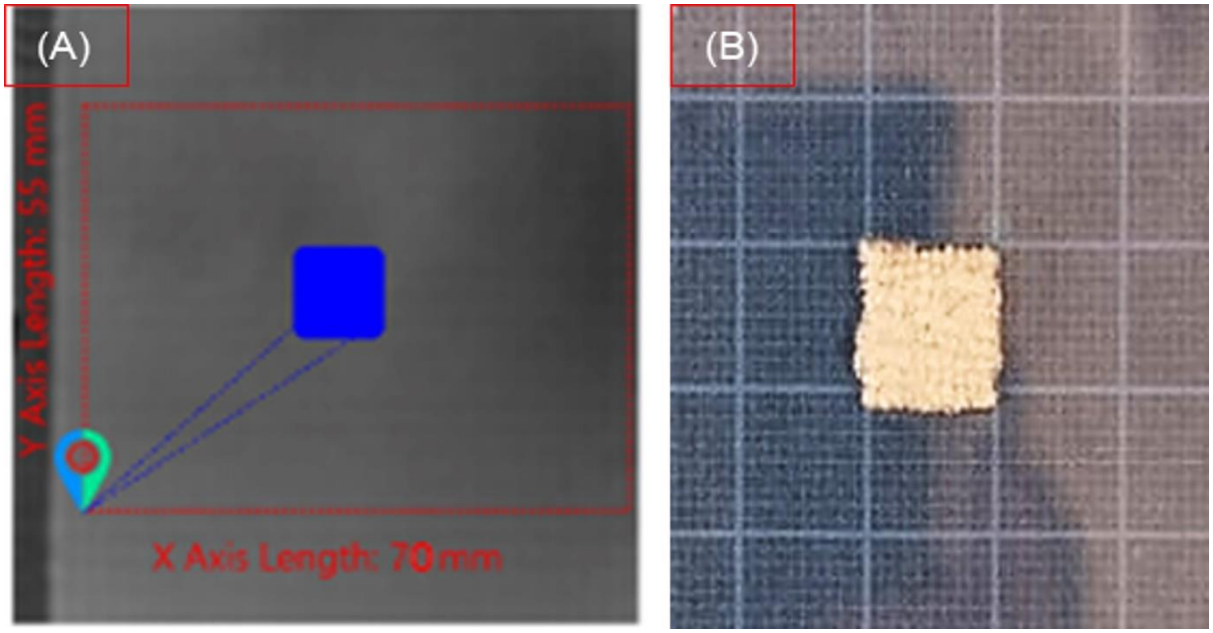

Figure 13

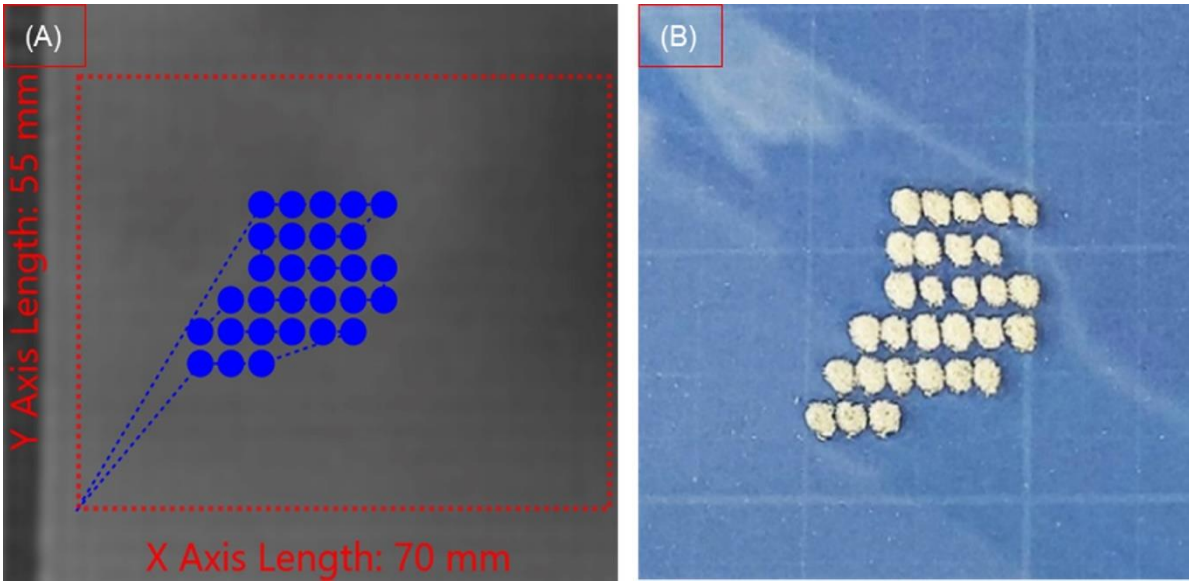

Figure 14

Physica Medica

Workflow of a preclinical robotic MRI-guided FUS body system

--Manuscript Draft--

Manuscript Number:	EJMP-D-23-00436
Article Type:	Original article
Keywords:	workflow; MRgFUS; ultrasound; robotic system; software; planning
Corresponding Author:	Christakis Damianou Cyprus University of Technology CYPRUS
First Author:	Nikolas Evripidou
Order of Authors:	Nikolas Evripidou
	Anastasia Antoniou
	George Lazarou
	Leonidas Georgiou
	Antreas Chrysanthou
	Cleanthis Ioannides
	Christakis Damianou
Abstract:	Purpose: Establishing an efficient workflow is crucial for the success of Magnetic Resonance guided Focused Ultrasound (MRgFUS) procedures. The current study provides a comprehensive description of the MRgFUS workflow of a customized preclinical robotic MRgFUS body device and accompanied software through experiments in excised porcine tissue. Methods: The employed system comprises a single element spherically focused transducer of 2.6 MHz that can be moved along four PC-controlled axes. Detailed description of essential software functionalities and its integration with a 3T Siemens MRI scanner via Access-i for interactive remote control of the scanner and real-time access to imaging data is provided. Following treatment planning on pre-operative MR images, porcine tissue samples were sonicated in rectangular and irregular grid patterns with varying ultrasonic parameters and spatial step under software-based monitoring. Results: MRgFUS ablations of ex-vivo porcine tissue were successfully performed utilizing a multimodal monitoring approach combining MRI-based temperature, thermal dose, and necrotic area mapping, thus demonstrating an efficient procedural workflow. The simulated necrotic regions were in excellent agreement with the actual lesions revealed upon tissue dissection, and highly consistent with the planned sonication patterns. The software's ability to accurately identify regions where necrosis did not occur and indicate to the user the specific points to be re-sonicated was demonstrated. Conclusions: Overall, the study highlights critical aspects in accurately planning and executing MRgFUS protocols within an efficient workflow. The provided data could serve as the basis for other researchers in the field.
Suggested Reviewers:	Costas Pattichis University of Cyprus pattichi@cs.ucy.ac.cy Experienced in the field.
	Jurgen Jenne mediri GmbH j.jenne@mediri.com Experienced in the field.
	Yves-Jean Chapelon National Institute of Health and Medical Research chapelon@lyon.inserm.fr Experienced in the field.

Opposed Reviewers:	

- MRgFUS workflow of preclinical robotic body device and accompanied software.
- Critical aspects in implementing MRgFUS protocols within an efficient workflow.
- Software integration with a 3T Siemens MRI scanner via Access-i.
- Ablations of *ex-vivo* porcine tissue successfully performed under MR-thermometry.
- Simulated necrotic areas agreed well with actual lesions and planned sonications.

Workflow of a preclinical robotic MRI-guided FUS body system

Nikolas Evripidou[a], Anastasia Antoniou[a], George Lazarou[a], Leonidas Georgiou[b], Antreas Chrysanthou[b], Cleanthis Ioannides[b], Christakis Damianou[a*]

[a] Department of Electrical Engineering, Computer Engineering, and Informatics, Cyprus University of Technology, Limassol, Cyprus.

[b] Department of Interventional Radiology, German Oncology Center, Limassol, Cyprus.

Authors' emails: nk.evripidou@edu.cut.ac.cy, anastasiaantoniou12@gmail.com, georgios.lazarou@gmail.com, leonidas.georgiou@goc.com.cy, antreas.chrysanthou@goc.com.cy, cleanthis.ioannides@goc.com.cy, christakis.damianou@cut.ac.cy.

* For correspondence contact:

Prof. Christakis Damianou,

Department of Electrical Engineering, Computer Engineering, and Informatics,

Cyprus University of Technology,

30 Archbishop Kyprianou Street, 3036 Limassol, Cyprus,

E-mail: christakis.damianou@cut.ac.cy

Tel: 0035725002039

Fax: 0035725002849

ABSTRACT

Purpose: Establishing an efficient workflow is crucial for the success of Magnetic Resonance guided Focused Ultrasound (MRgFUS) procedures. The current study provides a comprehensive description of the MRgFUS workflow of a customized preclinical robotic MRgFUS body device and accompanied software through experiments in excised porcine tissue.

Methods: The employed system comprises a single element spherically focused transducer of 2.6 MHz that can be moved along four PC-controlled axes. Detailed description of essential software functionalities and its integration with a 3T Siemens MRI scanner via Access-i for interactive remote control of the scanner and real-time access to imaging data is provided. Following treatment planning on pre-operative MR images, porcine tissue samples were sonicated in rectangular and irregular grid patterns with varying ultrasonic parameters and spatial step under software-based monitoring.

Results: MRgFUS ablations of *ex-vivo* porcine tissue were successfully performed utilizing a multimodal monitoring approach combining MRI-based temperature, thermal dose, and necrotic area mapping, thus demonstrating an efficient procedural workflow. The simulated necrotic regions were in excellent agreement with the actual lesions revealed upon tissue dissection, and highly consistent with the planned sonication patterns. The software's ability to accurately identify regions where necrosis did not occur and indicate to the user the specific points to be re-sonicated was demonstrated.

Conclusions: Overall, the study highlights critical aspects in accurately planning and executing MRgFUS protocols within an efficient workflow. The provided data could serve as the basis for other researchers in the field.

KEYWORDS: workflow; MRgFUS; ultrasound; robotic system; software; planning

1. INTRODUCTION

Magnetic Resonance-guided Focused Ultrasound (MRgFUS) is a non-invasive treatment modality that uses high-intensity ultrasonic waves to ablate targeted tissue within the body [1]. As a non-invasive modality, it may lead to quicker recovery, lower infection risks, and overall, to a superior life quality compared to standard surgical approaches [2]. Magnetic Resonance Imaging (MRI) guidance is deemed crucial for the success of FUS ablation since it provides real-time MR thermometry feedback, thereby allowing for the intraprocedural assessment of the therapeutic outcome and adjustment of the sonication protocol as necessary [1]. There are currently two commercial MRgFUS systems for treating body targets, both employing the phased array ultrasonic technology; the first one is the ExAblate 2000/2100 system owned by Insightec (InSightec Inc., Haifa, Israel) [3] and the second one is the Sonalleve system from Profound Medical (Profound Medical Corp., Mississauga, ON, Canada) [4]. Both systems have been approved by the US Food and Drug Administration (FDA) for the treatment of uterine fibroids and pain palliation of bone metastases. They can be integrated into the table of 1.5 and 3 T MRI scanners for a bottom-to-top ultrasonic delivery in prone-positioned patients.

An efficient treatment workflow is critical to the success of MRgFUS procedures since it ensures that patients receive the highest quality of care while minimizing discomfort and risk. It also contributes to efficient time management by optimizing the use of resources (equipment, staff, etc.), potentially improving patient throughput [5,6]. The workflow steps depend on and should be adjusted according to the specifications and unique features of each MRgFUS system. As an example, the ExAblate system performs point by point sonications leaving a cooling period between them, whereas a volumetric ablation technique based on a circular sonication pattern progressing from the inside towards the outside is employed by the Sonalleve system [7]. Accordingly, the ablation approach differentiates the treatment

planning and delivery process, and also affects other factors of the workflow, such as the treatment time. In this regard, each system has accompanying software platforms designed on its specific functionalities [7–9]. However, in a general overview, the basic steps employed in the treatment workflow of external MRgFUS body systems are similar.

Before the actual treatment session, the patient's medical history should be assessed and preliminary Computed Tomography (CT)/MRI scans may be acquired to determine the suitability and therapeutic strategy to be followed, as well as to outline a draft treatment plan [5]. On the day of treatment, the first step in the MRgFUS workflow is patient preparation, with skin preparation (e.g., complete removal of hair and air bubbles intervening the beam path) being crucial for achieving efficient ultrasonic transmission and avoiding skin burns.

The second step in the process is treatment planning, which involves acquiring pre-therapy planning images to determine the targeted tissue and optimal treatment parameters [5,10,11]. At this step, prior planning data may be incorporated into pre-therapy images. The treatment protocol is adjusted as required to minimize the risk of adverse events and ensure the best possible outcome for patients. Following segmentation of the regions of interest (ROIs), treatment volumes are distributed throughout the delineated area for ablation accounting for any sensitive structures that may interfere with the ultrasound beam and cause adverse effects [5,10,11]. The physician typically uses an advanced treatment planning software to map out the treatment path by overlaying a 3D map of the treatment area on anatomical images.

Before treatment delivery, the transducer is aligned with the target and low power (non-ablative) sonications are performed for focal spot verification [6]. The treatment is normally performed under conscious sedation or general anesthesia, depending on the patient's condition and preferences [6], with the patient lying on the MRI table, typically in the prone position. Continuous monitoring, including monitoring of the patient's vital signs and MR thermometry monitoring of the temperature evolution, is required to guarantee effectiveness

and safety [5,6], also by enabling interim modifications of the plan. Thermal dose calculation may be employed complementary to temperature measurements to determine coagulative necrosis of the targeted tissue and ensure that the surrounding healthy tissue is spared. Following treatment delivery, MRI is employed for assessing the treatment outcomes. Contrast agents are typically administered to identify the coagulated region, which is characterized as the non-perfused volume (NPV) [5,6,12].

Anneveldt et al. [13] conducted a retrospective analysis and discussed the strategies, challenges, and outcomes encountered during the implementation of MRgFUS as a non-invasive treatment option for uterine fibroids. The study covers practical aspects of this indication, from patient selection step to the post-treatment follow-up. Clinical outcomes, such as reduction in fibroid volume and relief of symptoms in the treated patients, are also examined. The study further underlines that the success of the procedure, highly relies on a productive collaboration between medical specialists. In this context, Payne et al [6] have recently published an informative guide for medical physicists regarding proper utilization of MRgFUS body systems based on the specifications of the Exablate system. Their study covers important technical considerations, safety measures, and quality assurance protocols aiming to ensure successful and effective implementation of this technology in clinical practice.

Meng et al. [10] outline the technical considerations of transcranial MRgFUS while presenting a range of neurological disorders where MRgFUS has shown promising results. A comprehensive overview of the technical principles and clinical workflow of transcranial MRgFUS is provided. Authors not only outline the different stages involved in the process, but also discuss specific patient selection criteria and common ultrasonic and MRI monitoring protocols employed in the treatment depending on the specific neurological indication. Follow-up MRI techniques for assessing tissue response and safety measures,

such as cooling techniques to prevent off-target heating, are also discussed. The importance of having a multidisciplinary team approach involving radiologists, neurologists, and neurosurgeons to ensure safe and effective implementation of the procedure is emphasized as well [10].

There have been proposed numerous algorithms aiming to advance and optimize different aspects of the MRgFUS treatment workflow, ultimately improving the safety, efficacy, and outcome of the procedure. For instance, there are algorithms dedicated to precise segmentation and sonication path planning for full coverage of the ROIs [11,14]. In this context, the impact of different ROI coverage algorithms on critical factors of the MRgFUS workflow, such as time management and near field heating, has been examined [15,16]. Other proposed algorithms aim to address the challenge of treating moving abdominal organs [17,18]. Indicatively, Schwenke et al. [18] have proposed a software tool that combines patient-specific simulation models of respiratory motion and motion tracking techniques to predict and compensate for organ motion intra-procedurally. Another noteworthy study by Zhang et al. [19] concerns the development of a flexible software architecture that can be used across different MRgFUS and MRI systems to guide the operator through the entire process, from the planning of treatment volumes to MRI-guided therapy under regular motion monitoring, and post-treatment assessment of NPVs. Interestingly, treatment execution is a three phase process involving the delivery of low and medium energy to respectively calibrate the beam position and dose, followed by sequential sonications using ablative energy levels [19].

Numerous studies provide insights on the MRgFUS workflow through sharing clinical experiences on specific MRgFUS indications. However, there is a limited number of studies dedicated to comprehensively describing the MRgFUS workflow and identifying critical aspects in the procedure. Researchers in the field and the medical physicist's community are

in need of such dedicated studies to openly exchange insights and expertise in a combined effort to address current limitations and challenges in the implementation of MRgFUS procedures, thus accelerating the adoption of this emerging technology in more clinical applications. The development of advanced MRgFUS software tools undeniably constitutes an integral part of this process.

The current study aimed to contribute in this effort by establishing a detailed workflow for preclinical MRgFUS studies through a series of ablation experiments in excised porcine tissue using a customized MRgFUS robotic device and accompanied software. The employed system [20] comprises a single element spherically focused transducer of 2.6 MHz that can be moved along four PC-controlled axes (X, Y, Z, Θ). The study provides a comprehensive description of essential software functionalities and its integration with a 3T Siemens MRI scanner via the Access-i software, which allows for remote control of the scanner and direct storage and process of MR images. Overall, an overview of the principles and workflow of a robotic MRgFUS body system is provided to the reader, which may serve as a baseline for other researchers in the field.

2. MATERIALS AND METHODS

2.1 Key features of the MRgFUS system

The device employed in the study consists of a mechanism enclosure hosting all the mechatronic components and a water enclosure, wherein a single-element spherically-focused ultrasonic transducer is actuated [20]. The positioning mechanism was designed with three linear and one angular piezoelectrically-actuated degrees of freedom (DOF) for steering the FUS beam into the subject. The water container includes a rectangular acoustic opening above the transducer's working space that is sealed with a coupling membrane, upon which the tissue of interest is placed. Degassed water is used as the coupling medium.

The system was designed to meet the specific requirements and challenges associated with robotic operation in an MRI setting. The robotic device was manufactured with MR compatible materials having dimensions compatible with the bore size of conventional MRI scanners. A custom made electronic driving system is externally wired to the device enabling the initiation and control of robotic movements through electronic signals. During motion, optical encoders (US Digital Corporation, Vancouver, WA 98684, USA) provide motion feedback to ensure accurate positioning of the ultrasonic source relevant to the target. The FUS system is supplied by an RF amplifier (AG1016, AG Series Amplifier, T & C Power Conversion, Inc., Rochester, USA) that is also located in the operator's room. Electronic signals are transferred by shielded cables passing through a penetration hole with integrated waveguides on the wall that separates the two rooms. Furthermore, the signals undergo filtering to ensure that interference frequencies are not transmitted into the MRI suite. The system further includes a water circulation system with integrated vacuum degassing pumps (DP-521, Baoding Shenchen Precision pump Co., Ltd, Baoding, China) and an MR-compatible camera (12M, MRC Systems GmbH, Heidelberg, Germany) for the direct visualization of acute tissue effects. Remote control of both the MRI and MRgFUS systems is available through an advanced dedicated software with treatment planning and monitoring features. The diagram of Figure 1 illustrates the communication between the MRgFUS and MRI systems.

2.2 MRgFUS software

2.2.1 Main functionalities

The software's main programming language is C# (Microsoft Corporation, Washington, USA) while python scripts (Python Software Foundation, Delaware, USA) were also incorporated to enhance its capabilities in parallel processing. It was built on the Windows

Presentation Foundation (WPF) platform, which allowed creating an advanced user-friendly graphical user interface (GUI), offering swift execution of commands and adaptability for future additions.

The software acts as the central control hub, facilitating communication and synchronization among the different system components. Figure 2A shows a schematic diagram of the software connection with the various peripheral devices. Figure 2B is a screenshot of the main software window that includes the treatment planning window and main toolbar (left side) with the various other functionality GUI buttons available. The software interfaces with the MRI system via Access-I for directly transferring imaging data and retrieving Digital Imaging and Communications in Medicine (DICOM) images from the scanner for both treatment planning and monitoring purposes.

Treatment planning is performed on preoperative DICOM images, where the ablation pattern is determined by the user using one of the three manual design options available in the drawing tool panel: 1) distribution of random sonication points, 2) selection of a rectangular area and specific motion resolution (grid sonication pattern), or 3) semi-automatic selection of a non-uniform area (irregular sonication pattern). In the latter case, the sonication pathway for full coverage of the segmented region is automatically generated by a dedicated algorithm utilizing a Zig-Zag pattern [14]. Otherwise, the user can select the desired sorting type among sequential, spiral, or Zig-Zag, determining the order in which the various sonication points will be visited (Sorting type menu). The extracted motion commands are then sent by the software to the motors through a Universal Serial Bus (USB) port to dynamically adjust the ultrasonic beam according to the planned sonication protocol. There is also a GUI panel dedicated to controlling the power output of the amplifier (Amplifier setup menu), which also connects with the software through USB interfaces.

Moreover, communication with an external water degassing system was successfully attained, enabling control of water inlet and circulation within the water container of the robotic device to ensure degassing of the water surrounding the transducer. Additionally, the same system ensures transducer cooling and cooling of the skin surface in future clinical use (Pump activation). Real-time visual inspection of the in-bore procedure is available on the software utilizing the MRI compatible camera (Camera monitoring).

2.2.2 Access-I

A major functionality added in the software is the Access-i that enables remote control of MAGNETOM MRI scanners manufactured by Siemens Healthineers (Erlangen, Germany). Specifically, the MRgFUS software was interfaced with a 3T Magnetom Vida scanner to establish a complete and efficient workflow. The Access-i software package was initially installed on the relevant scanner, acting as a middleware layer facilitating the communication between the scanner and the MRgFUS software. The existing software was then adapted by incorporating two Access-i functionalities utilizing dedicated software development kits provided by Siemens and according to the specific guidelines provided in the Access-i Developer Guide document.

The first functionality establishes a passive connection with the Access-i server of the scanner based on a python script that allows for real time image storage and processing. The second functionality establishes an interactive connection with the scanner enabling remote overall control and triggering of the MRI system. This interactive functionality can be simply activated by double-clicking on the “Access-i” button on the toolbar of the main window (Figure 2). The relevant panel includes the 3 main subpanels shown in Figure 3. The user should initially request access to the Access-i functionality and then control of the MRI scanner. Note that planning of imaging sequences was not employed under this functionality.

The sequences are planned as normally on the MRI console and collected in a list at the "Available programs" subpanel, provided that they were previously made available to the software by attaching the Access-i Dot-AddIn within the Dot Cockpit interface of the scanner. The sequences of interest are then moved by the user to the "Templates in the queue" subpanel. The ones to be executed are finally transferred to the "Executed Templates" subpanel, from which they can be manually started. Also, the user can select from this list the desired sequence to be used for thermometry by clicking the "Use for thermometry" button (Figure 3) and then initiate online thermometry through the relevant Thermometry monitoring panel of the main window toolbar (Figure 2).

As a result, the software allows interactive remote control of the MRI scanner and access to imaging data. The scanner can be remotely triggered to initiate imaging while the acquired images are directly transferred to and processed by the software in near real-time for monitoring purposes. The user can terminate a sequence at any time if necessary.

2.2.3 MR thermometry and thermal dose calculation

The real time acquisition and transfer of MR images via Access-i allowed the integration of MR thermometry tools in the software. The main treatment planning software runs in parallel to a separate MR thermometry script written in Python for dynamically generating and displaying temperature and thermal dose maps during execution of the planned sonication protocol.

During ultrasonic heating, the software determines the temperature changes within the ROI by employing the proton resonance frequency (PRF) shift method [21]. This method involves comparing the phase between an initial baseline image acquired at a reference temperature (φ_0) and subsequent images taken at different time points intra- and post-procedurally (φ). These phase changes arise from the temperature dependent PRF changes in

the ROI, and can be converted into the respective temperature changes (ΔT) by applying the following relation:

$$\Delta T = \frac{\varphi - \varphi_0}{\gamma \, \alpha \, B_0 \, TE} \quad [1]$$

where γ is the gyromagnetic ratio, α is the PRF change coefficient, B_0 is the magnetic field strength (3T), and TE is the echo time. The maps are typically constructed using a 2D Fast Low Angle Shot (FLASH) sequence.

The thermal dose is used as the main metric for assessing whether tissue necrosis has been successfully achieved. The software calculates the thermal dose according to the method proposed by Sapareto and Dewey using the following equation [22]:

$$CEM43°\text{C} = \sum_{t=0}^{t=final} R^{(43-T)} \Delta t \quad [2]$$

where $CEM43°\text{C}$ is the cumulative number of equivalent minutes at 43 °C, T is the average temperature during the elapsed time Δt, and R is the temperature-dependent rate of cell death (a constant of 0.25 is used for temperatures smaller than 43 °C and 0.5 for temperatures higher than 43 °C). Generally, a thermal dose equal to 240 $CEM43°\text{C}$ is considered sufficient for achieving coagulative necrosis of tissue (i.e., the tissue needs to be exposed to a cumulative equivalent of 240 minutes at 43 °C) [23,24].

The treatment monitoring tools are available in the Thermometry monitoring panel (Figure 2), which is divided into several subpanels enabling the user to set essential parameters required for MR thermometry (e.g., number of reference images, T tolerance, thermal dose threshold, etc.) and visualize dynamic temperature maps, thermal dose maps, necrosis maps, and time-series temperature data in parallel. The estimated temperatures and accumulated thermal dose are represented as colour-coded maps, which can be overlaid on anatomical images to provide a comprehensive visualization of the treatment area. Notably, the thermal

dose values are expressed in a color-coded (blue-to-red) logarithmic scale. The simulated area of tissue necrosis is also overlaid on the corresponding magnitude image of the subject as a red region. Quantitative information on the necrotic region (i.e., the extent of necrosis in mm^2) is also extracted automatically and displayed on the relevant monitoring panel and updated for each individual sonication and timepoint during treatment. Additionally, the software identifies and indicates to the user the regions that did not receive ablative thermal dose during the initial sonication and should be re-exposed. This process may require adjusting the FUS parameters (e.g., the acoustic intensity, duration) to deliver sufficient thermal dose for tissue necrosis in the relevant regions.

2.3 Treatment workflow

The main steps followed for performing an MRgFUS procedure with the proposed preclinical robotic system are summarized in the workflow diagram of Figure 4. The first step in the MRgFUS workflow concerns the positioning and registration of the robot in the MRI coordinates. Localizer images are initially acquired to assess successful subject-transducer setup and determine the appropriate FOV for subsequent sequences. For instance, air bubbles may be identified in the treatment pathway and removed using the degassing pumps, thus optimizing the acoustic coupling. Transducer tracking in the MRI coordinates and identification of the ROI in relation to the transducer home position is simply achieved by acquiring parallel slices at the level of the transducer (located at the axes origin) and targeted tissue. Fast Spin Echo (FSE) sequences are typically employed for this purpose, or the localizer images may be used alternatively. Once the user specifies the transducer location, a marker appears at its center, which is subsequently superimposed onto the DICOM images utilized for treatment planning.

The treatment planning process begins with the creation of a layer on a specific DICOM image of the subject, which includes an overlay of the transducer position and available working area, as defined by the motion range limits of the robot. The user specifies the Z-position of this specific layer, which is then translated into the corresponding height along the Z-axis of the device so that ultrasonic energy can be delivered to the particular layer.

The next planning step involves defining the region for ablation and motion parameters (step size, sorting type, etc.), followed by automatic prescription of sonication foci to cover the ROI. The amplifier parameters (power, frequency, sonication duration) and time delay between successive sonications are then defined by the user. Notably, for treatment in a three-dimensional space, the planning procedure should be repeated for multiple layers at different height (Z-axis).

Before initiating sonication, the user should select the desired sequence for thermometry from the Access-i panel and initiate the process though the MR thermometry monitoring panel (as described in section 2.2.2). After the acquisition of at least 3 references images, the sonication protocol can be activated. A test low power sonication may be carried out once the transducer is moved to the first point of sonication to verify accurate location of the focal point before proceeding to full power sonication.

During execution of the planned sonication, a multi-fold monitoring approach is available combining FLASH-based temperature, thermal dose, and necrotic area mapping. The latest thermometry data are displayed on-screen at time intervals equal to the image acquisition time of the employed MR imaging sequence. The necrosis map is overlaid on anatomical images of the ROI revealing potential ’viable’ regions where sonication should be repeated. The software returns a true or false value for each sonicated point indicating the presence or absence of necrosis, respectively. Thereby, the user can repeat unsuccessful sonications following adjustment of the sonication protocol if required.

By the end of the sonication, T1-Weighted (T1-W) or T2-Weighted (T2-W) FSE imaging is employed for assessing the treatment effects, including lesion formation and potential off-target tissue effects.

2.4 MRgFUS ablation in *ex-vivo* porcine tissue

The robotic device was placed on the table of the 3T Magnetom Vida scanner as shown in the photo of Figure 5. A piece of freshly excised porcine tissue was securely positioned on the acoustic opening. Degassed water was used to completely fill the space between the membrane and tissue to allow for efficient ultrasound transmission. A plastic structure was attached on the MRI table to support the imaging coil at a small distance above the ROI. Notably, isolation of the coil from the sonicated sample is considered essential to prevent the transfer of vibrations to the coil [25].

A single element spherical focused transducer (Piezohannas, Wuhan, China) with a frequency of 2.6 MHz, diameter of 50 mm, radius of curvature of 65 mm, and efficiency of 30 % was employed in all the experiments. The tissue sample was sonicated in different grid patterns with varying spatial step and a 60-s delay between sequential sonications. Each grid spot was exposed at acoustic power of 75-90 W for a duration of 20-30 s, with the focal depth set at 35 mm. The tissue effects were monitored using MR thermometry according to equation [1], where the magnitude of α was set at 0.0094 ppm/ºC [26]. The temperature and thermal dose distribution were mapped on a pixel-by-pixel basis by dynamic acquisition of 2D FLASH images with repetition time (TR) = 25 ms, echo time (TE) = 10 ms, flip angle (FA) = 30°, echo train length (ETL) =1, pixel bandwidth = 250 Hz/pixel, field of view (FOV) = 280x280x3 mm^3, acquisition matrix size = 96x96, and acquisition time/slice = 2.4 s, using the multi-channel Spine-72-RS coil (Siemens).

Post sonication assessment of lesion formation included T2-W imaging followed by tissue dissection to determine the actual size of lesions. T2-W FSE images were acquired with a multichannel body coil (Body18, Siemens) using TR = 4000 ms, TE =52 ms, FA = 110°, ETL = 20, pixel bandwidth = 250 Hz/pixel, FOV =245 x 261 x 3 mm^3, matrix size =256 x 240, and slice thickness = 3 mm.

3. RESULTS

MRgFUS ablation of *ex-vivo* porcine tissue was successfully performed without any identified FUS-related off-target effects, thus demonstrating an efficient procedural workflow. Indicative results of the MRgFUS procedure from treatment planning to post-sonication assessment are presented by Figures 6 to 11.

The first example concerns a 6x6 rhomboid grid, where each spot was exposed at 75 W acoustic power for 30 s, using a 60-s delay between adjacent sonications. The spatial step was set at 10 mm in both the X- and Y-axes. Figure 6 is a screenshot of the software acquired during execution of the planned sonication. As shown, the software interface allowed the user to visualize in real-time the temperature, thermal dose, and necrosis evolution in the relevant monitoring sub-panels. Note that the treatment planning window appears at the right side of this window showing the planned sonication pattern overlaid on the relevant reference image of the tissue.

Figure 7 is a collection of thermal maps acquired during the 6x6 sonication, providing a visual representation of the temperature distribution within the imaged region over time, with the color scale ranging from yellow to red representing temperatures from the lowest to the highest value. The temperature profiles recorded at the various focal spots during the sequential sonications are combined in the graph of Figure 8, where the various peaks indicate the maximum temperature achieved in each sonication spot. The maximum recorded

temperatures varied from a minimum value of 67°C to a maximum value of 93 °C. This graph reveals a clear increase in the baseline temperature with time owing to heat dissipation from previously sonicated areas.

Figure 9 provides a visual representation of the accuracy and effectiveness of the sonication. The planned sonication foci can be seen in the software screenshot of Figure 9A. Tissue necrosis was successfully monitored interprocedurally by dynamic thermal dose and necrotic area mapping, resulting in the final maps of Figure 9B and 9C, respectively, following completion of the sonication. The tissue effects were directly examined by T2-W FSE imaging and then by visual examination. An indicative MR image and a photo of the sonicated tissue are respectively shown in Figures 9D and 9E. Note that the mean lesion diameter as measured on the T2-W image of 6.6 ± 0.8 mm was smaller than the actual lesion size of 7.6 ± 0.9 mm measured with a caliper (0.1 mm resolution). Note also that the thermal dose and necrosis maps, as well as the actual lesions revealed upon tissue dissection, were in excellent agreement with the planned sonication pattern.

The overlapping lesion shown in Figure 10 was created by sonication in irregular pattern (Figure 10A) using similar acoustic power applied for 20 s, a smaller cooling time of 60 s, and a smaller spatial step of 3 mm. The T2-W image of the sonicated tissue revealed an oval lesion area of 13.6 cm^2 (Figure 10 B) compared to the actual area of 17.5 cm^2 measured on the tissue slice (Figure 10C).

Finally, Figure 11 presents the results of a test conducted to evaluate the software's capability to accurately identify regions where incomplete necrosis occurred. For this purpose, the amplifier was intentionally deactivated at two random points (No.6 and No.10) of a 4x4 grid pattern, simulating a particular scenario where sonication at these specific points was unsuccessful, potentially due to obstacles obstructing the beam pathway or an amplifier malfunctioning. In that case, each spot was exposed at 90 W acoustic power for 30

s using a step of 15 mm and leaving a 60-s delay between them. As shown in Figure 11A, the accumulated thermal dose remained below the set threshold for necrosis (240 $CEM43°C$), indicating that tissue necrosis was not achieved at these specific regions. The software successfully generated the corresponding necrosis map shown in Figure 11B, which coincides perfectly with the thermal dose map, indicating the regions of tissue that are spared and should be re-sonicated. Figure 11C shows the list of the sonication status returned to the user. Note that the relevant points (No.6 and No.10) have a “false” status, whereas the remaining points are flagged as "true", proving the software’s ability to accurately identify and indicate to the user which specific grid points should be re-visited.

4. DISCUSSION

The current study outlines the various steps involved in the MRgFUS workflow utilizing an MRgFUS body system and accompanied software. A thorough description of essential software features and how these were enhanced by incorporating Access-i functionalities to allow remote triggering of Siemens Magnetom scanners and real-time access to imaging data is provided. The effectiveness of the employed MRgFUS system is demonstrated by providing indicative results of MRgFUS ablation in *ex-vivo* animal tissue. In this context, an efficient procedural workflow, from treatment planning to intra-procedural MR thermometry-based monitoring, and post-sonication MRI assessment of acute tissue effects is established. Remarkably, the creation of a comprehensive MRgFUS preclinical workflow could serve as the basis for the protocol optimization of our robots [20,27-38].

In commercial MRgFUS body systems, electronic steering is used to scan the beam throughout the target volume and is typically performed complementary to mechanical positioning of the source depending on the ROI size [3,4]. The need to control each array element individually results in the need of advanced signal processing algorithms [39]

complicating and prolonging the procedure. The MRgFUS system used in the present study is considered much simpler and more ergonomic compared to systems employing phased arrays, thereby simplifying the overall treatment workflow.

Various MRgFUS protocols were planned and executed by the MRgFUS system with high precision and accuracy. Successful communication between the MRgFUS and MRI systems was established via dedicated Access-i functionalities, enabling the software to directly retrieve DICOM images of the porcine tissue sample and remotely trigger the MRI for the acquisition and display of MR images in actual time. MR thermometry monitoring of tissue ablation was successfully performed in a quite fast pulse sequence. The monitoring panel allowed the user to monitor the FUS-induced tissue effects through a dynamic display of temperature maps, thermal dose maps, and the simulated necrotic region overlaid on magnitude images of the subject (Figure 6). The software was also proven efficient in determining whether tissue necrosis was successfully achieved and indicating to the user the specific grid points that should be re-sonicated (Figure 11).

The positioning mechanism precisely navigated the ultrasonic beam aligning it with the desired treatment locations within the porcine tissue sample. The selected ultrasonic parameters resulted in tissue necrosis (accumulated thermal dose > 240 $CEM43°C$), also confirming that an efficient coupling with the target was achieved. For instance, in the 6x6 grid where the various sonication points were exposed at a focal intensity of about 17440 W/cm^2 for 30 s, the recorded focal temperatures reached 67-93 °C, depending on the specific tissue characteristics (e.g., presence of fat and inhomogeneities) and pre-focal heat accumulation. The thermal dose distribution and simulated necrotic regions were highly consistent with the intended sonication pattern (Figure 9).

Post-sonication T2-W images showed a decrease in the signal intensity (SI) of the treated points, which served as an additional indication of successful sonication. The pattern of

inflicted lesions as visualized on the T2-W images agreed well with the planned sonication pattern, thermal dose distribution, and simulated regions of necrosis (Figure 9). Being in agreement with prior literature, the present findings reveal that MRI imaging may underestimate the size of FUS lesions [40], potentially owning to limitations in spatial resolution or inability to precisely delineate the lesion borders. Consequently, it is crucial for researchers to consider increasing the imaging resolution or possibly using other pulse sequences to ensure an accurate assessment of the extent of tissue necrosis following MRgFUS procedures. Notably, T1-W imaging may be preferable for lesion assessment in live tissue owing to the utilization of contrast agents. Finally, visual examination of the sonicated tissue confirmed that the formed lesions were precisely inflicted in tissue in the desired arrangement (Figure 9). Remarkably, none of the assessment methods revealed FUS-related off-target effects.

A potential limitation of these experiments is that sonications were limited in a single layer for the sake of simplicity, and thus, only the horizontal motion stages were activated. The described planning procedure could be repeated for multiple layers to enable treatment in the three-dimensional space. Motion along the Z-axis will be required in the case of sonicating different Z-layers. Furthermore, in the case of *in-vivo* application, beam angulation will most likely be necessary to prevent beam interference with critical structures such as bones, air regions, etc.

In this study, a cooling time of 60 s between consecutive sonications was considered sufficient to mitigate pre-focal heating phenomena [16]. However, the time-series plot of recorded temperatures (Figure 8) reveals clear evidence of heat dissipation among neighboring grid points (6x6 grid). Note that following completion of each sonication, the subsequent sonication point could not return to the baseline temperature within the 60-s cooling time, thus resulting in a progression increase in the baseline temperature over time.

This unavoidably led to an increasing heat accumulation (Figure 9B) and extend of tissue necrosis as the sonication pattern progressed towards its final points. Consequently, the discrete lesions gradually increased in diameter, ultimately merging into overlapping lesions within the final two (top) rows of the sonication grid (Figure 9E). It is thus crucial that during the planning process the pre-focal thermal dose accumulation is accounted in order to avoid damage of healthy tissue. In this context, cooling of the skin surface is also required to avoid skin burns, which constitute the most common FUS-induced complications, with the common reported rates being up to 10% [41,42].

Successful implementation of the planned sonication protocols further demonstrates the system's compatibility with the MRI. In this context, optimization of the coil position is deemed essential in achieving satisfactory signal to noise ratio (SNR) values for high quality imaging and thermometry [25]. A specific measure employed in this study is the isolation of the coil from the subject so that during sonication potential subject vibrations are not transferred to the coil. Additionally, the mechatronic parts of the robot were not included within the coil imaging area to minimize the possibilities for susceptibility artifacts. Generally, the operator should select the coil position carefully to ensure adequate proximity to the region of interest but not direct contact with the subject, and the absence of any interference with the beam. Notably, in clinical systems employing the phased array technology, MR thermometry is typically performed during electronic beam steering and not while the transducer is moving to avoid the introduction of susceptibility artifacts in thermal maps [6].

Although, in the general sense, the presented workflow applies also in the clinical setting, there exist additional considerations regarding applications in human subjects. Patient motion, far-field protection, and skin preparation are some of the safety considerations that should be taken into account within the clinical workflow [6]. Another essential safety

measure considered critical for *in-vivo* applications but not discussed in this study is the employment of a thermal dose verification sonication within the treatment planning process [6]. Such verification sonication is conducted to assess whether the predicted power levels for achieving the desired thermal dose accumulation are either excessive or insufficient, given that the temperature elevation is influenced not only by the energy applied but also by the intricate heat transfer mechanisms within tissues. Thereby, thermal dose testing is crucial to determining if any protocol calibration is required. Furthermore, the present study does not concern pre-treatment planning imaging, neither short- and long-term follow up [5]. The treatment duration constitutes an additional consideration not addressed herein. Although more crucial for clinical applications, the procedure duration is an important factor in preclinical MRgFUS applications as well, given that the MRI time is expensive and valuable. Researchers should thus carefully plan and optimize experimental protocols to make efficient use of the limited MRI time available.

Advantageously, the study provides a comprehensive description of the Access-i functionalities incorporated in the software to allow remote control of the scanner and the direct storage and processing of acquired images. To the best of the authors' knowledge, there is a lack of prior documentation on this topic. The absence of relevant documentation constitutes a significant challenge for the researchers, who encounter difficulties in establishing an efficient workflow in MRgFUS studies and waste valuable time to uncover insights that could have been extracted from existing literature. Therefore, this study holds potential to benefit other researchers in the field and accelerate future studies by enabling a basic understanding of the Access-i functionality. However, it is important to highlight that integration of any software in the Access-i MR Scanner Interface should be performed following the specific guidelines provided in the Access-I Developer Guide of Siemens and according to the unique features and intended application of the software.

Overall, the study outcomes prove the effectiveness of the employed MRgFUS system in accurately planning and executing MRgFUS protocols. The employed software integrates all the key functionalities required for establishing an efficient MRgFUS workflow, including direct acquisition of MRI images, transducer localization, treatment planning, and automatic execution of the planned sonication protocol under continuous software-based monitoring of the thermal dose accumulation and tissue necrosis in near real time. While these functionalities are satisfactory for preclinical applications, they should be potentially enhanced (e.g., to allow for motion compensation) to enable clinical translation. Through this paper, a comprehensive overview of the MRgFUS workflow of a preclinical body system is provided to the reader, highlighting critical aspects and potential matters of concern in establishing a successful workflow and maintaining optimal conditions for the delivery of MRgFUS. Therefore, it could be of benefit to researchers in the field aiming to implement similar studies, simultaneously contributing to advance the understanding of how to develop MRgFUS applications that could be more easily translated to the clinic.

LIST OF FIGURE CAPTIONS

Figure 1: Wiring diagram indicating the connection among components of the MRI and MRgFUS systems.

Figure 2: **(A)** Schematic diagram of software connection and communication with peripheral devices. **(B)** Screenshot of the initial main software window with the treatment planning window and the various functionality GUI buttons: [1] Drawing tool panel, [2] Sorting type menu, [3] Amplifier setup menu, [4] Manual motion control, [5] 'Homing' process, [6] Layer creation, [7] Access-I control, [8] Thermometry monitoring, [9] Pump activation, and [10] Camera monitoring.

Figure 3: Screenshot of the Access-i panel with three main subpanels: [1] Available programs, [2] Templates in the queue, and [3] Executed templates.

Figure 4: Schematic diagram of the treatment workflow with the proposed MRgFUS software.

Figure 5: The experimental setup for MRgFUS ablation of *ex-vivo* porcine tissue in the 3T Siemens MRI scanner.

Figure 6: Screenshot of the software with the MR thermometry monitoring panel activated, indicating the 4 main subpanels: [1] thermal maps, [2] thermal dose maps, [3] a timeseries temperature graph and [4] thermal necrosis area overlaid on magnitude image.

Figure 7: Coronal thermal maps acquired at the focal spot level using FLASH sequence showing the temperature evolution during the 6x6 sonication.

Figure 8: Timeseries plot of the focal temperature evolution during the 30-s of sonication and 60-s time delay at each of the 36 sonicated points.

Figure 9: (A) The 6x6 sonication pattern as planned on the DICOM image of the sample tissue. **(B)** Thermal dose map after the end of sonication expressed in log scale. The black bar

corresponds to a thermal dose of 240 CEM43℃. **(C)** The necrosis map after the end of sonication. **(D)** Post-sonication T2-W FSE coronal image of tissue showing the 36 formed lesions and axial image showing the lesions formed in a random grid row. **(E)** Photo of the tissue following dissection revealing the actual formed lesions.

Figure 10: (A) Irregular sonication pattern (overlapping) as planned on the DICOM reference image of the porcine tissue sample. **(B)** Post-sonication T2-W FSE coronal image of the tissue**. (C)** Photo of the tissue following dissection revealing the actual formed lesion.

Figure 11: Example of unsuccessful sonication: **(A)** The thermal dose map after a 4x4 grid sonication where the amplifier was de-activated at points No.6 and No.10. The black bar corresponds to a thermal dose of 240 CEM43℃. **(B)** The corresponding necrosis map; the necrotic regions appear in red and planned sonication points in blue. **(C)** The sonication status list returned to the user indicating the two points that were not successfully sonicated.

ACKNOWLEDGMENTS

The study was co-funded by the European Structural & Investment Funds (ESIF) and the Republic of Cyprus through the Research and Innovation Foundation (RIF) under the projects SOUNDPET (INTEGRATED/0918/0008) and FUSVET (SEED/1221/0080).

We would also like to acknowledge Prof. Samuel Pichardo (Cumming School of Medicine, University of Calgary, Calgary, Alberta, Canada) for providing the MR thermometry code.

DECLARATION OF INTEREST STATEMENT

All authors declare NO conflicts of interest.

ETHICS APPROVAL DECLARATION

The study does not involve animals or human participants. Therefore, no ethical approval is available.

REFERENCES

[1] Lee EJ, Fomenko A, Lozano AM. Magnetic resonance-guided focused ultrasound: Current status and future perspectives in thermal ablation and blood-brain barrier opening. J Korean Neurosurg Soc 2019;62:10–26. https://doi.org/10.3340/jkns.2018.0180.

[2] Izadifar Z, Izadifar Z, Chapman D, Babyn P. An Introduction to High Intensity Focused Ultrasound: Systematic Review on Principles, Devices, and Clinical Applications. J Clin Med 2020;9:460. https://doi.org/10.3390/jcm9020460.

[3] INSIGHTEC. Exablate Body. https://insightec.com/exablate-body/ (accessed May 24, 2023).

[4] Medical P. Sonalleve. https://profoundmedical.com/sonalleve/ (accessed May 24, 2023).

[5] Loeve AJ, Al-Issawi J, Fernandez-Gutiérrez F, Langø T, Strehlow J, Haase S, et al. Workflow and intervention times of MR-guided focused ultrasound-Predicing the impact of new techniques. J Biomed Inform 2016;60:38–48. https://doi.org/10.1016/j.jbi.2016.01.001.

[6] Payne A, Chopra R, Ellens N, Chen L, Ghanouni P, Sammet S, et al. AAPM Task Group 241_A medical physicist's guide to MRI- guided focused ultrasound body systems. Med Phys 2021;48:772–806. https://doi.org/10.1002/mp.15076.

[7] Gunderman A, Montayre R, Ranjan A, Chen Y. Review of Robot-Assisted HIFU Therapy. Sensors (Basel) 2023;23:1–27. https://doi.org/10.3390/s23073707.

[8] Zaporzan B, Waspe AC, Looi T, Mougenot C, Partanen A, Pichardo S. MatMRI and

MatHIFU: Software toolboxes for real-time monitoring and control of MR-guided HIFU. J Ther Ultrasound 2013;1. https://doi.org/10.1186/2050-5736-1-7.

[9] Abdullah B, Subramaniam R, Omar S, Wragg P, Ramli N, Wui A, et al. Magnetic resonance-guided focused ultrasound surgery (MRgFUS) treatment for uterine fibroids. Biomed Imaging Interv J 2010;5. https://doi.org/10.2349/biij.5.4.e33.

[10] Meng Y, Jones RM, Davidson B, Huang Y, Pople CB, Surendrakumar S, et al. Technical Principles and Clinical Workflow of Transcranial MR-Guided Focused Ultrasound. Stereotact Funct Neurosurg 2021;99:329–42. https://doi.org/10.1159/000512111.

[11] Vargas-Olivares A, Navarro-Hinojosa O, Pichardo S, Curiel L, Alencastre-Miranda M, Chong-Quero JE. Image Segmentation for the Treatment Planning of Magnetic Resonance-Guided High-Intensity Focused Ultrasound (MRgFUS) Therapy: A Parametric Study. Appl Sci 2019;9:1–23. https://doi.org/10.3390/app9245296.

[12] Kociuba J, Łoziński T, Zgliczyńska M, Byrczak M, Vitale SG, Skrzypczak M, et al. Adverse events and complications after magnetic resonance-guided focused ultrasound (MRgFUS) therapy in uterine fibroids–a systematic review and future perspectives. Int J Hyperth 2023;40. https://doi.org/10.1080/02656736.2023.2174274.

[13] Anneveldt KJ, Verpalen IM, Nijholt IM, Dijkstra JR, van den Hoed RD, van't Veer-ten Kate M, et al. Lessons learned during implementation of MR-guided High-Intensity Focused Ultrasound treatment of uterine fibroids. Insights Imaging 2021;12. https://doi.org/10.1186/s13244-021-01128-w.

[14] Antoniou A, Georgiou A, Evripidou N, Damianou C. Full coverage path planning algorithm for MRgFUS therapy. Int J Med Robot Comput Assist Surg 2022;18:1–10.

https://doi.org/10.1002/rcs.2389.

[15] Zhou Y, Kargl SG, Hwang JH. The Effect of the Scanning Pathway in High-Intensity Focused Ultrasound Therapy on Lesion Production. Ultrasound Med Biol 2011;37:1457–68. https://doi.org/10.1016/j.ultrasmedbio.2011.05.848.

[16] Filippou A, Drakos T, Giannakou M, Evripidou N, Damianou C. Experimental evaluation of the near-field and far-field heating of focused ultrasound using the thermal dose concept. Ultrasonics 2021;116:106513. https://doi.org/10.1016/j.ultras.2021.106513.

[17] Ferrer CJ, Bos C, de Senneville BD, Borman P, Stemkens B, Tijssen R, et al. A planning strategy for combined motion-assisted/gated MR guided focused ultrasound treatment of the pancreas. Int J Hyperth 2019;36:702–11. https://doi.org/10.1080/02656736.2019.1629650.

[18] Schwenke M, Strehlow J, Haase S, Jenne J, Tanner C, Lango T, et al. An integrated model-based software for FUS in moving abdominal organs. Int J Hyperth 2015;31:240–50. https://doi.org/10.3109/02656736.2014.1002817.

[19] Zhang S, Tang N, Shen G, Wang H, Qiao S. Universal Software Architecture of Magnetic Resonance-Guided Focused Ultrasound Surgery System and Experimental Study. J Shanghai Jiaotong Univ 2021;26:471–81. https://doi.org/10.1007/s12204-021-2325-1.

[20] Drakos T, Giannakou M, Menikou G, Filippou A, Evripidou N, Spanoudes K, et al. MRI-Guided Focused Ultrasound Robotic System for Preclinical use. J Vet Med Anim Sci 2021;4:1–11.

[21] Rieke V, Pauly KB. MR Thermometry. J Magn Reson Imaging 2008;27:376–90.

https://doi.org/10.1002/jmri.21265.MR.

[22] Sapareto SA, Dewey WC. Thermal dose determination in cancer therapy. Int J Radiat Oncol Biol Phys 1984;10:787–800. https://doi.org/10.1016/0360-3016(84)90379-1.

[23] Dewhirst MW, Viglianti BL, Lora-Michiels M, Hanson M, Hoopes PJ. Basic principles of thermal dosimetry and thermal thresholds for tissue damage from hyperthermia. Int J Hyperth 2003;19:267–94. https://doi.org/10.1080/0265673031000119006.

[24] Yarmolenko PS, Moon EJ, Landon C, Manzoor A, Hochman DW, Viglianti BL, et al. Thresholds for thermal damage to normal tissues: An update. Int J Hyperth 2011;27:320–43. https://doi.org/10.3109/02656736.2010.534527.

[25] Antoniou A, Georgiou L, Evripidou N, Ioannides C, Damianou C. Challenges regarding MR compatibility of an MRgFUS robotic system. J Magn Reson 2022;344:107317. https://doi.org/10.1016/j.jmr.2022.107317.

[26] Bing C, Staruch R, Tillander M, Köhler MO, Mougenot C, Ylihautala M, et al. Drift correction for accurate PRF shift MR thermometry during mild hyperthermia treatments with MR-HIFU. Int J Hyperth 2017;32:673–87. https://doi.org/10.1080/02656736.2016.1179799.

[27] Epaminonda E, Drakos T, Kalogirou C, Theodoulou M, Yiallouras C, Damianou C. MRI guided focused ultrasound robotic system for the treatment of gynaecological tumors. Int J Med Robot Comput Assist Surg 2016;12:46–52. https://doi.org/10.1002/rcs.1653.

[28] Yiannakou M, Menikou G, Yiallouras C, Ioannides C, Damianou C. MRI guided focused ultrasound robotic system for animal experiments. Int J Med Robot Comput

Assist Surg 2017;13:e1804. https://doi.org/10.1002/rcs.1804.

[29] Menikou G, Yiallouras C, Yiannakou M, Damianou C. MRI-guided focused ultrasound robotic system for the treatment of bone cancer. Int J Med Robot Comput Assist Surg 2017;13:1–11. https://doi.org/10.1002/rcs.1753.

[30] Antoniou A, Giannakou M, Evripidou N, Evripidou G, Spanoudes K, Menikou G, et al. Robotic system for magnetic resonance guided focused ultrasound ablation of abdominal cancer. Int J Med Robot Comput Assist Surg 2021;17. https://doi.org/10.1002/rcs.2299.

[31] Damianou C, Giannakou M, Menikou G, Ioannou L. Magnetic resonance imaging-guided focused ultrasound robotic system with the subject placed in the prone position. Digit Med 2020;6:24–31. https://doi.org/10.4103/digm.digm_2_20.

[32] Antoniou A, Giannakou M, Evripidou N, Stratis S, Pichardo S, Damianou C. Robotic system for top to bottom MRgFUS therapy of multiple cancer types. Int J Med Robot Comput Assist Surg 2022. https://doi.org/10.1002/rcs.2364.

[33] Giannakou M, Antoniou A, Damianou C. Preclinical robotic device for magnetic resonance imaging guided focussed ultrasound. Int J Med Robot Comput Assist Surg 2022:1–10. https://doi.org/10.1002/rcs.2466.

[34] Antoniou A, Giannakou M, Georgiou E, Kleopa KA, Damianou C. Robotic device for transcranial focussed ultrasound applications in small animal models. Int J Med Robot Comput Assist Surg 2022:1–11. https://doi.org/10.1002/rcs.2447.

[35] Damianou C, Yiannakou M. Multi-purpose robotic system for MRI guided focused ultrasound treatment. EP3254731A1, 2017.

[36] Filippou A, Evripidou N, Damianou C. Robotic system for magnetic resonance

imaging-guided focused ultrasound treatment of thyroid nodules. Int J Med Robot 2023. https://doi.org/10.1002/rcs.2525.

[37] Giannakou M, Drakos T, Menikou G, Evripidou N, Filippou A, Spanoudes K, et al. Magnetic resonance image-guided focused ultrasound robotic system for transrectal prostate cancer therapy. Int J Med Robot 2021;7:e2237. https://doi.org/10.1002/rcs.2237.

[38] Yiallouras C, Yiannakou M, Menikou G, Damianou C. A multipurpose positioning device for magnetic resonance imaging-guided focused ultrasound surgery. Digit Med 2017;3:138–44. https://doi.org/10.4103/digm.digm_33_17.

[39] Hynynen K, Jones RM. Image-guided ultrasound phased arrays are a disruptive technology for non-invasive therapy. Phys Med Biol 2016;61:206–248. https://doi.org/10.1088/0031-9155/61/17/R206.

[40] Allen SP, Prada F, Xu Z, Gatesman J, Feng X, Sporkin H, et al. A preclinical study of diffusion-weighted MRI contrast as an early indicator of thermal ablation. Magn Reson Med 2021;85:2145–59. https://doi.org/10.1002/mrm.28537.

[41] Hurwitz MD, Ghanouni P, Kanaev S V., Iozeffi D, Gianfelice D, Fennessy FM, et al. Magnetic resonance-guided focused ultrasound for patients with painful bone metastases: Phase III trial results. J Natl Cancer Inst 2014;106:1–9. https://doi.org/10.1093/jnci/dju082.

[42] Lin X, Chen W, Wei F. Technique Success, Technique Efficacy and Complications of HIFU Ablation for Palliation of Pain in Patients With Bone Lesions: A Meta-Analysis of 28 Feasibility Studies. Ultrasound Med Biol 2021;47:1182–91. https://doi.org/10.1016/j.ultrasmedbio.2021.01.018.

Figure 1

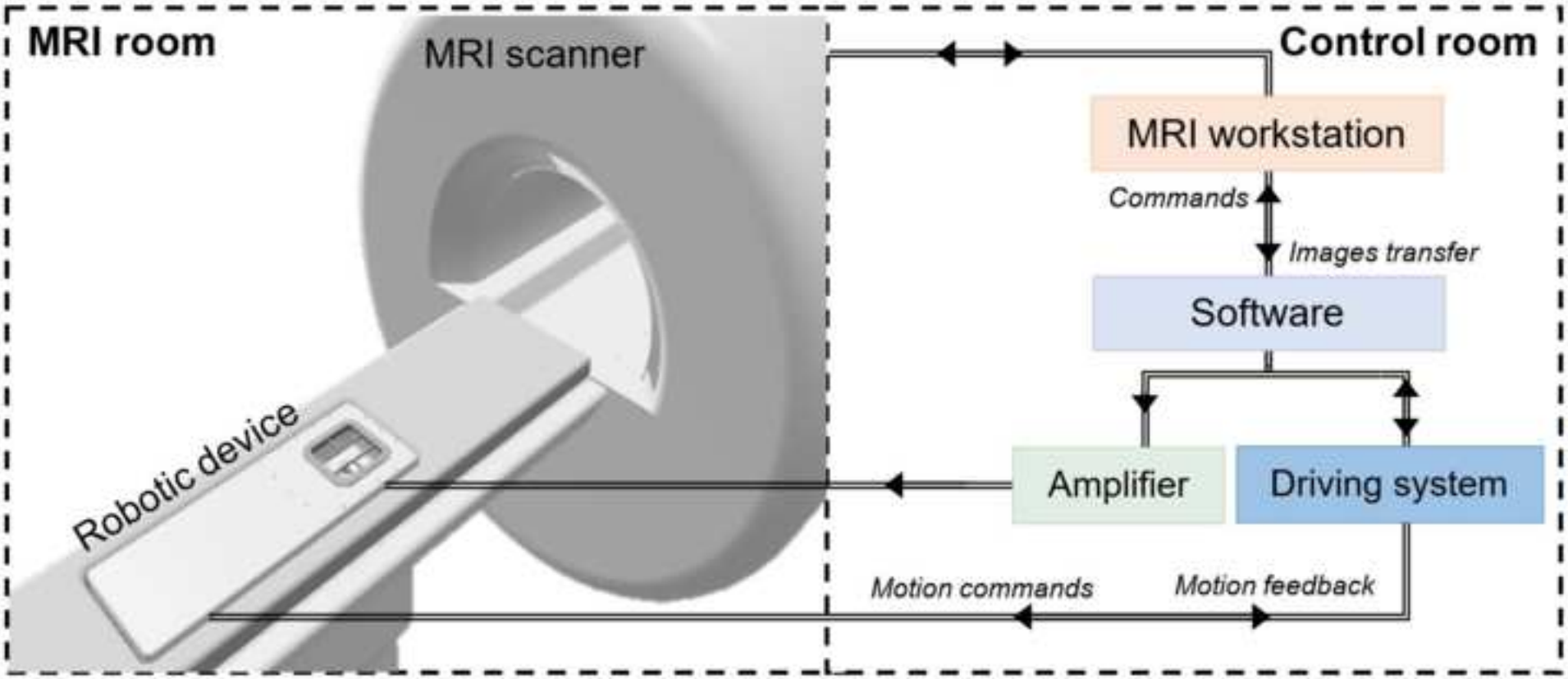

Figure 2

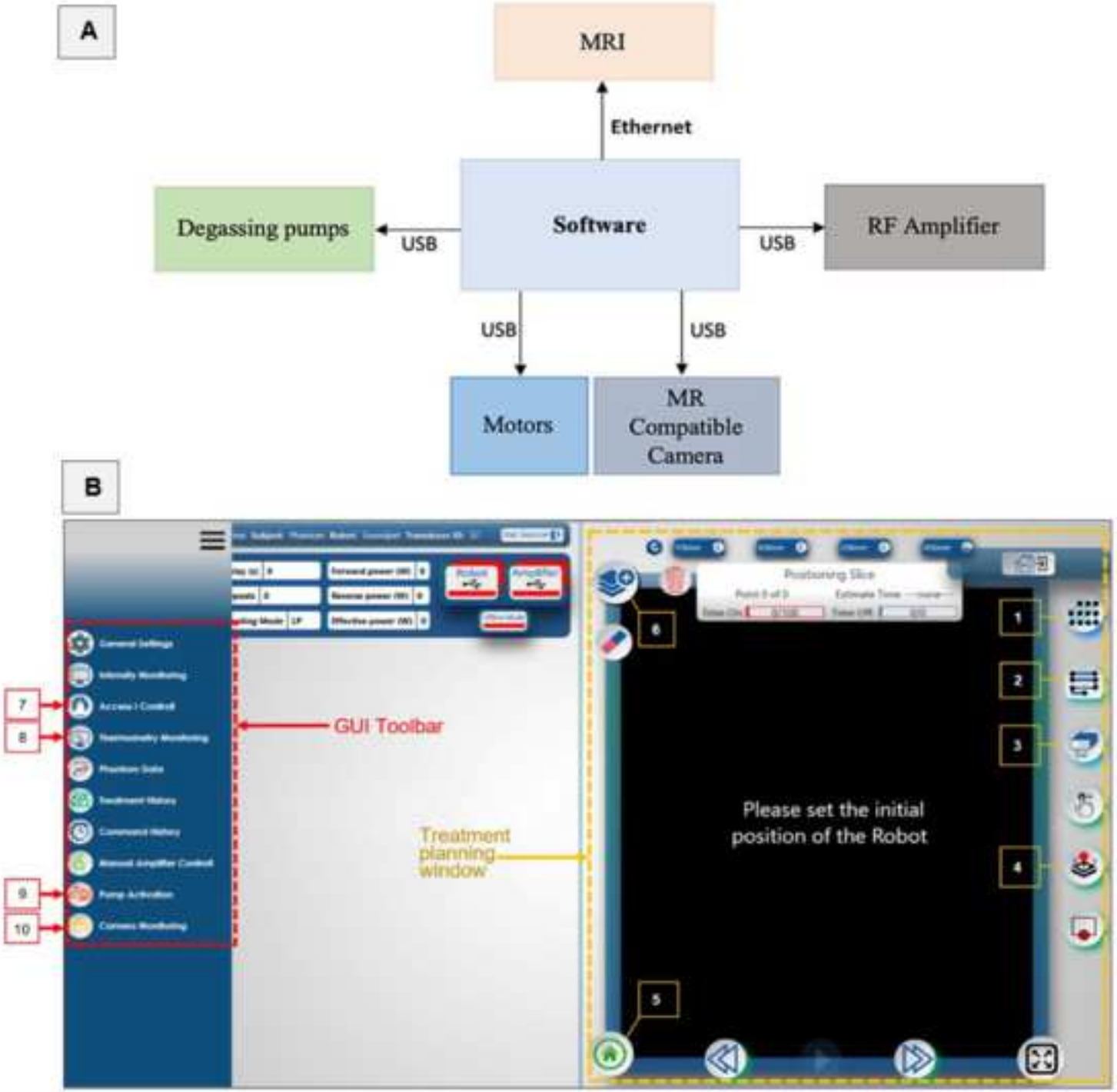

Figure 3

Click here to access/download;Figure;Figure 3.tiff

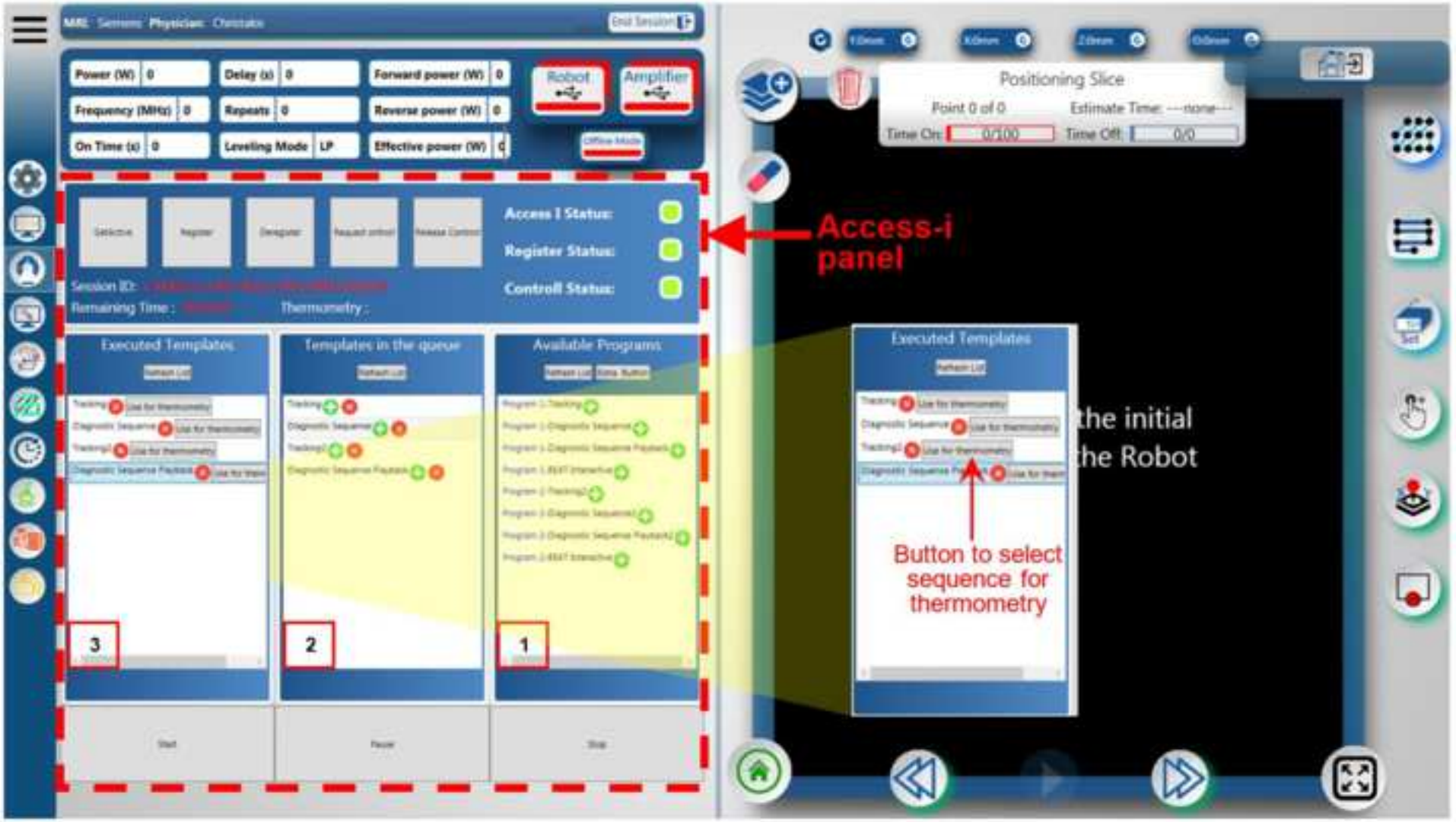

Figure 4

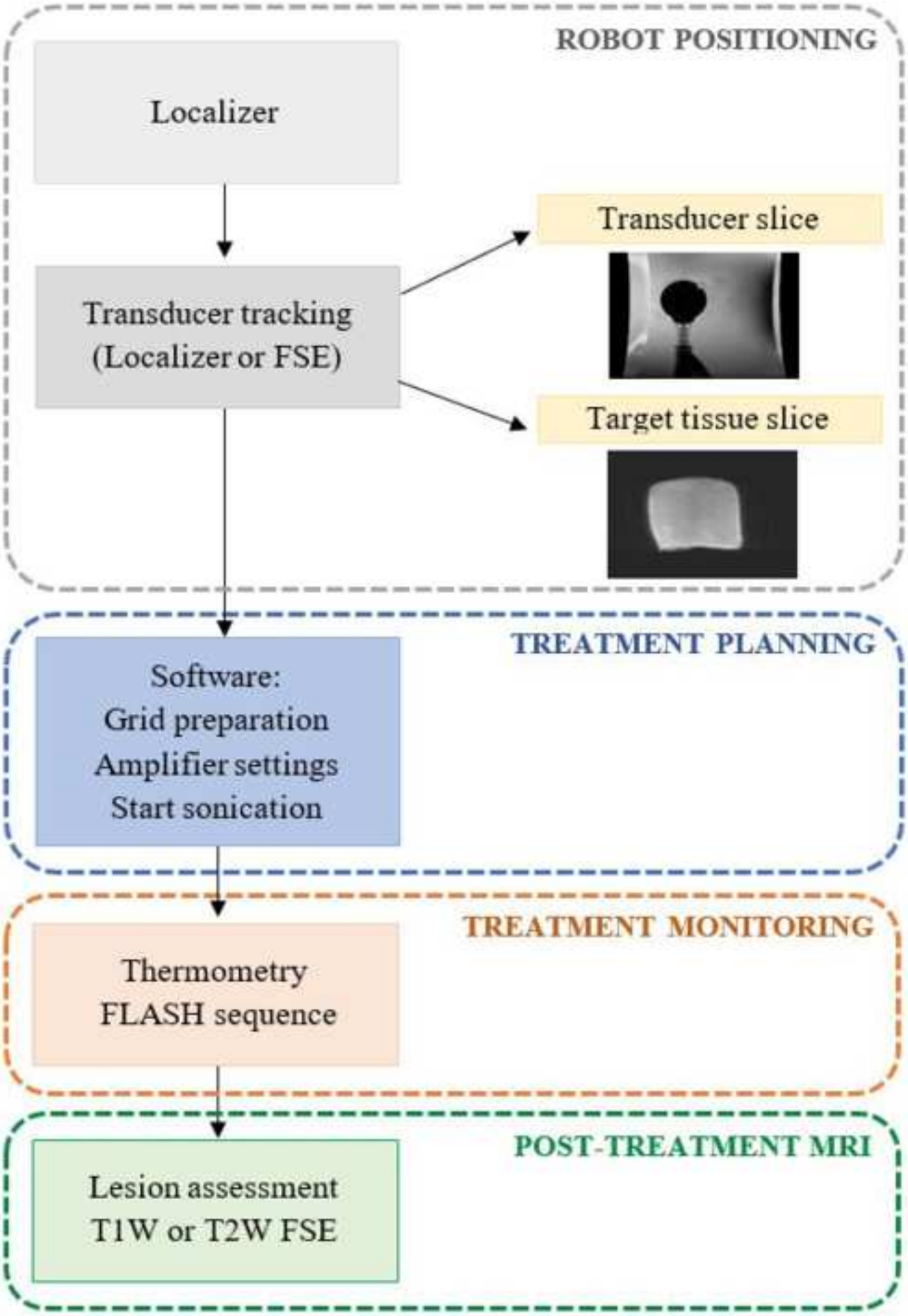

Figure 5

Click here to access/download;Figure;Figure 5.tiff

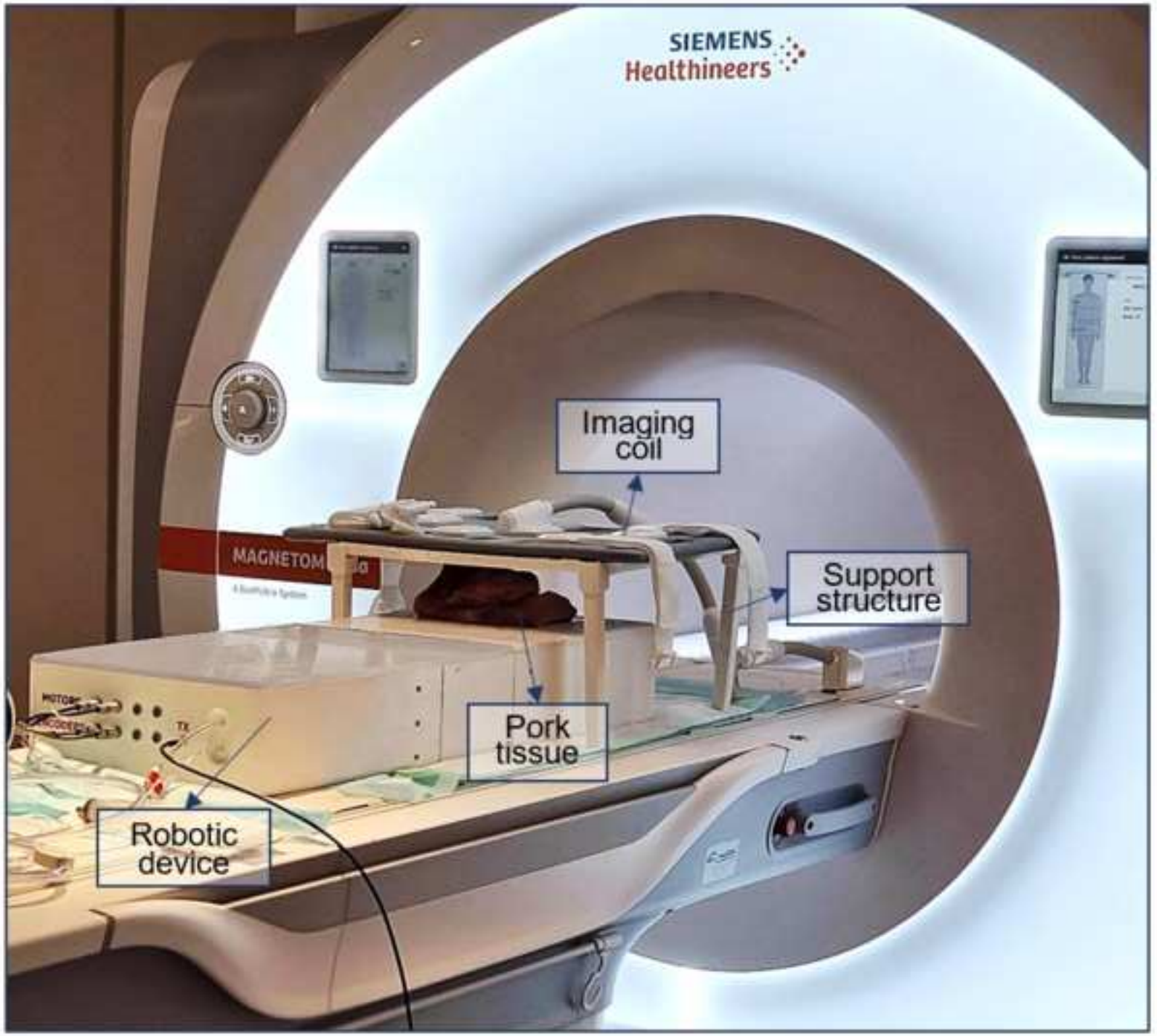

Figure 6

Click here to access/download;Figure;Figure 6.tiff

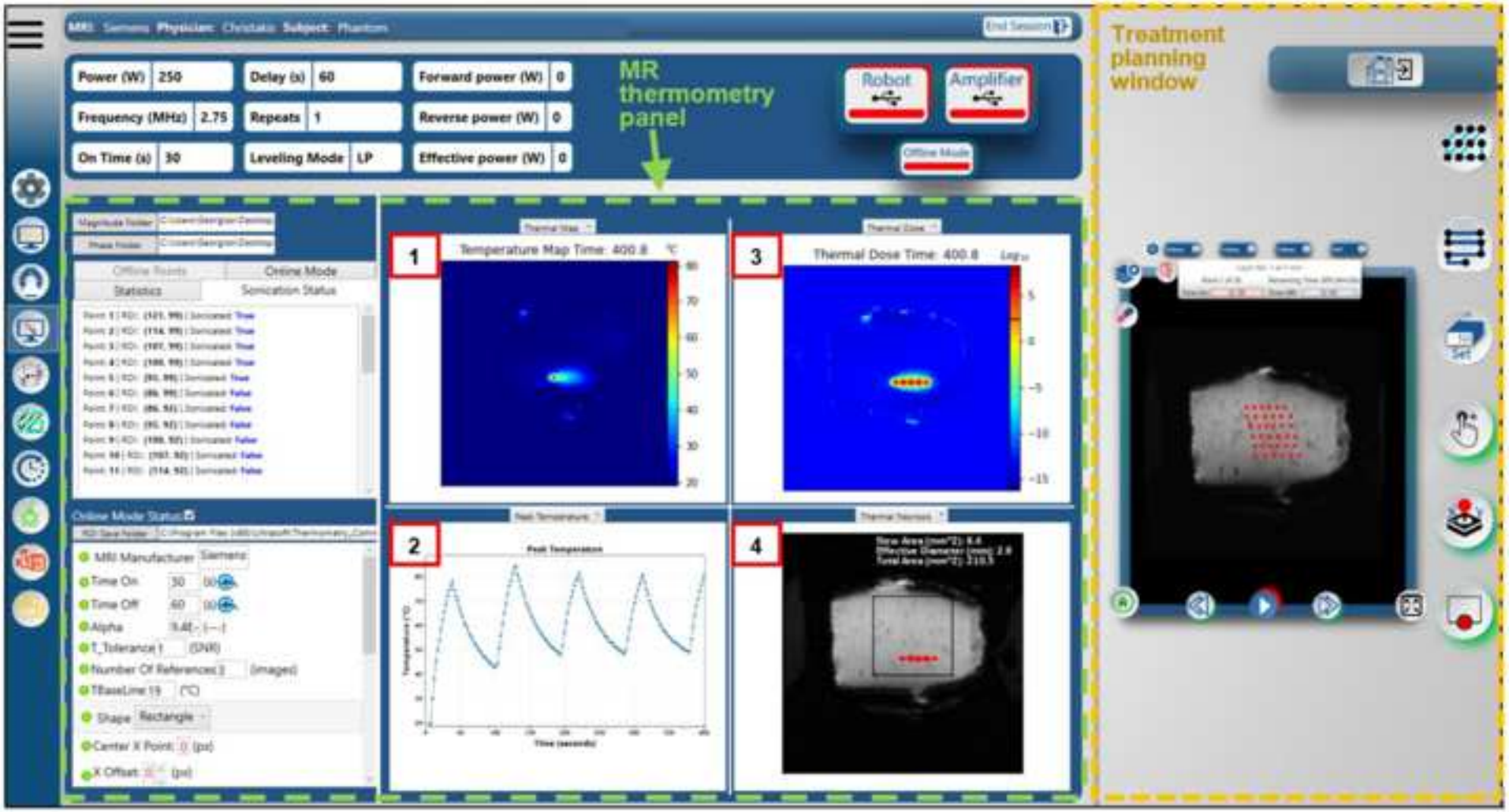

Figure 7

Click here to access/download;Figure;Figure 7.tiff

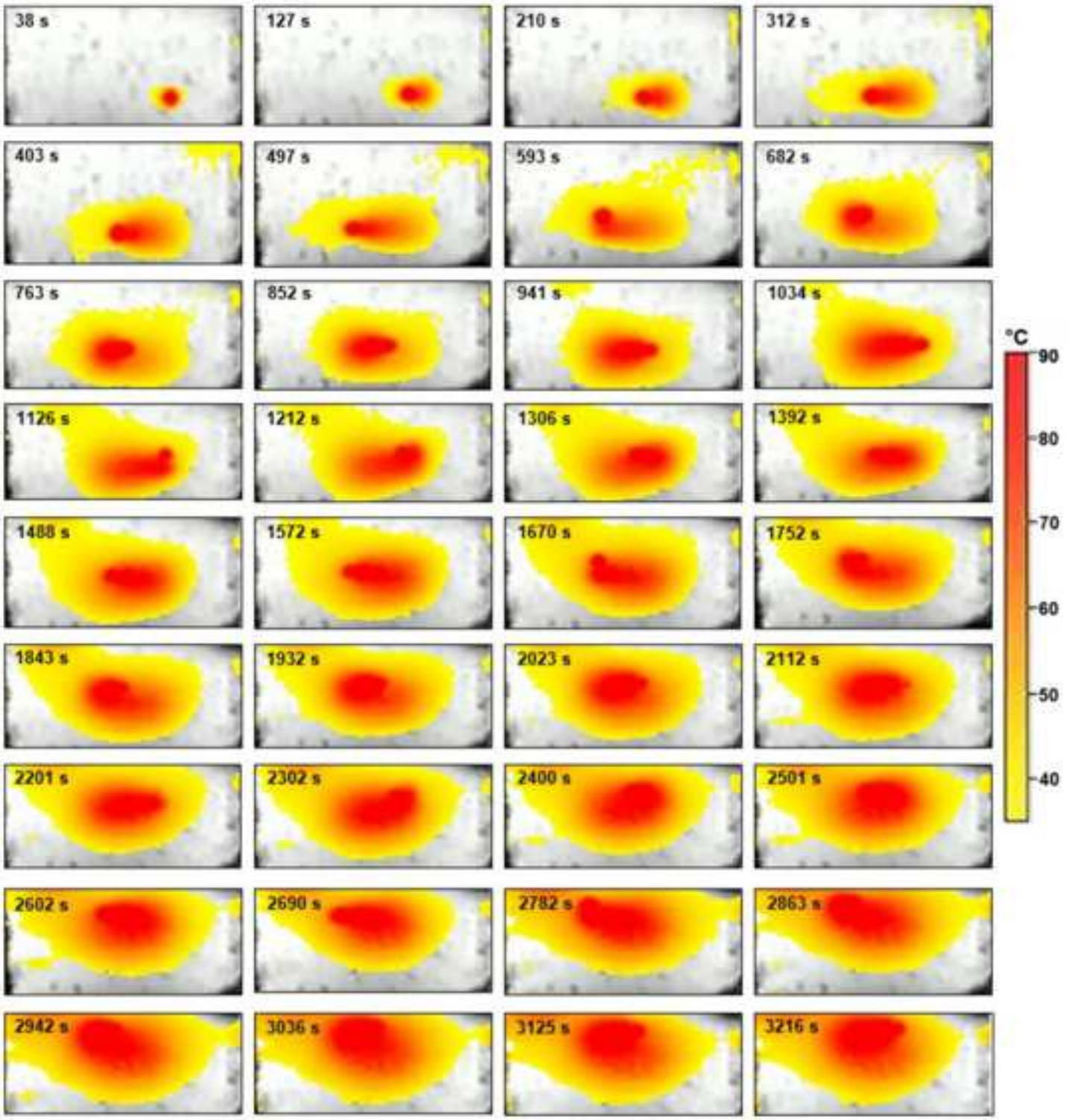

Figure 8

Click here to access/download;Figure;Figure 8.tiff

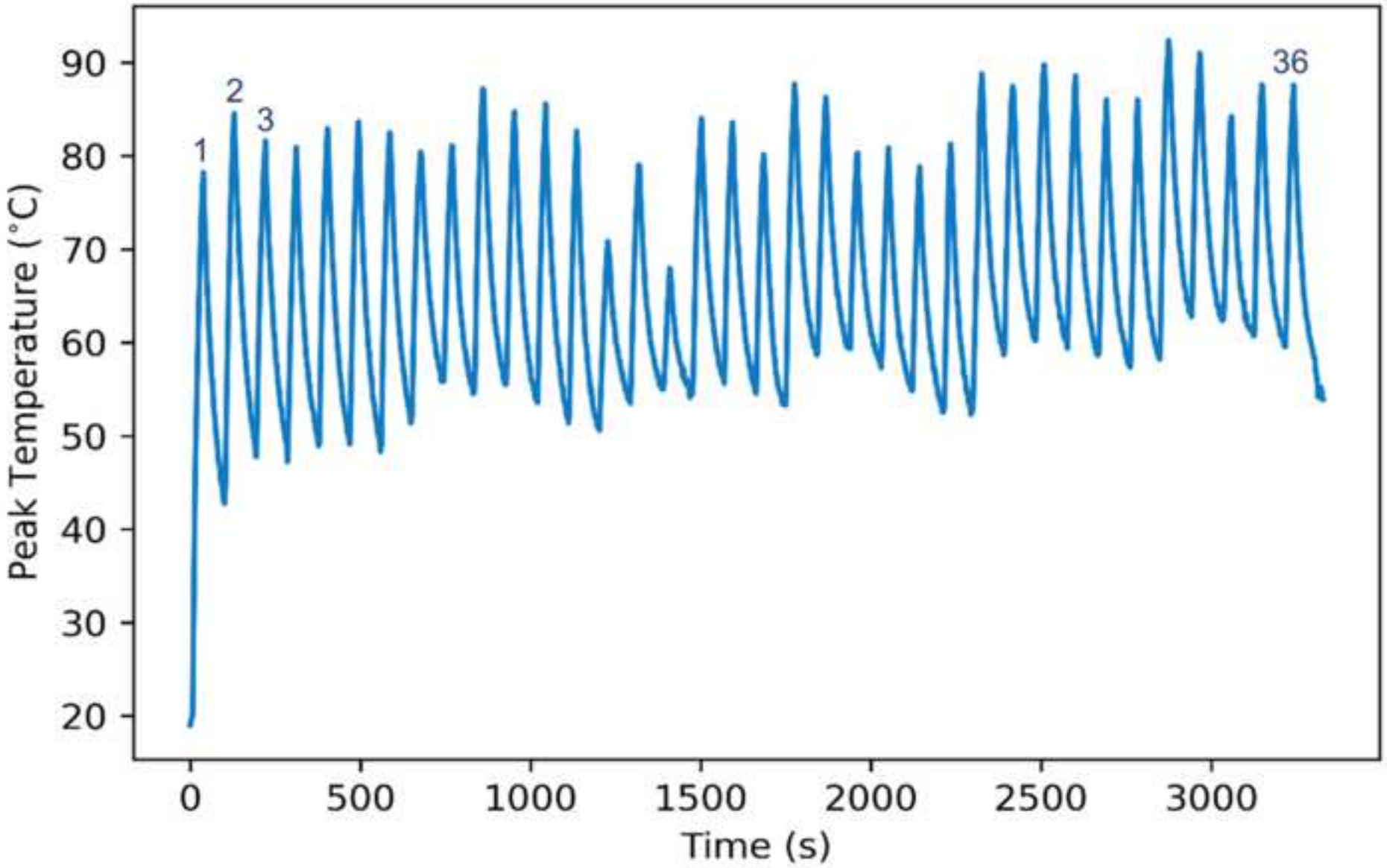

Figure 9

Click here to access/download;Figure;Figure 9.tiff

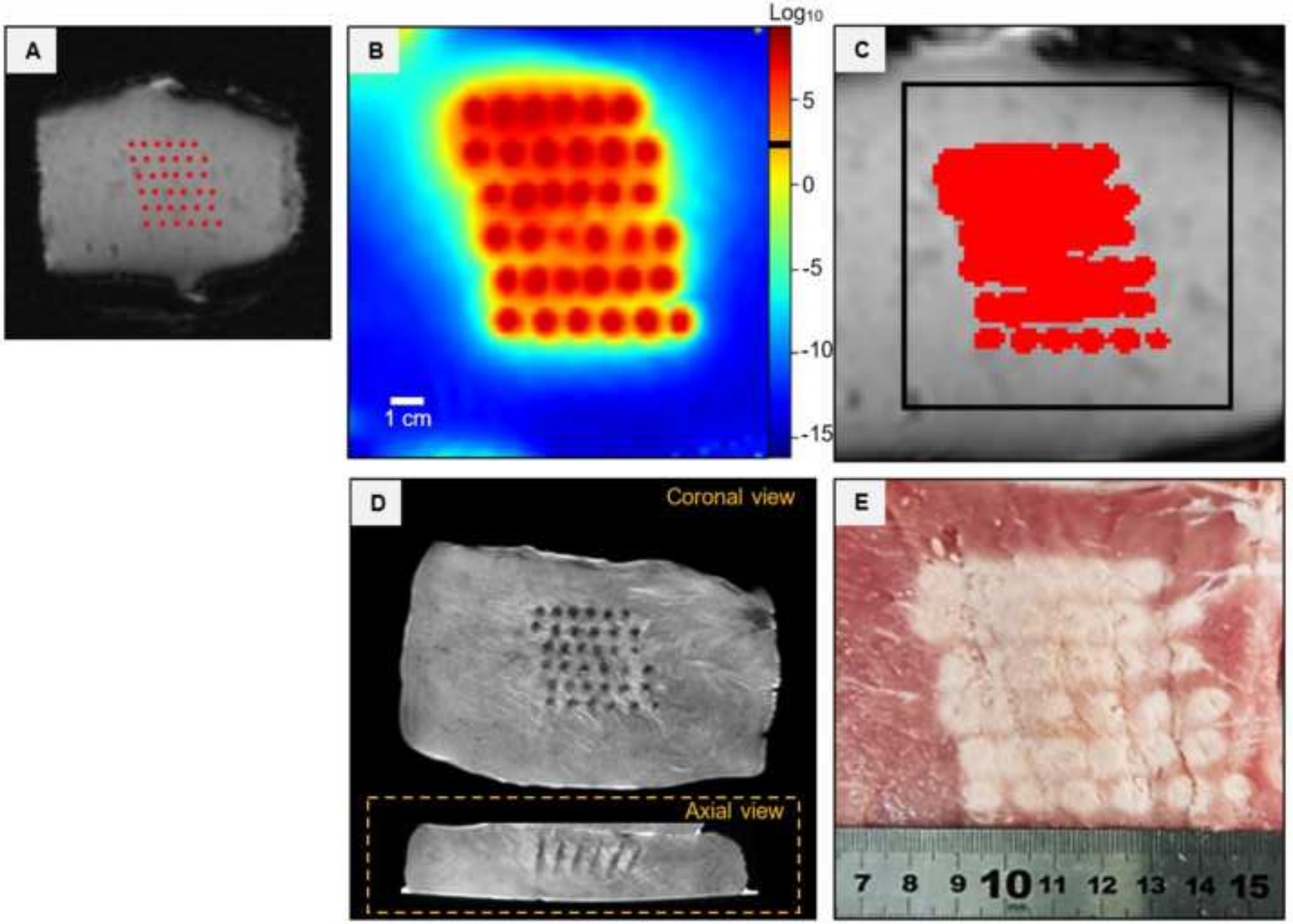

Figure 10

Click here to access/download;Figure;Figure 10.tiff

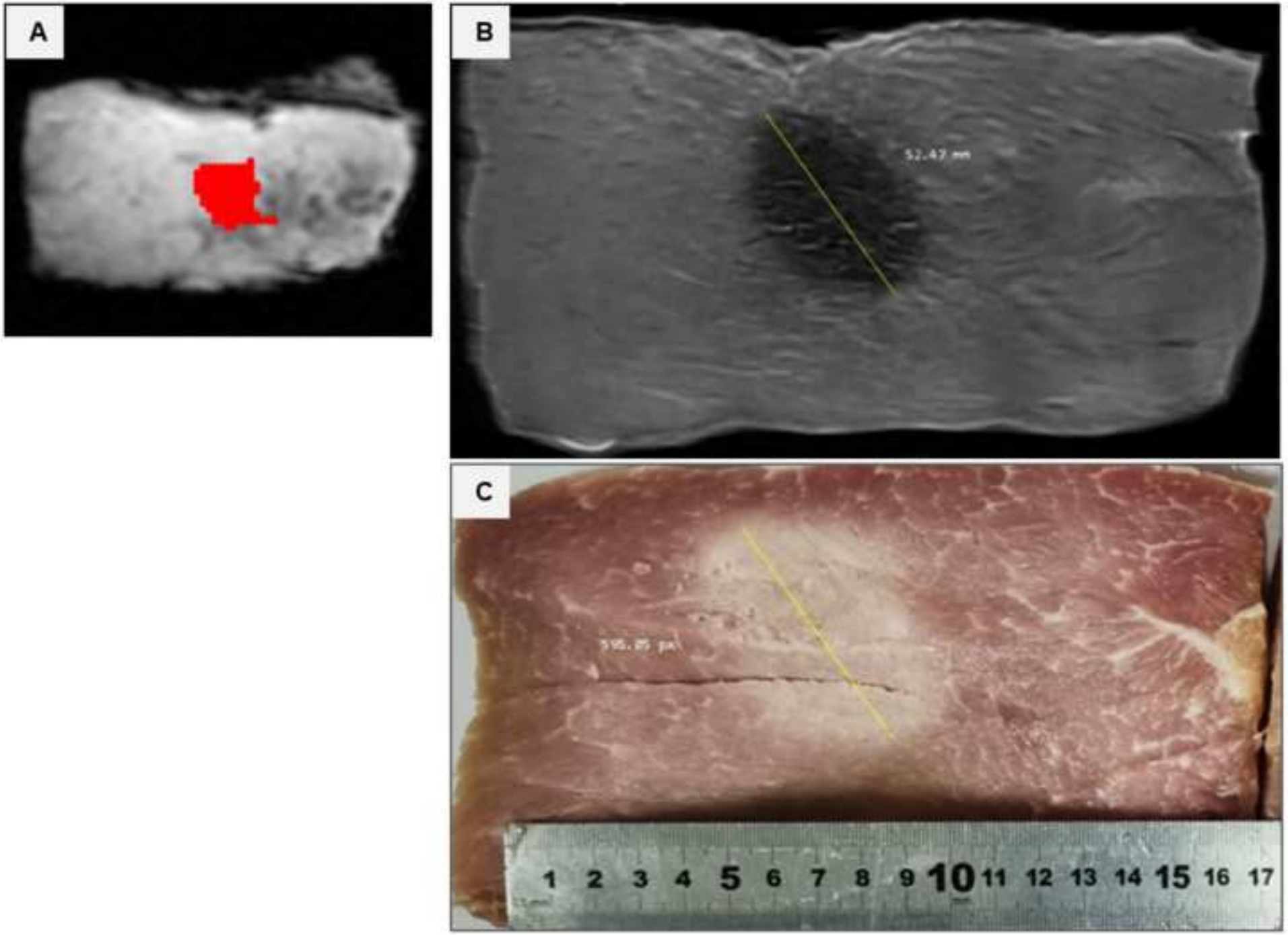

Figure 11

Click here to access/download;Figure;Figure 11.tiff

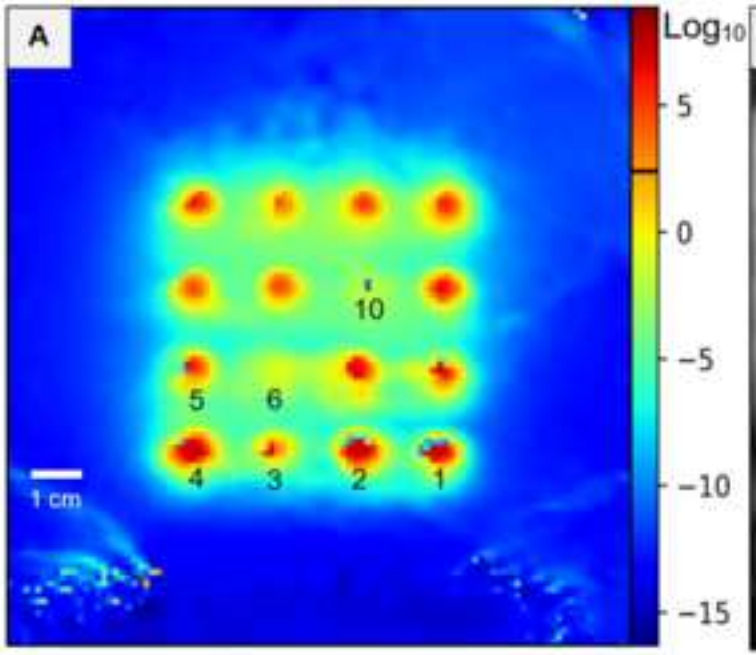

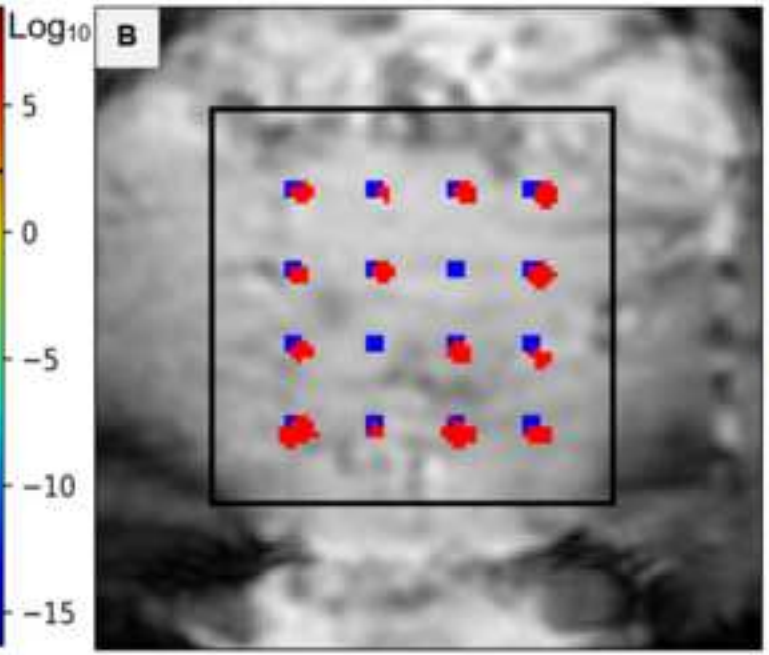

C

Point	Coordinate	Sonication Status
1	(160, 152)	True
2	(147, 152)	True
3	(133, 152)	True
4	(119, 152)	True
5	(119, 138)	True
6	(133, 138)	False
7	(147, 138)	True
8	(160, 138)	True
9	(160, 125)	True
10	(147, 125)	False
11	(133, 125)	True
12	(119, 125)	True
13	(119, 111)	True
14	(133, 111)	True
15	(147, 111)	True
16	(160, 111)	True

Physica Medica

MRI compatibility testing of commercial High Intensity Focused Ultrasound transducers

--Manuscript Draft--

Manuscript Number:	EJMP-D-23-00432
Article Type:	Original article
Keywords:	transducer; commercial; HiFU; MRI; compatibility; artifacts
Corresponding Author:	Christakis Damianou Cyprus University of Technology CYPRUS
First Author:	Nikolas Evripidou
Order of Authors:	Nikolas Evripidou
	Anastasia Antoniou
	Leonidas Georgiou
	Cleanthis Ioannides
	Kyriakos Spanoudes
	Christakis Damianou
Abstract:	Purpose: The study aimed to compare the performance of eight commercially available single-element High Intensity Focused Ultrasound (HIFU) transducers in terms of Magnetic Resonance Imaging (MRI) compatibility. Methods: Imaging of an agar-based MRI phantom was performed in a 3T MRI scanner utilizing T2-Weighted Fast Spin Echo (FSE) and Fast low angle shot (FLASH) sequences, which are typically employed for high resolution anatomical imaging and thermometry, respectively. Reference magnitude and phase images of the phantom were compared with images acquired in the presence of each transducer in terms of the signal to noise ratio (SNR), introduced artifacts, and overall image quality. Results: The degree of observed artifacts highly differed among the various transducers. The transducer whose backing material included magnetic impurities showed poor performance in the MRI, introducing significant susceptibility artifacts such as geometric distortions and signal void bands. Additionally, it caused the most significant SNR drop. Other transducers were shown to exhibit high level of MRI compatibility as the resulting images closely resembled the reference images with minimal to no apparent artifacts and comparable SNR values. Conclusions: The study findings may facilitate researchers to select the most suitable transducer for their research, simultaneously avoiding unnecessary testing. The study further provides useful design considerations for MRI compatible transducers.
Suggested Reviewers:	Costas Pattichis University of Cyprus pattichi@cs.ucy.ac.cy Experienced in the field.
	Jurgen Jenne mediri GmbH j.jenne@mediri.com Experienced in the field.
	Yves-Jean Chapelon National Institute of Health and Medical Research chapelon@lyon.inserm.fr Experienced in the field.
Opposed Reviewers:	

- MRI compatibility testing of eight commercially available HIFU transducers.
- Assessment of MRI phantom images in terms of SNR and introduced artifacts.
- The degree of observed artifacts highly differed among the various transducers.
- Transducer with magnetic impurities caused significant susceptibility artifacts.
- Some transducers caused minimal to no apparent artifacts and acceptable SNR level.

MRI compatibility testing of commercial High Intensity Focused Ultrasound transducers

Nikolas Evripidou[a], Anastasia Antoniou[a], Leonidas Georgiou[b], Cleanthis Ioannides[b], Kyriakos Spanoudes[c], Christakis Damianou[a*]

[a] Department of Electrical Engineering, Computer Engineering, and Informatics, Cyprus University of Technology, Limassol, Cyprus.

[b] Department of Interventional Radiology, German Oncology Center, Limassol, Cyprus.

[c]VET EX MACHINA Limited, Nicosia, Cyprus

Authors' emails: nk.evripidou@edu.cut.ac.cy, anastasiaantoniou12@gmail.com, leonidas.georgiou@goc.com.cy, cleanthis.ioannides@goc.com.cy, kyriakos.spanoudes@gmail.com, christakis.damianou@cut.ac.cy.

* For correspondence contact:

Prof. Christakis Damianou,

Department of Electrical Engineering, Computer Engineering, and Informatics,

Cyprus University of Technology,

30 Archbishop Kyprianou Street, 3036 Limassol, Cyprus,

E-mail: christakis.damianou@cut.ac.cy

Tel: 0035725002039, Fax: 0035725002849

ABSTRACT

Purpose: The study aimed to compare the performance of eight commercially available single-element High Intensity Focused Ultrasound (HIFU) transducers in terms of Magnetic Resonance Imaging (MRI) compatibility.

Methods: Imaging of an agar-based MRI phantom was performed in a 3T MRI scanner utilizing T2-Weighted Fast Spin Echo (FSE) and Fast low angle shot (FLASH) sequences, which are typically employed for high resolution anatomical imaging and thermometry, respectively. Reference magnitude and phase images of the phantom were compared with images acquired in the presence of each transducer in terms of the signal to noise ratio (SNR), introduced artifacts, and overall image quality.

Results: The degree of observed artifacts highly differed among the various transducers. The transducer whose backing material included magnetic impurities showed poor performance in the MRI, introducing significant susceptibility artifacts such as geometric distortions and signal void bands. Additionally, it caused the most significant SNR drop. Other transducers were shown to exhibit high level of MRI compatibility as the resulting images closely resembled the reference images with minimal to no apparent artifacts and comparable SNR values.

Conclusions: The study findings may facilitate researchers to select the most suitable transducer for their research, simultaneously avoiding unnecessary testing. The study further provides useful design considerations for MRI compatible transducers.

KEYWORDS: transducer; commercial; HIFU; MRI; compatibility; artifacts

1. INTRODUCTION

High Intensity Focused Ultrasound (HIFU) has emerged in the oncological sector as a non-invasive modality to ablate tissue [1]. By combining HIFU with Magnetic Resonance Imaging (MRI), physicians can precisely guide and monitor the therapeutic procedure [2]. There are though numerous challenges in safely integrating and operating a HIFU system in the MRI environment due to the potential interference caused by the strong magnetic fields [3]. Ensuring MRI compatibility of HIFU transducers constitutes a critical step in the evaluation process of MRI-guided HIFU systems.

Evaluation of MRI compatibility typically involves acquiring a series of MR images under different activation states of the transducer to assess how the overall image quality is affected [4–11]. Standard MRI sequences employed for planning and guiding HIFU procedures are selected for compatibility testing. High resolution T1-Weighted (T1-W) and T2-Weighted (T2-W) Spin Echo (SE) and Fast Spin Echo (FSE) sequences are routinely tested [4–7]. Such sequences are extensively used for planning and post-sonication assessment purposes since they offer good information of the target anatomy and HIFU-induced tissue effects [8–11].

Treatment monitoring involves the use of fast thermosensitive sequences that enable accurate tracking of temperature changes to achieve controlled coagulative necrosis of tissue [12–14]. Therefore, fast pulse sequences that are sensitive to magnetic susceptibility effects, such as Gradient Echo (GRE) and Spoiled gradient echo (SPGR) sequences, are also selected for transducer compatibility analysis to assess whether proton resonance frequency shift (PRFS) thermometry can be accurately performed [4,5,15–18]. Other studies report the use of Echo Planar Imaging (EPI) [5,7] and Fast Low Angle Shot (FLASH) [19,20] sequences, which are also characterized by high temporal resolution, thus allowing for rapid temperature mapping.

MRI compatibility assessment of equipment intended for operation within or in close proximity to an MRI scanner is normally performed in commercial dose-quality assurance (DQA) and calibration phantoms [4,6,21] or homemade gel phantoms [5,15,16,18,22]. The signal to noise ratio (SNR) constitutes a main metric examined for quantitative compatibility assessment since it plays a crucial role in high-quality imaging and temperature mapping [23]. In the context of HIFU, the SNR fluctuations between a baseline image of the phantom and images acquired in the presence (passive mode) and under various activation states (active mode) of the transducer are evaluated [16–18,22]. SNR is typically measured by calculating the difference in signal intensity (SI) between a region of interest (ROI) in the phantom and a background ROI placed in the surrounding air (noise) [16–18,22]. Researchers often follow specific guidelines such as those of the National Electrical Manufacturers Association (NEMA), which provide a comprehensive description of proper ROI placement and SNR calculation accounting for additional correction factors [5,7,15]. Qualitative assessment of image quality may also be performed visually by examining loss of detail and introduced artifacts. As an example, Qiu et al. [24] assessed the MRI compatibility of a newly developed array transducer made of piezo-crystal material by examining the artifacts introduced in T1-W SE images of an ultrasound surgery phantom due to the inclusion of the transducer in the imaging field.

MRI generates strong magnetic fields that are possible to interfere with nearby electromagnetic devices compromising both the quality of diagnostic imaging and device functionality. Thereby, careful manufacturing is required to avoid the introduction of noise by HIFU transducers. In fact, ferromagnetic components constitute the main source of noise causing significant susceptibility artifacts [25,26]. For instance, nickel plating may be applied to piezoelectric elements or ferromagnetic particles may be added as fillers in the backing and acoustic matching materials to enhance density and acoustic impedance [25]. Metals with magnetic susceptibility comparable to human tissue are expected to generate negligible

artifacts in MRI and could be used instead to address this issue. For instance, Gerold et al. [26] proposed the use of other additives, such as Copper (Cu) and Alumina powder. Cu-loaded epoxy was shown to provide both electromagnetic shielding and appropriate acoustic impedance for sufficient ultrasonic coupling with piezoelectric materials [26]. It is also crucial that any conductive components are properly shielded since eddy currents may be generated under magnetic field changes, leading to SNR loss and image distortion [25]. Lastly, it is essential to employ suitable materials for the housing of the piezoelectric element. 3D-printed plastic holders have been identified as an ideal solution [27].

Generally, previous studies report compatibility tests of an individual HIFU transducer mainly in the framework of evaluating newly developed HIFU systems. However, the scientific community would be highly benefited from a direct comparison of the MRI performance of commercial HIFU transducers. Therefore, the current study reports the results of compatibility testing of eight single-element HIFU transducers from six well-known transducer manufacturers in a 3T MRI scanner. The effect of each transducer (in passive mode) on the imaging quality was assessed by acquiring high resolution T2-W FSE and FLASH images of an in-house made agar-based MRI phantom. Image degradation was assessed qualitatively by visual inspection of introduced magnetic susceptibility artifacts, as well as quantitatively by SNR calculation. To our knowledge, the current paper stands out as the only one that compares most of the marketed HIFU transducers, allowing researchers in the field to assess and compare their performance.

2. MATERIALS AND METHODS

Single-element spherically focused ultrasonic transducers from six different companies were tested for compatibility with a 3T Siemens MRI scanner (Magnetom Vida, Siemens Healthineers, Erlangen, Germany) utilizing an in-house-made MRI phantom. The operating

frequency and structural characteristics of each tested transducer can be found in Table 1. As per manufacturer documentation, metal-loaded epoxy serves as the backing material for transducer No.1, whereas the rest transducers include a metal-free backing material. Note in the table that in some cases, a fully developed transducer was provided by the company; otherwise, only the piezoelectric element was provided, and manufacturing was completed in-house. In the latter case, the element was layered with metal-free epoxy resin (two-component epoxy adhesive, ASonic, Ljubljana, Slovenia) serving as the backing material and hosted in a 3D-printed plastic structure.

The MRI phantom was prepared in-house by dissolving proper amounts of agar (Merck KGaA, EMD Millipore Corporation, Darmstadt, Germany) and silicone dioxide (Sigma-Aldrich, St. Louis, Missouri, United States) in degassed-deionized water to achieve a weight per volume (w/v) concentration of 6 % and 4 %, respectively. The mixture was poured into a dedicated mold and left to solidify forming a cubic phantom with dimensions of $8 \times 8 \times 8\ cm^3$. The detailed process for phantom development can be found in previous literature [28]. Note that the phantom composition was based on previous experiments [29,30] proving that the specific recipe imparts tissue-like MRI visibility, as well as acoustic and thermal properties comparable to human tissues.

The MRI phantom was submerged in a plastic tank filled with degassed and deionized water using a dedicated holder. Each transducer was successively fixed to the bottom of the tank facing towards the bottom surface of the phantom, as shown in Figure 1A. The transducer element was located about 3.5 cm from the phantom surface. The tank was positioned on the MRI table and covered by a multichannel body coil (Body 12, Siemens Healthineers), which was centered a few mm above the phantom. Figure 1B shows a photo of the experimental setup arranged in the MRI scanner.

The phantom was imaged without any transducer present (reference images) and then with each transducer present to assess its impact on the overall image quality. 2D FLASH and FSE sequences were employed. FLASH images were acquired in both axial and coronal planes with repetition time (TR) = 25 ms, echo time (TE) = 10 ms, flip angle (FA) = 30°, echo train length (ETL) =1, number of averages (NEX) = 1, pixel bandwidth (pBW) = 250 Hz/pixel, field of view (FOV) = 280x280x3 mm^3, acquisition matrix size = 96x96, and acquisition time/slice = 3.1 s. T2-W FSE imaging was performed in axial plane using TR = 2500 ms, TE = 52 ms, FA = 110°, ETL =30, NEX = 2, pBW = 250 Hz/pixel, FOV = 260x260x3 mm^3, acquisition matrix size = 256x256, and acquisition time/slice = 150 s.

The resulting images were visually analyzed to assess the level of detail and presence of any unwanted artifacts. The SNR in the phantom served as the primary quantitative metric for image quality assessment. The SNR of magnitude images was calculated as the ratio of the mean SI in a circular ROI (area of 5.35 cm^2) placed at the center of the phantom to the standard deviation of a similar ROI placed in the surrounding air (representing noise) [31]. The ROIs were consistently placed at the same locations in all cases.

3. RESULTS

The series of images acquired for each transducer are shown in Figures 2 to 9. As can be seen from Figure 2, transducer No.1 introduced significant susceptibility artifacts in the MR images owing to the presence of ferromagnetic particles in its backing material. FLASH phase images were completely distorted. Complete loss of phase information occurred in both axial and coronal planes, resulting in image blurring, abnormal changes in SI, and reversal of contrast. A large circular area of signal void appears on the axial magnitude image covering a large part of the phantom. Similarly, a semi-circular band of increased signal was created on the T2-W FSE image overlapping the phantom.

The second transducer of this company (No.2) also showed poor compatibility, but much better compared to transducer No.1. Note that while the coronal magnitude and phase images of Figure 3 resemble well the reference images, the quality of axial images (both FLASH and T2-W) is highly compromised in the presence of the transducer. The axial magnitude images present similar artifacts with those generated by transducer No.1, albeit of smaller dimensions, remaining confined within the water region. However, if the transducer is positioned closer to the phantom is possible that these artifacts will shift towards the phantom.

The corresponding results for transducers No.3 to No.6 are respectively presented in Figures 4 to 7. Note that none of these transducers caused noticeable effects on the coronal phantom images. Visual assessment suggests that the phase information is mostly retained, except for some apparent SI reduction in the phantom interior. Regarding the axial images, no phantom distortion was observed, and the image details, contrast, and uniformity were mostly preserved. However, noticeable susceptibility artifacts appeared as signal voids surrounding the transducers but were not spread beyond that area. Notably, this phenomenon is more prominent in the case of transducers No.4 (Figure 5) and No.5 (Figure 6).

Transducers No.7 and No.8 introduced minimal to no apparent artifacts, preserving the overall quality of both FLASH and T2-W FSE images, as revealed by Figures 8 and 9. No susceptibility artifacts were detected on the T2-W images, apart from a slight signal decrease above the transducer element.

The bar chart of Figure 10 illustrates the SNR measurements obtained for the various transducers in comparison to the reference SNR. Among the tested transducers, transducer No.1 exhibited the worst performance, as it yielded the lowest SNR values for both tested sequences. The rest transducers demonstrated comparable performance in FLASH imaging. Transducers No.2 and No.7 resulted in the highest SNR values in T2-W FSE imaging.

4. DISCUSSION

As the utilization of the MRI-guided HIFU technology continues to expand, it's deemed necessary to address the challenges associated with safe operation of HIFU equipment within the MRI environment, thus facilitating the wider adoption of this promising modality in clinical practice. HIFU transducers constitute a main source of noise that may compromise the quality of diagnostic and therapeutic information and should thus be carefully selected to minimize or ideally eliminate any potential interference with the MRI magnet [3]. The market offers a wide range of HIFU transducers, with some of them labeled as "MRI compatible," suggesting their potential to safely operate within the MRI environment under proper conditions. We herein report the findings of the MRI compatibility testing of eight commercially-available single-element HIFU transducers.

The transducers were assessed for their compatibility with a 3T Siemens MRI scanner by imaging an agar-based MRI phantom. FLASH and T2-W FSE images were acquired in the presence of each transducer and compared with the relevant reference phantom images. The specific sequences were selected because the first one is used for MR thermometry [19,20], and the latter one for high resolution imaging [4,5]. The extent of introduced artifacts varied greatly across the different transducers.

The transducer whose backing material consists of a (ferromagnetic) metal-loaded epoxy resin (No.1) had a poor performance in the MRI. Grainy images and significant susceptibility artifacts, such as geometric distortions and signal void bands overlapping with the phantom, were generated by this transducer, clearly indicating important compatibility issues. Overall, the introduced artifacts affected the image quality to a level compromising the reliability of imaging in both axial and coronal planes. The quantitative assessment verified these findings since the SNR of T2-W FSE phantom images was reduced to approximately 48 % of the reference value. The second transducer from the same company (No.2) demonstrated higher

compatibility with the scanner, with only a 5 % reduction in the SNR and less pronounced artifacts occurring only in the axial plane. Nevertheless, the introduced artifacts remained substantial, undermining the accuracy of imaging and thermometry. The source of these artifacts remains unclear because of the lack of detailed documentation of the transducer's manufacturing technique, and it is left for future investigation.

On the contrary, transducers No.7 and No.8 from the Zibo Yuhai Electronic Ceramic Co. (China) company showed excellent performance. The intensity and phase information of FLASH images were completely retained. The FLASH and T2-W FSE magnitude images of the phantom acquired in the presence of the transducers presented similar image resolution and contrast with the reference images and no susceptibility artifacts. Notably, the transducer of a smaller diameter (No.7) yielded higher SNR values reaching 95 % of reference, compared to the larger one, which reduced the SNR to 65 % of the reference value (in T2-W imaging). Overall, these transducers exhibit a high level of MRI compatibility as the resulting images closely resembled the reference images.

The rest transducers (No.3 – No.6) showed a moderate to very good performance, with the quality of both FLASH and T2-W FSE images remaining sufficiently high. In T2-W FSE imaging, the reference SNR was decreased by 14 to 22 % while still remaining high enough for reliable imaging. Some localized susceptibility artifacts (signal voids) surrounding the transducers' elements were clearly identified on T2-W images. Therefore, caution should be given if these transducers are to be placed directly underneath the phantom, as there is a possibility of these artifacts propagating within the phantom, potentially altering useful imaging data. These localized artifacts may originate from the electric circuit of the transducer and specifically from the soldering used to join the transducer element with the copper cabling. Further investigation is though needed to confirm this.

Generally, devices intended for operation in the MRI should be constructed with non-magnetic materials, otherwise enclosed in shielded boxes [32]. The existence of magnetic impurities disrupts the uniformity of the external field, causing variations in the resonance frequency of protons and signal dephasing [33]. This phenomenon subsequently results in image readout errors and susceptibility artifacts, such those observed in the current study. Different types of artifacts may be generated depending on how intense these field strength fluctuations are, varying from slight geometric distortions to complete signal distortion and loss of image information [33]. In particular, signal displacement in the slice selection direction can cause signal loss in certain regions and signal accumulation in other regions [33].

In summary, the present study compared the performance of various HIFU transducers from key HIFU transducer manufacturers in terms of MRI compatibility with a 3T MRI scanner. Both qualitative and quantitative evaluation of the impact of each employed transducer (in passive mode) on the imaging quality was conducted, and transducer design considerations were discussed. Among the tested transducers, varying levels of compatibility with the MRI scanner were observed, with some being incompatible, others highly compatible, and some performing moderately. Such direct comparisons of marketed HIFU equipment are expected to benefit the scientific community by facilitating researchers to select the most suitable equipment for their specific applications, simultaneously avoiding unnecessary testing.

LIST OF FIGURE AND TABLE CAPTIONS

Figure 1: (A) Drawing of the water container hosting the phantom and transducer. (B) Photo of the experimental setup for assessing the compatibility of HIFU transducers with a 3T MRI scanner, with the essential components indicated.

Figure 2: MR images of the phantom acquired without the transducer (reference) and in the presence of the transducer No.1: (A) FLASH coronal magnitude image, (B) FLASH axial magnitude image, (C) FLASH coronal phase image, (D) FLASH axial phase image, and (E) T2-W FSE axial magnitude image.

Figure 3: MR images of the phantom acquired without the transducer (reference) and in the presence of the transducer No.2: (A) FLASH coronal magnitude image, (B) FLASH axial magnitude image, (C) FLASH coronal phase image, (D) FLASH axial phase image, and (E) T2-W FSE axial magnitude image.

Figure 4: MR images of the phantom acquired without the transducer (reference) and in the presence of the transducer No.3: (A) FLASH coronal magnitude image, (B) FLASH axial magnitude image, (C) FLASH coronal phase image, (D) FLASH axial phase image, and (E) T2-W FSE axial magnitude image.

Figure 5: MR images of the phantom acquired without the transducer (reference) and in the presence of the transducer No.4: (A) FLASH coronal magnitude image, (B) FLASH axial magnitude image, (C) FLASH coronal phase image, (D) FLASH axial phase image, and (E) T2-W FSE axial magnitude image.

Figure 6: MR images of the phantom acquired without the transducer (reference) and in the presence of the transducer No.5: (A) FLASH coronal magnitude image, (B) FLASH axial

magnitude image, (C) FLASH coronal phase image, (D) FLASH axial phase image, and (E) T2-W FSE axial magnitude image.

Figure 7: MR images of the phantom acquired without the transducer (reference) and in the presence of the transducer No.6: (A) FLASH coronal magnitude image, (B) FLASH axial magnitude image, (C) FLASH coronal phase image, (D) FLASH axial phase image, and (E) T2-W FSE axial magnitude image.

Figure 8: MR images of the phantom acquired without the transducer (reference) and in the presence of the transducer No.7: (A) FLASH coronal magnitude image, (B) FLASH axial magnitude image, (C) FLASH coronal phase image, (D) FLASH axial phase image, and (E) T2-W FSE axial magnitude image.

Figure 9: MR images of the phantom acquired without the transducer (reference) and in the presence of the transducer No.8: (A) FLASH coronal magnitude image, (B) FLASH axial magnitude image, (C) FLASH coronal phase image, (D) FLASH axial phase image, and (E) T2-W FSE axial magnitude image.

Figure 10: Bar chart of the SNR values obtained for the various transducers compared to the reference SNR for the FLASH and T2-W FSE sequences. Errors bars represent the standard deviation.

Table 1: Operating frequency and structural characteristics of commercial HIFU transducer employed in the study. Complete transducers or only piezoelectric elements were provided. *Due to bad performance, we prefer not to disclose the manufacturer of this transducer.

Table 1

Transducer No.	Frequency (MHz)	Diameter (mm)	Radius of curvature (mm)	Manufacturer of piezoelectric	Complete transducer provided
1	3.0	40	40	X*	✓
2	1.0	40	100	X*	✓
3	0.5	50	100	CNIRHurricane Tech., *Shenzhen, China*	✓
4	1.0	50	100	PIEZO HANNAS, *Wuhan, Hubei, China*	✗
5	2.6	45	70	Sonic Concepts, *Bothell, Washington, USA*	✓
6	3.0	50	50	Meggitt, *Coventry, UK*	✗
7	1.0	90	100	Zibo Yuhai Electronic Ceramic Co., *Zibo, Shandong, China*	✗
8	2.5	100	100	Zibo Yuhai Electronic Ceramic Co., *Zibo, Shandong, China*	✗

ACKNOWLEDGMENTS

The study was co-funded by the European Structural & Investment Funds (ESIF) and the Republic of Cyprus through the Research and Innovation Foundation (RIF) under the projects SOUNDPET (INTEGRATED/0918/0008) and FUSVET (SEED/1221/0080).

DECLARATION OF INTEREST STATEMENT

All authors declare no conflicts of interest.

REFERENCES

[1] Izadifar Z, Izadifar Z, Chapman D, Babyn P. An Introduction to High Intensity Focused Ultrasound: Systematic Review on Principles, Devices, and Clinical Applications. J Clin Med 2020;9:460. https://doi.org/10.3390/jcm9020460.

[2] Lee EJ, Fomenko A, Lozano AM. Magnetic resonance-guided focused ultrasound: Current status and future perspectives in thermal ablation and blood-brain barrier opening. J Korean Neurosurg Soc 2019;62:10–26. https://doi.org/10.3340/jkns.2018.0180.

[3] Antoniou A, Georgiou L, Evripidou N, Ioannides C, Damianou C. Challenges regarding MR compatibility of an MRgFUS robotic system. J Magn Reson 2022;344:107317. https://doi.org/10.1016/j.jmr.2022.107317.

[4] Menikou G, Yiallouras C, Yiannakou M, Damianou C. MRI-guided focused ultrasound robotic system for the treatment of bone cancer. Int J Med Robot Comput Assist Surg 2017;13:1–11. https://doi.org/10.1002/rcs.1753.

[5] Drakos T, Giannakou M, Menikou G, Filippou A, Evripidou N, Spanoudes K, et al. MRI-Guided Focused Ultrasound Robotic System for Preclinical use. J Vet Med Anim Sci 2021;4:1–11.

[6] Epaminonda E, Drakos T, Kalogirou C, Theodoulou M, Yiallouras C, Damianou C. MRI guided focused ultrasound robotic system for the treatment of gynaecological tumors. Int J Med Robot Comput Assist Surg 2016;12:46–52. https://doi.org/10.1002/rcs.1653.

[7] Price KD, Sin VW, Mougenot C, Pichardo S, Looi T, Waspe AC, et al. Design and validation of an MR-conditional robot for transcranial focused ultrasound surgery in infants. Med Phys 2016;43:4983–95. https://doi.org/10.1118/1.4955174.

[8] Fite BZ, Wang J, Ghanouni P, Ferrara KW. A Review of Imaging Methods to Assess Ultrasound-Mediated Ablation. BME Front 2022;2022:1–17.

https://doi.org/10.34133/2022/9758652.

[9] Damianou C, Ioannides K, Hadjisavvas V, Mylonas N, Couppis A, Iosif D, et al. MRI monitoring of lesions created at temperature below the boiling point and of lesions created above the boiling point using high intensity focused ultrasound. J Biomed Sci Eng 2010;03:763–75. https://doi.org/10.4236/jbise.2010.38102.

[10] Damianou C, Ioannides K, Hadjisavvas V, Mylonas N, Couppis A, Iosif D. In vitro and in vivo brain ablation created by high-intensity focused ultrasound and monitored by MRI. IEEE Trans Ultrason Ferroelectr Freq Control 2009;56:1189–98. https://doi.org/10.1109/TUFFC.2009.1160.

[11] Keil VC, Borger V, Purrer V, Groetz SF, Scheef L, Boecker H, et al. MRI follow-up after magnetic resonance-guided focused ultrasound for non-invasive thalamotomy: the neuroradiologist's perspective. Neuroradiology 2020;62:1111–22. https://doi.org/10.1007/s00234-020-02433-9.

[12] Zhu M, Sun Z, Ng CK. Image-guided thermal ablation with MR-based thermometry. Quant Imaging Med Surg 2017;7:356–368. https://doi.org/10.21037/qims.2017.06.06.

[13] Rieke V, Pauly KB. MR Thermometry. J Magn Reson Imaging 2008;27:376–90. https://doi.org/10.1002/jmri.21265.MR.

[14] Kickhefel A, Roland J, Weiss C, Schick F. Accuracy of real-time MR temperature mapping in the brain: A comparison of fast sequences. Phys Medica 2010;26:192–201. https://doi.org/10.1016/j.ejmp.2009.11.006.

[15] Antoniou A, Giannakou M, Evripidou N, Evripidou G, Spanoudes K, Menikou G, et al. Robotic system for magnetic resonance guided focused ultrasound ablation of abdominal cancer. Int J Med Robot Comput Assist Surg 2021;17. https://doi.org/10.1002/rcs.2299.

[16] Giannakou M, Antoniou A, Damianou C. Preclinical robotic device for magnetic

resonance imaging guided focussed ultrasound. Int J Med Robot Comput Assist Surg 2022:1–10. https://doi.org/10.1002/rcs.2466.

[17] Damianou C, Giannakou M, Menikou G, Ioannou L. Magnetic resonance imaging-guided focused ultrasound robotic system with the subject placed in the prone position. Digit Med 2020;6:24–31. https://doi.org/10.4103/digm.digm_2_20.

[18] Yiannakou M, Menikou G, Yiallouras C, Ioannides C, Damianou C. MRI guided focused ultrasound robotic system for animal experiments. Int J Med Robot Comput Assist Surg 2017;13:e1804. https://doi.org/10.1002/rcs.1804.

[19] Filippou A, Evripidou N, Damianou C. Robotic system for magnetic resonance imaging-guided focused ultrasound treatment of thyroid nodules. Int J Med Robot 2023. https://doi.org/10.1002/rcs.2525.

[20] Zhang X, Greiser S, Roy U, Lange F, van Gorkum R, Fournelle M, et al. Evaluation of a Developed MRI-Guided Focused Ultrasound System in 7 T Small Animal MRI and Proof-of-Concept in a Prostate Cancer Xenograft Model to Improve Radiation Therapy. Cells 2023;12. https://doi.org/10.3390/cells12030481.

[21] Fischer GS, Krieger A, Iordachita I, Csoma C, Whitcomb LL, Fichtinger G. MRI Compatibility of Robot Actuation Techniques – A Comparative Study. Med Image Comput Comput Assist Interv 2008;11:509–17. https://doi.org/10.1007/978-3-540-85990-1_61.

[22] Antoniou A, Giannakou M, Georgiou E, Kleopa KA, Damianou C. Robotic device for transcranial focussed ultrasound applications in small animal models. Int J Med Robot Comput Assist Surg 2022:1–11. https://doi.org/10.1002/rcs.2447.

[23] Winter L, Oberacker E, Paul K, Ji Y, Oezerdem C, Ghadjar P, et al. Magnetic resonance thermometry: Methodology, pitfalls and practical solutions. Int J Hyperth 2015;32:63–75. https://doi.org/10.3109/02656736.2015.1108462.

[24] Qiu Z, Habeshaw R, Fortine J, Huang Z, Démoré C, Cochran S. New piezocrystal material in the development of a 96-element array transducer for MR-guided focused ultrasound surgery. AIP Conf Proc 2012;1503:282–7. https://doi.org/10.1063/1.4769958.

[25] Speicher D, Bartscherer T, Becker FJ, Jenne JW, Mrosk K, Degel C, et al. MRI compatible ultrasound transducers for simultaneous acquisition of coregistered ultrasound to MRI data. Phys Procedia 2015;70:1002–6. https://doi.org/10.1016/j.phpro.2015.08.209.

[26] Gerold B, Reynolds S, Melzer A, Cochran S. Early exploration of MRI-compatible diagnostic ultrasound transducers. Proc. - IEEE Ultrason. Symp., IEEE; 2010, p. 2404–7. https://doi.org/10.1109/ULTSYM.2010.5935882.

[27] Wang J, Xiao X, Huang Z, Melzer A. 3D-printing based Transducer Holder for Robotic Assisted Ultrasound Guided HIFU. Procedia Manuf., vol. 30, Elsevier B.V.; 2019, p. 3–10. https://doi.org/10.1016/j.promfg.2019.02.002.

[28] Drakos T, Giannakou M, Menikou G, Constantinides G, Damianou C. Characterization of a soft tissue-mimicking agar/wood powder material for MRgFUS applications. Ultrasonics 2021;113: 10635. https://doi.org/10.1016/j.ultras.2021.106357.

[29] Drakos T, Antoniou A, Evripidou N, Alecou T, Giannakou M, Menikou G, et al. Ultrasonic Attenuation of an Agar, Silicon Dioxide, and Evaporated Milk Gel Phantom. J Med Ultrasound 2021;29:239–49. https://doi.org/10.4103/JMU.JMU.

[30] Antoniou A, Georgiou L, Christodoulou T, Panayiotou N, Ioannides C, Zamboglou N, et al. MR relaxation times of agar- based tissue- mimicking phantoms. J Appl Clin Med Phys 2022:213533. https://doi.org/10.1002/acm2.13533.

[31] Goerner FL, Clarke GD. Measuring signal-to-noise ratio in partially parallel imaging MRI. Med Phys 2011;38:5049–57. https://doi.org/10.1118/1.3618730.

[32] Elhawary H, Tse ZTH, Hamed A, Rea M, Davies BL, Lamperth MU. The case for MR-compatible robotics: a review of the state of the art. Int J Med Robot Comput Assist Surg 2008;4:105–13. https://doi.org/10.1002/rcs.192.

[33] Hargreaves B, Worters PW, Pauly KB, Pauly JM, Koch KM, Gold GE. Metal Induced Artifacts in MRI. Am J Roentgenol 2011;197:547–55. https://doi.org/10.2214/AJR.

Figure 1

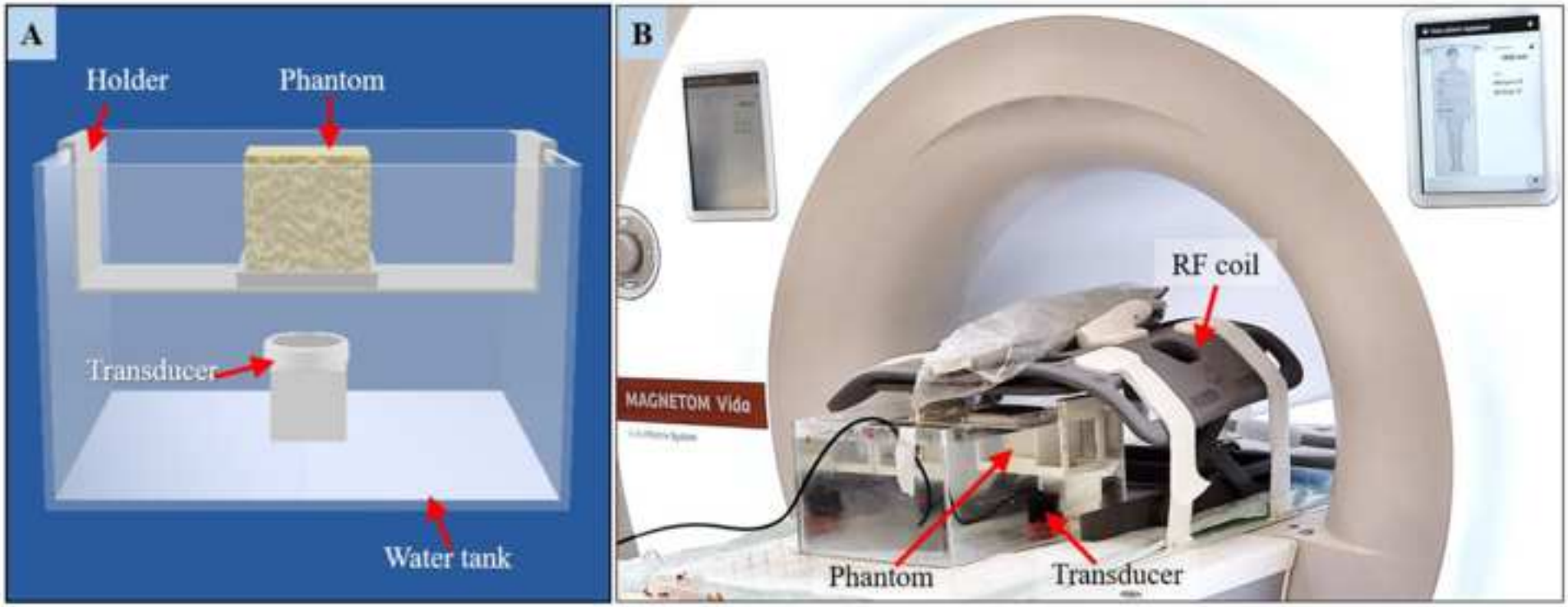

Figure 2

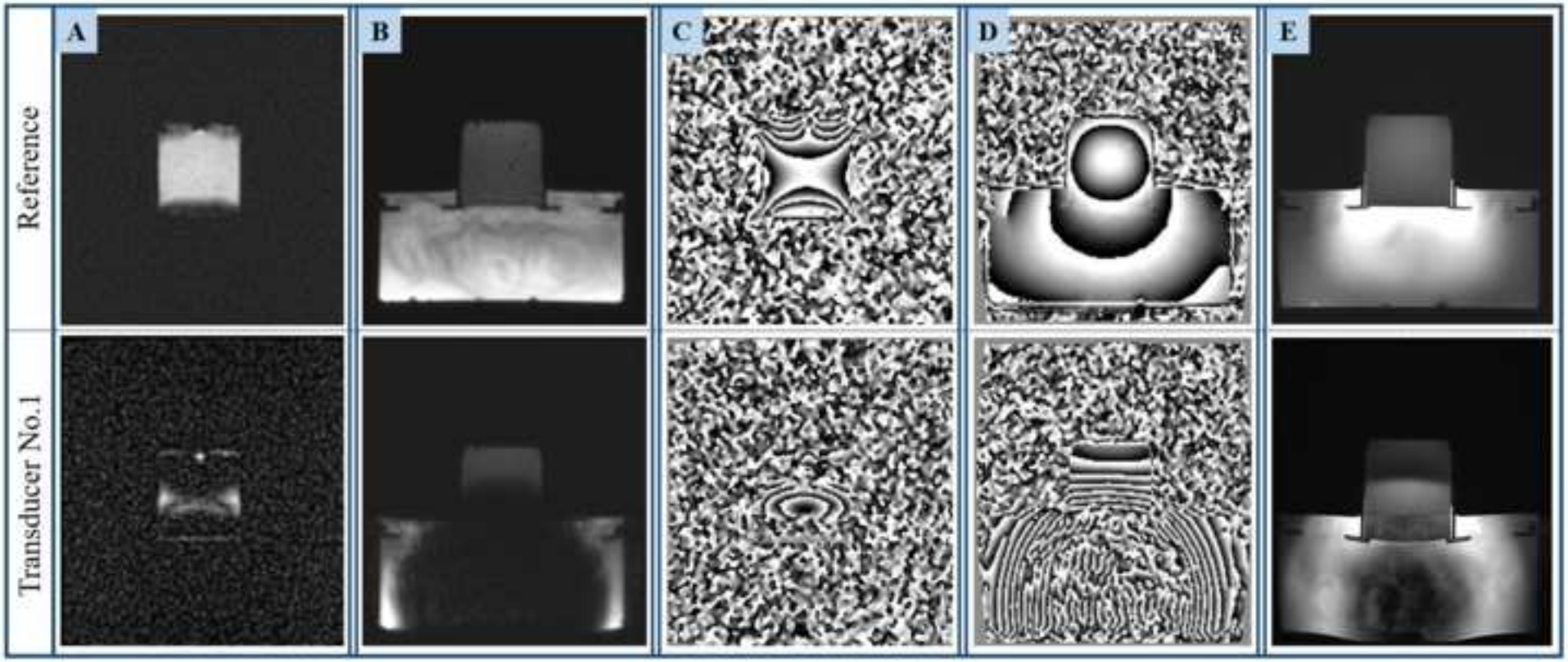

Figure 3

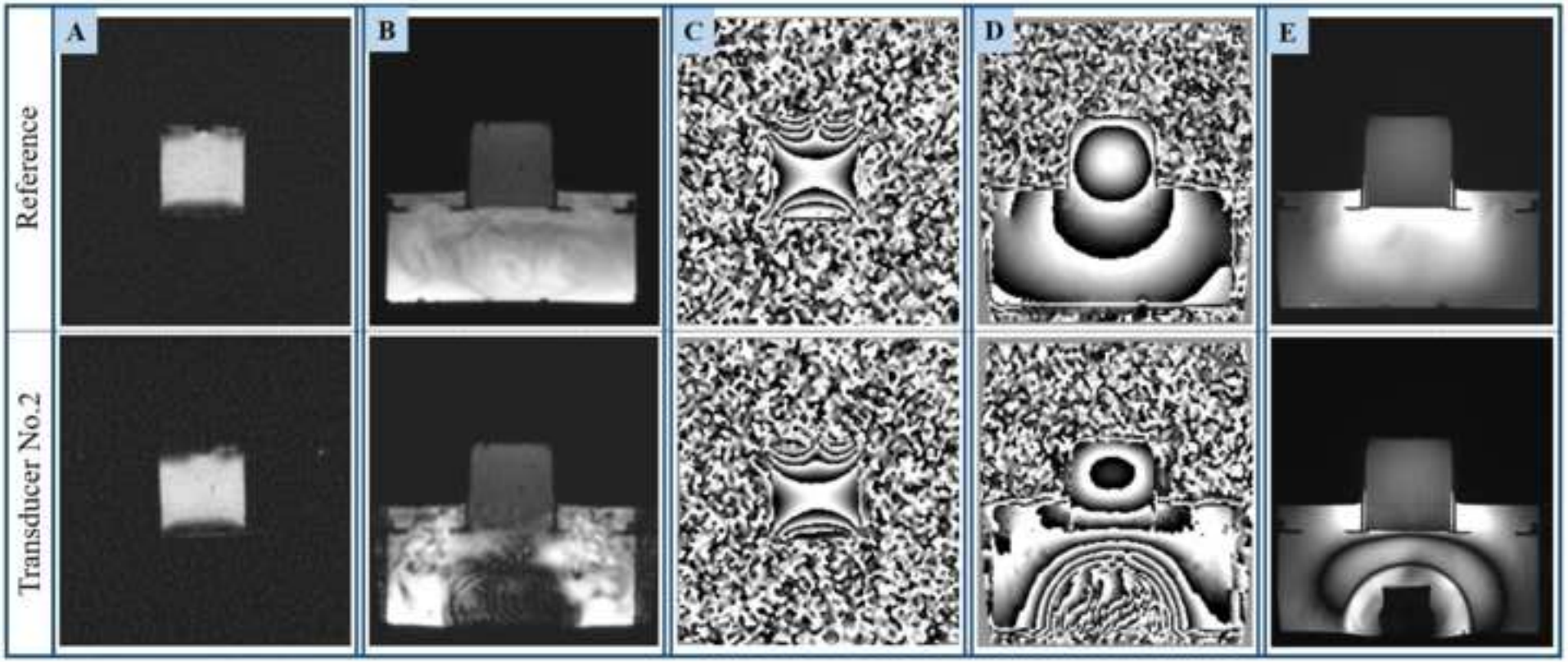

Figure 4

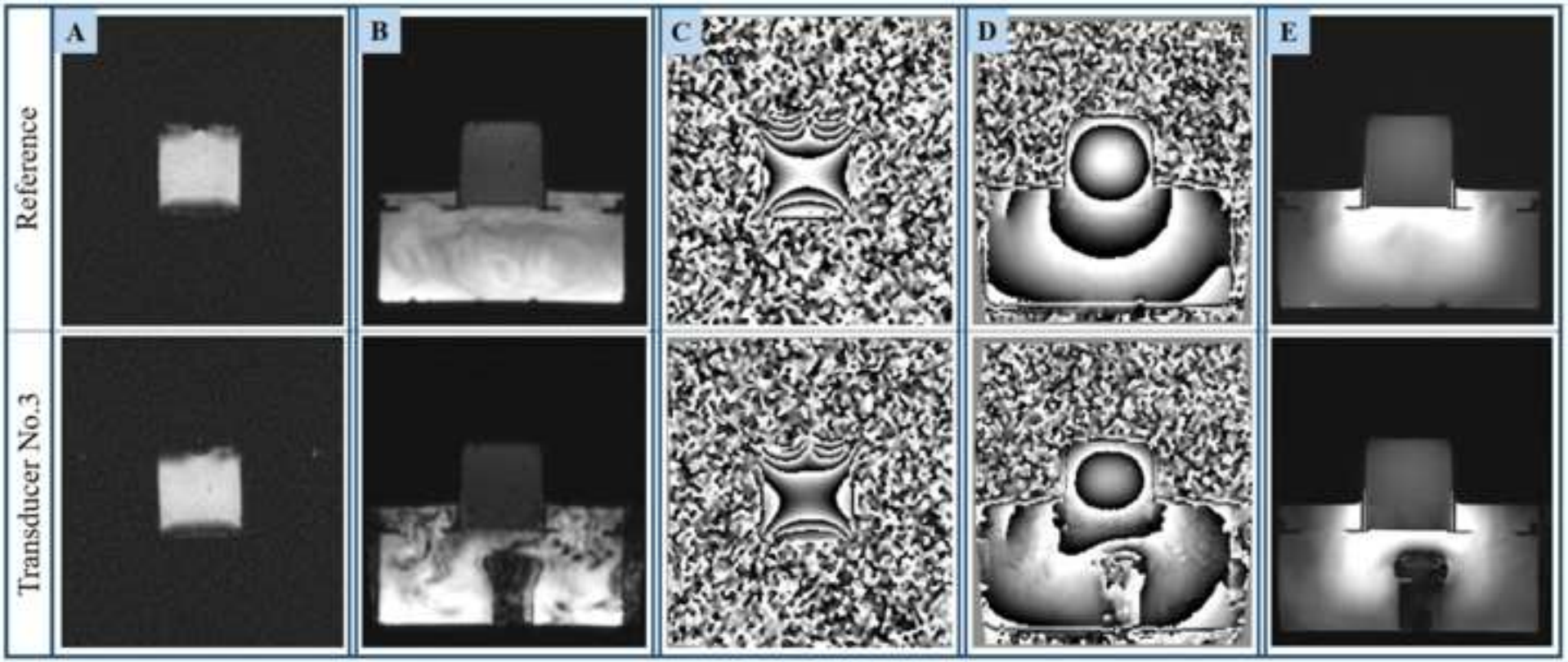

Figure 5

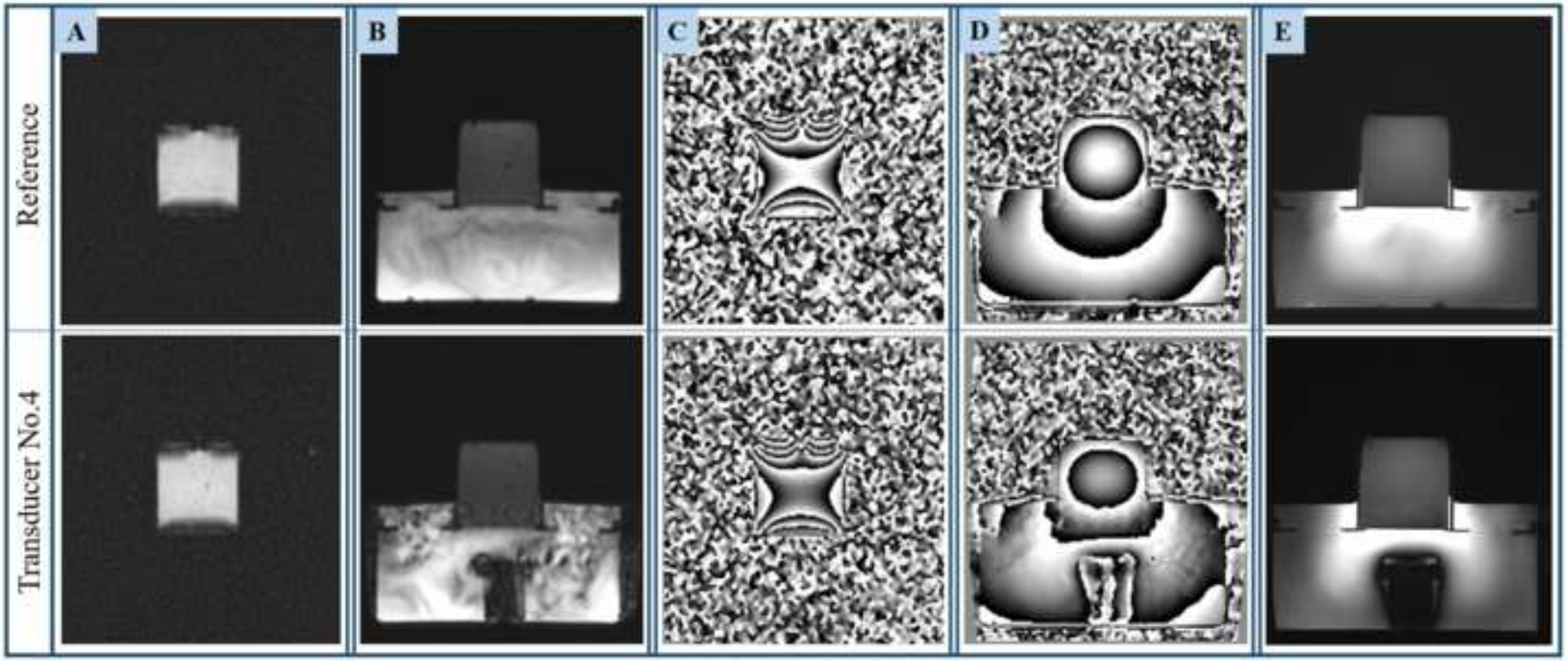

Figure 6

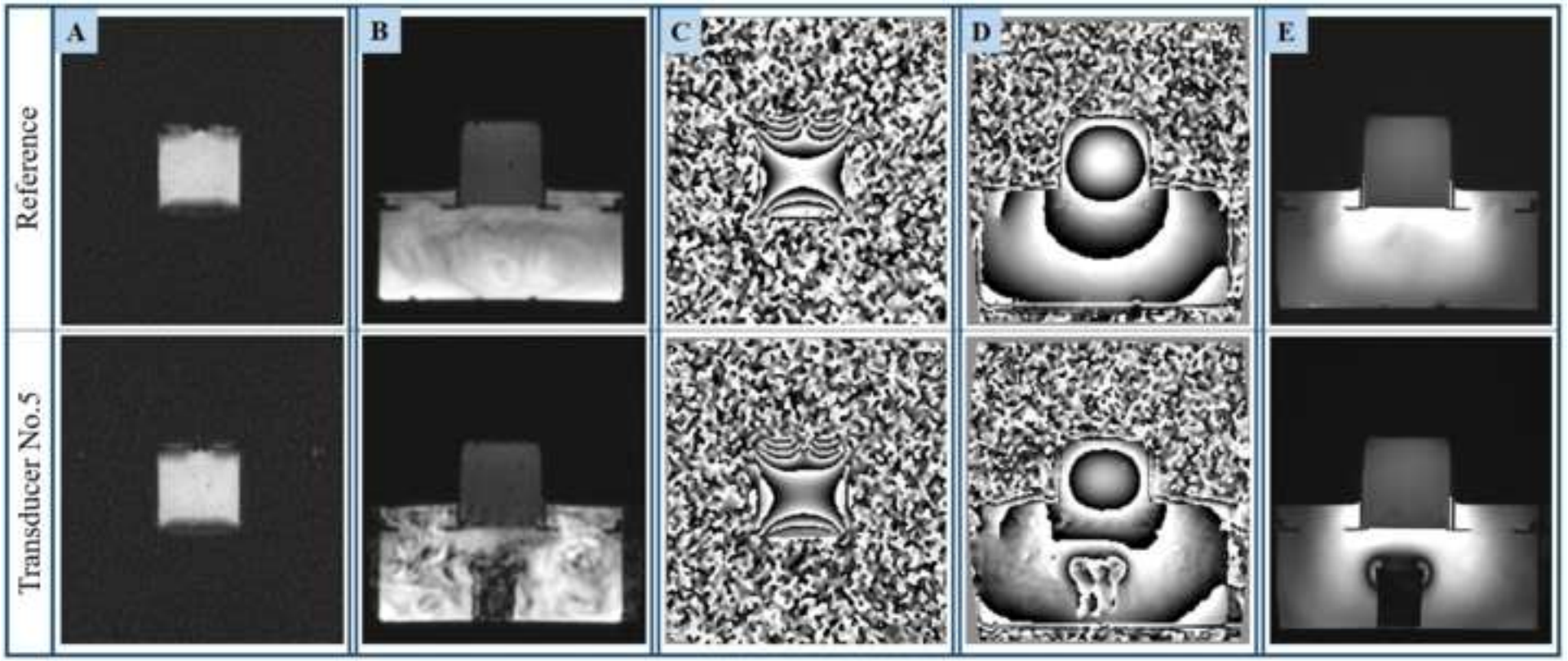

Figure 7

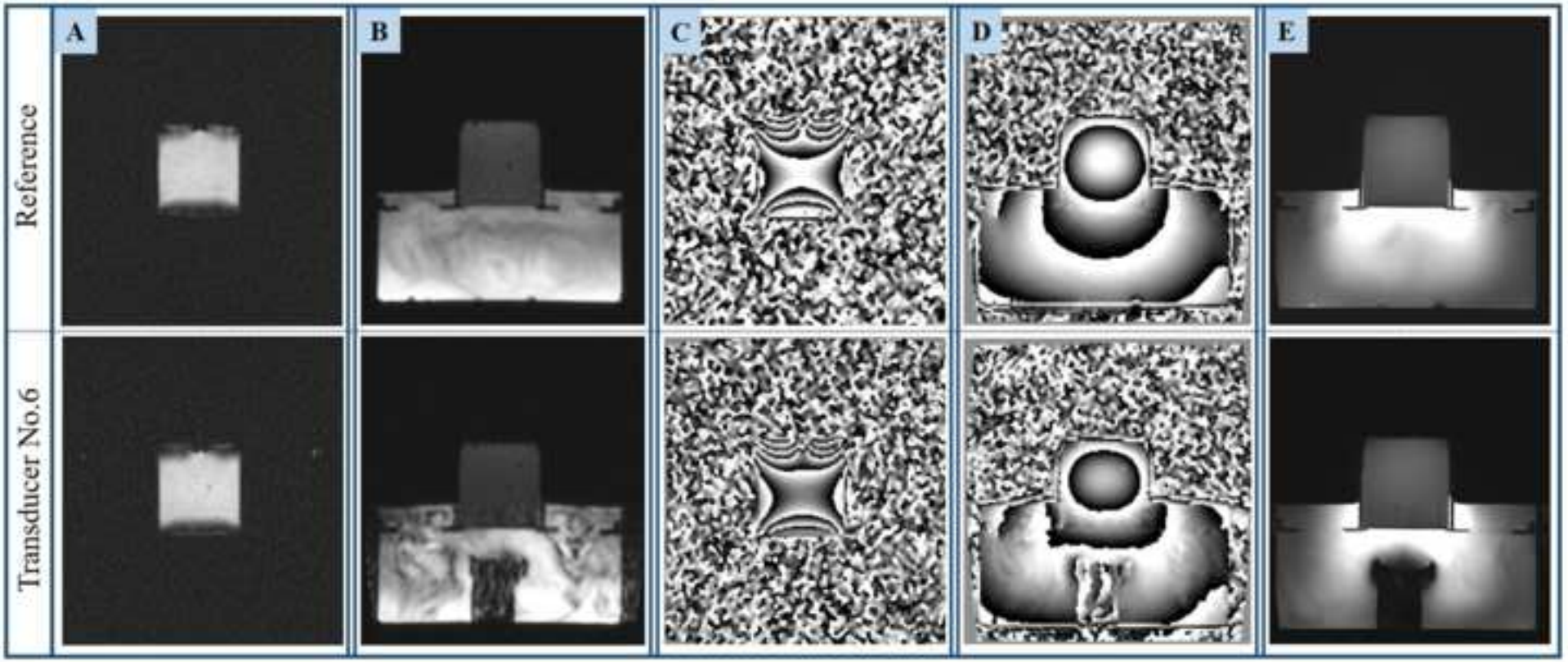

Figure 8

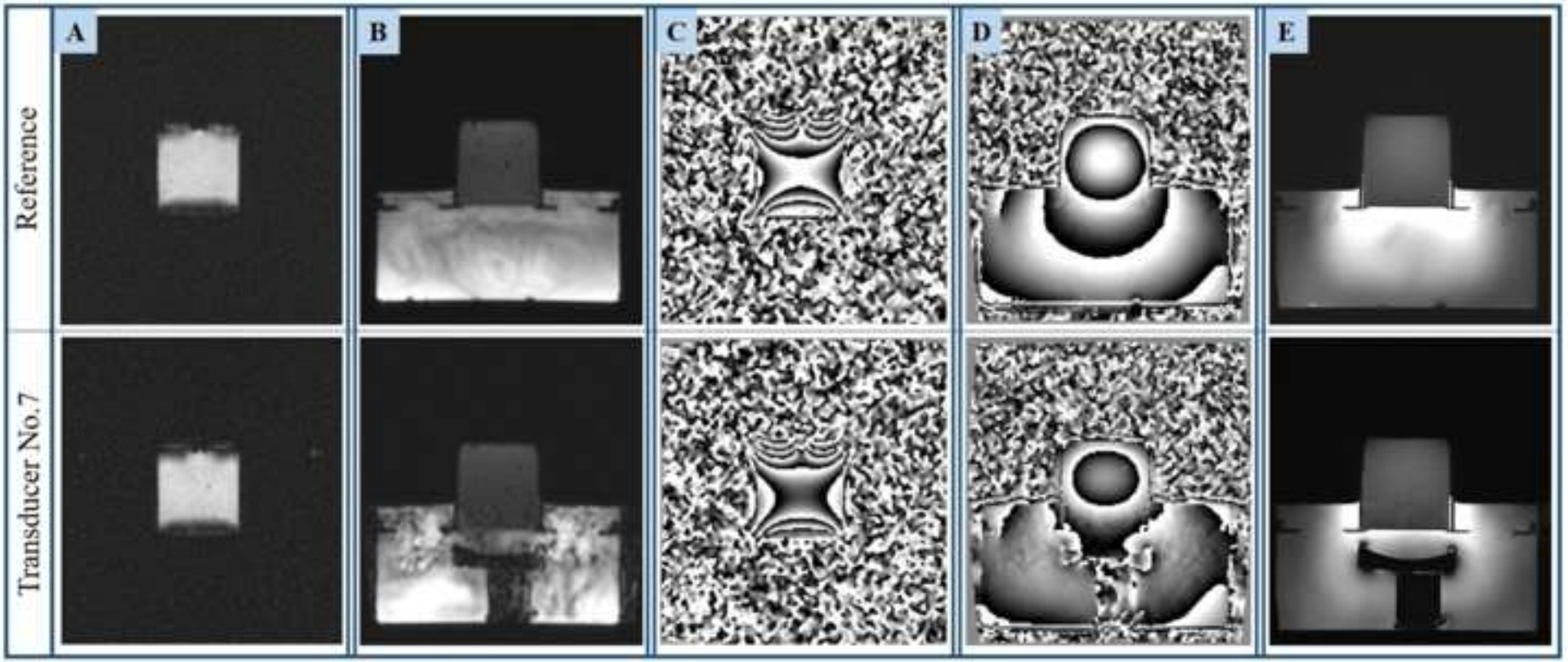

Figure 9

Click here to access/download;Figure;Figure 9.tiff

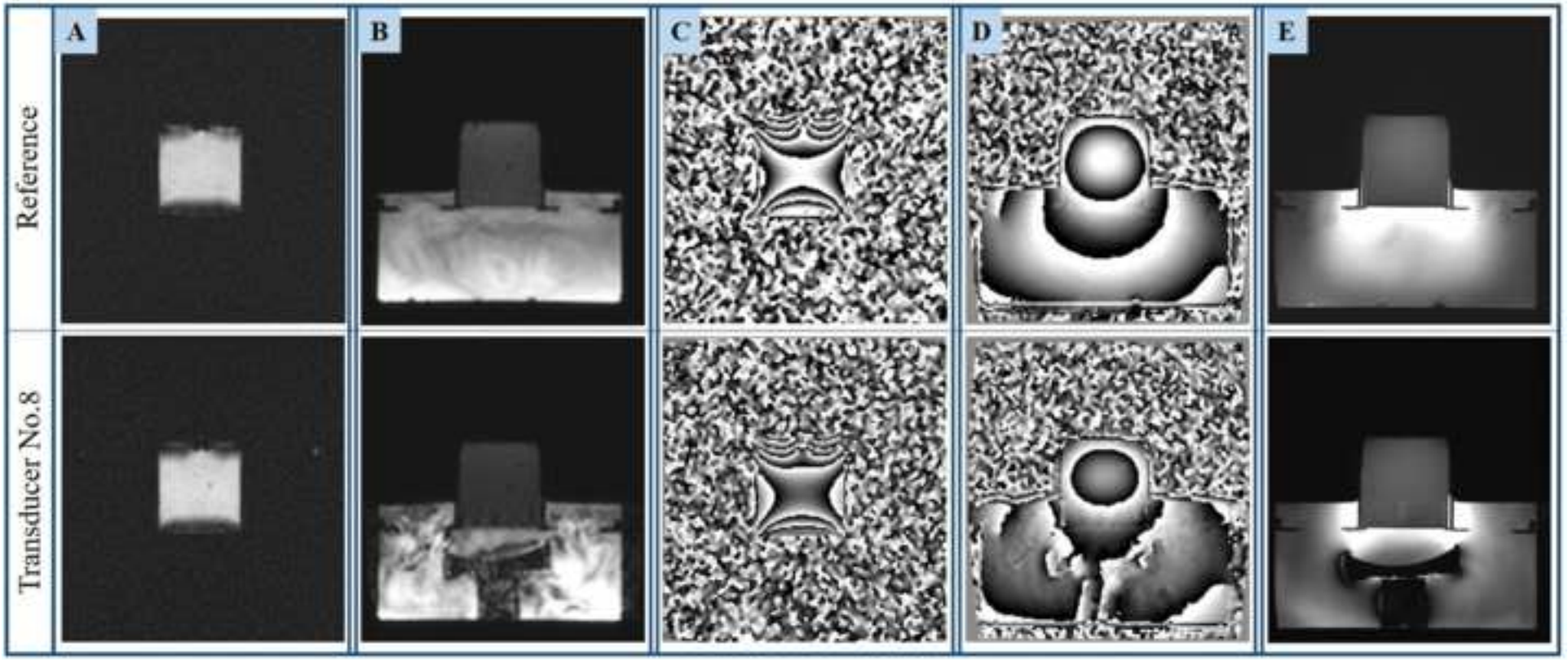

Figure 10

Click here to access/download;Figure;Figure 10.tiff

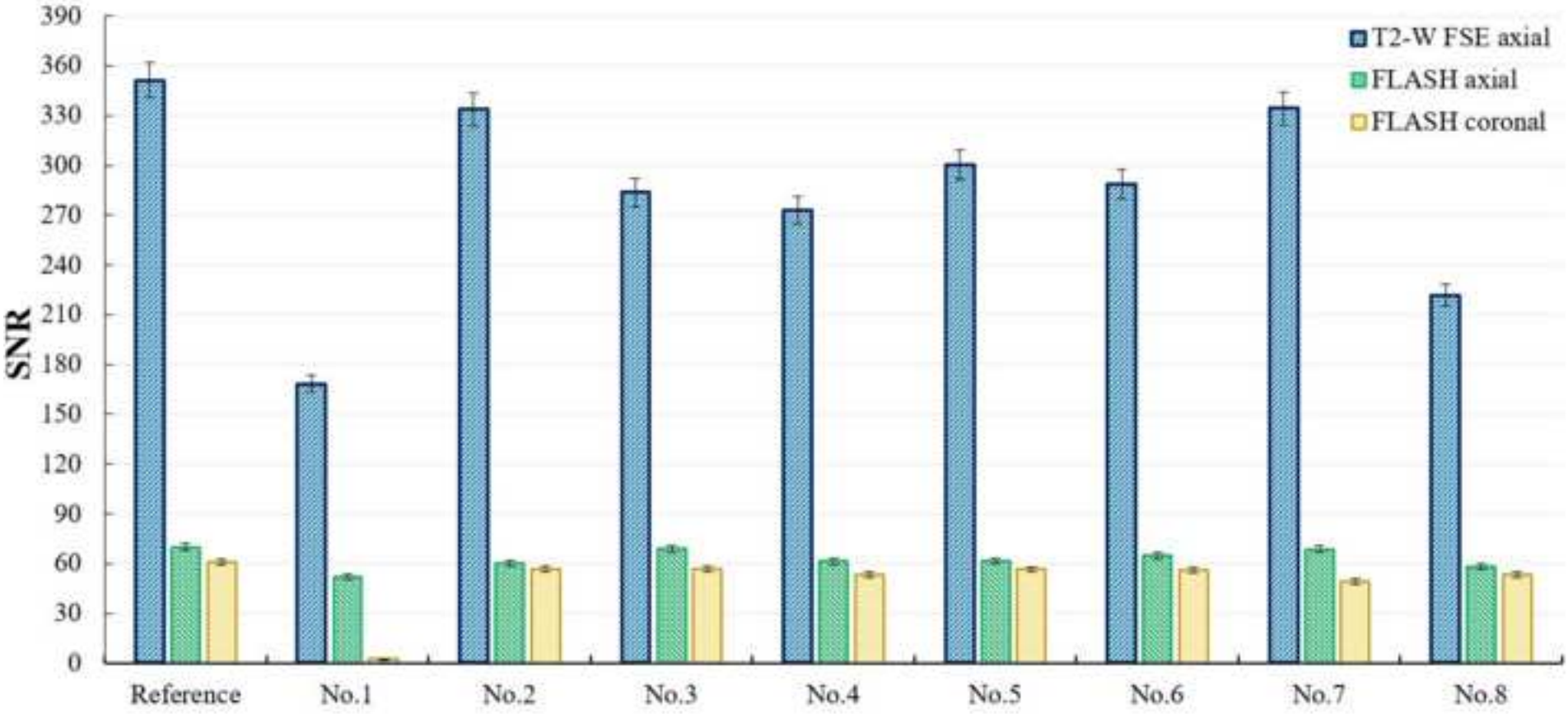

Received: 24 May 2022 | Revised: 12 September 2022 | Accepted: 27 September 2022

DOI: 10.1002/rcs.2466

ORIGINAL ARTICLE

The International Journal of Medical Robotics and Computer Assisted Surgery

WILEY

Preclinical robotic device for magnetic resonance imaging guided focussed ultrasound

Marinos Giannakou[1] | Anastasia Antoniou[2] | Christakis Damianou[2]

[1]R&D, Medsonic Ltd, Limassol, Cyprus

[2]Department of Electrical Engineering, Computer Engineering, and Informatics, Cyprus University of Technology, Limassol, Cyprus

Correspondence
Christakis Damianou, Department of Electrical Engineering, Computer Engineering, and Informatics, Cyprus University of Technology, 30 Archbishop Kyprianou Street, Limassol 3036, Cyprus.
Email: christakis.damianou@cut.ac.cy

Funding information
European Structural & Investment Funds and Research and Innovation Foundation of Cyprus, Grant/Award Number: SOUNDPET (INTEGRATED/0918/0008)

Abstract

Background: A robotic device featuring three motion axes was manufactured for preclinical research on focussed ultrasound (FUS). The device comprises a 2.75 MHz single element ultrasonic transducer and is guided by Magnetic Resonance Imaging (MRI).

Methods: The compatibility of the device with the MRI was evaluated by estimating the influence on the signal-to-noise ratio (SNR). The efficacy of the transducer in generating ablative temperatures was evaluated in phantoms and excised porcine tissue.

Results: System's activation in the MRI scanner reduced the SNR to an acceptable level without compromising the image quality. The transducer demonstrated efficient heating ability as proved by MR thermometry. Discrete and overlapping thermal lesions were inflicted in excised tissue.

Conclusions: The FUS system was proven effective for FUS thermal applications in the MRI setting. It can thus be used for multiple preclinical applications of the emerging MRI-guided FUS technology. The device can be scaled-up for human use with minor modifications.

KEYWORDS
focussed ultrasound, MRI guidance, preclinical research, robotic device

1 | INTRODUCTION

Focussed ultrasound (FUS) therapy is a promising treatment method against various diseases.[1] By focussing the ultrasonic beam, an increase in temperature is achieved due to the absorption of the ultrasonic energy by the tissue.[2] Accordingly, local therapy is possible even for targets located deep in the body.[3] The focal point is just a few mm in diameter depending on the transducer characteristics. This has the advantage of accessing targets with high precision and no damage on the surrounding tissue.[4] So far, therapeutic ultrasound has been evaluated in multiple oncological[5–8] and neurological applications[9–11] with very promising results. Due to its numerous benefits and wide range of potential applications, FUS play an important role in the future of medicine.

Magnetic Resonance Imaging (MRI) provides high resolution imaging of soft tissues. In addition, the imaging sequences used in MRI are temperature sensitive. Due to this property, it is possible to monitor the temperature evolution with the use of image processing.[12] It is therefore the ideal diagnostic method for FUS guidance.[13] MRI with fast imaging sequences can monitor temperature changes and estimate the delivered thermal dose during heating in almost real time.

Due to the small size of the focus, multiple overlapping lesions must be formed for ablating a large tissue volume. Thus, a robotic system is needed to accurately guide the transducer without intervention by the medical personnel, which would result in extremely long treatment sessions. Simultaneously, robotic operation offers the accuracy and precision required for such procedures, and thus, it is clearly safer. In addition, a robotic system allows treatment in a non-sequential pattern, thus reducing the prefocal heating and treatment duration.[14]

Various companies are involved in the development of preclinical FUS systems. One of them is the FUS Instruments company[15] owing two MRI compatible devices. The first one was specifically developed for 9.4 T MRI scanners, which have a small bore diameter.[16] The second device is larger in size and is compatible with MRI scanners of 1.5–3 T.[17] Image guided therapy is another company offering a wide range of products in the field of therapeutic ultrasound, including positioning systems.[18] Another company known for its wide range of ultrasound research systems is Verasonics.[19] This company offers a platform for FUS applications under diagnostic ultrasound guidance.[19] Although ultrasound is cheaper and can be easily integrated to a robotic system, it has lower image quality and does not provide any temperature information.

The development of MRI-compatible robotic systems is challenging due to the limitations related to the materials, motion actuators and encoders employed. A careful selection of materials and mechatronic components is required so that there is no significant interference with the scanner. In addition, the available space of the MRI scanner is very limited.[20] Thereby, the device must be able to fit inside the MRI bore while allowing enough space for the patient.

An emerging application that is still in the preclinical phase and has already attracted the attention of the research community is the FUS-mediated transient opening of the blood brain barrier (BBB).[21] The permeability of the BBB to large molecules prevents most of the drugs from entering the brain tissue.[21] Therefore, therapeutic drugs cannot normally reach the brain in the appropriate concentration to trigger the desired effect.

BBB opening could be beneficial in the treatment of numerous neurological diseases as it allows therapeutic agents to enter the brain parenchyma.[22] With FUS it is possible to reversibly disrupt the BBB for several hours allowing sufficient drug delivery while maintaining its defensive mechanism unaffected.[22] The benefits of FUS-mediated BBB disruption were proven in numerous animal studies.[23,24] Most studies were conducted in rodents, which are usually easier in handling and require less expensive facilities.[25,26]

Before a new device can be used in humans, it must be extensively evaluated ex-vivo in phantoms and excised animal tissue, as well as in vivo in animals. The purpose of pre-clinical trials is to extract data on the safety and the efficiency of the device and therapeutic protocol for the specific intended application. For this reason, there is a great interest from the research community for preclinical systems to accelerate the evaluation process of emerging applications in the field.

In prior studies, a lot of FUS robotic systems with varying functionalities and intended applications have been proposed.[27–34] Motion was established through different mechanisms including linear ball,[28] brass racks and pinion,[29] and jackscrew[34] mechanisms. Both piezoelectric[28,29,31,34] and pneumatic[30] motors were utilised for actuating motion. So far, our group manufactured numerous MRI-guided FUS (MRgFUS) systems by 3D printing, which comprise piezoelectric motors and MR compatible optical encoders for precisely actuating and monitoring motion, respectively.[31–34]

In the current study, we propose an in-house developed robotic device with advanced ergonomics for preclinical studies on MRI-guided FUS. The proposed device has compact dimensions, which make it capable for integration with all commercial scanners of cylindrical bore. Specifically, it can be sited on or fitted in the MRI table with the animal laying above an acoustic opening for ultrasonic coupling. The positioning mechanism actuates motion of the FUS transducer in the three cartesian axes. Movement in each axis is established by piezoelectric motors and controlled by a set of MR compatible optical encoders. Due to the non-invasive nature of therapeutic ultrasound, recovery of the animals will be faster and postoperative pain will be minimised.

The main innovation of the system is its mechanical design that addresses the issue of water volume fluctuation during motion occurred in previously proposed systems,[27,34] thereby avoiding the use of vacuum mechanisms. Specifically, the transducer is actuated in a water container along with all the moving parts, whereas the motors and encoders are accommodated in a separate enclosure. The motion is transferred into the water container via shafts that are sealed using O-rings to avoid water leakage to the motors' enclosure. The design of the various mechanical assemblies was proven challenging since they had to be compactly arranged in a single enclosure leaving sufficient space for the transducer to move. Special gear mechanisms and shaft guides were incorporated to achieve a smooth and reliable motion. The wide range of motion will enable adaptation of the system for human applications upon minor changes. Furthermore, in contrast to previously developed systems,[28,29,33] the proposed one has all its electronic and mechanical components hosted in a single compact enclosure, thus offering improved safety and ergonomics. Another key benefit is the highly accurate motion achieved through the use of a set of optical encoders for each individual motion axis. The combination of all the aforementioned benefits makes the system unique.

2 | MATERIALS AND METHODS

2.1 | Focussed ultrasound (FUS) setup

The device comprises an in-house manufactured piezoelectric transducer made out of non-magnetic materials. A concave piezoelectric element with a frequency of 2.75 MHz, an active diameter of 50 mm, and a geometric focussing radius of 65 mm (Piezo Hannas Tech co. Ltd) was hosted in a plastic case and secured with epoxy (2-

part epoxy adhesive, Asonic). Note that the transducer specifications were selected to achieve a sharp beam focussing at sufficient depth in tissue following simulation of the FUS beam and heating effects of candidate transducers with varying characteristics (frequency, diameter, and radius of curvature).

The impedance of the transducer was matched to a high-power amplifier (AG1016, AG Series Amplifier, T & C Power Conversion, Inc.) using a custom manufactured matching circuit. Its acoustic efficiency was experimentally determined by the radiation force balance method[35] and found to be 30%. Based on the power capacity of the transducer the maximum depth that lesions can be created is 10 cm.

2.2 | Positioning device

A robotic system with three degrees of freedom (DOF) was developed. The device manoeuvres the ultrasonic transducer in the *X*, *Y* and *Z* linear axes, with an available motion range of 80, 90, and 62 mm, respectively. Most of the device components were manufactured using a Fused Deposition Modelling (FDM) 3D printing machine (FDM 270, Stratasys). Some parts of the device that needed to have a highly accurate design and solid infill were manufactured using a polyjet 3D printing machine (Object30 pro, Stratasys). The FDM parts were made out of Acrylonitrile styrene acrylate (ASA) thermoplastic, whereas the polyjet parts were made out of Vero-White resin material.

The robotic system utilises ultrasonic motors (USR60-S3N, Shinsei Kogyo Corp.), whose motion is controlled by optical encoders (EM1-2-2500, US Digital Corporation) with a resolution of 2500 lines per 360°. The angular motion produced by the motors is converted into linear motion by jackscrew-based mechanisms.

The *X*-stage is shown in Figure 1. The rotational motion of the *X*-stage motor is transferred into the water container by a brass shaft, which rotates a gear mechanism. The gear mechanism was linked with the two jackscrews, which were in turn coupled with the *X*-plate as shown in Figure 1. Rotation of the motor induces linear motion of the *X*-plate along the respective jackscrews. Four guiding rods with a diameter of 8 mm were incorporated in the mechanism to ensure stable and smooth positioning in the *X*-axis.

The *Y*-stage shown in Figure 2 involves bevel gears coupled to a hexagonal driveshaft, thus transferring the motion at 90° (along the *Y* axis). During motion in the *X*-axis, the bevel gears mechanism slides along the driveshaft following the *X*-stage motion. During motion in *Y*-axis, the gears rotate at a specific point in the *X*-axis, thus transmitting the motion to the *Y*-stage independently. Specifically, the *Y*-stage motor as coupled to the hexagonal driveshaft rotates the bevel gears, which in turn rotate the *Y*-stage jackscrew. Similar to the *X*-stage, the *Y*-plate is coupled to and moves along the respective jackscrew and two guiding rods.

The *Z*-stage has a more complex mechanism involving additional moving parts, as shown in Figure 3. This stage required the use of two hexagonal driveshafts so as to transfer the motion to the *Z*-axis. Specifically, the *Z*-stage motor was coupled to the primary hexagonal driveshaft rotating the first stage bevel gears. The first stage bevel gears were in turn coupled to the secondary hexagonal driveshaft, thus rotating the second stage bevel gears. The second stage bevel gears rotate a set of spur gears, which are located under the *Y*-plate and are coupled to the *Z*-stage jackscrew. Rotation of the jackscrew causes motion of the *Z*-plate in the vertical direction along two guiding rods. With this configuration, the *Z*-stage is able to move independently from the *X*-stage and *Y*-stage. The FUS transducer is attached to the respective coupling of the *Z*-plate.

Figure 4A,B show Computer-aided design (CAD) drawings of the assembled robotic system. The moving parts were placed inside the water container, whereas the motors were placed in a separate mechanism enclosure located behind the water container. A simple and reliable mechanism with an O-ring was used in each axis to seal the water container since ultrasonic motors cannot operate in water. The main advantage of placing the moving parts inside the water container is that water level fluctuation during positioning is prevented. Figure 4C,D show photos of the manufactured device.

The device is compact with a length of 50 cm, a width of 23 cm, and a height of 13 cm. Therefore, it can be placed in the table of all conventional scanners up to 7T. The patient lies above the device with the ultrasound reaching the target from bottom to top via the acoustic opening. Since a part of the device protrudes above the table, a mattress will be added forming a comfortable flat bed for the animal or patient in potential future clinical applications. Note that the mattress is placed around the device and not between the device and subject under test.

The hardware is interfaced with a controlling software that allows for remote control of the FUS system and robotic motion. Multiple sonications in grid and irregular patterns can be executed following path planning. The software also implements algorithms for treatment planning on pre-operative MR images and monitoring of ultrasonic exposures through MR thermometry.[36]

2.3 | Evaluation of the system

2.3.1 | Accuracy and repeatability of robotic motion

The robotic device was initially assessed in terms of the accuracy of positioning. Evaluation was done in the benchtop setting using a high precision digital calliper. The method was based on comparing specific steps (1, 5, and 10 mm) commanded through the controlling software with the actual displacements of the motion stage as estimated by the calliper. A detailed description of this calliper-based technique can be found in previous work of our group.[37]

2.3.2 | Phantom preparation

An agar-based phantom was prepared with 6% weight per volume (w/v) agar (Merck KGaA, EMD Millipore Corporation) as described in

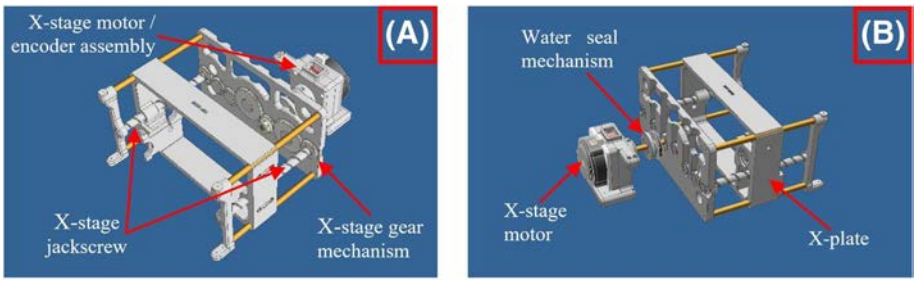

FIGURE 1 Computer-aided design (CAD) drawing of the *X*-stage mechanism: (A) Front view, (B) Rear view

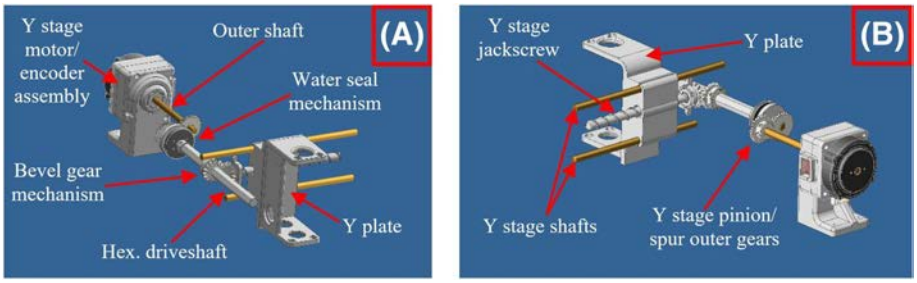

FIGURE 2 Computer-aided design (CAD) drawing of the *Y*-stage mechanism: (A) Front view, (B) Rear view

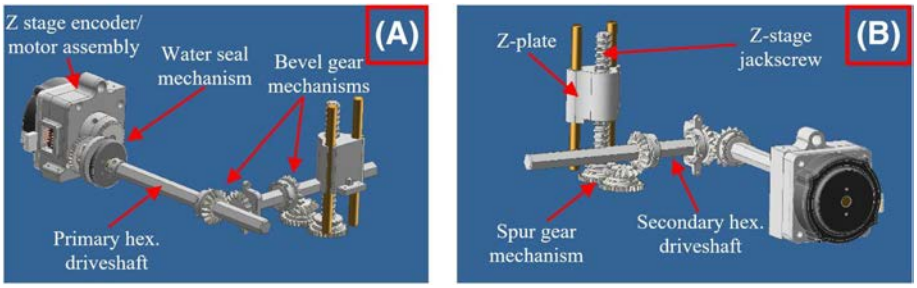

FIGURE 3 Computer-aided design (CAD) drawing of the *Z*-stage mechanism: (A) Front view, (B) Rear view

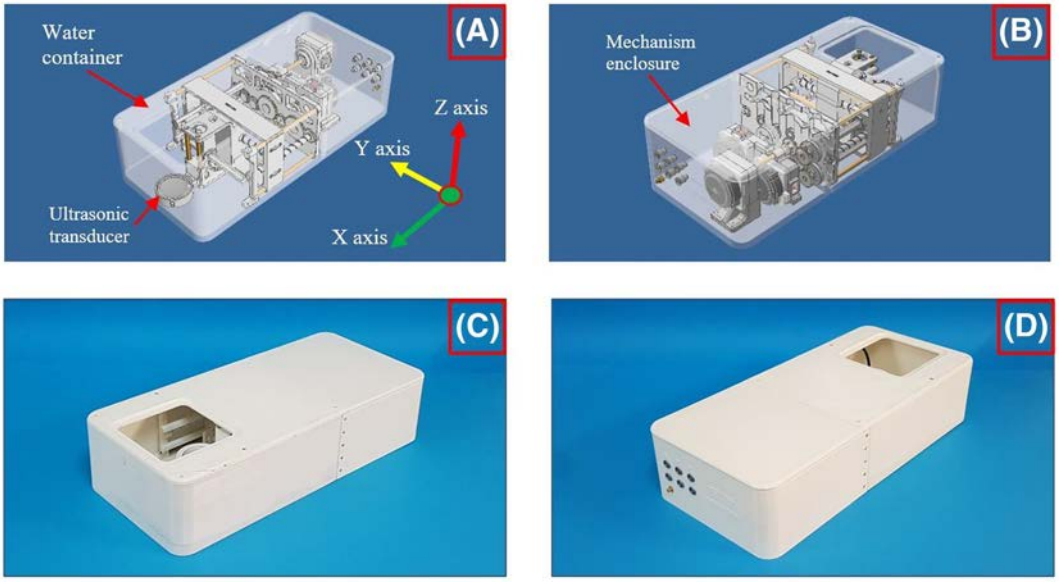

FIGURE 4 Computer-aided design (CAD) drawing of the assembled robotic device with transparent covers: (A) Front view, (B) Rear view, and photos of the manufactured device: (C) Front view, (D) Rear view

a previous study.[38] The selection of agar was based on the fact that agar-based phantoms can be easily prepared at low cost and have tissue-like MRI signal.[39] Additionally, this phantom has similar acoustical properties as human tissue.[39,40] The phantom was specially designed to securely fit the acoustic opening of the device so that vibrations during ultrasonic heating are minimised.

The phantom was used for assessing the MRI compatibility of the robotic device and heating ability of the FUS transducer using MR thermometry. Notably, image homogeneity in the MRI was achieved by continuous agitation of the agar mixture during preparation.[39]

2.3.3 | MRI compatibility

The robotic device was placed on the bed of a 1.5 T MRI scanner (GE Signa HD16, General Electric, Fairfield). The phantom was fitted in the acoustic opening. A body coil (Signa 1.5T 12 Channel, GE Healthcare Coils) was placed above the phantom using a custom-made positioner made out of Polylactic acid (PLA) thermoplastic. The MRI compatibility of the system components was evaluated by estimating the influence on the Signal to noise ratio (SNR).

Images of the agar phantom were acquired under different activations of the positioning device using a Spoiled Gradient Echo (SPGR) sequence with the following parameters: repetition time (TR) = 22 ms, echo time (TE) = 10.5 ms, field of view (FOV) = 28 × 28 cm^2, matrix = 192 × 160, flip angle = 30° and number of excitations (NEX) = 2. Image acquisition was performed with the cables disconnected (reference), cables connected, and DC ON (i.e., electronic system activated). Accordingly, the compatibility of the transducer with the scanner was evaluated by comparing SPGR images acquired with the amplifier activated (zero power applied) and electric power applied using the following parameters: TR = 22 ms, TE = 8.4 ms, FOV = 28 × 28 cm^2, matrix = 192 × 160, flip angle = 30° and NEX = 2. In each case, the SNR was calculated as follows:

$$SNR = \frac{SI_{phantom}}{\sigma_{noise}} \quad (1)$$

where the nominator represents the mean signal intensity (SI) of a region of interest (ROI) in the agar phantom and the denominator represents the standard deviation from the background ROI.

2.3.4 | MRI evaluation of thermal heating

The developed phantom was also used for evaluating the heating abilities of the FUS transducer. The transducer was fitted in a special plastic holder facing towards the bottom surface of the phantom. This setup was fitted in a water-filled tank to achieve proper ultrasonic transmission. The tank was sited on the MRI scanner and phantom sonications were performed. MR thermometry maps were extracted by comparing 2D SPGR images acquired using the following parameters: TR = 22 ms, TE = 8.4 ms, FOV = 28 × 28 cm^2, matrix = 192 × 160, flip angle = 30° and NEX = 2, according to the proton resonance frequency shift (PRFS)-based technique previously described in detail by Menikou et al.[41,42] This method takes advantage of the change in the resonance frequency of water protons upon heating. The phase difference between a baseline image $\varphi(T_0)$ and an image acquired at a specific time during heating $\varphi(T)$ is proportional to the corresponding PRFS and it can be easily converted to temperature change as follows:[43]

$$\Delta T = \frac{\varphi(T) - \varphi(T_0)}{\gamma \alpha B_0 TE} \quad (2)$$

where γ is the gyromagnetic ratio, α is the PRF change coefficient, B_0 is the magnetic field strength, and TE is the echo time. The range of temperatures (from a minimum to a maximum value) as calculated by MR thermometry were colour-coded by adjusting a colour map from blue to red.

2.3.5 | Lesion creation in excised tissue

The effectiveness of the transducer in terms of thermal ablation was then evaluated by sonicating freshly excised porcine tissue. The piece of freshly excised porcine tissue was fitted to the acoustic opening above the FUS transducer, which was moved in grid patterns with a 60 s time delay and varying spatial step. Each spot was sonicated using electric power of 150 or 200 W for a duration of 10–30 s at a focal depth of 25 mm.

3 | RESULTS

3.1 | Accuracy and repeatability of robotic motion

Motion steps of 1, 5, and 10 mm were tested. The maximum mean positioning error (n = 10) occurred at the 1 mm step and was 0.044 ± 0.019 mm, 0.051 ± 0.023 mm, and 0.072 ± 0.034 mm for motion in the *X*, *Y*, and *Z* axes, respectively. These results demonstrate high accuracy and repeatability of robotic motion in all incorporated axes, with a maximum positioning error of about 0.1 mm.

3.2 | MR compatibility

The effect of activating different system components on the SNR was calculated. Initially, the phantom was imaged with all its electronics deactivated. At this condition, the highest SNR value of 161 was recorded providing the reference value for comparison with the different activations tested, as shown in the graph of Figure 5. Connection of the cables to the electronic driving system did not

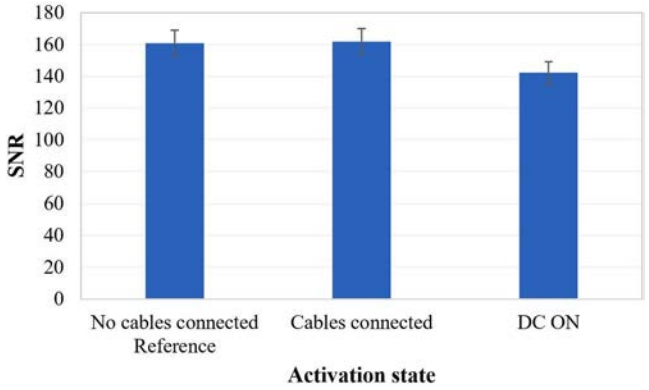

FIGURE 5 Signal-to-noise ratio (SNR) measurements from spoiled gradient echo (SPGR) phantom images acquired under different activation states of the positioning mechanism (MR parameters used: TR = 22 ms, TE = 10.5 ms, FOV = 28 × 28 cm^2, matrix = 192 × 160, flip angle = 30° and NEX = 2)

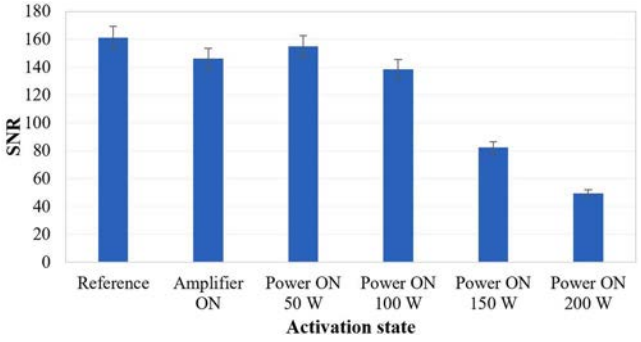

FIGURE 6 Signal-to-noise ratio (SNR) measurements from spoiled gradient echo (SPGR) phantom images acquired under different activation states of the focussed ultrasound (FUS) transducer (MR parameters used: TR = 22 ms, TE = 8.4 ms, FOV = 28 × 28 cm^2, matrix = 192 × 160, flip angle = 30° and NEX = 2)

affect the image quality since the estimated SNR value was almost equal to the reference value. Activation of the DC supply dropped the SNR to approximately 142.

Next, the impact the transducer's activation has on the image quality for different electric power levels was investigated, as shown in Figure 6. Initially, the amplifier was activated (zero output power) resulting in an SNR value of 146, which is similar to that obtained when the positioning mechanism was activated (Figure 5). For electric power values of 50–200 W the estimated SNR values were in the range of 155–50 (respectively). The amplifier's activation seemed to introduce noise in almost linear fashion as the power increases (50–200 W).

3.3 | MRI evaluation of thermal heating

Thermal maps were generated using SPGR images of the phantom acquired every 7 s. Figure 7 shows a thermal map constructed at 50 s of sonication at electrical power of 150 W in a plane perpendicular to the ultrasonic transmission (coronal), indicating a peak temperature of about 70°C at the focal spot (baseline temperature of 37°C).

3.4 | Lesion creation in excised tissue

Discrete lesions were initially produced on freshly excised porcine tissue. Figure 8A shows the lesions induced using electric power of 150 W for 15 s at the focal depth in tissue of 25 mm. Sequential sonications were performed in a 3 × 1 grid using a spatial step of 20 mm with a time delay of 120 s. Tissue was cut vertically (parallel to the ultrasonic beam) through the centre of lesions. The lesion diameter was approximately 3 mm and their length ranged from 10 to 15 mm. Note that the intervening tissue between the top surface of the meat and the focal depth does not seem to have been affected.

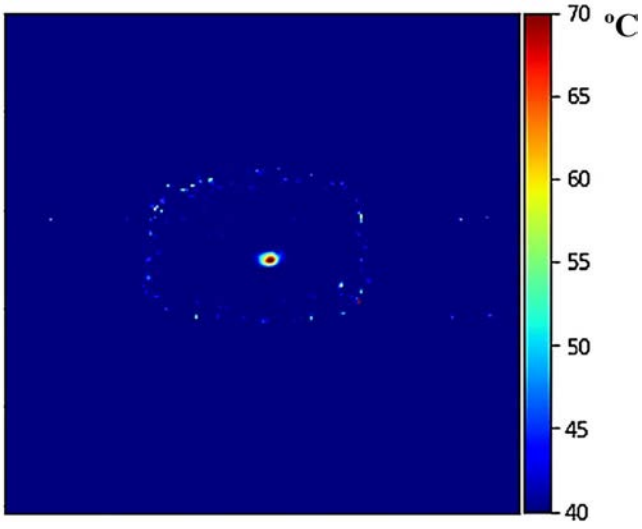

FIGURE 7 Coronal MR thermal map obtained in the focal plane at 50 s of sonication with electric power of 150 W using the spoiled gradient echo (SPGR) sequence (transducer specifications: frequency = 2.75 MHz, radius of curvature = 65 mm, diameter = 50 mm)

The lesions shown in Figure 8B were created using higher electric power of 200 W applied for a longer duration of 20 s while keeping the spatial and temporal step constant at the same focal depth (25 mm). In this case, the inflicted lesions were larger due to the increased power and were shifted towards the top surface of the meat. They had a larger diameter (approximately 5 mm) and a length in the range of 25–45 mm. The variation in lesion length is assumed to be the result of uneven tissue surface or other inhomogeneities and trapped air bubbles.

Sonications of similar electric power (200 W) applied for 30 s in a 4 × 4 grid with a smaller spatial step of 4 mm (60 s time delay) resulted in 16 overlapping lesions in tissue. Figure 9 shows the top surface of the meat where the ablated tissue covers an area of approximately 40 × 40 mm^2.

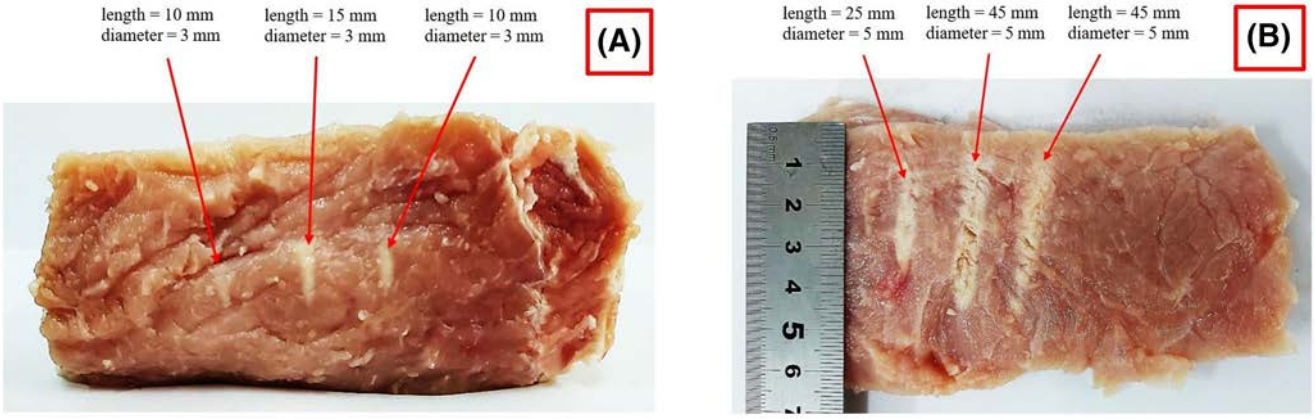

FIGURE 8 Photo of vertically dissected porcine meat showing lesions that were formed (on a plane parallel to the beam) in a 3 × 1 grid with a 20 mm step using electric power of (A) 150 W for 15 s, (B) 200 W for 20 s, at a focal depth of 25 mm (transducer specifications: frequency = 2.75 MHz, radius of curvature = 65 mm, diameter = 50 mm). Lesion's dimensions are indicated

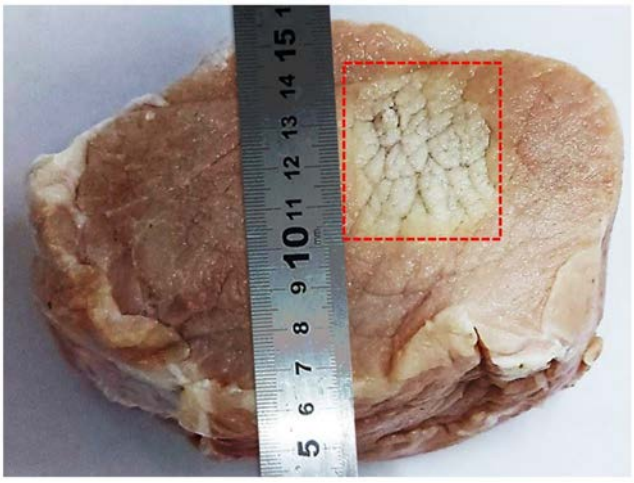

FIGURE 9 Photo of the top surface of excised meat after sonication in a 4 × 4 grid with a 4 mm step (60 s time delay) at a 25 mm focal depth using electric power of 200 W for 30 s at each spot (transducer specifications: frequency = 2.75 MHz, radius of curvature = 65 mm, diameter = 50 mm)

4 | DISCUSSION

A 3-DOF robotic device was developed to facilitate preclinical research on MRgFUS. The FUS transducer and all the mechanical assemblies are actuated in a water container, whereas the motion actuators and controllers are hosted in a separate enclosure located at the rear of the device. This allows easy access to the mechanical and electronic components of the system. Piezoelectric motors are used for motion actuation. Note that this type of motors was widely used in the development of MRI compatible FUS devices.[27,34,44–48] The angular motion of the motors is transmitted inside the water container via sealed shafts.

The robotic mechanism was specially designed to prevent water volume changes in the container during motion. By placing the motion stages inside the water container, fluctuation of the water volume is prevented since the mechanical parts are always occupying the same space. This approach eliminates the need for a bellow, which was used in previous studies to seal the coupling between the water container and the mechanism enclosure.[27,34] The bellow displaces the water especially during forward and reverse motion (*X*-axis motion); hence the water container should include a vacuum system, thereby complicating the system's design and use.

The device is intended to be used in the MRI environment; hence magnetic materials were not incorporated. To ensure safe operation of the device inside the strong magnetic field of the scanner, several experiments were carried out. The SNR was the main metric for evaluating the effect of the system's activation on image quality. The acquired SNR values suggest that the quality of the SPGR images was not affected significantly by the presence of the device in the imaging field of the scanner, and thus the incorporated materials were considered appropriate. Activation of the various electronics (i.e., motors and encoders) did not seem to impact the SNR considerably as the SNR measurements were close to the reference value of 161. Noticeable SNR reduction occurred when electric power was applied. The SNR reduced gradually from about 155 to 50 with increasing electric power from 50 to 200 W. Note that a 3-fold SNR reduction occurred at the highest acoustic power of 200 W. This is most probably attributed to the intense phantom vibrations occurring during intense heating. However, the SNR remained sufficiently high for the acquisition of thermal maps using MR thermometry algorithms. Note that the effect of power on image quality could be reduced substantially in higher field MRI scanners (3 and 7T), thus enabling the acquisition of high resolution images even at high power sonications.

The compact dimensions of the robotic device allow its placement in any commercial MRI scanner. The only requirement is to fit in the bore of the scanner. Due to its low weight (5.5 kg), it can be easily transported from the laboratory to the MRI setting. In addition, it can be easily prepared for use in a matter of few minutes. After use, it can be stored away as it is not integrated into the MRI bed permanently. Furthermore, the system is easy to be operated by the users.

Regarding future applications in humans, the 13 cm height of the device allows placement of humans for 3 and 7T scanners since the bore diameter is wide enough. For a 1.5 T scanner, the size of the robot would have to be reduced in order to accommodate humans with this robotic system. Basically, this design can be potentially fitted in all the scanners up to 7 T. For mice-dedicated scanners (9.4 T), the space available when the coil is inserted is only 6–7 cm, and thus this device cannot be hosted in such scanners. It is also clarified that the device cannot be used in combination with the head coil, since the subject under preclinical testing should be placed above the acoustic window. Therefore, only surface type coils can be used with this device.

The FUS system was then tested for its effectiveness in producing sufficient heating using MR thermometry maps. Initially, low power sonication was performed to detect the focus location where the peak temperature occurs. Thermal maps were then acquired at the focal plane during intense heating, demonstrating the ability of the transducer to induce lethal temperature in the agar phantom without any recorded self-heating effects.

After confirming efficient performance of the FUS transducer, the device was evaluated for its ability to produce thermal lesions in grid patterns through ex-vivo experiments. Multiple sonications were performed in freshly excised porcine tissue using the automatic grid operation of the software. Discrete and overlapping lesions were successfully created in tissue. Unlike agar-based phantoms, lesions in tissue are permanent. The production of lesions suggests that the temperature reached lethal levels, which is the main goal in oncological applications.

Discrete lesions were consistently created at the focal depth of 25 mm having similar diameter and length. This is a good indication of the thermal dose consistency and targeting accuracy of the device. Furthermore, the almost equal spacing arrangement of the formed lesions indicates high accuracy and repeatability of motion. Accurate motion is largely due to the high tolerances on the guides and stable driving mechanisms, as well as to the incorporation of a set of optical encoders on each axis that verify each other's operation.

It is interesting to note that the lesion size was proportional to the applied acoustic energy. Specifically, it was observed that an increase in the applied acoustic energy from 2250 to 4000 J (while keeping the other sonication parameters constant) resulted in discrete lesions of bigger dimensions, with a more than 2-fold increase in lesion length. Further increase of the acoustic energy to 6000 J resulted in overlapping lesions and the creation of a single homogeneous ablation area. These experiments also proved that the system offers proper coupling with the target, as well as reliable isolation between water container and electronic parts (motors and encoders) since no water leakage was observed.

It is also worth noting that a small variability in the size of adjacent lesions was observed. This is most probably attributed to tissue inhomogeneities and the presence of fat layers that cause scattering and phase aberrations, thus affecting the ultrasonic propagation and penetration depth. It is also possible that air bubbles are trapped in the tissue causing intense acoustic reflection also affecting the formation of uniform lesions.

The intended applications of the system include testing and optimising therapeutic protocols, as well as assessing the performance of FUS software and treatment algorithms in the preclinical setting; in tissue-mimicking phantom, excised tissue, and experimental animals. The available motion range is sufficient for the FUS beam to reach both shallow and deep tissue in animals of small to large size. Regarding BBB studies, a special holder could be fixed to the acoustic opening to accommodate rodents above the FUS transducer. Note that three DOF are more than enough for targeting the mouse brain, given its very small volume. However, the transducer should be replaced with one of proper characteristics for the specific application of BBB opening in mice. Typically, an operating frequency close to 1 MHz is suitable for minimising energy losses due to the skull. It should be also clarified that BBB opening is based on the mechanical (non-thermal) effects of pulsed FUS.

The proposed device constitutes an evolution of previously proposed robotic systems.[27,34] Drakos et al.[34] developed an MRgFUS robotic system for similar use. However, this device comprises a bellow for water sealing, which unavoidably induces water level fluctuations during robotic motion. As previously explained, the device proposed herein has a novel design that address this issue offering advanced ergonomics. In addition, it offers smoother motion that is mainly attributed to the use of gear mechanisms. Potential disadvantages of the system compared to the one proposed by Drakos et al.[34] are its greater height and the lack of an angular motion stage. Note that an angular stage could be easily added in the positioning mechanism, but at the cost of increased complexity. Although angular motion of the transducer offers access to more challenging locations (e.g., behind the ribs), it complicates the system and might not be necessary for preclinical use. The next evaluation step is to test the device in animals, such as rabbits.

5 | CONCLUSIONS

In summary, the current study proposes a robotic device with advanced ergonomics intended for preclinical research on the MRgFUS technology. The motion accuracy and MRI compatibility of the system in terms of proper imaging and thermal maps acquisition were demonstrated. The FUS system was proven safe and effective for thermal applications through MR thermometry experiments and visual assessment of lesion formation in excised porcine tissue. Overall, the results showed accuracy and consistency in the performance of the developed system throughout the sonication process. Further ex-vivo and in vivo experiments in animals are needed to identify any malfunctions of the system and optimise the therapeutic protocol for applications in animals with cancer.

AUTHOR CONTRIBUTIONS

Marinos Giannakou contributed to the development of the robotic device and draughting of the manuscript. Anastasia Antoniou contributed to the draughting of manuscript and implementation of the scientific methods. Christakis Damianou supervised the overall study, as well as the draughting of the manuscript.

ACKNOWLEDGEMENTS

The study was co-funded by the European Structural & Investment Funds (ESIF) and the Republic of Cyprus through the Research and Innovation Foundation (RIF) under the project SOUNDPET (INTEGRATED/0918/0008).

CONFLICT OF INTEREST

Marinos Giannakou declares no conflict of interest. Anastasia Antoniou declares no conflict of interest. Christakis Damianou declares no conflict of interest.

DATA AVAILABILITY STATEMENT

The data that support the findings of this study are available from the corresponding author upon reasonable request.

ORCID

Marinos Giannakou https://orcid.org/0000-0002-6777-0515
Christakis Damianou https://orcid.org/0000-0003-0424-2851

REFERENCES

1. Izadifar Z, Izadifar Z, Chapman D, Babyn P. An introduction to high intensity focused ultrasound: systematic review on principles, devices, and clinical applications. *J Clin Med*. 2020;9(2):460. https://doi.org/10.3390/jcm9020460
2. Andreeva TA, Berkovich AE, Bykov NY, Kozyrev SV, Lukin AY. High-intensity focused ultrasound: heating and destruction of biological tissue. *Tech Phys*. 2020;65(9):1455-1466. https://doi.org/10.1134/S1063784220090030
3. Elhelf IAS, Albahar H, Shah U, Oto A, Cressman E, Almekkawy M. High intensity focused ultrasound: the fundamentals, clinical applications and research trends. *Diagn Interv Imaging*. 2018;99(6):349-359. https://doi.org/10.1016/j.diii.2018.03.001
4. Bachu VS, Kedda J, Suk I, Green JJ, Tyler B. High-intensity focused ultrasound: a review of mechanisms and clinical applications. *Ann Biomed Eng*. 2021;49(9):1975-1991. https://doi.org/10.1007/s10439-021-02833-9
5. Kovatcheva R, Guglielmina J.-N, Abehsera M, Boulanger L, Laurent N, Poncelet E. Ultrasound-guided high-intensity focused ultrasound treatment of breast fibroadenoma—a multicenter experience. *J Ther Ultrasound*. 2015;3(1):1. https://doi.org/10.1186/s40349-014-0022-3
6. Dobrotwir A, Pun E. Clinical 24 month experience of the first MRgFUS unit for treatment of uterine fibroids in Australia. *J Med Imag Radiat Oncol*. 2012;56(4):409-416. https://doi.org/10.1111/j.1754-9485.2012.02376.x
7. Rodrigues DB, Stauffer PR, Vrba D, Hurwitz MD. Focused ultrasound for treatment of bone tumours. *Int J Hyperther*. 2015;31(3):260-271. https://doi.org/10.3109/02656736.2015.1006690
8. Dervishi E, Larrat B, Pernot M, et al. Transcranial high intensity focused ultrasound therapy guided by 7 TESLA MRI in a rat brain tumour model: a feasibility study. *Int J Hyperther*. 2013;29(6):598-608. https://doi.org/10.3109/02656736.2013.820357
9. King RL, Brown JR, Pauly KB. Localization of ultrasound-induced in vivo neurostimulation in the mouse model. *Ultrasound Med Biol*. 2014;40(7):1512-1522. https://doi.org/10.1016/j.ultrasmedbio.2014.01.020
10. Mehić E, Xu JM, Caler CJ, Coulson NK, Moritz CT, Mourad PD. Increased anatomical specificity of neuromodulation via modulated focused ultrasound. *PLoS One*. 2014;9(2):e86939. https://doi.org/10.1371/journal.pone.0086939
11. Hersh DS, Kim AJ, Winkles JA, Eisenberg HM, Woodworth GF, Frenkel V. Emerging applications of therapeutic ultrasound in neuro-oncology. *Neurosurgery*. 2016;79(5):643-654. https://doi.org/10.1227/NEU.0000000000001399
12. Vykhodtseva N, Sorrentino V, Jolesz FA, Bronson RT, Hynynen K. MRI detection of the thermal effects of focused ultrasound on the brain. *Ultrasound Med Biol*. 2000;26(5):871-880. https://doi.org/10.1016/S0301-5629(00)00216-7
13. Köhler MO, Mougenot C, Quesson B, et al. Volumetric HIFU ablation under 3D guidance of rapid MRI thermometry. *Med Phys*. 2009;36(8):3521-3535. https://doi.org/10.1118/1.3152112
14. Yiannakou M, Trimikliniotis M, Yiallouras C, Damianou C. Evaluation of focused ultrasound algorithms: issues for reducing pre-focal heating and treatment time. *Ultrasonics*. 2016;65:145-153. https://doi.org/10.1016/j.ultras.2015.10.007
15. Home | FUS Instruments. Accessed May 22, 2022. https://www.fusinstruments.com/
16. Wu S.-K, Santos MA, Marcus SL, Hynynen K. MR-Guided focused ultrasound facilitates sonodynamic therapy with 5-aminolevulinic acid in a rat glioma model. *Sci Rep*. 2019;9(1):10465. https://doi.org/10.1038/s41598-019-46832-2
17. Santos MA, Wu S.-K, Li Z, Goertz DE, Hynynen K. Microbubble-assisted MRI-guided focused ultrasound for hyperthermia at reduced power levels. *Int J Hyperther*. 2018;35(1):599-611. https://doi.org/10.1080/02656736.2018.1514468
18. Image Guided Therapy—TargetedFUS. Accessed May 15, 2022. http://www.imageguidedtherapy.com/Focused-ultrasounds/MR-guided-Focused-Ultrasounds-System-for-experimental-research.html
19. HIFUPlex Options—Verasonics. Accessed May 15, 2022. https://verasonics.com/hifuplex-options/
20. Hata N, Moreira P, Fischer G. Robotics in MRI-guided interventions. *Top Magn Reson Imag*. 2018;27(1):19-23. https://doi.org/10.1097/RMR.0000000000000159
21. Choi JJ, Wang S, Tung Y.-S, Morrison B, Konofagou EE. Molecules of various pharmacologically-relevant sizes can cross the ultrasound-induced blood-brain barrier opening in vivo. *Ultrasound Med Biol*. 2010;36(1):58-67. https://doi.org/10.1016/j.ultrasmedbio.2009.08.006
22. Sheikov N, McDannold N, Sharma S, Hynynen K. Effect of focused ultrasound applied with an ultrasound contrast agent on the tight junctional integrity of the brain microvascular endothelium. *Ultrasound Med Biol*. 2008;34(7):1093-1104. https://doi.org/10.1016/j.ultrasmedbio.2007.12.015
23. Bing C, Ladouceur-Wodzak M, Wanner CR, Shelton JM, Richardson JA, Chopra R. Trans-cranial opening of the blood-brain barrier in targeted regions using astereotaxic brain atlas and focused ultrasound energy. *J Ther Ultrasound*. 2014;2(1):1-11. https://doi.org/10.1186/2050-5736-2-13
24. Karakatsani ME, Blesa J, Konofagou EE. Blood–brain barrier opening with focused ultrasound in experimental models of Parkinson's disease. *Mov Disord*. 2019;34(9):1252-1261. https://doi.org/10.1002/mds.27804
25. Sabbagh A, Beccaria K, Ling X, et al. Opening of the blood–brain barrier using low-intensity pulsed ultrasound enhances responses

to immunotherapy in preclinical glioma models. *Clin Cancer Res*. 2021:1-14. https://doi.org/10.1158/1078-0432.ccr-20-3760
26. Englander ZK, Wei HJ, Pouliopoulos AN, et al. Focused ultrasound mediated blood–brain barrier opening is safe and feasible in a murine pontine glioma model. *Sci Rep*. 2021;11(1):1-10. https://doi.org/10.1038/s41598-021-85180-y
27. Spanoudes K, Evripidou N, Giannakou M, Drakos T, Menikou G, Damianou C. A high intensity focused ultrasound system for veterinary oncology applications. *J Med Ultrasound*. 29(3):195-202. https://doi.org/10.4103/JMU.JMU_130_20
28. Chopra R, Curiel L, Staruch R, Morrison L, Hynynen K. An MRI-compatible system for focused ultrasound experiments in small animal models. *Med Phys*. 2009;36(5):1867-1874. https://doi.org/10.1118/1.3115680
29. Mylonas N, Damianou C. MR compatible positioning device for guiding a focused ultrasound system for the treatment of brain diseases. *Int J Med Robot Comput Assist Surg*. 2014;10:1-10. https://doi.org/10.1002/rcs.1501
30. Krafft AJ, Jenne JW, Maier F, et al. A long arm for ultrasound: a combined robotic focused ultrasound setup for magnetic resonance-guided focused ultrasound surgery. *Med Phys*. 2010;37(5):2380-2393. https://doi.org/10.1118/1.3377777
31. Menikou G, Yiallouras C, Yiannakou M, Damianou C. MRI-guided focused ultrasound robotic system for the treatment of bone cancer. *Int J Med Robot Comput Assist Surg*. 2017;13(1):1-11. https://doi.org/10.1002/rcs.1753
32. Drakos T, Giannakou M, Menikou G, Damianou C. Magnetic resonance imaging–guided focused ultrasound positioning system for preclinical studies in small animals. *J Ultrasound Med*. 2020;40(7):1-10. https://doi.org/10.1002/jum.15514
33. Damianou C, Giannakou M, Menikou G, Ioannou L. Magnetic resonance imaging-guided focused ultrasound robotic system with the subject placed in the prone position. *Digit Med*. 2020;6(1):24-31. https://doi.org/10.4103/digm.digm_2_20
34. Drakos T, Giannakou M, Menikou G, et al. MRI-guided focused ultrasound robotic system for preclinical use. *J Vet Med Anim Sci*. 2021;4(1):1-11.
35. Shou W, Huang X, Duan S, et al. Acoustic power measurement of high intensity focused ultrasound in medicine based on radiation force. *Ultrasonics*. 2006;44:17-20. https://doi.org/10.1016/j.ultras.2006.06.034
36. Antoniou A, Georgiou A, Evripidou N, Damianou C. Full coverage path planning algorithm for MRgFUS therapy. *Int J Med Robot Comput Assist Surg*. 2022;18(3):1-10. https://doi.org/10.1002/rcs.2389
37. Antoniou A, Drakos T, Giannakou M, et al. Simple methods to test the accuracy of MRgFUS robotic systems. *Int J Med Robot Comput Assist Surg*. 2021;17(4). https://doi.org/10.1002/rcs.2287
38. Drakos T, Giannakou M, Menikou G, Constantinides G, Damianou C. Characterization of a soft tissue-mimicking agar/wood powder material for MRgFUS applications. *Ultrasonics*. 2021;113:10635. https://doi.org/10.1016/j.ultras.2021.106357
39. Antoniou A, Damianou C. MR relaxation properties of tissue-mimicking phantoms. *Ultrasonics*. 2022;119:106600. https://doi.org/10.1016/j.ultras.2021.106600
40. Drakos T, Antoniou A, Evripidou N, et al. Ultrasonic attenuation of an agar, silicon dioxide, and evaporated milk gel phantom. *J Med Ultrasound*. 2021;29(4):239-249. https://doi.org/10.4103/JMU.JMU
41. Menikou G, Damianou C. Acoustic and thermal characterization of agar based phantoms used for evaluating focused ultrasound exposures. *J Ther Ultrasound*. 2017;5(1):14. https://doi.org/10.1186/s40349-017-0093-z
42. Drakos T, Giannakou M, Menikou G, Ioannides C, Damianou C. An improved method to estimate ultrasonic absorption in agar-based gel phantom using thermocouples and MR thermometry. *Ultrasonics*. 2020;103:106089. https://doi.org/10.1016/j.ultras.2020.106089
43. Rieke V, Pauly KB. MR thermometry. *J Magn Reson Imag*. 2008;27(2):376-390. https://doi.org/10.1002/jmri.21265.MR
44. Antoniou A, Giannakou M, Evripidou N, Stratis S, Pichardo S, Damianou C. Robotic system for top to bottom MRgFUS therapy of multiple cancer types. *Int J Med Robot Comput Assist Surg*. 2022;18. https://doi.org/10.1002/rcs.2364
45. Giannakou M, Drakos T, Menikou G, et al. MRI-guided focused ultrasound robotic system for transrectal prostate cancer therapy. *Int J Med Robot Comput Assist Surg*. 2021;17:1-15. https://doi.org/10.1002/rcs.2237
46. Yiallouras C, Mylonas N, Damianou C. MRI-compatible positioning device for guiding a focused ultrasound system for transrectal treatment of prostate cancer. *Int J Comput Assist Radiol Surg*. 2014;9(4):745-753. https://doi.org/10.1007/s11548-013-0964-x
47. Antoniou A, Giannakou M, Evripidou N, et al. Robotic system for magnetic resonance guided focused ultrasound ablation of abdominal cancer. *Int J Med Robot Comput Assist Surg*. 2021;17(5). https://doi.org/10.1002/rcs.2299
48. Epaminonda E, Drakos T, Kalogirou C, Theodoulou M, Yiallouras C, Damianou C. MRI guided focused ultrasound robotic system for the treatment of gynaecological tumors. *Int J Med Robot Comput Assist Surg*. 2016;12(1):46-52. https://doi.org/10.1002/rcs.1653

How to cite this article: Giannakou M, Antoniou A, Damianou C. Preclinical robotic device for magnetic resonance imaging guided focussed ultrasound. *Int J Med Robot*. 2022;e2466. https://doi.org/10.1002/rcs.2466

Journal of Magnetic Resonance 344 (2022) 107317

Contents lists available at ScienceDirect

Journal of Magnetic Resonance

journal homepage: www.elsevier.com/locate/jmr

Challenges regarding MR compatibility of an MRgFUS robotic system

Anastasia Antoniou [a], Leonidas Georgiou [b], Nikolas Evripidou [a], Cleanthis Ioannides [b], Christakis Damianou [a,*]

[a] Department of Electrical Engineering, Computer Engineering, and Informatics, Cyprus University of Technology, Limassol, Cyprus
[b] German Oncology Center, Department of Interventional Radiology, Limassol, Cyprus

ARTICLE INFO

Article history:
Received 15 April 2022
Revised 11 October 2022
Accepted 13 October 2022
Available online 18 October 2022

Keywords:
MRI compatibility
SNR
MRgFUS
Robotic device
Artifacts

ABSTRACT

Numerous challenges are faced when employing Magnetic Resonance guided Focused Ultrasound (MRgFUS) hardware in the Magnetic Resonance Imaging (MRI) setting. The current study aimed to provide insights on this topic through a series of experiments performed in the framework of evaluating the MRI compatibility of an MRgFUS robotic device. All experiments were performed in a 1.5 T MRI scanner. The main metric for MRI compatibility assessment was the signal to noise ratio (SNR). Measurements were carried out in a tissue mimicking phantom and freshly excised pork tissue under various activation states of the system. In the effort to minimize magnetic interference and image distortion, various set-up parameters were examined. Significant SNR degradation and image distortion occurred when the FUS transducer was activated mainly owing to FUS-induced target and coil vibrations and was getting worse as the output power was increased. Proper design and stable positioning of the imaged phantom play a critical role in reducing these vibrations. Moreover, isolation of the phantom from the imaging coil was proven essential for avoiding FUS-induced vibrations from being transferred to the coil during sonication and resulted in a more than 3-fold increase in SNR. The use of a multi-channel coil increased the SNR by up to 50 % compared to a single-channel coil. Placement of the electronics outside the coil detection area increased the SNR by about 65 %. A similar SNR improvement was observed when the encoders' counting pulses were deactivated. Overall, this study raises awareness about major challenges regarding operation of an MRgFUS system in the MRI environment and proposes simple measures that could mitigate the impact of noise sources so that the monitoring value of MR imaging in FUS applications is not compromised.

1. Introduction

High intensity focused ultrasound (HIFU) is a non-invasive modality for tumour treatment by local thermal ablation [1,2]. To achieve these localized biological effects, piezoelectric transducers are used to converge ultrasound waves at a pre-selected focal point of interest [1,2]. Accordingly, precise navigation of the ultrasonic transducer is needed for the ablation of a large tissue volume. Focused ultrasound (FUS) can eliminate the risks associated with surgical incisions and exposure to ionizing radiation and allows for multiple treatment repetitions in case of disease recurrence. So far, the most common side effect of HIFU therapy is thermal injury (e.g., skin burns), which is caused by energy deposition in the beam pathway [3].

Since Lynn's et al. [4] early studies in 1942 introducing the concept of HIFU and Fry's et al. [5,6] groundbreaking studies in the 1950 s, in which HIFU was used for brain surgery in animals and people, this intriguing technology has come a long way in terms of development and maturation. This was made feasible by a number of factors, including improvements in transducer design and particularly the introduction of the phased array technology, as well as in monitoring of ultrasonic delivery, with the major improvement being the development of Magnetic Resonance (MR) thermometry [7,8].

When FUS is combined with MR imaging (MRI) guidance, precise targeting and real-time temperature monitoring with closed-loop control of energy deposition are achieved with an ideal safety profile [9,10]. The thermometric data help to adjust the ablation strategy *in situ* through feedback control of the HIFU power, as well as to assess the tissue necrosis and hence define the therapeutic

* Corresponding author at: Department of Electrical Engineering, Computer Engineering, and Informatics, Cyprus University of Technology, 30 Archbishop Kyprianou Street, 3036 Limassol, Cyprus.
E-mail addresses: anastasiaantoniou12@gmail.com (A. Antoniou), leonidas.georgiou@goc.com.cy (L. Georgiou), nk.evripidou@edu.cut.ac.cy (N. Evripidou), cleanthis.ioannides@goc.com.cy (C. Ioannides), christakis.damianou@cut.ac.cy (C. Damianou).

https://doi.org/10.1016/j.jmr.2022.107317
1090-7807/

endpoint [11]. Currently, MRI is the only imaging technique that provides quantitative temperature measurements in vivo [9,10]. This technological combination is known as MR-guided FUS (MRgFUS). Because of its clinical advantages, MRgFUS therapy is an appealing alternative to surgical resection for the treatment of cancer and other diseases [12].

Image quality and the accuracy of temperature mapping are largely dependent on the signal to noise ratio (SNR) [13]. In conventional MRI, high spatiotemporal resolution is achieved by employing multiple channel coil arrays that are placed in close proximity to the patient [14]. It is well known that phased array coils yield higher SNR compared to single-channel coils for identical parameters of imaging [15–18]. An example in the context of FUS is a study by Werner et al. [19], in which a custom built 8-channel head array was proven to offer a 3.5 times higher SNR than that of a standard body coil, thereby providing more anatomical details and better image guidance for MRgFUS neurosurgery. The coil characteristics, such as the number and size of its elements [17], as well as its rigidness [20], have an impact on SNR as well. Random motion of the patient (e.g., due to respiration) and the imaging coil is a common source of image blurring in the MRI and can also impact the measured SNR [21].

Different sources of noise and artifacts may influence the quality of diagnostic and therapeutic information negatively, and may be related to the MRI hardware itself or its interaction with the patient/imaging object or other equipment in the MRI room [22]. In this regard, there are a lot of challenges regarding the development of hardware for robotic assisted MRI-guided therapeutic interventions. The main sources of noise for robotic devices operating within an MRI environment are the employed construction materials, motion actuators and controllers, which are possible to interfere with the static magnetic field, the magnetic field gradients, and RF signals of the scanner depending on their activation condition (passive or active mode).

Materials should be electrically nonconductive, nonmetallic, and nonmagnetic in order to be classified as ‘‘MR safe” according to the ASTM standards (F2503) [23]. ‘‘MR Conditional” devices are anticipated to enter and operate in a specific MRI environment safely (with no hazards) only under specific conditions (e.g., magnetic field strength, spatial gradient, RF fields, etc.). MR unsafe devices are those that should remain outside the MRI room because they are known to pose hazards in all MRI environments. Generally, electrically active medical devices could be either MR Conditional or MR Unsafe since they contain electrically conductive components.

Materials are typically classified for MR safety based on their susceptibility property. Materials with very low susceptibility magnitude such as plastics (e.g., Acrylonitrile butadiene styrene (ABS), nylon, Polycarbonate (PC), and Teflon), rubber, glass, wood, copper, and high-alumina ceramic do not induce detectable image artifacts [24–26]. It is interesting to note that in recent years, rapid prototyping with plastic using 3D computer aided design (CAD) data offers an ergonomic way to manufacture MR-safe components of any geometry [27], and was widely used for manufacturing motion stages of MR compatible FUS robots [28–31]. Easily noticed artifacts can be produced by metals such as titanium, molybdenum, tungsten, tantalum, zirconium, aluminium, as well as by graphite [26,32]. However, their influence on imaging can be minimized if they are placed at specific locations in the MRI room and at smaller quantities [26,32]. Since imaging relies on tissue excitation by RF pulses under a strong static magnetic field, ferromagnetic materials such as iron and nickel that are characterized by very high magnetic susceptibility produce significant artifacts and are easily magnetized in the field direction. Therefore, their use should be precluded if possible. Otherwise, in case such materials are to be employed in the MRI room, they should be housed in fixed structures to ensure that they will not be attracted towards the magnet [32].

In robotic devices, magnetic materials are typically found in the mechatronic components (motion actuators and encoders), which are typically arranged in the motion mechanism, thus not raising any safety concerns. However, their presence perturbates the homogeneity of the external field causing errors in the image readout process. Specifically, the magnetic field variations in the presence of magnetic impurities induce variations of the resonance frequency of protons and signal dephasing, and thus, signal loss [33]. Displacement of signal in the slice selection direction can also cause signal loss in specific regions (black areas) and accumulation of signal in other regions, thus creating another type of artifact known as the ‘‘pile-up” artifact [33]. In case the field variations are smooth, the image may exhibit milder artifacts such as geometric distortions [33]. In general, the artifacts originating from magnetic field strength variation at regions with different magnetic susceptibility are commonly known as susceptibility artifacts.

Another concern regarding safe operation of robotic devices in the MRI environment is the use of motion actuators. Piezoelectric motors completely designed with non-ferrous materials are available in the market and are widely incorporated in MR guided robotics [24,28,34–37]. Despite that they are generally considered to be safe for operation in proximity to high field scanners, it was observed that they interfere with the MRI equipment when not used properly [38]. The major issue is the use of electric circuits, which drastically reduce the SNR if not shielded properly [24,32]. To address this issue, the motors can be placed far away from the scanner’s isocenter [24,27] so as to function properly, with Larson et al. [39] suggesting a distance of at least 0.5 m. Accordingly, this often creates the need to use mechanical means to transmit the motion to the workspace [24,40], which unavoidably introduces a source of error since the system is more prone to friction and backlash [24]. Notably, introduction of the motors inside the isocenter of the scanner while maintaining acceptable SNR reduction was proven feasible when placing the electronics into an enclosure acting as a Faraday cage while simultaneously filtering the control lines [41]. Furthermore, accurate motion in robotics requires continuous feedback from sensors. Optical encoders are widely implemented for position sensing, but the generated electric pulses can also introduce noise [32].

Further challenges are faced when employing MRgFUS hardware in the scanner. A technical limitation of an MRgFUS experimental setup relates to the coil position. It is important that coil arrays do not obstruct the beam’s propagation since a clean path is required for proper ultrasonic delivery to the target. It is interesting to note that recently, Corea et al. [14] reported that 3D printed coil arrays exhibit significant transparency to the acoustic energy and proposed their use as a way to enhance image resolution by placing the coil in the beam path.

Caution should also be paid to potential noise that may be introduced by the ultrasonic transducer. Piezoelectric elements are sometimes plated with nickel while backing materials and acoustic matching layers often contain ferromagnetic particles, which are included to increase their density and thus their acoustic impedance [42]. As already mentioned, ferromagnetic components should be avoided since they are known to induce significant susceptibility artifacts [4243]. Alternatively, Gerold et al. [43] have suggested the inclusion of other fillers such as Al2O3 or Cu powder. Cu-epoxy composites were shown to offer electromagnetic shielding and proper acoustic impedance for ultrasonic matching with piezocomposite materials [43]. Furthermore, conductive components may develop eddy currents when experiencing magnetic field changes, thereby arising additional safety concerns [42]. Eddy currents can induce not only SNR degradation, but also consider-

able image distortion [44]. Small components such as wiring and printed circuit boards produce acceptable field disturbance, whereas other bigger conductive structures must be shielded [42]. Finally, it is necessary that the housing of the piezoelectric element is manufactured with proper materials. 3D printed plastic holders were found to be fully compatible with MRI and constitute an ergonomic and cost-effective solution [45].

The current study concerned the evaluation of a robotic device dedicated to MRgFUS preclinical use in terms of MR compatibility. In this paper, the term "MR-compatibility" refers to an MR-conditional device that can be operated in an MRI setting properly without affecting the quality of imaging and diagnostic information significantly. The device used is classified as MRI conditional according to the ASTM standards because it contains metallic and electronic components.

The SNR served as the main metric for evaluating the MR image quality and compatibility of the various system's components (i.e., employed materials, actuators, encoders, and ultrasonic source) with a 1.5 T clinical MRI scanner. In addition, various set-up parameters such as the coil stability and its positioning relative to the target, target size and stability, as well as the positioning of electronic components relative to the imaging coil and activation status of encoders (i.e., counting pulses on/off), were examined for optimizing the SNR and quality of image acquisition. Imaging was performed in a tissue mimicking phantom and freshly excised pork tissue using common MR sequences. By summarizing all the experimental data, the study aims to contribute to addressing major challenges regarding operation of a robotically positioned MRgFUS system in the MRI environment and raising awareness for potential sources of noise and distortion that may not be obvious to researchers in the field.

2. Materials and methods

All described experiments were performed in the framework of evaluating the performance of an MRgFUS robotic device for preclinical applications in terms of safe and efficient operation in the MRI environment. No data on patients or animals were included in the study and thus no ethical approval is available.

2.1. Robotic device for MRgFUS applications

The robotic device used in the current study comprises a mechanism with three linear (X, Y, Z) and one angular (Θ) stages of motion dedicated to positioning a single element spherically focused transducer relative to the target. All the mechanical components are installed in a compact housing, thereby enabling ease integration of the device into the MRI table so that thermal ablation can be accurately performed under the guidance of MRI. The ultrasonic transducer operates in a separate enclosure that includes an acoustic opening at the top for ultrasonic coupling with the target through water. A CAD drawing of the device is shown in Fig. 1A, whereas Fig. 1B shows its integration into the MRI table. A dedicated software is used for therapy planning, kinematic control of the positioning mechanism, therapeutic ultrasound control, and monitoring of ultrasonic delivery through the use of MR thermometry, thereby offering an efficient procedural workflow.

Piezoelectric motors (USR30-S3N, Shinsei Kogyo Corp., Tokyo, Japan) serve as the actuators of motion. The rotational motion of the motors is converted into linear mainly through jackscrew mechanisms, which amplify the motor torque. Motion of each positioning stage is controlled by an optical encoder set up (US Digital Corporation,Washington, USA), which increases the motion accuracy and eliminates the possibilities of mechanical problems not being detected. The location of the motors and encoder modules is indicated in Fig. 1A.

The mechatronic parts (motors and encoders) are wired up to medical non-magnetic connectors (S 103 A053-130+, Fischer Connectors, Saint-prex, Vaud, Switzerland) at the rear of the mechanism enclosure. The driving electronics, i.e., the motor drivers (D6030, Shinsei corporation, Tokyo, Japan) and the Microcontroller card (Arduino cc, Ivrea, Italy) used to convert analog signals into digital signals that are recognized by the software, are housed in a compact enclosure located outside of the MRI room.

The driving system is powered by a DC supply (24 V, 6A) and is wired up to the device through the grounded MRI penetration panel using rubber-shielded copper cables (Shinsei Kogyo Corp., Tokyo, Japan) for the motors and a copper-shielded coaxial cable (RJ58, 50 Ω) for transducer supply. Note that each cable has its own shielding layer for reducing electromagnetic emissions. Outside of the MRI room, the transducer is paired to a custom-made low pass RF filter (10 MHz cutoff frequency), which is in turn connected to the amplifier (AG1016, AG Series Amplifier, T & C Power Conversion, Inc., Rochester, US) to block harmonic currents and prevent image distortions effects.

All individual embodiments employed were specially selected to ensure MR compatibility of the system. The structural and moving parts were 3D printed using non-magnetic ABS thermoplastic material on a rapid prototyping machine (FDM400, STRATASYS, 7665 Commerce Way, Eden Prairie, Minnesota, 55344, USA). Regarding the FUS transducer, the element is made of MR-safe piezoceramic material (Piezo Hannas Tech co. ltd, Wuhan, China, central frequency of 2.45 MHz, radius of curvature of 65 mm, and diameter of 50 mm) and is housed in a plastic case that was also manufactured using 3D printing thermoplastic. The conductive surfaces of the piezoelectric element were connected to the electric circuit required for transducer activation through contacts and layered with epoxy (ASonic, Tržaška c. 134, 1000 Ljubljana, Slovenia). The epoxy encapsulant serves as the backing material immobilizing the element inside the housing while providing electrical isolation. The encapsulant is a two-component epoxy adhesive prepared by mixing metal-free resin glue with hardener (1 kg glue to 0.4 kg hardener).

Despite the careful selection of materials and mechatronic parts and the use of cable shielding, the impact of their existence and/or operation in the scanner should be assessed extensively. Evaluation was done as described in the following sections.

2.2. Experimental setup in MRI

The MRI experiments took place at the German Oncology Center (GOC) in Cyprus using a 1.5 T MRI scanner (GE Signa HD16, Chicago, Wisconsin, USA). For each experiment, the robotic system was sited on the MRI table, with an agar-based phantom or freshly excised pork tissue being positioned at the acoustic opening. The phantom/excised tissue sample was scanned under different activation conditions and setup parameters. The water container was filled with degassed and deionized water up to the bottom of the phantom/tissue sample so that proper ultrasonic coupling is achieved. The acoustic opening was not covered by a membrane, so the target was in direct contact with water. The phantom was prepared with a 6 % weight per volume (w/v) concentration of agar (Merck KGaA, EMD Millipore Corporation, Darmstadt, Germany). Notably, agar gels have demonstrated tissue-like signal in MRI and are predominantly used for quality assurance of imaging equipment and protocols [46]. The phantom was carefully prepared with constant stirring to achieve MRI homogeneity.

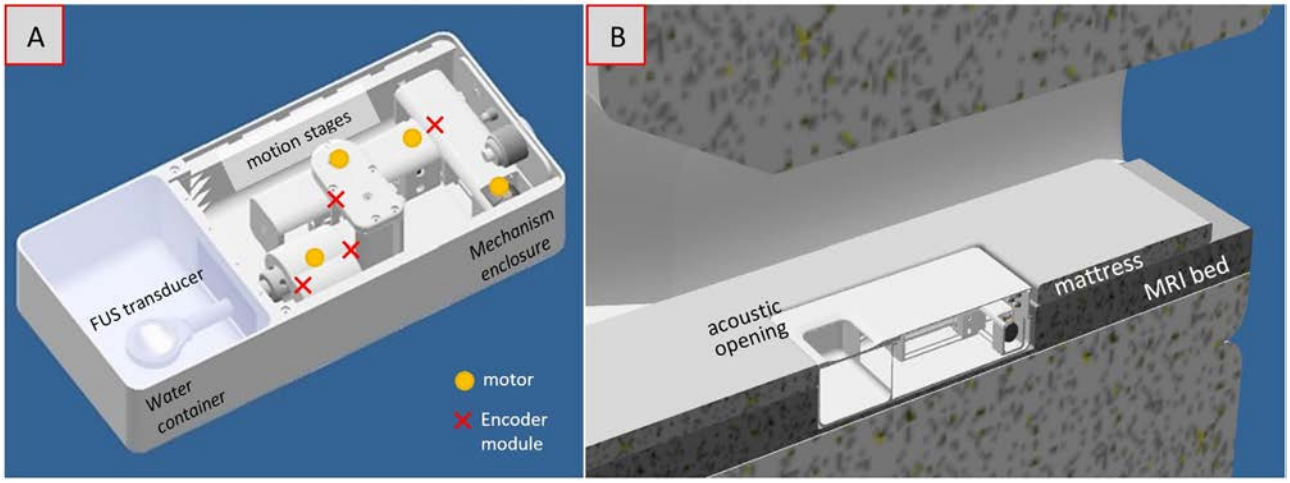

Fig. 1. CAD drawings of the robotic device (A) without top covers, (B) with top covers as integrated in the MRI table, with the main components and location of motors and encoders indicated.

2.3. SNR assessment of MR compatibility

To determine the SNR, the ratio of the mean signal intensity of a preselected ROI in the target (SI_{target}) to the standard deviation (σ_{noise}) from a ROI placed in the air (background signal - noise) was simply calculated as follows assuming a gaussian distribution of noise [47]:

$$SNR = SI_{target}/\sigma_{noise} \quad (1)$$

Specifically, the signal was estimated as the mean intensity and standard deviation of five consecutive measurements in a circular ROI of 5-mm diameter placed in the phantom/excised tissue sample. In all the experiments, the ROI was placed in such a way so that its center coincided with the focus location, i.e., 65 mm above the transducer's surface and 25 mm deep in the phantom. For the SNR measurements, the phantom was centered at the isocenter of the magnet (0,0) using the external laser positioning system so that the ROI is defined at isocenter level. Both the single- and multichannel coils were centered at constant vertical distance above the phantom/ROI to avoid inhomogeneity due to inconsistent coil placement among the various experiments. Accordingly, the background ROI was also defined at a location with identical offset for all experiments (in the air).

With the above described configuration, the closer motor is located at 24 cm from the isocenter while other mechatronic components are located further away. Connection of motors and encoders with the driving system (located outside of the MRI room) was achieved through the penetration panel using specially shielded cables.

Image acquisition was mainly performed using a spoiled gradient recalled echo (SPGR) sequence with the following parameters: repetition time (TR) = 23 ms, echo time (TE) = 16 ms, flip angle (FA) = 35°, echo train length (ETL) = 1, pixel bandwidth (PB) = 45 Hertz/pixel, field of view (FOV) = 280 × 280 × 10 mm^3, matrix = 128 × 128, number of excitations (NEX) = 2, and acquisition time/slice = 7 s. A Fast Spin Echo (FSE) pulse sequence was also implemented in a few experiments. The corresponding parameters were: TR = 500 ms, TE = 13 ms, FA = 90°, ETL = 13, PB = 130 Hertz/pixel, FOV: 260 × 260 × 10 mm^3, NEX = 1, matrix = 256 × 256, and acquisition time/slice = 128 s.

MRI k-space data were used for image reconstruction. Raw data were transferred to MATLAB (MathWorks, Natick, MA, United States) for offline reconstruction using inverse Fourier transform. No filtering was applied. For the multichannel coil, k-space samples were obtained for each coil. The individual coil data was combined using a sum of squares. In all experiments, signal to image conversion was performed using similar scaling, where the recorded signal values were distributed over the gray scale range.

2.4. Impact of activation states on SNR

The noise introduced by the presence and operation of the device in the MRI scanner and potential remedies for enhancing compatibility with the scanner were investigated through a series of experiments. Each of the following experiments consisted of a target being imaged with the system in power off and then in power on or moving configuration. Specifically, SNR measurements were performed under different activation states of the robotic mechanism and ultrasonic transducer [30,31,48]. Regarding ultrasonic control, the following states were tested: Ultrasonic RF cable not connected, ultrasonic RF cable connected, amplifier energized (zero ultrasonic power applied), and electrical power applied (50–200 W). Regarding motion control, the following states were tested: motor/encoder cable not connected, motor/encoder cable connected, electronic control system energized (no motion command initiated, herein referred to as "DC ON"), and motion command initiated (referred to as "motor moving"). SNR evaluation was mainly carried out in a tissue mimicking phantom, but also in freshly excised pork tissue for comparison purposes.

2.5. Effect of magnetic impurities in the transducer on image quality

Initially, the potential effect of magnetic impurities contained in the transducer's backing material on image quality was assessed qualitatively. For this purpose, two different transducers were used; the one manufactured with a metal-free epoxy encapsulant and the other one containing ferromagnetic, iron particles. Both transducers were manufactured in house using a similar methodology, where a concave piezoelectric element with central frequency of 2.45 MHz, radius of curvature of 65 mm, and diameter of 50 mm was housed in a 3D printed plastic case which was filled with epoxy (2-part epoxy adhesive, Asonic, Slovenia, Ljubljana). For the "iron-doped" transducer, the epoxy mixture was loaded with iron particles. Specifically, iron filler powder (GF51431240, Sigma-Aldrich, St. Louis, Missouri, United States) was added during the preparation of the epoxy adhesive.

The transducer was located under the phantom/tissue sample and its location was adjusted so that its focal point was located

2.5 cm deep in the phantom coinciding with the ROI center. The transducer was centered in the horizontal plane with respect to the phantom. Imaging was done with the transducers deactivated using the FSE sequence with identical parameters (listed in section 2.3). Visual assessment was performed by comparing the quality of imaging (e.g., signal loss, image distortion and introduced artifacts) in the presence of each transducer.

At this point, it should be noted that all subsequent experiments were carried out using the transducer containing iron-free epoxy encapsulant that was proven proper for operation in the MRI scanner.

2.6. Impact of set-up parameters on SNR

In the effort to eliminate image distortion, several set-up parameters were examined. Initially, the SNR was obtained using a single-channel general-purpose flex surface coil (Signa 1.5 T Receiver only, GE Medical Systems, Milwaukee, Wisconsin, USA), as well as a 12-channel body coil (Signa 1.5 T, GE Healthcare Coils, Aurora, Ohio, USA) to confirm the SNR advantage of the multichannel-coil and how significant it is in the context of HIFU.

Subsequently, the impact of coil stability and positioning in relation to the target was evaluated by comparing the SNR results of the multichannel coil being placed in the two different configurations shown in Fig. 2. In the former case, the coil was placed directly above the phantom using positioning pads and supporting objects (Fig. 2A), whereas in the latter case it was securely stabilized at sufficient distance above the top of the phantom using a dedicated 3D printed plastic structure with 6 legs (Fig. 2B).

Similarly, the impact of target stability on image quality was assessed by comparing the SNR estimates in the preselected ROI in a small square phantom and a larger phantom of dedicated shape, as illustrated in Fig. 3A and Fig. 3B, respectively. In the second case, the phantom's dimensions and shape were modified so that its bottom protruding part to be submerged in water through the acoustic opening while its top part is being supported on the plastic top cover, thus improving the phantom's stability during exposures. Stability is also enhanced by the increased weight. Specifically, the square phantom had a weight of about 0.8 kg, whereas the bigger dedicated phantom weighted about 1.3 kg.

Other set-up parameters examined in the effort to eliminate electromagnetic interference between the various components and the magnet were the positioning of the actuators relative to the imaging coil and encoders' activation status (i.e., counting pulses ON and OFF). The placement of electronic components relative to the coil is illustrated in Fig. 4. In Fig. 4A, the electronic parts are placed within the coil detection area, whereas in Fig. 4B the electronic parts are placed outside of the coil detection area.

3. Results

3.1. Effect of magnetic impurities in the transducer on image quality

The effect of transducer material on image quality is revealed by Fig. 5, in which the FSE images acquired in the presence of the iron-doped (Fig. 5A) and iron-free (Fig. 5B) transducers (deactivated) are compared. It is clearly seen that image quality is compromised in the presence of ferromagnetic impurities due to susceptibility artifacts. Notice that the susceptibility artifacts near the "iron-doped" transducer in Fig. 5A are more pronounced than susceptibility artifacts in Fig. 5B.

3.2. Effect of transducer operation on SNR

The impact of the various activation states of the transducer containing iron-free epoxy encapsulant on SNR for the SPGR and FSE sequences is revealed by the bar charts of Fig. 6. The greatest reduction in SNR occurred during transducer's operation at the highest power level of 200 W for both sequences.

Fig. 7 compares the SNR values acquired in (6 % w/v) agar phantom and freshly excised pork tissue with the SPGR pulse sequence and the 12-channel coil being properly stabilized above the target. The bar chart shows a slightly higher SNR (approximately 5 on average) in the agar phantom for each tested activation condition of the system. This shows that the developed phantom provides similar SNR with excised tissue. The corresponding SPGR slices of the tissue sample are shown in Fig. 8.

3.3. Impact of set-up parameters on SNR

Fig. 9 reveals the impact of coil type (single-channel versus multi-channel coil) on SNR for the various activation states of the FUS transducer. Note that the change in SNR among the various

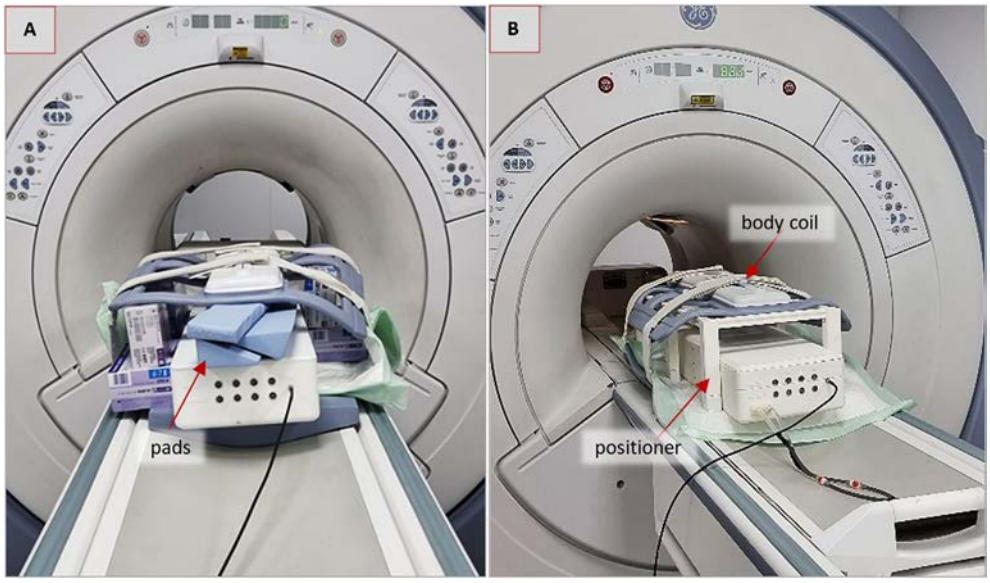

Fig. 2. The robotic device sited on the table of the 1.5 T MRI scanner, with the multi-channel body coil (A) placed directly above the phantom using pads and supporting objects and (B) securely mounted using a dedicated 3D printed plastic structure.

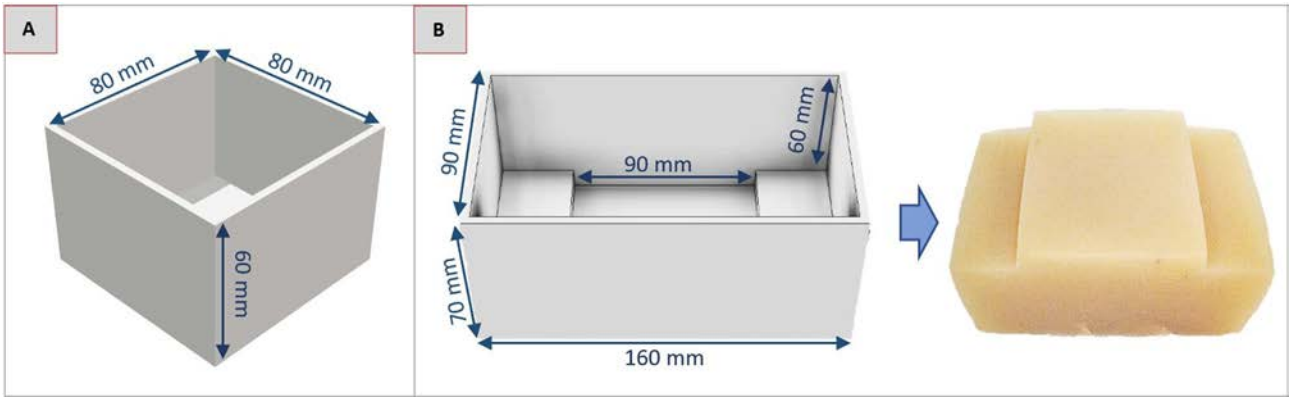

Fig. 3. 3D printed molds used for manufacturing the (A) small size square phantom and (B) the larger phantom of dedicated shape.

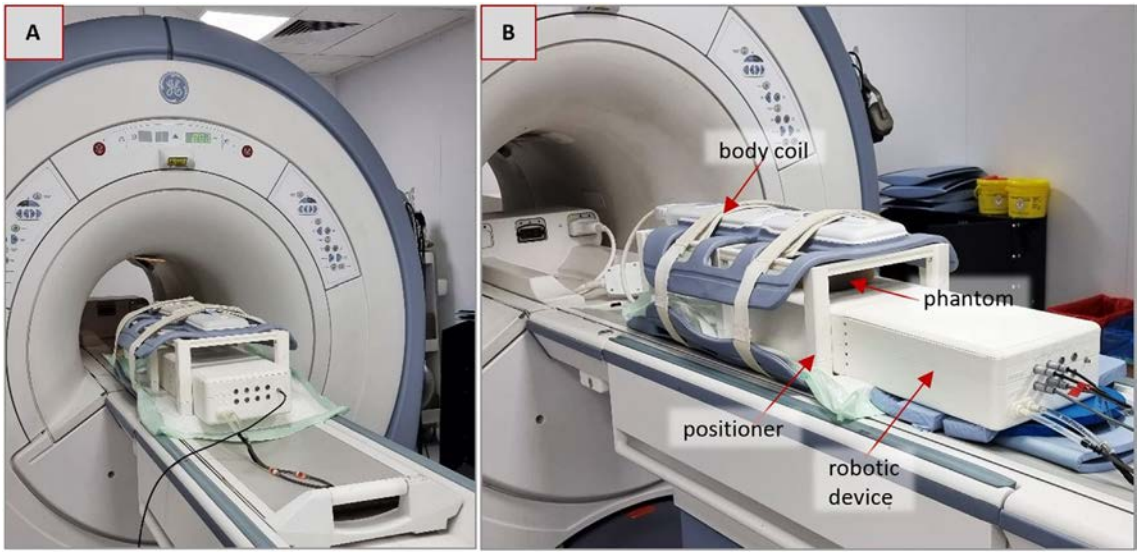

Fig. 4. The robotic device sited on the table of the 1.5 T MRI scanner with the multi-channel body coil securely mounted on the positioner with the electronic parts (A) within the coil detection area and (B) outside of the coil detection area.

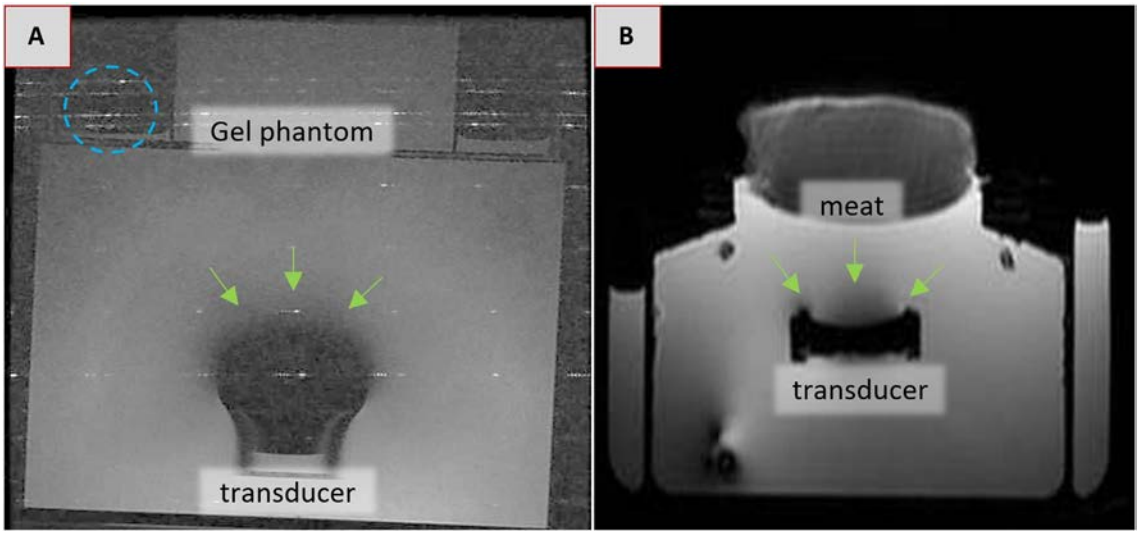

Fig. 5. FSE axial images of a ROI containing (A) an iron-doped transducer and a gel phantom as the target and (B) an iron-free transducer and tissue sample as the target. Green arrows indicate susceptibility-induced signal loss artifacts around the transducer. The blue dotted circle indicates Zipper artifacts.

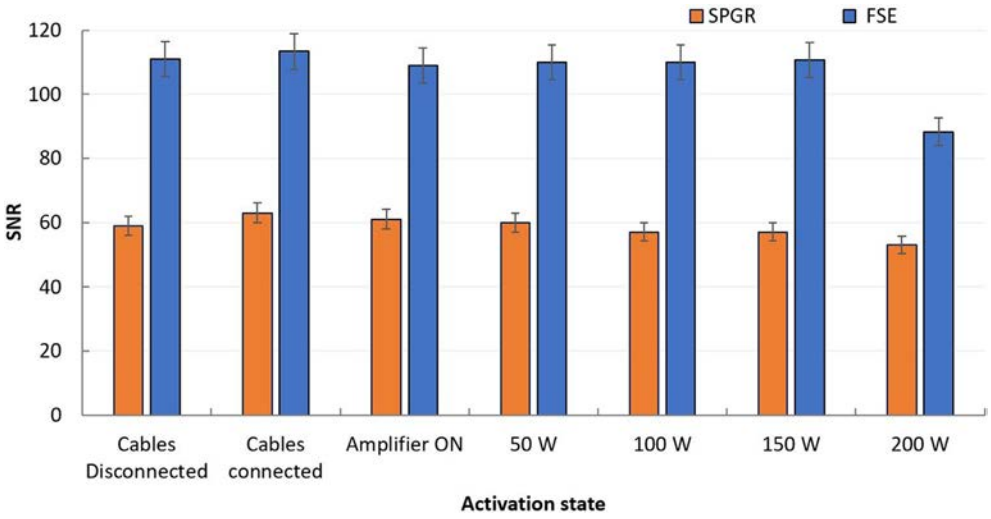

Fig. 6. Bar charts of the SNR acquired using the SPGR and FSE pulse sequences under different activation states of the ultrasonic transducer.

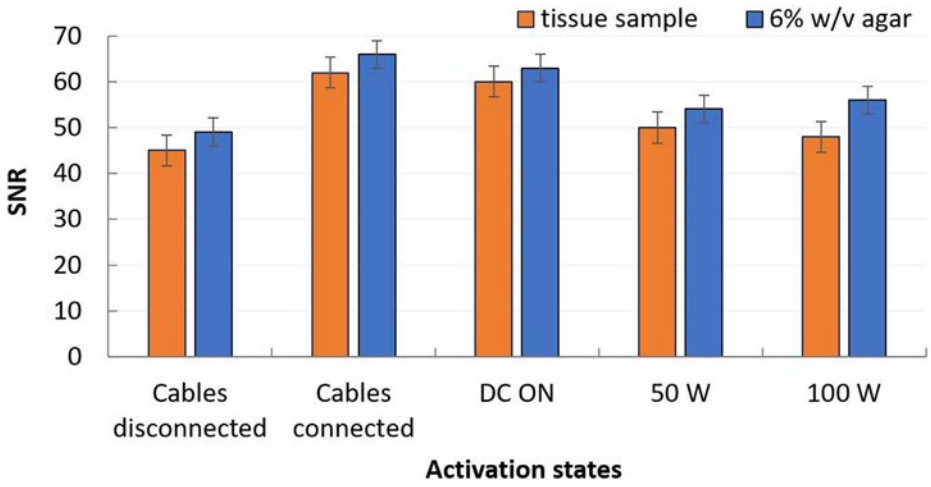

Fig. 7. Bar charts of the SNR acquired in excised tissue sample and 6 % w/v agar phantom using the SPGR sequence under different activation states of the ultrasonic transducer.

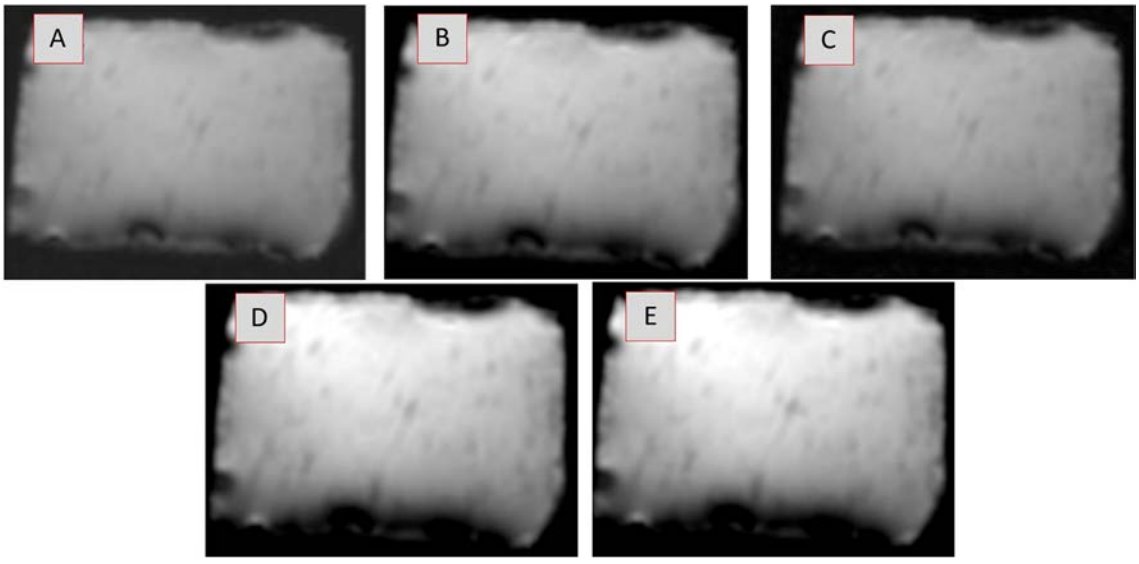

Fig. 8. SPGR coronal images of the pork tissue sample acquired with (A) the cables disconnected, (B) cables connected, (C) DC ON, and power on at (D) 50 W and (E) 100 W.

conditions follows a similar trend. Also, note that the SNR advantage of the multi-channel coil is more prominent during FUS sonication. Similarly, Fig. 10 shows the SNR evaluation for different transducer activation states for two different positionings of the multi-channel body coil with respect to the phantom. Note that the use of the dedicated supporting structure raises the coil at sufficient distance above the phantom so that it is not prone to target vibrations during sonication. These results prove that the use of properly stabilized multi-channel coils and their isolation from the target can help towards maintaining sufficiently high SNR during high-power sonications of up to 200 W (electrical power).

Further results on the effect of FUS-induced coil vibrations are presented in Fig. 11. Image acquisition during heating at 200 W electrical power using the SPGR sequence resulted in completely noisy images when the coil was not secured properly at sufficient distance above the phantom. Note that Fig. 11C was acquired just after deactivation of the transducer. Normal image contrast and detail occurred when the transducer was deactivated.

The effect of target size was also evaluated. The bar chart of Fig. 12 reveals a distinct SNR improvement owing to the higher stability of the large phantom compared to the small-size phantom. Insights on target size and stability are also given in Fig. 13, which presents SPGR images of excised pork tissue sample obtained with the transducer being at different activation states. In this case, image quality during heating is getting degraded as the power is increased from 10 to 100 W, with complete loss of detail and contrast at 100 W owing to the small size of the tissue sample.

Finally, the SNR impact of placing the electronic parts outside of the coil detection area is revealed by Fig. 14, whereas Fig. 15 shows the corresponding SNR improvement occurred after switching off the encoder's counting pulses.

4. Discussion

The current study aimed to provide insights on major challenges faced when implementing a FUS robotic system in the MRI by evaluating the compatibility of an MRgFUS robotic device with a 1.5 T scanner. Imaging was performed in tissue mimicking agar-based phantoms (6 % w/v agar) and freshly excised pork tissue. The SNR served as the main metric for quantitative assessment of MR compatibility of the various system's components. MR compatibility was investigated under different activation states of the system and set-up parameters. Simultaneously, potential sources of SNR degradation and image quality distortion in an MRgFUS system were identified through quantitative and visual examination.

As previously mentioned, there are numerous issues impeding the design of robotic devices for MRI-guided interventions, including the employed construction materials. In the proposed robotic device, metallic components are incorporated in the motion mechanism, which is housed in a plastic enclosure, and thus do not raise any safety concerns. However, their presence perturbates the homogeneity of the external field and may cause susceptibility artifacts. In this study, such artifacts were observed as signal loss and distortion around the transducer, especially at the upper side (Fig. 5A), due to the magnetic field inhomogeneity introduced by the iron particles contained in the backing material. In line with previous studies [42], these results highlight that caution should be given not to include ferromagnetic particles during the manufacturing process of ultrasonic transducers, despite that this constitutes a common way for enhancing backing material's density to the desirable level [42].

Note also that some zipper artifacts (appear as white lines) are aligned in phase encode direction for the iron-doped transducer. In the first place, this appears to be a case of RF interference. However, this type of RF artifact is not expected to appear when the transducer is in passive state. We thus speculate that the source of these artifacts is unexpected noise from the amplifier, possibly due to high frequency harmonics that could not be filtered by the low pass filter used. Such kind of RF artifacts were observed by Shokrollahi et al [49] and were attributed to interference with the RF field caused by electric signals between motors and drivers during imaging with the motor being in active mode. However, since such artifacts can arise for any cable that is not properly installed through the RF waveguides and not related to the MRgFUS setup, further investigation is required to identify their source.

Image acquisition was performed using two standard MR sequences (FSE and SPGR). Both sequences present similar behavior in terms of SNR drop compared to the baseline for the various activation modes. Thermometry maps are typically constructed by proton resonance frequency shift (PRFS) calculation; a method that is typically implemented with an SPGR sequence [10]. Generally, the sensitivity of this sequence type to the PRFS effect makes them ideal for MR thermometry [10]. Therefore, the rest of experiments were carried out using the specific sequence, given also that it produced SNR values sufficiently high for the purposes of the current study.

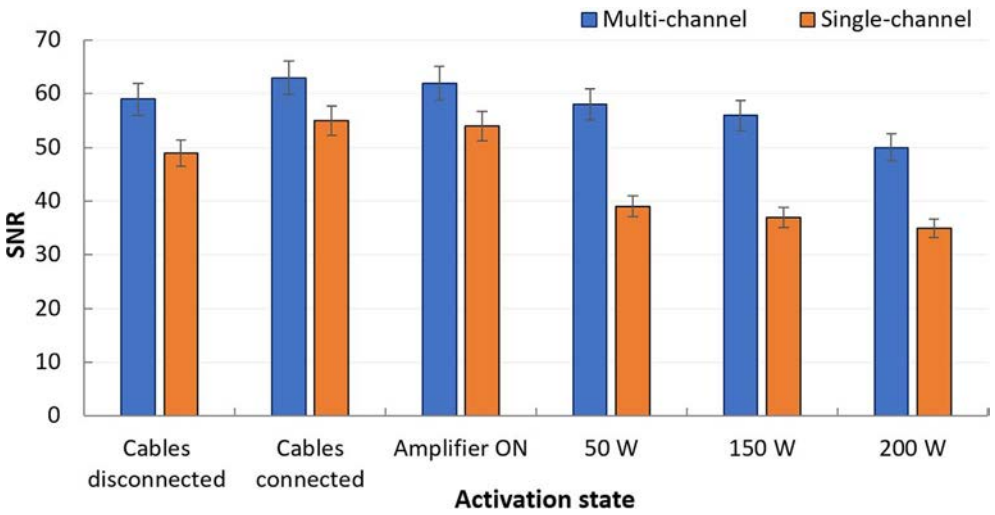

Fig. 9. Bar charts of the SNR acquired with the multi-channel and single-channel coils using the SPGR sequence under different activation states of the ultrasonic transducer.

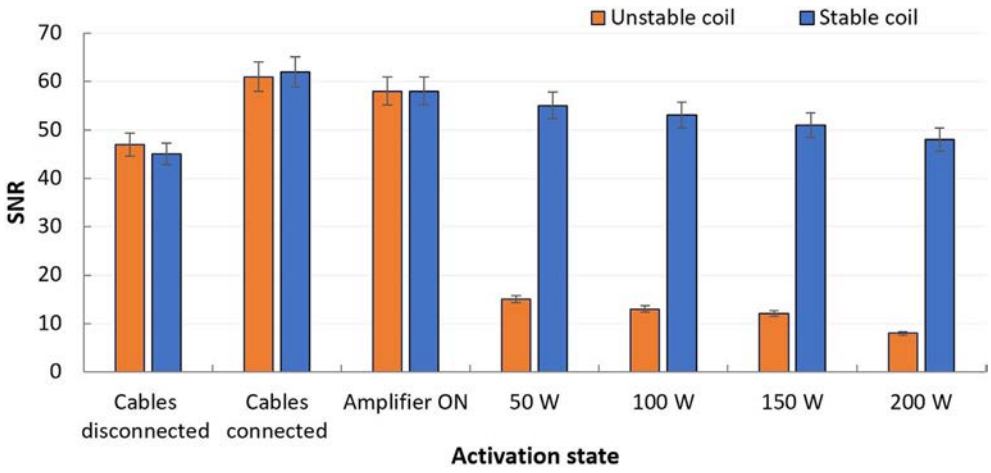

Fig. 10. Bar charts of the SNR acquired using the SPGR sequence with the multi-channel body coil being placed without any supporting structure above the phantom (unstable) and securely mounted on a dedicated plastic supporting structure (stable) for different activation states of the ultrasonic transducer.

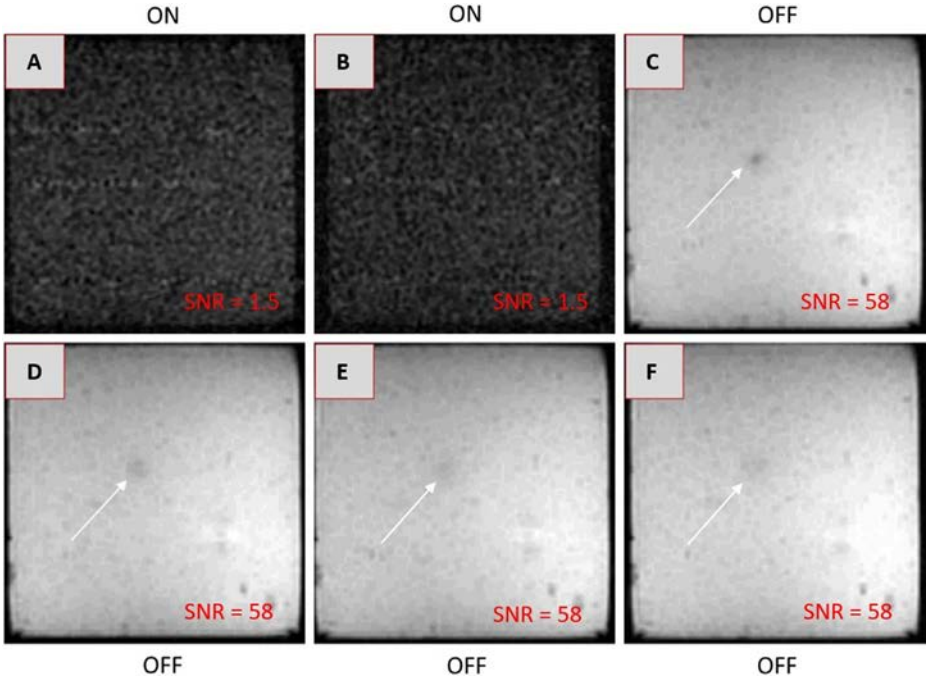

Fig. 11. SPGR axial images acquired in a 6 % agar phantom with the coil placed directly above the phantom (without supporting structure) during sonication at 200 W for 12 s and after sonication. Images were acquired (A) 4 s, (B) 8 s, (C) 12 s, (D) 16 s, (E) 20 s, and (F) 24 s after the start of sonication. The corresponding SNR is overlaid on each image. White arrows indicate the focal area where temperature increase occurred.

The results also verified that the proposed agar based phantom (6 % w/v) produces tissue-like signal in the MRI, with an average SNR difference of approximately 5 compared to the pork tissue sample. This conclusion is consistent with literature findings suggesting that agar gels are ideal for MR studies not only due to their tissue-like properties, but also due to their ease and cost-effective preparation, as well as their ability to withstand ablative temperatures [46].

It is by now widely accepted that multi-channel coils provide substantially higher SNR compared to single-channel coils. In this study, their SNR advantage was examined in the context of FUS, and specifically under different activation states of the FUS transducer. The multi-channel coil increased the SNR compared to the single-channel coil by up to 50 % (Fig. 9). It is important to note that the SNR improvement differs between activation states, with the highest difference occurring when the transducer is powered on. Therefore, in line with previous studies [19], the use of a multi-channel coil is crucial for proper imaging during MRgFUS.

It is obvious that proper stabilization of the imaging coil is required for proper imaging. The current results go beyond this, showing that the coil placement technique plays a more important role in the context of MRgFUS procedures. When the coil was placed above the phantom without any dedicated supporting fixture was being subject to vibrations of the target during transducer's activation, and consequently the SNR dropped drastically (to about 25 %), and imaging was affected severely (Fig. 10). To solve this issue, a specially designed positioner was developed using 3D printing in order to securely position the coil a few mm above the phantom. With this arrangement, more than 3-fold improvement in SNR was observed for electric power values of

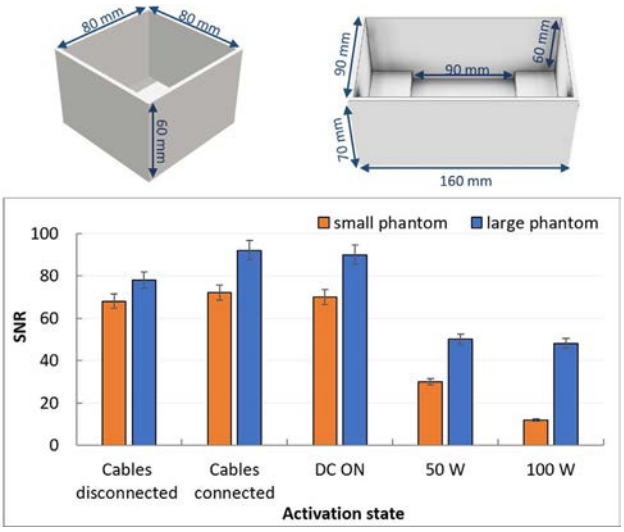

Fig. 12. Bar chart of the SNR acquired in the small and large phantom using the SPGR sequence under different activation states of the ultrasonic transducer.

50–200 W (Fig. 10). Although the SNR is slightly affected by increasing the ultrasonic power it remains at sufficiently high levels for high quality imaging. This was true whether a surface or body coil was used.

Visual assessment of SPGR images acquired during and after heating at 200 W yields similar conclusions (Fig. 11). Specifically, when the transducer was activated, the coil with no support structure caused intense granular noise and resulted in severe image distortion with complete loss of detail. Deactivation of the transducer allowed for proper imaging and visualization of the heated region as a slightly black circular spot that was fading with time due to heat diffusion (Fig. 11), thus revealing the coil interaction with the target and instability (and resultant vibration) as the main image polluter in that case.

The weight and shape of the target (phantom/tissue sample) play a very important role as these parameters define its stability under acoustic pressure. It was observed that due to the force exerted by ultrasound on the phantom, the image during a fast MRI pulse sequence was affected severely. In fact, the SNR dropped drastically in the lightweight phantom compared to the heavier phantom. For the highest tested power of 100 W, the SNR during activation with the 0.8 Kg phantom was about 12, whereas for the 1.3 Kg phantom the SNR was increased by 4-fold to 48. Note that the impact of using a stable phantom is more pronounced at higher applied electrical power. Furthermore, it is notable that the SNR for the heavy phantom was not affected by increasing the electrical power from 50 to 100 W. Further results on image degradation arising from small and unstable targets were obtained using an excised pork tissue sample. The details of SPGR images of a ROI including the excised tissue sample placed on a special holder above the transducer (Fig. 13) were gradually blurred as the electrical power was increased from 10 to 100 W. Note that complete loss of details and contrast occurred at the highest tested power of 100 W.

Although the above experiments do not represent a clinical scenario, it is a possible scenario in the preclinical setting or in the process of quality assurance (QA) of clinical MRgFUS equipment. Phantoms are the most commonly used QA tools in this regard [46]. Therefore, the above conclusions may contribute towards optimizing QA methodologies by providing insights on key set-up parameters, given also that methods for QA of MRgFUS devices are still to be established and standardized.

By comparing the SNR among different activation states and experiments, some other interesting observations can be made. Firstly, it is observed that in many cases (e.g., Fig. 10) connected cables provide higher SNR than disconnected cables. This is attributed to that disconnected cables act like antennas and they can easily pick up RF noise, whereas connected cables are grounded and are less likely to cause noise emission. In addition, noise from disconnected cables is somewhat random, and thus, SNR fluctuations are typically observed. It is also worth noting that some

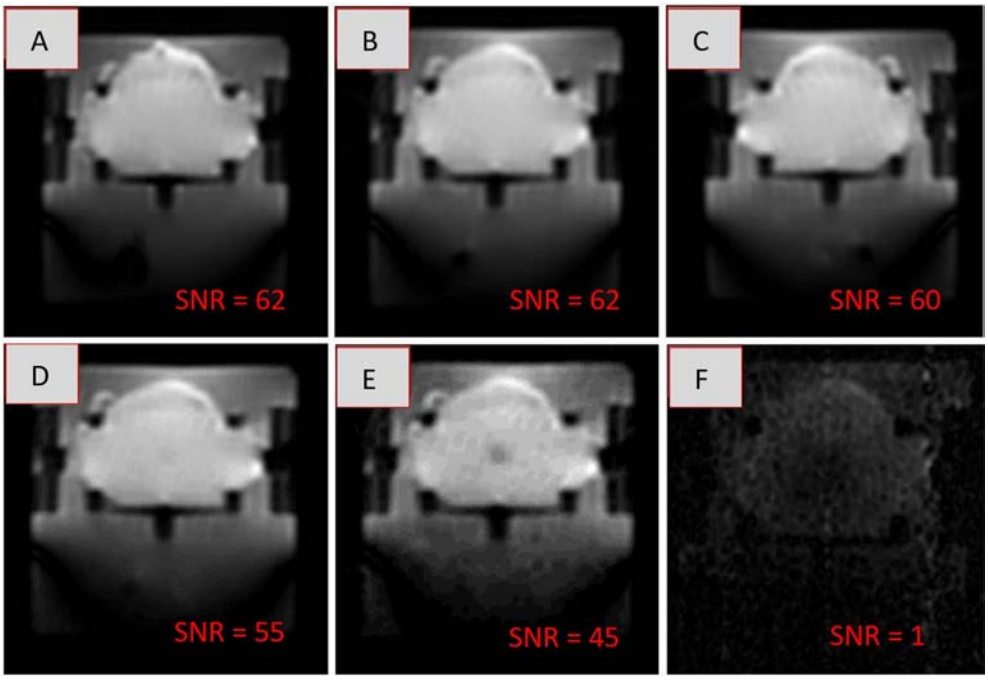

Fig. 13. Example of SPGR coronal images acquired in excised tissue sample with the (A) Cables disconnected, (B) Cables connected, (C) DC ON, and power ON at (D) 10 W, (E) 50 W, and (F) 100 W. The corresponding SNR is overlaid on each image.

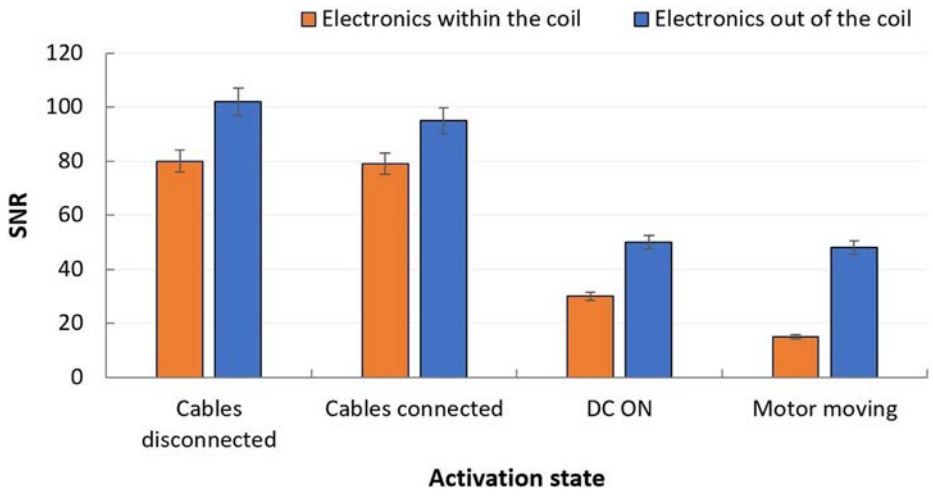

Fig. 14. Bar charts of the SNR acquired with the electronic parts inside and outside of the coil detection area using the SPGR sequence under different activation states of the positioning mechanism.

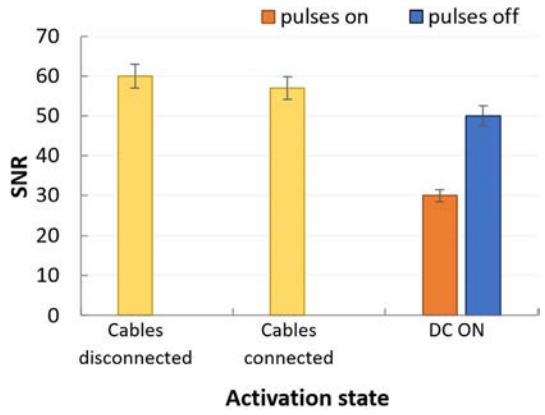

Fig. 15. SNR measured using the SPGR sequence with the cables disconnected (reference image), cables connected, and electronic driving system energized (DC ON) for two different cases: encoders' pulses activated and deactivated.

SNR variability should be expected among experiments due to HIFU electromagnetic noise. When the transducer is in active mode, unexpected noise may be generated from the transducer cable. To be more specific, harmonic components that cannot be eliminated by the filter may fall into the MRI-sensitive frequency band, thus generating noise. Note that this phenomenon is more pronounced at high power operation.

Other main "polluters" of MRI quality existing in an MRgFUS system are the motors and motor control electronics. As explained previously, the presence and operation of the motors can cause both susceptibility and RF interference problems, which unavoidable result in signal loss and significant image distortion [49]. Signal voids and pileup artifacts were observed by Shokrollahi et al. [49] and were attributed to inhomogeneities of the external and gradient fields caused by the presence of the motor (deactivated). Herein, a serious SNR degradation occurred when the electronic control system was energized, and motion command was initiated. In this regard, an important measure for SNR improvement was proven to be the placement of motors and encoder electronics outside of the coil detection area (Fig. 14). It is interesting to note that the effect of motor orientation and location on image artifacts has already been assessed previously and it was shown that susceptibility artifacts are reduced when the motor's shaft is aligned with the z-axis [49]. In our case, the SNR is affected by the presence of all motors, each one having different location and orientation, since they are all housed in a single enclosure.

According to previous studies, SNR reduction of up to 80 % can be caused from harmonic motors, such as the Shinsei motors used in this study, whereas non-harmonic motors cause much less interference [50]. For the specific MRgFUS system proposed herein, it was proven essential to keep the motors and encoders outside of the coil detection area. However, it is possible that other designs allow operation of the electronics within the coil detection area without substantial impact on SNR, maybe through additional shielding or the use of specially designed actuators and encoders. For instance, in a study by Hofstetter et al. [51], imaging remained largely unaffected (in terms of SNR) by the presence and operation of a specially designed electromagnetic servomotor (and the encoder) at 15 cm distance from the object. In comparison with the current study, the closest motor was located 24 cm from the phantom center (ROI location). Generally, the compatibility requirements depend not only on the type, but also on the specific characteristics of motors and encoders.

The tested MRgFUS system incorporates purchased optical encoders, which are considered to be MRI compatible and are widely used in robotic design. Deactivation of the encoders' counting pulses during image acquisition was proven essential for maintaining high SNR (Fig. 15). Specifically, the acquired SNR with the pulsing system deactivated was increased by about 70 % compared to that obtained with the counting pulses activated. To our knowledge, this aspect was not examined previously.

Generally, various techniques exist to mitigate MRI artifacts so as to obtain images of diagnostic value, especially through the optimization of the scanning parameters [33]. For instance, the signal loss resulting from dephasing effects of field inhomogeneities can be avoided by employing SE sequences [33]. However, this type of sequences is not suitable for PRFS thermometry. While this study investigated general MRI compatibility and illustrated the impact of the various activation states of an MRgFUS system on SNR under different setup parameters, further investigations of long-term measurement stability, scanning parameters as well as clinical thermometry sequences are the next step in line.

5. Conclusions

It is by now generally accepted that ferromagnetic components should not be employed in the transducer's manufacturing. Among the various activations states of the FUS system, the most signifi-

cant distortion occurs when the transducer is activated mainly owing to coil and target vibrations and is getting worse as the output power is increased. It is thus crucial to securely stabilize both the coil and imaging object. In this regard, isolation of the imaging coil from the sonicated target is essential to avoid FUS-induced vibrations from being transferred to the coil. The use of a multichannel coil is also critical in increasing SNR in the context of HIFU. Regarding robotic motion, the study raises concerns about proper use of motion actuators and sensors. Piezoelectric motors and optical encoders are extensively employed in MRgFUS devices; nevertheless, the current study suggests that they should be located outside of the coil detection area during imaging, otherwise the image quality may be compromised severely. It is also crucial to have the counting pulses of encoders turned off during image acquisition since this was also proven to increase SNR remarkably. By summarizing all the experimental data, the study contributes towards addressing major challenges regarding operation of an MRgFUS system in the MRI environment and raises awareness for potential sources of noise and distortion to researchers in the field.

Ethics Approval Declaration.

The study does not include data on patients or animals. No ethical approval is available.

Author Contribution Statement.

Anastasia Antoniou contributed to the drafting of manuscript and implementation of the scientific methods. Leonidas Georgiou, Nikolas Evripidou, and Cleanthis Ioannides contributed to the MRI experiments and data analysis. Christakis Damianou supervised the overall study, as well as the drafting of the manuscript.

Data availability

Data will be made available on request.

Declaration of Competing Interest

The authors declare that they have no known competing financial interests or personal relationships that could have appeared to influence the work reported in this paper.

Acknowledgments

The study was co-funded by the European Structural & Investment Funds (ESIF) and the Republic of Cyprus through the Research and Innovation Foundation (RIF) under the projects SOUNDPET (INTEGRATED/0918/0008) and FUSROBOT (ENTERPRISES/0618/0016). The robotic device was developed in the framework of the FUSROBOT project, whereas all described experiments were carried out as part of the SOUNDPET project.

References

[1] I.A.S. Elhelf, H. Albahar, U. Shah, A. Oto, E. Cressman, M. Almekkawy, High intensity focused ultrasound: The fundamentals, clinical applications and research trends, Diagn. Interv Imaging. 99 (2018) 349–359, https://doi.org/10.1016/j.diii.2018.03.001.

[2] Z. Izadifar, Z. Izadifar, D. Chapman, P. Babyn, An Introduction to High Intensity Focused Ultrasound: Systematic Review on Principles, Devices, and Clinical Applications, J. Clin. Med. 9 (2020) 460, https://doi.org/10.3390/jcm9020460.

[3] J.J. Li, M.F. Gu, G.Y. Luo, L.Z. Liu, R. Zhang, G.L. Xu, Complications of high intensity focused ultrasound for patients with hepatocellular carcinoma, Technol. Cancer Res. Treat. 8 (2009) 217–224, https://doi.org/10.1177/153303460900800306.

[4] J.G. Lynn, R.L. Zwemer, A.J. Chick, The biological application of focused ultrasonic waves, Science 96 (1942) 119–120, https://doi.org/10.1126/science.96.2483.119.

[5] W.J. Fry, Intense ultrasound in investigations of the central nervous system, Adv. Biol. Med. Phys. 6 (1958) 281–348, https://doi.org/10.1016/b978-1-4832-3112-9.50012-8.

[6] W.J. Fry, F.J. Fry, Fundamental Neurological Research and Human Neurosurgery Using Intense Ultrasound, IRE Trans. Med. Electron. ME-7 (1960) 166–181, https://doi.org/10.1109/IRET-ME.1960.5008041.

[7] K. Hynynen, G.T. Clement, N. McDannold, N. Vykhodtseva, R. King, P.J. White, S. Vitek, F.A. Jolesz, 500-Element ultrasound phased array system for noninvasive focal surgery of the brain: A preliminary rabbit study with ex vivo human skulls, Magn. Reson. Med. 52 (2004) 100–107, https://doi.org/10.1002/mrm.20118.

[8] B.R. Shah, V.T. Lehman, T.J. Kaufmann, D. Blezek, J. Waugh, D. Imphean, F.F. Yu, T.R. Patel, S. Chitnis, R.B. Dewey, J.A. Maldjian, R. Chopra, Advanced MRI techniques for transcranial high intensity focused ultrasound targeting, Brain. 143 (2020) 2664–2672, https://doi.org/10.1093/brain/awaa107.

[9] Y. Ishihara, A. Calderon, H. Watanabe, K. Okamoto, Y. Suzuki, K. Kuroda, Y. Suzuki, A precise and fast temperature mapping using water proton chemical shift, Magn. Reson. Imaging. 34 (1995) 814–823, https://doi.org/10.1002/mrm.1910340606.

[10] V. Rieke, K.B. Pauly, M.R. Thermometry, J Magn Reson Imaging. 27 (2008) 376–390, https://doi.org/10.1002/jmri.21265.MR.

[11] K. Hynynen, MRIgHIFU: A Tool for Image-Guided Therapeutics, J. Magn. Reson. Imaging. 34 (2011) 482–493, https://doi.org/10.1002/jmri.22649.

[12] E.J. Lee, A. Fomenko, A.M. Lozano, Magnetic resonance-guided focused ultrasound: Current status and future perspectives in thermal ablation and blood-brain barrier opening, J. Korean Neurosurg. Soc. 62 (2019) 10–26, https://doi.org/10.3340/jkns.2018.0180.

[13] L. Winter, E. Oberacker, K. Paul, Y. Ji, C. Oezerdem, P. Ghadjar, A. Thieme, V. Budach, P. Wust, T. Niendorf, Magnetic resonance thermometry: Methodology, pitfalls and practical solutions, Int. J. Hyperth. 32 (2015) 63–75, https://doi.org/10.3109/02656736.2015.1108462.

[14] J. Corea, P. Ye, D. Seo, K. Butts-Pauly, A.C. Arias, M. Lustig, Printed Receive Coils with High Acoustic Transparency for Magnetic Resonance Guided Focused Ultrasound, Sci. Rep. 8 (2018) 1–10, https://doi.org/10.1038/s41598-018-21687-1.

[15] S.M. Wright, L.L. Wald, Theory and application of array coils in MR spectroscopy, NMR Biomed. 10 (1998) 394–410, https://doi.org/10.1002/(SICI)1099-1492(199712)10:8<394::AID-NBM494>3.0.CO;2-0.

[16] P.B. Roemer, W.A. Edelstein, C.E. Hayes, S.P. Souza, O.M. Mueller, The NMR phased array, Magn. Reson. Med. 16 (1990) 192–225, https://doi.org/10.1002/mrm.1910160203.

[17] K.N. Kim, D. Hernandez, J.H. Seo, Y. Noh, Y. Han, Y.C. Ryu, J.Y. Chung, Quantitative assessment of phased array coils with different numbers of receiving channels in terms of signal-to-noise ratio and spatial noise variation in magnetic resonance imaging, PLoS ONE 14 (2019) 1–13, https://doi.org/10.1371/journal.pone.0219407.

[18] O. Dietrich, J.G. Raya, S.B. Reeder, M.F. Reiser, S.O. Schoenberg, Measurement of signal-to-noise ratios in MR images: Influence of multichannel coils, parallel imaging, and reconstruction filters, J. Magn. Reson. Imaging. 26 (2007) 375–385, https://doi.org/10.1002/jmri.20969.

[19] B. Werner, E. Martin, R. Bauer, R. O'Gorman, Optimizing MR imaging-guided navigation for focused ultrasound interventions in the brain, in pp. 120001–1–120001–5 AIP Conf. Proc. (2017), https://doi.org/10.1063/1.4977641.

[20] B. Gruber, R. Rehner, E. Laistler, S. Zink, Anatomically Adaptive Coils for MRI—A 6-Channel Array for Knee Imaging at 1.5 Tesla, Front. Phys. 8 (2020) 1–17, https://doi.org/10.3389/fphy.2020.00080.

[21] W.C.G. Peh, J.H.M. Chan, Artifacts in musculoskeletal magnetic resonance imaging: identification and correction, Skelet. Radiol. 30 (2001) 179–191, https://doi.org/10.1007/s002560100341.

[22] K. Krupa, M. Bekiesińska-Figatowska, Artifacts in magnetic resonance imaging, Polish J. Radiol. 80 (2015) 93–106, https://doi.org/10.12659/PJR.892628.

[23] ASTM F2503–13: Standard Practice for Marking Medical Devices and Other Items for Safety in the Magnetic Resonance Environment, (n.d.). http://compass.astm.org/EDIT/html_annot.cgi?%0AF2503+13.

[24] N.V. Tsekos, E. Christoforou, A. Ozcan, A general-purpose MR-compatible robotic system: implementation and image guidance for performing minimally invasive interventions, IEEE Eng. Med. Biol. Mag. 27 (2008) 51–58, https://doi.org/10.1109/EMB.2007.910270.A.

[25] D. Stoianovici, C. Jun, S. Lim, P. Li, D. Petrisor, S. Fricke, K. Sharma, K. Cleary, Multi-Imager Compatible, MR Safe, Remote Center of Motion Needle-Guide Robot, IEEE Trans Biomed Eng. 65 (2018) 165–177, https://doi.org/10.1109/TBME.2017.2697766.

[26] D. Stoianovici, Multi-imager compatible actuation principles in surgical robotics, Int. J. Med. Robot. 1 (2005) 86–100, https://doi.org/10.1002/rcs.19.

[27] S.S. Cheng, Challenges on the Development of MRI-Compatible Neurosurgical Robotic Systems, Int. J. Robot. Res. Appl. Autom. 1 (2019) 2–5, https://doi.org/10.18689/ijra-1000102.

[28] M. Giannakou, T. Drakos, G. Menikou, N. Evripidou, A. Filippou, K. Spanoudes, L. Ioannou, C. Damianou, MRI-guided focused ultrasound robotic system for transrectal prostate cancer therapy, Int. J. Med. Robot. Comput. Assist. Surg. (2021) 1–15, https://doi.org/10.1002/rcs.2237.

[29] G. Menikou, C. Yiallouras, M. Yiannakou, C. Damianou, MRI-guided focused ultrasound robotic system for the treatment of bone cancer, Int. J. Med. Robot. Comput. Assist. Surg. 13 (2017) 1–11, https://doi.org/10.1002/rcs.1753.

[30] A. Antoniou, M. Giannakou, N. Evripidou, G. Evripidou, K. Spanoudes, G. Menikou, C. Damianou, Robotic system for magnetic resonance guided focused ultrasound ablation of abdominal cancer, Int. J. Med. Robot. Comput. Assist. Surg. 17 (2021), https://doi.org/10.1002/rcs.2299.

[31] A. Antoniou, M. Giannakou, N. Evripidou, S. Stratis, S. Pichardo, C. Damianou, Robotic system for top to bottom MRgFUS therapy of multiple cancer types, Int. J. Med. Robot. Comput. Assist. Surg. (2022), https://doi.org/10.1002/rcs.2364.
[32] H. Elhawary, Z.T.H. Tse, A. Hamed, M. Rea, B.L. Davies, M.U. Lamperth, The case for MR-compatible robotics: a review of the state of the art, Int. J. Med. Robot. Comput. Assist. Surg. 4 (2008) 105–113, https://doi.org/10.1002/rcs.192.
[33] B. Hargreaves, P.W. Worters, K.B. Pauly, J.M. Pauly, K.M. Koch, G.E. Gold, Metal Induced Artifacts in MRI, Am J Roentgenol. 197 (2011) 547–555, https://doi.org/10.2214/AJR.
[34] M. Yiannakou, G. Menikou, C. Yiallouras, C. Ioannides, C. Damianou, MRI guided focused ultrasound robotic system for animal experiments, Int. J. Med. Robot. Comput. Assist. Surg. 13 (2017) e1804.
[35] M. Yiannakou, G. Menikou, C. Yiallouras, C. Damianou, MRI-guided coupling for a focused ultrasound system using a top-to-bottom propagation, J. Ther. Ultrasound. 5 (2017) 1–8, https://doi.org/10.1186/s40349-017-0087-x.
[36] C. Damianou, M. Giannakou, N. Evripidou, S. Kegel, P. Huber, J. Jenne, Focused ultrasound robotic system for very small bore magnetic resonance imaging, Int. J. Med. Robot. Comput. Assist. Surg. 16 (2020) 1–9, https://doi.org/10.1002/rcs.2165.
[37] T. Drakos, M. Giannakou, G. Menikou, A. Filippou, N. Evripidou, K. Spanoudes, L. Ioannou, C. Damianou, MRI-Guided Focused Ultrasound Robotic System for Preclinical use, J. Vet. Med. Anim. Sci. 4 (2021) 1–11.
[38] P. Shokrollahi, J.M. Drake, A.A. Goldenberg, Signal-to-noise ratio evaluation of magnetic resonance images in the presence of an ultrasonic motor, Biomed. Eng. Online. 16 (2017) 1–12, https://doi.org/10.1186/s12938-017-0331-1.
[39] B.T. Larson, A.G. Erdman, N.V. Tsekos, E. Yacoub, P.V. Tsekos, I.G. Koutlas, Design of an MRI-Compatible Robotic Stereotactic Device for Minimally Invasive Interventions in the Breast, J Biomech Eng. 126 (2004) 458–465.
[40] F. Tajima, K. Kishi, K. Kan, H. Ishii, K. Nishizawa, M.G. Fujie, T. Dohi, K. ichi Sudo, S. ichi Takamoto, An MR-compatible master–slave manipulator with interchangeable surgical tools, Int. Congr. Ser. 1256 (2003) 529–537. https://doi.org/10.1016/S0531-5131(03)00212-7.
[41] H. Elhawary, A. Zivanovic, M. Rea, B.L. Davies, C. Besant, D.M.C. Robbie, N.M. Desouza, A Modular Approach to MRI-Compatible Robotics, IEEE Eng. Med. Biol. Mag. 27 (2008) 35–41, https://doi.org/10.1109/EMB.2007.910260.
[42] D. Speicher, T. Bartscherer, F.J. Becker, J.W. Jenne, K. Mrosk, C. Degel, M. Günther, S. Tretbar, MRI compatible ultrasound transducers for simultaneous acquisition of coregistered ultrasound to MRI data, Phys. Procedia. 70 (2015) 1002–1006, https://doi.org/10.1016/j.phpro.2015.08.209.
[43] B. Gerold, S. Reynolds, A. Melzer, S. Cochran, Early exploration of MRI-compatible diagnostic ultrasound transducers, in: Proc. - IEEE Ultrason. Symp., IEEE, 2010: pp. 2404–2407. https://doi.org/10.1109/ULTSYM.2010.5935882.
[44] S.M. Lechner-Greite, N. Hehn, B. Werner, E. Zadicario, M. Tarasek, D. Yeo, Minimizing eddy currents induced in the ground plane of a large phased-array ultrasound applicator for echo-planar imaging-based MR thermometry, J. Ther. Ultrasound. 4 (2016) 1–14, https://doi.org/10.1186/s40349-016-0047-x.
[45] J. Wang, X. Xiao, Z. Huang, A. Melzer, 3D-printing based Transducer Holder for Robotic Assisted Ultrasound Guided HIFU, in: Procedia Manuf., Elsevier B.V., 2019: pp. 3–10. https://doi.org/10.1016/j.promfg.2019.02.002.
[46] A. Antoniou, C. Damianou, MR relaxation properties of tissue-mimicking phantoms, Ultrasonics 119 (2022), https://doi.org/10.1016/j.ultras.2021.106600.
[47] F.L. Goerner, G.D. Clarke, Measuring signal-to-noise ratio in partially parallel imaging MRI, Med. Phys. 38 (2011) 5049–5057, https://doi.org/10.1118/1.3618730.
[48] C. Yiallouras, N. Mylonas, C. Damianou, MRI-compatible positioning device for guiding a focused ultrasound system for transrectal treatment of prostate cancer, Int. J. Comput. Assist. Radiol. Surg. 9 (2014) 745–753, https://doi.org/10.1007/s11548-013-0964-x.
[49] P. Shokrollahi, J.M. Drake, A.A. Goldenberg, A study on observed ultrasonic motor-induced magnetic resonance imaging (MRI)artifacts, Biomed. J. 42 (2019) 116–123, https://doi.org/10.1016/j.bj.2018.12.007.
[50] G. Li, H. Su, G.A. Cole, W. Shang, K. Harrington, A. Camilo, J.G. Pilitsis, G.S. Fischer, Robotic system for MRI-guided stereotactic neurosurgery, IEEE Trans Biomed Eng. 62 (2015) 1077–1088, https://doi.org/10.1109/TBME.2014.2367233.
[51] L.W. Hofstetter, J.R. Hadley, R. Merrill, H. Pham, G.C. Fine, D.L. Parker, MRI-compatible electromagnetic servomotor for image-guided medical robotics, Commun. Eng. 1 (2022), https://doi.org/10.1038/s44172-022-00001-y.

Journal of Ultrasound
https://doi.org/10.1007/s40477-022-00740-w

Simple, inexpensive, and ergonomic phantom for quality assurance control of MRI guided Focused Ultrasound systems

Anastasia Antoniou[1] · **Christakis Damianou**[1]

Received: 28 June 2022 / Accepted: 3 October 2022

Abstract

Purpose The popularity of Magnetic Resonance guided Focused Ultrasound (MRgFUS) as a beneficial therapeutic solution for many diseases is increasing rapidly, thus raising the need for reliable quality assurance (QA) phantoms for routine testing of MRgFUS systems. In this study, we propose a thin acrylic film as the cheapest and most easily accessible phantom for assessing the functionality of MRgFUS hardware and software.

Methods Through the paper, specific QA tests are detailed in the framework of evaluating an MRgFUS preclinical robotic device comprising a single element spherically focused transducer with a nominal frequency of 2.75 MHz. These tests take advantage of the reflection of ultrasonic waves at a plastic–air interface, which results in almost immediate lesion formation on the film at a threshold of applied acoustic energy.

Results The phantom offered qualitative information on the power field distribution of the FUS transducer and the ability to visualize different FUS protocols. It also enabled quick and reliable assessment of various navigation algorithms as they are used in real treatments, and also allowed for the assessment of the accuracy of robotic motion.

Conclusion Therefore, it could serve as a useful tool for detecting defects in system's performance over its lifetime after establishing a baseline while concurrently contributing to establish QA and calibration guidelines for clinical routine controls.

Keywords Quality assurance · Phantom · MRI · Acrylic film · Cheap · Ultrasound

Introduction

The therapeutic benefits of focused ultrasound (FUS) have been widely exploited in the area of oncology [1]. Malignant cells can be necrotized by concentrating the ultrasonic energy within the target region, thus increasing the temperature to lethal levels non-invasively [1]. The popularity of this technology is increasing substantially while quality assurance (QA) tools for FUS devices and protocols remain to be standardized, thus raising the need for dedicated high-quality QA phantoms.

So far, gel-based tissue mimicking materials (TMMs) have been the main tool for testing FUS hardware in the research and development (R&D) stage, including assessment of the thermal heating abilities of ultrasonic transducers [2–4] and the Magnetic Resonance Imaging (MRI) compatibility of devices intended for MRI-guided FUS (MRgFUS) applications [2–6]. To begin with, gel phantoms are considered suitable for thermal studies in that they enable insertion of thermocouples for benchtop temperature measurements [7]. In addition, their tissue-like MRI signal [8] is beneficial in monitoring thermal exposures in the MRI setting through the use of MR thermometry. Accordingly, they serve as a valuable tool for evaluating and optimizing therapeutic protocols before in-vivo applications, for example, by examining the impact of various scanning pathways on the off-target heating [9] and the formation of asymmetric lesions [10] owning to thermal diffusion phenomena.

Polyacrylamide (PAA) gels containing thermosensitive ingredients, such as thermochromic ink that progressively changes colour under heating [11], BSA protein [11], and egg-white [12], were proposed for FUS studies, having the advantage of visualizing the formed lesions due to protein denaturation. Agar gels were also proven effective for FUS studies having the benefit of easy and cost-effective

✉ Christakis Damianou
christakis.damianou@cut.ac.cy

[1] Department of Electrical Engineering, Computer Engineering, and Informatics, Cyprus University of Technology, 30 Archbishop Kyprianou Street, 3036 Limassol, Cyprus

Published online: 04 November 2022

preparation, as well as the ability to simulate the critical thermal, acoustical, and MRI properties of several soft tissues depending on the type and concentration of added complementary ingredients [13]. On the contrary, gelatin-based phantom are only suitable for hyperthermia applications because they cannot withstand ablative temperatures [14]. Notably, the use of 3D printed materials and plastics to mimic bony tissues is becoming popular in multi-modality phantoms intended for MRI and/or US imaging [15–17].

In terms of evaluating the motion accuracy of robotic mechanisms designed to navigate the ultrasonic transducer relative to the subject, the so far proposed R&D techniques include digital calliper-based methods [3], MRI imaging of the ultrasonic transducer or other dedicated MRI visible objects during step motion [18], and visual assessment of lesion formation in transparent thermosensitive phantoms [2, 19].

Regarding clinical use of test phantoms, the basic functionalities of a clinical MRgFUS device can also be tested by mapping the temperature rise during heating in a dedicated phantom. Several studies report on the use of MR thermometry during sonication in US/MRI phantoms as a simple QA method for clinical routine testing [20, 21]. In fact, this method has been the mainstay for clinical QA allowing for testing the acoustic power output, the targeting accuracy, the noise level introduced into the picture, and well as the size and shape of the focal spot. An indicative example is a 4-years retrospective study [21], which was performed to assess the basic functionalities of the first clinical MRgFUS system; ExAblate 2000 (InSightec Inc., Haifa, Israel) before each of 148 uterine fibroid treatment sessions.

The aforementioned QA measures are also employed before clinical deployment since they are extremely essential in the process of a system's technical acceptance [22]. In this regard, the MRgFUS system ExAblate 2000 has been tested by employing MR thermometry in TMMs designed to match the ultrasonic properties of tissue [22]. The focus positioning accuracy was examined by performing grid sonications in coronal and axial planes and comparing the commanded position with the actual position of the focus as defined by the peak temperature location through the controlling software.

Similarly, Vicari et al. [23] proposed a series of radiation force measurements, 3D modelling and geometrical tests for daily in-vitro QA of the InSightec ExAblate 2100 equipment, with emphasis on the delivered power and position of the focus. The authors followed an interesting technique to assess the focus positioning accuracy and software reliability by sonicating a 96 well plate filled with a thermosensitive BSA-doped PAA gel [23].

While the need for phantoms dedicated to QA of FUS equipment has long been recognized [24], their development was delayed until recently, when two relevant studies were published [25, 26]. The proposed QA phantoms are both based on the concept of placing ultrasonic calibration equipment in a plastic container that is filled with a TMM. To be more specific, Acri et al. [25] developed an ergonomic phantom for clinical routine QA of MRgFUS devices consisting of a hollow polymethyl methacrylate (PMMA) cylinder that can host various movable inserts. These could be PMMA holders specially designed to support instruments, such as a precision balance or a thermometer, or small teflon pieces simulating microcalcifications. According to the authors, it is filled with different fluids depending on the tested parameters, which may be the precision and dimension of the FUS spot, the target temperature, and the linearity of output power.

Ambrogio et al. [26] developed a QA phantom of similar design to evaluate the performance of the Sonalleve commercial MRgFUS system (Philips, Canada) over a 12-month period. The developed phantom is a PMMA cubic structure that embeds a 3D-printed bone-mimic disk made of VeroWhite Plus material and 4 T-type thermocouples within an agar-based soft TMM in clinically relevant places for the specific intended therapeutic modalities of this system.

It becomes clear that gel phantom-based techniques have been essential in both R&D and clinical testing of MRgFUS devices. Although widely accepted, these techniques suffer from many potential sources of error related to human or instrument failures, which may cause the results of assessment to be interpreted incorrectly. For instance, gel phantoms are prone to air or other inhomogeneities that may be introduced during the preparation process, as well as to gradual water loss, which are very possible to influence the formation of uniform lesions and thus the reliability of measurements. Furthermore, since phantoms have limited lifetime, different phantoms will be used at different days, which is not ideal when examining the functionality and loss of precision on a routine basis.

Following the aforementioned unmet needs, in this study, we propose the use of an acrylic thin film as the most cost-effective and ergonomic way of evaluating the functionality and stability of MRgFUS equipment over time. A robotic device dedicated to MRgFUS preclinical applications, and the relevant treatment planning/monitoring software were employed in the study. The QA methodology is detailed through a series of experiments designed to assess the performance of this system in terms of targeting accuracy, heating effects of the ultrasonic transducer, software functionality, and proper communication between hardware and software.

Materials and methods

Quality assurance acrylic film

The QA phantom proposed in this study is a clear film made of acrylic plastic with a thickness of 0.9 mm (FDM400mc

print plate, Stratasys, Minnesota, USA). The ultrasonic attenuation of the film was estimated at 8.5 dB/cm-MHz (at 2 MHz) according to the transmission through technique [27]. The following QA tests take advantage of the almost complete reflection of ultrasonic waves at the plastic–air interface, which results in almost immediate lesion formation on the upper side of the film at a threshold of applied acoustic energy. Accordingly, in all experiments, the upper side of the film involved air while degassed water was used as the coupling media between the transducer and the bottom surface of the film, as shown in Fig. 1, so lesion formation was mainly based on reflection.

MRgFUS robotic device for preclinical use

A preclinical MRgFUS robotic device previously described in detail by Drakos et al. [3] was employed in the study. In brief, the system comprises a mechanism enclosure where all the mechanical and electronic components are hosted and another separate water enclosure where the transducer is actuated. The water enclosure includes an acoustic opening at the top for placing the target.

For the purpose of the current study, the transducer comprised a single element spherically focused ultrasonic piezoelectric (Piezohannas, Wuhan, China) with a nominal frequency of 2.75 MHz (Radius of curvature: 65 mm, Diameter: 50 mm, efficiency: 30%). The transducer was powered by an RF amplifier (AG1016, AG Series Amplifier, T & C Power Conversion, Inc., Rochester, US).

The system was integrated with and controlled by a custom made treatment planning-monitoring software which provided the ability to plan sonications in rectangular grids or complex patterns for full coverage of any segmented area on MRI images, as well as to define the sonication (acoustic power and sonication time) and grid parameters (spatial and temporal step).

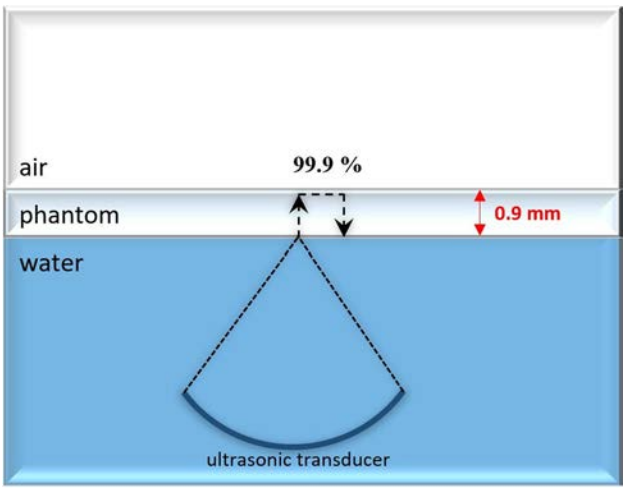

Fig. 1 Concept of lesion formation on the plastic film

Power field assessment

The power field of the 2.75 MHz ultrasonic transducer was evaluated by sonicating the plastic film at varying distance from its surface. The transducer was securely mounted on the bottom part of a plastic holder facing upwards to the plastic film. Careful design of the holder was followed to ensure horizontal placement of the film, thus minimizing sound refraction phenomena. The holder also included a height adjustment mechanism for changing the transducer-film distance with a 10-mm step. The setup was hosted in a tank, which was filled with degassed, deionized water up to the upper surface of the plastic film to achieve the aforementioned "water-plastic-air" configuration. Electrical power of 150 W (acoustic power of 45 W) was applied for 30 s in continuous mode for different transducer-film distances of 40–90 mm. The diameter of the formed lesion at each tested distance was measured using a digital caliper.

Assessment of change in lesion size by varying sonication parameters

In this experimental part, the QA film was securely mounted on the acoustic opening of the device using a dedicated holder, as shown in Fig. 2. The distance from the transducer was adjusted to equal the radius of curvature. Degassed water was used as described above to ensure ultrasonic coupling with the bottom surface of the film. The effect of the power (10–70 W electric power) and duration of sonication (1–11 s) on lesion formation was examined independently by performing sonications spaced by 1 cm.

Accuracy and repeatability of motion assessment

This experimental part was carried out to assess the accuracy and repeatability of motion, as well as whether the software commands are properly executed using a similar setup as detailed above. The film was sonicated by robotically moving the transducer along predefined pathways; square or irregular grids using the commands of the relevant software. The planned sonication spots were visited in a Zig-Zag pathway using varying motion step. An acoustical power of 6 W was applied for 5 s to each spot while a waiting time of 60 s was left between successive sonications to ensure adequate heat dissipation in the phantom.

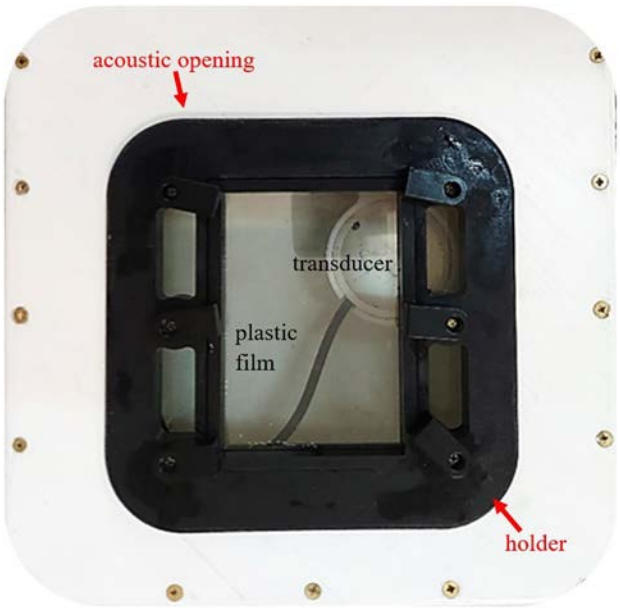

Fig. 2 Photo of the experimental setup with the phantom fixed to the acoustic opening of the MRgFUS device above the FUS transducer

Results

Lesions of different dimensions were formed by sonicating the acrylic film at varying distance from the transducer surface and served as indicators of the power film distribution. The sonicated films are shown in Fig. 3 with the measured lesion diameter indicated. Among the tested distances, the largest lesion is observed at 40 mm and gradually decreases in size until the distance of 60 mm, whereas at 80 mm it increases again, thus demonstrating heating in the far-field region. This change in lesion size with varying distance gives a good approximation of the power field distribution in that lesion dimensions can be defined as the half width and length of a Gaussian power distribution at each distance.

The lesion size at a specific distance from the transducer surface can be controlled by varying the sonication parameters. Figure 4 shows the change in lesion size by varying the electric power from 10 to 70 W while keeping constant the sonication duration at 6 s at the focal plane. The distance between successive sonications was set at 1 cm.

Figures 5, 6 and 7 show indicative results of multiple lesions formed on the phantom following pathway planning on the dedicated software. Figure 5 shows discrete

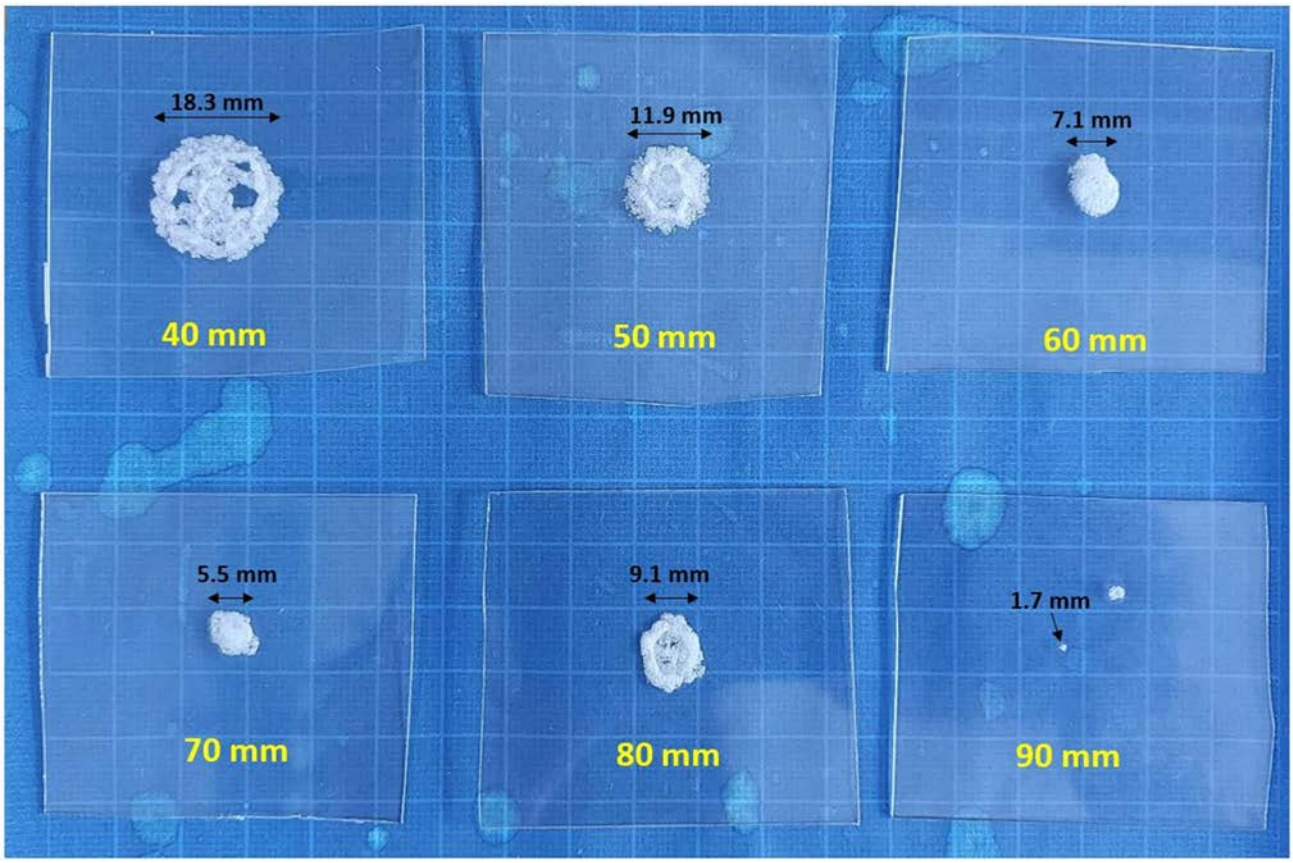

Fig. 3 Photo of acrylic films sonicated at increasing distance from the transducer using acoustical power of 45 W for 30 s and the 2.75 MHz transducer (radius of curvature of 65 mm and diameter of 50 mm), indicating the diameter of the formed lesions

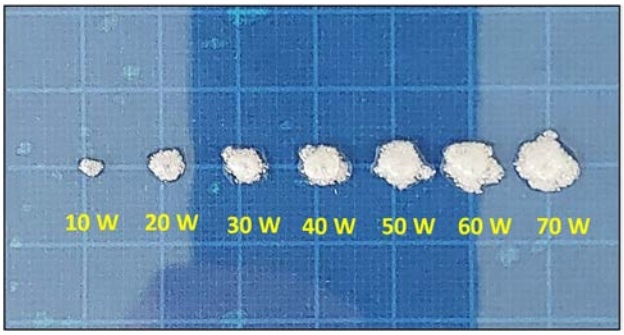

Fig. 4 Photo of lesions formed using varying electric power of 10 to 70 W for a constant sonication duration of 6 s

lesions formed in a 5 × 5 square grid using a spatial step of 10 mm (each spot exposed to 20 W electric power/6 W acoustical power for 5 s). The overlapping lesions shown in Fig. 6 were created after sonication in a 20 × 20 grid using identical ultrasonic parameters but a smaller spatial step of 1 mm. An indicative result of sonication in irregular pattern with similar sonication protocol and a 3-mm step is shown in Fig. 7. Note that the ablated area matches well the segmented area in the software. The selection of grid step defined the formation of discrete or overlapping lesions. Overall, the lesion patterns demonstrate good motion and alignment accuracy.

Discussion

Through a literature search, it can be easily concluded that while there are well established methods for calibrating FUS equipment, the methods and tools for QA of MRgFUS robotic devices are still far from being standardized. Herein, a thin acrylic film was proposed as the cheapest and most easily accessible quality assurance phantom for assessing the performance of MRgFUS hardware and software. Although, in this study, we used a 0.9 mm-thick print plate obtained from a Stratasys printer, one can simply buy a similar product from a bookstore at a very low price.

Specific methods involving the use of the proposed film were utilized for assessing the functionality of an MRgFUS preclinical robotic device. The setup is extremely simple and is based on the concept of "water-plastic-air" described previously, where lesion formation is mainly the result of sound reflection at the plastic/air boundary.

Regarding quality assurance of the FUS transducer, the phantom provides indication of the beam's cross section. By collecting several slices in cross section, it is possible to get qualitative information for the power field distribution of the FUS transducer in axial direction. In addition, by adjusting the power and time it is possible to control the size of the individual lesions, thus simulating different focused ultrasound protocols. Following experiments with varying power and time, an acoustic energy of 18 W was proven sufficient to produce a lesion of easily measurable dimensions (≈ 2 mm in diameter) on the proposed phantom. A

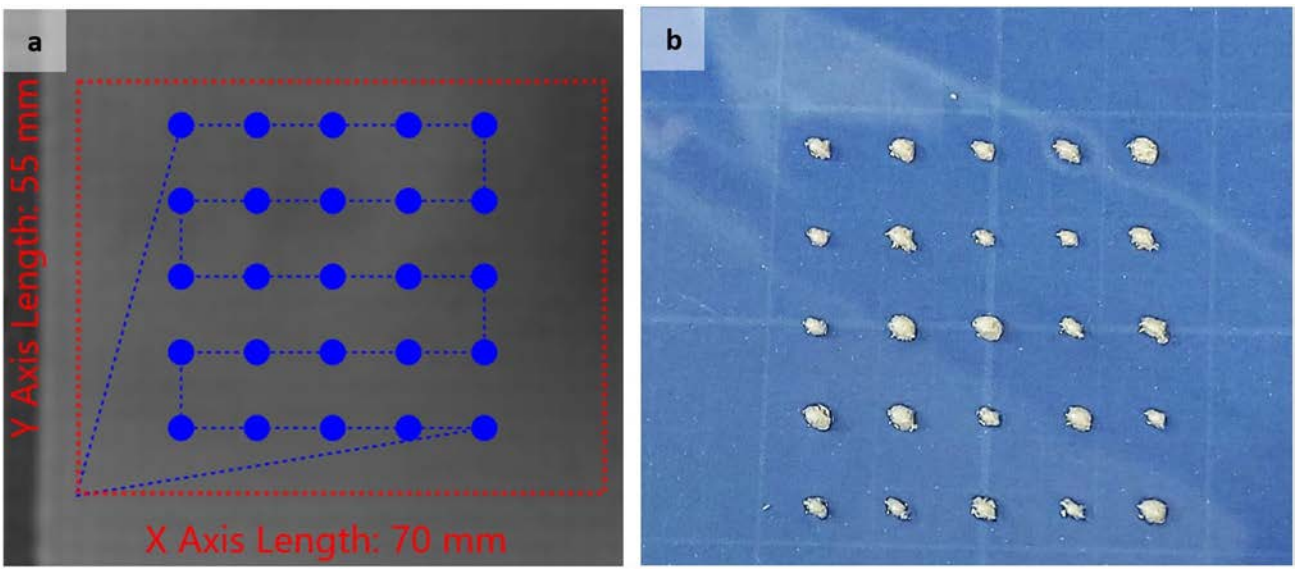

Fig. 5 **a** Software screenshot showing the sonication spots (5 × 5 grid) and Zig-Zag pathway as planned on an MRI image of an agar phantom. **b** The corresponding lesions formed on the plastic film using acoustic power of 6 W for 5 s at each spot, with a spatial step of 10 mm, using the 2.75 MHz transducer (radius of curvature of 65 mm and diameter of 50 mm)

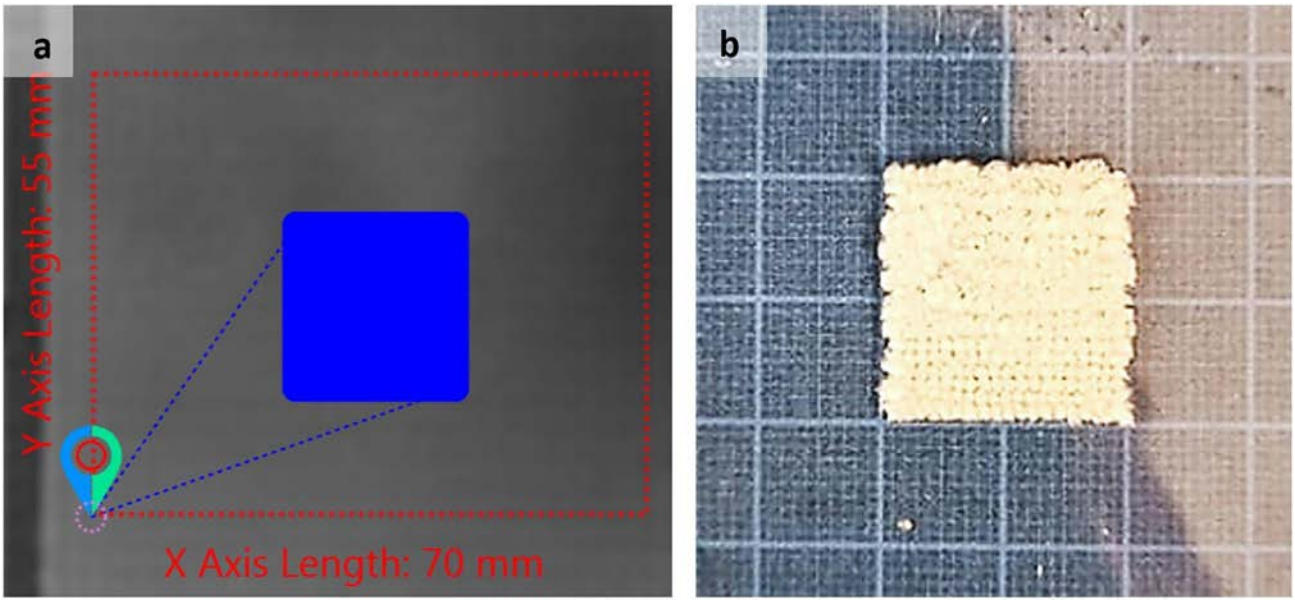

Fig. 6 **a** Software screenshot showing the sonication area (20×20 grid) as planned on an MRI image of an agar phantom. **b** The corresponding overlapping lesions formed on the plastic film using acoustic power of 6 W for 5 s at each spot, with a spatial step of 1 mm, using the 2.75 MHz transducer (radius of curvature of 65 mm and diameter of 50 mm)

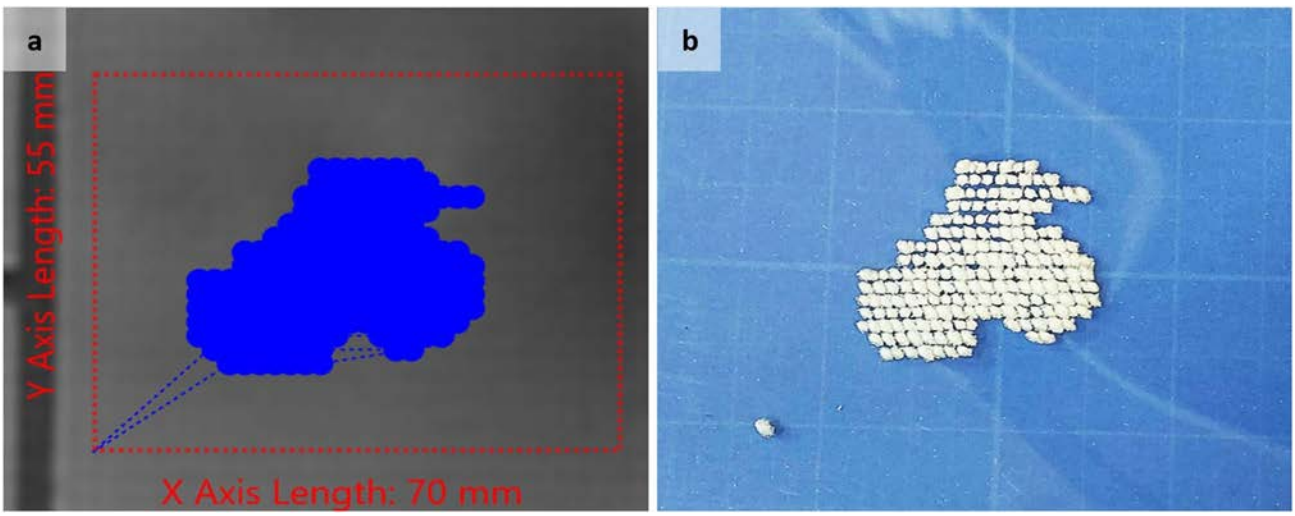

Fig. 7 **a** Software screenshot showing the segmented irregular area on an MRI image of an agar phantom. **b** The corresponding almost overlapping lesions formed on the plastic film using acoustic power of 6 W for 5 s at each spot, with a spatial step of 3 mm, using the 2.75 MHz transducer (radius of curvature of 65 mm and diameter of 50 mm)

limitation of this approach is that evaluation is not possible in the axial direction.

Furthermore, the phantom was proven an efficient tool for assessing the accuracy and repeatability of robotic motion by navigating the robotic system in grid patterns and producing discrete lesions. Note that this was also demonstrated in a previous study [18], but it was further assessed with extensive experimentation of various motion algorithms. It is interesting to note that the formed lesion patterns did not show evidence of thermal diffusion.

By using small spacing during navigation, it is also possible to assess several navigation algorithms as they are used in actual treatments. In this study, complex shapes were sonicated successfully as evidenced by the lesions created on the plastic film, following planning of the sonication sequence on the software. This method helps to assess not

only the software performance, but also its communication with the integrated robotic system and whether motion commands are properly executed.

The main limitation of the proposed QA methodology is that it cannot be used as a stand-alone tool to optimize clinical therapeutic protocols since it has different acoustic properties and response to heat than soft tissues. The mechanism of thermal diffusion that affects the formation of uniform lesions and treatment outcome in tissue [10, 28] is less effective in plastic due to the difference in thermal conductivity. Besides, the mechanism of lesion formation is completely different. This limitation is also considered a benefit in that it allows for reliable assessment of the planning algorithms and robotic motion without phantom-dependent parameters affecting the lesion's size and shape significantly.

So far, tissue-mimicking gel phantoms have been the major tool for characterizing the performance of preclinical and clinical MRgFUS systems. However, they have a limited lifetime and are prone to air or other inhomogeneities, which are very likely to shift or distort the formed lesions. In this regard, they are not ideal for assessing the system's functionality and stability over time or the motion accuracy of robotically positioned MRgFUS devices. Furthermore, in case a thermosensitive TMM is utilized that forms permanent lesions, it should be replaced after each QA test. Notably, two recently published articles report the development of more complex phantoms containing TMMs and FUS measurement tools for QA of clinical MRgFUS devices [25, 26]. In this study, the proposed QA phantom and relevant methodology are simpler and more ergonomic, highly cost-effective, universal, and do not depend on human or instrument-related factors. Although it is not reusable since the formed lesions are permanent, this is not a problem due to its very low cost.

Conclusions

Overall, the obtained results qualify the proposed acrylic phantom as a reliable QA tool for routine testing of MRgFUS robotic devices through a series of simple and quick tests. Accordingly, it could be used for the detection of defects in system's performance and ease maintenance over its lifetime, while concurrently contributing towards developing quality control and calibration guidelines for clinical practices. It is though underlined that state-of-the-art gel-based methods should also be employed when testing therapeutic protocols to optimize the efficiency and safety before in-vivo use.

Acknowledgements The study was co-funded by the European Structural & Investment Funds (ESIF) and the Republic of Cyprus through the Research and Innovation Foundation (RIF) under the project SOUNDPET (INTEGRATED/0918/0008).

Author contributions AA contributed to the drafting of manuscript and scientific methods. CD had the overall supervision of the study.

Funding This research was supported by Research and Innovation Foundation of Cyprus, SOUNDPET (INTEGRATED/0918/0008).

Declarations

Conflict of interests The authors declare that they have no conflicts of interest.

Ethical approval The study does not involve animals or human participants.

Consent to participate/consent to publish Not applicable.

References

1. Abe K, Taira T (2017) Focused ultrasound treatment, present and future. Neurol Med Chir (Tokyo) 57:386–391. https://doi.org/10.2176/nmc.ra.2017-0024
2. Damianou C, Giannakou M, Menikou G, Ioannou L (2020) Magnetic resonance imaging-guided focused ultrasound robotic system with the subject placed in the prone position. Digit Med 6:24–31. https://doi.org/10.4103/digm.digm_2_20
3. Drakos T, Giannakou M, Menikou G, Filippou A, Evripidou N, Spanoudes K et al (2021) MRI-guided focused ultrasound robotic system for preclinical use. J Vet Med Anim Sci 4:1–11
4. Antoniou A, Giannakou M, Evripidou N, Stratis S, Pichardo S, Damianou C (2022) Robotic system for top to bottom MRgFUS therapy of multiple cancer types. Int J Med Robot Comput Assist Surg 18(2):e2364. https://doi.org/10.1002/rcs.2364
5. Antoniou A, Giannakou M, Evripidou N, Evripidou G, Spanoudes K, Menikou G et al (2021) Robotic system for magnetic resonance guided focused ultrasound ablation of abdominal cancer. Int J Med Robot Comput Assist Surg. https://doi.org/10.1002/rcs.2299
6. Giannakou M, Drakos T, Menikou G, Evripidou N, Filippou A, Spanoudes K et al (2021) MRI-guided focused ultrasound robotic system for transrectal prostate cancer therapy. Int J Med Robot Comput Assist Surg 17(3):e2237. https://doi.org/10.1002/rcs.2237
7. Dabbagh A, Abdullah BJJ, Ramasindarum C, Abu Kasim NH (2014) Tissue-mimicking gel phantoms for thermal therapy studies. Ultrason Imaging 36:291–316. https://doi.org/10.1177/0161734614526372
8. Antoniou A, Damianou C (2022) MR relaxation properties of tissue-mimicking phantoms. Ultrasonics. https://doi.org/10.1016/j.ultras.2021.106600
9. Filippou A, Drakos T, Giannakou M, Evripidou N, Damianou C (2021) Experimental evaluation of the near-field and far-field heating of focused ultrasound using the thermal dose concept. Ultrasonics 116:106513. https://doi.org/10.1016/j.ultras.2021.106513
10. Zhou Y, Kargl SG, Hwang JH (2011) The effect of the scanning pathway in high-intensity focused ultrasound therapy on lesion production. Ultrasound Med Biol 37:1457–1468. https://doi.org/10.1016/j.ultrasmedbio.2011.05.848
11. Eranki A, Mikhail AS, Negussie AH, Katti PS, Wood BJ, Partanen A (2019) Tissue-mimicking thermochromic phantom for characterization of HIFU devices and applications. Int J Hyperth 36:518–529. https://doi.org/10.1080/02656736.2019.1605458
12. Takegami K, Kaneko Y, Watanabe T, Maruyama T, Matsumoto Y, Nagawa H (2004) Polyacrylamide gel containing egg white as new model for irradiation experiments using focused ultrasound.

Ultrasound Med Biol 30:1419–1422. https://doi.org/10.1016/j.ultrasmedbio.2004.07.016
13. Antoniou A, Georgiou L, Christodoulou T, Panayiotou N, Ioannides C, Zamboglou N et al (2022) MR relaxation times of agar-based tissue-mimicking phantoms. J Appl Clin Med Phys. https://doi.org/10.1002/acm2.13533
14. Madsen EL, Hobson MA, Shi H, Varghese T, Frank GR (2005) Tissue-mimicking agar/gelatin materials for use in heterogeneous elastography phantoms. Phys Med Biol 50:5597–5618. https://doi.org/10.1088/0031-9155/50/23/013
15. Menikou G, Dadakova T, Pavlina M, Bock M, Damianou C (2015) MRI compatible head phantom for ultrasound surgery. Ultrasonics 57:144–152. https://doi.org/10.1016/j.ultras.2014.11.004
16. Menikou G, Yiannakou M, Yiallouras C, Ioannides C, Damianou C (2018) MRI-compatible breast/rib phantom for evaluating ultrasonic thermal exposures. Int J Med Robot Comput Assist Surg 14:1–12. https://doi.org/10.1002/rcs.1849
17. Menikou G, Yiannakou M, Yiallouras C, Ioannides C, Damianou C (2016) MRI-compatible bone phantom for evaluating ultrasonic thermal exposures. Ultrasonics 71:12–19. https://doi.org/10.1016/j.ultras.2016.05.020
18. Antoniou A, Drakos T, Giannakou M, Evripidou N, Georgiou L, Christodoulou T et al (2021) Simple methods to test the accuracy of MRgFUS robotic systems. Int J Med Robot Comput Assist Surg. https://doi.org/10.1002/rcs.2287
19. Yiallouras C, Mylonas N, Damianou C (2014) MRI-compatible positioning device for guiding a focused ultrasound system for transrectal treatment of prostate cancer. Int J Comput Assist Radiol Surg 9:745–753. https://doi.org/10.1007/s11548-013-0964-x
20. Chen L, Ma C, Meyer J (2014) Quality assurance for MR guided focused ultrasound treatment of bone metastasis: a clinical experience. Int J Radiat Oncol 90:S703. https://doi.org/10.1016/j.ijrobp.2014.05.2059
21. Mcdannold N, Hynynen K (2006) Quality assurance and system stability of a clinical MRI-guided focused ultrasound system: four-year experience. Med Phys 33:4307–4313. https://doi.org/10.1118/1.2352853
22. Gorny KR, Hangiandreou NJ, Hesley GK, Gostout BS, McGee KP, Felmlee JP (2006) MR guided focused ultrasound: technical acceptance measures for a clinical system. Phys Med Biol 51:3155–3173. https://doi.org/10.1088/0031-9155/51/12/011
23. Vicari F, Russo G, Cammarata FP, Cirincione R, Forte GI, Borasi G et al (2014) A daily quality assurance routine for ultrasounds in vitro experiments. Transl Cancer Res 3:421–429. https://doi.org/10.3978/j.issn.2218-676X.2014.09.02
24. Schätzle U, Reuner T, Jenne J, Heilingbrunner A (1998) Quality assurance tools for therapeutic ultrasound. Ultrasonics 36:679–682. https://doi.org/10.1016/S0041-624X(97)00138-8
25. Acri G, Caridi F, Testagrossa B, Gurgone S, Anfuso C, Paladini G, et al. (2022) A "user-friendly" phantom to conduct Quality Controls on MRgFUS device. J Phys Conf Ser, vol. 2162, IOP Publishing; p. 012004. https://doi.org/10.1088/1742-6596/2162/1/012004
26. Ambrogio S, Baêsso RM, Bosio F, Fedele F, Ramnarine KV, Zeqiri B et al (2022) A standard test phantom for the performance assessment of magnetic resonance guided high intensity focused ultrasound (MRgHIFU) thermal therapy devices. Int J Hyperth 39:57–68. https://doi.org/10.1080/02656736.2021.2017023
27. Antoniou A, Evripidou N, Giannakou M, Constantinides G, Damianou C (2021) Acoustical properties of 3D printed thermoplastics. J Acoust Soc Am 149:2854–2864. https://doi.org/10.1121/10.0004772
28. Curiel L, Chavrier F, Gignoux B, Pichardo S, Chesnais S, Chapelon JY (2004) Experimental evaluation of lesion prediction modelling in the presence of cavitation bubbles: Intended for high-intensity focused ultrasound prostate treatment. Med Biol Eng Comput 42:44–54. https://doi.org/10.1007/BF02351010

Journal of Ultrasound
https://doi.org/10.1007/s40477-022-00746-4

ORIGINAL PAPER

Characterization of a fat tissue mimicking material for high intensity focused ultrasound applications

Antria Filippou[1] · Irene Louca[1] · Christakis Damianou[1]

Received: 20 July 2022 / Accepted: 11 October 2022

Abstract

Purpose Tissue-mimicking materials (TMMs) have a prominent role in validating new high intensity focused ultrasound (HIFU) therapies. Agar-based TMMs are often developed mimicking the thermal properties of muscle tissue, while TMMs simulating fat tissue properties are rarely developed. Herein, twelve agar-based TMMs were iteratively developed with varied concentrations of agar, water, glycerol and propan-2-ol, and characterized for their suitability in emulating the thermal conductivity of human fat tissue.

Methods Varied agar concentrations (2%, 4%, 6%, 8%, 12%, 16% and 20% w/v) were utilized for developing seven water-based TMMs, while a 20% w/v agar concentration was utilized for developing two water/alcohol-based TMMs (50% v/v water and 50% v/v either glycerol or propan-2-ol) and three alcohol-based TMMs (varied glycerol and propan-2-ol concentrations). Thermal conductivity was measured for all TMMs, and the tissue mimicking material (TMM) exhibiting thermal conductivity closest to human fat was considered the optimum fat TMM and was further characterized using ultrasound (US) and Magnetic Resonance Imaging (MRI).

Results For the seven water-based TMMs an inverse linear trend was observed between thermal conductivity and increased agar concentration, being between 0.524 and 0.445 W/m K. Alcohol addition decreased thermal conductivity of the two water/alcohol-based TMMs to about 0.33 W/m K, while in the alcohol-based TMMs, increased concentrations of propan-2-ol emerged as a modifier of thermal conductivity. The optimum fat TMM (33.3% v/v glycerol and 66.7% v/v propan-2-ol) exhibited a 0.231 W/m K thermal conductivity, and appeared hypoechoic on US images and with increased brightness on T1-Weighted MRI images.

Conclusion The optimum fat TMM emulates the thermal conductivity of human fat tissue and exhibits a fat-like appearance on US and MRI images. The TMM is cost-effective and has a long lifespan and possesses great potential for use in HIFU applications as a fat TMM.

Keywords Fat · Phantom · TMM · Thermal conductivity · HIFU

Introduction

Tissue-mimicking materials (TMMs) otherwise known as phantoms, have a prominent role in biomedical research, since they are manufactured to mimic biological tissue for enabling easy and accurate validation and quality control of emerging systems and therapies [1]. Employment of TMMs with tissue-like properties can provide an understanding on the efficacy and hazards of the investigated system or therapy, prior to clinical trials [1]. With the continuous development of novel applications, different types of therapies are being examined. One of these, is the use of High Intensity Focused Ultrasound (HIFU) for therapeutic and palliative purposes. HIFU employs ultrasonic transducers that focus within the targeted tissue to raise its temperature to necrotic levels [2]. As a result, characteristic lesions of coagulative necrotic cells are formed in the tissue at the focus of the transducer [2].

To enable data reproducibility, TMMs should maintain structural, chemical, and mechanical stability over time [3]. Additionally, the materials utilized should be non-toxic,

✉ Christakis Damianou
christakis.damianou@cut.ac.cy

[1] Department of Electrical Engineering, Computer Engineering and Informatics, Cyprus University of Technology, 30 Archbishop Kyprianou Street, 3036 Limassol, Cyprus

Published online: 21 November 2022

provide ease of use as well as be cost-effective [3]. The time and shape of lesion formation for any emerging HIFU systems or applications must be well examined before use in clinical trials. For this purpose, TMMs developed with materials that mimic the magnetic, acoustic, and thermal properties of human tissues are much needed. Generally, human soft tissues include a combination of muscles, fat, ligaments, tendons, fibrous tissue, nerves, synovial membranes and blood vessels [4]. Commonly, the majority of TMMs are developed to mimic soft tissue, with numerous anthropomorphic phantoms accurately mimicking the anatomy, shape and functionality of several soft tissue types [5]. Nevertheless, the majority of soft TMMs have a homogeneous structure [5]. Due to variations in the physical properties of different soft tissue types, the homogeneous TMMs should be developed to largely mimic soft tissues [5], and through judicious selection of additional inclusions further customized for mimicking specific tissue types.

Normally, for diagnostic and therapeutic applications of ultrasound (US) the developed tissue alternatives have an aqueous base [5], following the vast use of water in the calibration of US systems [6, 7]. However, water has a substantially lower propagation speed of sound (1480 m/s) and a relatively minimal attenuation coefficient (0.0022 dB/cm MHz) compared to human soft tissues and therefore alone is not a suitable soft tissue mimicking material (TMM) [5]. Nevertheless, the use of an ethanol–water solution provides increased propagation speed of sound, similar to soft tissue levels (1540 m/s) [8]. Notably, aqueous phantoms consisting of an agar [9] or gelatin base [10] are widely available, easily reproduced, and with their mixture with a variety of materials, can mimic the acoustic, magnetic or thermal characteristics of human tissues [5, 11]. Agar is a biopolymer, arising from algae, that is soluble in hot water, where it undergoes hysteresis to form a gel once the agar-water solution is cooled below 45 °C [12]. Gel creation occurs for temperatures up to 60 °C, due to the formation of intra- and inter-molecular hydrogen bonds between the agar and water molecules [13], as evidenced by spectroscopic techniques [14]. Increased concentrations of agar are related to a decreased pore size [12, 15] that leads to closer formation of the water-agar hydrogen bonds [15], and thus increased mechanical properties of the water-agar gel [16]. Specifically, agar-based TMMs have reported emulating soft tissue properties, while simultaneously reporting with a comparative mechanical strength [1]. Moreover, the agar or gelatin-based hydrogels enable reproducible results since several chemical compounds such as methyl paraben [17], thimerosal [16], Germall-plus [16], sodium azide [18], benzoic acids [19] or benzalkonium chloride [20] are often added to prevent bacterial growth, thus prolonging the lifespan of the TMMs. Use of chemical preservatives combined with TMM storage in airtight containers, with the TMM surrounded by a solution of its liquid components [20] or distilled water [19], results in stability of the TMM and reusability for a period of several months [19, 20].

A water-agar or water-gelatin mixture is most frequently used for muscle-like TMMs [21] due to water having similar thermal conductivity with muscle tissue [22], thus resulting in a TMM with muscle-like thermal conductivity [21]. The thermal conductivities of human tissues were measured by Hatfield et al. [23], and were found between 0.435 and 0.510 W/m K for muscle tissues and 0.161–0.197 W/m K for fat tissues. Materials having a low thermal conductivity are of great interest due to their potential use in phantoms simulating fat tissues. Ogiwara et al. [24] measured the thermal conductivity of ten liquid alcohols between 20 and 70 °C. Thermal conductivity decreased with increasing temperature, with pure ethanol ranging between 0.155 and 0.161 W/m K [24]. Woolf et al. [25] measured the thermal conductivity of olive oil between 0 and 140 °C. The thermal conductivity was inversely proportional to increasing temperature, acquiring values between 0.161 and 0.169 W/m K [25]. Similarly, Turgut et al. [26] measured the thermal conductivity of olive, sunflower and corn oils between temperatures of 25 and 80 °C. Olive oil had the smallest variation with temperature, with its conductivity having values of 0.163 and 0.166 W/m K, while sunflower oil had thermal conductivity values between 0.162 and 0.168 W/m K [26]. Corn oil exhibited the greatest effect on its thermal conductivity with temperature difference, with its thermal conductivity having values between 0.154 and 0.165 W/m K [26]. Wrenick et al. [27] examined the thermal conductivity of two different groups, II and V, of engine oils between 50 and 200 °C. Group II had thermal conductivities in the interval 0.13–0.138 W/m K, while the values for Group V were in the range of 0.12–0.15 W/m K [27]. Lavrykov et al. [28] examined the thermal properties of different types of commercially available paper sheets with the thermal conductivity of each sample dependent upon its density, thickness and percentage ash content. All 57 samples had their thermal conductivities between 0.0740 and 0.1816 W/m K [28]. Watson et al. [29] measured the thermal properties of butter containing 80% fat and 16% moisture between −40 and 30 °C, with the thermal conductivity increasing with increasing temperature, obtaining values in the range of 0.243–0.31 W/m K. In the study by Eltom et al. [30] the thermal conductivities of charcoal were measured between a temperature range of 30–90 °C with the thermal conductivity varying with increasing temperature. The thermal conductivity was ranging between 0.07 and 0.1 W/m K; increasing until 40 °C, having constant values between 40 and 70 °C and decreasing from 70 to 90 °C [30]. Takizawa et al. [31] examined the thermal conductivity of liquid glycerol between the temperatures of 20–70 °C with the values obtained being approximately constant and ranging from

0.291 to 0.297 W/m K. Maccarthy et al. [32] measured the thermal conductivities of samples of granulated, extra-fine, caster and icing sugar with the measurements performed between 17.2 and 64.8 °C. The authors [32] concluded that the thermal conductivity increased with increasing particle size and temperature, having values in the interval 0.085–0.167 W/m K.

Although a vast literature exists for phantoms mimicking muscle tissue, not much literature exists for agar or gelatin-based phantoms thermally simulating fat tissue. Robinson et al. [33] developed two TMMs that dielectrically replicated muscle and fat, and calculated their dielectric and thermal properties. For the fat TMM, the authors [33] utilized a mixture of gelatin, ethanediol and polyethene powder and reached a thermal conductivity of 0.29 W/m K. In a study by Yuan et al. [34], a recipe proposed by Lazebnik et al. [35] was modified to simulate both electrical and thermal properties of human fat tissue, for developing a heterogeneous TMM for radiofrequency (RF) ablation. Yuan et al. [34] concluded that the initial use of kerosene by Lazebnik [35], would result in different thermal properties of the developed phantom compared to human fat tissue. Therefore, the authors [34] utilized a water-based solution with added gelatin, saline, pure vegetable oil, and a surfactant to allow for a homogeneous mixture of oil with the aqueous solution. The fat-mimicking compartment of the phantom consisted of 85% oil with its thermal conductivity measured at 0.20 W/m K, thus being in good agreement with the literature value for the thermal conductivity of fat tissue [34]. Similarly, in a study by Liu et al. [36], a heterogeneous agar-based TMM was developed with specific concentrations of sucrose and sodium chloride and varied concentrations of a fat-saturated oil. Notably, a 90% concentration of the fat-saturated oil resulted in a fat TMM having a thermal conductivity of 0.23 W/m K [36]. Correspondingly, Kim et al. [37] developed an agar-based fat TMM for HIFU applications using a combination of water, olive oil, glycerol, surfactant, aluminum oxide and silicon carbide at varied concentrations. Although a 15% concentration of olive oil resulted in a phantom with similar acoustic properties as fat tissue, no measurements of the thermal properties of the fabricated phantom were reported [37].

A TMM with fat tissue-like thermal properties would be of great interest for the HIFU field, due to the presence of intervening fat in extracorporeal use of HIFU [2], as well as the increasing use of HIFU for noninvasive fat-reduction [38, 39]. In an attempt to enhance the available literature for TMMs with thermal properties representative of fat tissue, agar-based TMMs were developed herein and characterized for their suitability in emulating thermal properties of human fat. Agar was preferred since it provides easy handling with minimal change of its properties over time [3], as well as the ability to withstand the high temperatures induced by thermal therapies [21]. Several TMMs were developed in an iterative approach utilizing different concentrations of agar, water and various types of alcohols, to find the ultimate recipe that best resembles the thermal characteristics of human fat tissue. Different alcohols were used, according to their literature values for thermal conductivity; glycerol with a thermal conductivity of 0.291–0.297 W/m K [31] and propan-2-ol with thermal conductivity between 0.127 and 0.133 W/m K [24]. The idea of adding alcohols was based on the fact that the abovementioned alcohols have low conductivity, thus ultimately reducing the thermal conductivity of the fabricated TMMs to desirable levels. More importantly, alcohols have hydroxyl groups (–OH) [40], therefore intra- and inter-molecular hydrogen bondings were expected between the alcohols and agar.

In the literature, alcohols have reportedly been utilized in varied concentrations as additives in agar or gelatin-based hydrogels for adjusting certain physical properties of the TMMs. Most commonly, glycerol is employed to adjust the ultrasonic propagation speed of the TMM [16, 37, 41], while varied concentrations of 1-propanol have also been utilized in this regard in gelatin-based hydrogels [19]. Varied alcohol concentrations have an insignificant effect on the attenuation coefficient of the TMM [16], with additional inclusions such as graphite [19] or aluminum oxide powder [20] employed in varying concentrations to regulate the attenuation coefficient of agar or gelatin-based water/alcohol TMMs [19, 20]. Nevertheless, the effect of varied alcohol concentrations on the thermal properties of TMMs has not been investigated. Therefore, in this study, the effect of varied concentrations of two types of alcohol (glycerol and propan-2-ol) on the thermal properties of agar-based TMMs is described, with the TMM exhibiting a thermal conductivity closest to human fat tissue [23] selected and further characterized for its suitability as a fat TMM using US and magnetic resonance imaging (MRI).

Materials and methods

Preparation of fat TMM

Seven water-based TMMs were initially developed with different percent (%) weight per volume (w/v) concentrations of agar (101,614, Merck KGgA, Darmstadt, Germany) for examining the effect of the varied agar concentration (2%, 4%, 6%, 8%, 12%, 16% and 20% w/v) on the thermal properties of the developed phantom. A similar and simple preparation procedure was followed for production of the seven water-based TMMs. Initially, 500 ml of purified deionized water that had undergone degasification, were placed in a beaker and moderately heated utilizing a hotplate magnetic stirrer (SBS A160, Steinberg Systems, Hamburg, Germany).

During the heating process, the water volume was continuously magnetically stirred with its temperature periodically monitored with a digital thermometer (HH806AU, Omega Engineering, Connecticut, USA). Concurrently, an appropriate proportion of granulated agar (101614, Merck KGgA) was pulverized into a fine powder, that was steadily added to the water volume once its temperature slightly exceeded 50 °C. The proportion of agar was carefully selected each time, to result in the corresponding % w/v concentration (2%, 4%, 6%, 8%, 12%, 16%, or 20% w/v). Thereafter, the water-agar solution was continuously stirred and heated until its temperature exceeded 85 °C. This results in breaking of the agar bonds and allows the free hydroxyl groups to form hydrogen bonds with the water solution. Subsequently, the water-agar solution was allowed to cool down to between 50 and 60 °C, while continuously being magnetically stirred. Notably, the water volume that evaporated during the heating procedure was carefully replaced so that the water volume equated the volume that was initially placed in the beaker (500 ml). Once the temperature of the water-agar mixture dropped, the solution was poured inside a specially designed mold. The mold was designed with specific dimensions (6 cm (w) × 15 cm (l) × 6 cm (h)) and was 3D-printed (CR-10, Creality, Shenzhen, China) with Polylactic Acid (PLA) thermoplastic. The mixture was placed in a refrigerator where it was allowed overnight to jellify and completely solidify.

Subsequently, five TMMs were developed with a constant % w/v agar concentration (20% w/v) and utilizing various alcohols, for examining the effect of alcohol addition on the thermal properties. Initially, glycerol (15523, Honeywell, Seelze, Germany) and propan-2-ol (34863, Honeywell) were individually added to a water base with equal % volume per volume (v/v) concentrations of water and alcohol, for investigating the effect of the alcohol type on the thermal properties. In this sense, the following two water/alcohol-based TMMs were developed; one with 50% v/v water and 50% v/v propan-2-ol, and one with 50% v/v water and 50% v/v glycerol. These TMMs were developed following the abovementioned preparation procedure that was slightly differentiated in the sense that initially 500 ml of the water-alcohol mixture were placed in the beaker and heated. The agar concentration was added at the aforementioned temperature threshold (50 °C), with heating and cooling of the solution performed until the mixture reached the aforesaid temperatures (85 °C and 60 °C). The water/alcohol-based TMMs were developed in the PLA mold and were refrigerated overnight. The 0% v/v water and 50% v/v propan-2-ol TMM presented with a slight brown colour and moderate stiffness as shown in Fig. 1.

Additionally, glycerol (15523, Honeywell) and propan-2-ol (34863, Honeywell) were utilized together in varied % v/v concentrations for forming a binary liquid alcohol base

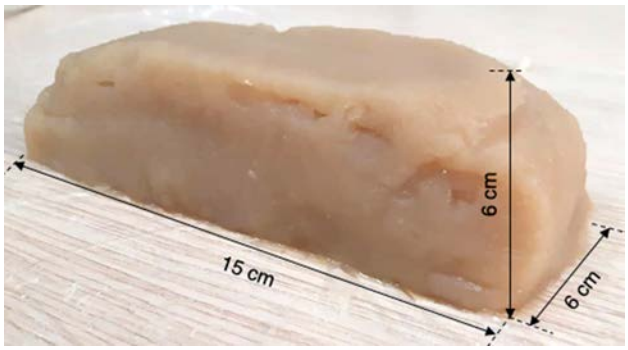

Fig. 1 Photo of the agar/water/propan-2-ol-based TMM (20% w/v agar, 50% v/v water and 50% v/v propan-2-ol)

for examining the effect of a varied alcohol concentration on the thermal properties. In this regard, the following three alcohol-based TMMs were developed; a sample with 100% v/v concentration of glycerol, a sample with 40% v/v glycerol and 60% v/v propan-2-ol and one sample with 33.3% v/v glycerol and 66.7% v/v propan-2-ol. Notably, compared to the water-based and water/alcohol-based phantoms, these three alcohol-based TMMs were developed utilizing a slightly differentiated preparation procedure. Initially, for each sample, the appropriate % v/v alcohol concentrations were placed in the 500 ml beaker for a total alcohol volume of 500 ml. The 500 ml beaker with the alcohol solution was immersed in 300 ml water inside a 1000 ml beaker that was placed on the hotplate magnetic stirrer (SBS A160, Steinberg Systems), thus creating a water bath. The water was continuously heated and magnetically stirred, while during the heating procedure the alcohol solution was manually stirred. The alcohol solution was heated until its temperature was within 70–80 °C, whereupon the agar was added with the appropriate concentration (20% w/v). The powdered agar was gradually added to diminish the formation of agar powder clusters and ensure homogeneous dissolution of agar in the alcohol solution. Thereafter, the agar-alcohol solution continued to be heated in the water bath for approximately half an hour at about 80 °C as shown in Fig. 2. Afterwards, the agar-alcohol solution was removed from the water bath and while manually being stirred was allowed to cool to about 50 °C, whereupon it was poured in the PLA mold and refrigerated overnight. In cases propan-2-ol was utilized in the alcohol base, the propan-2-ol volume that had evaporated throughout the heating procedure was replaced to maintain the appropriate % v/v concentration. The evaporated volume of propan-2-ol was measured by inserting the corresponding initial volume of propan-2-ol in a separate beaker and following the heating procedure for the propan-2-ol solely (no added glycerol or agar) over the same temperatures and timeframe. Therefore, the evaporated volume was equal to the difference between the initial propan-2-ol volume and

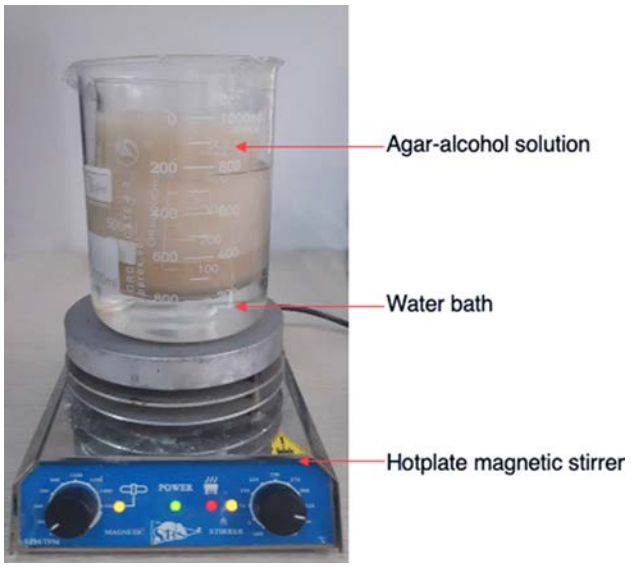

Fig. 2 Photo of the preparation procedure of the agar/alcohol-based TMM with the agar-alcohol solution heated in a water bath

the volume of propan-2-ol remaining after the end of the heating procedure. The alcohol-based TMMs presented with a light brown colour with their stiffness varying according to the % v/v concentration of the alcohol types. In this regard, the 100% v/v glycerol TMM presented with the highest stiffness as shown in Fig. 3. Contrary, the 33.3% v/v glycerol and 66.7% v/v propan-2-ol TMM presented with the fairest stiffness and was wrapped in a plastic membrane as shown in Fig. 4.

Experimental estimation of the thermal properties of the fat TMMs

The thermal conductivity of the various TMMs was experimentally measured within 24 h of fabrication. Prior to the measurements, the TMMs were removed from the

Fig. 3 Photo of the agar/glycerol-based TMM (20% w/v agar and 100% v/v glycerol)

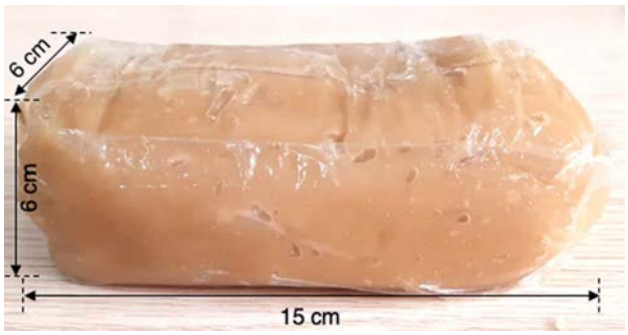

Fig. 4 Photo of the agar/glycerol/propan-2-ol-based TMM (20% w/v agar, 33.3% v/v glycerol and 66.7% v/v propan-2-ol)

refrigerator and were allowed to reach thermal equilibrium with the laboratory environment. The thermal conductivity of each TMM was measured by employing a portable heat transfer analyzer (Isomet model 2104, Applied Precision, Bratislava, Slovakia). Various sensors can be incorporated on the analyzer for automatic measurement of the thermal conductivity, thermal diffusivity, and volumetric heat capacity by utilizing the transient method, where the sensors heat the material under investigation and measure thermal properties from the temperature change rate [42]. A needle sensor (S/N 09030019, Applied Precision) with a measurement range of 0.2–1 W/m K was employed for experimental measurement of the thermal properties of each TMM. The needle sensor was inserted in its entirety centrally along the longitudinal axis of each TMM, since according to the manufacturer a minimum radius of 4 cm of material is required around the needle probe for accurate measurements of the thermal conductivity (5% of reading + 0.001 W/m K). In this sense, the dimensions of the PLA molds that were utilized for production of the TMMs were carefully selected to account for these requirements for accurate experimental measurements of the thermal properties. Although all three thermal properties (thermal conductivity, thermal diffusivity, and volumetric heat capacity) were acquired for each TMM, only thermal conductivity values are reported in the present study. For each TMM, four measurements of the thermal conductivity were acquired, and the average value of thermal conductivity was calculated. Individual measurements of thermal conductivity were rapid, requiring approximately 15–20 min.

Characterization of the fat-soft TMM

The TMM exhibiting the lowest thermal conductivity with a value closest to the range of thermal conductivity for human fat tissue [23], was considered as the ultimate fat TMM and is referred to as such for the rest of this study. For the purposes of simulating the anatomy of human soft tissue [4],

the homogeneous fat TMM was placed with an approximate height of 2 cm on top of a homogeneous agar-based phantom doped with silicon dioxide [42–45]. The agar-based phantom was developed with 6% w/v agar (101614, Merck KGgA) and 4% w/v silicon dioxide (S5631, Sigma Aldrich, Missouri, USA) following the same preparation procedure reported by Drakos et al. [43]. These concentrations of agar (6% w/v) and silicon dioxide (4% w/v) were specifically chosen to result in a TMM with similar acoustic properties with human muscle tissue [43] as well as comparable magnetic properties with different body tissues [46]. The agar/silicon dioxide TMM was developed in a 3D-printed (CR-10, Creality) PLA mold with dimensions 7 cm (w) × 9 cm (l) × 6 cm (h). For the rest of the manuscript, the combined fat TMM and agar/silicon dioxide TMM are referred to as the fat-soft TMM.

US imaging of the fat-soft TMM

The fat-soft TMM was imaged utilizing a conventional diagnostic US system (DP-50, Shenzhen Mindray Bio-Medical Electronics Co., Shenzhen, China). The US images were utilized for examining the sonographic appearance and echogenicity of the fat-soft TMM. US images were individually acquired for the soft TMM, the fat TMM as well as the interface of the fat-soft TMM.

MRI imaging of the fat-soft TMM

The fat-soft TMM was placed in a 3 T MRI scanner (Magneton Vida, Siemens Healthineers, Erlangen, Germany) and imaged utilizing a body coil (Body 18, Siemens Healthineers). High-resolution images were acquired on axial plane using T1-Weighted Turbo Spin Echo (T1-W TSE) and T2-Weighted Turbo Spin Echo (T2-W TSE) sequences. The T1-W TSE image was acquired with the following parameters: Repetition Time (TR) = 700 ms, Echo Time (TE) = 12 ms, Echo Train Length (ETL) = 2, Matrix = 256 × 256, Field of View (FOV) = 20 × 20 cm^2, Flip Angle (FA) = 160°, Number of Excitations (NEX) = 1 and slice thickness = 10 mm. Correspondingly, the T2-W TSE image was acquired with TR = 2500 ms, TE = 48 ms, ETL = 16, Matrix = 320 × 320, FOV = 20 × 20 cm^2, FA = 180°, NEX = 1 and slice thickness = 10 mm.

Results

Experimental estimation of the thermal properties of the fat TMMs

Initially, the thermal conductivities of the seven water-based TMMs having varied % w/v agar concentrations (2%, 4%, 6%, 8%, 12%, 16% and 20% w/v) were measured for assessing the effect of the increasing agar concentration on the thermal conductivity. Increased stiffness of the phantoms was observed with increasing % w/v concentrations of agar. For each TMM, the average value of thermal conductivity from four individual measurements was reported. Figure 5 shows the average thermal conductivity as measured for each of the TMMs having varied % w/v concentrations of agar. Following linear regression analysis ($R^2 = 0.969$), an inverse correlation was observed between thermal conductivity and increased % w/v concentration of agar, with thermal conductivities in the range of 0.524–0.445 W/m K for 2–20% w/v agar concentrations. Nevertheless, only a small decrement of thermal conductivity was observed with increasing % w/v agar concentration, with the thermal conductivity decreased by 0.0042 W/m K for a unit increase in the % w/v agar concentration.

Thereafter, thermal conductivity was measured for the five TMMs developed with 20% w/v agar and varied % v/v concentrations of water, glycerol, and propan-2-ol. The thermal conductivity was measured for the two water/alcohol-based TMMs (one 50% v/v water and 50% v/v propan-2-ol, and one 50% v/v water and 50% v/v glycerol) for examining the effect of alcohol type on the thermal conductivity, as well as the three alcohol-based TMMs (one 100% v/v glycerol, one 40% v/v glycerol and 60% v/v propan-2-ol, and one 33.3% v/v and 66.7% propan-2-ol) for investigating the effect of alcohol concentration on the thermal conductivity. Similarly, thermal conductivity measurements for each of the five TMMs were performed four times and the average value of the four measurements was acquired. Figure 6 shows the average value of the thermal conductivity for each of the five TMMs containing alcohols. Figure 6 additionally includes the thermal conductivity value (0.445 W/m K) of the water-based TMM (100% v/v water) with the analogous agar concentration (20% w/v) for comparison purposes. The addition of alcohol decreased the thermal conductivity, with

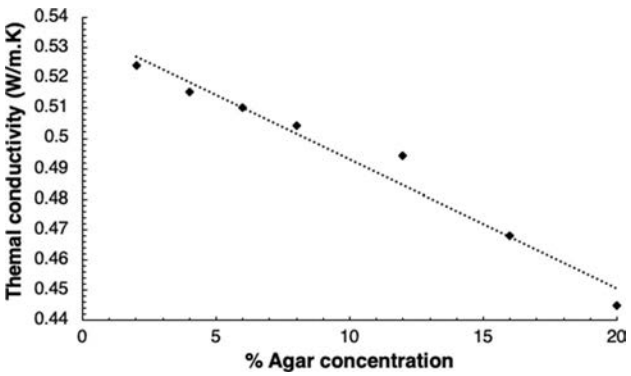

Fig. 5 Average thermal conductivity of the agar/water-based TMMs having varied % w/v concentrations of agar

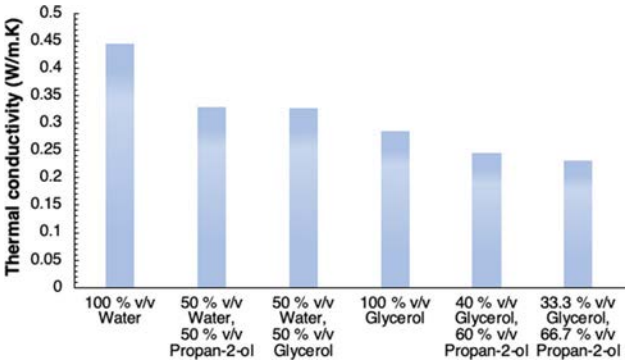

Fig. 6 Average thermal conductivity of the 20% w/v agar-based TMMs having varied concentrations of water, glycerol and propan-2-ol

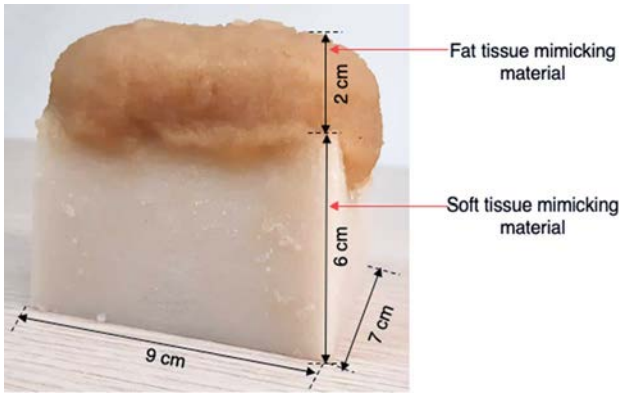

Fig. 7 Photo of the fat-soft TMM with the soft TMM developed with a muscle-like recipe (6% w/v agar and 4% w/v silicon dioxide) and the fat TMM developed with the optimum recipe (20% w/v agar, 33.3% v/v glycerol and 66.7% v/v propan-2-ol)

the average thermal conductivity values of the two water/alcohol-based TMMs approximately similar for a 50% v/v concentration of either propan-2-ol (0.33 W/m K) or glycerol (0.327 W/m K). Further reductions in the average thermal conductivity were observed for the three alcohol-based TMMs, with the 100% v/v glycerol TMM reporting a mean thermal conductivity of 0.286 W/m K. Similarly, addition of propan-2-ol in either 60% or 66.7% v/v concentrations further reduced the thermal conductivity to 0.246 W/m K and 0.231 W/m K respectively.

Characterization of the fat-soft TMM

The alcohol-based TMM developed with 20% w/v agar, 33.3% v/v glycerol and 66.7% v/v propan-2-ol exhibited the lowest thermal conductivity (0.231 W/m K) and was thus considered as the fat TMM. Therefore, it was removed from the plastic membrane and placed on top of the agar/silicon dioxide, resulting in the fat-soft TMM as shown in Fig. 7.

US imaging of the fat-soft TMM

Figure 8 shows the US images acquired for the soft TMM (Fig. 8A), fat TMM (Fig. 8B), and the interface of the fat-soft TMM (Fig. 8C). The soft TMM appeared homogeneous and highly echogenic as shown in Fig. 8A. Contrary, the fat TMM appeared with reduced echogenicity on its acquired US image (Fig. 8B), while it was shown hypoechoic relative to the soft TMM on the US image acquired on the interface of the fat-soft TMM (Fig. 8C).

MRI imaging of the fat-soft TMM

Figure 9A and B respectively show the acquired axial T1-W TSE and T2-W TSE images of the fat-soft TMM. Generally, the fat-soft TMM appeared relatively homogeneous with no artifacts on the acquired MRI images. The soft TMM appeared with similar intensity on both images (bottom layer in Fig. 9A and B), while the fat TMM appeared with increased brightness on the T1-W TSE image (top layer in Fig. 9A) and with relatively low brightness on the T2-W TSE image (top layer in Fig. 9B).

Discussion

In the present study, agar-based TMMs intended for HIFU applications were developed and characterized for their suitability to mimic the thermal properties of human fat tissue, and specifically thermal conductivity. Twelve TMMs were developed in an iterative approach using varied concentrations of agar, water, glycerol, and propan-2-ol, with experimental measurements of their thermal conductivity performed with the transient method [42]. The TMM exhibiting a thermal conductivity closest to the range of thermal conductivities reported for human fat tissue [23], was considered as the optimum fat TMM and was further characterized for its appearance on US and MRI images.

Following the vast use of agar in an aqueous base for TMMs for MRI-guided HIFU applications [44, 45, 47], seven TMMs were initially developed with a water base and varied concentrations of agar (2%, 4%, 6%, 8%, 12%, 16% and 20% w/v) for investigating the effect of the agar concentration on the thermal conductivity. Agar concentration emerged as a modifier of thermal conductivity, with increased % w/v concentrations resulting in reduced thermal conductivity values. Notably, the inverse correlation between increased agar concentration and thermal conductivity observed herein is corroborated by similar relations reported in the studies by Cho et al. [48] and Zhang et al. [49] for the thermal conductivities of other agar-based TMMs. Nevertheless, herein, increased % w/v agar concentrations resulted in minor reductions in thermal conductivity

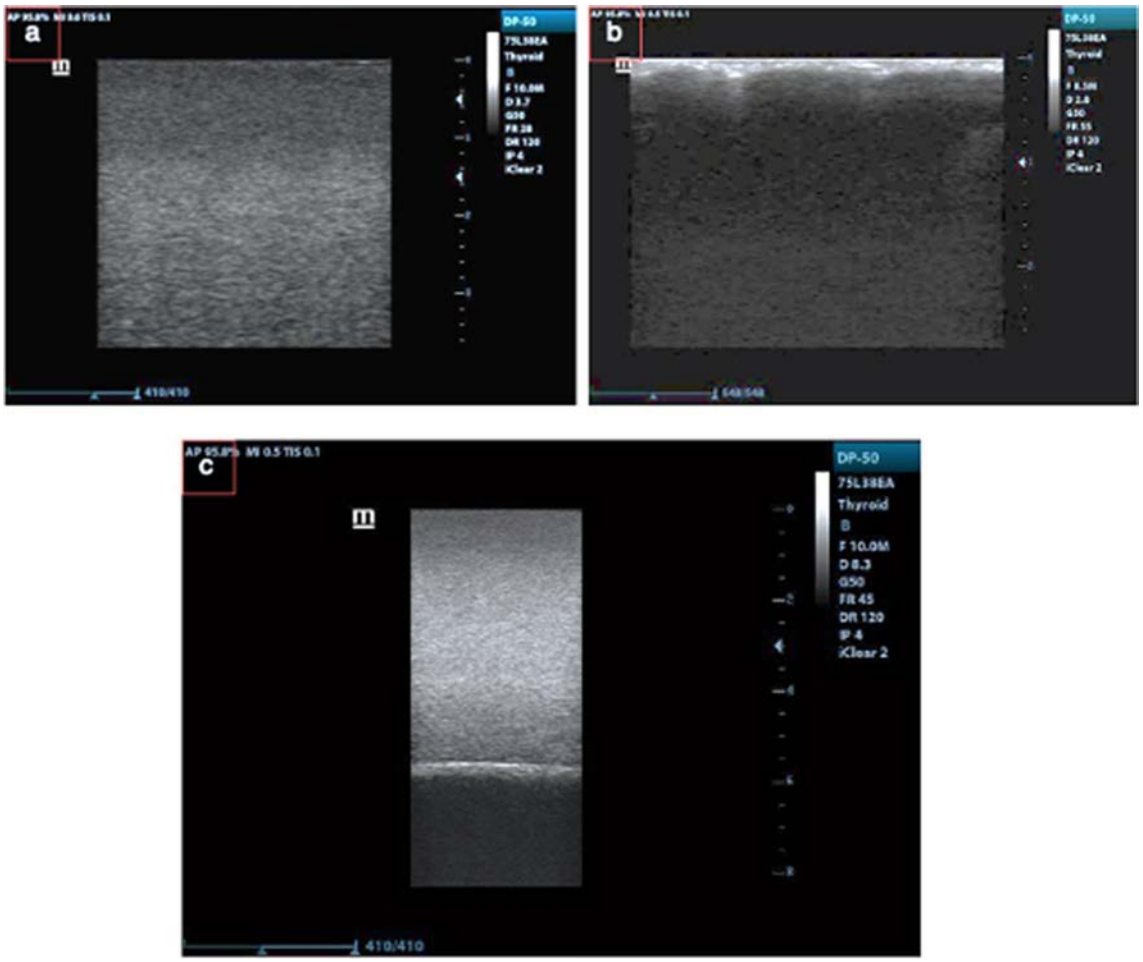

Fig. 8 Ultrasound images of the fat-soft TMM individually acquired for **a** the soft TMM, **b** fat TMM, and **c** the interface of the fat-soft TMM with the soft TMM on top and the fat TMM on the bottom

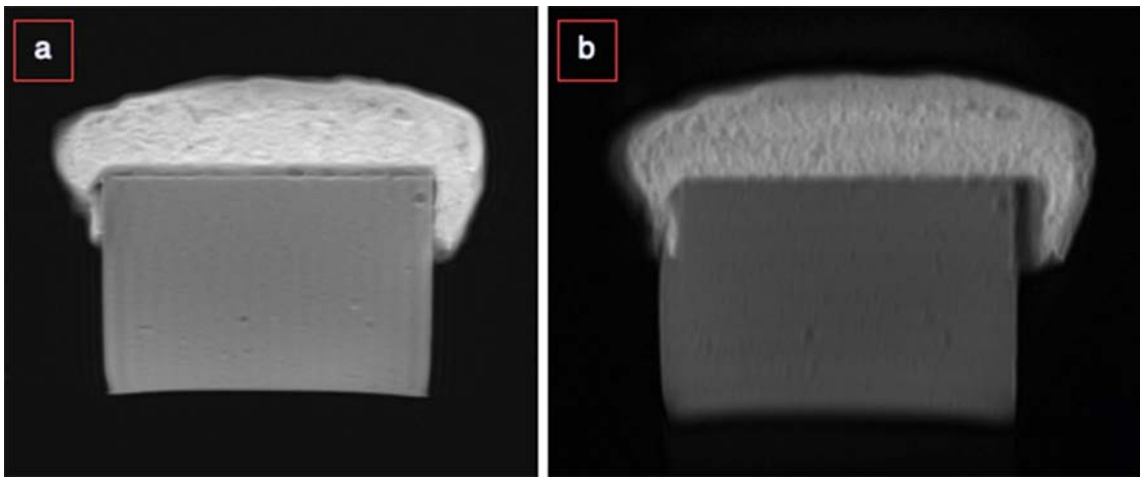

Fig. 9 MRI images of the fat-soft TMM acquired on axial plane with **a** T1-W TSE, and **b** T2-W TSE sequences. Soft TMM in bottom layer and fat TMM in top layer

as well as increased stiffness of the phantoms. The latter was expected, since it is widely known that increased mechanical stiffness is observed with increased agar concentrations [16]. Therefore, TMMs with agar concentrations greater than 20% w/v were not investigated, since these would result in TMMs of extreme stiffness that would not only prohibit insertion of the needle sensor in the TMM for measurement of the thermal conductivity, but would also be atypical of the stiffness of human fat tissue.

In this regard, agar concentration was limited to 20% w/v, and glycerol and propan-2-ol were individually added with a 50% v/v concentration in a water base, for forming two water/alcohol-based TMMs. Addition of alcohol decreased the thermal conductivity of the TMM by approximately 25% from the thermal conductivity value of the water-based TMM with the corresponding agar concentration (20% w/v). Alcohol type (glycerol or propan-2-ol) did not seem to affect the thermal conductivity value, since no significant difference was observed between the thermal conductivities of the two water/alcohol-based TMMs, despite the lower range of thermal conductivities reported in the literature for propan-2-ol (0.127–0.133 W/m K) [24] compared to glycerol (0.291–0.297 W/m K) [31].

Notably, utilization of the two alcohols (glycerol and propan-2-ol) for three alcohol-based TMMs further reduced the thermal conductivity of the TMM. As expected, agar easily dissolved and bonded with the alcohol solutions, with the thermal conductivity of the glycerol-based TMM (100% v/v glycerol) substantially lower than the thermal conductivity of the respective water-based or water/glycerol-based TMMs. Moreover, the thermal conductivity of the 100% v/v glycerol-based TMM reported herein, was comparative to and somewhat lower than the literature value for the thermal conductivity of pure glycerol [31], probably as a result of the added agar. Moreover, due to the lower thermal conductivity of propan-2-ol [24], its addition respectively decreased the thermal conductivity of the TMMs. An increased % v/v concentration of propan-2-ol was a significant modifier of the thermal conductivity of the TMM, reaching up to 20% reduction from the thermal conductivity of the 100% v/v glycerol-based TMM. Notably, utilization of 33.3% v/v glycerol and 66.7% propan-2-ol for a 20% w/v agar concentration, resulted in a TMM with a thermal conductivity value (0.231 W/m K) approximately close to the range of thermal conductivities reported for human fat tissue [23]. In this regard, this specific phantom was considered as the fat TMM and was further evaluated.

US and MRI characterization of the fat TMM was performed following its placement on an agar/silicon dioxide TMM [43] exhibiting similar acoustic [43] and magnetic properties [46] with human soft tissue. In this regard, the combination of the homogeneous fat and soft TMMs were macroscopically simulating human anatomy, where tissues and organs are surrounded by fat [4]. US images of the soft TMM (6% w/v agar and 4% w/v silicon dioxide) showed the developed TMM appearing with similar texture and echogenicity with a phantom of the same recipe as reported in the study by Drakos et al. [43], thus approximating US signal of human soft tissues. Contrary, acquired US images of the fat TMM resulted in minimal echogenicity. Similar US imaging difficulties were previously reported for an agar-based breast fat TMM developed for US and microwave imaging with the artifacts attributed to the increased attenuation of fat tissue [50]. In this regard, hypoechogenicity of the fat TMM developed herein could indicate increased acoustic attenuation, with the fat TMM resembling the sonographic appearance reported clinically for breast fat tissue [51] as well as perirenal and abdominal fat tissues [52]. Correspondingly, the MRI appearance of the fat TMM simulated the MRI visibility of fatty tissues that appear with increased and decreased intensity on T1-Weighted and T2-Weighted images respectively [53].

Generally, utilization of glycerol and propan-2-ol in appropriate concentrations (33.3% v/v glycerol and 66.7% v/v propan-2-ol) resulted in an agar-based (20% w/v) fat TMM with the desirable thermal conductivity. The measured thermal conductivity of the fat TMM (0.231 W/m K) was similar to the thermal conductivity value of the fat-like compartment (90% fat saturated-oil) of a heterogeneous agar-based TMM intended for RF ablation [36], slightly higher than the thermal conductivity of a gelatin-based fat TMM for RF ablation [34], and lower than the thermal conductivity of other gelatin-based fat TMMs [33]. More importantly, the fat TMM proposed in the present study resembles the US and MRI visibility of human fat tissue. As a result, the proposed TMM possesses fat-like thermal, US and MRI properties and could thus have potential use in HIFU applications as a fat TMM, simulating and accounting for thermal energy lost due to intervening fat tissue. Development of the fat TMM is easy and requires a moderate amount of preparation time (~ 1.5 h). Moreover, the materials utilized for the fat TMM are non-toxic, cost-effective, and have a long lifespan, therefore minimal perishability and bacterial contamination are expected. Nevertheless, storage of the fat TMM developed herein is recommended to be performed in an airtight container to prevent the evaporation of propan-2-ol.

Author contributions All authors contributed to the study conception and design. AF contributed to the drafting of the manucript and the experimental work. IL contributed to the experimental work. CD supervised the experimental work and the drafting of the manuscript. All authors read and approved the final manuscript.

Funding This work was funded by the Research & Innovation Foundation of Cyprus under the project SOUNDPET (INTEGRATED/0918/0008).

Availability of data and material All data generated or analyzed in the present study are available from the authors upon request.

Code availability Not applicable.

Declarations

Conflict of interest The authors have no relevant financial or non-financial interests to disclose.

Ethical approval This study was performed on tissue mimicking materials and no human participants or animals were included. In this regard, an approval from an institutional review board or ethics committee was not required.

Consent to participate Not applicable.

Consent for publication Not applicable.

References

1. Mobashsher AT, Abbosh AM (2015) Artificial human phantoms: Human proxy in testing microwave apparatuses that have electromagnetic interaction with the human body. IEEE Microw Mag 16(6):42–62. https://doi.org/10.1109/MMM.2015.2419772
2. ter Haar G, Coussios C (2007) High intensity focused ultrasound: Physical principles and devices. Int J Hyperth 23(2):89–104. https://doi.org/10.1080/02656730601186138
3. Ahmad MS, Suardi N, Shukri A, Mohammad H, Oglat AA, Alarab A, Makhamrah O (2020) Chemical characteristics, motivation and strategies in choice of materials used as liver phantom: a literature review. J Med Ultrasound 28(1):7–16. https://doi.org/10.4103/JMU.JMU_4_19
4. Hazari A, Maiya AG, Nagda TV (2021) Cellular biomechanics of soft tissues. Conceptual biomechanics and kinesiology. Springer, Singapore, pp 19–27. https://doi.org/10.1007/978-981-16-4991-2_2
5. Culjat MO, Goldenberg D, Tewari P, Singh RS (2010) A review of tissue substitutes for ultrasound imaging. Ultrasound Med Biol 36(6):861–873. https://doi.org/10.1016/j.ultrasmedbio.2010.02.012
6. Shen C, Lyu L, Wang G, Wu J (2019) A method for ultrasound probe calibration based on arbitrary wire phantom. Cogent Eng. https://doi.org/10.1080/23311916.2019.1592739
7. Wen T, Wang C, Zhang Y, Zhou S (2020) A novel ultrasound probe spatial calibration method using a combined phantom and stylus. Ultrasound Med Biol 46(8):2079–2089. https://doi.org/10.1016/j.ultrasmedbio.2020.03.018
8. Glacomini A (1947) Ultrasonic velocity in ethanol-water mixtures. J Acoust Soc Am 19(4):701–702. https://doi.org/10.1121/1.1916541
9. Burlew MM, Madsen EL, Zagzebski JA, Banjavic RA, Sum SW (1980) A new ultrasound tissue-equivalent material. Radiology 134(2):517–520. https://doi.org/10.1148/radiology.134.2.7352242
10. Cook JR, Bouchard RR, Emelianov SY (2011) Tissue-mimicking phantoms for photoacoustic and ultrasonic imaging. Biomed Opt Express 2(11):3193–3206. https://doi.org/10.1364/boe.2.003193
11. McGarry CK, Grattan LJ, Ivory AM et al (2020) Tissue mimicking materials for imaging and therapy phantoms: a review. Phys Med Biol 65:23TR01. https://doi.org/10.1088/1361-6560/abbd17
12. Gustavsson PE, Son POL (2003) Monolithic polysaccharide materials. Journal of chromatography library, vol 67. Elsevier Science, Amsterdam, pp 121–141
13. Tako M, Tamaki Y, Teruya T, Takeda Y (2014) The principles of starch gelatinization and retrogradation. Food Nutr Sci 5(3):280–291. https://doi.org/10.4236/fns.2014.53035
14. Gamini A, Toffanin R, Murano E, Rizzo R (1997) Hydrogen-bonding and conformation of agarose in methyl sulfoxide and aqueous solutions investigated by 1H and 13C NMR spectroscopy. Carbohyd Res 304(3–4):293–302. https://doi.org/10.1016/S0008-6215(97)00232-2
15. Kaczmarek K, Mrówczyński R, Hornowski T, Bielas R, Józefczak A (2019) The effect of tissue-mimicking phantom compressibility on magnetic hyperthermia. Nanomaterials 9(5):803. https://doi.org/10.3390/nano9050803
16. Madsen EL, Hobson MA, Shi H, Varghese T, Frank GR (2005) Tissue-mimicking agar/gelatin materials for use in heterogeneous elastography phantoms. Phys Med Biol 50(23):5597–5618. https://doi.org/10.1088/0031-9155/50/23/013
17. Holt RG, Roy RA (2001) Measurements of bubble-enhanced heating from focused, MHz-frequency ultrasound in a tissue-mimicking material. Ultrasound Med Biol 27(10):1399–1412. https://doi.org/10.1016/S0301-5629(01)00438-0
18. Kato H, Hiraoka M, Ishida T (1986) An agar phantom for hyperthermia. Med Phys 13(3):396–398. https://doi.org/10.1118/1.595882
19. Madsen EL, Zagzebski JA, Banjavie RA, Jutila RE (1978) Tissue mimicking materials for ultrasound phantoms. Med Phys 5(5):391–394. https://doi.org/10.1118/1.594483
20. Ramnarine KV, Anderson T, Hoskins PR (2001) Construction and geometric stability of physiological flow rate wall-less stenosis phantoms. Ultrasound Med Biol 27(2):245–250. https://doi.org/10.1016/S0301-5629(00)00304-5
21. Dabbagh A, Abdullah BJJ, Ramasindarum C, Abu Kasim NH (2014) Tissue-mimicking gel phantoms for thermal therapy studies. Ultrason Imaging 36(4):291–316. https://doi.org/10.1177/0161734614526372
22. Demirel Y (2013) Nonequilibrium thermodynamics transport and rate processes in physical, chemical and biological systems, 3rd edn. Elsevier Science, Amsterdam
23. Hatfield HS, Pugh LGC (1951) Thermal conductivity of human fat and muscle. Nature 168(4282):918–919. https://doi.org/10.1038/168918a0
24. Ogiwara K, Arai Y, Saito S (1982) Thermal conductivities of liquid alcohols and their binary mixtures. J Chem Eng Jpn 15(5):335–342. https://doi.org/10.1252/jcej.15.335

25. Woolf JR, Sibbitt WL (1954) Thermal Conductivity of Liquids. Ind Eng Chem 46(9):1947–1952. https://doi.org/10.1021/ie50537a049
26. Turgut A, Tavman I, Tavman S (2009) Measurement of thermal conductivity of edible oils using transient hot wire method. Int J Food Prop 12(4):741–747. https://doi.org/10.1080/10942910802023242
27. Wrenick S, Sutor P, Pangilinan H, Schwarz EE (2005) Heat transfer properties of engine oils. Proc World Tribol Congr III 1:595–596. https://doi.org/10.1115/wtc2005-64316
28. Lavrykov SA, Ramarao BV (2012) Thermal properties of copy paper sheets. Drying Technol 30(3):297–311. https://doi.org/10.1080/07373937.2011.638148
29. Watson E (1975) Thermal properties of butter. Can Agric Eng 17(2):68–71
30. Eltom OMM, Sayigh AAM (1994) A simple method to enhance thermal conductivity of charcoal using some additives. Renew Energy 4(1):113–118. https://doi.org/10.1016/0960-1481(94)90072-8
31. Takizawa S, Murata H, Nagashima A (1978) Measurement of the thermal conductivity of liquids by transient hot-wire method I : measurement at atmospheric pressure. Bull Jpn Soc Mech Eng 21(152):273–278. https://doi.org/10.1299/jsme1958.21.273
32. Maccarthy DA, Fabre N (1989) Thermal conductivity of sucrose. In: Singh RP, Medina AG (eds) Food properties and computer-aided engineering of food processing systems, vol 168. Springer, Dordrecht, pp 105–111
33. Robinson MP, Richardson MJ, Green JL, Preece AW (1991) New materials for dielectric simulation of tissues. Phys Med Biol 36(12):1565–1571. https://doi.org/10.1088/0031-9155/36/12/002
34. Yuan Y, Wyatt C, Maccarini P et al (2012) A heterogeneous human tissue mimicking phantom for RF heating and MRI thermal monitoring verification. Phys Med Biol 57(7):2021–2037. https://doi.org/10.1088/0031-9155/57/7/2021
35. Lazebnik M, Madsen EL, Frank GR, Hagness SC (2005) Tissue-mimicking phantom materials for narrowband and ultrawideband microwave applications. Phys Med Biol 50(18):4371–4384. https://doi.org/10.1088/0031-9155/50/18/001
36. Liu Z, Ahmed M, Weinstein Y, Yi M, Mahajan RL, Goldberg NS (2006) Characterization of the RF ablation-induced 'oven effect': the importance of background tissue thermal conductivity on tissue heating. Int J Hyperth 22(4):327–342. https://doi.org/10.1080/02656730600609122
37. Kim MS, Kim JY, Du Jung H, Kim JY, Choi HH (2014) A fat-tissue mimic phantom for therapeutic ultrasound. IEIE Trans Smart Process Comput 3(3):153–157. https://doi.org/10.5573/IEIESPC.2014.3.3.153
38. Jewell ML, Solish NJ, Desilets CS (2011) Noninvasive body sculpting technologies with an emphasis on high-intensity focused ultrasound. Aesthetic Plast Surg 35(5):901–912. https://doi.org/10.1007/s00266-011-9700-5
39. Gadsden E, Aguilar MT, Smoller BR, Jewell ML (2011) Evaluation of a novel high-intensity focused ultrasound device for ablating subcutaneous adipose tissue for noninvasive body contouring: Safety studies in human volunteers. Aesthetic Surg J 31(4):401–410. https://doi.org/10.1177/1090820X11405027
40. Chen C, Li WZ, Song YC, Yang J (2009) Hydrogen bonding analysis of glycerol aqueous solutions: a molecular dynamics simulation study. J Mol Liq 146(1–2):23–28. https://doi.org/10.1016/j.molliq.2009.01.009
41. Oglat AA, Matjafri MZ, Suardi N et al (2018) Chemical items used for preparing tissue-mimicking material of wall-less flow phantom for Doppler ultrasound imaging. J Med Ultrasound 26(3):123–127. https://doi.org/10.4103/JMU.JMU_13_17
42. Menikou G, Damianou C (2017) Acoustic and thermal characterization of agar based phantoms used for evaluating focused ultrasound exposures. J Ther Ultrasound 5:14. https://doi.org/10.1186/s40349-017-0093-z
43. Drakos T, Antoniou A, Evripidou N et al (2021) Ultrasonic attenuation of an agar, silicon dioxide, and evaporated milk gel phantom. J Med Ultrasound 29(4):239–249. https://doi.org/10.4103/JMU.JMU_145_20
44. Menikou G, Dadakova T, Pavlina M, Bock M, Damianou C (2015) MRI compatible head phantom for ultrasound surgery. Ultrasonics 57:144–152. https://doi.org/10.1016/j.ultras.2014.11.004
45. Menikou G, Yiannakou M, Yiallouras C, Ioannides C, Damianou C (2018) MRI-compatible breast/rib phantom for evaluating ultrasonic thermal exposures. Int J Med Robot Comput Assist Surg 14(1):1–12. https://doi.org/10.1002/rcs.1849
46. Antoniou A, Georgiou L, Christodoulou T, Panayiotou N, Ioannides C, Zamboglou N, Damianou C (2022) MR relaxation times of agar-based tissue-mimicking phantoms. J Appl Clin Med Phys 23:e13533. https://doi.org/10.1002/acm2.13533
47. Drakos T, Giannakou M, Menikou G, Constantinides G, Damianou C (2021) Characterization of a soft tissue-mimicking agar/wood powder material for MRgFUS applications. Ultrasonics 113:106357. https://doi.org/10.1016/j.ultras.2021.106357
48. Cho J, Prasad B, Kim JK (2018) Near-infrared laser irradiation of a multilayer agar-gel tissue phantom to induce thermal effect of traditional moxibustion. J Innov Opt Health Sci. https://doi.org/10.1142/S1793545818500335
49. Zhang M, Che Z, Chen J, Zhao H, Yang L, Zhong Z, Lu J (2011) Experimental determination of thermal conductivity of water-agar gel at different concentrations and temperatures. J Chem Eng Data 56(4):859–864. https://doi.org/10.1021/je100570h
50. Li S, Fear E, Curiel L (2021) Breast tissue mimicking phantoms for combined ultrasound and microwave imaging. Phys Med Biol 66:245011. https://doi.org/10.1088/1361-6560/ac3d18
51. Venta LA, Dudiak CM, Salomon CG, Flisak ME (1994) Sonographic evaluation of the breast. Radiographics 14(1):29–50. https://doi.org/10.1148/radiographics.14.1.8128064
52. Spencer GM, Rubens DJ, Roach DJ (1995) Hypoechoic fat: a sonographic pitfall. Am J Roentgenol 164(5):1277–1280. https://doi.org/10.2214/ajr.164.5.7717247
53. Bloem JL, Reijnierse M, Huizinga TWJ, Van Der Helm-Van Mil AHM (2018) MR signal intensity: staying on the bright side in MR image interpretation. Rheum Musculoskelet Dis Open 4:e000728. https://doi.org/10.1136/rmdopen-2018-000728

Received: 10 May 2022 | Revised: 22 July 2022 | Accepted: 23 July 2022

DOI: 10.1002/rcs.2447

ORIGINAL ARTICLE

The International Journal of Medical Robotics and Computer Assisted Surgery

WILEY

Robotic device for transcranial focussed ultrasound applications in small animal models

Anastasia Antoniou[1] | Marinos Giannakou[2] | Elena Georgiou[3] | Kleopas A. Kleopa[3] | Christakis Damianou[1]

[1]Department of Electrical Engineering, Computer Engineering, and Informatics, Cyprus University of Technology, Limassol, Cyprus

[2]R&D, Medsonic Ltd, Limassol, Cyprus

[3]Department of Neuroscience, The Cyprus Institute of Neurology and Genetics, Nicosia, Cyprus

Correspondence
Christakis Damianou, Department of Electrical Engineering, Computer Engineering, and Informatics, Cyprus University of Technology, 30 Archbishop Kyprianou Street, 3036 Limassol, Cyprus.
Email: christakis.damianou@cut.ac.cy

Funding information
Research and Innovation Foundation of Cyprus, Grant/Award Number: SOUNDPET (INTEGRATED/0918/0008); Piccolo Grande Guerriero - Associazione Malattia PMLD, Grant/Award Number: 2020-22 Grant

Abstract

Background: Focussed Ultrasound (FUS) combined with microbubbles (MBs) was proven a promising modality for non-invasive blood brain barrier disruption (BBBD). Herein, two devices for FUS-mediated BBBD in rodents are presented.

Methods: A two-axes robotic device was manufactured for navigating a single element FUS transducer of 1 MHz relative to the brain of rodents. A second more compact device featuring a single motorized vertical axis was also developed. Their performance was assessed in terms of motion accuracy, MRI compatibility and trans-skull BBBD in wild type mice using MBs in synergy with pulsed FUS.

Results: Successful BBBD was evidenced by the Evans Blue dye method, as well as by Fibronectin and Fibrinogen immunostaining. BBB permeability was enhanced when the applied acoustic intensity was increased.

Conclusions: The proposed devices constitute a cost-effective and ergonomic solution for FUS-mediated BBBD in small animal models. Further experimentation is needed to examine the repeatability of results and optimise the therapeutic protocol.

KEYWORDS
BBB disruption, focussed ultrasound, mice, MRI compatible, robotic device, transcranial

1 | INTRODUCTION

Penetration of the blood-brain barrier (BBB) to deliver medication into the brain is a subject that has aroused the interest of many research groups. The techniques available so far are not very effective. The BBB, which is the body's defence against toxic substances, also provides resistance to the supply of therapeutic agents. Therefore, the provision of medication to the brain is a main problem to overcome. In this regard, focussed ultrasound (FUS) seems to be an alternative completely non-invasive method that can enhance treatment against neurodegenerative diseases.[1]

It has been shown that opening of the BBB can be achieved with the use of therapeutic ultrasound and the administration of microbubbles (MBs).[2] This process is reversible, thus maintaining the ability of the brain to stay protected against harmful substances. Specifically, application of pulsed FUS induces various mechanical phenomena in tissue, which in synergy with MBs, loosen the endothelial cell connections allowing medication to reach the brain.[3] This method is targeted since the ultrasonic energy is focussed at a specific area of the brain, thus reducing the risk for complications from the process.[4] The relaxation of the endothelial ligaments is completely reversible, with complete recovery occurring within a few hours after the treatment.[5] Since low intensity FUS is used, the temperature remains at safe levels.

The application of this method for disrupting the BBB has been tested in various animal models, but mostly evaluated in mice and

rats.[6–8] Due to their small size, mice are easier to handle and allow the use of more economical infrastructure, compared to larger animals. However, their small size also appeared to be a challenge in terms of accurate targeting in the laboratory environment, where MRI feedback is not available. For this reason, various experimental devices have been used by several research groups involved in the field to facilitate studies in small animal models.

The team of Konofagou did remarkable work in the field using a 3-axis robotic system (Velmex Inc., Lachine, QC, Canada).[9–13] The FUS transducer was attached to the positioning system, as well as to a water-filled cone. Another water tank featuring an acoustic opening at the bottom was used,[9–12] and coupled to the mouse head using ultrasound gel.[13] The water tank was stable allowing the transducer as integrated with the water-filled cone to move inside the tank relative to the target, without affecting the coupling with the mouse head.

A manual mounting system was proposed by the team of Hynynen.[5] The mouse was placed in the supine position above a water container. The transducer was positioned in the container under the mouse head and acoustic coupling was achieved using a bag filled with water. Similar experimental setups as the ones described above with some modifications were used in relevant studies.[14–17]

There are also systems available in the market that were developed for research activities. An example is the PK50 system offered by the FUS Instruments company (Toronto, Canada). The system has 3 degrees of freedom (DOF) for transducer positioning.[18] This company also offers another mounting device with 3 DOF, which approaches the target from the bottom (LP100, FUS Instruments, Toronto, Canada).[18] Another company that offers robotic devices for research purposes is Verasonics (Kirkland WA, USA).[19] The company owns a robotic system with 2 DOF, where ultrasonic coupling is achieved using a water filled bladder. The guidance of the system is achieved with diagnostic ultrasound.[19]

Image guided therapy manufactures robotic systems compatible with MRI. This company offers 2 different robotic systems[20] featuring 5 DOF. These systems are intended for various therapeutic ultrasound applications. However, they are complex and thus not ergonomic, especially for small animal experiments.[20]

The company Sonovol focuses on imaging modalities for preclinical applications,[21] but it also offers a preclinical device for FUS applications guided by three-dimensional ultrasound combined with acoustic angiography. The system was designed to assist research with therapeutic ultrasound, given that fusion of ultrasound imaging and angiography can be beneficial for guiding BBB disruption (BBBD). Notably, the system offers a wide field of view combining the two imaging modalities.

Robotic-assistance was introduced in many studies to improve the accuracy of ultrasonic targeting.[22–27] As an example, Kujawska et al.[25,26] developed a computer-controlled robotic system with 4 DOF for FUS ablation preclinical studies. The 4 DOF positioner is attached on a water-filled tank to maneuver a dedicated platform that carries the target relative to the FUS transducer, which is fixed coaxially with an ultrasound imaging probe on the bottom of the tank facing towards the underside of the target.

There is an increasing demand for preclinical robotic devices, as various FUS applications are continuously being developed and should be investigated to demonstrate the accuracy and repeatability needed for their clinical translation. Preclinical devices are the most cost-effective solution because medical certification is not necessary. Although numerous devices with different functionalities have been developed and tested so far, more simplistic and ergonomic devices dedicated for small experimental animals would be of great usefulness in accelerating research in the field.

In this study, we propose two systems dedicated to manoeuvering a single element FUS transducer for preclinical research in small animal models. The first system had the ability to manoeuver the transducer in two dimensions. The operation of the system is simplistic since all the moving parts are placed in a single water tank that includes an acoustic window on the top. A target supporting platform was specially designed to securely position rodents above the ultrasonic source.

A second system was built to simplify targeting given the very small size of the mouse head and offer improved ergonomics. In this version, the mouse is placed in the more stable prone position on a flat platform, with the transducer reaching the head with a top to bottom approach. In fact, the transducer is located inside a cone that is acoustically coupled to the mouse head using ultrasound gel. With this design, the administration of anaesthesia is more flexible.

Both devices were made MRI compatible. Even though the two devices were primarily developed for laboratory use, MRI compatibility is important since it allows for treatment planning and accurate targeting in the MRI setting, as well as confirmation of BBBD by contrast agent enhanced imaging directly after treatment.

The proposed devices will provide the researchers with means to perform research on FUS applications in small animals. The two devices were engineered in a way that ensures ease of use, with adjustment tools to suit the different species. Especially for very small animals such as mice, the accuracy benefits of the proposed experimental setup are of high importance. Overall, the proposed systems are easy to make at an affordable price and were developed based on the knowledge gained from our previously introduced robotic systems.[28–33]

2 | MATERIALS AND METHODS

2.1 | Focussed ultrasound setup

A custom-made FUS transducer was manufactured in-house using a single piezoceramic element (Piezo Hannas Tech Co. Ltd, Wuhan, China), with a radius of curvature of 80 mm, an active diameter of 50 mm, and an operating frequency of 1 MHz. A dedicated housing was 3D printed using Acrylonitrile styrene acrylate (ASA) material on a STRATASYS (F270, Eden Prairie, Minnesota, USA) printer having a circle-shaped cavity, wherein the element was soldered. An electric circuit was created and encapsulated with epoxy, which serves as electric isolator and simultaneously as a backing material preventing

excessive vibration of the element and improving the acoustic performance of the transducer. The acoustic efficiency of the transducer was experimentally determined at 33% by the radiation force balance method.[34] Note that the selection of the various transducer components was based on MR-compatibility.

The transducer is tuned to an RF amplifier (AG series, T&G Power conversion Inc., Rochester, NY) and its actuation is controlled via an in house developed software, which allows selection between continuous and pulsed ultrasound sonication. There is also the possibility to set the sonication parameters, such as the electric power, sonication duration, frequency, and duty cycle.

2.2 | Positioning devices

2.2.1 | Robotic positioning device V1

A 2 DOF motorized device was manufactured using a 3D printing machine (FDM 270, Stratasys, Minnesota, USA). Figure 1 shows computer-aided design (CAD) drawings of the device revealing its components and how they are assembled. The various parts were produced using the fused disposition modelling (FDM) technology with ASA thermoplastic. The positioning mechanism maneuvers the proposed transducer in the *X* and *Y* linear axes, with a motion range of 60 and 130 mm, respectively. Specifically, the rotational motion of two piezoelectric motors (USR30-S3; Shinsei Kogyo Corp., Tokyo, Japan) located outside the water enclosure is converted into linear motion via complex mechanisms located inside the enclosure, as shown in Figure 1.

The *X* axis angular motion is converted into linear motion by a Jack screw mechanism. The motor rotates the Jack screw that is linked with the *X*-plate (Figure 1A). The rotation of the Jack screw in turn causes the *X* plate to move forward (upon counterclockwise rotation) or back (upon clockwise rotation) along dedicated guides of the *X*-frame, which has also a supportive role increasing structural rigidity. The pitch of the Jack screw is 1.44 cm, meaning that for each complete rotation, the *X* stage moves 1.44 cm.

The *Y* axis mechanism involves additional moving parts since the motion has to be delivered at a 90° angle (Figure 1B). The motor was placed outside the water container and was connected to a hexagonal drive shaft for transferring the motion to the interior parts. Bevel gears were coupled to the shaft transferring the motion at 90° (along the *Y* axis). Bevel gears refers to a type of gears with conically shaped teeth that transmit motion at an angle. The gear rotates the *Y* axis jackscrew, thus converting rotational motion into linear motion of the *Y* plate. The angular to linear motion ratio of the *X* and *Y* axes is equal, thus establishing uniformity.

The entire mechanism operates within the water container (Figure 1C), which is sealed by a cover (Figure 1D) having a square acoustic opening on the top. A platform with adjustable plates is fixed to the opening to secure the mouse above the FUS transducer.

2.2.2 | Robotic positioning device V2

The second version of the device is shown in Figure 2A and was developed to achieve more efficient ultrasonic delivery in the mouse brain using a top to bottom approach. The main advantage of this approach is the ability to visually confirm proper coupling with the mouse head. Furthermore, this device was made smaller in size, and hence, it is lighter and easier to transport. Another essential benefit of this version is that intravenous injections and anaesthesia

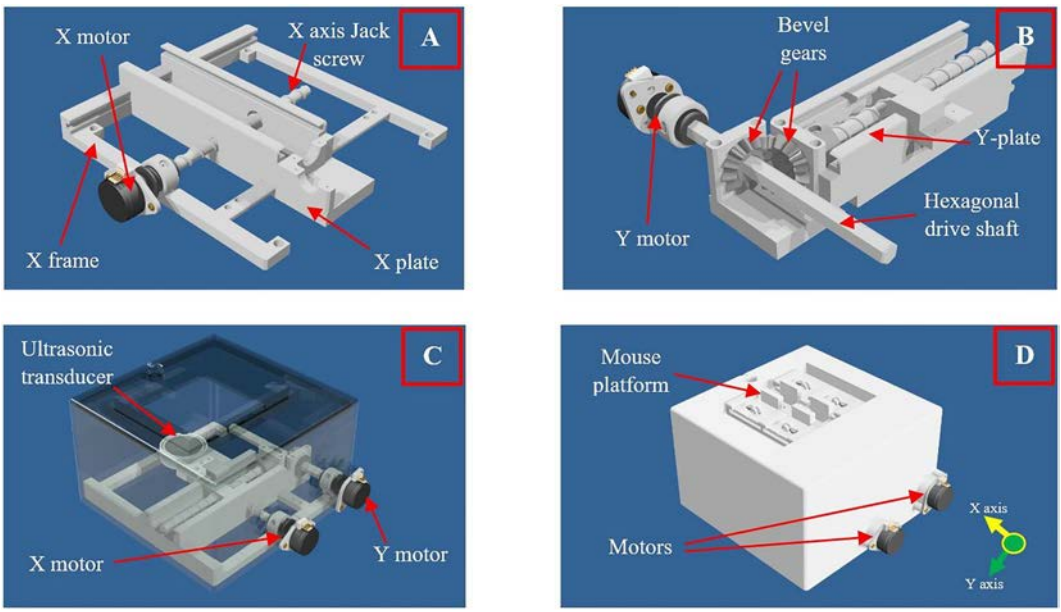

FIGURE 1 CAD drawings of the (A) X-stage, (B) Y-stage, (C) positioning device with transparent enclosure, and (D) positioning device

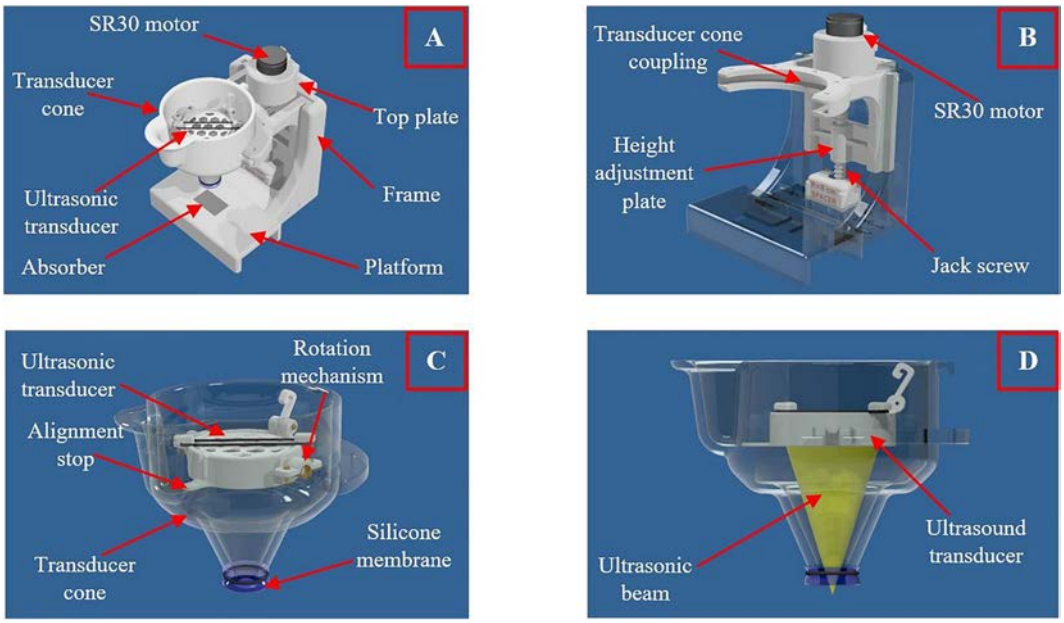

FIGURE 2 CAD drawings of the (A) robotic positioning device V2, (B) height adjustment mechanism, (C) transducer cone, and (D) transducer cone showing the ultrasonic beam

administration can be performed without removing the mouse from the device. For these reasons, it is considered more ideal for small animal experiments.

The device was manufactured on a polyjet 3D printing machine (Object30 pro, Stratasys, Minnesota, USA) using resin, which is cured when exposed to ultraviolet radiation. This technology offers high resolution, thus enabling the production of dimensionally accurate parts. The surface finish is also superior compared to the FDM technology where the layer lines are more visible.

This version of the device includes a flat platform where the mouse is positioned. Notably, an absorber was embedded in the centre of the platform for minimising ultrasound reflections. This platform is connected to a frame that includes linear guides for height adjustment via a moving plate (Figure 2B). The height adjustment plate carries a conical holder, which was designed to accommodate the FUS transducer (transducer cone in Figure 2C).

The height adjustment plate is operated in conjunction with a Jack screw having its first side attached to the platform and its second side connected to the top plate. The jackscrew is rotated by an ultrasonic motor (USR30, Shinsei, Tokyo, Japan) inducing vertical motion of the height adjustment plate so that the transducer cone can be fixed on targets of different size. Notably, its bottom part is securely sealed with a thin silicone membrane that is held by an O-ring (Figure 2C). Upon operation, this cone is filled with degassed-deionised water and is coupled to the target using ultrasound gel for proper ultrasonic transmission.

The transducer was mounted on the upper section of the cone using a special mechanism that enables its manual angulation. Angulation of the transducer is limited by a stop, thus ensuring the alignment of the ultrasonic beam with the acoustic opening (Figure 2D). This mechanism allows for easy removal of the air that is usually trapped on the transducer element during filling of the cone with water.

2.3 | Power field assessment

The axial and radial power field of the designed transducer operating at its fundamental frequency of 1 MHz was evaluated by FUS field scanning with a hydrophone. A dedicated plastic holder was utilised to accommodate the designed transducer and the needle hydrophone (NH0500, Precision Acoustic, Dorset, UK) in an acrylic tank filled with degassed, deionised water. The transducer was precisely moved along the axial and radial directions by a system of stepping motors (VXM, Velmex Inc, Bloomfield, NY, USA) while the hydrophone was aligned to the beam axis to record the pressure waves at increasing distance from the transducer's surface. The hydrophone signal was displayed on a digital oscilloscope (TDS 2012, Tektronix, Inc., 14150 SW Karl Braun Drive, United States) and the peak to peak voltage recordings were collected. In total, 65 measurements were acquired with 2 mm intervals, in the range of 3–16 cm from the transducer's surface. At the estimated focal distance, 80 measurements were acquired in radial direction with 0.1 mm intervals. A voltage of 50 mV was applied in each case.

2.4 | Motion accuracy assessment

The accuracy and repeatability of robotic motion for the two versions of the robot was assessed following a calliper-based method as previously detailed in the literature.[35] Briefly, motion steps of 1, 5, and 10 mm were commanded through the motion commands of the

relevant software and compared with the actual displacements as measured with a high-precision digital calliper. Additionally, the speed of motion in each axis was estimated by the activation time of the motion actuators, which is provided by the controlling software and equals to the time needed for the stage to cover the commanded step.

2.5 | MRI compatibility assessment

The developed robotic devices were then evaluated in terms of proper operation in the MRI environment. Evaluation was carried out in a 1.5 T MRI scanner. The SNR served as the main tool for assessing the compatibility of the transducer with the scanner.

Imaging of an agar-based tissue mimicking phantom (6% weight per volume agar; Merck KGaA, EMD Millipore Corporation, Darmstadt, Germany) was performed using the spoiled gradient recalled echo (SPGR) sequence with the following parameters: repetition time (TR) = 23 ms, echo time (TE) = 16 ms, flip angle (FA) = 35°, echo train length (ETL) = 1, pixel bandwidth (PB) = 45 Hz/pixel, field of view (FOV) = 280 × 280 × 10 mm^3, matrix = 128 × 128, number of excitations (NEXs) = 2, and acquisition time/slice = 7 s.

The following activation states of the positioning mechanism were tested: motor/encoder cable not connected, motor/encoder cable connected, electronic control system energised but no motion command initiated (referred to as: DC ON), and motion command initiated (referred to as: motor moving). Regarding the FUS system, the following states were tested: RF cable not connected, RF cable connected, amplifier energised (zero power applied), and ultrasonic power applied. Electrical power values of 50–200 W were tested. In each case, the SNR was determined using the following formula[36]:

$$SNR = SI_{target}/\sigma_{noise} \quad (1)$$

where the numerator is the mean signal intensity of a preselected target ROI while the denominator represents the standard deviation from a ROI placed in the air (noise).

2.6 | Feasibility study in mice

Feasibility experiments were conducted in wild type (WT) mice (1-month old, body weight 10–12 g) in collaboration with the Cyprus Institute of Neurology and Genetics to obtain proof of concept for the first version of the device. All the experimental procedures were approved by the Cyprus Veterinary Service under the protocol number CY/EXP/PR.L05/2021.

Initially, the transducer's location was adjusted to coincide with the circle-shaped opening of the mouse holder (where the mouse head is fixed) through the motion commands of the interfaced software. The mouse head was shaved using hair removal cream. The mouse was then anaesthetized with isoflurane (Chanelle Pharm, I-sovet®, Loughrea, Co Galway, Ireland) following administration of 10 or 20 μL of SonoVue MBs (Bracco Imaging, Turin, Italy) intravenously through the tail vein with a 30G syringe. Once the mouse was sufficiently anaesthetized, it was mounted on the device above the FUS transducer in the supine position and immobilised by properly adjusting the holder's handles. The container was filled with degassed-deionised water up to the mouse head to ensure efficient ultrasonic coupling. It is essential to mention that before fixing the mouse to the holder, the transducer was energised enabling visual localization of the beam at the water surface, thus providing an additional reference for mouse positioning. Each mouse received a single sonication using FUS pulses of 10 ms length, applied at a repetition frequency of 1 Hz, for a total duration of 60 s using electrical power of 20 or 30 W.

In total, 6 mice were included in the study. Four (4) mice were treated using MBs-enhanced FUS. The Evans Blue (EB) dye method was used to assess the success of BBBD. Specifically, 5 μL/g of body weight of a 4% EB stain solution (Sigma, St. Louis, MO, USA) was injected intravenously into each mouse immediately after sonication; 30 min before they were sacrificed. One mouse received EB only and another mouse served as the control mouse and received no treatment or EB.

All mice were sacrificed approximately 30 min after the sonication or/and EB administration. Slides containing brain sections were directly visualised using a Nikon eclipse-Ni (Tokyo, Japan) fluorescence microscope to examine the EB extravasation. Furthermore, cryosections from brain were immunostained for fibronectin (DAKO, Glostrup, Denmark, 1:100) and FITC-labelled polyclonal fibrinogen antibody (DAKO, 1:500) to assess the protein leakage into the parenchyma. DAPI staining (Sigma-Aldrich, St. Louis, MO, USA) was used for nuclear localization (blue).

3 | RESULTS

3.1 | Power field assessment

Ultrasonic pressure field characterisation was performed using a hydrophone. The voltage recordings show a maximum pressure at 7.5 cm indicating that the actual focal spot is slightly shifted towards the transducer's surface. The axial pressure profile follows a Gaussian distribution with a full width half maximum (FWHM) of about 10 mm around the focus location (half pressure length). Accordingly, the radial pressure profile at the estimated focal distance of 7.5 cm also follows a Gaussian distribution around the central axis, which is characterised by a FWHM of about 4 mm (half pressure width). These measurements provide a good indication of the size of the focal spot.

3.2 | Motion accuracy assessment

The results on motion accuracy as obtained by the calliper based method are summarised in Table 1, which lists the range of the measured actual displacements and the corresponding mean error

for each axis direction and each commanded step. Note that the motion error decreases with increasing motion step, with a maximum mean positioning error of 0.080 ± 0.027 mm and 0.077 ± 0.026 mm for the first and second versions of the robot, respectively. Accordingly, the speed of motion was estimated at 9.90 ± 0.12 mm/s and 11.07 ± 0.17 mm/s in the *X* and *Y* directions, respectively. Regarding the second version of the robot, the Z-stage was found to move with a speed of 8.65 ± 0.08 mm/s.

3.3 | MRI compatibility assessment

The bar charts of Figures 3 and 4 reveal how the SNR of SPGR images of the phantom is affected by changing the activation status of the system. The bar chart of Figure 3 shows the SNR estimations with the positioning mechanism being at different activation states. The greatest SNR reduction occurred when the ultrasonic motor was moving during image acquisition. The corresponding results for the FUS transducer are shown in Figure 4, which shows a gradual SNR reduction with increasing electric power from 50 to 200 W, most probably owing to the increasing target vibration. The MR compatibility was tested for version 1, which represents the worst case since it accommodates two motors.

3.4 | Feasibility study in mice

BBB opening was evidenced in all cases (4/4). Representative microscopy photos of EB extravasation in the brain parenchyma adjacent to the lateral ventricles are shown in Figure 5. No leakage was observed in the brain parenchyma of the control mouse (Figure 5A) and the mouse injected with EB only (Figure 5B). EB leakage is clearly visible in red colour in mice treated with FUS in synergy with MBs (Figure 5C,D). Note that the mouse treated with higher acoustic power showed higher levels of EB dye in the brain tissue covering a larger area.

The BBB permeability was also characterised using Fibrinogen and Fibronectin immunofluorescent staining. The mice treated with

TABLE 1 The range of actual displacements as measured by the digital calliper at commanded motion steps of 1, 5, and 10 mm in each axis direction of the two robotic devices (version I and II), and the corresponding mean motion error and standard deviation

Version I	Commanded step (mm)	Range (mm)	Mean error ± SD forward (mm)	Mean error ± SD reverse (mm)
X	1	0.9–1.09	0.061 ± 0.031	0.064 ± 0.025
	5	4.9–5.06	0.046 ± 0.021	0.048 ± 0.022
	10	9.97–10.03	0.039 ± 0.010	0.036 ± 0.012
	Commanded step (mm)	**Range (mm)**	**Mean error ± SD right (mm)**	**Mean error ± SD left (mm)**
Y	1	0.88–1.1	0.08 ± 0.027	0.076 ± 0.032
	5	4.88–5.07	0.057 ± 0.029	0.051 ± 0.023
	10	9.95–10.04	0.023 ± 0.020	0.025 ± 0.016
Version II	**Commanded step (mm)**	**Range (mm)**	**Mean error ± SD upward (mm)**	**Mean error ± SD downward (mm)**
Z	1	0.86–1.1	0.073 ± 0.038	0.077 ± 0.026
	5	4.9–5.05	0.042 ± 0.026	0.05 ± 0.03
	10	9.92–10.03	0.028 ± 0.02	0.033 ± 0.024

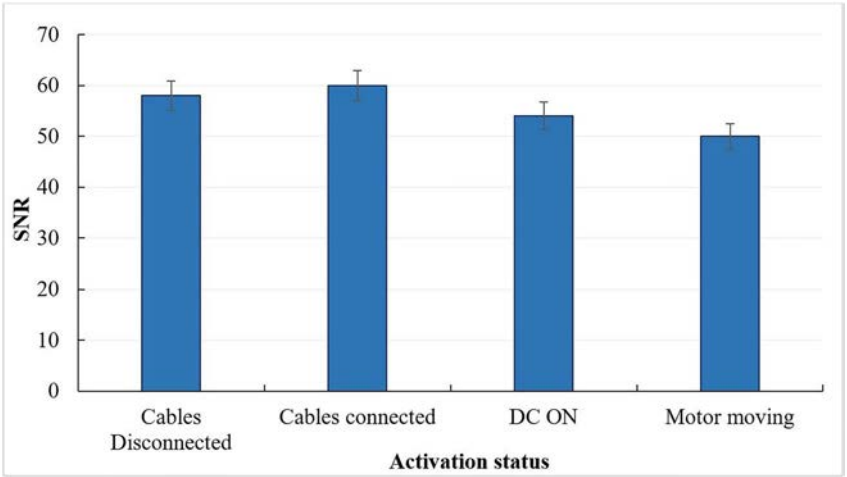

FIGURE 3 Bar chart of the SNR of SPGR images of an agar phantom acquired for different activation states of the robotic device (Cables Disconnected, Cables Connected, DC ON, and Motor moving). Error bars represent the standard deviation of the mean

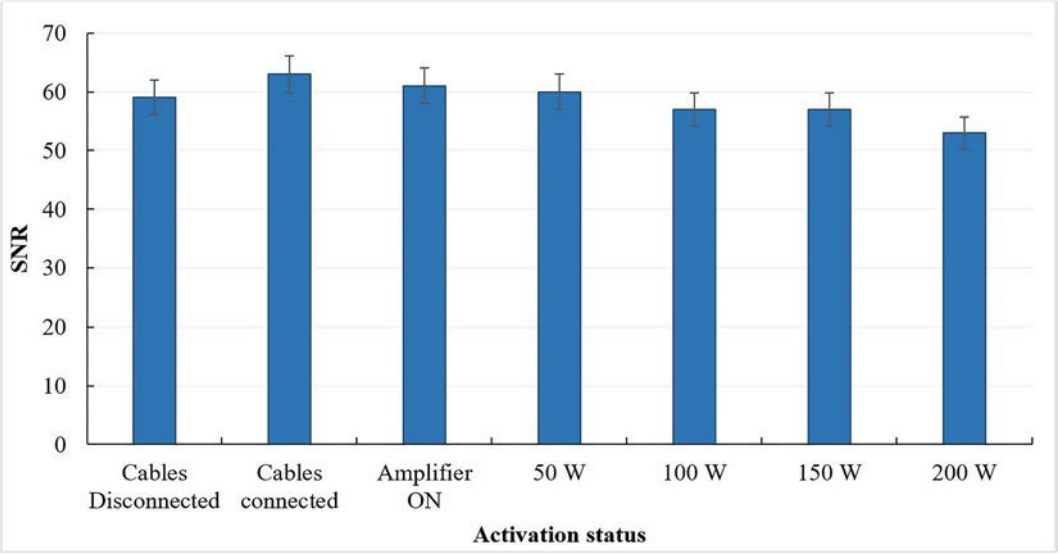

FIGURE 4 Bar chart of the SNR of SPGR images of an agar phantom acquired for different activation states of the FUS transducer (Cables Disconnected, Cables Connected, Amplifier ON, and power set at 50, 100, 150, and 200 W). Error bars represent the standard deviation of the mean

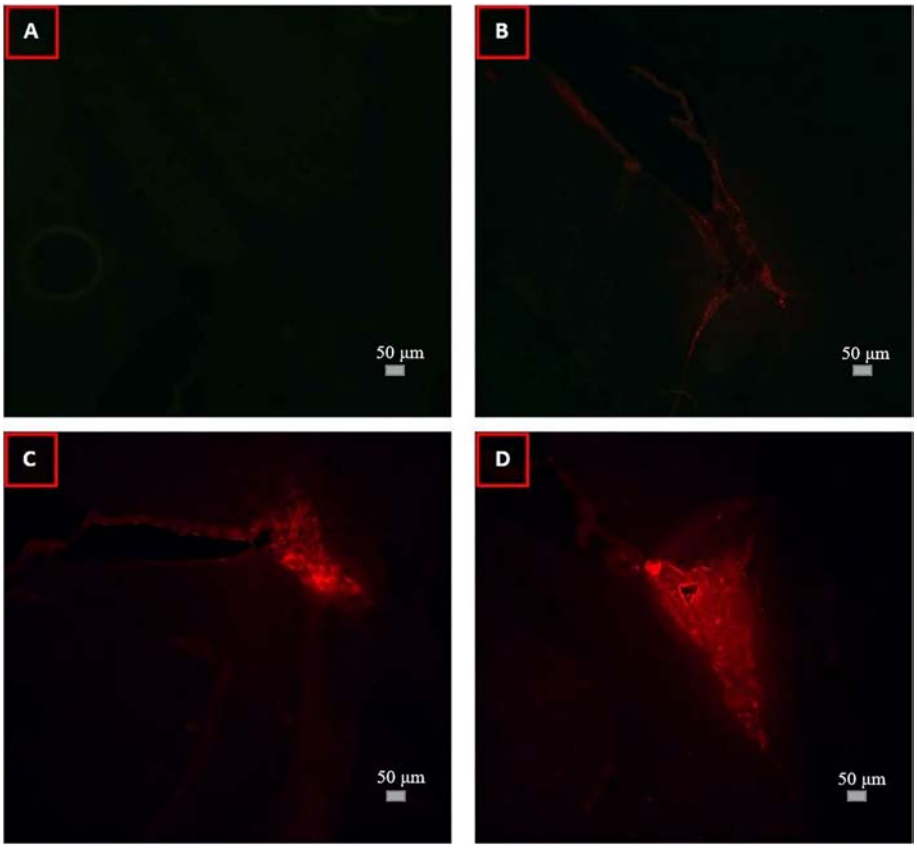

FIGURE 5 Fluorescence images of unstained brain sections at the level of the lateral ventricles taken from (A) a control mouse, (B) a mouse injected with EB only, and mice treated using (C) 20 W and 10 µL MBs, and (D) 30 W and 10 µL MBs (Scale bar: 50 µm)

FUS plus MBs showed higher levels of the protein in all examined brain areas compared to the control mice. Images of fluorescence microscopy from the corpus callosum are presented in Figure 6, where the fibronectin is stained green, and the cell nuclei are stained blue. It seems that for the control mouse (Figure 6A) and the mouse that received EB only (Figure 6B) the protein remained in the

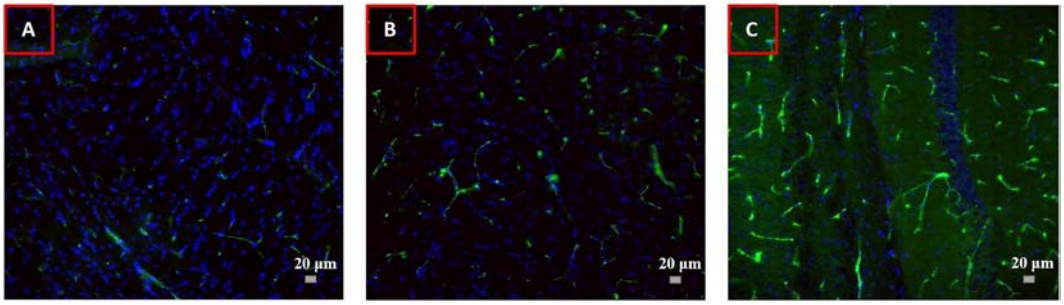

FIGURE 6 Fluorescence images of immunostained brain sections at the level of the corpus callosum for a (A) control mouse, (B) a mouse injected with EB only, and (C) a mouse treated with 30 W plus 20 μL MBs. The Fibronectin protein is stained green, and the cell nuclei are counterstained blue with DAPI (Scale bar: 20 μm)

perivascular extracellular matrix. On the contrary, in the case of the mouse treated using electrical power of 30 W and 20 μL MBs (Figure 6C), the fibronectin leakage is clearly visualised as a diffused green dye in the brain tissue.

4 | DISCUSSION

The current study presents two robotic devices intended to facilitate preclinical research on transcranial applications of FUS in small animal models, such as mice. The specific application of the system is the FUS-mediated BBB opening for the delivery of therapeutic drugs that are normally hampered by the BBB into the brain parenchyma.

The first version of the robotic system was developed with two piezoelectric-actuated motion axes. The mechanical parts and FUS transducer were arranged in a single water enclosure. The rotational motion of the motors located outside the container is converted into linear motion of the respective stages inside the enclosure by Jack screw mechanisms. The system incorporates a custom made single element FUS transducer operating at a frequency of 1 MHz. Note that MBs-enhanced pulsed FUS around 1 MHz was predominantly selected for similar applications in mice by numerous studies.[9,10,37,38] A specialised platform featuring four moving plates with locking levers was designed and fitted in the acoustic opening to safely immobilise rodents of different size and type above the transducer. During operation, the enclosure is filled with degassed water that serves as the coupling medium for proper beam propagation from the transducer to the mouse head.

The FUS transducer was also manufactured in-house using a purchased piezoelectric element that was housed in a plastic case and covered by an epoxy encapsulant. The acoustic efficiency of the transducer was experimentally determined at 33% by the radiation force balance method. The produced FUS field was scanned using a hydrophone. The collected sound pressure signals were displayed on a digital oscilloscope, thus allowing assessment of the pressure field distribution. The obtained results revealed an actual location of the focal spot shifted at 7.5 cm, compared to the focal distance of 8 cm reported by the manufacturer for the element. This method also provided good indication of the size of the focal spot.

The most parts of the device were developed on a rapid prototyping machine using plastic to avoid interference with the scanner. The MRI compatibility of the developed system was assessed in a 1.5 T MRI scanner by comparing the SNR of SPGR images of an agar-based MRI phantom obtained under different activations of the system. Regarding the positioning mechanism, noticeable SNR reduction was observed when the motion command was initiated (motor moving). Regarding activation of the FUS transducer, the image quality was getting degraded as the output power was increasing, thus resulting in some loss of detail. However, the induced SNR reductions were not considered significant. In other words, all tested activations resulted in SNR values sufficiently high for proper imaging, and thus, the efficacy of anatomical targeting and MR thermometry are not influenced. It should be though noted that since activation of the various components requires the use of electricity the system is classified as MR conditional (American Society for Testing and Materials (ASTM) standards).

The feasibility of the system in opening the BBB of small animal models using pulsed FUS in synergy with MBs was examined in WT mice. The mouse platform provided proper immobilisation of the mouse in the supine position. Targeting was though proven challenging due to the inability to directly visualise the exact location of the transducer relative to the mouse brain. However, promising results were obtained indicating successful opening of the BBB. Specifically, EB leakage in the brain parenchyma was clearly evidenced in microscopy images of brain cryosections only in the case of mice treated with FUS in synergy with MBs. It is interesting to note that the mouse treated with higher acoustic power showed higher levels of EB dye diffusing through a larger brain area. The BBB permeability was also confirmed by Fibronectin and Fibrinogen immunofluorescent staining. Again, the FUS treated mice showed higher levels of the protein in all examined brain areas, whereas for the control mouse the protein remained in the extracellular matrix.

Some issues identified during these preliminary experiments led to the development of a second improved version of the system. The first system comprises a relatively large water container that has to be filled up to the top so that the animal's head is in direct contact with the water and efficient ultrasonic propagation is achieved. However, the large water volume needed to achieve acoustic

coupling makes the device heavy and less ergonomic. It was also observed that this design is prone to water leakage from the acoustic opening. Additionally, targeting the animal's brain in the laboratory setting was proven challenging due to the inability to directly visualise the transducer's location. Another identified limitation relates to the intravenous injections and administration of anaesthesia, which cannot be performed properly without removing the mouse from the device.

The second version was designed to address these issues, thus facilitating mice experiments even more. This device uses a top to bottom approach and features motion only in the vertical direction. To be more specific, the FUS transducer was integrated in a coupling cone that can be moved vertically and tightly fit the mouse head. Accordingly, the dimensions of the system were reduced considerably making the device even more compact, lightweight, and ergonomic in its use. A silicone membrane was used to seal to bottom opening of the coupling cone. The membrane unavoidably reduces the efficacy of acoustic coupling. For this reason, it was selected to be thin (0.2 mm) to minimise ultrasonic attenuation. Also, ultrasound gel was applied to displace air and maximise ultrasonic transmission. It is noted that this is a simplified device suitable for single-shot FUS applications. A more advanced device could be developed in the future with the addition of horizontal motion stages, thus enabling sequential placement of the transducer at multiple brain locations, but at the cost of increasing size and complexity.

Additionally, the top to bottom approach allows the placement of the animal in the prone position that is much more stable, simultaneously offering better immobilisation of the mouse and visual confirmation of proper acoustic coupling. Furthermore, there is no possibility for water leakage from the cone. Finally, since the animal lies in a flat platform, there is direct access for the administration of anaesthesia, MBs and contrast agents through needles. An absorbent material was incorporated into the animal platform, thus reducing ultrasound reflections.

It is important to ensure that no bubbles obstruct the beam path. In this regard, the manual rotational mechanism of the transducer incorporated in the second version of the system is extremely useful. A simple method to remove air bubbles is to rotate the transducer at 90°, and then, once the coupling cone is filled with degassed water, rotate it back in its horizontal position. An elastic band was included in the mechanism to stabilise the transducer.

The motion accuracy of both systems was assessed following a calliper-based methodology as previously detailed in the literature.[35] The obtained results demonstrate that the motion error is decreasing with increasing motion step in all axes, with a maximum positioning error of about 0.1 mm for the 1-mm step.

The single-element spherically focussed transducer of 1 MHz that was developed in-house was proven suitable for the specific trans-skull application of FUS-induced BBBD in mice, most probably due to their small skull thickness. Although very promising results were obtained, further experiments should be performed using the second version of the device, which is expected to address all the difficulties faced during the feasibility studies of the first version.

Despite the fact that the systems are mostly intended to be used in the laboratory setting, their MRI compatibility constitutes a great benefit since it allows for treatment planning and accurate targeting based on high resolution anatomical images, as well as confirmation of BBB opening by contrast agent enhanced imaging directly after treatment without moving the device from the scanner. Therefore, subsequent experiments may be benefited by treatment planning and post-treatment BBBD assessment in the MRI setting. Note that MRI has been already employed in numerous studies mostly for assessing whether the BBB was successfully disrupted,[9,38–40] and less often for focus positioning and targeting.[39,40]

It is essential to clarify that the current study focuses on the development of the two FUS robotic systems while a feasibility study on a small number of mice was only included to provide proof of concept for their intended application. Therefore, a dedicated targeting method such as the use of a stereotactic frame was not adapted. Instead, a global approach was followed, where the transducer's location was adjusted so that the FUS beam targets the skull centrally roughly focussing at the level of the hippocampus. This approach was efficient to obtain proof of successful ultrasonic coupling and disruption of the BBB. Follow up studies will focus on evaluating the second optimised version in a large number of mice accounting for specific parameters affecting the location and extent of the BBBD, as well as on assessing the ability of delivering chemotherapeutic drugs through the opened BBB.

5 | CONCLUSIONS

Overall, the proposed devices constitute a cost-effective and ergonomic solution for FUS mediated non-invasive and reversible disruption of the BBB in small animal models, such as mice and rats. It should be though noted that both devices could also be used for other brain or body applications in various types of rodents, provided that their size is appropriate. The preparation of the experimental setup can be completed within a few minutes taking up minimal space. The user can remotely adjust the transducer's position and initiate sonication through a dedicated user-friendly software. Such ergonomic devices are expected to facilitate research in the relevant field, thus accelerating clinical translation of the technology to offer an alternative therapeutic solution for neurological diseases.

AUTHOR CONTRIBUTION

Marinos Giannakou contributed to the development of the robotic devices and draughting of the manuscript. Anastasia Antoniou contributed to the draughting of manuscript and implementation of the scientific methods. Elena Georgiou and Kleopas Kleopa contributed to the execution of the mice experiments. Christakis Damianou supervised the overall study, as well as the draughting of the manuscript.

ACKNOWLEDGEMENTS

The study was funded by the Research and Innovation Foundation of Cyprus under the project SOUNDPET (INTEGRATED/0918/0008) and by the Piccolo Grande Guerriero - Associazione Malattia PMLD, Italy (2020-22 Grant to KAK).

CONFLICT OF INTEREST

All authors declares no conflict of interest.

DATA AVAILABILITY STATEMENT

The data that support the findings of this study are available from the corresponding author upon reasonable request.

ORCID

Marinos Giannakou https://orcid.org/0000-0002-6777-0515
Christakis Damianou https://orcid.org/0000-0003-0424-2851

REFERENCES

1. Lin CY, Hsieh HY, Pitt WG, et al. Focused ultrasound-induced blood-brain barrier opening for non-viral, non-invasive, and targeted gene delivery. *J Contr Release*. 2015;212:1-9. https://doi.org/10.1016/j.jconrel.2015.06.010
2. Mesiwala AH, Farrell L, Wenzel HJ, et al. High-intensity focused ultrasound selectively disrupts the blood-brain barrier in vivo. *Ultrasound Med Biol*. 2002;28(3):389-400. https://doi.org/10.1016/S0301-5629(01)00521-X
3. Yang Y, Zhang X, Ye D, et al. Cavitation dose painting for focused ultrasound-induced blood-brain barrier disruption. *Sci Rep*. 2019;9(1):1-10. https://doi.org/10.1038/s41598-019-39090-9
4. Sheikov N, McDannold N, Vykhodtseva N, Jolesz F, Hynynen K. Cellular mechanisms of the blood-brain barrier opening induced by ultrasound in presence of microbubbles. *Ultrasound Med Biol*. 2004;30(7):979-989. https://doi.org/10.1016/j.ultrasmedbio.2004.04.010
5. Hynynen K, Mcdannold N, Sheikov NA, Jolesz FA, Vykhodtseva N. Local and reversible blood – brain barrier disruption by noninvasive focused ultrasound at frequencies suitable for trans-skull sonications. *Neuroimage*. 2005;24(1):12-20. https://doi.org/10.1016/j.neuroimage.2004.06.046
6. Chopra R, Vykhodtseva N, Hynynen K. Influence of exposure time and pressure amplitude on blood - brain-barrier opening using transcranial ultrasound exposures. *ACS Chem Neurosci*. 2010;1(5):391-398. https://doi.org/10.1021/cn9000445
7. Tung Y-S, Vlachos F, Feshitan JA, Borden MA, Konofagou EE. The mechanism of interaction between focused ultrasound and microbubbles in blood-brain barrier opening in mice. *J Acoust Soc Am*. 2011;130(5):3059-3067. https://doi.org/10.1121/1.3646905
8. McDannold N, Vykhodtseva N, Hynynen K. Blood-brain barrier disruption induced by focused ultrasound and circulating preformed microbubbles appears to Be characterized by the mechanical index. *Ultrasound Med Biol*. 2008;34(5):834-840. https://doi.org/10.1016/j.ultrasmedbio.2007.10.016
9. Choi JJ, Pernot M, Small SA, Konofagou EE. Noninvasive, transcranial and localized opening of the blood-brain barrier using focused ultrasound in mice. *Ultrasound Med Biol*. 2007;33(1):95-104. https://doi.org/10.1016/j.ultrasmedbio.2006.07.018
10. Choi JJ, Wang S, Tung Y-S, Morrison B, Konofagou EE. Molecules of various pharmacologically-relevant sizes can cross the ultrasound-induced blood-brain barrier opening in vivo. *Ultrasound Med Biol*. 2010;36(1):58-67. https://doi.org/10.1016/j.ultrasmedbio.2009.08.006
11. Konofagou EE. Optimization of the ultrasound-induced blood-brain barrier opening. *Theranostics*. 2012;2(12):1223-1237. https://doi.org/10.7150/thno.5576
12. Chen H, Konofagou EE. The size of blood-brain barrier opening induced by focused ultrasound is dictated by the acoustic pressure. *J Cerebr Blood Flow Metabol*. 2014;34(7):1197-1204. https://doi.org/10.1038/jcbfm.2014.71
13. Karakatsani ME, Blesa J, Konofagou EE. Blood–brain barrier opening with focused ultrasound in experimental models of Parkinson's disease. *Mov Disord*. 2019;34(9):1252-1261. https://doi.org/10.1002/mds.27804
14. Sheikov N, McDannold N, Sharma S, Hynynen K. Effect of focused ultrasound applied with an ultrasound contrast agent on the tight junctional integrity of the brain microvascular endothelium. *Ultrasound Med Biol*. 2008;34(7):1093-1104. https://doi.org/10.1016/j.ultrasmedbio.2007.12.015
15. Jalali S, Huang Y, Dumont DJ, Hynynen K. Focused ultrasound-mediated bbb disruption is associated with an increase in activation of AKT: experimental study in rats. *BMC Neurol*. 2010;10(1):114. https://doi.org/10.1186/1471-2377-10-114
16. Burgess A, Ayala-Grosso CA, Ganguly M, Jordão JF, Aubert I, Hynynen K. Targeted delivery of neural stem cells to the brain using MRI-guided focused ultrasound to disrupt the blood-brain barrier. *PLoS One*. 2011;6(11):e27877. https://doi.org/10.1371/journal.pone.0027877
17. Etame AB, Diaz RJ, O'Reilly MA, et al. Enhanced delivery of gold nanoparticles with therapeutic potential into the brain using MRI-guided focused ultrasound. *Nanomedicine*. 2012;8(7):1133-1142. https://doi.org/10.1016/j.nano.2012.02.003
18. Home | FUS Instruments. Accessed May 22, 2022. https://www.fusinstruments.com/
19. HIFUPlex Options - Verasonics. Accessed May 15, 2022. https://verasonics.com/hifuplex-options/
20. Image Guided Therapy - TargetedFUS. Accessed May 15, 2022. http://www.imageguidedtherapy.com/Focused-ultrasounds/MR-guided-Focused-Ultrasounds-System-for-experimental-research.html
21. Focused Ultrasound - SonoVol, Inc. Accessed April 7, 2022. https://sonovol.com/applications/focused-ultrasound/
22. Groen MHA, Slieker FJB, Vink A, et al. Safety and feasibility of arterial wall targeting with robot-assisted high intensity focused ultrasound: a preclinical study. *Int J Hyperther*. 2020;37(1):903-912. https://doi.org/10.1080/02656736.2020.1795278
23. Thomas GPL, Khokhlova TD, Khokhlova VA. Partial respiratory motion compensation for abdominal extracorporeal boiling histotripsy treatments with a robotic arm. *IEEE Trans Ultrason Ferroelectrics Freq Control*. 2021;68(9):2861-2870. https://doi.org/10.1109/TUFFC.2021.3075938
24. Bove T, Zawada T, Serup J, Jessen A, Poli M. High-frequency (20-MHz) high-intensity focused ultrasound (HIFU) system for dermal intervention: preclinical evaluation in skin equivalents. *Skin Res Technol*. 2019;25(2):217-228. https://doi.org/10.1111/srt.12661
25. Fura Ł, Dera W, Dziekoński C, Świątkiewicz M, Kujawska T. Experimental assessment of the impact of sonication parameters on necrotic lesions induced in tissues by HIFU ablative device for preclinical studies. *Arch Acoust Q*. 2021;46(2):341-352. https://doi.org/10.24425/aoa.2021.136573
26. Fura Ł, Dera W, Dziekoński C, Świątkiewicz M, Kujawska T. Experimental evaluation of targeting accuracy of ultrasound imaging-guided robotic HIFU ablative system for the treatment of solid tumors in pre-clinical studies. *Appl Acoust*. 2021:184. https://doi.org/10.1016/j.apacoust.2021.108367
27. Yiannakou M, Menikou G, Yiallouras C, Ioannides C, Damianou C. MRI guided focused ultrasound robotic system for animal experiments. *Int J Med Robot Comput Assist Surg*. 2017;13(4):e1804. https://doi.org/10.1002/rcs.1804

28. Damianou C, Giannakou M, Evripidou N, Kegel S, Huber P, Jenne J. Focused ultrasound robotic system for very small bore magnetic resonance imaging. *Int J Med Robot Comput Assist Surg*. 2020;16(6):1-9. https://doi.org/10.1002/rcs.2165
29. Drakos T, Giannakou M, Menikou G, et al. MRI-guided focused ultrasound robotic system for preclinical use. *J Vet Med Anim Sci*. 2021;4(1):1-11.
30. Giannakou M, Drakos T, Menikou G, et al. MRI-guided focused ultrasound robotic system for transrectal prostate cancer therapy. *Int J Med Robot Comput Assist Surg*. 2021;17(3):e2237. https://doi.org/10.1002/rcs.2237
31. Antoniou A, Giannakou M, Evripidou N, et al. Robotic system for magnetic resonance guided focused ultrasound ablation of abdominal cancer. *Int J Med Robot Comput Assist Surg*. 2021;17(5). https://doi.org/10.1002/rcs.2299
32. Spanoudes K, Evripidou N, Giannakou M, Drakos T, Menikou G, Damianou C. A high intensity focused ultrasound system for veterinary oncology applications. *J Med Ultrasound*;29(3):195-202. https://doi.org/10.4103/JMU.JMU_130_20
33. Antoniou A, Giannakou M, Evripidou N, Stratis S, Pichardo S, Damianou C. Robotic system for top to bottom MRgFUS therapy of multiple cancer types. *Int J Med Robot Comput Assist Surg*. 2022;18(2). https://doi.org/10.1002/rcs.2364
34. Shou W, Huang X, Duan S, et al. Acoustic power measurement of high intensity focused ultrasound in medicine based on radiation force. *Ultrasonics*. 2006;44:17-20. https://doi.org/10.1016/j.ultras.2006.06.034
35. Antoniou A, Drakos T, Giannakou M, et al. Simple methods to test the accuracy of MRgFUS robotic systems. *Int J Med Robot Comput Assist Surg*. 2021;17(4). https://doi.org/10.1002/rcs.2287
36. Goerner FL, Clarke GD. Measuring signal-to-noise ratio in partially parallel imaging MRI. *Med Phys*. 2011;38(9):5049-5057. https://doi.org/10.1118/1.3618730
37. Choi JJ, Selert K, Gao Z, Samiotaki G, Baseri B, Konofagou EE. Noninvasive and localized blood—brain barrier disruption using focused ultrasound can be achieved at short pulse lengths and low pulse repetition frequencies. *J Cerebr Blood Flow Metabol*. 2011;31(2):725-737. https://doi.org/10.1038/jcbfm.2010.155
38. Wang S, Samiotaki G, Olumolade O, Feshitan JA, Konofagou EE. Microbubble type and distribution dependence of focused ultrasound-induced blood-brain barrier opening. *Ultrasound Med Biol*. 2014;40(1):130-137. https://doi.org/10.1016/j.ultrasmedbio.2013.09.015
39. Mooney SJ, Shah K, Yeung S, Burgess A, Aubert I, Hynynen K. Focused ultrasound-induced neurogenesis requires an increase in blood-brain barrier permeability. *PLoS One*. 2016;11(7):1-11. https://doi.org/10.1371/journal.pone.0159892
40. Ishida J, Alli S, Bondoc A, et al. MRI-guided focused ultrasound enhances drug delivery in experimental diffuse intrinsic pontine glioma. *J Control ReleaseJ Control Release*. 2021;330:1034-1045. https://doi.org/10.1016/j.jconrel.2020.11.010

How to cite this article: Antoniou A, Giannakou M, Georgiou E, Kleopa KA, Damianou C. Robotic device for transcranial focussed ultrasound applications in small animal models. *Int J Med Robot*. 2022;18(6):e2447. https://doi.org/10.1002/rcs.2447

Ultrasonics xxx (xxxx) 106955

Contents lists available at ScienceDirect

Ultrasonics

journal homepage: www.elsevier.com/locate/ultras

Development of an US, MRI, and CT imaging compatible realistic mouse phantom for thermal ablation and focused ultrasound evaluation

Anastasia Antoniou, Anastasia Nikolaou, Andreas Georgiou, Nikolas Evripidou, Christakis Damianou *

Department of Electrical Engineering, Computer Engineering, and Informatics, Cyprus University of Technology, Limassol, Cyprus

ARTICLE INFO

Keywords:
Mouse phantom
Focused ultrasound
MRI
CT
Realistic
3D printing

ABSTRACT

Tissue mimicking phantoms (TMPs) play an essential role in modern biomedical research as cost-effective quality assurance and training tools, simultaneously contributing to the reduction of animal use. Herein, we present the development and evaluation of an anatomically accurate mouse phantom intended for image-guided thermal ablation and Focused Ultrasound (FUS) applications. The proposed mouse model consists of skeletal and soft tissue mimics, whose design was based on the Computed tomography (CT) scans data of a live mouse. Advantageously, it is compatible with US, CT, and Magnetic Resonance Imaging (MRI). The compatibility assessment was focused on the radiological behavior of the phantom due to the lack of relevant literature. The X-ray linear attenuation coefficient of candidate materials was estimated to assess the one that matches best the radiological behavior of living tissues. The bone part was manufactured by Fused Deposition Modeling (FDM) printing using Acrylonitrile styrene acrylate (ASA) material. For the soft-tissue mimic, a special mold was 3D printed having a cavity with the unique shape of the mouse body and filled with an agar-based silica-doped gel. The mouse phantom accurately matched the size and reproduced the body surface of the imaged mouse. Tissue-equivalency in terms of X-ray attenuation was demonstrated for the agar-based soft-tissue mimic. The phantom demonstrated excellent MRI visibility of the skeletal and soft-tissue mimics. Good radiological contrast between the skeletal and soft-tissue models was also observed in the CT scans. The model was also able to reproduce realistic behavior during *trans*-skull sonication as proved by thermocouple measurements. Overall, the proposed phantom is inexpensive, ergonomic, and realistic. It could constitute a powerful tool for image-guided thermal ablation and FUS studies in terms of testing and optimizing the performance of relevant equipment and protocols. It also possess great potential for use in transcranial FUS applications, including the emerging topic of FUS-mediated blood brain barrier (BBB) disruption.

1. Introduction

Preclinical evaluation of new diagnostic and therapeutic systems and protocols is initially carried out in tissue-mimicking phantoms (TMPs) [1,2] or/and excised animal tissue [3], followed by in-vivo evaluation, which may involve rodents [4], large animal models [5,6], and non-human primates [7]. Realistic TMPs could serve as a valuable tool in this process, offering advanced ergonomics while contributing towards reducing animal experimentation [8].

TMPs have been widely used in all aspects of medical physics, with various phantom types being available for use with almost all imaging modalities [9]. The phantom design and composition is determined by its specific intended task, such as the assessment of dose accuracy, image quality, geometric accuracy, etc. [9]. Water-based gel phantoms representing the human body constitute a cost effective tool in biomedical research both for evaluation purposes and the training of medical students, provided that low cost supplementary ingredients can be included to adjust phantom properties [9–11].

Over the last decades, there has been a lot of research on the development of Magnetic Resonance Imaging (MRI) [12,13] and Ultrasound (US) [14] imaging phantoms, which are typically based on hydrogels such as agar, gelatin, and polymeric materials mainly due to the ability of these materials to mimic the soft-tissue composition [11]. Except from a wide variety of in-house made phantoms, there are standards

* Corresponding author at: Department of Electrical Engineering, Computer Engineering, and Informatics, Cyprus University of Technology, 30 Archbishop Kyprianou Street, 3036 Limassol, Cyprus.
E-mail addresses: am.antoniou@edu.cut.ac.cy (A. Antoniou), ann.nikolaou@edu.cut.ac.cy (A. Nikolaou), andreas-georgiou1@outlook.com (A. Georgiou), nk.evripidou@edu.cut.ac.cy (N. Evripidou), christakis.damianou@cut.ac.cy (C. Damianou).

https://doi.org/10.1016/j.ultras.2023.106955
Received 30 June 2022; Received in revised form 9 November 2022; Accepted 10 February 2023
0041-624/

available by the International Electrotechnical Commission (IEC) regarding imaging phantoms and methods for quality assurance of medical ultrasound systems [15–17]. Agar [18], gelatin [19], and Polyvinyl alcohol (PVA) [20] served also as gelling agents for the construction of gel-based radiographic phantoms [21]. Notably, such biopolymers have high water content and therefore water evaporation might cause them to degrade more rapidly than synthetic polymers [11]. However, they offer tissue-like mechanical responses to interventional tools, and thus, they have been predominantly selected for the construction of surgical phantoms [11].

Regarding thermal studies, agar and Polyacrylic acid (PAA) are the preferable gelling agents because they meet the main criterion of withstanding ablative temperatures without decomposing or deforming [10]. In fact, for most cell types, irreversible tissue damage and coagulative necrosis happens almost instantly (1 s) at temperatures over 56 °C [22,23] while agar gels have a higher melting point of near 85 °C [24]. Furthermore, in order for phantoms to exhibit potential for use with thermal applications, they should possess similar thermal properties with living tissues while concurrently being compatible with the relevant imaging modalities used for therapy guidance. Although both gel types can fulfil these requirements by adding proper concentration of specific ingredients, agar gels are generally considered cheaper and more ergonomic in preparation, storage and handling [10].

The increasing popularity of Focused Ultrasound (FUS) [25] as a non-invasive therapeutic modality in many disciplines led to an increased need for dedicated TMPs to facilitate and accelerate preclinical research on emerging FUS applications. High quality TMPs could also be used as a practical tool for quality control of FUS systems and the establishment of quality assurance (QA) standards, given that the methodologies for QA of FUS are still to be standardized. Although the requirement for such phantoms has long been realized [26], their creation was delayed until recently when two relevant studies were published [27,28]. Both studies report the development of phantoms intended specifically for QA of FUS. Authors followed a similar approach of embedding ultrasonic calibration tools, such as a precision balance and thermometers, in a plastic container filled with a TMM [27,28].

The application of FUS in the brain ranging from thermal ablation to drug delivery is currently of intense clinical interest [29]. In the last decade, microbubble-enhanced FUS has emerged as a novel modality enabling safe and transient disruption of the blood brain barrier (BBB) so that molecules of pharmacologically relevant size can enter the brain parenchyma [30–34]. Both wild type and genetically-modified mice serving as models of various neurological diseases have been widely used in the evaluation process and have allowed for a greater understanding of the mechanisms underlying the effects of FUS [30–34]. Thus, there is an urgent need for further research on this topic, so that clinical translation of transcranial FUS applications is accelerated. Accordingly, realistic mouse phantoms would constitute a powerful tool in this effort, given that they are inexpensive, easily accessible, and ergonomic.

3D printing has become a popular means of creating 3D phantoms for multiple purposes. This emerging technology offers the ability for cost-effective rapid prototyping of complex geometries with high precision and has been extensively employed in the development of bone substitutes [1,35,36]. As an example in the context of FUS, 3D-printed parts mimicking the skull [36], femur bone [1], and ribs [37] were developed for FUS exposures, all replicating the ultrasonic attenuation property of human bones.

The use of 3D-printed real-size replicas of mice has already been suggested by numerous studies as an efficient and cost-effective way to replace live mice in a wide range of applications. The 3D printing of both hard and soft tissue anatomical structures is based on data collection from computerized tomography (CT) scans followed by surface rendering and smoothing techniques [38]. Doney et al. [38] described in detail the process of constructing plastic models of a full rat skeleton as derived from CT scans on three different 3D printers using different printing plastics (acrylic, nylon, and Acrylonitrile butadiene styrene (ABS)) and compared their performance in terms of cost-effectiveness and manufacturing resolution.

Current literature suggest that 3D printed small animal models could be of great value in preclinical medical imaging. Zhang et al. [39] developed an anthropomorphic mouse phantom intended for CT, MRI, and PET imaging. The bone part was manufactured by 3D printing on a Polyjet printer using VERO-WHITE Resin. The skin shell was manufactured on a Fused Deposition Modeling (FDM) printer using ABS thermoplastic and filled with an in-house made agar gel. Micro-pearl powder and magnevist solution were included in the gel serving as the X-ray attenuation and T1 relaxation time modifiers, respectively [39].

Dann et al. [40] proposed the use of PA2200; a commercial polyamide powder composed of Nylon-12 and TiO2 titanium dioxide, as a novel substrate for 3D printing optical imaging phantoms using a different additive manufacturing technique called selective laser sintering (SLS). The authors discovered that this 3D printing material exhibited photoluminescent properties owing to the anatase derivative of TiO2 and proceed to the development of a PA2200 rat skeleton phantom to be used as a training/teaching tool.

Anthropomorphic mouse models are also gaining popularity as radiation dosimetry tools. Welch et al [41] developed a realistic model mimicking the bone, lung, and tissue of a mouse, in which radiographic films were included to establish dose mapping capabilities. The bone parts were made of an epoxy resin-based material, whereas a tissue equivalent urethane-based mixture containing polystyrene microbeads was used to develop the lung tissue equivalent part.

Similarly, Esplen et al. [42] proposed a real-size heterogeneous mouse phantom containing a radiochromic film and a plastic scintillating detector, thus enabling radiation dose measurements. The phantom was constructed on a Stratasys Polyjet printing machine using low-density photopolymer materials (translucent VeroClear Resin for the body and white Rigur for the bone), which were chosen to simulate polymethyl methacrylate (PMMA) as closely as possible. A Polyester-filled void served as the lung model. Notably, authors clarified that a careful dosimetric characterization of the phantom is required since the employed materials are not tissue equivalent.

It is interesting to note that in a study by Price et al. [43], a bone-equivalent material composed of ABS and CaTiO3 powder has been proposed as a novel substrate for FDM printing. Authors developed a bone/soft tissue mouse phantom for preclinical radiation dosimetry, in which the soft-tissue mimic was made of ABS and the lungs were represented by air-filled voids.

Notably, Bainier et al. [44] explored the utility of 3D printed rodent phantoms for neurosurgical training. The rodent models consisted of a 3D printed skull mimic that was filled with Polyurethane expanding foam to simulate the brain tissue while a thin silicone sheet was added to simulate the skin [44].

The use of 3D printed phantoms filled with TMMs in preclinical therapeutic applications is still under investigation and development. In this regard, the in-house construction of high quality multipurpose phantoms with anthropomorphic characteristics and tissue-equivalent properties remains a challenge. For thermal ablation studies, phantoms should possess similar thermal properties with living tissues while concurrently being compatible with the relevant imaging modalities used for guidance, which may be US [45], MRI [46], or, more rarely, CT [47]. The thermal behavior of biological tissues is mostly controlled by the specific heat capacity and thermal conductivity [48,49]. TMPs designed for FUS studies should also possess tissue-like acoustic behavior. In this regard, the most important parameters to be considered are the attenuation coefficient and speed of sound in the medium [48,49]. Regarding imaging parameters, expect from excellent US visibility, it is critical for phantoms to offer tissue-like MR signal given that MRI is currently the only imaging modality allowing for almost real-time ther-

mometry during heating [50]. The T1 and T2 relaxation properties are considered the critical MR properties since they greatly affect the contrast between normal tissue and thermal lesions [51]. Monitoring of thermal heating is also based on changes in these properties [50]. Although less common, CT was also employed for planning and guiding thermal ablation procedures, and thus, phantom compatibility with CT scanners constitute an additional advantage for phantoms enabling their wider use [47].

Previously proposed 3D-printed rodent-morphic phantoms matched only imaging properties [39,40] or they were specifically designed for radiation dosimetry purposes [41,42]. This may be partly attributed to the difficulty in simultaneously mimicking a wider range of properties. In the effort to contribute in this regard, we herein present the development and evaluation of an US, MRI, and CT imaging compatible and anatomically accurate mouse phantom intended for image-guided thermal ablation and FUS applications, which can mimic all the aforementioned critical properties.

The proposed mouse model consists of skeletal and soft tissue mimics, both being manufactured according to the CT scans data of a male mouse. The skeletal structure was constructed by 3D printing on a Stratasys printer using Acrylonitrile styrene acrylate (ASA) material, whereas the mouse body was mimicked by an in-house made agar-based phantom doped with silicon dioxide. The specific materials and their composition were selected to best approximate the critical properties of the mouse tissue for the intended applications. Note that the thermal, acoustical, and MRI properties of agar-based phantoms have already been investigated in previous studies of our group [48,52], and were taken into consideration in this study. The candidate 3D printing thermoplastics were also proven suitable for MRI and FUS studies [1, 35,36]. Therefore, in this study, material characterization was focused on the radiographic properties of the candidate materials. The developed phantom was evaluated to assess whether it provides tissue-like signal in MRI and CT. trans-skull sonications with a single-element ultrasonic transducer were performed to assess its feasibility for transcranial FUS studies.

The proposed mouse phantom could serve as a valuable tool for testing thermal ablation and FUS systems and protocols in the preclinical setting while simultaneously addressing the need for realistic rodent phantoms to facilitate *trans*-skull FUS studies, also given the increasing utilization of FUS as a novel method for non-invasive and transient BBB disruption.

2. Materials and methods

2.1. Selection of materials

The mouse skeleton was developed using 3D printing, which was proven a cost-effective rapid prototyping method that offers the ability to develop complex, high resolution parts [42,53], given also that there is literature data proving that 3D printed thermoplastics can match the acoustical properties of the human skull and other bony structures sufficiently [1,35,36,54]. Polylactic Acid – PLA (3DJ, Essex, UK), polypropylene – PP (ULTIMAKER, Utrecht, Netherlands), ASA (Stratasys, Minnesota, USA), and VeroWhite Resin (RGD835, Stratasys, Minnesota, USA) served as the candidate materials for manufacturing the skeleton bones.

Agar (Merck KGaA, EMD Millipore Corporation, Darmstadt, Germany) was selected as the gelling agent for the construction of the soft-tissue mimicking phantom for three main reasons. Firstly, it is an easily sourced and cheap material that can be formed in any shape following a simple procedure [55]. Secondly, the capacity of agar gels to withstand the high temperatures used for tissue ablation make them suitable for HIFU applications [52]. Thirdly, agar is the most common type of gelling agent used for the development of MRI phantoms mainly because it offers tissue-like MRI signal [10,56–58]. Silicon dioxide was included as a modifier of the attenuation property to enhance ultrasonic scattering [10].

The concentration of inclusions in the agar-based soft-tissue mimic was selected so as to replicate as closely as possible the aforementioned critical properties for the intended uses of the phantom. Selection was based both on results from the current study as well as previous studies of the group. It should be noted that so far, a great effort has been placed on the investigation of the acoustical behavior of agar gels, through which key modifiers of the ultrasonic attenuation and velocity have been identified [59,11,48,60,61] allowing the development of a wide variety of phantoms simulating different types of tissue in ultrasonic applications. The ability of agar-based gels to simulate critical thermal and MR properties of tissue has also been demonstrated [52, 59]. In this effort, the acoustical, thermal, and MRI properties of agar gels doped with silicon dioxide and evaporated milk were investigated by our group [48,52,60].

There is though limited literature on the radiological properties of these candidate materials, and thus, their suitability for imaging with CT remains to be demonstrated. Therefore, in the framework of selecting proper materials that will enable the development of a multimodality phantom, the radiological behavior of candidate materials was examined by measuring their X-ray linear attenuation coefficient using CT scans.

Overall, the current work aimed to combine previous knowledge on the acoustical, thermal, and MRI properties of candidate materials with the current fundings regarding the X-ray attenuation properties, along with the recent advances of the 3D printing technology, to produce a more realistic and accurate model suitable for multimodality imaging and thermal ablation studies, including transcranial FUS applications.

2.2. X-ray attenuation in candidate materials

Samples of the candidate soft-tissue and bone mimicking materials were prepared as shown in Fig. 1. Four agar-based mixtures were prepared and contained in rectangular plastic containers of 64 mm^3 inner volume. Fig. 1 shows the composition of the corresponding materials used in each phantom. Three phantoms contained different agar concentrations of 2 – 6 % weight per volume (w/v) to assess the role of agar as a modifier of radiographic attenuation. A fourth phantom was

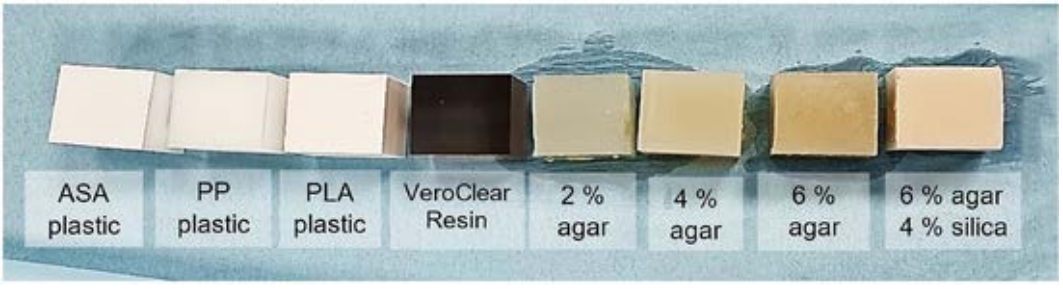

Fig. 1. 3D-printed thermoplastics samples (ASA, PP, PLA, and VeroClear resin) and agar-based samples prepared for X-ray imaging.

prepared with 6 % w/v agar and 4 % w/v silicon dioxide (Sigma-Aldrich, St. Louis, Missouri, United States). Agar is a plant-originated substance that can be easily formed into a gel when mixed with water and heated to a temperature of around 85 °C and left to cool down naturally. The preparation process of agar-based phantoms can be found in detail in the literature [55]. It is important that during heating the mixture should be continuously agitated in order to achieve proper image homogeneity [10].

The candidate thermoplastic materials were 3D printed into cubes with 4 cm side length using 100 % infill. The ASA (Stratasys) sample was manufactured on a Stratasys printer (F270, Eden Prairie, Minnesota, USA) using the Fused Deposition Modeling (FDM) technique. The same technique was used for 3D printing the PP (Ultimaker) and PLA (3DJ) samples. The former was manufactured on an Ultimaker printer (3 Extended, Utrecht, Netherlands) and the latter on a Creality printer (CR10, Shenzhen, China). The fourth phantom was manufacturing using VeroWhite Resin (Stratasys) on a polyjet 3D printing machine (Object30 pro, Stratasys, Minnesota, USA).

The X-ray attenuation coefficient of the candidate materials was measured using CT scans and compared with that of body tissues. The samples were imaged with a General Electric (GE) CT scanner (Optima CT580, GE Medical Systems, Wisconsin, United States) using a tube voltage of 120 kV and a tube current of 300 mA. The CT number (expressed in Hounsfield Units (HU)) for each sample was converted into linear attenuation coefficient (μ) using equation (1) [62]:

$$\mu = \frac{HU * \mu_{water}}{1000} + \mu_{water} \quad (1)$$

where μ_{water} represents the linear attenuation coefficient of water (0,16 cm^{-1}).

2.3. Mouse phantom fabrication

The phantom was designed to resemble the skeletal bone and main body of a mouse. CT images of a healthy mouse provided by the Cyprus Institute of Neurology and Genetics (under the study license CY/EXP/PR.L05/2021) were acquired on the GE Optima CT scanner using the following parameters: tube voltage = 120 kV, tube current: 80 mA, exposure time: 2.26 s, and slice thickness = 1.25 mm. Fig. 2 shows indicative CT images of the mouse. The acquired images were processed in an open source software (3D slicer) [63] to isolate the bone and soft-tissue volumes. Specifically, thresholds were applied to separately delineate the mouse body and skeleton. The extracted geometries were converted into stereolithographic (STL) format and further processed by an open source 3D modelling software (Blender, Blender Foundation, Amsterdam, the Netherland) to achieve a continuous and smooth surface and improve feature resolution. The smoothed STL model of the skeletal bone shown in Fig. 3 was imported in the printer's software for final processing and printing.

The mouse body was modeled using an agar-based recipe. The fabrication process was carried out in two steps. Initially, a multi-part mold was 3D printed using PLA having a cavity with the unique shape of the mouse body as extracted from the CT data. Fig. 4A shows a computer-aided design (CAD) drawing of the mold in exploited view revealing the multiple layers, each one consisting of multiple parts. This quite complex design was required so that the mold can be easily dissembled, thus enabling proper demolding of the mouse model, and avoiding any deformation or other surface defects. The assembled 3D printed mouse mold is shown in Fig. 4B. Prior to the molding procedure, the 3D printed skeletal bone was placed inside the mold cavity. The agar mixture was poured into the mold and left to solidify overnight. Note that the concentration of included materials was selected based on previous literature and the experimental work performed on the X-ray properties of candidate materials.

2.4. Phantom imaging

The mouse phantom was imaged in a 1.5 T MRI scanner (GE Signa HD16, Chicago, Illinois, USA) using the quad knee/foot/ankle coil (Signa 1.5 T Transmitter/Receiver, GE Medical Systems, Milwaukee, Wisconsin, USA). The coil was sited on the MRI table and the phantom was placed inside the coil cavity. For image acquisition, a proton density (PD) Cube 3D sequence was used with the following parameters: repetition time (TR) = 2000 ms, echo time (TE) = 30, 60 ms, Flip Angle (FA) = 90°, echo train length (ETL) = 64, Pixel Bandwidth (PB) = 244 kHz, field of view (FOV) = 160 × 160 × 1.6 mm^3, acquisition matrix size = 224 × 224, number of excitations (NEX) = 0.5, acquisition time/ slice = 58.6 s. Image acquisition was then performed on the GE CT scanner with the following parameters: tube voltage = 120 kVp, tube current = 440 mA, exposure time = 2.34 s, and slice thickness = 1.25 mm.

2.5. Trans-skull sonication in the mouse phantom

This experimental part was focused on investigating the utility of the mouse phantom in FUS applications. The phantom was mounted on

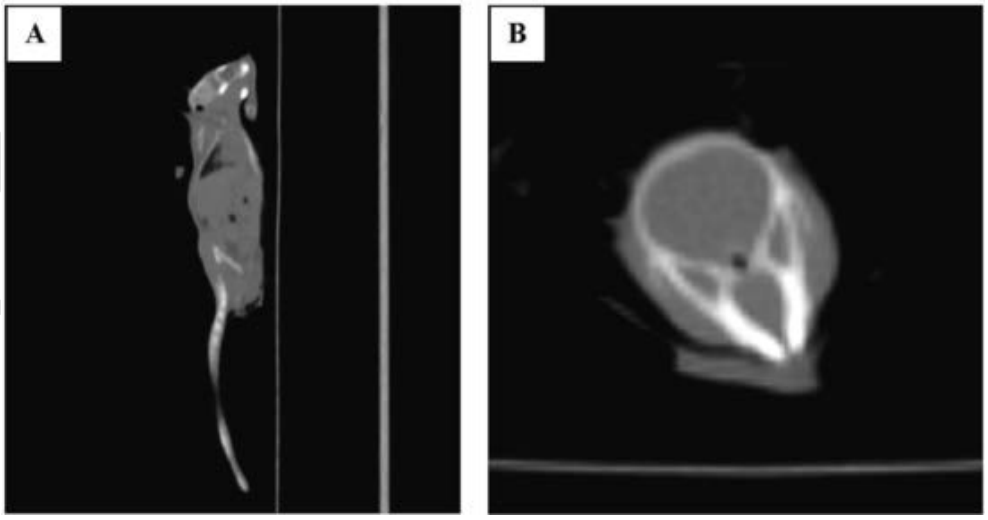

Fig. 2. CT images of the mouse (A) Sagittal plane, (B) Axial plane at the skull level (tube voltage: 120 kV, tube current: 80 mA, exposure time: 2.26 s, slice thickness = 1.25 mm).

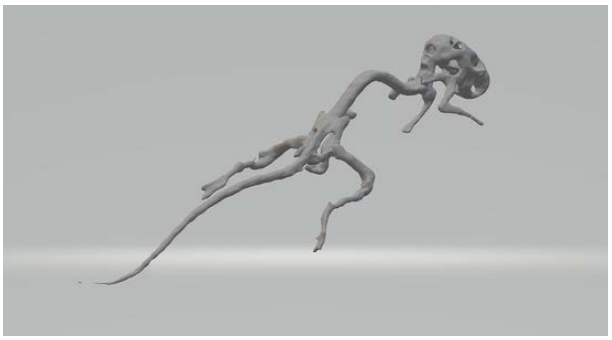

Fig. 3. The final STL model of the segmented skeletal structure after rendering and smoothing.

a dedicated holder inside a tank filled with degassed, deionized water. An in-house manufactured transducer comprising a single element spherically focused piezoelectric (Piezohannas, Wuhan, China) of 1 MHz (diameter of 50 mm and radius of curvature of 100 mm) was fixed to the bottom part of the holder facing upwards to the phantom, as shown in Fig. 5. The distance between the transducer and the phantom was adjusted so that the focal point is located 2 cm deep in the head part. Sonications were performed at electric power of 30 W using continuous FUS and pulsed FUS with duty factor (DF) of 1 % for a total duration of 60 s, and the temperature changes at the focus were recorded using a thermocouple (HH806AU, HH806 Series, OMEGA, CT, USA). The transducer was powered by an AG1016 RF amplifier (AG Series Amplifier, T & C Power Conversion, Inc., Rochester, US). Note that the experimental setup used in this study was not designed to simulate a real scenario of a live mouse study, but to facilitate *trans*-skull sonication and thermocouple measurements. However, the phantom could be used in any scenario relevant to a live rodent study due to its rodent-morphic shape.

3. Results

3.1. X-ray attenuation in candidate materials

Table 1 lists the estimated CT numbers (expressed in HU) for each sample and the corresponding linear attenuation coefficient, as well the CT numbers of mouse and human tissues for comparison purposes [39, 64–67]. Fig. 6 shows indicative CT images for selected samples. The estimated HU values for the ASA, PLA, and VeroClear Resin samples were in the range of 100 to 200, whereas the PP sample was found to possess a negative HU value (−1 7 1). Regarding the agar samples, increasing agar concentration from 2 to 6 % w/v, resulted in a gradual small increase of the CT number, which translated to a minimal increase of the linear attenuation coefficient. Further increase of the CT number occurred when silica was added, yielding a slightly higher X-ray attenuation coefficient.

3.2. Mouse phantom fabrication

The mouse skeleton was 3D printed to actual scale having a length of approximately 13 cm using ASA thermoplastic. Since none of the tested thermoplastic materials were shown to have the proper radiographic behavior in terms of mimicking bone, selection was based on other criteria. Firstly, ASA was found to possess the highest HU value, which was essential for achieving good radiographic contrast in the fi-

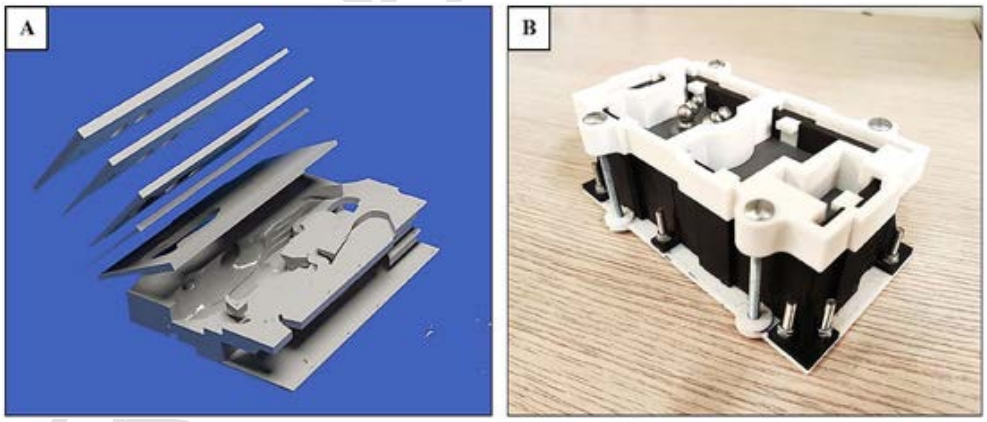

Fig. 4. (A) Exploited view of the mouse mold showing the multiple structure layers, (B) Assembled 3D printed mouse model.

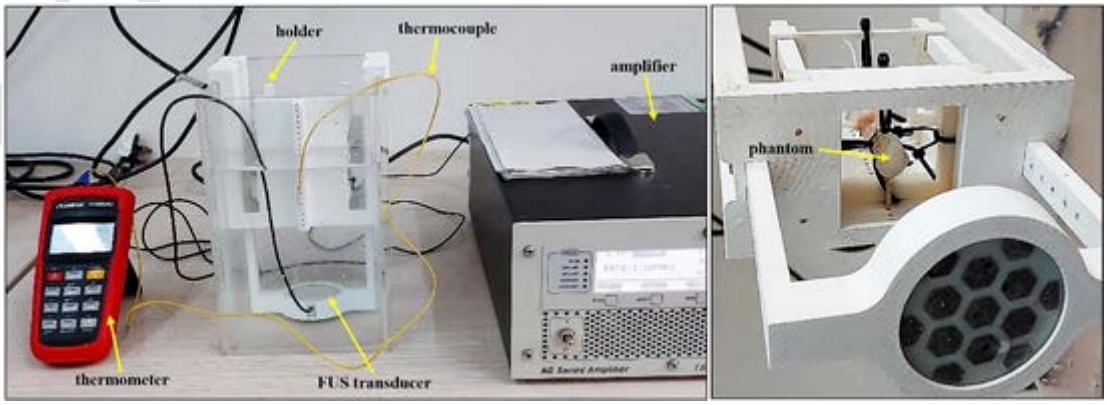

Fig. 5. Experimental setup used for performing FUS sonications in the mouse phantom showing the location of each compartment.

Table 1
The estimated CT number of each sample expressed in Hounsfield units (HU) and the corresponding X-ray linear attenuation coefficient (μ) for 120 kV tube voltage and 300 mA tube current (using μ_{water} = 0,16 cm^{-1}), along with the CT numbers of mouse and human tissues as extracted from the literature.

Material	CT number (HU)	μ (cm^{-1})	Source
ASA plastic	191.4	0.1906	Self-measured
PP plastic	−171.0	0.1326	
PLA plastic	154.1	0.1847	
VeroClear resin	111.9	0.1779	
VERO-WHITE	130 ± 10	–	[39]
Cortical bone	1524	–	[64]
Cancellous bone	265 ± 135	–	[65]
Mouse skeleton	108 ± 20	–	[39]
Rabbit skeleton	146 ± 20		
2 % agar	10.2	0.1616	
4 % agar	16.9	0.1627	Self-measured
6 % agar	24.4	0.1639	
6 % agar & 4 % silica	54.3	0.1687	
Human muscle	45 ± 5	–	[64]
Brain tissue	20–40	–	[6667]
	28 ± 19		

nal phantom. In addition, it was previously proven to possess bone tissue-like ultrasonic properties. It is also a benefit that ASA models have higher durability and high temperature resistance [68], and they are 3D printed using the FDM method that is considered more cost-effective than Polyjet printing due to the use of minimal support material [68], thus enabling lower cost production.

The mouse body consisted of 6 % w/v agar and 4 w/v silica. The specific composition of inclusions resulted in a CT number similar to that reported in the literature for soft tissues [39,64]. The ultrasonic and MR relaxation properties of the soft-tissue mimic as estimated in previous studies were also taken into consideration for the recipe selection. Table 2 summarizes the critical properties of the proposed phantom by combining results of the current and previous studies and compares them with literature values of live tissue [39,52,54,60,64,69–72]. Fig. 7A shows the 3D printed skeleton as placed inside the mouse mold cavity before pouring the agar mixture. Fig. 7B shows the mouse skeleton model and the whole mouse phantom side by side.

3.3. Phantom imaging

Fig. 8 shows PD Cube images of the phantom from a 1.5 T MRI scanner. Note that the brightness in PD images is determined by the hydrogen content of the imaging object. Thereby, the 3D printed mouse skeleton appears black due to the lack of protons. On the contrary, the agar-based mouse body phantom is rich in protons due to its large water component, thus producing stronger signal and appearing brighter in the image. CT scans of the phantom are shown in Fig. 9. Note that there is a good radiological contrast between the mouse skeletal bone and body.

3.4. Trans-skull sonication in the mouse phantom

Sonication with continuous FUS at 30 W (for 60 s) resulted in a total temperature increase of 11.2 °C at the focus, whereas pulsed FUS (DF = 1 % for 60 s) caused a temperature rise of 2.9 °C. The corresponding temperature profiles (focal temperature versus time) can be seen in Fig. 10. Note that a substantial (about 4-fold) decrease in temperature change is observed when using pulsed FUS (compared to continuous FUS) owing to the very low intensities produced in the phantom. Also, note that the thermal profile presents plateaus where the temperature remains constant for several seconds indicating a very slow rate of heat deposition.

4. Discussion

The current study focused on the development of an US, MRI, and CT imaging compatible realistic mouse phantom for thermal ablation and FUS studies. The thermal ablation modalities could be radiofrequency ablation (RFA), microwave ablation (MWA), and laser thermal ablation (LTA) [73]. The mouse model consists of the mouse body and skeletal bone (excluding the ribs) and was developed according to the segmentation data derived from CT scans of a mouse. The skeletal structure was isolated by thresholding and manufactured by 3D printing with ASA material following further smoothing on a dedicated software. Similarly, the mouse body was constructed by molding an agar-based gel in a 3D printed mold, which was specially-designed having a cavity with the unique shape of the imaged mouse. Careful mold design with multiple layers was followed to allow the mouse model to freely separate from the cavity. Accordingly, proper demolding allowed the creation of a smooth phantom surface, which is essential for achieving proper ultrasonic transmission in FUS applications.

The selection of an agar-based phantom to mimic soft tissue was based on numerous criteria, including its ability to replicate critical properties of living tissues (Table 2). It is also of paramount importance that agar has a melting temperature near 85 °C, which makes it suitable for thermal applications, such as FUS [10]. Accordingly, numerous studies have suggested the use of agar-based phantoms replicating critical acoustical and thermal properties of soft tissue [10,52,55,60,74] with the FUS technology.

Our results further demonstrated the ability of agar gels to induce similar radiographic attenuation with soft tissues. The X-ray attenuation coefficient of the four candidate soft-tissue mimicking materials was measured using CT scans and compared with that of living tissues. The results suggest that increasing agar concentration (2 to 6 % w/v) increases the CT number at a low rate (10 to 24 HU). The addition of silicon dioxide (4 % silica, 6 % agar) resulted in a more than 2-fold in-

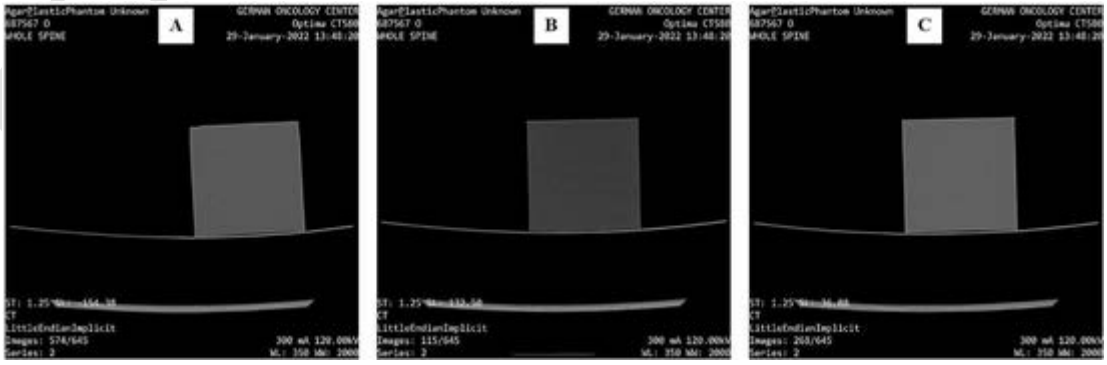

Fig. 6. CT images of the (A) sample containing 6 % w/v agar and 4 % w/v silica, (B) PP sample, and (C) Vero Clear Resin sample (120 kV tube voltage and 300 mA tube current).

Table 2
The critical properties of the mouse phantom compared to literature values for live human/mouse tissue.

Property	Agar-based phantom	Live tissue	ASA skeleton	Live tissue
Hounsfield Units	54.3	Human muscle: 45 ± 5 [64] Mouse muscle: 41 ± 5 [39]	191.4	Mouse skeleton: 107.91 ± 20 [39]
Attenuation coefficient (dB/cm)	1.1 ± 0.09 (1 MHz) [60]	Rabbit Muscle: 1.18 ± 0.46 [60]	16.8 ± 1.8 (1 MHz) [54]	Skull bone: 13–24 (1 MHz) [69]
Ultrasonic velocity (m/s)	–	–	3041 ± 27 (2.7 MHz) [54]	Skull bone: 2840 ± 158 [69]
T1 relaxation time at 1.5 T (ms)	1251 ± 3 [52]	Human muscle: 1060 ± 155 [70]	–	–
T2 relaxation time at 1.5 T (ms)	23.4 ± 0.2 [52]	Human muscle: 35 ± 4 [70]	–	–
Thermal conductivity (W/m-K)	Agar gel: 0.59 [71]	Human muscle: 0.5–0.6 [72]		

crease of the CT number (54 HU), which is slightly higher than the value of 45 ± 5 HU reported for human muscle [64]. The silica doped phantom also matches sufficiently the value of 41 ± 5 HU reported by Zhang et al [39] for mouse muscle.

The methodology used for manufacturing the skeleton mimic including bone segmentation by thresholding, image processing, and 3D printing resulted in a smooth and detailed model, which matched the size and accurately reproduced the shape of the imaged mouse skeleton. Advantageously, several studies have demonstrated the efficacy of 3D printed thermoplastics to mimic bone in terms of acoustic properties and have suggested their use with the FUS technology [1,35,36].

Ideally, bone-mimicking materials should also be X-ray attenuation equivalent to bone in order to be suitable for radiographic imaging. According to the evaluation results, none of the tested thermoplastic samples was found to be radiographically representative of human bones [75], which have significantly higher CT numbers in the range of 300–2000 HU depending on whether they are cancellous or cortical [75]. However, the estimated CT numbers are close to the value of 107.91 ± 20 HU reported by Zhang et al. [39] for mouse bone (at 120 kVp and 100 mAs).

The developed phantom was evaluated by MRI and CT imaging to assess whether it provides tissue-like signal. The agar-based mouse body mimic demonstrated tissue-like MRI signal as expected. In addition, the mouse skeleton was delineated well by MRI imaging (Fig. 8). Accordingly, the CT images (Fig. 9) reveal good radiological contrast between the mouse skeletal bone and body, which is similar to that observed for the live mouse (Fig. 2).

Finally, the mouse phantom was able to reproduce realistic behavior during *trans*-skull sonication as proved by thermometry measurements with a thermocouple. As demonstrated in Fig. 10, the temperature increased due to heat absorption and then decreased gradually after transducer deactivation due to heat dissipation through conduction mechanisms. As expected, heat dissipation is a slower process, and its rate decreases with time. In this regard, the phantom demonstrated realistic response to heat, except from the absence of blood flood, which contributes to post-sonication heat loss and would result in steeper drop of the focal temperature. The obtained preliminary results further suggest that the phantom can develop high temperatures during heating, and thus, it can be used for assessing thermal protocols, given also that it possess tissue-like acoustic, thermal, and MRI properties (Table 2). However, further investigation is required to comprehensively assess the phantom's response to thermal heating. Regarding pulsed FUS, the recorded temperature change is important in the sense that it was maintained below the safety threshold where thermal effects can be considered negligible [76]. It is also essential that the phantom enabled the insertion of thermocouples without losing its structural integrity. As expected, the presence of the ASA skull affected the results by decreasing the rate of heat deposition through beam spreading and focal shifting [54]. Note also that although single element transducers cannot compensate these energy losses, they were proven suitable for *trans*-skull applications in mice due to their thin skull bone [30,77–79].

The phantom offers realistic visualization in US, MRI, and CT, which constitute the modalities that have been used so far for the positioning of thermal applicators, as well as for therapy guidance or/and determi-

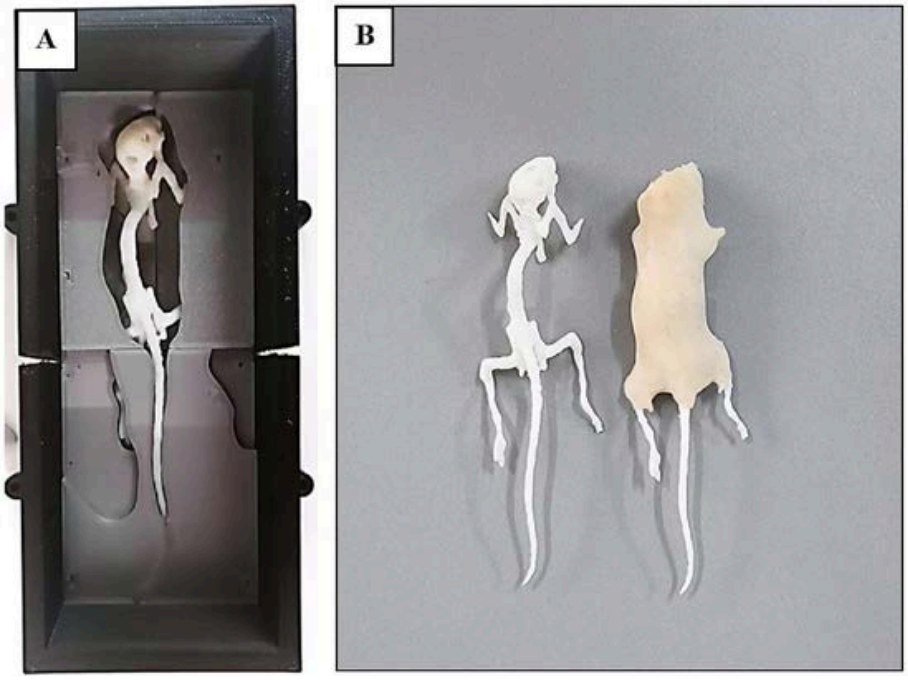

Fig. 7. Photos of the (A) 3D printed skeleton as placed inside the mouse mold cavity, (B) 3D printed mouse skeleton and whole mouse phantom.

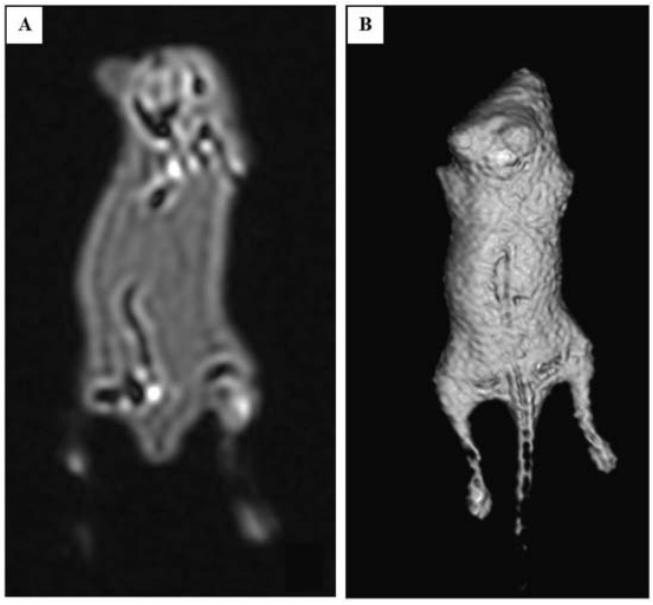

Fig. 8. MRI image of the mouse phantom acquired using PD 3D FSE Cube sequence: (A) coronal plane with TE = 60 ms, and (B) 3D reconstruction with TE = 30 ms.

nation of tissue destruction [45–47]. In the context of transcranial FUS, although the proposed phantom is not physiologically accurate, replication of the main acoustic, thermal, and MRI properties is considered adequate in terms of assessing the spatial accuracy of ultrasound delivery and how it is affected by the skull-induced beam aberration, the dimensions of the FUS spot, thermal effects at the region of interest and potential off-target effects, such as thermal deposition near to the skull, as well as the focal acoustic pressure in the case of pulsed FUS. Such information are required for adjusting the setup and/or sonication parameters so as to correct beam shifting, avoid off-target bioeffects, and compensate for energy losses, thus achieving the desired thermal or mechanical effects at the desired location. In terms of equipment testing, examples of particular applications we anticipate the phantom being useful for are the testing of the *trans*-skull heating abilities of newly-developed FUS transducers or the steering abilities of phased array ones, the linearity of output power, the response to increasing power and the limit for safe operation, as well as the assessment of shelf-heating effects and identification of malfunctions in equipment's operation.

The feasibility experiments performed in this study demonstrated the functionality of the phantom for the evaluation of thermal protocols. Future studies are though needed to further assess the thermal response of the phantom when exposed to continuous FUS at increasing ultrasonic power, as well as the acoustic pressure field generated by pulsed FUS with varying ultrasonic parameters. In this regard, its MRI compatibility will enable temperature monitoring in real-time through MR thermometry. It is clarified that the phantom is not intended to replace mouse studies but rather to minimize the required number of studies by allowing optimization of experimental features and parameters before in-vivo experimentation.

5. Conclusions

The current study presented a method to rapidly produce an anatomically accurate mouse phantom based on CT scans data of a live mouse. The proposed phantom is inexpensive, accessible, realistic, and do not require ethical approval. It can be manufactured in house following a relatively easy and cost-effective process to accelerate biomedical research, given that commercial phantoms are offered at very high cost [39]. The phantom could constitute a powerful tool in small animal studies enabling the testing and optimization of thermal ablation and FUS systems and protocols before performing experiments in live mice, thereby avoiding the unnecessary use of live mice. It also possess great potential for use in transcranial FUS applications.

Ethics approval declaration

The study does not include data on patients.

The healthy mouse imaged for the purposes of this study was provided by the Cyprus Institute of Neurology and Genetics under the study license CY/EXP/PR.L05/2021.

Declaration of Competing Interest

The authors declare that they have no known competing financial interests or personal relationships that could have appeared to influence the work reported in this paper.

Data availability

Data will be made available on request.

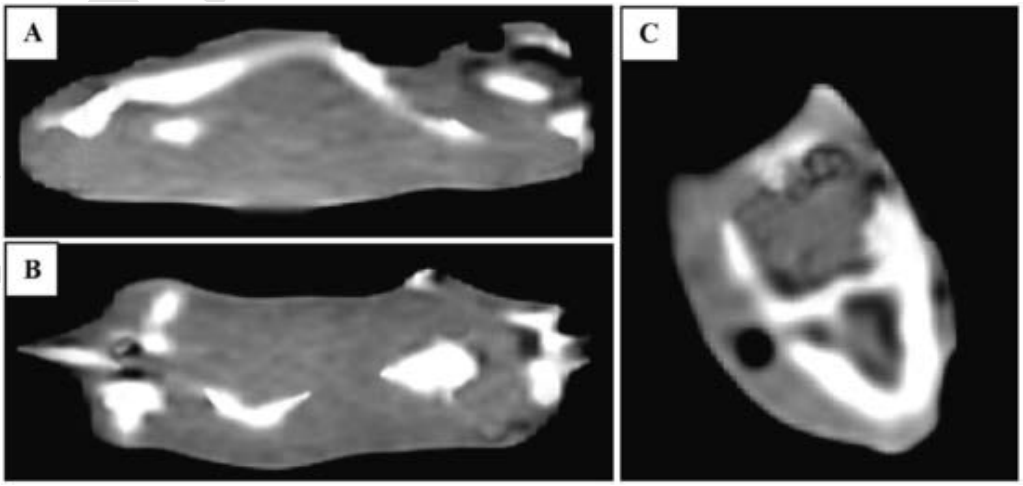

Fig. 9. CT image of the whole mouse phantom (tube voltage = 120 kV, tube current = 440 mA, exposure time = 2.34 s, slice thickness = 1.25 mm): (A) Side view center slice, (B) Top view slice, and (C) Front view slice of mouse head.

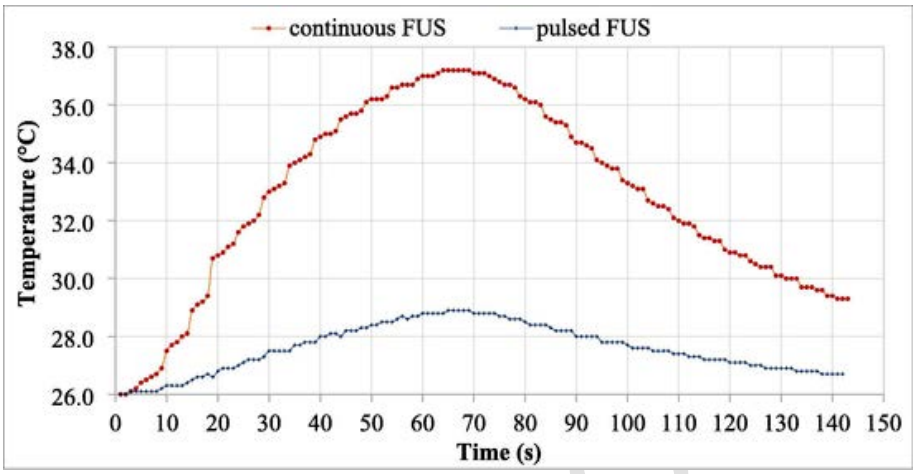

Fig. 10. Temperature change versus time recorded in the phantom at focal depth of 2 cm during continuous and pulsed (DF of 1 %) sonication at acoustic power of 30 W for 60 s using the 1 MHz transducer.

Acknowledgments

The study was co-funded by the European Structural & Investment Funds (ESIF) and the Republic of Cyprus through the Research and Innovation Foundation (RIF) under the project SOUNDPET (INTEGRATED/0918/0008).

References

[1] G. Menikou, M. Yiannakou, C. Yiallouras, C. Ioannides, C. Damianou, MRI-compatible bone phantom for evaluating ultrasonic thermal exposures, Ultrasonics 71 (2016) 12–19, https://doi.org/10.1016/j.ultras.2016.05.020.

[2] A. Kozana, T. Boursianis, G. Kalaitzakis, M. Raissaki, T.G. Maris, Neonatal brain: Fabrication of a tissue-mimicking phantom and optimization of clinical T1w and T2w MRI sequences at 1.5 T, Phys. Medica 55 (2018) 88–97, https://doi.org/10.1016/j.ejmp.2018.10.022.

[3] M. Giannakou, et al., MRI-guided focused ultrasound robotic system for transrectal prostate cancer therapy, Int. J. Med. Robot. Comput. Assist. Surg. 17 (3) (2021) 1–15, https://doi.org/10.1002/rcs.2237.

[4] A. Antoniou, M. Giannakou, E. Georgiou, K.A. Kleopa, C. Damianou, Robotic device for transcranial focussed ultrasound applications in small animal models, Int. J. Med. Robot. Comput. Assist. Surg. 18 (6) (2022) 1–11, https://doi.org/10.1002/rcs.2447.

[5] A. Antoniou, et al., Robotic system for magnetic resonance guided focused ultrasound ablation of abdominal cancer, Int. J. Med. Robot. Comput. Assist. Surg. 17 (5) (2021) pp, https://doi.org/10.1002/rcs.2299.

[6] J. Bini, J.M. David Izquierdo-Garcia, J. Machac, J. Narula, V. Fuster, Z.A. Fayad, Preclinical evaluation of MR-attenuation correction versus CT-attenuation correction on a sequential whole-body MR/PET scanner, Invest Radiol. 48 (5) (2013) 313–322, https://doi.org/10.1097/RLI.0b013e31827a49ba.

[7] A.N. Pouliopoulos, S.Y. Wu, M.T. Burgess, M.E. Karakatsani, H.A.S. Kamimura, E.E. Konofagou, A Clinical System for Non-invasive Blood-Brain Barrier Opening Using a Neuronavigation-Guided Single-Element Focused Ultrasound Transducer, Ultrasound Med. Biol. 46 (1) (2020) 73–89, https://doi.org/10.1016/j.ultrasmedbio.2019.09.010.

[8] C.K. McGarry, et al., Tissue mimicking materials for imaging and therapy phantoms: A review, Phys. Med. Biol. 65 (23) (2020) pp, https://doi.org/10.1088/1361-6560/abbd17.

[9] L.A. Dewerd, M. Kissick, Biological and Medical Physics, Biomedical Engineering - The Phantoms of Medical and Health Physics: Devices for Research and Development, Springer, New York, 2014.

[10] A. Antoniou, C. Damianou, MR relaxation properties of tissue-mimicking phantoms, Ultrasonics 119 (2022), https://doi.org/10.1016/j.ultras.2021.106600.

[11] C.K. McGarry, et al., Tissue mimicking materials for imaging and therapy phantoms: A review, Phys. Med. Biol. 65 (23) (2020) 1–43, https://doi.org/10.1088/1361-6560/abbd17.

[12] G.P. Mazzara, R.W. Briggs, Z. Wu, B.G. Steinbach, Use of a modified polysaccharide gel in developing a realistic breast phantom for MRI, Magn. Reson. Imaging 14 (6) (1996) 639–648, https://doi.org/10.1016/0730-725X(96)00054-9.

[13] K. Yoshimura, et al., Development of a Tissue-Equivalent MRI Phantom Using Carrageenan Gel, Magn. Reson. Med. 50 (2003) 1011–1017, https://doi.org/10.1002/mrm.10619.

[14] C. Bai, M. Ji, A. Bouakaz, Y. Zong, M. Wan, Design and Characterization of an Acoustically and Structurally Matched 3-D-Printed Model for Transcranial Ultrasound Imaging, IEEE Trans. Ultrason. Ferroelectr. Freq. Control 65 (5) (2018) 741–748, https://doi.org/10.1109/TUFFC.2018.2811756.

[15] Technical Committee EPL/87, "IEC 61685:2001," Ultrasonics - Flow measurement systems - Flow test object, 2001. [Online]. Available: https://webstore.iec.ch/publication/5721. [Accessed: 07-Nov-2022].

[16] Technical Committee EPL/87, "IEC TS 62791:2022," Ultrasonics - Pulse-echo scanners - Low-echo sphere phantoms and method for performance testing of grey-scale medical ultrasound scanners applicable to a broad range of transducer types, 2022. [Online]. Available: https://webstore.iec.ch/publication/68146. [Accessed: 07-Nov-2022].

[17] S. Rajagopal, N. Sadhoo, B. Zeqiri, Reference Characterisation of Sound Speed and Attenuation of the IEC Agar-Based Tissue-Mimicking Material Up to a Frequency of 60 MHz, Ultrasound Med. Biol. 41 (1) (2015) 317–333, https://doi.org/10.1016/j.ultrasmedbio.2014.04.018.

[18] G. Cloutier, et al., A multimodality vascular imaging phantom with fiducial markers visiblein DSA, CTA, MRA, and ultrasound, Med Phys 31 (6) (2004) pp, https://doi.org/10.1118/1.1739300.

[19] E. Dahal, et al., Stable gelatin-based phantom materials with tunable x-ray attenuation properties and 3D printability for x-ray imaging, Phys. Med. Biol. 63 (9) (2018) pp, https://doi.org/10.1088/1361-6560/aabd1f.

[20] J. Laing, J. Moore, R. Vassallo, D. Bainbridge, M. Drangova, T. Peters, Patient-specific cardiac phantom for clinical training and preprocedure surgical planning, J Med Imaging 5 (2) (2018) pp, https://doi.org/10.1117/1.JMI.5.2.021222.

[21] D.R. Jacobson, Gel-Based Phantoms for Diagnostic Radiology, Radiat. Prot. Dosimetry 49 (1–3) (1993) 199–200, https://doi.org/10.1093/rpd/49.1-3.199.

[22] C. Damianou, K. Hynynen, The effect of various physical parameters on the size and shape of necrosed tissue volumeuring ultrasound surgery, J. Acoust. Soc. Am. 95 (3) (1994) 1641–1649, https://doi.org/10.1121/1.408550.

[23] J.E. Kennedy, G.R. TER Haar, D. Cranston, High intensity focused ultrasound: surgery of the future? Br. J. Radiol. 76 (2003) 590–599, https://doi.org/10.1259/bjr/17150274.

[24] M. Zeece, "Food additives," in Introduction to the Chemistry of Food, 2020, pp. 251–311.

[25] K. Abe, T. Taira, Focused ultrasound treatment, present and future, Neurol. Med. Chir. (Tokyo) 57 (8) (2017) 386–391, https://doi.org/10.2176/nmc.ra.2017-0024.

[26] U. Schätzle, T. Reuner, J. Jenne, A. Heilingbrunner, Quality assurance tools for therapeutic ultrasound, Ultrasonics 36 (1–5) (1998) 679–682, https://doi.org/10.1016/S0041-624X(97)00138-8.

[27] G. Acri, et al., A 'user-friendly' phantom to conduct Quality Controls on MRgFUS device, Journal of Physics: Conference Series 2162 (1) (2022) 012004, https://doi.org/10.1088/1742-6596/2162/1/012004.

[28] S. Ambrogio, et al., A standard test phantom for the performance assessment of magnetic resonance guided high intensity focused ultrasound (MRgHIFU) thermal therapy devices, Int. J. Hyperth. 39 (1) (2022) 57–68, https://doi.org/10.1080/02656736.2021.2017023.

[29] J. Jagannathan, et al., High Intensity Focused Ultrasound surgery of the brain: Historical Perspective, With Modern Applications, Phys. Med. Biol. 55 (7) (2014) 201–211, https://doi.org/10.1227/01.NEU.0000336766.18197.8E.High.

[30] J.J. Choi, S. Wang, Y.-S. Tung, B. Morrison, E.E. Konofagou, Molecules of various pharmacologically-relevant sizes can cross the ultrasound-induced blood-brain barrier opening in vivo, Ultrasound Med Biol 36 (1) (2010) 58–67, https://doi.org/10.1016/j.ultrasmedbio.2009.08.006.

[31] J.J. Choi, K. Selert, Z. Gao, G. Samiotaki, B. Baseri, E.E. Konofagou, Noninvasive and localized blood-brain barrier disruption using focused ultrasound can be achieved at short pulse lengths and low pulse repetition frequencies, J. Cereb. Blood Flow Metab. 31 (2) (2011) 725–737, https://doi.org/10.1038/jcbfm.2010.155.

[32] S. Wang, G. Samiotaki, O. Olumolade, J.A. Feshitan, E.E. Konofagou, Microbubble Type and Distribution Dependence of Focused Ultrasound Induced Blood Brain Barrier Opening, Bone 23 (1) (2008) 1–7, https://doi.org/10.1016/j.ultrasmedbio.2013.09.015.

[33] N.A. Lapin, K. Gill, B.R. Shah, R. Chopra, Consistent opening of the blood brain barrier using focused ultrasound with constant intravenous infusion of microbubble agent, Sci. Rep. 10 (1) (2020) 1–11, https://doi.org/10.1038/s41598-020-73312-9.
[34] C.D. Arvanitis, et al., Mechanisms of enhanced drug delivery in brain metastases with focused ultrasound-induced blood–tumor barrier disruption, Proc. Natl. Acad. Sci. U. S. A. 115 (37) (2018) E8717–E8726, https://doi.org/10.1073/pnas.1807105115.
[35] V. Hadjisavvas, N. Mylonas, K. Ioannides, C. Damianou, An MR-compatible phantom for evaluating the propagation of high intensity focused ultrasound through the skull, AIP Conf. Proc. 1481 (2012) 119–124, https://doi.org/10.1063/1.4757321.
[36] G. Menikou, T. Dadakova, M. Pavlina, M. Bock, C. Damianou, MRI compatible head phantom for ultrasound surgery, Ultrasonics 57 (2015) 144–152, https://doi.org/10.1016/j.ultras.2014.11.004.
[37] G. Menikou, M. Yiannakou, C. Yiallouras, C. Ioannides, C. Damianou, MRI-compatible breast/rib phantom for evaluating ultrasonic thermal exposures, Int. J. Med. Robot. Comput. Assist. Surg. 14 (1) (2018) 1–12, https://doi.org/10.1002/rcs.1849.
[38] E. Doney, et al., 3D printing of preclinical X-ray computed tomographic data sets, J. Vis. Exp. 22 (73) (2013) 1–6, https://doi.org/10.3791/50250.
[39] H. Zhang et al., "Fabrication of an anthropomorphic heterogeneous mouse phantom for multimodality medical imaging," Phys. Med. Biol., vol. 63, no. 19, 2018, doi: 10.1088/1361-6560/aadf2b.
[40] T. Dann, et al., Anatase titanium dioxide imparts photoluminescent properties to PA2200 commercial 3D printing material to generate complex optical imaging phantoms, Materials (Basel) 14 (7) (2021) 1–9, https://doi.org/10.3390/ma14071813.
[41] D. Welch, A.D. Harken, G. Randers-Pehrson, D.J. Brenner, Construction of mouse phantoms from segmented CT scan data for radiation dosimetry studies, Phys. Med. Biol. 60 (9) (2015) 3589–3598, https://doi.org/10.1088/0031-9155/60/9/3589.
[42] N. Esplen, E. Alyaqoub, M. Bazalova-Carter, Technical Note: Manufacturing of a realistic mouse phantom for dosimetry of radiobiology experiments, Med. Phys. 46 (2) (2019) 1030–1036, https://doi.org/10.1002/mp.13310.
[43] G. Price et al., "An open source heterogeneous 3D printed mouse phantom utilising a novel bone representative thermoplastic," Phys. Med. Biol., vol. 65, no. 10, 2020, doi: 10.1088/1361-6560/ab8078.
[44] M. Bainier, A. Su, R.L. Redondo, 3D printed rodent skin-skull-brain model: A novel animal-free approach for neurosurgical training, PLoS One 16 (6) (2021) 1–12, https://doi.org/10.1371/journal.pone.0253477.
[45] Z. Cheng, P. Liang, Advances in ultrasound-guided thermal ablation for symptomatic benign thyroid nodules, Adv Clin Exp Med 29 (9) (2020) 1123–1129, https://doi.org/10.17219/acem/125433.
[46] M. Zhu, Z. Sun, C.K. Ng, Image-guided thermal ablation with MR-based thermometry, Quant Imaging Med Surg. 7 (3) (2017) 356–368, https://doi.org/10.21037/qims.2017.06.06.
[47] E. Botsa, S. Mylona, I. Koutsogiannis, A. Koundouraki, L. Thanos, CT image guided thermal ablation techniques for palliation of painful bone metastases, Ann Palliat Med 3 (2) (2014) 47–53, https://doi.org/10.3978/j.issn.2224-5820.2014.04.02.
[48] G. Menikou, C. Damianou, Acoustic and thermal characterization of agar based phantoms used for evaluating focused ultrasound exposures, J. Ther. Ultrasound 5 (2017), https://doi.org/10.1186/s40349-017-0093-z.
[49] R.L. King, B.A. Herman, S. Maruvada, K.A. Wear, G. Harris, Development of a HIFU phantom, AIP Conf. Proc. 911 (2007) 351–356, https://doi.org/10.1063/1.2744296.
[50] V. Rieke, K.B. Pauly, MR Thermometry, J Magn Reson Imaging 27 (2) (2008) 376–390, https://doi.org/10.1002/jmri.21265.MR.
[51] V. Hadjisavvas, K. Ioannides, M. Komodromos, N. Mylonas, C. Damianou, Evaluation of the contrast between tissues and thermal lesions in rabbit in vivo produced by high intensity focused ultrasound using fast spin echo MRI sequences, J Biomed. Sci. Eng. 4 (1) (2010) 51–61, https://doi.org/10.4236/jbise.2011.41007.
[52] A. Antoniou et al., "MR relaxation times of agar-based tissue-mimicking phantoms," J. Appl. Clin. Med. Phys., vol.23, no.5, 2022, doi: 10.1002/acm2.13533.
[53] N. Esplen, F. Therriault-Proulx, L. Beaulieu, M. Bazalova-Carter, Preclinical dose verification using a 3D printed mouse phantom for radiobiology experiments, Med. Phys. 46 (11) (2019) 5294–5303, https://doi.org/10.1002/mp.13790.
[54] A. Antoniou, N. Evripidou, M. Giannakou, G. Constantinides, C. Damianou, Acoustical properties of 3D printed thermoplastics, J. Acoust. Soc. Am. 149 (4) (2021) 2854–2864, https://doi.org/10.1121/10.0004772.
[55] T. Drakos, M. Giannakou, G. Menikou, G. Constantinides, C. Damianou, Characterization of a soft tissue-mimicking agar/wood powder material for MRgFUS applications, Ultrasonics 113 (2021) 10635, https://doi.org/10.1016/j.ultras.2021.106357.
[56] A. Hellerbach, V. Schuster, A. Jansen, J. Sommer, MRI Phantoms – Are There Alternatives to Agar? PLoS One 8 (8) (2013) e70343.
[57] M.D. Mitchell, H.L. Kundel, L. Axel, P.M. Joseph, Agarose as a tissue equivalent phantom material for NMR imaging, Magn. Reson. Imaging 4 (3) (1986) 263–266, https://doi.org/10.1016/0730-725X(86)91068-4.
[58] J.O. Christoffersson, L.E. Olsson, S. Sjöberg, Nickel-doped agarose gel phantoms in MR imaging, Acta radiol. 32 (5) (1991) 426–431, https://doi.org/10.3109/02841859109177599.
[59] A. Dabbagh, B.J.J. Abdullah, C. Ramasindarum, N.H. Abu Kasim, Tissue-mimicking gel phantoms for thermal therapy studies, Ultrason. Imaging 36 (4) (2014) 291–316, https://doi.org/10.1177/0161734614526372.
[60] T. Drakos, et al., Ultrasonic Attenuation of an Agar, Silicon Dioxide, and Evaporated Milk Gel Phantom, J. Med. Ultrasound 29 (4) (2021) 239–249, https://doi.org/10.4103/JMU.JMU.
[61] A. Filippou, C. Damianou, Evaluation of ultrasonic scattering in agar-based phantoms using 3D printed scattering molds, J. Ultrasound 25 (3) (2022) 597–609, https://doi.org/10.1007/s40477-021-00630-7.
[62] T.E. Reeves, P. Mah, W.D. McDavid, Deriving Hounsfield units using grey levels in cone beam CT: A clinical application, Dentomaxillofacial Radiol. 41 (6) (2012) 500–508, https://doi.org/10.1259/dmfr/31640433.
[63] A. Fedorov, et al., 3D Slicer as an Image Computing Platform for the Quantitative Imaging Network, Magn. Reson. Imaging 30 (9) (2012) 1323–1341, https://doi.org/10.1016/j.mri.2012.05.001.
[64] W. Schneider, T. Bortfeld, W. Schlegel, Correlation between CT numbers and tissue parameters needed for Monte Carlo simulations of clinical dose distributions, Phys. Med. Biol. 45 (2) (2000) 459–478, https://doi.org/10.1088/0031-9155/45/2/314.
[65] S. V G, M. K, and B.-F. P, "Electrical properties of phantoms for mimicking breast tissue," in 39th Annual International Conference of the IEEE Engineering in Medicine and Biology Society, 2017, pp. 157–160.
[66] A.A. Konstas, G.V. Goldmakher, T.-Y. Lee, M.H. Lev, Theoretic basis and technical implementations of CT perfusion in acute ischemic stroke, Part 2: Technical implementations, Am. J. Neuroradiol. 30 (5) (2009) 885–892.
[67] D.N. Makris, et al., Characterization of a novel 3D printed patient specific phantom for quality assurance in cranial stereotactic radiosurgery applications, Phys. Med. Biol. 64 (10) (2019) pp, https://doi.org/10.1088/1361-6560/ab1758.
[68] F. Fischer, FDM and Polyjet 3D Printing, Pop. Plast. Packag. 60 (6) (2015) 7.
[69] F.J. Fry, J.E. Barger, Acoustical properties of the human skull, J. Acoust. Soc. Am. 63 (5) (1978) 1576–1590, https://doi.org/10.1121/1.381852.
[70] G.J. Stanisz, et al., T1, T2 relaxation and magnetization transfer in tissue at 3T, Magn. Reson. Med. 54 (3) (2005) 507–512, https://doi.org/10.1002/mrm.20605.
[71] J. Huang, R.G. Holt, R.O. Cleveland, R.A. Roy, Experimental validation of a tractable numerical model for focused ultrasound heating in flow-through tissue phantoms, J. Acoust. Soc. Am. 116 (2004), https://doi.org/10.1121/1.1787124.
[72] J. Crezee, J.J.W. Lagendijk, Temperature uniformity during hyperthermia: the impact of large vessels, Phys. Med. Biol. 37 (6) (1992) 1321–1337, https://doi.org/10.1088/0031-9155/37/6/009.
[73] H. Webb, M.G. Lubner, J.L. Hinshaw, Thermal Ablation, Semin. Roentgenol. 46 (2) (2011) 133–141, https://doi.org/10.1053/j.ro.2010.08.002.
[74] A. Partanen, C. Mougenot, T. Vaara, Feasibility of agar-silica phantoms in quality assurance of MRgHIFU, AIP Conf. Proc. 1113 (2009) 296–300, https://doi.org/10.1063/1.3131434.
[75] S. Patrick, N.P. Birur, K. Gurushanth, A.S. Raghavan, S. Gurudath, Comparison of gray values of cone-beam computed tomography with hounsfield units of multislice computed tomography: An in vitro study, Indian J. Dent. Res. 28 (1) (2017) 66–70.
[76] J. Foley, J. Snell, A. Hananel, N. Kassell, J. Aubry, Image-guided focused ultrasound: state of the technology and the challenges that lie ahead, Imaging Med. 5 (2013) 357–370, https://doi.org/10.2217/IIM.13.38.
[77] J.J. Choi, M. Pernot, S.A. Small, E.E. Konofagou, Noninvasive, transcranial and localized opening of the blood-brain barrier using focused ultrasound in mice, Ultrasound Med. Biol. 33 (1) (2007) 95–104, https://doi.org/10.1016/j.ultrasmedbio.2006.07.018.
[78] J.J. Choi, K. Selert, Z. Gao, G. Samiotaki, B. Baseri, E.E. Konofagou, Noninvasive and Localized Blood—Brain Barrier Disruption using Focused Ultrasound can be Achieved at Short Pulse Lengths and Low Pulse Repetition Frequencies, J. Cereb. Blood Flow Metab. 31 (2) (2011) 725–737, https://doi.org/10.1038/jcbfm.2010.155.
[79] S. Wang, G. Samiotaki, O. Olumolade, J.A. Feshitan, E.E. Konofagou, Microbubble type and distribution dependence of focused ultrasound-induced blood-brain barrier opening, Ultrasound Med. Biol. 40 (1) (2014) 130–137, https://doi.org/10.1016/j.ultrasmedbio.2013.09.015.

Ultrasonics 132 (2023) 106974

Contents lists available at ScienceDirect

Ultrasonics

journal homepage: www.elsevier.com/locate/ultras

Treatment of mammary cancer with focused ultrasound: A pilot study in canine and feline patients

Anastasia Antoniou, Kyriakos Spanoudes, Christakis Damianou *

Department of Electrical Engineering, Computer Engineering, and Informatics, Cyprus University of Technology, Limassol, Cyprus

ARTICLE INFO

Keywords:
Focused ultrasound ablation
Mammary cancer
Robotic
Dogs
Cats

ABSTRACT

In recent years, veterinary medicine has expanded its practices beyond conventional methods, gradually integrating the Focused Ultrasound (FUS) technology in the care of companion animals like dogs and cats. The current study aimed to examine the feasibility and provide insights into the application of thermal FUS in canine and feline mammary cancer therapy. FUS was delivered by a 2-MHz single-element spherically focused ultrasonic transducer as integrated with an existing robotic positioning device. The functionality of the FUS system and sonication protocol in efficiently and safely ablating live tissue was initially validated in a rabbit thigh model in a laboratory environment. Nine (9) dogs and cats with superficial mammary cancer were recruited through a dedicated campaign according to specific safety criteria. The veterinary patients underwent FUS ablation followed by immediate surgical resection of the entire malignancy. Histopathology examination demonstrated well-defined regions of coagulative necrosis in all treated tumors with no off-target damage. Further study with a larger patient population is needed to confirm the current findings and demonstrate the safety and feasibility of complete FUS ablation of deep-seated tumors.

1. Introduction

Mammary cancer constitutes the most common malignant neoplasm observed in female dogs [1,2], accounting for about 70 % of all diagnosed cancers according to a previous study on the occurrence of canine tumors covering cases from 1985 to 2002 [1]. An incidence rate of approximately 2 and 192 per 100,000 dog-years is reported for male and female dogs, respectively [1]. Notably, dog age is considered an important factor in disease development since the recorded cancer incidence rates increase drastically with age [1,2].

Although less common than in dogs, mammary neoplasia belongs to the three most prevalent types of tumor in female cats, accounting for about 17 % of all neoplasms [3]. There is an estimated number of 230 neoplasia cases per 100,000 female cats annually, with 80 to 90 % of them being malignant [4]. In fact, the majority of feline mammary tumors are malignant and usually diagnosed at an advanced stage when already metastasized [5]. Accordingly, mammary carcinomas have a very poor survival prognosis of eight to twelve months after surgical resection [4].

Dogs and cats with cancer have been proposed as effective models for studying human cancer, offering significant benefits over genetically engineered rodent models, which have so far been the main *in-vivo* model in preclinical oncological research [5–8]. Firstly, while mice within an inbred strain possess identical genomes, dogs and cats are genetically heterogeneous, thus enhancing experimental variability. Furthermore, compared to rodent genes, canine cancer genes are more homologous to their human counterparts [6]. Great homology exists between the feline and human genomes as well [7,8]. Being exposed to the same environmental risk factors as humans, cats and dogs reflect the complex interactions between genetics and environment more accurately [5].

Key genes involved in the development of mammary gland cancer have been found to be remarkably homologous in humans, dogs, and cats. Human and feline mammary gland tumors share similar epidemiological features, including key risk factors such as increasing age and exposure to specific hormones [5]. De Maria et al. [8] demonstrated a close resemblance between the molecular subtype of the feline mammary carcinoma and a particular breast cancer caused by the overexpression of the HER2 gene. Canine mammary cancer also shares similar epidemiological and histological characteristics with breast

* Corresponding author at: Department of Electrical Engineering, Computer Engineering, and Informatics, Cyprus University of Technology, 30 Archbishop Kyprianou Street, 3036 Limassol, Cyprus.
E-mail addresses: am.antoniou@edu.cut.ac.cy (A. Antoniou), kyriakos.spanoudes@gmail.com (K. Spanoudes), christakis.damianou@cut.ac.cy (C. Damianou).

https://doi.org/10.1016/j.ultras.2023.106974
Received 1 December 2022; Received in revised form 30 January 2023; Accepted 27 February 2023
Available online 10 March 2023

cancer in women [9]. In fact, cancer in both species is linked to mutations in the BRCA1 gene, with the canine gene being 84 % identical to its human counterpart [9].

Therefore, canine and feline mammary cancers could serve as effective models not only for studying breast cancer but also for evaluating the therapeutic efficiency of newly developed and emerging technologies. Besides enhancing our understanding of cancer biology, comparative oncology accelerates the development and clinical translation of beneficial cancer treatments for both human and pet patients. At the same time, veterinary trials make alternative therapies accessible to household pets.

The majority of mammary carcinomas in dogs are still treated by surgery, which is though insufficient as a stand-alone therapy in cases of metastatic tumors [10]. Surgical resection is considered the method of choice for managing resectable feline mammary cancer as well [11]. Complete removal of all malignant tissue with sufficient surgical margins constitutes the optimum surgical strategy for dogs [12]. More radical approaches, such as mastectomies, are advised for cats, given the more aggressive nature of the feline disease, and have demonstrated a noticeably lower rate of local recurrence in comparison to cats undergoing conservative surgery [13,14]. Chemotherapy may be employed as adjuvant therapy in cases of metastatic disease or to prevent disease relapse [15,16].

Nowadays, driven by the increasing demand of pet owners to offer new methods of care of higher quality to their pets, alternative therapeutics are gradually emerging over conventional ones transforming the way we approach animal health care. Veterinary medicine has recently expanded its practices beyond traditional methods integrating the Focused Ultrasound (FUS) technology in the care of companion animals. FUS is a therapeutic tool that can thermally ablate tissue non-invasively. This becomes possible by precisely focusing high-intensity ultrasonic energy inside the target to induce coagulative necrosis, which occurs almost instantly at temperatures over 56 °C [17–19]. So far, FUS has been employed in the management of many oncological diseases [20] while its clinical adaption has been accelerated through the introduction of Magnetic Resonance (MR) thermometry as the guidance tool enabling almost direct acquisition of thermal maps [21,22]. At the same time, a wide variety of robotic systems offering precise navigation of the ultrasonic source relative to the subject has been developed to facilitate preclinical research in the field [23–27].

The FUS technology was introduced in veterinary medicine a few years ago with the FUS Foundation reporting that the majority of FUS-based veterinary research involves canine patients and is currently focused on oncological and pain relief applications [28]. The FUS treatment of soft tissue tumors, including mast cell tumors and sarcomas in dogs, has been reported for the first time in clinical practice in 2018 [29]. In the same year, Ryu et al. [30] published the results of a retrospective study, in which 11 cases of canine solid tumors that were treated by US-guided FUS using the “VIFU2000” system (Alpinion Medical Systems, Gyeonggi-do, South Korea) were analyzed. In almost 50 % of patients, clinical symptoms were alleviated while 40 % of patients presented tumor size reduction. During the same period, Seward et al. [31] attempted to target soft tissue sarcomas in 53 dogs located at multiple anatomical sites, including the head, truncal, and spine, using the “Sonalleve V2” MRI-guided FUS system (Profound Medical, Ontario, Canada). Authors report that despite the fact that up to 81.1 % of tumors could be targeted, only 5.7 % of canine patients would be able to have their full tumor volume treated safely without off-target adverse effects. More recently, Ranjan et al. [32] examined the feasibility of US-guided FUS to treat an oral tumor in a canine patient by thermal ablation. Histological analysis showed gradual remission of the tumor while simultaneously antitumor immune responses seemed to be triggered since enhanced immune cell multiplication occurred in the FUS-exposed area, with the main adverse event being thermal burns in the buccal mucosa [32]. The feasibility of treating soft tissue sarcomas in dogs and cats was also demonstrated in a previous study [33]. Partial ablation of sarcomas in the neck, back, belly, and face was attempted, with the histopathological examination revealing necrosis in 8 of a total of 10 cases [33].

Driven by the increasing utilization of FUS in veterinary clinical trials and its potential impact, we herein report the results of a pilot study investigating the feasibility of FUS in the management of canine and feline mammary cancer. The main goal of the study was to test the suitability and efficiency of a robotic device from a series of robots developed by our group [34–36] being equipped with a 2-MHz single element FUS transducer to induce controllable and well-defined necrosis in naturally occurring mammary tumors, following *ex-vivo* assessment in a rabbit thigh model. The study further aimed to obtain data on the safety and efficiency of the proposed FUS protocol for the ablation of superficial mammary malignancies, so far lacking in the scientific literature, simultaneously providing a good starting point for further FUS trials in veterinary patients with mammary neoplasia.

2. Materials and methods

2.1. Study workflow

Ethical approval for the described animal studies was obtained from the authorities of Veterinary Services (Ministry of Agriculture, Rural Development and Environment) of the Republic of Cyprus under the study licenses CY/EXP/PR.*L*01/2020 (rabbits) and CY/EXP/PR.*L*01/2020/R1/2021 (dogs and cats).

The first series of experiments was carried out to examine the efficiency and safety of FUS-induced thermal necrosis in a rabbit thigh model using an existing FUS robotic system, simultaneously optimizing the therapeutic protocol and addressing potential technical problems in the system before proceeding to the main study, which involved pets with naturally occurring mammary gland tumors.

For the purpose of the current study, an MRI-compatible robotic device from a series of robots developed by our group [34–36], was employed for guiding the ultrasonic source relative to the target. Regarding the driving electronics, robotic motion is actuated by piezoelectric motors while optical encoders provide accurate position feedback, thus creating a closed loop control system. An in-house manufactured ultrasonic transducer comprising a single element spherically focused piezoelectric element (Piezo Hannas Tech Co. ltd, Wuhan, China) with a nominal frequency of 2 MHz, a 65 mm radius of curvature, a 50 mm diameter, and acoustic efficiency of 30 % was incorporated as the end effector of the robotic mechanism. The transducer produces an ellipsoid focus of approximately 0.95 mm width (short axis) and 8.7 mm length (long axis). An amplifier with a built-in signal generator (AG1016, T & C Power Conversion, Inc., Rochester, USA) was used to supply the FUS transducer.

The employed robotic device comprises 3 linear and one angular PC-controlled stages arranged in a compact enclosure. The transducer is actuated in a separate enclosure that includes an acoustic opening for positioning the subject above the transducer’s workspace and is filled with degassed/deionized water for efficient ultrasonic transmission to the region of interest. The linear axes allow maneuvering the transducer in three orthogonal directions (left–right, forward-reverse, and top–bottom), and the Θ-axis, rotating it around its axis, thus enabling targeting from different angles. Both the ultrasonic and motion parameters were remotely controlled through a specially developed FUS software with treatment planning and monitoring capabilities. A schematic diagram of the communication between software and hardware is shown in Fig. 1.

2.2. Feasibility study in a rabbit thigh model

The rabbit experiments (n = 40) were carried out at the premises of the Cyprus University of Technology (Limassol, Cyprus) by a qualified veterinarian, who supervised all relevant procedures following the

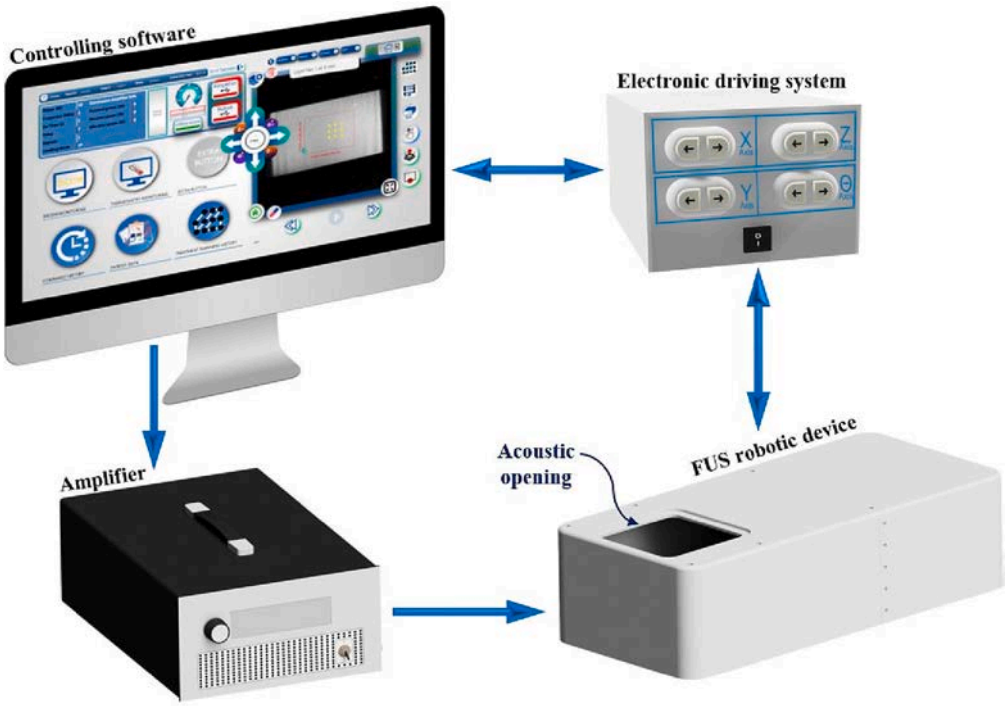

Fig. 1. Schematic of communication between the main hardware components and software.

requirements set by the Animal Welfare Committee to ensure maximal animal wellbeing. In each experiment, continuous monitoring of vital signs was performed, and a detailed record containing the anesthesia timeline and vital signs monitoring was kept.

Rabbits underwent injectable anesthesia with a combination of 0.5 mg/kg medetomidine (Medeson, Livisto GmbH, Senden, Germany) and 0.15 mg/kg ketamine (Narketan–10, Vetoquinol ltd, Towcester, UK), which offered 40–60 min of surgical anesthesia. Prior to the experiments, the thighs of the rabbit were depilated (VEET, Reckitt Benkiser, Slough, UK). The rabbit was then carefully placed on the acoustic opening of the device with its thigh immersed in degassed water. Fig. 2 illustrates the arrangement of the various system components in the laboratory and rabbit placement on the device.

Sonications were performed on the outer side of the thighs. In each case, the sonication parameters were chosen based on X-ray images (IMS001, Shenzhen Browiner Tech Co., ltd, Shenzhen, China) of the rabbit taken to calculate the muscle area available for ablation, thereby avoiding sonicating the bone and other undesirable effects. The animal was placed on left recumbency above a Computed Radiography (CR) cassette for image acquisition. After X-ray exposure, a CR reader (Vita Flex, Carestream Health, Inc., Rochester, NY, USA) was used to convert the data into a digital image. Due to limitations in the target size, linear vertical or rotational motion of the transducer was not required. Thereby, all the sonication patterns were executed in a horizontal plane in grid patterns of varying size (1×3 to 5×5). The spatial step between adjacent sonication spots as well as the ultrasonic parameters (acoustic power and sonication time) were varied to observe their effect on the dimensions (length and diameter) of the formed discrete lesions or the size of the ablated area created by overlapping lesions. Acoustic power values in the range of 23–69 W, corresponding to ultrasonic intensities in the range of 810 to 2433 W/cm^2 were tested at different sonication times of 3, 5, 10, 20 and 30 s. In all cases, the vertical distance between the transducer and acoustic opening was adjusted so that the focal depth equals 1 cm, given the small thickness of the rabbit thighs.

Upon completion of the ablation procedure, the animals were humanely euthanized with intracardial injection of an agent containing embutramide, mebezonium, and tetracaine (T61, MSD Animal Health, New Jersey, USA). Photos of the rabbit thigh were taken above and below the skin and upon exposure of the ablated muscle to capture the inflicted discrete lesions or ablated area in a plane perpendicular to the beam, as well as after cross-sectioning tissue to allow visualization in a plane parallel to the beam.

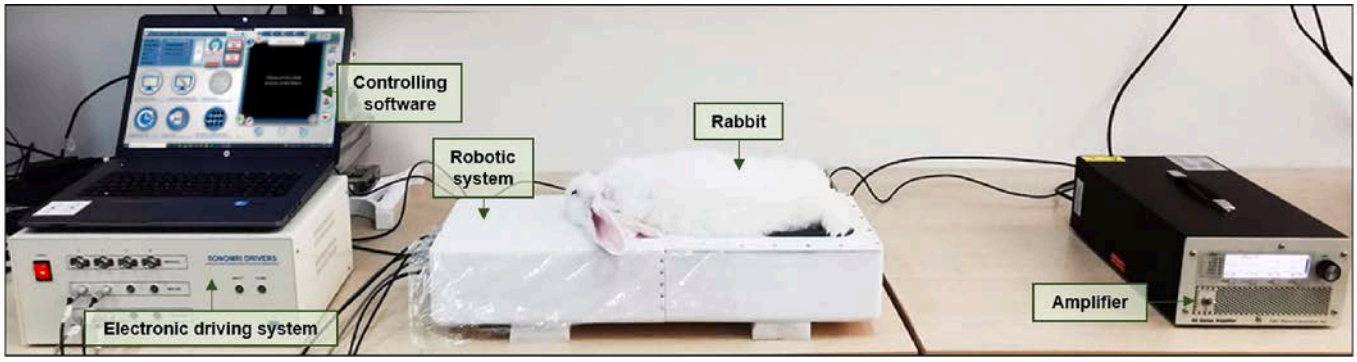

Fig. 2. Experimental set-up for rabbit thigh ablation indicating the various components.

2.3. Trial in pet cancer patients

2.3.1. Case selection

Pet recruitment was achieved by personally contacting veterinarians and informing them about the study rationale and procedure to be followed. Three veterinarians agreed to participate and provided a total of 11 referrals. Female dogs or cats heavier than 2 kg with diagnosed mammary cancer were considered eligible for enrollment on the condition that the tumor had not metastasized neither regionally, nor distantly while its volume was>20 × 20 × 30 mm^3. An owner's informed consent was obtained in all cases. Table 1 lists the main characteristics of the enrolled pets and treated tumors.

2.3.2. Ablation protocol

The pet experiments were carried out at the premises of the referring veterinarians. The pet was anesthetized using a combination of 1 mg/kg Dexmedetomidine (Dexdomitor, Elanco, Indiana, USA), 5 mg/kg Thiopental (Pentothal, Abbott Chicago, USA), and Isoflurane (IsoFlo Zoetis, New Jersey, USA) and then positioned on the device with the tumor located directly above the ultrasonic transducer in a way to eliminate any possibilities of accidentally heating healthy tissue. Specifically, the dog/cat was placed on its side so that thermal heating was entirely applied to the tumor. The concept of animal placement is shown in Fig. 3. Similar to the rabbit thigh ablation study, ultrasonic energy was delivered through degassed water, which served as the coupling agent.

The sonication protocol was adjusted mainly depending on the size of the tumor. Initially, a low power sonication was performed to assess safety. If with this exposure there was no indication of pain, then full power was applied. Tumors with dimensions of up to 60 × 50 × 30 mm^3 were treated with single sonication using acoustic power of 30 – 60 W, corresponding to focal ultrasonic intensities in the range of 1058 – 2116 W/cm^2. Otherwise, a grid sonication was performed. Table 1 lists the range of ultrasonic parameters employed for single and multiple sonications. During the experiment, the heart rate, respiration rate, urination, absence of movement/ pedal reflex, and temperature of the animal were monitored.

2.3.3. Tumor resection and histopathology

The treatment outcome was assessed by histological examination. Immediately after FUS ablation, the entire tumor was surgically removed by the pet's veterinarian and fixed in (10 %) formalin to be sent for histology to a specialized center (SGS Diagnostic Centre of Histopathology and Cytology Limited, Limassol, Cyprus). The H & E stained slides were visualized on a microscope (Olympus BX51, Shinjuku City, Tokyo, Japan), and a bright field slider scanner (VENTANA DP 200, Roche Diagnostics International AG, Rotkreuz, Switzerland) was utilized to create digital slides of high-resolution.

Table 1
Characteristics of recruited cases and ablation protocol employed for pain check and ablation.

CHARACTERISTICS OF RECRUITED PETS		
Weight of cats (kg)	2.7 – 8.0	
Weight of dogs (kg)	8.0 – 28.0	
Age (years)	9 – 12	
Size of tumor (mm^3)	60 × 30 × 30 – 80 × 60 × 30	
SONICATION PROTOCOL		
Single lesion		
Acoustic Power (W)	Pain check: 1.5 – 15	Ablation: 30 – 60
Time (s)	Pain check: 10	Ablation: 10 – 20
Overlapping lesion		
Grid size	2 × 2/3 × 3	
Acoustic Power (W)	60	
Time ON (s)	10	
Cooling time (s)	30	
Step size (mm)	3	
Focal depth (mm)	25	

The animal welfare was followed-up via phone communications with the corresponding veterinarian. Follow-ups were scheduled at 1, 3, 6 and 12 months post-treatment.

2.3.4. MR and CT imaging of pet anatomy

In the framework of these trials, the FUS system was tested in a veterinary MRI system (Vet-MR Grande, Esaote, Genoa, Italy), as shown in Fig. 4a, with the purpose to evaluate its MRI compatibility in terms of maintaining the quality and diagnostic value of imaging. A case dog was imaged with a T2-Weighted (T2-W) Fast Spin Echo (FSE) sequence with Repetition time (TR) = 2600 ms, Echo time (TE) = 125 ms, Field of view (FOV) = 256 × 256 mm^2, and slice thickness = 3 mm to visualize its anatomy.

The FUS system was also utilized with a CT scanner (SOMATOM, Siemens Healthineers, Erlangen, Germany) with the purpose to visualize the experimental setup, as well as the pet anatomy and tumor in relation to the transducer location. The robotic device was fixed to the bed of the scanner and a mattress was added around it, thus forming a flat comfortable surface for animal placement, as shown in Fig. 4b. The following parameters were used for image acquisition: tube voltage = 130 kV, tube current = 70 mA, FOV = 348 × 348 mm^2, and slice thickness = 1.5 mm.

3. Results

3.1. Feasibility study in a rabbit thigh model

During the entire procedure, all the rabbits remained in deep general anesthesia without indication of suffering until euthanasia. The size of the sonication pattern was determined by the total thigh area available for ablation as determined on X-ray images of the rabbit, as shown in Fig. 5a. By adjusting the spatial step between successive sonications and the ultrasonic parameters applied to each spot, both discrete and overlapping lesions with variable diameter and length were produced successfully, thus demonstrating the efficacy of the system in creating reproducible and controllable lesions.

Intensities of 810 and 1216 W/cm^2 applied for increasing sonication time of 5–30 s resulted in lesions with varying diameters of 3–9 mm and lengths of 2–16 mm. Accordingly, for higher ultrasonic intensities of 1622 and 2045 W/cm^2 applied for 5–20 s, lesions with a diameter ranging from 2 to 11 mm and a length ranging from 2 to 14 mm were observed. For the smallest tested intensity of 810 W/cm^2, the minimum time for creating easily observable lesions with measurable dimensions (diameter > 2 mm) was 20 s. For the maximum tested intensity, this time was reduced to 3 s. In all cases, sonications in grid patterns with a 15-mm step resulted in discrete lesions. Overlapping lesions were consistently inflicted in tissue at a 4-mm step. Using the specific spatial step, the area of necrosis was increased by increasing the duration of sonication or applied ultrasonic intensity. As an example, for sonications in a 3 × 3 grid with a 4-mm step using constant focal intensity of 1622 W/cm^2, increasing sonication time of 5, 10, and 20 s, resulted in increased ablation areas of 14 × 10 × 15 mm^3, 15 × 15 × 11 mm^3, and 19 × 19 × 12 mm^3 (in plane area × length), respectively. Remarkably, an increased intensity of 2433 W/cm^2 applied for 5 s (to each grid spot) ablated a total area of 20 × 18 × 12 mm^3, which is similar to that observed for the 1690 W/cm^2, but in 4 times less sonication time.

Fig. 5 presents indicative results of rabbit thigh ablation. Fig. 5b is a sample photo of the thigh after muscle exposure showing discrete lesions formed by sonication in a 1 × 3 grid pattern with a 10-mm step, where the three spots were successively exposed at acoustic power of 60 W (focal intensity of 2116 W/cm^2) for 10 s with a 60 s delay. The lesions from left to right have diameters of 8, 8, and 7 mm. Fig. 5c is a top view of rabbit muscle following multiple sonications at acoustic power of 60 W (focal intensity of 2116 W/cm^2) for 10 s in a 3 × 3 pattern, with a 60 s delay and a 5-mm step between adjacent sonications. Note that compared to the discrete lesions of Fig. 5b, the use of a smaller spatial

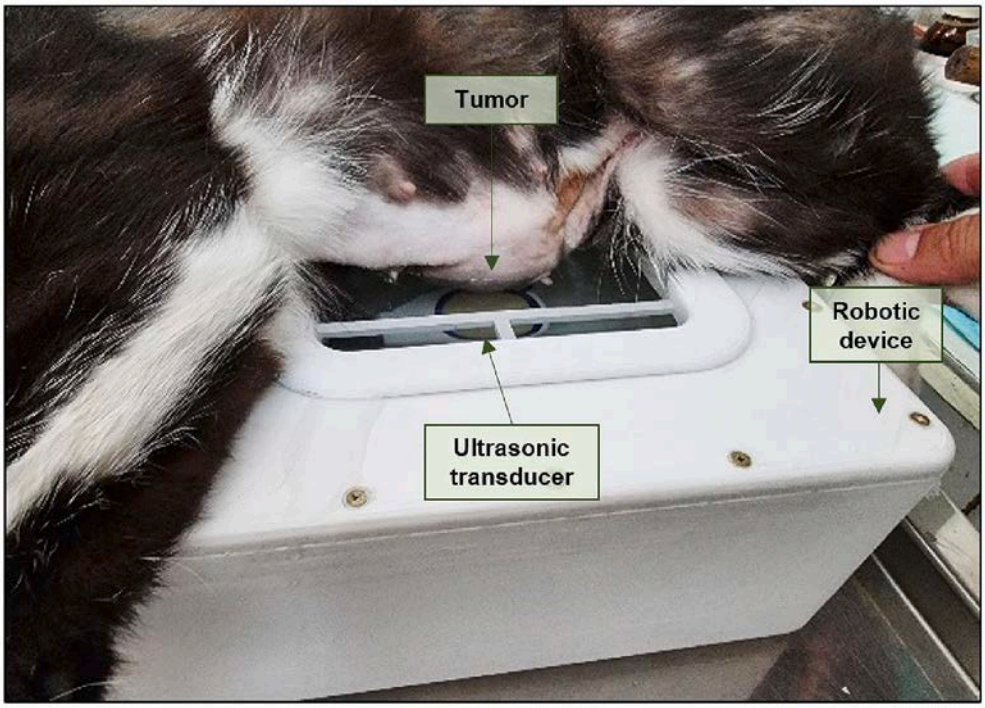

Fig. 3. Example of cat placement on the robotic device with the tumor located above the ultrasonic transducer.

Fig. 4. (a) The FUS system integrated with a veterinary MRI system (Vet-MR Grande, Esaote, Genoa, Italy) located at the premises of V3ts Veterinary Clinic (Larnaca, Cyprus). (b) The FUS system integrated with a CT scanner (SOMATOM, Siemens Healthineers) located at the premises of V3ts Veterinary Clinic (Larnaca, Cyprus).

step while keeping the sonication parameters constant resulted in the formation of overlapping lesions covering an area of 19 × 15 mm^2 and extending at a depth of 10 mm. A photo of overlapping lesions after cross-sectioning tissue is shown in Fig. 5d. In this case, the application of similar acoustic power of 60 W for a longer time of 20 s with a 60 s delay and a 4-mm step created a larger lesion of 19 × 19 × 12 mm^3. In all cases, ablation was limited within the targeted tissue without damaging other areas.

3.2. Trial in pet cancer patients

In total, 11 referrals for dogs and cats with mammary malignancies were received, from which 2 cases were excluded because the tumor size was smaller than the minimum permitted according to the set safety criteria (20 × 20 × 30 mm^3). Eventually, the trial involved 7 dogs and 2 cats with superficial solid mammary tumors.

Imaging of the pet in the presence of the robotic device in the veterinary MR scanner was proven feasible. Fig. 6a shows an indicative T2-W image of a case dog with excellent visualization of the dog anatomy and tumor and no noticeable susceptibility artifacts. CT imaging allowed visualization of the pet's placement on the robotic device and confirmation of accurate transducer positioning in relation to the targeted tumor, as shown in the indicative axial slice of Fig. 6b.

An example of lesion formation by thermal coagulation is shown in Fig. 7. Thermal necrosis was evidenced by histological examination using H&E staining in all 9 treated tumors. Typical histology slides with apparent thermal necrosis are presented in Fig. 8. A small area of hemorrhage was observed in one case and is indicated in Fig. 8a. Note also in Fig. 8b that an intact cancer structure can be clearly identified within the necrotic area at higher magnification (5X).

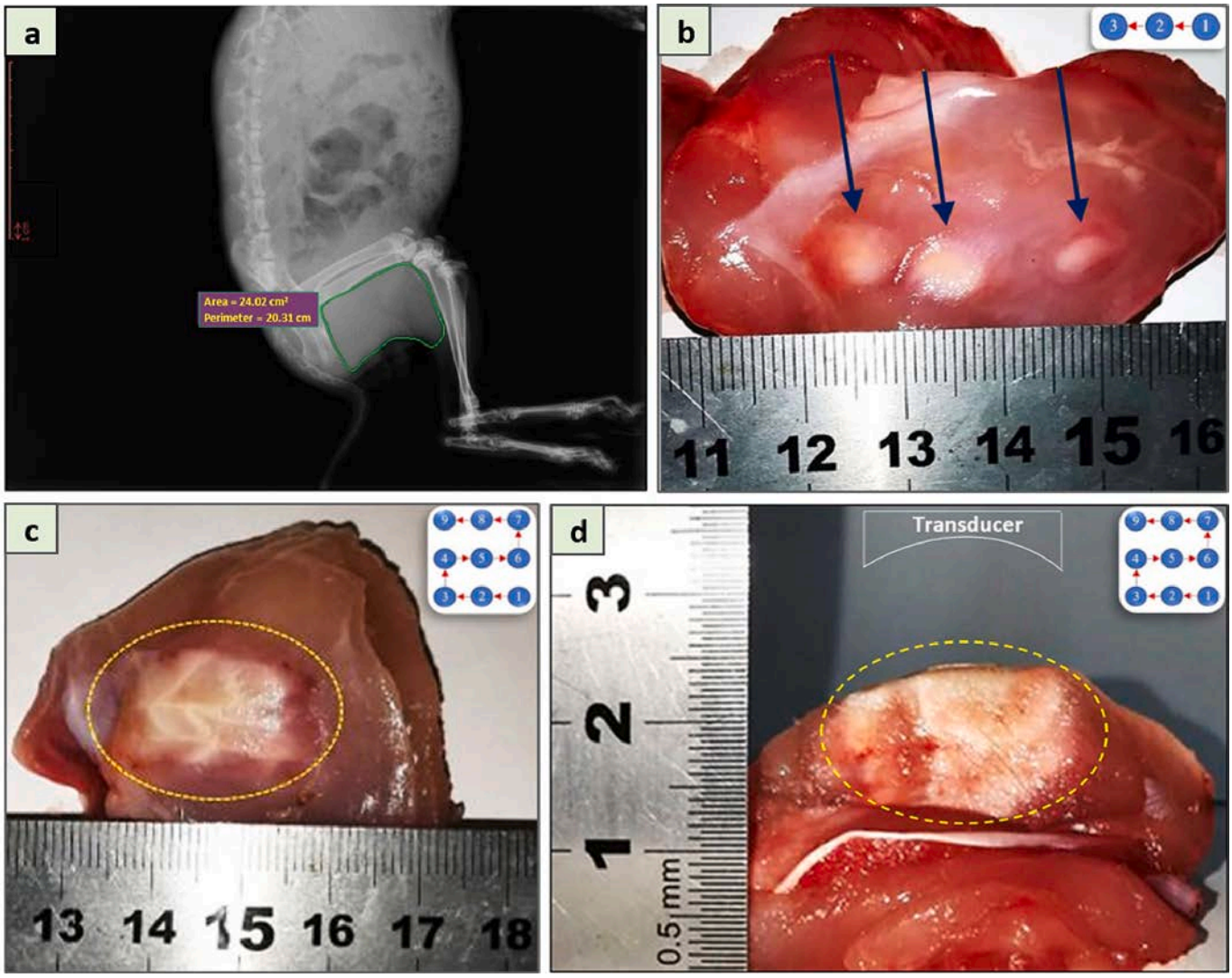

Fig. 5. (a) X-ray image of a rabbit taken to allow calculation of thigh muscle area available for ablation (voltage = 50 kV, current = 45 mA, exposure time = 45 ms). (b) Top photo of rabbit thigh after muscle exposure showing discrete lesions for a grid pattern of 1 × 3 (acoustic power = 60 W, sonication duration = 10 s, step = 10 mm, delay = 60 s, and focal depth = 1 cm). The blue arrows indicate the lesions. (c) Sample image of 3 × 3 overlapping lesions from top view after rabbit muscle exposure (acoustic power = 60 W, sonication duration = 10 s, step = 5 mm, delay = 60 s, and focal depth = 1 cm). (d) Sample image of 3 × 3 overlapping lesions on cross-sectioned tissue (acoustic power = 60 W, sonication duration = 20 s, step = 4 mm, delay = 60 s, and focal depth = 1 cm). The yellow dotted circles indicate the ablated area. The ablation pattern followed is shown at the top right corner of each photo.

4. Discussion

In recent days, driven by the increasing expectations of pet owners, there is an apparent need for making beneficial minimally-invasive therapeutic solutions available to our pet patients. As a non-invasive therapeutic modality, FUS is considered to have a beneficial competitive role against gold standard therapeutics in that it minimizes the likelihood of infections, complications and side effects related to invasive surgery. Pets can benefit from a major improvement in the quality of their lives since the specific therapy does not require stitches and the use of Elizabethan collars [28]. Pet owners may also benefit by cheaper medical care due to shorter hospitalizations. In the case of recurrent disease, the capacity to administer treatment more than once is a crucial advantage of this technology as well [28]. This pilot study reports data on the feasibility of treating canine and feline mammary cancer by FUS ablation.

Preliminary experiments were carried out in a rabbit thigh model with the purpose to test the functionality of the employed robotic system and ultrasonic transducer in live tissue and ensure an effective procedural workflow before proceeding to trials in companion animals. Notably, rabbit models have been quite widely employed in the process of evaluating the performance of newly developed FUS robotic systems and protocols [36–39]. Various sonication protocols were tested, where the acoustic power and sonication time, as well as the grid size and relevant spatial step were varied to evaluate their effect on lesion creation and the extent of coagulative necrosis. With the 2 MHz FUS transducer (focal diameter of ~ 0.9 mm) used, the minimum tested peak focal intensity of 810 W/cm^2 was able to produce lesions of easily measurable dimensions (>2 mm in diameter) that were clearly identified with the naked eye after muscle exposure extending 4–5 mm deep in tissue when applied for approximately 20 s. In case the power and duration of sonication remained the same, the creation of discrete or overlapping lesions was determined by the selected step between adjacent sonication spots. Note that the time delay was typically set at 60 s to eliminate thermal diffusion and unwanted near-field heating effects [40]. The results further suggest that by increasing the applied ultrasonic intensity, the sonication time can be drastically decreased, thus producing similar extent of necrosis at a shorter time. It is though

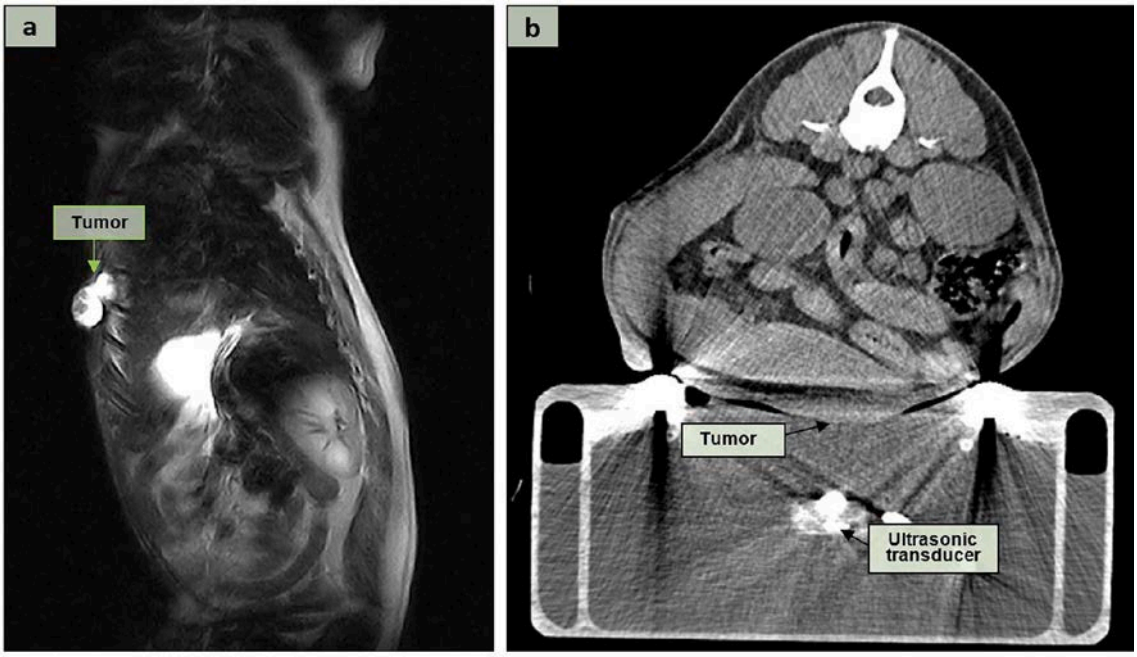

Fig. 6. (a) T2-W FSE image of the dog (TR = 2600 ms, TE = 125 ms, FOV = 256 × 256 mm^2, and slice thickness = 3 mm) in the presence of the FUS robotic device. (b) CT axial image of the experimental setup (voltage = 130 kV, current = 70 mA, FOV = 348 × 348 mm^2, and slice thickness = 1.5 mm).

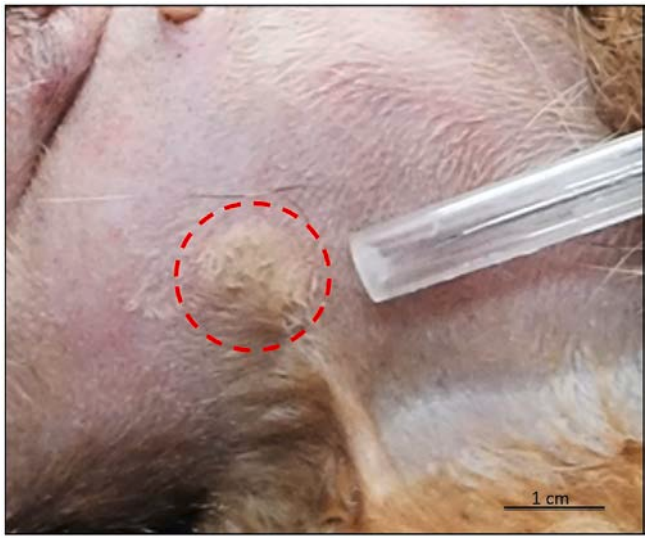

Fig. 7. Example photo of a mammary tumor in cat after FUS sonication. The dotted circle indicates the lesion formed by thermal coagulation (acoustic power = 45 W, duration = 20 s).

clarified that rabbit and canine/feline mammary tissues are very dissimilar, and therefore, the treatment protocol must be optimized for each.

Overall, the system was proven capable of accurately delivering FUS to safely ablate live rabbit tissue with no recorded operational malfunctions that could compromise the animal's safety. Rabbits were examined for adverse events by continuous monitoring of vital signs and visual inspection of FUS-induced changes in the surrounding tissue. No off-target skin redness or burns were observed.

Nine (9) pets (7 dogs and 2 cats) with well-defined superficial malignancies of the mammary glands were recruited through a recruitment campaign and received FUS treatment prior to surgical tumor excision. The superficial location of the treated tumors allowed direct targeting by visual assessment. For safety reasons, a comprehensive approach was followed with the pet placed on its side so that the beam is not directed to the thorax perpendicularly, thus ensuring no interference of the beam with the ribs or off-target tissue. Thereby, the success of thermal ablation was predominantly dependent on efficient through-water-transmission of ultrasonic waves to the tumor and complete immobilization of the subject during the entire procedure, which was ensured through systematic monitoring of the anesthesia level. An additional safety measure was the application of low ultrasonic energy prior to full ultrasonic exposure to ensure no indication of pain.

All pet trials were implemented successfully, without any recorded adverse events compromising welfare. The selected frequency of 2 MHz was proven suitable for the size of mammary cancer in that it offered good focusing and sufficient penetration. H&E staining demonstrated well-defined regions of coagulative necrosis in all 9 treated tumors with no off-target damage (100 %), except from minor extravasation of red blood cells observed at the borderline of the thermal lesion in one case (11 %). In the sonicated areas, the architecture of malignant cells was destroyed completely. Characteristically, the cells in the necrotic area appeared eosinophilic and discohesive. This hyper-eosinophilic behavior is linked to both cytoplasmic RNA loss and proteins' denaturation, which constitutes a common characteristic of coagulative necrosis [41]. The microscopic examination showed mammary gland tumor after FUS with predominately central tumor necrosis with hyalinized tumor stroma with pigment laden foamy macrophages (hemosiderin like pigment). Small solitary tumor structures were occasionally found within the hyalinized stroma. This might be attributed to the fact that the specific tumor type is characterized by the existence of a large number of blood vessels and ducts that possibly attenuate the ultrasonic beam; however, further investigation is required to confirm this. At the periphery of the tumor necrosis, focused fresh and old hemorrhage with hemosiderin laden macrophages was identified in one case. The surrounding tumor was composed of small and large-sized irregular ducts lined by malignant epithelial cells and within the lumina were hemosiderin laden macrophages and polymorphs.

According to a 12-month phone-call follow up with the referring veterinarians, all dogs and cats were in good condition within this 1-year period with no recurrence of the tumor or other study-related health

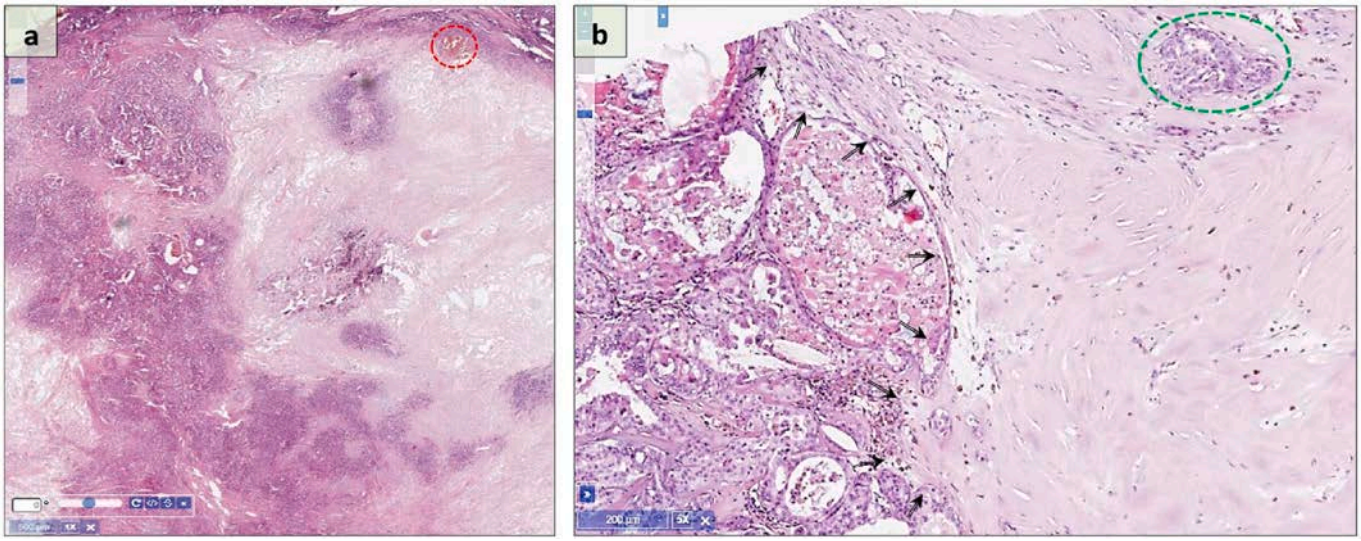

Fig. 8. Indicative histological slides demonstrating thermal necrosis with (a) no magnification and (b) 5X magnification. The red dotted circle indicates the hemorrhagic area and the black arrows the area of thermal necrosis. The green dotted circle indicates an intact cancer structure within the necrotic area.

issues. It is though important to note that the employed "treat and resect" approach minimizes the possibilities for side effects. Since the adopted protocol included immediate tumor excision, superficial ablation of tumors was considered beneficial because it allowed visual inspection of inflicted lesions, without considering potential skin damages. However, in case surgical excision will not be performed, lesions should be created deeper in tissue to avoid thermal damage of the skin. In case of incomplete ablation, adjuvant chemotherapy may be used to kill the remaining cancer [42].

The long treatment time required to cover the entire region of interest by multiple sonications while leaving sufficient cooling time between them is one of the key considerations in the clinical adaption of FUS and its feasibility compared to the standard of care; surgery. In the current study, for the maximum grid size of 3×3 with a sonication time of 10 s and a 30 s delay between sonications, the total FUS treatment duration was about 6 min. For complete tumor ablation, the time will depend on the tumor size and employed sonication parameters. With the parameters used in the current study and assuming a typical lesion diameter of 3 cm, a minimum grid size of $10 \times 10 \times 2$ (i.e., 10×10 grid repeated at different depth) is estimated to be required, thus resulting in a relatively long treatment duration of just under 2.5 h. Thereby, with the specific sonication protocol only small tumors can be treated in a reasonable time. However, one could use a transducer with a smaller beam size (i.e., different structural geometry and/or sonication frequency) to achieve stronger focusing, which will allow reducing the sonication time and time delay between successive sonications, thereby reducing the total treatment duration. Further investigation is definitely needed to assess the feasibility in terms of treatment time relative to surgery. Notably, the length of treatment for both US- and MRI-guided breast tumor ablation was widely varied among clinical studies, from less than one to several hours, depending on a number of factors [43].

In this pilot study, MRI and CT imaging was occasionally used to visualize the pet anatomy and determine the tumor size. Generally, the acquisition of anatomical images is needed in the context of treatment planning for accurate tumor targeting and post-ablation assessment of infected thermal lesions. While CT does not provide the ability to monitor intraprocedural temperature changes, MR thermometry provides precise monitoring of the temperature distribution within the targeted tissue and prediction of the treatment outcome. Additionally, intra-operative acquisition of MR images may allow for monitoring individual lesions while being formed in grid patterns. Tissue ablation under MR thermometry guidance would thus constitute the ideal scenario, but unfortunately, it was not feasible with the available experimental setup. The Esaote veterinary MRI system comprises dedicated rigid ring-shaped coils that should be placed around the body region of interest, thus making ultrasonic penetration impossible. Anatomical imaging with the dog lying on the device and the coil placed around the device was attempted with no success. It was thus concluded that the employed robotic system and any other system with a similar design (for bottom to top ultrasonic delivery) cannot be properly integrated with the specific MRI scanner. It is though important that high-quality anatomical imaging of the pet in the presence of the device in the scanner was feasible, confirming the MR compatibility of the system in terms of maintaining the diagnostic value of imaging. It is also important that the device fits within the scanner, leaving sufficient space for animal placement due to its compact design (Fig. 4a). Therefore, if the vendor redesigns the coils to address this limitation, MRI-guided thermal ablation with this equipment will be feasible.

Thermal ablation of breast masses using FUS has been reported in various studies [43–45]. Breast cancer patients were managed with both partial ablation followed by surgical excision of tumors [46] and full ablation by multiple FUS sonications to cover the entire tumor, including a small safety margin [47]. Most studies followed a «treat and resect» approach where the tumor was resected at different time points post-treatment [43–45]. The rates of complete ablation over the treated area largely range among studies [43]. Incomplete ablation can be attributed to numerous factors, including inefficient patient immobilization and monitoring of the ablation process. The more conservative approach of partial ablation is considered more suitable for assessing safety and the success/extend of necrosis and may also be adopted so that the procedure can be completed within a reasonable timeframe. The partial ablative approach has also been adopted clinically in the context of breast cancer therapy using FUS in combination with chemotherapy [42]. Although the current study adapted a partial ablative approach to ensure the pet's safety, the treatment of whole tumors should be addressed in follow up studies since it could give insights into translational potentials.

The conservative approach utilized in the current study suffers from the limitation that only superficial tumors were targeted, whereas in most clinical cases, tumors are located deeper in tissue. Since the study concerned only superficial tumors, direct visual targeting sufficed. The 2-MHz transducer used for tissue ablation offered good ultrasonic penetration in both rabbit thighs and superficial mammary tumors. However, the sonication protocol should be further examined and

adjusted in future studies involving non-superficial tumors, thus more accurately reflecting potential clinical outcomes. Ablation of deep-seated tumors would, of course, be far more challenging. Firstly, the targeting of non-superficial tumors in follow-up studies will require the guidance of an imaging modality, such as US or MRI. MRI compatibility of the robotic device used for transducer positioning is considered essential in this regard. Furthermore, while in this study, angular motion of the transducer was not used, in future studies involving deep-seated tumors, beam angulation may be required to safely guide the ultrasonic beam close to sensitive structures and avoid bones.

It is important that future research further investigate potential inflammatory reaction after FUS ablation of mammary cancer in veterinary patients. Preclinical and clinical data reveal an immune response following FUS ablation of breast and other types of tumors, which may be associated with additional therapeutic effects such as slower tumor growth and metastatic progression [48,49]. Since this study was focused on the ablative effects of FUS, investigation of inflammatory markers is left for follow up trials and may provide useful data on the therapeutic efficacy of FUS compared to the surgical treatment, which still constitutes the standard of care.

To our knowledge, this is the first study to report results on FUS-induced coagulative necrosis of mammary tumors in canine and feline patients, adding to a growing corpus of research showing that FUS could constitute an alternative beneficial therapy, especially in cases of unresectable or recurrent tumors. Further research is required to examine the phenomenon of residual cancer and potential inflammatory reactions, as well as the feasibility of safely ablating the entire tumor volume. Further study with a larger patient population is needed to confirm the findings and expand the application of FUS in the management of other cancer types as well. Another promising application to be investigated is the use of FUS to enhance the delivery of chemotherapeutic drugs to the tumor site [50]. Given that mammary tumors have already been validated as efficient models of the human disease [8,9], veterinary trials on FUS therapy of canine and feline mammary malignancies would definitely be beneficial to the scientific community.

Ethics Approval Declaration

All animal experiments were approved by the authorities of Veterinary Services (Ministry of Agriculture, Rural Development and Environment) of the Republic of Cyprus under the study licenses CY/EXP/PR.*L*01/2020 (rabbits) and CY/EXP/PR.*L*01/2020/R1/2021 (dogs and cats).

Declaration of Competing Interest

The authors declare that they have no known competing financial interests or personal relationships that could have appeared to influence the work reported in this paper.

Data availability

Data will be made available from the corresponding author upon reasonable request.

Acknowledgments

The study was co-funded by the European Structural & Investment Funds (ESIF) and the Republic of Cyprus through the Research and Innovation Foundation (RIF) under the projects SOUNDPET (INTEGRATED/0918/0008) and FUSVET (SEED/1221/0080).

References

[1] D.F. Merlo, et al., Cancer Incidence in Pet Dogs: Findings of the Animal Tumor Registry of Genoa, Italy, J Vet Intern Med 22 (2008) 976–984, https://doi.org/10.1111/j.1939-1676.2008.0133.x.

[2] K. Gupta, Epidemiological Studies on Canine Mammary Tumour and its Relevance for Breast Cancer Studies, IOSR J. Pharm. 2 (2) (2012) 322–333, https://doi.org/10.9790/3013-0220322333.

[3] V. Zappulli, et al., Prognostic Evaluation of Feline Mammary Carcinomas: A Review of the Literature, Vet. Pathol. 52 (1) (2015) 46–60, https://doi.org/10.1177/0300985814528221.

[4] F. Chocteau, V. Mordelet, E. Dagher, D. Loussouarn, J. Abadie, F. Nguyen, One-year conditional survival of dogs and cats with invasive mammary carcinomas: A concept inspired from human breast cancer, Vet. Comp. Oncol. 19 (1) (2021) 140–151, https://doi.org/10.1111/vco.12655.

[5] C.M. Cannon, Cats, cancer and comparative oncology, Vet. Sci. 2 (3) (2015) 111–126, https://doi.org/10.3390/vetsci2030111.

[6] M. Paoloni, C. Khanna, Translation of new cancer treatments from pet dogs to humans, Nat. Rev. Cancer 8 (2) (2008) 147–156, https://doi.org/10.1038/nrc2273.

[7] L.A. Lyons, The Feline Genome and Clinical Implications, Cat (2012) 1263–1269, https://doi.org/10.1016/B978-1-4377-0660-4.00043-0.

[8] R. De Maria, et al., Spontaneous feline mammary carcinoma is a model of HER2 overexpressing poor prognosis human breast cancer, Cancer Res. 65 (3) (2005) 907–912.

[9] K. Todorova, P. Dimitrov, R. Milcheva, S. Roga, R. Russev, Comparative Study of Several Cases of Human Breast Cancer and Mammary Caner in Domestic Dogs and Cats, Acta Morphol. Anthropol. 23 (2016).

[10] C.M. Tran, A.S. Moore, A.E. Frimberger, Surgical treatment of mammary carcinomas in dogs with or without postoperative chemotherapy, Vet. Comp. Oncol. 14 (3) (2016) 252–262, https://doi.org/10.1111/vco.12092.

[11] C.A. Novosad, Principles of treatment for mammary gland tumors, Clin. Tech. Small Anim. Pract. 18 (2) (2003) 107–109, https://doi.org/10.1053/svms.2003.36625.

[12] G. Rutterman, S.J. Withrow, E. MacEwan, Tumors of mammary gland, in: S. Withrow, E. MacEwan (Eds.), Small Animal Clinical Oncology, 3rd ed., PA, Philadelphia, 2001, pp. 455–473.

[13] A.A. Hayes, S. Mooney, Feline Mammary Tumors, Vet. Clin. North Am. Small Anim. Pract. 15 (3) (1985) 513–520, https://doi.org/10.1016/S0195-5616(85)50054-6.

[14] E. MacEwen, A. Hayes, H. Harvey, A. Patnaik, S. Mooney, S. Passe, Prognostic factors for feline mammary tumors, J Am Vet Med Assoc. 185 (2) (1984) 201–204.

[15] G.E. Lavalle, C.B. De Campos, A.C. Bertagnolli, G.D. Cassali, Canine malignant mammary gland neoplasms with advanced clinical staging treated with carboplatin and cyclooxygenase inhibitors, In Vivo 26 (3) (2012) 375–379.

[16] C.J. McNeill, et al., Evaluation of Adjuvant Doxorubicin-Based Chemotherapy for the Treatment of Feline Mammary Carcinoma, J Vet Intern Med 23 (2009) 123–129, https://doi.org/10.1111/j.1939-1676.2008.0244.x.

[17] M.R. Bailey, V. Khokhlova, O.A. Sapozhnikov, S.G. Kargl, L.A. Crum, Physical Mechanisms of the Therapeuctic Effect of Ultrasound, Acoust. Phys. 49 (4) (2003) 369–388.

[18] C. Damianou, K. Hynynen, The effect of various physical parameters on the size and shape of necrosed tissue volumeuring ultrasound surgery, J. Acoust. Soc. Am. 95 (3) (1994) 1641–1649, https://doi.org/10.1121/1.408550.

[19] J.E. Kennedy, G.R. TER Haar, D. Cranston, High intensity focused ultrasound: surgery of the future? Br. J. Radiol. 76 (2003) 590–599, https://doi.org/10.1259/bjr/17150274.

[20] I.A.S. Elhelf, H. Albahar, U. Shah, A. Oto, E. Cressman, M. Almekkawy, High intensity focused ultrasound: The fundamentals, clinical applications and research trends, Diagn. Interv. Imaging 99 (6) (2018) 349–359, https://doi.org/10.1016/j.diii.2018.03.001.

[21] V. Rieke, K.B. Pauly, MR Thermometry, J Magn Reson Imaging 27 (2) (2008) 376–390, https://doi.org/10.1002/jmri.21265.MR.

[22] E.J. Lee, A. Fomenko, A.M. Lozano, Magnetic resonance-guided focused ultrasound: Current status and future perspectives in thermal ablation and blood-brain barrier opening, J. Korean Neurosurg. Soc. 62 (1) (2019) 10–26, https://doi.org/10.3340/jkns.2018.0180.

[23] M. Giannakou, C. Yiallouras, G. Menikou, C. Ioannides, C. Damianou, MRI-guided frameless biopsy robotic system with the inclusion of unfocused ultrasound transducer for brain cancer ablation, Int. J. Med. Robot. Comput. Assist. Surg. 15 (1) (2019) 1–9, https://doi.org/10.1002/rcs.1951.

[24] E. Epaminonda, T. Drakos, C. Kalogirou, M. Theodoulou, C. Yiallouras, C. Damianou, MRI guided focused ultrasound robotic system for the treatment of gynaecological tumors, Int. J. Med. Robot. Comput. Assist. Surg. 12 (2016) 46–52, https://doi.org/10.1002/rcs.1653.

[25] C. Yiallouras, C. Damianou, Review of MRI positioning devices for guiding focused ultrasound systems, Int. J. Med. Robot. Comput. Assist. Surg. 11 (2015) 247–255, https://doi.org/10.1002/rcs.1601.

[26] M. Yiannakou, G. Menikou, C. Yiallouras, C. Ioannides, C. Damianou, MRI guided focused ultrasound robotic system for animal experiments, Int. J. Med. Robot. Comput. Assist. Surg. 13 (4) (2017) e1804.

[27] G. Menikou, C. Yiallouras, M. Yiannakou, C. Damianou, MRI-guided focused ultrasound robotic system for the treatment of bone cancer, Int. J. Med. Robot. Comput. Assist. Surg. 13 (1) (2017) 1–11, https://doi.org/10.1002/rcs.1753.

[28] Veterinary Medicine: At a Glance, Focused Ultrasound Foundation. [Online]. Available: https://www.fusfoundation.org/the-foundation/initiatives/focused-ultrasound-for-veterinary-medicine-at-a-glance/ (Accessed: 29-Nov-2022).

[29] Focused Ultrasound Foundation Launches Veterinary Program., Focused Ultrasound Foundation, 2017. [Online]. Available: https://www.fusfoundation.org/posts/focused-ultrasound-foundation-launches-veterinary-program/ (Accessed: 29-Nov-2022).

[30] M.O. Ryu, S.H. Lee, J.O. Ahn, W.J. Song, Q. Li, H.Y. Youn, Treatment of solid tumors in dogs using veterinary high-intensity focused ultrasound: A retrospective clinical study, Vet. J. 234 (2018) 126–129, https://doi.org/10.1016/j.tvjl.2018.02.019.

[31] M.C. Seward, G.B. Daniel, J.D. Ruth, N. Dervisis, A. Partanen, P.S. Yarmolenko, Feasibility of targeting canine soft tissue sarcoma with MR-guided high-intensity focused ultrasound, Int. J. Hyperth. 35 (1) (2018) 205–215, https://doi.org/10.1080/02656736.2018.1489072.

[32] A. Ranjan, D. Kishore, H. Ashar, T. Neel, A. Singh, S. More, Focused ultrasound ablation of a large canine oral tumor achieves efficient tumor remission: a case report, Int. J. Hyperthermia 38 (1) (2021) 552–560, https://doi.org/10.1080/02656736.2021.1903582.

[33] A. Antoniou, N. Evripidou, S. Panayiotou, K. Spanoudes, C. Damianou, Treatment of canine and feline sarcoma using MR-guided focused ultrasound system, J. Ultrasound 25 (4) (2022) 895–904, https://doi.org/10.1007/s40477-022-00672-5.

[34] C. Damianou, M. Giannakou, N. Evripidou, S. Kegel, P. Huber, J. Jenne, Focused ultrasound robotic system for very small bore magnetic resonance imaging, Int. J. Med. Robot. Comput. Assist. Surg. 16 (6) (2020) 1–9, https://doi.org/10.1002/rcs.2165.

[35] T. Drakos, M. Giannakou, G. Menikou, C. Damianou, Magnetic Resonance Imaging-Guided Focused Ultrasound Positioning System for Preclinical Studies in Small Animals, J. Ultrasound Med. 40 (7) (2020) 1343–1352, https://doi.org/10.1002/jum.15514.

[36] T. Drakos, et al., MRI-Guided Focused Ultrasound Robotic System for Preclinical use, J. Vet. Med, Anim. Sci. 4 (1) (2021).

[37] A. Antoniou, et al., Robotic system for magnetic resonance guided focused ultrasound ablation of abdominal cancer, Int. J. Med. Robot. Comput. Assist. Surg. 17 (5) (2021), https://doi.org/10.1002/rcs.2299.

[38] C. Damianou, V. Hadjisavvas, N. Mylonas, A. Couppis, K. Ioannides, MRI-guided Sonothrombolysis of Rabbit Carotid Artery, J. Stroke Cerebrovasc. Dis. 23 (2) (2014) E113–E121, https://doi.org/10.1016/j.jstrokecerebrovasdis.2013.09.005.

[39] T. Alecou, M. Giannakou, C. Damianou, Amyloid β plaque reduction with antibodies crossing the blood-brain barrier, which was opened in 3 sessions of focused ultrasound in a rabbit model, J. Ultrasound Med. 36 (11) (2017) 2257–2270, https://doi.org/10.1002/jum.14256.

[40] A. Filippou, T. Drakos, M. Giannakou, N. Evripidou, C. Damianou, Experimental evaluation of the near-field and far-field heating of focused ultrasound using the thermal dose concept, Ultrasonics 116 (2021), 106513, https://doi.org/10.1016/j.ultras.2021.106513.

[41] M. A. Miller, J.F. Zachary, Mechanisms and Morphology of Cellular Injury, Adaptation, and Death. Pathologic Bases of Veterinary Disease, J. F. Zachary, Ed., 2017, pp. 2-43.

[42] M. Dahan, M. Cortet, C. Lafon, F. Padilla, Combination of Focused Ultrasound, Immunotherapy, and Chemotherapy: New Perspectives in Breast Cancer Therapy, J. Ultrasound Med. 42 (2022) 559–573, https://doi.org/10.1002/jum.16053.

[43] M.C.L. Peek, F. Wu, High-intensity focused ultrasound in the treatment of breast tumours, Ecancermedicalscience 12 (2018) 794, https://doi.org/10.3332/ecancer.2018.794.

[44] D.R. Brenin, Ablative Treatment of Breast Cancer; Are We There Yet? Curr. Breast Cancer Rep. 11 (2) (2019) 43–50, https://doi.org/10.1007/s12609-019-0307-1.

[45] L. Feril, R. Fernan, K. Tachibana, High-Intensity Focused Ultrasound in the Treatment of Breast Cancer, Curr Med Chem 28 (25) (2021) 5179–5188, https://doi.org/10.2174/0929867327666201111143206.

[46] L.G. Merckel, et al., First clinical experience with a dedicated MRI-guided high-intensity focused ultrasound system for breast cancer ablation, Eur Radiol 26 (11) (2016) 4037–4046, https://doi.org/10.1007/s00330-016-4222-9.

[47] M. Hahn, et al., High intensity focused ultrasound (HIFU) for the treatment of symptomatic breast fibroadenoma, Int. J. Hyperth. 35 (1) (2018) 463–470, https://doi.org/10.1080/02656736.2018.1508757.

[48] Z.-L. Xu, X.-Q. Zhu, P. Lu, Q. Zhou, J. Zhang, F. Wu, Activation of Tumor-Infiltrating Antigen Presenting Cells by High Intensity Focused Ultrasound Ablation of Human Breast Cancer, Ultrasound Med. Biol. 35 (1) (2009) 50–57, https://doi.org/10.1016/j.ultrasmedbio.2008.08.005.

[49] T. Tonguc, et al., US-guided high-intensity focused ultrasound (HIFU) of abdominal tumors: outcome, early ablation-related laboratory changes and inflammatory reaction. A single-center experience from Germany, Int. J. Hyperth. 38 (2) (2021) 65–74, https://doi.org/10.1080/02656736.2021.1900926.

[50] O. Couture, J. Foley, N.F. Kassell, B. Larrat, J.F. Aubry, Review of ultrasound mediated drug delivery for cancer treatment: Updates from pre-clinical studies, Transl. Cancer Res. 3 (5) (2014) 494–511, https://doi.org/10.3978/j.issn.2218-676X.2014.10.01.

Received: 16 December 2022 | Revised: 24 March 2023 | Accepted: 2 May 2023

DOI: 10.1002/mp.16480

RESEARCH ARTICLE

MEDICAL PHYSICS

Tumor phantom model for MRI-guided focused ultrasound ablation studies

Anastasia Antoniou[1] | **Nikolas Evripidou**[1] | **Leonidas Georgiou**[2] | **Antreas Chrysanthou**[2] | **Cleanthis Ioannides**[2] | **Christakis Damianou**[1]

[1]Department of Electrical Engineering, Computer Engineering, and Informatics, Cyprus University of Technology, Limassol, Cyprus

[2]Department of Interventional Radiology, German Oncology Center, Limassol, Cyprus

Correspondence
Christakis Damianou, Department of Electrical Engineering, Computer Engineering, and Informatics, Cyprus University of Technology, 30 Archbishop Kyprianou Street, 3036 Limassol, Cyprus.
Email: christakis.damianou@cut.ac.cy

Funding information
Research and Innovation Foundation of Cyprus

Abstract

Background: The persistent development of focused ultrasound (FUS) thermal therapy in the context of oncology creates the need for tissue-mimicking tumor phantom models for early-stage experimentation and evaluation of relevant systems and protocols.

Purpose: This study presents the development and evaluation of a tumor-bearing tissue phantom model for testing magnetic resonance imaging (MRI)-guided FUS (MRgFUS) ablation protocols and equipment based on MR thermometry.

Methods: Normal tissue was mimicked by a pure agar gel, while the tumor simulator was differentiated from the surrounding material by including silicon dioxide. The phantom was characterized in terms of acoustic, thermal, and MRI properties. US, MRI, and computed tomography (CT) images of the phantom were acquired to assess the contrast between the two compartments. The phantom's response to thermal heating was investigated by performing high power sonications with a 2.4 MHz single element spherically focused ultrasonic transducer in a 3T MRI scanner.

Results: The estimated phantom properties fall within the range of literature-reported values of soft tissues. The inclusion of silicon dioxide in the tumor material offered excellent tumor visualization in US, MRI, and CT. MR thermometry revealed temperature elevations in the phantom to ablation levels and clear evidence of larger heat accumulation within the tumor owing to the inclusion of silicon dioxide.

Conclusion: Overall, the study findings suggest that the proposed tumor phantom model constitutes a simple and inexpensive tool for preclinical MRgFUS ablation studies, and potentially other image-guided thermal ablation applications upon minimal modifications.

KEYWORDS
ablation, focused ultrasound, MRI, phantom, thermometry, tumor

1 | INTRODUCTION

Ex vivo tumor models have an essential role in early-stage experimentation and validation of imaging and therapeutic modalities and protocols in the context of oncology, provided that the use of animal tumor models is not only costly and resource-intensive, but also against the minimization of animal testing.[1] Accordingly, as part of the effort to enable cost-effective and easily implemented research methods to optimize such modalities and identify beneficial advancements prior to in vivo application, there exist numerous tumor models mainly involving the use of gel phantoms proposed in the literature.

One category of tumor-bearing tissue phantoms concerns imaging applications. High-quality test objects are needed for examining the performance of newly developed imaging applications or even routine testing of well-established imaging systems and techniques.[1–4] Recently, the 3D printing technology allowed the development of more realistic tumor phantoms for x-ray radiographic imaging.[5,6] Phantoms simulating tumor heterogeneity in imaging have been employed in radiomic studies as well.[7–9] Besides their usefulness for imaging applications, tumor phantom models constitute a critical asset for the training and experimentation on interventional procedures including needle biopsies, and the assessment of relevant robotic-assisted equipment.[10–13]

Image guided thermal ablation has arisen as a feasible alternative to invasive surgery for patients with malignancies,[14] and it may be minimally invasive with the use of percutaneous radiofrequency ablation (RFA) and microwave ablation (MWA) applicators,[15] or completely non-invasive with the extracorporeal use of focused ultrasound (FUS).[16] Although a wide variety of gel-based phantom models have been proposed as ergonomic tools for preclinical thermal therapy studies,[17] only some of them incorporate tumor simulators. Thermally sensitive polyacrylamide (PAA) phantoms are considered advantageous in that they offer visualization of the thermal damage owing to the inclusion of heat-responsive materials, such as Bovine serum albumin (BSA) protein,[18] egg white,[19] and thermochromic ink.[20] As an example, Zhou et al.[21] proposed a tumor model for testing ablation protocols that consists of a 3-cm spherical tumor mimic embedded in a PAA gel loaded with thermochromic ink.

Driven by the increasing utilization of RFA and MWA as the prevalent non-invasive modalities for the management of hepatocellular carcinoma (HCC), gel phantom models intended for RFA and MWA of the liver were quite widely described in the literature,[22] but with only few of them involving thermal heating of a tumor model. In a relevant study,[23] authors constructed a 5% agar cylindrical phantom featuring a cylindrical hole of 2 cm in diameter, which was filled with an agar solution of smaller agar concentration of 0.25% to represent a tumor. The outer section also included an oil-based solute, the amount of which was varied to achieve different thermal conductivities. According to thermocouple measurements, changes in RF heating occurred as a result of this difference, with the authors concluding that lower values of thermal conductivity in the background material can increase the temperatures produced within the tumor target significantly.[23] A two-section phantom was also utilized by Haemmerich et al.[24] for the purpose of evaluating the functionality of low frequency RFA in tumor destruction by thermocouple thermometry. The tumor phantom was a thin layer of 5% agar gel laid on the top of a piece of ex vivo bovine liver tissue. In a similar study regarding MWA, thermocouple measurements were performed in an agar-based breast tumor phantom to evaluate the thermal effects of three types of microwave antennas.[25] The breast tissue was mimicked by a mixture of detergent, oil, and agarose in water having embedded 1 and 1.5 cm spherical tumor inserts made of Sodium chloride (NaCl), ethanol, and agarose, which served as modifiers of the conductivity, permittivity, and solidity, respectively.[25]

Tumor-bearing phantom models for interventional and thermal studies should ideally combine both tissue-like imaging and therapeutic features provided the apparent need for image guidance of such procedures. An indicative phantom model featuring a tumor was presented by Zhong et al.[26] for the purpose of performing thermal ablations and tumor puncture studies under US, CT, or MRI guidance. The phantom was formed by embedding a PAA-based 3 cm spherical tumor mimic in a PAA gel loaded with thermochromic ink. Iohexol and psyllium husk were added in the tumor mimic serving as the CT and US/MR contrast agents, respectively. Another example is a study by Kim et al.,[27] who developed a two-compartment phantom for RF studies, where normal and tumor tissues were mimicked by agar gels doped with $CuSO_4$ solution serving as the electrical conductivity controller. The tumor compartment was differentiated from the surrounding with the inclusion of a Fe_3O_4 nanoparticle suspension and 4% sodium carboxymethyl cellulose. Temperature changes were intermittently recorded during RF heating by performing MR thermometry in a 3T scanner, demonstrating that nanoparticle-doped regions developed higher temperatures than the background. Carrageenan was also used as the gelling agent for developing a tumor-bearing phantom as a tool for evaluating RF ablation margins in HCC by contrast-enhanced ultrasound-CT/MR image fusion.[28] Notably, while carrageenan gels possess proper physical properties, they are not considered the material of choice for evaluating thermal ablation protocols.[28,29]

Among the thermal ablation techniques, the rapidly evolving technology of FUS has proven a promising non-invasive alternative to traditional cancer therapy and has been so far employed for multiple oncological applications.[16,30] In this process, tissue mimicking phantoms provided a test environment for the preliminary evaluation of equipment and protocols. Hassanuddin et al.[31] investigated the impact of obstacles such as bone and metallic implants on FUS thermal therapy in a novel tumor-bearing phantom. This phantom was a mixture of PAA gel and BSA protein containing several metallic and plastic objects, as well as a water-filled rubber balloon mimicking a cyst.[32] In another study,[33] an agar-based tumor model was utilized to evaluate the effectiveness of a newly proposed dual modality combining magnetic and FUS heating for cancer therapy.

Numerous gelling agents have been proposed so far for the development of phantoms for diagnostic and therapeutic ultrasound applications, with gelatin and PAA being two of the most widely investigated materials.[17,29] The critical properties of these phantom types were shown to fall within the literature-reported ranges of soft tissues upon inclusion of appropriate supplementary materials. However, gelatin-based phantoms lack the capacity to withstand ablation temperatures.[34,35] Their low melting temperature makes them unsuitable for thermal studies in which temperatures exceed 50°C and material melting or/and alteration of their characteristics may occur. They are thus only recommended for hyperthermia applications. It is possible to include cross-linkers in order to increase the melting temperature of gelatin gels,[34] but this makes the manufacturing process more complicated, and may also alter other critical phantom properties. On the contrary, agar gels have high melting point, thus being able to withstand ablative temperatures,[17,29] which is crucial for FUS thermal studies. Regarding PAA gels, their major advantage over agar gels is that they are thermally sensitive offering the ability to directly visualize the ablated region. However, they are typically characterized by other limitations, including their complex preparation and storage process, as well as their neurotoxic nature.[36]

Although the use of agar-based phantoms in FUS ablation studies is widespread,[17,37–42] there is an identified need for more realistic tissue-mimicking phantoms embedding tumor simulators. Despite that agar gels do not possess optical transparency, they are considered ideal in mimicking biological tissues by replicating their most critical thermal, acoustic, and MR properties when mixed with proper concentration of other ingredients,[37,43–45] as well as withstanding ablative temperatures while maintaining their integrity.[46] They can be easily created in any size and shape with inexpensive non-toxic materials and tailored to suit different applications. Accordingly, we herein present the development and evaluation of an agar-based single-tumor phantom model with tissue-like US, CT, and MR visibility for MRI-guided FUS (MRgFUS) ablation studies and the performance assessment of relevant equipment and protocols. The proposed two-section phantom is based on two inexpensive ingredients; agar and silicon dioxide, whose concentration was selected to impart tissue-like properties and good US, CT, and MRI contrast of the tumor simulator. The most critical acoustic, thermal, and MRI properties of the phantom were investigated. High power single and grid FUS sonications were performed in selected regions of interest (ROIs) in and out of the tumor simulator. The temperature evolution was recorded using MR thermometry to assess the suitability of the proposed phantom model for the evaluation of FUS thermal protocols. The phantom was sonicated using an MRgFUS robotic system featuring a 2.4-MHz single-element FUS transducer.

2 | MATERIALS AND METHODS

2.1 | Tumor phantom model design

The tumor phantom model was developed in the laboratory following a simple procedure. The main ingredient was agar in granular form (particle size of 1400 μm, Merck KGaA, EMD Millipore Corporation, Darmstadt, Germany). This ingredient acts as a solidifier, but also by varying its concentration, it is possible to adjust the MR relaxation properties of the gel.[29] The second ingredient was silicon dioxide (Sigma-Aldrich, St. Louis, Missouri, USA) that was previously proven an effective modifier of ultrasonic attenuation.[29,45]

The two-compartment phantom model was developed with the assistance of dedicated molds that were 3D printed using polylactic acid (PLA) plastic on a rapid prototyping machine (FDM400, Stratasys, 7665 Commerce Way, Eden Prairie, Minnesota, USA). The background material was prepared by dissolving proper amount of agar grounded into powder in degassed/deionized water that was previously heated to 50°C so as to achieve the desired weight per volume (w/v) concentration of 6%. A mixture containing similar amount of 6% w/v agar and 4% w/v silicon dioxide was selected as the tumor material. Silicon dioxide was slowly added a few minutes after agar was poured while continuously stirring to avoid aggregation of ingredients.[37] The tumor material was poured into the mold shown in Figure 1a and left to solidify to form a 3 cm spherical tumor mimic (volume of about 14 cm^3) having a thread running through it. Following demolding, the tumor mimic was fixed in the center of the rectangular mold shown in Figure 1b by mounting the thread at opposite sides of the mold and finally the background material was poured in the container to form the final phantom, which is shown in Figure 1c.

2.2 | Characterization of tumor phantom model

2.2.1 | Acoustical properties

The ultrasonic attenuation in the tumor and background materials was investigated using the transmission-through variable thickness technique.[45] The specific method is based on comparing the ultrasonic signals acquired through samples of different thickness (2 and 4 cm). Planar transducers of 30-mm diameter and operating frequency of 1.1 MHz were employed (CeramTec, Plochingen, Germany); one as the transmitter and one for receiving the attenuated signals, which were displaced on a digital oscilloscope (TDS 2012, Tektronix, Inc., Beaverton, USA).

The well-established pulse-echo methodology was employed for estimating the ultrasonic velocity in the two

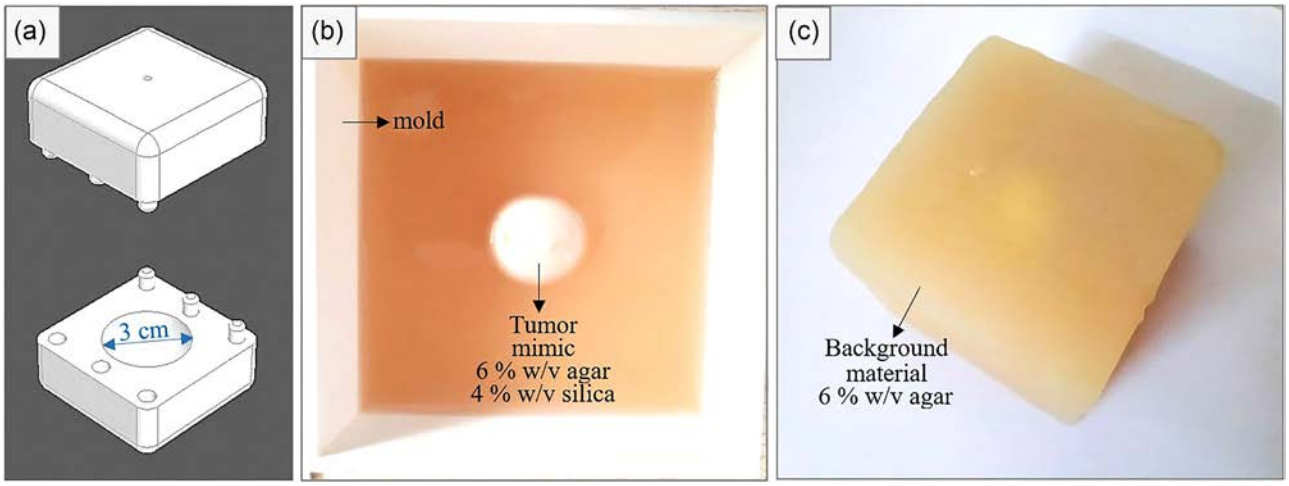

FIGURE 1 (a) The mold used for tumor mimic development. (b) Photo during phantom development showing the tumor mimic within the rectangular mold. (c) Photo of the developed agar-based tumor phantom model.

phantom compartments.[47] Samples of 2 cm thickness were fixed between a planar transducer (diameter of 10 mm, central frequency of 2.7 MHz) and a reflector. The transducer was connected to a pulser/receiver (model 500 PR, GE Panametrics, Waltham, Massachusetts, USA; 25 MHz bandwidth) and the reflection signals returning from the samples were recorded on the oscilloscope. The characteristic acoustic impedance was then determined by multiplying the density of each sample with the corresponding estimated speed of sound.

The absorption coefficient was estimated according to the procedure described by Drakos et al.[48] The rate of temperature change (dT/dt) during phantom sonication was recorded using a thermocouple (type K insulated beaded wire, Omega Thermometer, HH806AU, Omega Engineering, USA) for a short time so that the effect of conduction is minimized, and a liner increase of temperature with time can be assumed. This is a reasonable approach also given the low conductivity of the phantom (estimated in Section 2.2.2). Finally, the ultrasonic backscatter coefficient was extracted from previous work of the group.[49]

2.2.2 | Thermal properties

The thermal properties (thermal conductivity, thermal diffusivity, and specific heat capacity) of both phantom compartments were measured using a portable heat transfer analyzer (Isomet model 2104; Applied Precision, Bratislava, Slovakia). A dedicated needle sensor (S/N 09030019; Applied Precision) with a measurement range of 0.2–1 W/m K was used for the measurements. The detailed description of the employed methodology can be found in the study by Filippou et al.[50]

2.2.3 | MR relaxation properties

The MR relaxation properties of the phantom were investigated as well. For this purpose, the phantom was imaged in a 3T MRI scanner (Magnetom Vida) using a multichannel body coil (Body18, Siemens Healthineers) that was securely positioned at a small distance above its top surface.

Variable Echo Time T2 Mapping was employed for estimating the T2 relaxation times of the tumor and background materials using a T2-Weighted (T2-W) Turbo Spin Echo (TSE) sequence with Repetition time (TR) = 250 ms, Flip Angle (FA) = 180°, Field of view (FOV) = 260 × 260 mm^2, Slice thickness = 10 mm, matrix size = 128 × 128, Number of averages (NEX) = 2, Echo train length (ETL) = 12, and varying Echo time (TE) values in the range from 8 to 69 ms. Similarly, for T2* mapping, the TE value was varied from 4 to 67 ms and the parameters were as follows: TR = 445 ms, FA = 60°, FOV = 220 × 220 mm^2, Slice thickness = 5 mm, matrix size = 384 × 384, NEX = 1, and ETL = 10. The measured signal intensity in the ROI plotted against the TE value was fitted to the exponential decay function describing the gradual decrease in the transverse magnetization and measured signal strength for T2 relaxation time estimation.[51]

Accordingly, for T1 relaxation time mapping, images were obtained using a Gradient Echo (GRE) sequence at variable FA values in the range of 3 °–15° using the following parameters: TR = 15 ms, TE = 1.93 ms, slice thickness = 5 mm, FOV = 250×250 mm^2, matrix size = 256×256, ETL = 1, and NEX = 1. The obtained data were fitted into the formula describing the recovery of the longitudinal magnetization to its equilibrium value for calculating the relevant T1 relaxation time values.[51]

2.2.4 | Imaging features

The sonographic appearance of the developed tumor phantom model was evaluated using a portable ultrasound machine (UMT-150, Shenzhen Mindray Bio-Medical Electronics Co., Ltd., Shenzhen, P.R. China). The phantom was then scanned in a high-resolution CT system [Optima CT580, General Electric (GE) Medical Systems, Wisconsin, USA] to examine its radiographic appearance. The employed parameters were tube voltage = 100 kVp, tube current = 300 mA, exposure time = 2.0 s, and slice thickness = 1.25 mm. The radiographic properties of the phantom were also extracted from a previous study of the group. Finally, MR images of the phantom were acquired in a 3T scanner (Magnetom Vida, Siemens Healthineers, Erlangen, Germany) using a T2-W TSE sequence with the following parameters: TR = 2500 ms, TE = 52 ms, FA = 180 °, ETL = 12, slice thickness = 10 mm, FOV = 260×260×10 mm^3, matrix size = 128×128, and NEX = 2, to assess the MR contrast between the tumor mimic and surrounding material.

2.3 | Phantom response to thermal heating

The phantom was sonicated with a FUS transducer incorporating a single spherically focused piezoelectric element (Piezo Hannas Tech Co. Ltd, Wuhan, China) with a nominal frequency of 2.4 MHz, a diameter of 50 mm, and a radius of curvature of 65 mm. The transducer's acoustic efficiency was 30%. An MRI compatible positioning device featuring 4 degrees of freedom was employed in the study allowing for robotic movement and placement of the transducer relative to the tumor location.[52] A dedicated software was interfaced with the system enabling remote control of the FUS transducer and positioning mechanism, as well as with the MR scanner enabling sonication planning on preoperative MR images and the use of MR thermometry for thermal ablation monitoring.

The robotic device was positioned on the MRI couch (Magnetom Vida) with the phantom securely placed on the acoustic opening above the transducer, which was supplied by an RF amplifier (AG1016, AG Series Amplifier, T & C Power Conversion, Inc., Rochester, USA). Communication between the robotic device and software was achieved through an electronic driving system placed outside of the MRI room. The phantom was scanned using the 18-channel body coil (Siemens Healthineers) that was securely fixed a few mm above its surface with the assistance of a rigid supporting structure, as illustrated in the experimental setup of Figure 2. The distance between the phantom surface and the transducer was set at 30 mm resulting in a focal depth of 35 mm.

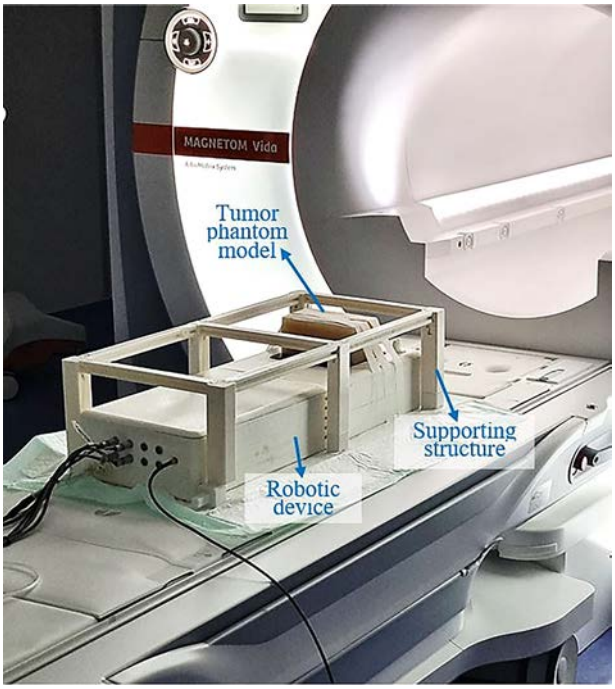

FIGURE 2 The experimental setup arranged on the MRI table for phantom sonications.

Single and grid ultrasonic sonications were performed, where an electric power of 150–200 W (corresponding to focal intensities of 8000–11 000 W/cm^2) was applied for 60 s to each sonication spot. The temperature change in the ROI during and after heating was calculated using the well-known proton resonance frequency (PRF) shift method.[53] This technique makes use of the PRF change that occurs upon temperature change in the subject. This PRF change is proportional to the difference in phase between an initial image acquired at a specific baseline temperature (φ_0) and images obtained at various pre- and post-sonication time spots (φ), making it simple to translate phase differences ($\varphi - \varphi_0$) into temperature changes ($\Delta\tau$) through the following equation:[53]

$$\Delta\tau = \frac{\varphi - \varphi_0}{\gamma\, \alpha\, \beta_0\, \tau\epsilon} \quad (1)$$

where γ is the gyromagnetic ratio, α is the PRF change coefficient, β_0 is the magnetic field strength, and $\tau\epsilon$ is the echo time. The magnitude of α was set at 0.0094 ppm/°C.[54,55,56]

Accordingly, a pixel-by-pixel analysis of phase differences was followed to determine the temperature change in a given ROI in the tumor mimic or surrounding material. Coronal and axial thermal maps were derived from Fast Low Angle Shot (FLASH) images acquired with the following parameters: TR = 25 ms, TE = 10 ms, FOV = 280×280 mm^2, Slice thickness = 3 mm, NEX = 1,

TABLE 1 The acoustic, thermal, MRI, and CT properties of the proposed phantom as measured in the current study or extracted from previous studies of the group, compared with literature values for soft tissues.

Property	6% agar	6% agar + 4 % silica	Source	Soft tissues
Attenuation coefficient (dB/cm-MHz) at 1.1 MHz	0.63 ± 0.05	0.75 ± 0.06	Self-measured	0.54 ± 0.37 [57]
Absorption coefficient (dB/cm-MHz) at 1 MHz	0.10	0.15	Self-measured	0.16–0.34 (brain, heart, liver, kidney) [58]
Group velocity (m/s) at 2.7 MHz	1512 ± 16	1535 ± 17	Self-measured	1561 ± 51 [57]
Mass density (kg/m^3)	945.5 ± 17.7	1020.0 ± 20.2	Self-measured	1043 ± 42 [57]
Acoustic impedance (MRayls)	1.45 ± 0.03	1.61 ± 0.03	Self-measured	≈ 1.6 [59]
Backscatter coefficient (dB/cm-MHz) at 1.1 MHz	–	0.078 ± 0.014	[49]	–
Thermal conductivity (W/m-K)	0.520 ± 0.002	0.543 ± 0.002	Self-measured	0.545–0.587 [60]
Thermal diffusivity (10^{-6} m^2/s)	0.296 ± 0.001	0.306 ± 0.001	Self-measured	0.13–0.15 [60]
Specific heat capacity (J/kg-K)	1859 ± 40	1738 ± 39	Self-measured	3590–3890 [60]
T1 (ms)	2135.8	2099.2	Self-measured	500–1000 [61,62]
T2 (ms)	40.0	35.7	Self-measured	40–80 [61,62]
T2*(ms)	21.7	18.5	Self-measured	–
CT number (HU)	24.4	54.3	[63]	20–80 [64]

FA = 30°, ETL = 1, matrix size = 96×96, and Acquisition time/slice = 2.4 s. Color maps were produced by color-coding the measured temperatures from the minimum to the maximum value from yellow to red.

3 | RESULTS

3.1 | Characterization of tumor phantom model

Table 1 summarizes the acoustic, thermal, MRI, and CT properties of both the tumor mimic and surrounding materials, as measured in the current study or extracted from previous studies of the group, along with indicative literature values for biological tissues. Data are presented as mean ± standard deviation (n = 10). Note that the tumor-mimicking material was found to attenuate ultrasonic waves to a greater extent. Similarly, it possesses higher ultrasonic velocity and acoustic impedance. The results of relaxation time mapping in the 3T scanner revealed lower relaxation times in the tumor material. The estimated thermal properties suggest that the tumor mimic heats up more quickly owing to the addition of silicon dioxide.

The US, CT, and MR images of the developed tumor phantom model are shown in Figure 3. The inclusion of silicon dioxide in the tumor material provided sufficient contrast for clear tumor delineation in all three imaging modalities. Note that the tumor mimic appears more echogenic (Figure 3a) than the surrounding due to the property of silicon dioxide to scatter ultrasound waves. Note also in the CT image (Figure 3b) that some air spaces were created within the tumor mimic due to insufficient stirring. The case shown was the worst case that was encountered. The tumor mimic appeared with decreased intensity compared to the surrounding in the T2-W MR image (Figure 3c) due to its lower water concentration.

3.2 | Phantom response to thermal heating

Figures 4 and 5 present indicative thermal maps for a single sonication within the tumor mimic acquired in coronal and axial planes, respectively. The phantom was exposed at 60 W acoustic power for 60 s at a focal depth of 35 mm. The specific sonication parameters yielded ablative temperatures in the tumor. In fact, peak temperatures of 75°C and 70°C were estimated in coronal and axial planes, respectively, each starting from a baseline temperature of 37°C. The corresponding results for single sonication outside of the tumor are shown in Figure 6, which is a collection of coronal thermal maps acquired at specific time spots during and after sonication. In this case, a smaller peak temperature of 65°C was recorded. Note that some artifacts occur in these maps due to phantom vibration caused by the ultrasound waves.

Typical results for a 3×3 grid sonication with a spatial step of 10 mm and a time delay of 60 s between

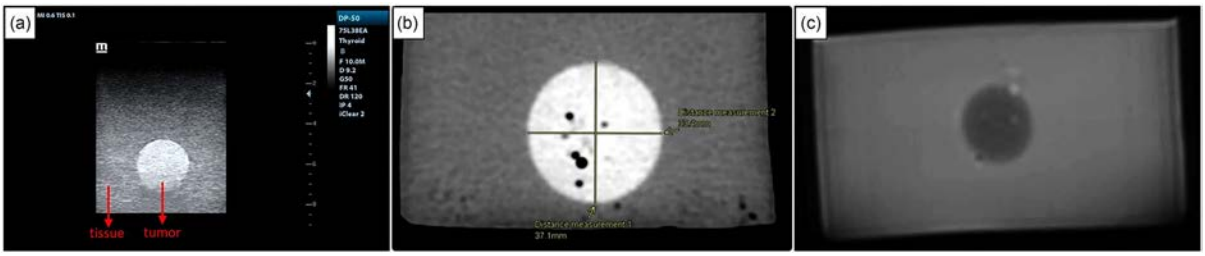

FIGURE 3 (a) US, (b) CT (tube voltage = 100 kVp, tube current = 300 mA, exposure time = 2.0 s, and slice thickness = 1.25 mm), and (c) T2-W TSE coronal (TR = 2500 ms, TE = 52 ms, FA = 180 °, ETL = 12, slice thickness = 10 mm, FOV = 260×260×10 mm^3, matrix size = 128×128, and NEX = 2) images of the developed tumor phantom model.

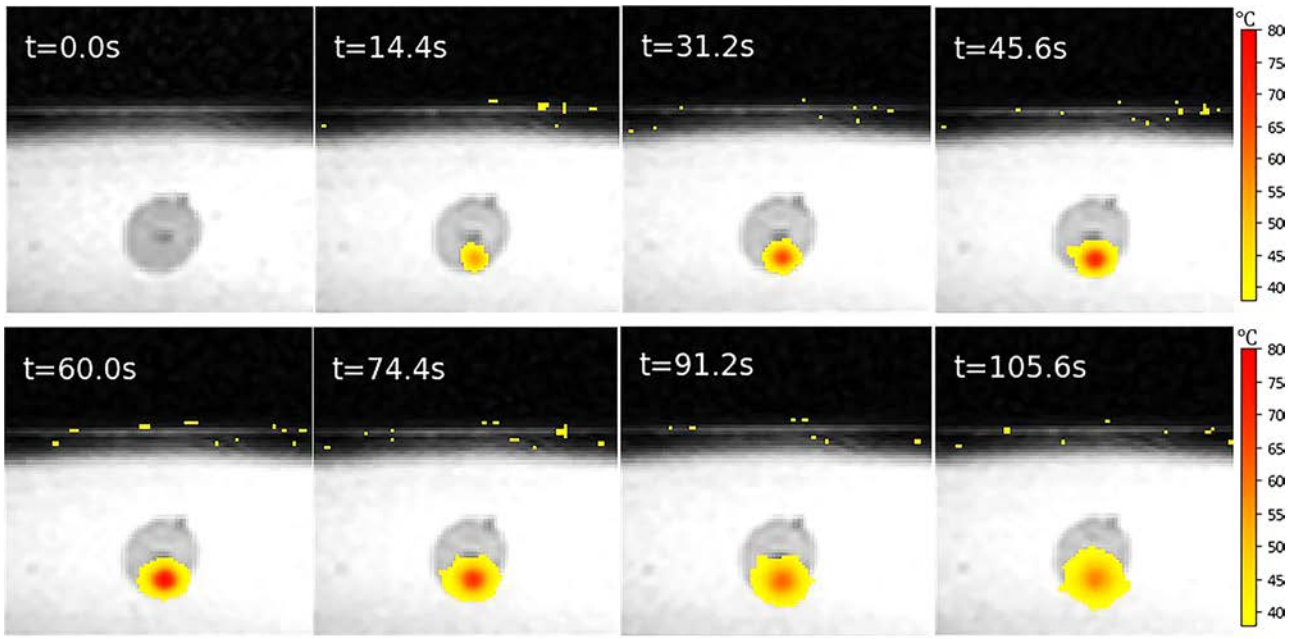

FIGURE 4 Coronal thermal maps extracted from FLASH images (TR = 25 ms, TE = 10 ms, FOV = 280×280 mm^2, slice thickness = 3 mm, NEX = 1, FA = 30°, ETL = 1, matrix size = 96×96, and Acquisition time/slice = 2.4 s) during and after sonication within the tumor mimic with acoustic power of 60 W, sonication duration of 60 s, and focal depth of 35 mm at 2.4 MHz.

adjacent sonications are shown in Figure 7. In this case, an acoustic power of 45 W was applied for 60 s at each sonication spot. Figure 7a shows the sonication points overlaid on a thermal map acquired 4 s post-sonication. The temperature evolution over time recorded for the nine grid points is shown in Figure 7b. Note that the recorded temperature changes were smaller compared to the single sonication due to the use of a smaller acoustic power. Note also that a progressive temperature increase occurred due to near-field heating while during heating the largest temperature changes were observed within the tumor material.

4 | DISCUSSION

Tissue-mimicking phantoms are becoming more and more common for the performance characterization of therapeutic and imaging systems and applications in the context of oncology.[1] Given that image-guided thermal ablation techniques including MRgFUS are continuously gaining popularity as beneficial methods for tumor destruction, the development of high-quality tumor-bearing phantoms dedicated for thermal ablation studies is of significant importance. Therefore, we herein presented the development and assessment of an US/CT/MRI compatible tumor-bearing tissue-mimicking phantom model for MRgFUS ablation studies.

In this study, the selection of phantom materials and their concentration was based on knowledge acquired through previous experimentation and published work of the group.[44,45,49] While previous studies were focused on assessing how specific properties of agar-based gels are affected by varying the concentration of inclusions, the current study aimed to design a phantom not

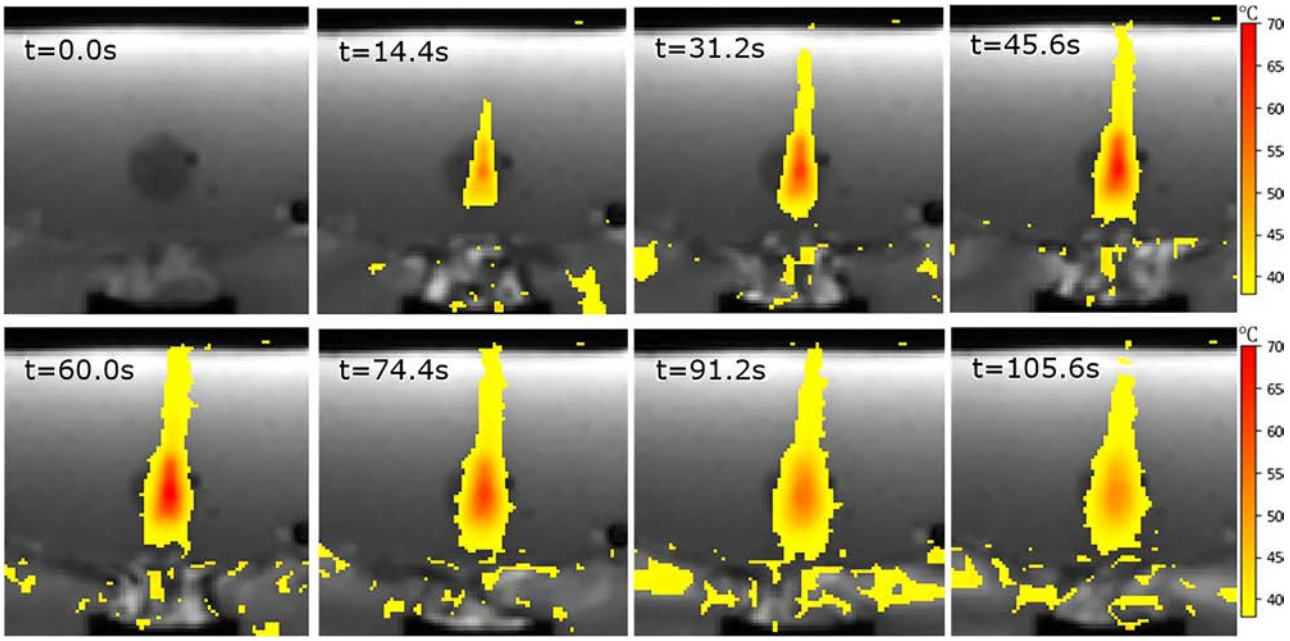

FIGURE 5 Axial thermal maps extracted from FLASH images (TR = 25 ms, TE = 10 ms, FOV = 280×280 mm^2, Slice thickness = 3 mm, NEX = 1, FA = 30°, ETL = 1, matrix size = 96×96, and Acquisition time/slice = 2.4 s) during and after sonication within the tumor mimic with acoustic power of 60 W, sonication duration of 60 s, and focal depth of 35 mm at 2.4 MHz.

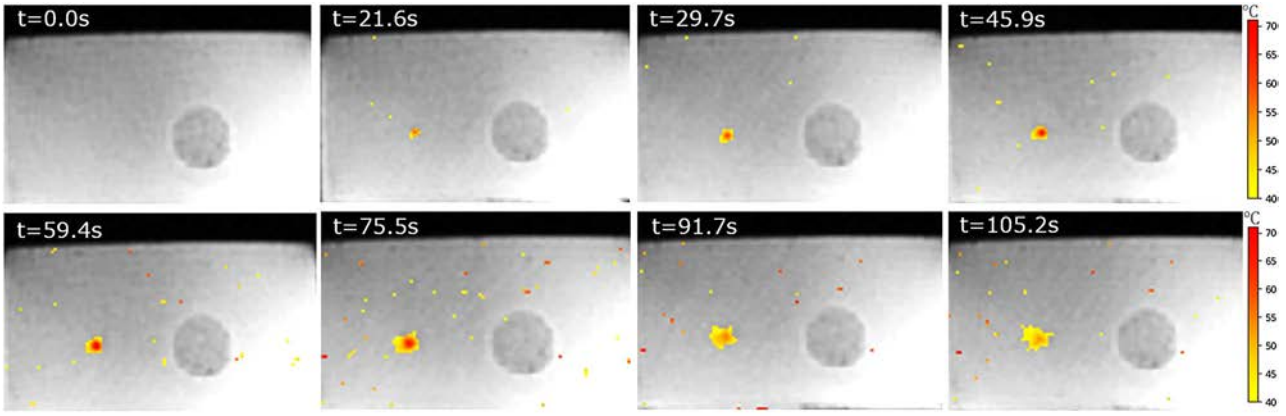

FIGURE 6 Coronal thermal maps extracted from FLASH images (TR = 25 ms, TE = 10 ms, FOV = 280×280 mm^2, Slice thickness = 3 mm, NEX = 1, FA = 30°, ETL = 1, matrix size = 96×96, and Acquisition time/slice = 2.4 s) during and after sonication outside of the tumor mimic with acoustic power of 60 W, sonication duration of 60 s, and focal depth of 35 mm at 2.4 MHz.

only replicating a wider range of properties (acoustic, thermal, and MRI) but also embedding a tumor simulator with different response to FUS heating from the surrounding material mimicking normal tissue.

The developed two-compartment phantom model consists of a 3 cm spherical tumor simulator embedded in a square tissue mimicking phantom. Agar was selected as the main ingredient for both compartments. The properties of the tumor mimic were differentiated from those of the surrounding material mimicking normal tissue by adding silicon dioxide. Although in this study a simplistic tumor model was adopted to obtain proof of concept of the proposed phantom, one could create patient-specific tumors, which may also be embedded in organ-specific phantoms to enable more realistic conditions. This could be achieved by 3D-printing dedicated molds having a cavity with the unique shape of the body part/ tumor to be mimicked, as extracted from CT data, and filling them with tissue-mimicking agar-based gels.

The estimated ultrasonic attenuation coefficient and velocity of the proposed phantom fall well within the range of literature-reported values for soft tissues (Table 1). The acoustic impedance was also found to be consistent between the phantom and live tissue, whereas both phantom compartments were found

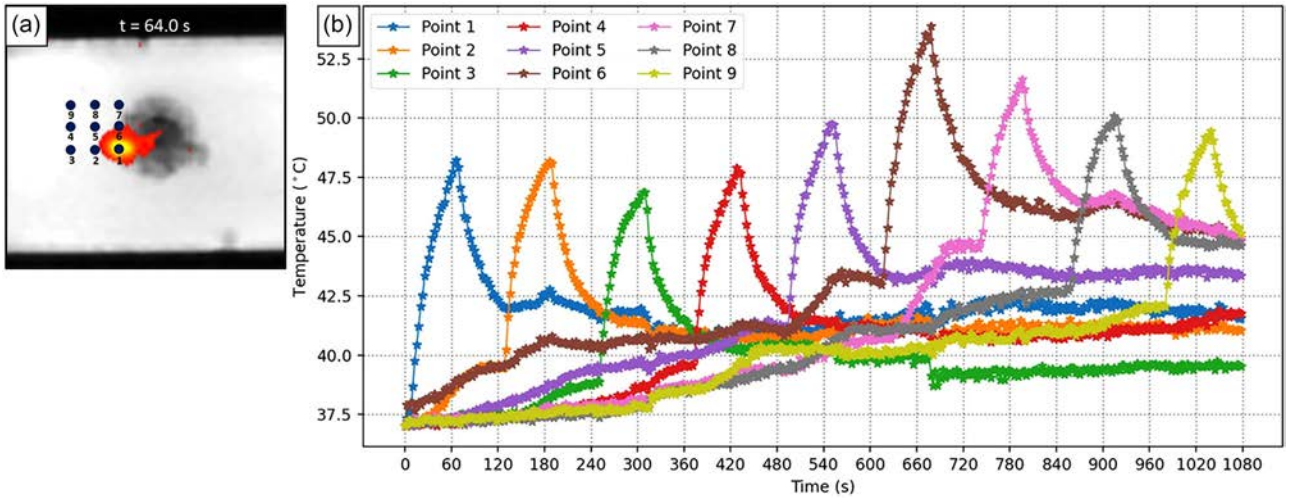

FIGURE 7 (a) The nine sonication points (3×3) overlaid on the thermal map acquired 4 s post-sonication. (b) The recorded thermal profiles for the nine spots sequentially exposed at 45 W acoustic power for 60 s, at 35 mm focal depth with the 2.4 MHz transducer.

to possess an absorption coefficient quite below the reported range for soft tissues. Notably, it was shown that the inclusion of a proper amount of milk in this phantom type can increase absorption to the level observed in tissue[45]; however, milk addition reduces the phantom robustness and shelf life. Note also that the tumor-mimicking material was found to attenuate ultrasonic waves to a greater extent verifying that silicon dioxide is an effective modifier of ultrasonic attenuation, as also demonstrated by previous research.[29,45] Similarly, it possesses higher ultrasonic velocity and acoustic impedance than the background material. Regarding thermal properties, while the phantom's thermal conductivity matches well that of soft tissues, the thermal diffusivity and specific heat capacity are roughly two-fold higher and smaller, respectively, than those reported by Giering et al.[60] for the kidney, heart, spleen, and liver (Table 1).

The imaging contrast between the two compartments should be sufficiently high to enable ease identification of the tumor mimic so that treatment planning and navigation of the ultrasonic beam relative to the target (using the motion commands of the relevant software) can be performed accurately. In the case of MRI monitoring, good contrast further enables monitoring whether thermal energy is delivered within the tumor with the required precision and as planned by intraprocedural MR imaging and thermometry. Herein, the selected concentration of 4 % w/v silicon dioxide resulted in shorter relaxation times and good delineation of the tumor in MRI. This result ties well with previous studies wherein increasing silicon dioxide concentration in agar gels resulted in gradual decrease of both relaxation times, with a greater effect on T1.[44] Notably, the estimated T2 relaxation times fall within the range of values reported literally for biological tissues, whereas the T1 relaxation times are longer than those observed in live tissues (Table 1).

The proposed phantom further demonstrated excellent tumor visualization in CT and US imaging. The silicon dioxide-doped tumor mimic has larger stiffness and appeared with increased radiographic density on CT images. It is also characterized by increased echogenicity due to the property of silicon dioxide to scatter ultrasound waves. Previous studies have also demonstrated that the inclusion of a metal or metalloid powder imparts noticeable ultrasonic attenuation.[29]

The phantom's response to thermal heating was investigated by performing high power sonications with a 2.4 MHz single element spherically focused ultrasonic transducer in a 3T MRI scanner. An acoustic power of 60 W applied for a duration of 60 s inside the tumor mimic yielded sufficient temperature elevation (> 30°C) resulting in maximum focal temperatures over 70°C, which fall within the ablative range. In fact, most human soft tissues undergo coagulative necrosis promptly when exposed at temperatures over 56°C.[65,66] Sonication in the background material with similar parameters resulted in a smaller focal temperature of 65°C, which is though sufficiently high for ablation purposes. Therefore, the selected recipes were deemed suitable in terms of achieving a different thermal response to heating between the tumor (6% agar and 4% silicon dioxide) and normal tissue (6% agar) phantoms. In fact, the tumor material is characterized by a higher ultrasonic absorption coefficient and a lower specific heat capacity, thus heating up more rapidly and being a better heat reservoir than the surrounding normal tissue. It is worth noting that the effect of silicon dioxide on ultrasonic absorption has also been explored in a prior study,[48] which found that the absorption coefficient increases at low silicon dioxide concentrations of up to 4%. It seems

that the scattering effect of this material becomes prominent decreasing ultrasonic absorption at silicon dioxide concentrations higher than 4%.[48] Therefore, the higher temperatures recorded in the tumor mimic can be attributed to the silicon dioxide-induced increase in ultrasonic absorption and reduction in specific heat capacity. At this point, it should be mentioned that the overall ultrasonic attenuation is higher in the tumor material while simultaneously ultrasonic waves encounter additional attenuation at the tumor borders due to beam reflection and scattering, which unavoidably reduces the ultrasonic energy reaching the tumor interior to some extent. Refraction and diffraction phenomena may also affect the energy deposition by causing distortion of the penetrating beam. In this example, the beam incidence was perpendicular to the tumor surface and transducer diameter was small, thus minimizing such energy losses. Although further investigation is needed to determine the significance of these energy losses, they do not seem to affect the thermal deposition to an extent that would reverse the effect of increased heat accumulation observed in the silica-doped material.

For grid sonications, the transducer was robotically moved in a horizontal plane to sequentially visit adjacent sonication spots using the relevant software commands. The thermal profiles obtained by MR thermometry (Figure 7b) reveal a rapid temperature increase within the 60 s of sonication followed by exponential decrease at a lower rate after transducer deactivation due to dissipation of heat through conduction mechanisms. Notably, smaller temperature changes (≅10°C) were recorded compared to the single sonication (≅30°C), resulting in smaller ablation areas, due to the use of a smaller acoustic power of 45 W. Generally, the ablation area can be easily increased by increasing the sonication time or applied power similarly to what is observed in biological tissue.

The various sonications points were visited in a sequential manner leaving a 60 s cooling period, which was previously suggested as the minimum required delay to reduce pre-focal heating for the specific sequential pattern.[67] However, the recorded temperature evolution at the nine sonication points (Figure 7b) provides clear evidence of heat dissipation. Generally, the baseline temperature at each point increased over time due to heat dissipation from adjacent previously sonicated regions. Notably, by increasing the time between grid points and adjusting the movement pattern it is possible to reduce the phenomenon of heat deposition in the near field region.[67] Furthermore, although all the recorded thermal profiles show similar trend in the rate of temperature increase and post-sonication decrease, bigger temperature changes occurred at the sonication points located within the tumor mimic (1 and 6) owing to the previously discussed silicon dioxide effects. Note for example that while the grid points 6 and 8 (Figure 7), respectively, located inside and outside the tumor, show similar thermal accumulation prior to sonication, the recorded temperature change at point 6 within the tumor was more than 50% larger.

The proposed phantom provides triple-modal imaging characteristics (US/CT/MR), which may provide the basis for other image-guided procedures involving tumor targeting. In fact, given the proven realistic haptic feedback of agar gels,[68] the phantom could also serve as a tool for tumor puncture training. Based on previous literature, the phantom could be further optimized for other thermal applications very easily by including additional ingredients during the preparation process. For instance, sodium chloride can be included to modify the electrical conductivity of the phantom for RFA and MWA studies.[25,28]

One limitation of our implementation is that no specific values of acoustic, thermal, and MRI properties were considered for the tumor model. However, since each tumor has its own specific characteristics, it is not practicable to create a model that mimics the specific properties of a single tumor type. Furthermore, it is not feasible to develop a model that sufficiently mimics all the critical properties of a specific tumor type given the wide variability of tumor features among subjects. Of course, individual researchers may modify the proposed recipes to fit their tumor of interest and create patient-specific tumor models. Furthermore, it could be argued that since the ultrasonic absorption and specific heat capacity of the phantom model differ from those of soft tissues, its response to thermal heating is not realistic and not adequately representative of the clinical scenario. Furthermore, in real tissue, a quicker focal temperature drop is expected due to the presence of blood flow. However, the phantom could be used as a quality assurance tool to assess the functionality of MRgFUS hardware (i.e., robotic devices and ultrasonic sources) and relevant software. Given the comprehensive characterization of phantom properties, it is also possible that precise dosimetry measurements and assessment of FUS ablation protocols before in vivo application can be accomplished by calibrating the relation between the phantom's and soft tissues' response to thermal heating using mathematical modeling and simulations. Good tumor visualization and delineation on US, MRI, and CT images could also provide the basis for a wider range of applications such image-guided tumor puncture and ablation using thermal applicators (such as RF applicators).

5 | CONCLUSION

Being in agreement with previous studies,[43–45] the current results provide sufficient evidence that the presented agar-based tumor phantom model possesses acoustic, thermal, and MRI properties well comparable with those of soft tissues. The low cost, ease handling,

and the capacity to withstand ablative temperatures and produce tissue-like US and MRI signal constitute additional benefits of this phantom type. The phantom model is also capable of generating multi-modality imaging contrast. MR thermometry revealed clear elevations of temperature to ablation levels in and out of the silicon dioxide-doped tumor simulator, with clear evidence of larger heat accumulation within the tumor. It was therefore concluded that the difference in materials between the tumor and surrounding is suitable to impart noticeable change in the thermal response of the two compartments. This simple and inexpensive tumor phantom model could facilitate preclinical MRgFUS studies, and potentially other image-guided thermal ablation techniques upon minimal modifications. It may also allow for reliable monitoring of thermal heating and assessment of ablation outcome through MR thermometry or alternatively thermocouple measurements for routine laboratory testing. The limitations of the phantom naturally include the absence of physiological procedures such as blood flow and the inability to directly visualize the ablated region. In future studies, anthropomorphic tumor-bearing phantoms could be easily created by 3D printing molds of dedicated shape depending on the specific tissue to be replicated.

ACKNOWLEDGMENTS

The project was funded by the Research and Innovation Foundation of Cyprus. The robotic device employed in the study was developed under the project FUSROBOT (ENTERPRISES/0618/0016), whereas the reported experiments were carried out under the project SOUNDPET (INTEGRATED/0918/0008) and FUSVET (SEED/1221/0080).

CONFLICT OF INTEREST STATEMENT

The authors have no conflicts to disclose.

DATA AVAILABILITY STATEMENT

The data that support the findings of this study are available from the corresponding author upon reasonable request.

REFERENCES

1. McGarry CK, Grattan LJ, Ivory AM, et al. Tissue mimicking materials for imaging and therapy phantoms: a review. *Phys Med Biol*. 2020;65(23):1-43. https://doi.org/10.1088/1361-6560/abbd17
2. Ahmad MS, Suardi N, Shukri A, et al. Dynamic hepatocellular carcinoma model within a liver phantom for multimodality imaging. *Eur J Radiol Open*. 2020;7:100257. https://doi.org/10.1016/j.ejro.2020.100257
3. Gan Q, Wang D, Ye J, et al. Benchtop and animal validation of a projective imaging system for potential use in intraoperative surgical guidance. *PLoS One*. 2016;11(7):e0157794. https://doi.org/10.1371/journal.pone.0157794
4. McHugh DJ, Zhou FL, Wimpenny I, et al. A biomimetic tumor tissue phantom for validating diffusion-weighted MRI measurements. *Magn Reson Med*. 2018;80(1):147-158. https://doi.org/10.1002/mrm.27016
5. LaRochelle EPM, Streeter SS, Littler EA, Ruiz AJ. 3D-printed tumor phantoms for assessment of in vivo fluorescence imaging analysis methods. *Mol Imaging Biol*. 2022; 25: 212–220. https://doi.org/10.1007/s11307-022-01783-5
6. Hatamikia S, Gulyas I, Birkfellner W, et al. Realistic 3D printed imaging tumor phantoms for validation of image processing algorithms. *Med Phys*. 2022:1-17. doi:10.48550/arXiv.2211.14861
7. Valladares A, Beyer T, Rausch I. Physical imaging phantoms for simulation of tumor heterogeneity in PET, CT, and MRI: an overview of existing designs. *Med Phys*. 2020;47(4):2023-2037. https://doi.org/10.1002/mp.14045
8. Presotto L, Bettinardi V, De Bernardi E, et al. PET textural features stability and pattern discrimination power for radiomics analysis: an "ad-hoc" phantoms study. *Phys Medica*. 2018;50:66-74. https://doi.org/10.1016/j.ejmp.2018.05.024
9. Waugh SA, Lerski RA, Bidaut L, Thompson AM. The influence of field strength and different clinical breast MRI protocols on the outcome of texture analysis using foam phantoms. *Med Phys*. 2011;38(9):5058-5066. https://doi.org/10.1118/1.3622605
10. Sramek MT, Shi Y, Quintanilla EA, et al. Development of a novel tumor phantom model for head and neck squamous cell carcinoma and its applications. *Med Imaging2020*. 2020; 11315: 741–751. https://doi.org/10.1117/12.2550597
11. Ng SY, Lin C. Low-cost and easily fabricated ultrasound-guided breast phantom for breast biopsy training. *Prepr (Version 1) available Res Sq*. 2020:1-22. doi:10.21203/rs.2.19957/v1
12. Groenhuis V, Siepel FJ, Veltman J, van Zandwijk JK, Stramigioli S. Stormram 4: an MR safe robotic system for breast biopsy. *Ann Biomed Eng*. 2018;46(10):1686-1696. https://doi.org/10.1007/s10439-018-2051-5
13. Daniel BL, Birdwell RL, Black JW, Ikeda DM, Glover GH, Herfkens RJ. Interactive MR-guided, 14-gauge core-needle biopsy of enhancing lesions in a breast phantom model. *Acad Radiol*. 1997;4(7):508-512. https://doi.org/10.1016/S1076-6332(97)80238-3
14. Webb H, Lubner MG, Hinshaw JL. Thermal Ablation. *Semin Roentgenol*. 2011;46(2):133-141. https://doi.org/10.1053/j.ro.2010.08.002
15. Glassberg MB, Ghosh S, Clymer JW, et al. Microwave ablation compared with radiofrequency ablation for treatment of hepatocellular carcinoma and liver metastases: a systematic review and metaanalysis. *Onco Targets Ther*. 2019;12:6407-6438. https://doi.org/10.2147/OTT.S204340
16. Izadifar Z, Izadifar Z, Chapman D, Babyn P. An introduction to high intensity focused ultrasound: systematic review on principles, devices, and clinical applications. *J Clin Med*. 2020;9(2):460. https://doi.org/10.3390/jcm9020460
17. Dabbagh A, Abdullah BJJ, Ramasindarum C, Abu Kasim NH. Tissue-mimicking gel phantoms for thermal therapy studies. *Ultrason Imaging*. 2014;36(4):291-316. https://doi.org/10.1177/0161734614526372
18. Lafon C, Zderic V, Noble ML, et al. Gel phantom for use in high-intensity focused ultrasound dosimetry. *Ultrasound Med Biol*. 2005;31(10):1383-1389. https://doi.org/10.1016/j.ultrasmedbio.2005.06.004
19. Takegami K, Kaneko Y, Watanabe T, Maruyama T, Matsumoto Y, Nagawa H. Polyacrylamide gel containing egg white as new model for irradiation experiments using focused ultrasound. *Ultrasound Med Biol*. 2004;30(10):1419-1422. https://doi.org/10.1016/j.ultrasmedbio.2004.07.016
20. Eranki A, Mikhail AS, Negussie AH, Katti PS, Wood BJ, Partanen A. Tissue-mimicking thermochromic phantom for characterization of HIFU devices and applications. *Int J Hyperthermia*. 2019;36(1):518–529. https://doi.org/10.1080/02656736.2019.1605458
21. Zhou Y, Zhao L, Zhong X, et al. A thermochromic tissue-mimicking phantom model for verification of ablation plans in thermal

ablation. *Ann Transl Med*. 2021;9(4):354. doi:10.21037/atm-21-523
22. Chen WJ, Wang Q, Kim CY. Gel phantom models for radiofrequency and microwave ablation of the liver. *Dig Dis Interv*. 2020;4(3):303-310. https://doi.org/10.1055/s-0040-1716737
23. Liu Z, Ahmed M, Weinstein Y, Yi M, Mahajan RL, Goldberg SN. Characterization of the RF ablation-induced "oven effect": the importance of background tissue thermal conductivity on tissue heating. *Int J Hyperth*. 2006;22(4):327-342. https://doi.org/10.1080/02656730600609122
24. Haemmerich D, Schutt DJ. RF ablation at low frequencies for targeted tumor heating: In vitro and computational modeling results. *IEEE Trans Biomed Eng*. 2011;58(2):404-410. https://doi.org/10.1109/TBME.2010.2085081
25. Ortega-Palacios R, Trujillo-Romero CJ, Cepeda-Rubio MFJ, Leija L, Hernández AV. Heat transfer study in breast tumor phantom during microwave ablation: modeling and experimental results for three different antennas. *Electronics*. 2020;9(3):535. https://doi.org/10.3390/electronics9030535
26. Zhong X, Zhou P, Zhao Y, Liu W, Zhang X. A novel tissue-mimicking phantom for US/CT/MR-guided tumor puncture and thermal ablation. *Int J Hyperth*. 2022;39(1):557-563. https://doi.org/10.1080/02656736.2022.2056249
27. Kim KS, Lee SY. Nanoparticle-mediated radiofrequency capacitive hyperthermia: a phantom study with magnetic resonance thermometry. *Int J Hyperth*. 2015;31(8):831-839. https://doi.org/10.3109/02656736.2015.1096968
28. Li K, Su Z, Xu E, Huang Q, Zeng Q, Zheng R. Evaluation of the ablation margin of hepatocellular carcinoma using CEUS-CT/MR image fusion in a phantom model and in patients. *BMC Cancer*. 2017;17(1):1-10. https://doi.org/10.1186/s12885-017-3061-7
29. Antoniou A, Damianou C. MR relaxation properties of tissue-mimicking phantoms. *Ultrasonics*. 2022;119. https://doi.org/10.1016/j.ultras.2021.106600
30. Duc NM, Keserci B. Emerging clinical applications of high-intensity focused ultrasound. *Diagnostic Interv Radiol*. 2019;25(5):398-409. https://doi.org/10.5152/dir.2019.18556
31. Hassanuddin A, Choi JH, Seo DW, et al. Factors affecting tumor ablation during high intensity focused ultrasound treatment. *Gut Liver*. 2014;8(4):433-437. https://doi.org/10.5009/gnl.2014.8.4.433
32. An CY, Hsu YL, Tseng CS. An ultrasound-guided robotic HIFU ablation system with respiration induced displacement and time delay compensation. *J Med Biol Eng*. 2019;39(5):796-805. https://doi.org/10.1007/s40846-019-00463-0
33. Kaczmarek K, Hornowski T, Antal I, Rajnak M, Timko M, Józefczak A. Sono-magnetic heating in tumor phantom. *J Magn Magn Mater*. 2020;500:166396. https://doi.org/10.1016/j.jmmm.2020.166396
34. Farrer AI, Odéen H, de Bever J, et al. Characterization and evaluation of tissue-mimicking gelatin phantoms for use with MRgFUS. *J Ther Ultrasound*. 2015;3(1):1-11. https://doi.org/10.1186/s40349-015-0030-y
35. Madsen EL, Zagzebski JA, Frank GR. An anthropomorphic ultrasound breast phantom containing intermediate-sized scatteres. *Ultrasound Med Biol*. 1982;8(4):381-392. https://doi.org/10.1016/S0301-5629(82)80006-9
36. Zell K, Sperl JI, Vogel MW, Niessner R, Haisch C. Acoustical properties of selected tissue phantom materials for ultrasound imaging. *Phys Med Biol*. 2007;52(20):N475–N484. https://doi.org/10.1088/0031-9155/52/20/N02
37. Drakos T, Giannakou M, Menikou G, Constantinides G, Damianou C. Characterization of a soft tissue-mimicking agar/wood powder material for MRgFUS applications. *Ultrasonics*. 2021;113: 10635. https://doi.org/10.1016/j.ultras.2021.106357
38. Menikou G, Dadakova T, Pavlina M, Bock M, Damianou C. MRI compatible head phantom for ultrasound surgery. *Ultrasonics*. 2015;57:144-152. https://doi.org/10.1016/j.ultras.2014.11.004
39. Menikou G, Yiannakou M, Yiallouras C, Ioannides C, Damianou C. MRI-compatible bone phantom for evaluating ultrasonic thermal exposures. *Ultrasonics*. 2016;71:12-19. https://doi.org/10.1016/j.ultras.2016.05.020
40. Pichardo S, Melodelima D, Curiel L, Kivinen J. Suitability of a tumour-mimicking material for the evaluation of high-intensity focused ultrasound ablation under magnetic resonance guidance. *Phys Med Biol*. 2013;58(7):2163-2183. https://doi.org/10.1088/0031-9155/58/7/2163
41. Menikou G, Yiannakou M, Yiallouras C, Ioannides C, Damianou C. MRI-compatible breast/rib phantom for evaluating ultrasonic thermal exposures. *Int J Med Robot Comput Assist Surg*. 2018;14(1):1-12. https://doi.org/10.1002/rcs.1849
42. Damianou C. The role of phantoms in magnetic resonance imaging-guided focused ultrasound surgery. *Digit Med*. 2019;5(2):52-55. https://doi.org/10.4103/digm.digm_13_19
43. Menikou G, Damianou C. Acoustic and thermal characterization of agar based phantoms used for evaluating focused ultrasound exposures. *J Ther Ultrasound*. 2017;5:14. https://doi.org/10.1186/s40349-017-0093-z
44. Antoniou A, Georgiou L, Christodoulou T, et al. MR relaxation times of agar-based tissue-mimicking phantoms. *J Appl Clin Med Phys*. 2022; 23:e13533. https://doi.org/10.1002/acm2.13533
45. Drakos T, Antoniou A, Evripidou N, et al. Ultrasonic attenuation of an agar, silicon dioxide, and evaporated milk gel phantom. *J Med Ultrasound*. 2021;29(4):239-249. https://doi.org/10.4103/JMU.JMU
46. Zeece M. Food additives. In: *Introduction to the Chemistry of Food*. 2020:251-311.
47. Antoniou A, Evripidou N, Giannakou M, Constantinides G, Damianou C. Acoustical properties of 3D printed thermoplastics. *J Acoust Soc Am*. 2021;149(4):2854-2864. https://doi.org/10.1121/10.0004772
48. Drakos T, Giannakou M, Menikou G, Ioannides C, Damianou C. An improved method to estimate ultrasonic absorption in agar-based gel phantom using thermocouples and MR thermometry. *Ultrasonics*. 2020;103. https://doi.org/10.1016/j.ultras.2020.106089
49. Filippou A, Damianou C. Evaluation of ultrasonic scattering in agar-based phantoms using 3D printed scattering molds. *J Ultrasound*. 2022;25(3):597-609. https://doi.org/10.1007/s40477-021-00630-7
50. Filippou A, Louca I, Damianou C. Characterization of a fat tissue mimicking material for high intensity focused ultrasound applications. *J Ultrasound*. 2022. https://doi.org/10.1007/s40477-022-00746-4
51. Bojorquez JZ, Bricq S, Acquitter C, Brunotte F, Walker PM, Lalande A. What are normal relaxation times of tissues at 3 T? *Magn Reson Imaging*. 2017;35:69-80. https://doi.org/10.1016/j.mri.2016.08.021
52. Drakos T, Giannakou M, Menikou G, et al. MRI-guided focused ultrasound robotic system for preclinical use. *J Vet Med Anim Sci*. 2021;4(1):1049.
53. Rieke V, Pauly KB. MR thermometry. *J Magn Reson Imaging*. 2008;27(2):376-390. https://doi.org/10.1002/jmri.21265.MR
54. Peters RD, Hinks RS, Henkelman RM. Heat-source orientation and geometry dependence in proton-resonance frequency shift magnetic resonance thermometry. *Magn Reson Med*. 1999;41(5):909-918. https://doi.org/10.1002/(SICI)1522-2594(199905)41:5<909::AID-MRM9>3.0.CO;2-N
55. Bing C, Staruch R, Tillander M, et al. Drift correction for accurate PRF shift MR thermometry during mild hyperthermia treatments with MR-HIFU. *Int J Hyperth*. 2017;32(6):673-687. https://doi.org/10.1080/02656736.2016.1179799
56. De Zwart JA, Vimeux FC, Delalande C, Canioni P, Moonen CTW. Fast lipid-suppressed MR temperature mapping with echo-shifted gradient- echo imaging and spectral-spatial

excitation. *Magn Reson Med*. 1999;42(1):53-59. https://doi.org/10.1002/(SICI)1522-2594(199907)42:1<53::AID-MRM9>3.0.CO;2-S
57. Mast TD. Empirical relationships between acoustic parametersin human soft tissues. *Acoust Res Lett Online*. 2000; 1(2). https://doi.org/10.1121/1.1336896
58. Goss SA, Frizzell LA, Dunn F. Ultrasonic absorption and attenuation in mammalian tissues. *Ultrasound Med Biol*. 1979;5(2):181-186. https://doi.org/10.1016/0301-5629(79)90086-3
59. Chan V, Perlas A. Basics of ultrasound imaging. In: *Atlas of Ultrasound-Guided Procedures in Interventional Pain Management*. 2011:13-19. https://doi.org/10.1007/978-1-4419-1681-5_2
60. Giering K, Minet O, Lamprecht I, Müller G. Review of thermal properties of biological tissues. In: *Proceedings of SPIE - The International Society for Optical Engineering*; 1995:45-65.
61. Stanisz GJ, Odrobina EE, Pun J, et al. T1, T2 relaxation and magnetization transfer in tissue at 3T. *Magn Reson Med*. 2005;54(3):507-512. https://doi.org/10.1002/mrm.20605
62. Bottomley PA, Foster TH, Argersinger RE, Pfeifer LM. A review of normal tissue hydrogen NMR relaxation times and relaxation mechanisms from 1–100 MHz: dependence on tissue type, NMR frequency, temperature, species, excision, and age. *Int J Med Phys Res Pract*. 1984;11(4):425-448. https://doi.org/10.1118/1.595535
63. Antoniou A, Nikolaou A, Georgiou A, Evripidou N, Damianou C. Development of an US, MRI, and CT imaging compatible realistic mouse phantom for thermal ablation and focused ultrasound evaluation. *Ultrasonics*. 2023;131:106955. https://doi.org/10.1016/j.ultras.2023.106955
64. Kalra A, Yang K-H. Developing FE human models from medical images. In: *Basic Finite Element Method as Applied to Injury Biomechanics*. Academic Press; 2018:389-415. https://doi.org/10.1016/B978-0-12-809831-8.00009-X
65. Damianou C, Hynynen K. The effect of various physical parameters on the size and shape of necrosed tissue volumeuring ultrasound surgery. *J Acoust Soc Am*. 1994;95(3):1641-1649. https://doi.org/10.1121/1.408550
66. Kennedy JE, Haar GR TER, Cranston D. High intensity focused ultrasound: surgery of the future? *Br J Radiol*. 2003;76:590-599. https://doi.org/10.1259/bjr/17150274
67. Filippou A, Drakos T, Giannakou M, Evripidou N, Damianou C. Experimental evaluation of the near-field and far-field heating of focused ultrasound using the thermal dose concept. *Ultrasonics*. 2021;116:106513. https://doi.org/10.1016/j.ultras.2021.106513
68. Ng SY, Lin C-L. A multilayered, lesion-embedded ultrasound breast phantom with realistic visual and haptic feedback for needle biopsy. *Ultrasound Med Biol*. 2022;48(8):1468-1483. https://doi.org/10.1016/j.ultrasmedbio.2022.03.009

How to cite this article: Antoniou A, Evripidou N, Georgiou L, Chrysanthou A, Ioannides C, Damianou C. Tumor phantom model for MRI-guided focused ultrasound ablation studies. *Med Phys*. 2023;1-13. https://doi.org/10.1002/mp.16480

Title of the article: Feasibility of ultrasonic heating through skull phantom using single-element transducer

Abstract:

Background: Non-invasive neurosurgery has become possible through the use of transcranial Focused Ultrasound (FUS). This study assessed the heating ability of single element spherically focused transducers operating at 0.4 and 1.1 MHz through 3D printed thermoplastic skull phantoms.

Methods: Phantoms with precise skull bone geometry of a male patient were 3D printed using common thermoplastic materials following segmentation on a Computed Tomography (CT) head scan image. The brain tissue was mimicked by an agar-based gel phantom developed in-house. The selection of phantom materials was mainly based on transmission-through attenuation measurements. Phantom sonications were performed through water, and then, with the skull phantoms intervening the beam path. In each case, thermometry was performed at the focal spot using thermocouples.

Results: The focal temperature change in the presence of the skull phantoms was reduced to less than 20 % of that recorded in free field when using the 0.4 MHz transducer, whereas the 1.1 MHz trans-skull sonication produced minimal or no change in focal temperature. The 0.4 MHz transducer showed better performance in trans-skull transmission, but still not efficient.

Conclusion: The inability of both tested single element transducers to steer the beam through the high attenuating skull phantoms and raise the temperature at the focus was confirmed, underlying the necessity to use a correction technique to compensate for energy losses, such those provided by phased arrays. The proposed phantom could be used as a cost-effective and ergonomic tool for trans-skull FUS preclinical studies.

Key-words: single element transducer; 3D printed skull; agar phantom; heating; trans-skull

Key messages:

- Thermoplastic phantoms with precise human skull bone geometry were 3D printed.
- Trans-skull HIFU sonications were performed in a brain-tissue/skull phantom using single element spherically focused transducers of 0.4 and 1.1 MHz central frequency under temperature monitoring.
- The propagation of ultrasonic waves by single element emissions was blocked to a great degree by the human-like skull phantoms, leading to minimal temperature increase at the focal point.
- The 0.4 MHz transducer showed better performance in trans-skull transmission attributed to less scattering effects.

Introduction:

The last couple of decades, special research interest has been placed to the therapeutic value of ultrasound and the benefits it brings to many disciplines of modern medicine.[1-2] The non- invasive nature of Focused Ultrasound (FUS) constitutes its main advantage over conventional surgery. When operating at high intensities (in continuous mode), the mechanical energy is converted into heat inducing hyperthermic and ablative effects that were mainly exploited in the area of oncology for the ablative therapy of both shallow and deep tissue.[2] On the other hand, pulsed FUS is associated with various mechanical bioeffects from tissue vibrations to acoustic cavitation, which are caused by the fast pressure changes in tissue.[1]

In the 1950s, revolutionary studies were conducted by Fry et al.[3-4] to assess the High Intensity Focused Ultrasound (HIFU) effects on human brain tissue. However, transcranial focusing was unattainable because of the strong aberrating and attenuating nature of the skull resulting in significant beam defocusing.[5] Thereby, for many years, studies involved craniotomy for precise delivery of ultrasonic energy to the brain tissue through an acoustic window.[6]

In the 1990s, the multi-element ultrasonic technology has emerged as a way to actively form the beam compensating for such losses through regulating the phase of each element individually.[7-8] While this procedure was initially invasive, the introduction of numerical simulations for accurately estimating the resultant phase profile of the beam transmitted though the skull allowed for completely non-invasive transcranial applications.[9-10] In this regard, Magnetic Resonance Imaging (MRI) was also a significant milestone that accelerated the adoption of this technology mainly through the development of MR thermometry,[11] which is currently the only tool for monitoring temperature changes during sonication in almost real-time. Simultaneously, MRI is

considered ideal as a guidance modality since it offers non-invasive optimal imaging of brain tumours without exposing patients to ionizing radiation.[12] Overall, these technological advances offered the accuracy required to safely target areas in the Central Nervus System (CNS) without threatening adjacent or intervening tissues.

So far, the transcranial FUS technology has been investigated for its feasibility in treating essential tremor,[13] parkinson's disease,[14] obsessive-compulsive disorder,[15] major depressive disorder,[15] and epilepsy.[16] The last years, a lot of research was devoted in investigating the use of this technology for tumor ablation and drug delivery by selective disruption of the blood-brain barrier (BBB).[17]

Currently, the available devices for brain ultrasound therapy in the clinic are limited. The SonoCloud (CarThera, France)[18] and NaviFUS (NaviFUS, Taiwan)[19] systems offer FUS plus microbubbles mediated disruption of the BBB. The first one comprises a non-focused transducer that is implanted in the skull, whereas the later one offers neuronavigation-guided extracorporeal therapy. The ExAblate Neuro 4000 system (InSightec, Israel) is considered the leading Magnetic Resonance guided Focused Ultrasound (MRgFUS) brain system and the first to be approved by the Food and Drug administration (FDA) for targeted thermoablation of brain tissue.[20] Both extracorporeal systems use phased arrays for electronic steering of the beam.[19-20] The ExAblate system incorporates a helmet with 1024 elements operating at a frequency of 650 KHz, whereas the NaviFUS incorporates a more compact hemispherical transducer of fewer elements.

Though the phased array technology has immense benefits, it requires the use of sophisticated driving electronics that complicate its use and portability. Furthermore, it typically involves the use of a stereotactic frame making the procedure minimally

invasive.[20] The high cost of this technology constitutes another shortcoming limiting its wider adaption, especially in the preclinical setting.

The use of a single-element transducer could address these issues, but at the cost of difficulties in ultrasonic penetration through the skull. Successful trans-skull BBB disruption (BBBD) using a single element FUS transducer was achieved in experimental animals such as rabbits[21] and mice[22–25] by administration of microbubbles-enhanced pulsed FUS of 0.7 and 1.5 MHz, respectively. Single-element FUS transducers driven at a lower frequency of about 0.5 MHz were proven efficient for BBBD in larger animals, and particularly non-human primates.[26–31] Even lower frequencies of 0.4 and 0.25 MHz were chosen for similar applications in swine[32] and sheep,[33] respectively.

Simplified techniques for compensating for skull-induced energy losses were used in the effort to enable efficient trans-skull delivery of ultrasonic energy by single element transducers. As an example, a setup incorporating a single element 0.5 MHz spherical transducer for FUS-mediated BBBD was proposed by Marquet et al.[29] The proposed system is intended for use under stereotactic targeting and real-time monitoring by passive cavitation spectral analysis so as to enable MRI independent treatment sessions. In the framework of the system's evaluation, authors attempted BBBD of deep subcortical structures in macaque monkeys. The amplitude of ultrasonic emission was enhanced to compensate for the scalp and brain-induced attenuation losses as estimated by pressure measurements in vitro, thus leading to successful BBBD.

Pouliopoulos et al.[34] proposed a neuronavigation-guided system incorporating a single-element FUS transducer of 0.25 MHz nominal frequency, as well as a simulation framework for predicting the beam shift. The focusing properties of the transducer were assessed using a capsule hydrophone. The insertion of a human skull fragment in the

beam path resulted in a pressure attenuation of about 45% compared to that measured in free field for a normal incidence angle, whereas a focal shift of 0.5 (± 0.4) and 2.1 (± 1.1) mm was observed along the lateral and axial dimensions, respectively.[34] Notably, authors report a successful microbubbles-enhanced FUS-mediated BBB opening in the thalamus and dorsolateral prefrontal cortex of two non-human primates, which was evidenced by T1-weighted gadodiamide-enhanced MRI scans.[34] Notably, authors clarify that knowledge of the exact intracranial pressure with the proposed system is infeasible, and thus, the pressure field should be simulated utilizing computed tomography (CT) head scans of each subject individually.

More recently, the use of 3D printed holographic acoustic lenses customized to each skull geometry have been proposed as a more comprehensive low-cost way to compensate for skull losses, thereby enabling transcranial therapy with a single-element transducer.[35-36] Maimbourg et al.[35] demonstrated a 10-fold increase in the accumulated energy in the targeted area using the specific approach of aberration correction with lenses.

This article provides insights on the use of single element FUS transducers with no other means of defocusing corrections for transcranial FUS in humans by preclinical experimentation using a brain-tissue/skull phantom setup. The optimal phantom to mimic brain tissue was selected among twelve agar-based phantoms prepared in house with different concentrations of agar, silicon dioxide, and evaporated milk. The selection was based on the ultrasonic attenuation property of these phantoms as estimated by the transmission-through technique. Rapid prototyping was used for the construction of a skull model. The ultrasonic attenuation in three common thermoplastic materials was initially assessed, from which two were deemed suitable to replicate the attenuation observed in the skull bone adequately. Therefore, two

thermoplastic phantoms with the precise skull bone geometry of a male patient were 3D printed following segmentation on a CT head scan image.

The main part of the study involved HIFU sonications in the brain-tissue phantom through water (without any obstacle in the beam's path) and then, with each skull phantom intervening the beam under the same experimental conditions. Single element spherically focused transducers of 0.4 and 1.1 MHz central frequency were used. In each case, thermometry during heating was performed at the focal spot using thermocouples.

Materials and Methods:

No human participants or animals were included in the present study. Therefore, no informed consent or approval from an ethics committee was required.

Thermoplastic skull phantom

Development of block thermoplastic samples

Three (3) solid blocks (100% infill) were 3D printed using the Fused Deposition Modeling (FDM) technique with Acrylonitrile Butadiene Styrene (ABS, Stratasys) and VeroWhite Resin (RGD835, Stratasys) materials on a Stratasys printer (F270, Eden Prairie, Minnesota, USA), as well as with Polylactic Acid (PLA, 3DJ) thermoplastic on an Ultimaker printer (3 Extended, Utrecht, Netherlands). The samples were modeled into flat plates of 5-mm thickness and 63 x 63 mm area as shown in Figure 1.

Ultrasonic attenuation in thermoplastic samples

The ultrasonic attenuation in the thermoplastic samples was measured using a transmission-through immersion technique. Two identical transducers (custom-made,

central frequency of 2.1 MHz and diameter of 10 mm) and the test-thermoplastic were fixed into a specially designed plastic holder ensuring vertical incidence of the waves on the sample and minimizing energy losses due to refraction. The holder was submerged in degassed water and the first transducer was connected to the signal generator (33220A, Agilent, Santa Clara, CA 95051, United States), whereas the second transducer was connected to a digital oscilloscope (TDS 2012, Tektronix, Inc., 14150 SW Karl Braun Drive, United States) to display the received signal. The corresponding experimental setup is shown in Figure 2.

Pulsed ultrasound of 2.1 MHz frequency (20-cycle bursts with a period of 10 ms) was transmitted through the layered media. Initially, the peak-to-peak voltage was measured by the oscilloscope without any material between the transducers (reference signal). Then, the signal was recorded with the thermoplastic sample fixed in between the two transducers. The attenuation coefficient a of the sample was estimated by including the reference signal amplitude (A_w) and the one measured in the presence of the sample (A_s), together with the thickness of the sample x, and the transmission coefficient T of the water-sample interface in the following equation:[37]

$$a = a_w + \frac{20\,loge}{x} * ln\left(\frac{A_w}{A_s}T\right) \quad (1)$$

in which α_w represents the attenuation coefficient of water. The transmission coefficient was estimated by the speed of sound in the samples using the widely known pulse-echo technique as previously described by Selfridge et al.[38] All the measurements were conducted at room temperature (≅ 22 °C).

Development of phantoms with skull geometry

The skull bone of an anonymized male patient was isolated following segmentation on CT head scan images. Figure 3a shows the stereolithography (STL) format of the whole human skull. For the purpose of this study, a circle-shaped part was isolated from the temporal region of the human skull model, and then imported in each printer's software in STL format for further processing. Samples were 3D printed in solid mode having a diameter of approximately 60 mm and a thickness varying from 2.55 to 10.75 mm. The sample made with ABS (Stratasys) material is shown in Figure 3b.

Brain-tissue phantoms

Preparation of agar-based phantoms

Phantoms were prepared according to the procedure previously described by Drakos et al.[39] using agar (Merck KGaA, EMD Millipore Corporation, Darmstadt, Germany) as the gelling agent while silicon dioxide (Sigma-Aldrich, St. Louis, Missouri, United States) and evaporated milk (Nounou, Friesland Campina, Marousi, Greece) were included as modifiers of ultrasonic scattering and absorption, respectively.[40] Agar-only samples were prepared with different agar concentration of 2 %, 4 %, 6 % and 8 % weight per volume (w/v). Silica-doped phantoms were prepared using a silicon dioxide powder concentration of 2 %, 4 %, 6 %, 8 % and 10 % w/v for a constant agar concentration of 6 % w/v. The effect of evaporated milk concentration was assessed by including different volume per volume (v/v) concentrations of 10 %, 20 % and 30 % (replacing a percentage of the water component) at solutions with fixed concentrations of 6 % w/v agar and 4 % w/v silicon dioxide. For each recipe, the solution was poured in two molds of different thickness (20 and 40 mm) and left to solidify to form the final phantoms, as shown in the photo of Figure 4.

Ultrasonic attenuation in agar-based gels

The ultrasonic attenuation coefficient of the developed agar-based phantoms was estimated (at 22 °C) using the previously presented experimental set-up (Figure 2), but a quite different procedure known as the variable thickness method[41] to assess which one matches better the acoustic characteristics of brain tissue. The specific method involves comparison of ultrasonic signals acquired through samples of different thickness for estimating the attenuation coefficient (in units of dB/cm) through the following formula:[41]

$$a = \frac{20}{X_2 - X_1} * log\left(\frac{A_{x2}}{A_{x1}}\right) \quad (2)$$

where A_{x1} and A_{x2} symbolize the peak-to-peak voltages in the presence of the thinner (X_1 = 20 mm) and thicker (X_2 = 40 mm) samples (Figure 4), respectively.

Thermometry during HIFU in brain-tissue/skull phantom

The property of the skull phantoms to obstruct the propagation of acoustic waves generated by a single element transducer was evaluated by sonicating the agar-based phantom that was deemed suitable to mimic brain tissue (6 % w/v agar and 4% w/v silicon dioxide). For proper HIFU exposures, a special holder was 3D printed to accommodate the focused transducer and the phantom in a water tank, thus ensuring a normal incidence angle. Specifically, the transducer was fixed at the bottom part facing towards the phantom, as shown in Figure 5. The holder was geometrically designed to allow horizontal insertion of a thermocouple in the phantom every 5 mm. Therefore, the focal spot was easily located enabling recording of the temperature changes using a thermometer (Omega Thermometer, HH806AU, Omega Engineering, USA). As illustrated in Figure 5, the holder also included a special structure underneath the phantom's location to accommodate the skull sample. Degassed water was poured

inside the tank until it reached the top level of the phantom serving as the coupling medium.

The transducer was connected to an amplifier (AG1012, AG Series Amplifier, T&G Power Conversion, Inc.) with a build-in signal generator. Sonications were performed with two different single element spherically focused transducers (Sonic concepts, Washington, USA). The first one had a central frequency of 1.1 MHz, radius of curvature of 100 mm, and diameter of 40 mm, whereas the second one had a central frequency of 0.4 MHz, radius of curvature of 70 mm, and diameter of 40 mm. The acoustic efficacy of both transducers was approximately 100 %. The distance between the bottom of the phantom and each transducer was properly adjusted so that the focal depth is 2.5 cm for both. Temperature measurements were acquired using a thermometer (HH806AU, Omega Engineering, USA) with a sampling rate of 1s. Firstly, the temperature evolution during sonication was recorded through water path (without any plastic phantom), and then, in the presence of each skull phantom sequentially. For the sake of comparison, the experiment was also conducted with a 3-mm ABS flat plate inserted in the pathway of the beam.

Results:

Ultrasonic attenuation in thermoplastic samples

The attenuation of ultrasonic waves in the 3D printed thermoplastic samples (5-mm thick solid plates) was estimated using a common transmission-through technique and pulsed ultrasound of 2.1 MHz frequency. The mean attenuation coefficient was estimated at 8.4 ± 0.2 dB/cm for the Resin (Stratasys), at 14.9 ± 0.6 dB/cm for the PLA (3DJ), and at 37.7 ± 1.8 dB/cm for the ABS (Stratasys). The estimated coefficient of the Resin material was considered small compared to the values reported literally for

253 the skull bone.[42-43,5] Therefore, the PLA and ABS thermoplastics were used for the
254 construction of phantoms with precise geometry of a human skull, thus more accurately
255 replicating the distortion and attenuation effects of the skull.

256 **Ultrasonic attenuation in agar-based gels**

257 Twelve (12) agar-based phantoms were developed with varying concentrations of
258 agar, silicon dioxide and evaporated milk. The results suggest that the attenuation of
259 ultrasonic waves is enhanced with increasing concentration of each inclusion (agar,
260 silicone dioxide, and evaporated milk). Figure 6 shows the trend for the gels containing
261 only agar. The corresponding results for the silica- and evaporated milk-doped
262 phantoms are shown in Figures 7 and 8, respectively.

263 The phantom containing 6 % w/v agar and 4 % w/v silicon dioxide was found to
264 possess an attenuation coefficient (0.75 ± 0.06 dB/cm-MHz) in the range of 0.65 - 0.95
265 dB/cm-MHz reported literally for brain tissues[44] and deemed suitable to mimic brain
266 tissue in subsequent experiments.

267 **Thermometry during HIFU in brain-tissue/skull phantom**

268 These experiments aimed to assess the feasibility of two single element transducers
269 of different frequency to heat up the soft-tissue phantom through the skull mimics by
270 performing high power sonications. The selected phantom containing 6% agar and 4%
271 silicon dioxide served as the brain tissue mimic.

272 The thermometry data obtained by thermocouple measurements are listed in Table 1,
273 including the transducer characteristics and the corresponding temperature changes
274 achieved at the focal depth of 2.5 cm in free field (through water), as well as in the
275 presence of each skull phantom. Figures 9 and 10 show the corresponding

temperature profiles (temperature change versus time) recorded in the phantom using the 0.40 MHz (diameter of 40 mm and radius of curvature of 70 mm) and 1.10 MHz (diameter of 50 mm and radius of curvature of 100 mm) transducers, respectively. During sonication, heat absorption was responsible for the temperature rise while conduction decreased the rate of temperature elevation, whereas post-sonication only conduction mechanism remained, thus resulting in temperature reduction. As expected, the temperature change at the focal point is significantly reduced when the ultrasonic waves are obstructed by the skull phantoms.

Discussion:

This study aimed to examine the performance of single element spherically focused transducers in terms of trans-skull heating of tissue. Phantoms constitute a cost-effective and ergonomic tool for evaluating the performance of ultrasonic equipment.[40] In this study, an agar based phantom was prepared to mimic brain tissue, whereas the skull was mimicked by a 3D printed thermoplastic skull model. The selection of agar as the gelling agent was based on that agar gels were proven very promising for use with the FUS technology, as well as on their cost-effectiveness and ease of preparation.[40]

The 3D printing technology is continuously gaining popularity as a cost-effective tool for rapid prototyping, offering the ability to design structures of complex geometry with high precision.[45,46] In the last decade, it has been increasingly employed for the construction of bone mimicking phantoms using thermoplastic materials,[45,47–49] including MRI compatible skull phantoms embedding tissue-mimicking gels or freshly excised tissue.[47,49] Skull phantoms were initially manufactured with a simplified geometry[47] and later with the precise geometry of a real human skull as extracted from

300 brain CT scans. [49] More recently, a 3D printed skull filled with a phantom mimicking
301 both the vessels and tissue in the cranium has been proposed.[50] These phantoms
302 were designed to match the ultrasonic properties of human skull. Accordingly, in this
303 study, two anthropomorphic skull models were 3D printed using two different
304 thermoplastic materials, which were selected based on transmission-through
305 ultrasonic attenuation measurements.

306 The longitudinal attenuation coefficient of three common 3D printing thermoplastics
307 was estimated using a transmission-through technique. The estimated attenuation
308 coefficient of the Resin sample (8.4 ± 0.2 dB/cm) was considered small compared to
309 the literature values for skull bone. Ammi et al.[43] report attenuation values in the
310 temporal bone of 13.4 – 22.14 dB/cm at 1 MHz and 34.2 – 48.5 dB/cm at 2 MHz for
311 skulls not presenting temporal bone window insufficiency. Therefore, the PLA and ABS
312 samples with mean attenuation coefficients of 14.9 (± 0.6) and 37.7 (± 1.8) dB/cm
313 were deemed more suitable to replicate the insertion energy loss in human skull bone
314 and used for phantom development. Note that the high ultrasonic attenuation reported
315 for the skull bone is related to the varying thickness, porosity of the cancellous bone
316 and other inhomogeneities, which serve as additional sources of attenuation not
317 existing in thermoplastic samples.

318 Phantoms were then prepared following accurate geometrical replication of a human
319 skull to account for the defocusing effects induced by the varying thickness of the skull.
320 The skull bone geometry of a male adult was obtained from CT head scans and a circle
321 shape part was isolated from the temporal region, which constitutes an optimal window
322 for transcranial delivery of ultrasonic energy.[43] Phantoms were 3D printed in solid
323 mode using the selected thermoplastic materials (ABS, Stratasys and PLA, 3DJ).

The approach utilized in this study suffers from the limitation that the candidate thermoplastic materials were only investigated in terms of ultrasonic attenuation. However, thermoplastics were previously proven capable of sufficiently matching the propagation velocity of ultrasonic waves in the human skull as well.[37,50] Of course, given that in the real scenario ultrasonic waves interact with the complex microstructure of the bone (i.e., multilayer structure including cancellous bone), the proposed phantom constitutes a much simplified model of the human skull. However, since it was 3D printed with the exact geometry of a human skull, beam aberration mechanisms due to the varying skull thickness can be considered consistent between the phantom and real human skull. Overall, the phantom was considered sufficiently realistic for the purpose of the current study.

Gel phantoms were prepared with varying concentrations of agar, silicone dioxide, and evaporated milk to achieve different levels of ultrasonic attenuation. The attenuation results estimated by the variable thickness methodology suggest that attenuation increases with increasing w/v concentration of agar from 2 to 8% (Figure 6) following a second order polynomial (R^2=0.99). The influence of the evaporated milk concentration on the resultant attenuation followed a linear pattern (R^2=0.99). Increasing silicon dioxide concentration also enhanced attenuation, though not in a specific trend (Figure 7). In line with our findings, a positive linear relation between attenuation and concentration of milk was previously reported in the literature.[49] Notably, the role of these inclusions was examined in previous studies, in which silica particles were found to enhance acoustic scattering,[51] whereas evaporated milk was proven a key absorber of ultrasonic energy.[40]

Phantoms doped with silicon dioxide at concentrations of 2, 4, and 6 % w/v (6 % w/v agar) were found to possess attenuation coefficient values that fall well in the range of

0.65 - 0.95 dB/cm-MHz reported literally for brain tissues.[44] However, solutions with silica concentrations of more than 4 % undergo rapid solidification and are more likely to contain inhomogeneities. Therefore, the phantoms doped with 2-4 % w/v silicon dioxide were deemed suitable to mimic brain tissue. Since almost equal attenuation coefficient was estimated for both recipes, the one with 4 % w/v silica was selected to be used in subsequent experiments. Moreover, agar/silica phantoms are more stable and durable than milk-doped phantoms.

The heating properties of two single element transducers through the developed skull phantoms were investigated by thermocouple measurements in the brain tissue phantom (6 % w/v agar and 4 % w/v silica). The phantoms were mounted on a specially designed set-up being immersed in degassed water for proper ultrasonic propagation. Thermal profiles at the focus (2.5 cm) were recorded during sonications at acoustic power of 30 W. Absorption was the responsible mechanism for temperature rise in the agar gel, whereas upon deactivation of the transducer conduction-induced heat loss occurred. It is interesting that in the presence of the skull phantoms the thermal profiles presented plateaus where the temperature remained constant for several seconds revealing that the rate of heat deposition was very slow.

Without any sample along the beam's path, the 1.1 MHz sonication caused bigger temperature change (24.7 ˚C) compared to the 0.4 MHz sonication (15.7 ˚C) despite the use of similar acoustic parameters (acoustical power 30 W for 30 s). This is attributed to the fact that the 0.4 MHz beam is wider, and thereby, the produced intensities are lower. In fact, the focusing capability is determined by the transducer characteristics; frequency (f), radius of curvature (R), and diameter (D). Alternatively, when the focal depth and diameter are combined into the f-number (=R/D), the focus effect is determined by the f-number and frequency. For single element spherically

focused transducers the focal beam diameter (cross section) equals to $\lambda * \text{f-number}$ (where λ is the wavelength), thus being proportional to the f-number and inversely proportional to frequency. For the tested 1.1 and 0.4 MHz transducers, the beam radius at the focal depth equals to about 0.17 cm and 0.33 cm, respectively. Accordingly, the applied acoustic power of 30 W corresponds to focal intensities of 329 W/cm^2 and 89 W/cm^2 for the 1.1 and 0.4 MHz transducers. Therefore, without the skull mimic, the 1.1 MHz transducer results in higher temperature increase at the focus.

Nevertheless, in the presence of the skull phantoms a larger temperature change was recorded using the 0.4 MHz focused transducer. It seems that the phenomenon of scattering is the major factor responsible for this observation. Even though the 0.4 MHz transducer produces a wider beam, it seems that a larger amount of ultrasonic energy propagates through the thermoplastic samples due to the decreased scattering occurring at lower frequencies. Overall, the 0.4 MHz transducer showed better performance in trans-skull transmission. Notably, the use of such low frequencies is widely reported in studies involving non-human primates and large animals[26–33] and is driven by the highly aberrating nature of the skull bone. It should be though noted that these studies exploit the mechanical rather than the thermal effects of FUS.

The propagation of ultrasonic waves by single element emissions was blocked to a great degree by the skull phantoms, leading to minimal temperature increase at the focal point. In fact, the focal temperature change in the presence of the skull phantoms was reduced to less than 20 % of that recorded in free filed. This is attributed to the high ultrasonic attenuation occurring in the phantoms, but also to the defocusing effects of the varying thickness that were proven to cause spreading of the beam and focal shifting.[34] Notably, the strong defocusing effects of an ABS skull model were previously demonstrated using MR thermometry in a gel phantom[49] and were

associated with a great temperature reduction at the focal region.[49] This is where the phased array approach takes effect.

The specific mechanisms of energy loss through the skull phantoms such as the aforementioned beam defocusing were not explored quantitatively in the current study and may be addressed in a future study. Qualitative assessment was though performed by comparing the temperature evolution during sonication at 1.1 MHz through the ABS skull phantom with that recorded for a flat sample using similar acoustic parameters. With the skull phantom intervening the beam path, a minimal temperature change of 0.4 ˚C was achieved. The flat sample resulted in bigger temperature rise of 2.2 ˚C, confirming that the thickness variability of the skull phantom induced greater energy losses.

Single element transducers were proven efficient for transcranial applications in small experimental animals such as mice[22–25] because of their thin skull bone. Furthermore, many studies report successful use of this technology for BBB disruption in non-human primates,[26–31] whose skull resembles better the human skull. It should be though noted that these applications exploit the mechanical - cavitational effects of FUS rather than the thermal effects. Even in that case, there are many safety concerns, and thus, precise refocusing techniques are needed to compensate for energy losses and focal shifts, thus achieving accurate targeting and sufficient deposition of energy without threatening sensitive brain structures.

Overall, the herein findings confirm the inability of a single element transducer to efficiently steer the beam through the human skull to impart thermal effects to tissue unless a comprehensive correction technique is applied. The phased array technology is still considered the only tool offering optimal deposition of ultrasonic energy in the brain while maintaining the safety levels required in the clinical setting. Recently, the

use of 3D printed lenses to compensate beam aberrations while using single element transducers has been proposed;[35-36] however, further investigation is required to verify these findings and prove the feasibility of this approach. The proposed brain tissue-skull phantom could constitute a useful cost-effective tool for preclinical studies in the field of transcranial FUS.

References:

1. Izadifar Z, Izadifar Z, Chapman D, Babyn P. An Introduction to High Intensity Focused Ultrasound: Systematic Review on Principles, Devices, and Clinical Applications. *J Clin Med*. 2020;9(2):460. doi:10.3390/jcm9020460
2. Duc NM, Keserci B. Emerging clinical applications of high-intensity focused ultrasound. *Diagnostic Interv Radiol*. 2019;25(5):398-409. doi:10.5152/dir.2019.18556
3. Fry WJ, Mosberg Jr WH, Barnard JW, Fry FJ. Production of Focal Destructive Lesions in the Central Nervous System With Ultrasound. *J Neurosurg*. 1954;11(5):471-478.
4. Barnard JW, Fry WJ, Fry FJ, Krumins RF. Effects of high intensity ultrasound on the central nervous system of the cat. *J Comp Neurol*. 1955;103(3):459-484.
5. Fry FJ, Barger JE. Acoustical properties of the human skull. *J Acoust Soc Am*. 1978;63(5):1576-1590. doi:10.1121/1.381852
6. Guthkelch AN, Carter LP, Cassady JR, et al. Treatment of malignant brain tumors with focused ultrasound hyperthermia and radiation: results of a phase I trial. *J Neurooncol*. 1991;10:271-284.
7. Tanter M, Thomas J-L, Fink M. Focusing and steering through absorbing and aberrating layers: Application to ultrasonic propagation through the skull. *J Acoust Soc Am*. 1998;103(5). doi:10.1121/1.422759
8. Hynynen K, Jolesz FA. Demonstration of Potential Noninvasive Ultrasound Brain Therapy Through an Intact Skull. *Ultrasound Med Biol*. 1998;24(2):275-283. doi:10.1016/S0301-5629(97)00269-X
9. Sun J, Hynynen K. Focusing of therapeutic ultrasound through a human skull: a numerical study. *J Acoust Soc Am*. 1998;104:1705-1715. doi:10.1121/1.424383

10. Aubry J-F, Tanter M, Pernot M, Thomas J-L, Fink M. Experimental demonstration of noninvasive transskull adaptive focusing based on prior computed tomography scans. *J Acoust Soc Am*. 2003;113(1):84-93. doi:10.1121/1.1529663

11. Rieke V, Pauly KB. MR Thermometry. *J Magn Reson Imaging*. 2008;27(2):376-390. doi:10.1002/jmri.21265.MR

12. Hernando CG, Esteban L, Cañas T, Van Den Brule E, Pastrana M. The role of magnetic resonance imaging in oncology. *Clin Transl Oncol*. 2010;12(9):606-613. doi:10.1007/s12094-010-0565-x

13. Health Quality Ontario. Magnetic resonance-guided focused ultrasound neurosurgery for essential tremor: A health technology assessment. *Ont Health Technol Assess Ser*. 2018;18(4):1-141.

14. Foffani G, Trigo-damas I, Pineda-pardo JA, et al. Focused Ultrasound in Parkinson's Disease: A Twofold Path Toward Disease Modification. *Mov Disord*. 2019;34(9):1262-1273. doi:10.1002/mds.27805

15. Chang KW, Jung HH, Chang JW. Magnetic Resonance-Guided Focused Ultrasound Surgery for Obsessive-Compulsive Disorders: Potential for use as a Novel Ablative Surgical Technique. *Front Psychiatry*. 2021;12:1-9. doi:10.3389/fpsyt.2021.640832

16. Abe K, Yamaguchi T, Hori H, et al. Magnetic resonance-guided focused ultrasound for mesial temporal lobe epilepsy: A case report. *BMC Neurol*. 2020;20(1):1-7. doi:10.1186/s12883-020-01744-x

17. Lee EJ, Fomenko A, Lozano AM. Magnetic resonance-guided focused ultrasound: Current status and future perspectives in thermal ablation and blood-brain barrier opening. *J Korean Neurosurg Soc*. 2019;62(1):10-26.

480 doi:10.3340/jkns.2018.0180
481 18. Idbaih A, Canney M, Belin L, et al. Safety and feasibility of repeated and transient
482 blood-brain barrier disruption by pulsed ultrasound in patients with recurrent
483 glioblastoma. *Clin Cancer Res*. 2019;25(13):3793-3801. doi:10.1158/1078-
484 0432.CCR-18-3643
485 19. Chen K-T, Lin Y-J, Chai W-Y, et al. Neuronavigation-guided focused ultrasound
486 (NaviFUS) for transcranial blood-brain barrier opening in recurrent glioblastoma
487 patients: clinical trial protocol. *Ann Transl Med*. 2020;8(11):673-673.
488 doi:10.21037/atm-20-344
489 20. Meng Y, Jones RM, Davidson B, et al. Technical Principles and Clinical Workflow
490 of Transcranial MR-Guided Focused Ultrasound. *Stereotact Funct Neurosurg*.
491 2021;99(4):329-342. doi:10.1159/000512111
492 21. Hynynen K, Mcdannold N, Sheikov NA, Jolesz FA, Vykhodtseva N. Local and
493 reversible blood – brain barrier disruption by noninvasive focused ultrasound at
494 frequencies suitable for trans-skull sonications. *Neuroimage*. 2005;24:12-20.
495 doi:10.1016/j.neuroimage.2004.06.046
496 22. Choi JJ, Pernot M, Small SA, Konofagou EE. Noninvasive, transcranial and
497 localized opening of the blood-brain barrier using focused ultrasound in mice.
498 *Ultrasound Med Biol*. 2007;33(1):95-104.
499 doi:10.1016/j.ultrasmedbio.2006.07.018
500 23. Choi JJ, Wang S, Tung Y-S, Morrison B, Konofagou EE. Molecules of various
501 pharmacologically-relevant sizes can cross the ultrasound-induced blood-brain
502 barrier opening in vivo. *Ultrasound Med Biol*. 2010;36(1):58-67.
503 doi:10.1016/j.ultrasmedbio.2009.08.006
504 24. Choi JJ, Selert K, Gao Z, Samiotaki G, Baseri B, Konofagou EE. Noninvasive

and Localized Blood—Brain Barrier Disruption using Focused Ultrasound can be Achieved at Short Pulse Lengths and Low Pulse Repetition Frequencies. *J Cereb Blood Flow Metab*. 2011;31(2):725-737. doi:10.1038/jcbfm.2010.155

25. Wang S, Samiotaki G, Olumolade O, Feshitan JA, Konofagou EE. Microbubble type and distribution dependence of focused ultrasound-induced blood-brain barrier opening. *Ultrasound Med Biol*. 2014;40(1):130-137. doi:10.1016/j.ultrasmedbio.2013.09.015

26. Wu SY, Tung YS, Marquet F, et al. Transcranial cavitation detection in primates during blood-brain barrier opening-a performance assessment study. *IEEE Trans Ultrason Ferroelectr Freq Control*. 2014;61(6):966-978. doi:10.1109/TUFFC.2014.2992

27. Samiotaki G, Karakatsani ME, Buch A, et al. Pharmacokinetic analysis and drug delivery efficiency of the focused ultrasound-induced blood-brain barrier opening in non-human primates. *Magn Reson Imaging*. 2017;37:273-281. doi:10.1016/j.mri.2016.11.023

28. Wu SY, Aurup C, Sanchez CS, et al. Efficient blood-brain barrier opening in primates with neuronavigation-guided ultrasound and real-time acoustic mapping. *Sci Rep*. 2018;8(1):1-11. doi:10.1038/s41598-018-25904-9

29. Marquet F, Teichert T, Wu SY, et al. Real-time, transcranial monitoring of safe blood-brain barrier opening in non-human primates. *PLoS One*. 2014;9(2):1-11. doi:10.1371/journal.pone.0084310

30. Marquet F, Tung Y, Teichert T, Ferrera VP, Konofagou EE. Noninvasive, Transient and Selective Blood-Brain Barrier Opening in Non-Human Primates In Vivo. *Plus One.* 2011;6(7):1-7. doi:10.1371/journal.pone.0022598

31. Karakatsani ME, Samiotaki G, Downs ME, Ferrera VP, Konofagou EE. Targeting

Effects on the Volume of the Focused Ultrasound Induced Blood-Brain Barrier Opening in Non-Human Primates in vivo. *IEEE Trans Ultrason Ferroelectr Freq Control*. 2017;64(5):798–810. doi:10.1109/TUFFC

32. Wei K-C, Tsai H-C, Lu Y-J, et al. Neuronavigation-guided focused ultrasound-induced blood-brain barrier opening: a preliminary study in swine. *AJNR Am J Neuroradiol*. 2013;34(1):115-120. doi:10.3174/ajnr.A3150

33. Yoon K, Lee W, Chen E, et al. Localized blood-brain barrier opening in ovine model using image-guided transcranial focused ultrasound. *Ultrasound Med Biol*. 2019;45(9):2391–2404. doi:10.1016/j.ultrasmedbio.2019.05.023

34. Pouliopoulos AN, Wu SY, Burgess MT, Karakatsani ME, Kamimura HAS, Konofagou EE. A Clinical System for Non-invasive Blood–Brain Barrier Opening Using a Neuronavigation-Guided Single-Element Focused Ultrasound Transducer. *Ultrasound Med Biol*. 2020;46(1):73-89. doi:10.1016/j.ultrasmedbio.2019.09.010

35. Maimbourg G, Houdouin A, Deffieux T, Tanter M. 3D-printed adaptive acoustic lens as a disruptive technology for transcranial ultrasound therapy using single-element transducers 3D-printed adaptive acoustic lens as a disruptive technology for transcranial ultrasound therapy using single-element transdu. *Phys Med Biol*. 2018;63:1-14.

36. Ferri M, Bravo JM, Redondo J, Sanchez-Perez JV. Enhanced Numerical Method for the Design of 3-D-Printed Holographic Acoustic Lenses for Aberration Correction of Single-Element Transcranial Focused Ultrasound. *Ultrasound Med Biol*. 2019;45(3):867-884.

37. Antoniou A, Evripidou N, Giannakou M, Constantinides G, Damianou C. Acoustical properties of 3D printed thermoplastics. *J Acoust Soc Am*.

2021;149(4):2854-2864. doi:10.1121/10.0004772

38. Selfridge AR. Approximate Material Properties in Isotropic Materials. *IEEE Trans Sonics Ultrason*. 1985;SU-32(3):381-383.

39. Drakos T, Giannakou M, Menikou G, Constantinides G, Damianou C. Characterization of a soft tissue-mimicking agar/wood powder material for MRgFUS applications. *Ultrasonics*. 2021;113: 10635. doi:10.1016/j.ultras.2021.106357

40. Antoniou A, Damianou C. MR relaxation properties of tissue-mimicking phantoms. *Ultrasonics*. 2022;119. doi:10.1016/j.ultras.2021.106600

41. Menikou G, Damianou C. Acoustic and thermal characterization of agar based phantoms used for evaluating focused ultrasound exposures. *J Ther Ultrasound*. 2017;5. doi:10.1186/s40349-017-0093-z

42. Pichardo S, Sin VW, Hynynen K. Multi-frequency characterization of the speed of sound and attenuation coefficient for longitudinal transmission of freshly excised human skulls. *Phys Med Biol*. 2011;56(1):219-250. doi:10.1088/0031-9155/56/1/014

43. Ammi AY, Douglas Mast T, Huang I-H, et al. Characterization of Ultrasound Propagation Through Ex-vivo Human Temporal Bone HHS Public Access Author manuscript. *Ultrasound Med Biol*. 2008;34(10):1578-1589. doi:10.1016/j.ultrasmedbio.2008.02.012.Characterization

44. Selbekk T, Jakola AS, Solheim O, et al. Ultrasound imaging in neurosurgery: Approaches to minimize surgically induced image artefacts for improved resection control. *Acta Neurochir (Wien)*. 2013;155(6):973-980. doi:10.1007/s00701-013-1647-7

45. Menikou G, Yiannakou M, Yiallouras C, Ioannides C, Damianou C. MRI-

compatible breast/rib phantom for evaluating ultrasonic thermal exposures. *Int J Med Robot Comput Assist Surg*. 2018;14(1):1-12. doi:10.1002/rcs.1849

46. Shen Z, Yao Y, Xie Y, Guo C, Shang X, Dong X. The process of 3D-printed skull models for the anatomy education. *Comput Assist Surg*. 2017;24(1):1-14. doi:10.1080/24699322.2018.1560101

47. Hadjisavvas V, Mylonas N, Ioannides K, Damianou C. An MR-compatible phantom for evaluating the propagation of high intensity focused ultrasound through the skull. *AIP Conf Proc*. 2012;1481:119-124. doi:10.1063/1.4757321

48. Menikou G, Yiannakou M, Yiallouras C, Ioannides C, Damianou C. MRI-compatible bone phantom for evaluating ultrasonic thermal exposures. *Ultrasonics*. 2016;71:12-19. doi:10.1016/j.ultras.2016.05.020

49. Menikou G, Dadakova T, Pavlina M, Bock M, Damianou C. MRI compatible head phantom for ultrasound surgery. *Ultrasonics*. 2015;57:144-152. doi:10.1016/j.ultras.2014.11.004

50. Bai C, Ji M, Bouakaz A, Zong Y, Wan M. Design and Characterization of an Acoustically and Structurally Matched 3-D-Printed Model for Transcranial Ultrasound Imaging. *IEEE Trans Ultrason Ferroelectr Freq Control*. 2018;65(5):741-748. doi:10.1109/TUFFC.2018.2811756

51. Partanen A, Mougenot C, Vaara T. Feasibility of agar-silica phantoms in quality assurance of MRgHIFU. *AIP Conf Proc*. 2009;1113:296-300. doi:10.1063/1.3131434

Tables

Table 1: List of transducer specifications, including operating frequency (f), diameter (D), and radius of curvature (R) and the corresponding temperature changes recorded using acoustical power of 30 W for 30 s at the focal depth of 2.5 cm with no plastic, as well as with the ABS and PLA phantoms intervening the beam path.

Transducer characteristics			***Thermometry results*** **ΔT (˚C)**			
f (MHz)	**D (mm)**	**R (mm)**	**No Skull**	**PLA skull α ≅ 15 dB/cm**	**ABS skull α ≅ 38 dB/cm**	**ABS flat sample (3 mm)**
0.4	40	70	15.7	1.9	2.7	-
1.1	40	100	24.7	0	0.4	2.2

Figure legends

Figure 1: Photo of the 3-D printed ABS flat plate with indicated dimensions.

Figure 2: Photo of the experimental setup used to estimate the ultrasonic attenuation by the transmission-through method with indicated components.

Figure 3: a) STL format of the whole skull model. **b)** 3D printed skull phantom.

Figure 4: Top view of the thinner and thicker agar-based phantoms.

Figure 5: Photo of the experimental setup used to estimate temperature changes in the phantom during heating, showing the designed holder and the location of the compartments.

Figure 6: The mean attenuation coefficient (at 1.1 MHz) plotted against the agar concentration. The data points were fitted by polynomial regression. The error bars correspond to the standard deviation.

Figure 7: The mean attenuation coefficient (at 1.1 MHz) plotted against the silicon dioxide concentration for a fixed amount of 6 % w/v agar. The data points were fitted by linear regression. The error bars correspond to the standard deviation.

Figure 8: The mean attenuation coefficient (at 1.1 MHz) plotted against the evaporated milk concentration for a fixed amount of 6 % w/v agar and 4 % w/v silicon dioxide. The data points were fitted by linear regression. The error bars correspond to the standard deviation.

Figure 9: Temperature change versus time recorded in agar-based phantom at focal depth of 2.5 cm during sonication at acoustic power of 30 W for 30 s using the 0.4 MHz

632 transducer (diameter = 40 mm and radius of curvature = 70 mm) with no skull, as well
633 as with the skull phantoms inserted in the beam path.

634 **Figure 10:** Temperature change versus time recorded in agar-based phantom at focal
635 depth of 2.5 cm during sonication at acoustical power of 30 W for 30 s using the 1.1
636 MHz transducer (diameter = 40 mm and radius of curvature = 100 mm) with no skull,
637 as well as with the skull phantoms inserted in the beam path.

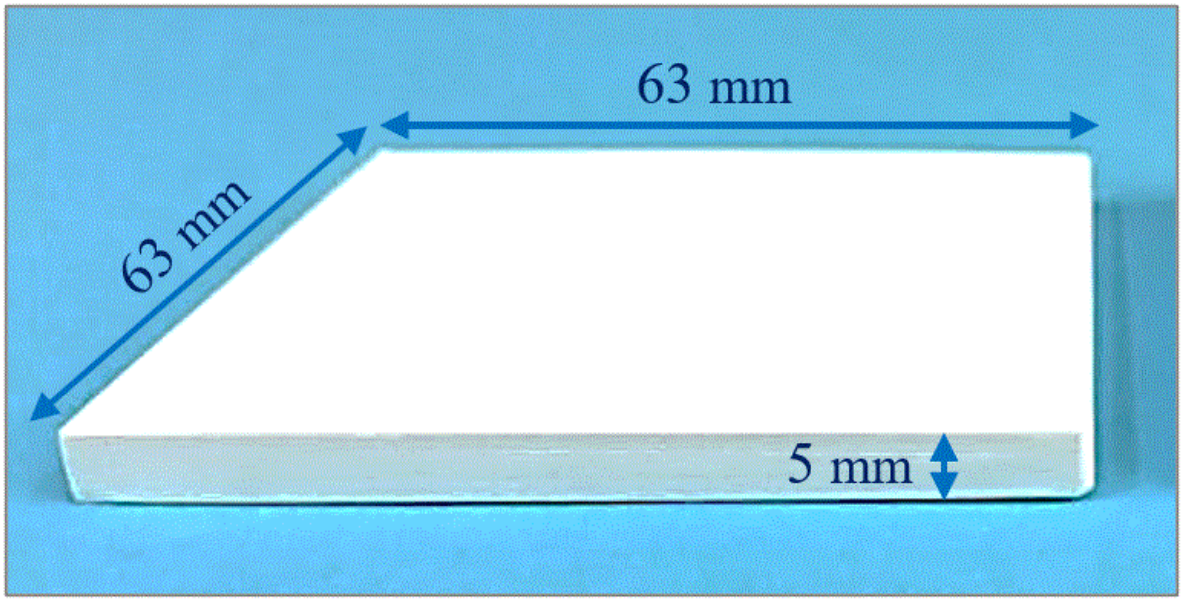

Figure 1

641 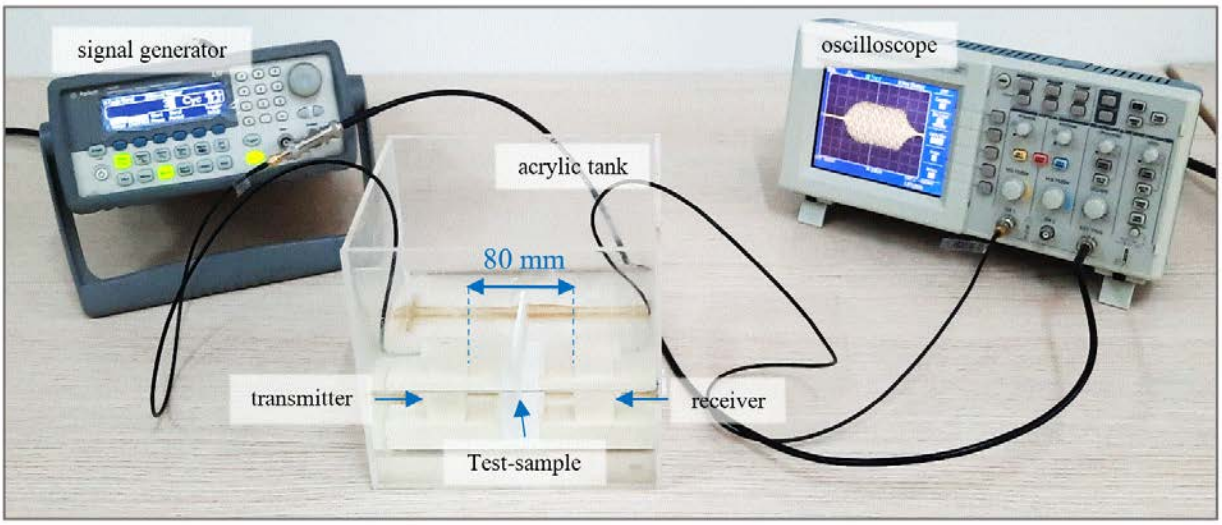

642 Figure 2

643

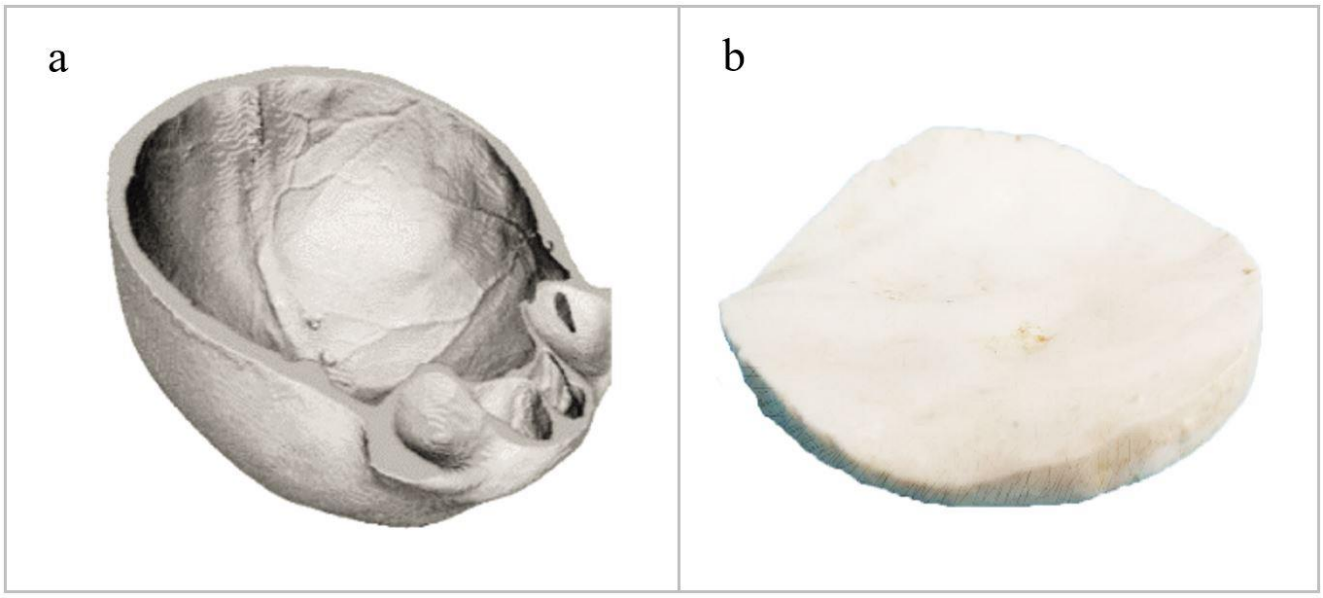

644

645 Figure 3

646

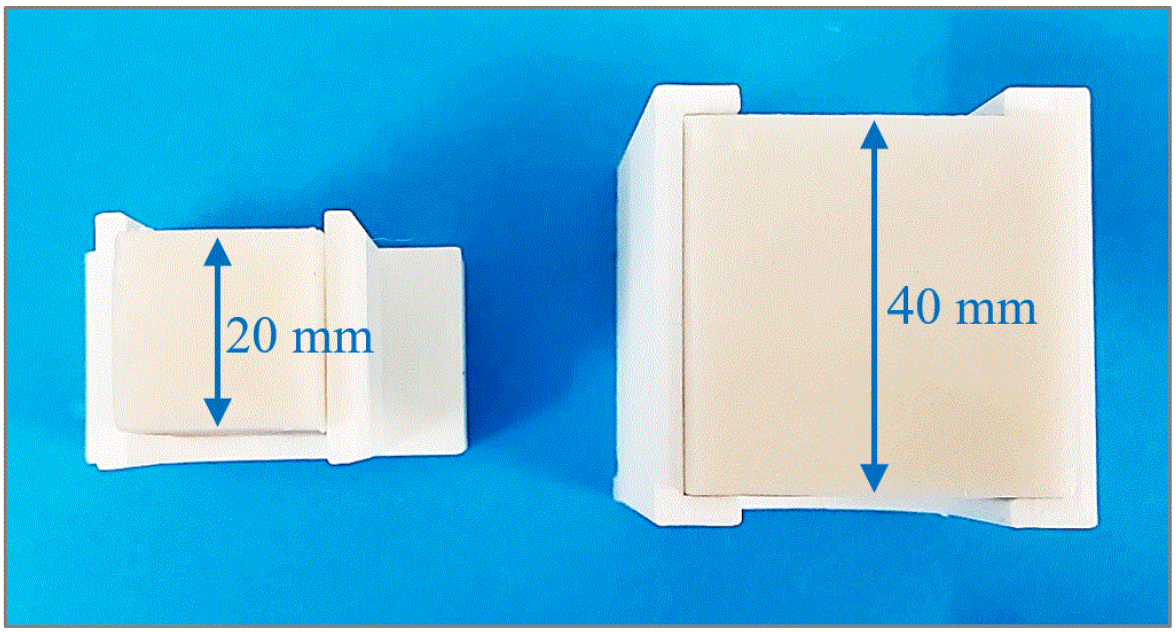

Figure 4

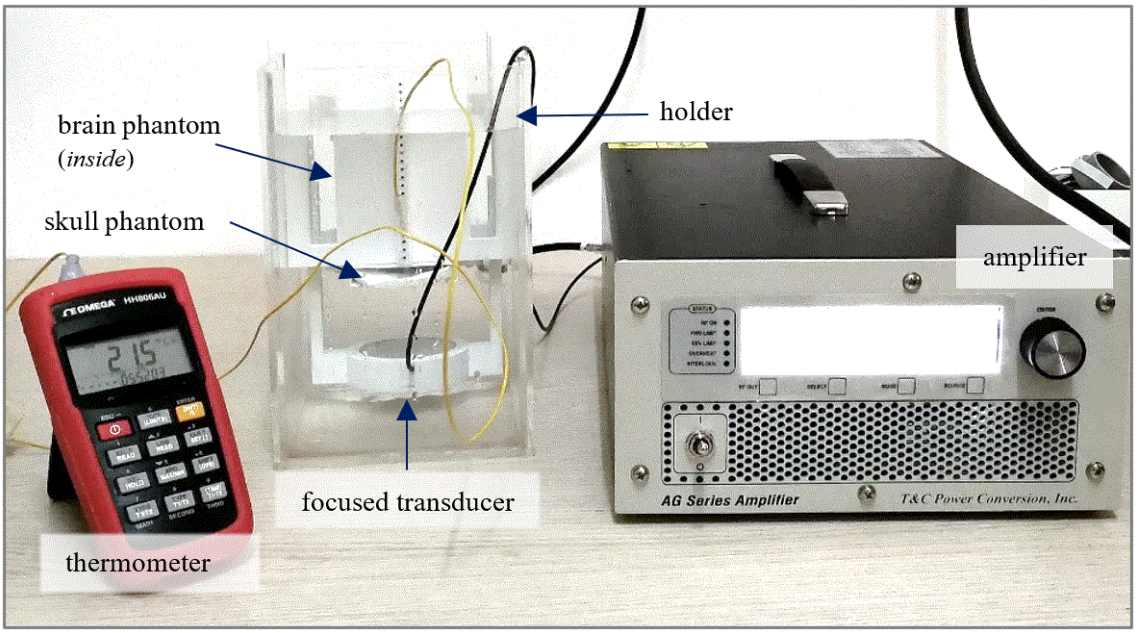

651

652 Figure 5

653

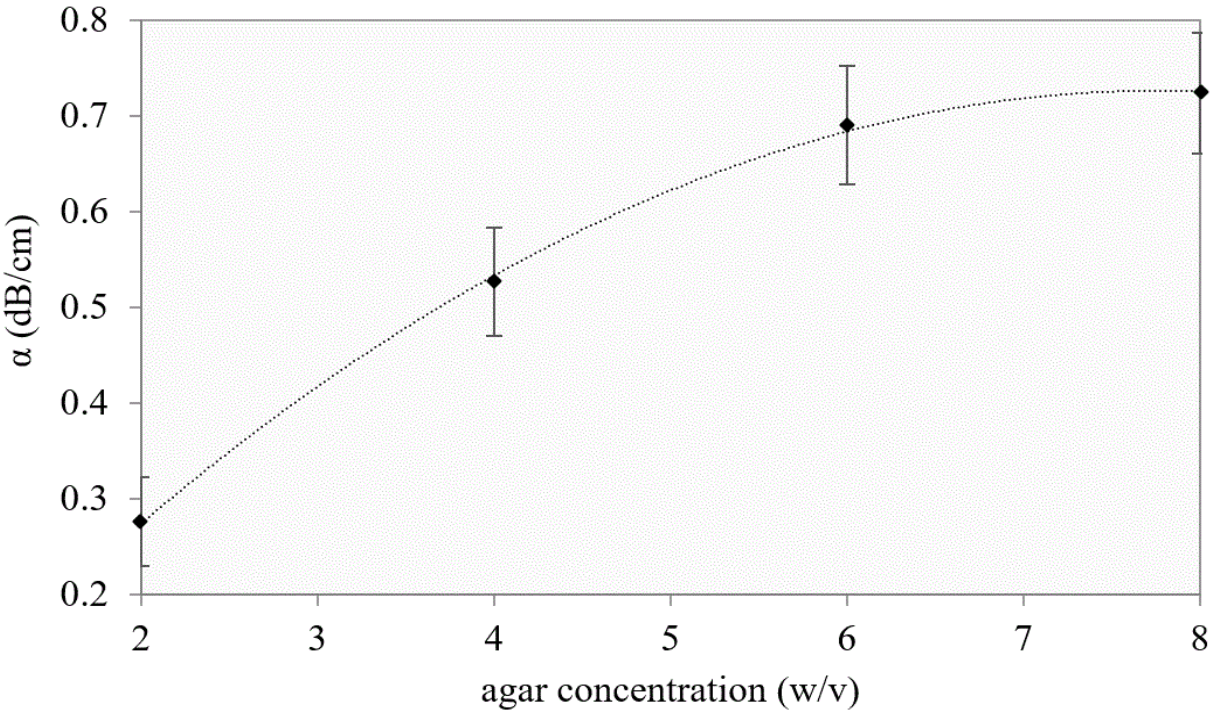

654

655 Figure 6

656

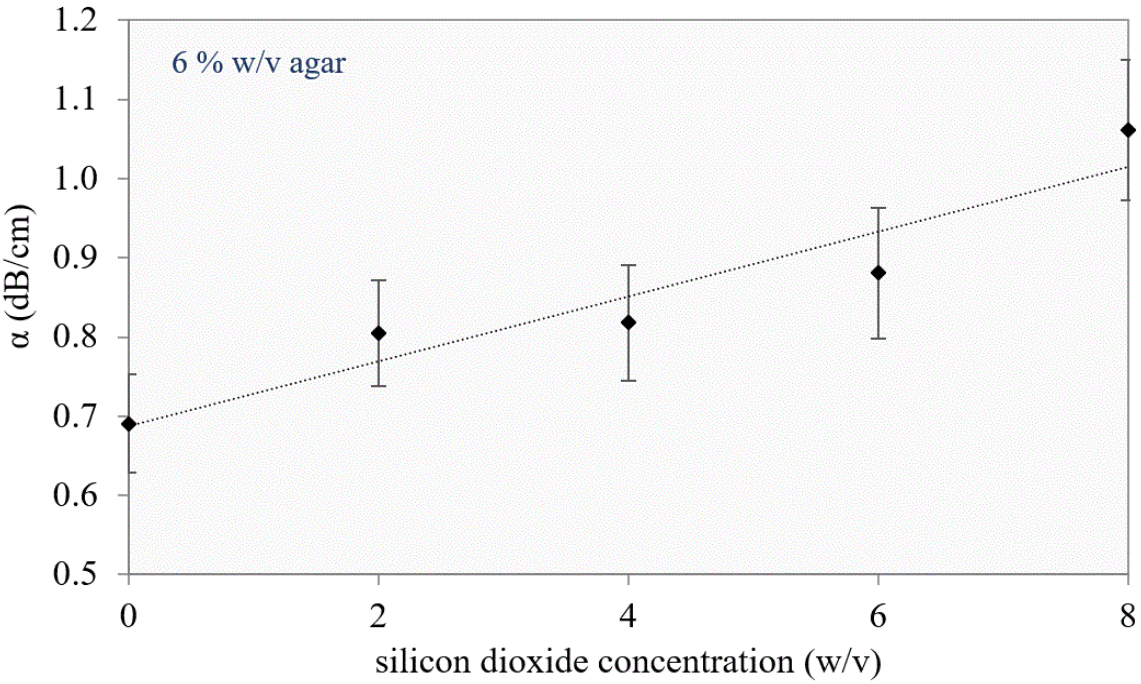

657

658 Figure 7

659

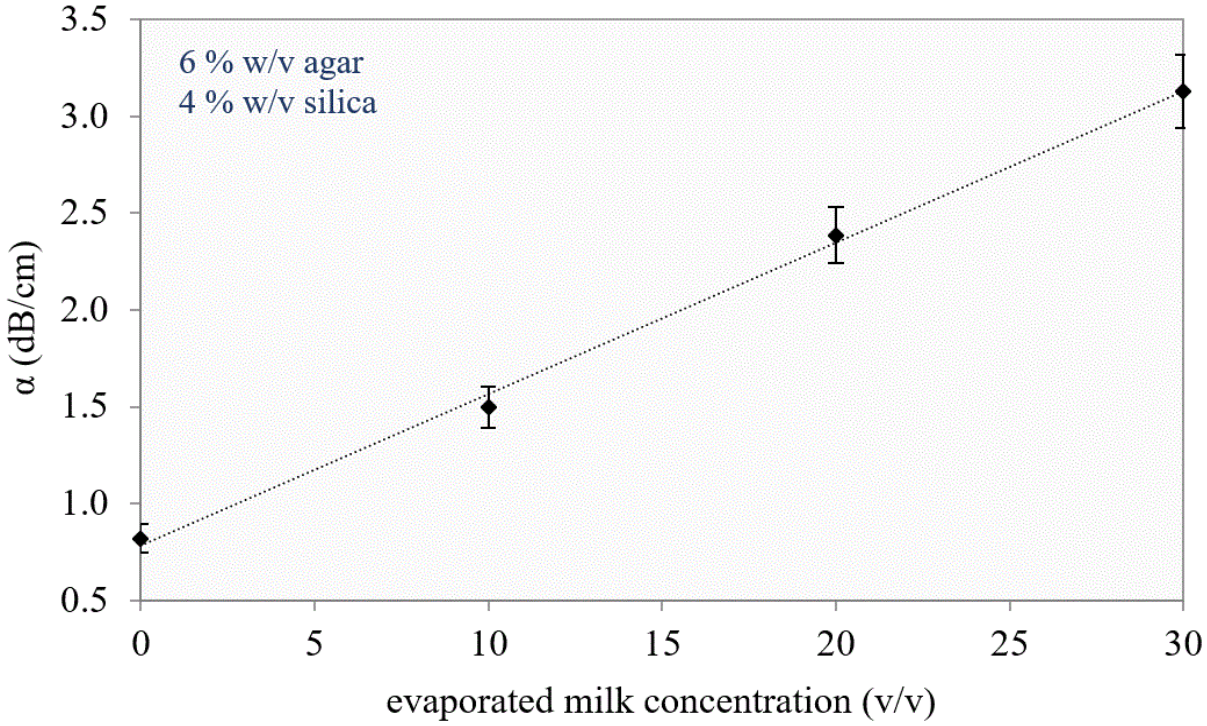

660

661 Figure 8

662

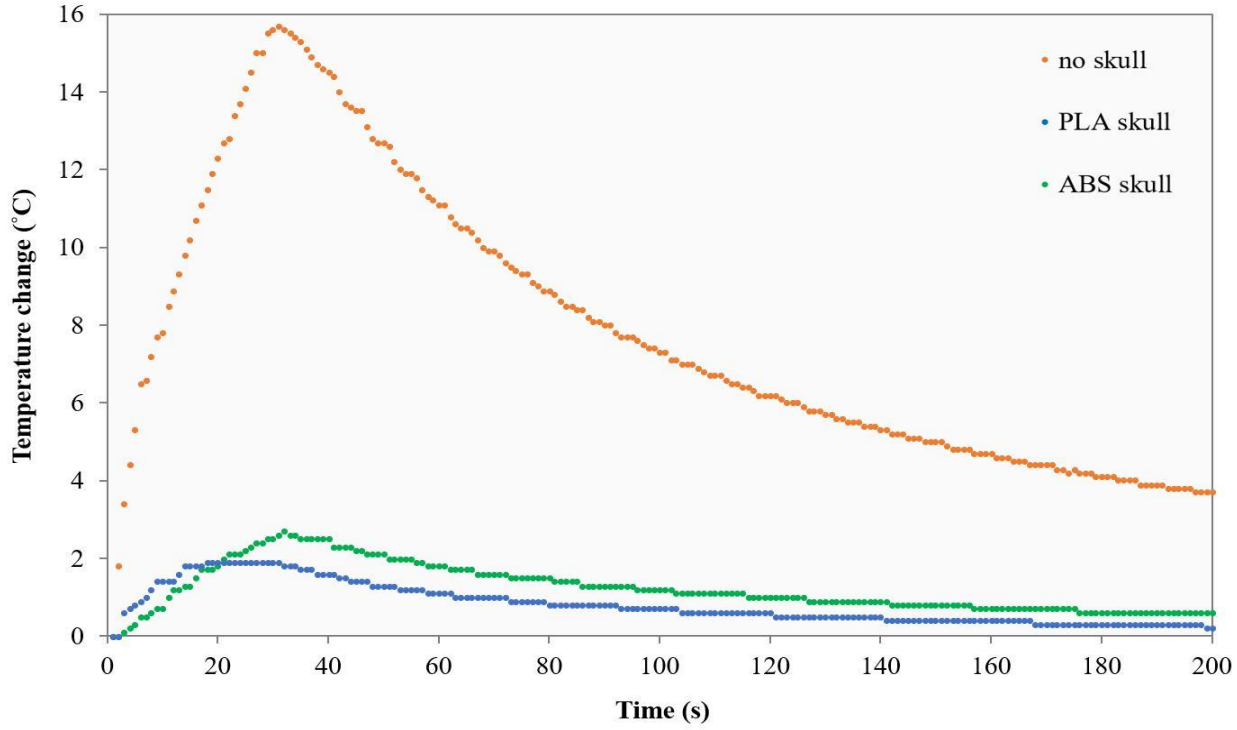

663

664 Figure 9

665

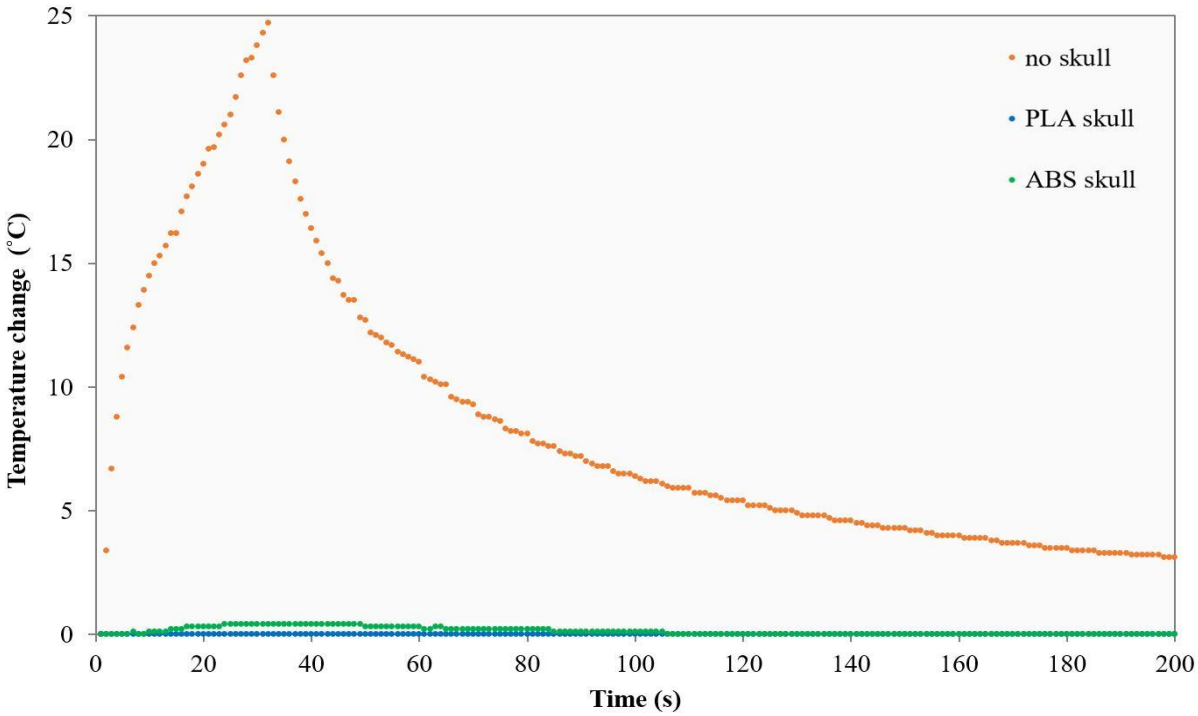
25
20
15
10
5
0
Temperature change (°C)
0
20
40
60
80
100
120
140
160
180
200
Time (s)
no skull
PLA skull
ABS skull

Figure 10

FUS-mediated Blood-brain barrier disruption for delivering anti-Aβ antibodies in 5XFAD Alzheimer's disease mice

ABSTRACT

Purpose: Amyloid-β (Aβ) peptides, the main component of amyloid plaques found in the Alzheimer's disease (AD) brain, are implicated in its pathogenesis, and are considered a key target in AD therapeutics. We herein propose a reliable strategy for non-invasively delivering a specific anti-Aβ antibody in a mouse model of AD by microbubbles-enhanced Focused Ultrasound (FUS)-mediated Blood-brain barrier disruption (BBBD), using a simple single stage MR-compatible positioning device.

Methods: The initial experimental work involved wild-type mice and was devoted to selecting the sonication protocol for efficient and safe BBBD. Pulsed FUS was applied using a single-element FUS transducer of 1 MHz (80 mm radius of curvature and 50 mm diameter). The success and extent of BBBD were assessed by Evans Blue extravasation and brain damage by hematoxylin and eosin staining. 5XFAD mice were divided into different subgroups; control (n=1), FUS+MBs alone (n=5), antibody alone (n=5), and FUS+antibody combined (n=10). The changes in antibody deposition among groups were determined by immunohistochemistry.

Results: It was confirmed that the antibody could not normally enter the brain parenchyma. A single treatment with MBs-enhanced pulsed FUS using the optimized protocol (1 MHz, 0.5 MPa *in-situ* pressure, 10 ms bursts, 1% duty factor, 100 s duration) transiently disrupted the BBB allowing for non-invasive antibody delivery to amyloid plaques within the sonicated brain regions. This was consistently reproduced in ten mice.

Conclusion: These preliminary findings should be confirmed by longer-term studies examining the antibody effects on plaque clearance and cognitive benefit to hold promise for developing disease-modifying anti-Aβ therapeutics for clinical use.

KEYWORDS: Alzheimer's disease; ultrasound; BBB; anti-Aβ; antibody; mice

1. INTRODUCTION

Blood-Brain-Barrier (BBB) protects the central nervous system (CNS) from drugs and toxins. It is composed of microvascular endothelial cells. Tight junctions (TJs) are formed between these cells, with several transporters regulating the influx and efflux of compounds, such as nutrients and small peptides [1]. Generally, paracellular permeability is limited to substances with a molecular weight up to 400-500 Da, thus prohibiting the delivery of most therapeutic agents into the brain [2]. The highly selective nature of BBB is the main obstacle against the application of potential disease-modifying therapies for diseases of the CNS, including neurodegenerative diseases such as the Alzheimer's disease (AD) [3,4]. Accordingly, drug delivery into the brain tissue has been a major challenge for researchers over a long period.

It is by now generally accepted that pulsed FUS in synergy with microbubbles (MBs) can cause temporal BBBD by causing alterations in the cell-to-cell interactions and endothelial cell cytoskeleton. In fact, MBs-enhanced FUS was shown to loosen the endothelial cell tight junctions (TJs) through a mechanism known as cavitation [7,8]. The junctions' disruption is mainly attributed to changes in the level of related trans- and peripheral membrane proteins [9]. In addition, FUS treatment was found to cause stimulation of transcytosis, sonoporation of the vascular endothelium, and increase in the paracellular diffusion due to the TJs disruption [9]. FUS can further cause disruption of drug efflux by temporally suppressing the expression of the permeability-glycoprotein (Pgp) [10].

BBBD by pulsed FUS in the presence of gaseous MBs has emerged as a feasible method of delivering large molecules normally hampered by the BBB to the brain. This strategy has been confirmed by numerous preclinical studies to enhance the penetration of therapeutic agents, such as therapeutic peptides, genes, and antibodies into the CNS of non-transgenic and transgenic mouse models of neurological diseases, with an increasing number of clinical trials exploring clinical utility [14–18]. Typically, initial evidence of the success and extend of

BBBD is obtained by contrast-enhanced MRI and the well-known Evans Blue (EB) dye method [15,16,18].

AD is the prevalent neurodegenerative disorder and cause of dementia and is characterized by the presence of intracellular neurofibrillary tangles and extracellular amyloid plaques owing to Amyloid β peptides (Aβ) aggregation [19,20]. Available treatments are not curative but may slow disease progression and alleviate symptoms. Given the urgent demand for disease-modifying therapies, the development of FUS therapeutics for AD receives remarkable research interest.

The ability of MBs-enhanced FUS without exogenous agents to reduce the Aβ pathology has been well demonstrated [21–23]. A single trans-skull MRgFUS treatment was shown to increase the levels of endogenous immunoglobulins (IgM and IgG) in the cortex of the TgCRND8 mouse model [21]. FUS-mediated endogenous antibody delivery and glia cells activation were considered as the mechanisms responsible for the observed plaque burden reduction [21]. Later, Shen et al. [22] reported that FUS in synergy with MBs applied twice a week for 6 weeks triggered behavioral changes and improved the spatial memory of triple transgenic AD mice. These changes were associated with reduced Aβ pathology and tau phosphorylation, as well as improved neuronal health of the sonicated hippocampus compared to the sham group.

The positive effects of FUS in the mitigation of AD pathological features can be enhanced by administrating exogenous therapeutic agents. According to a study by Hsu et al. [24], the effects of FUS on plaque reduction were enhanced using a specific inhibitor of the glycogen synthase kinase-3 (GSK-3); a key molecule in the onset of AD. Administration of this inhibitor in APPswe/PSEN1-dE9 transgenic mice prior to MBs-enhanced FUS reduced the Aβ plaque synthesis by suppressing the GSK-3 protein activity. Another study targeted an Aβ peptide species deposited in AD brain termed Pyroglutamate-3 Aβ (pGlu-3 Aβ) [25]. The FUS-

mediated administration of an anti-pGlu-3 Aβ vaccine was found to promote plaque clearance and partial protection from cognitive decline in APPswe/PS1ΔE9 mice [25]. Others attempted to support neuronal health as a measure for disease mitigation [26]. The repeated MRgFUS-mediated delivery of a pharmacological agent termed D3 (TrkA agonist) that promotes neuronal function was found to impart numerous therapeutic effects, including enhanced hippocampal neurogenesis and positive cognitive effects in TgCRND8 AD mice [26].

Several studies aimed to investigate the efficiency of FUS-mediated BBBD to facilitate the supply of large disease-specific antibodies in the brain and the resultant therapeutic effects. The feasibility of delivering an anti-Ab antibody called BAM-10 into the brain of the TgCRND8 mouse model using transcranial MRgFUS and reducing the plaque pathology has been demonstrated by Jordao et al. [27]. FUS-induced BBBD was also shown to facilitate the supply of an anti-pyroglutamate-3 Aβ monoclonal antibody (mAb) called 07/2a in the brain of aged APP/PS1dE9 transgenic mice [28]. Sun et al. [29] further demonstrated that three successive weekly treatments with the 07/2a mAb combined with FUS resulted in a faster improvement of spatial learning and memory of a higher percentage of aged APP/PS1dE9 mice compared to the mice group receiving only antibody.

Another anti-Aβ antibody tested for its efficacy to improve cognition in AD mice is the Aducanumab. Leinenga et al. [31] compared the effects of this antibody when administered alone or in synergy with MBs-enhanced scanning ultrasound in APP23 AD mice. The combined approach resulted in a 5-fold increase in the antibody amount compared to the non-sonicated mice a few days post-treatment and significant improvement in spatial memory. Notably, Aducanumab is the first therapeutic agent to be tested in combination with FUS in AD patients in a phase I ongoing clinical trial [32].

The Aβ (1-40) antibody targets the amyloid peptides Aβ(1-40) that represent the most abundant Aβ isoform in the AD brain [33]. The FUS-mediated delivery of the specific antibody was

previously tested in a very small mice population (n=3) [34]. A 3-fold increase in fluorescence intensity of the antibody staining was observed in the brain regions treated with MBs-enhanced MRgFUS in comparison with the non-sonicated regions, with hematoxylin and eosin (H&E) staining providing evidence of hemorrhages in the sonicated brain tissue [34]. While this study provides promising results on FUS-mediated enhanced Aβ (1-40) antibody delivery, further experiments in a larger mouse population are needed to confirm these early findings and optimize the therapeutic protocol for safe and efficient Aβ (1-40) antibody delivery.

In this study, we aimed to evaluate whether the application of FUS in synergy with MBs using an in-house manufactured manual positioning device comprising a single element FUS transducer of 1 MHz can facilitate the penetration of the Aβ (1-40) antibody into the brain of 5XFAD transgenic mice. We initially attempted to define the sonication protocol for safe and efficient BBBD. The success and extent of BBBD was assessed by EB extravasation while brain damage was assessed by H&E staining. We then examined the capability of the Aβ (1-40) antibody to consistently enter the brain parenchyma when administered alone and prior to MBs-enhanced FUS using the optimized protocol in a large 5XFAD mice group.

2. MATERIALS AND METHODS

All mice experiments were carried out at the premises of the Cyprus Institute of Neurology and Genetics under national guidelines and protocols authorized by the Veterinary Services of Cyprus under the study license CY/EXP/PR.L05/2021.

2.1 FUS system

FUS was delivered using a manual positioning system [35] comprising a single element, spherically focused, ultrasound transducer (Piezo Hannas, Wuhan, Hubei, China, 1 MHz central frequency, 80 mm radius of curvature, 50 mm diameter, and 32.5 % acoustic efficiency) tuned to an RF amplifier (AG 1016, AG series, T&G Power conversion Inc., Rochester, NY).

This system was specially designed to facilitate transcranial FUS studies in rodents. The transducer is hosted in a conical water tank whose bottom opening is sealed with a silicone membrane. The tank can be moved vertically via a manual positioning mechanism coupled to the mouse platform to attach to the mouse head via a top to bottom approach. A laser pointer accessory was implemented into the system to facilitate consistent targeting among experiments. The positioning device and animal placement on the dedicated platform can be seen in Fig. 1.

2.2 Protocol optimization for efficient and safe Blood-brain barrier disruption

Thirty-two (32) WT B6/SJL mice were used for protocol calibration/optimization. Intraperitoneal injection of Avertin (Sigma Aldrich, St. Louis, Missouri, United States) was used to cause rapid and deep anesthesia in mice and ensure no suffering. The dose of Avertin was weight-dependent for each animal (20 μL/g). The hair was removed from the mouse head using a commercial hair removal cream (Veet Hair Removal cream). Retro-orbital injection was then used to deliver a mixture of 5 μL of SonoVue® MBs (Bracco Imaging, Turin, Italy, 2 x 10^8 microbubbles/ mL suspension) along with 5 mL/kg of 3 % w/v EB solution (Sigma, St. Louis, MO, USA). Anesthetized animals were positioned in prone position on the platform as shown in Fig. 1. The tank was filled with degassed, deionized water and US coupling gel (Quick-Eco Gel, AB Medica group S.A., Barcelona, Spain) was applied on the mouse head to achieve efficient acoustic coupling. The position of the mouse was adjusted so that the FUS beam was targeted on the left hemisphere centrally with the assistance of the laser system. All mice received a single sonication within 3-4 minutes following the injection of MBs and EB using 1 MHz pulsed FUS of 10 ms bursts at a duty factor (DF) of 1% for a total duration of 100 s.

For protocol calibration purposes, electric power values of 20 to 70 W were tested (10 W step; 6 groups of 5 mice each). The relevant acoustic power ranged from 6.5 to 22.8 W, corresponding to *in situ* focal acoustic pressure in the range of 0.3 to 0.6 MPa. The output acoustic power was estimated based on the acoustic efficiency of the transducer of 32.5%. The respective focal pressures were initially determined in water using a needle hydrophone (HNC, ONDA, Sunnyvale, CA, USA) placed at the focal distance of the transducer. *In-situ* pressures were then calculated accounting for the transmission loss through the mouse skull. The transmission coefficient of a skull sample was measured according to the well-established through-transmission immersion technique [36] at the operating frequency of the transducer of 1 MHz. One mouse received only EB and one neither EB nor FUS, thus serving as the control mice.

Mice were sacrificed by transcardial perfusion with saline followed by 4% paraformaldehyde (PFA) 40 minutes post-treatment. This time period is well within the 4-hour window that the BBB was found to maintain open after FUS. Therefore it was considered sufficient for successful entry of EB into the brain, but also to allow for acute FUS-induced physiological responses to be resolved [37]. The brain tissue was then collected and preserved in paraformaldehyde (4%) and then sucrose (20%) diluted in Phosphate Buffer (0.1%) according to our protocol. Brain sections were prepared for fluorescence imaging. Slides containing brain sections were visualized using a Nikon eclipse-Ni (Tokyo, Japan) fluorescence microscope to visualize EB extravasation and determine the BBB-opened region.

2.3 Trans-BBB Aβ (1-40) antibody delivery in a mouse model of AD

2.3.1 Animals

5XFAD transgenic mice recapitulating major pathological features of AD were utilized. 5XFAD mice were bred as single transgenics. Male 5XFAD mice were crossed with female

SJL/B6 F1 mice to give hemizygous or wild-type offspring's, which were used for the purpose of the study. The pathologic phenotype of this mouse model consists of gliosis, amyloid plaques, neurodegeneration, memory deficits (at 4-5 months), as well as intraneuronal Aβ and neuron loss. Beginning at 8 weeks of age, amyloid deposition and gliosis become increasingly widespread, especially in the deep cortical layers and subiculum.

2.3.2 Experimental design

5XFAD transgenic mice of 5-months of age (n=21) were used to test the feasibility and efficacy of FUS-mediated delivery of the Aβ (1-40) antibody (150 kDa, Anti-β-Amyloid Protein (1-40) antibody produced in rabbit whole antiserum, A8326, Sigma Aldrich, 3050 Spruce Street, Saint Louis, MO 63103, USA) into the brain. The ability of the antibody to pass through the BBB and bind to the Aβ plaques when administered alone and in combination with FUS was investigated using a constant antibody amount of 50 µL (2.85 mg), which is the half quantity of the previously tested antibody dose [34].

Twenty one (21) mice were divided into 4 sub-groups: A. Staining with the Aβ (1-16) and Aβ (1-40) antibodies without injected antibody or FUS+MBs to confirm the presence of amyloid plaques in the cortex (referred to as control, n=1), B. Saline (50 µL) administration followed by FUS+MB-induced BBB opening (referred to as saline; n=5), C. Aβ (1-40) antibody (50 µL) administration alone (referred to as antibody, n=5), and D. Aβ (1-40) antibody (50 µL) administration followed by FUS+MB-induced BBB opening (referred to as FUS+MBs plus Ab; n=10).

The anesthesia protocol and treatment timeline were similar to that used for the calibration study. The Aβ (1-40) antibody was delivered instead of the EB dye via retro-orbital injection along with the MBs. Based on the data gathered from the protocol optimization study, an acoustic power of 16 W (*in situ* focal acoustic pressure of 0.5 MPa) was considered optimum

and used in this experimental part while the rest sonication parameters remained the same. The treatment protocol is summarized in the diagram of Fig. 2. Note that following FUS, a time window of 4 hours was left before mice sacrifice.

2.3.3 Mouse sacrifice and tissue preparation

Transcardial perfusion was used to clear blood and preserve the brain for immunostaining analysis. Following perfusion, the mouse head was dissected, and the skull was carefully removed using scissors and forceps, exposing the brain. The brain was washed in Phosphate Buffer Saline (PBS) and then placed for 2 hours in 4% Paraformaldehyde (PFA) solution. Subsequently, it was again washed with PBS and placed into 20% sucrose solution (diluted in Phosphate Buffer 0.1M) overnight at 4 °C for cryoprotection prior to embedding and freezing. For tissue embedding, the cryomould containing the brain tissues, was filled with OCT, and placed into acetone-dry ice bath. Finally, the frozen OCT containing the brain tissue was removed from the cryomould and stored in a -80°C freezer.

2.3.4 Immunohistochemistry

Double immunostaining of coronal brain sections (16 brain sections / mouse) was performed to determine whether the injected Aβ (1-40) antibody passed the BBB and bound to Aβ plaques. Staining with the Aβ (1-16) antibody (6E10, green colour) was used to identify the amyloid plaques. The tissue was permeabilized by immersing the frozen sections in acetone for 10 minutes at -20°C. It was then washed three times with 1X PBS and blocking solution (5% Bovine Serum Albumin + 0.5% Triton X-100) was applied for 1 hour on the sections at room temperature in a humidified chamber. The blocking solution was then removed and the primary antibody; anti-β-amyloid primary monoclonal 6E10 (1 mg/mL) (diluted in blocking solution, 1:400) was applied to the tissue sections and incubated overnight at 4°C. The following day, the primary antibody was removed, and the tissue sections were washed three times with 1X

PBS. The secondary antibodies; Fluorescein (FITC) goat anti-mouse (1.5 mg/mL), 1:100 and Alexa Fluor® 594 goat anti-rabbit (2 mg/mL), 1:500 (diluted in blocking solution) were next applied for 1 hour at room temperature for the detection of the injected antibody in the examined brain tissue, followed by three washes with 1X PBS and incubation for 30 seconds with 4',6-diamidino-2-phenylindole (DAPI, Sigma-Aldrich) for nuclear staining. The tissues were washed two times for 5 minutes with 1X PBS, dried and mounted with mounting media in order to prepare them for microscopy.

2.3.5 H&E staining

We also checked the tissue integrity and the lack of hemorrhage with H&E staining for the tested acoustic pressures ranging from 0.3 to 0.6 MPa. Tissue sections in OCT were stained with Harris's haematoxylin (freshly filtered) for 3 minutes, and then washed with distilled water and stained with aqueous eosin for 6 minutes. Next, they were dehydrated in ascending concentrations of alcohol and cleared in xylene (70 %, 95 %, 100 % x 2 and xylene x 3). Finally, the tissue slides were mounted with Dibutylphthalate Polystyrene Xylene (DPX).

3 RESULTS

3.1 Protocol optimization for efficient and safe Blood-brain barrier disruption

According to fluorescence microscopy all tested power levels in the range of 6.5 to 22.8 W (0.3−0.6 MPa *in situ* pressure) combined with 5 μL of MBs (for the specific sonication parameters employed) caused BBBD since increased fluorescence intensity of EB was observed compared to the control mouse (receiving only EB). Indicative fluorescence images for the various acoustic powers tested are presented in Fig. 3, revealing the power effect on the extent of EB extravasation. Note that a gradual increase of fluorescence intensity (indicating increase in the extent of BBBD) occurred as the power in the tested range was increased.

The optimal power was selected as the one resulting in the highest EB leakage (ideally spread throughout the sonicated region) without causing any adverse effects on tissue and having consistent behavior among subjects. The power value of 16 W (0.5 MPa *in situ* pressure) showed consistent EB leakage in all examined brain regions and no evidence of damage and was thus selected for follow-up experiments in the AD mouse model. Fig. 4 shows representative fluorescence microscopy images for the selected power taken from to cortex region. Photos of the freshly perfused excised brain of a mouse treated with the selected protocol and a brain section after fixation in OCT can be seen in Figs. 4b and 4c, respectively. Note that the EB dye was diffused throughout the entire left hemisphere that was sonicated. Figs. 4d and 4e compare magnified fluorescence images of unstained brain sections at the level of the cortex between a non-sonicated mouse and a sonicated mouse (pulsed FUS with 10 ms burst length and 1 % DF at 16 W for 100 s duration & 5 μL MBs) both injected with equal amount of EB solution (5 mL/kg of 3 % w/v). Note that no leakage was observed in the brain of the control mouse (EB only), whereas FUS-induced BBBD resulted in high levels of EB dye covering the examined cortex area. Indicative histological slides from H&E examination for the selected acoustic power (16 W) from two different brain areas can be seen in Fig. 5. No difference between the FUS treated and control cases in terms of tissue integrity was observed and there was no evidence of hemorrhage in none of the tested brain regions.

3.2 Trans-BBB Aβ (1-40) antibody delivery in a mouse model of AD

Indicative results of immunohistochemistry analysis of brain tissue sections from 5XFAD mice are presented in Figs. 6 and 7. Co-localization of red (injected Aβ (1-40) antibody) and green (Aβ (1-16) antibody) fluorescence in multiple brain regions of the sonicated hemisphere confirmed successful BBBD, as well as entry and binding of the injected Aβ (1-40) antibody to Aβ plaques. Indicative fluorescence images of brain sections at the level of the cortex for the various mice groups are shown in Fig. 6. As expected, the 5XFAD mice that were injected

with saline following FUS+MBs (saline group) did not have any signs of the Aβ (1-40) antibody in their brain. Similarly, the antibody was not present in any of the brain sections of the mice injected only with the Aβ (1-40) antibody (antibody group), confirming the inability of the specific therapeutic agent to normally pass through the BBB. On the contrary, immunohistochemistry analysis of brain sections from the FUS+MBs plus Ab group showed entry of the Aβ (1-40) antibody in the brain parenchyma. Note that the control mouse was not injected with the antibody neither received FUS+MBs; it was just stained with the Aβ (1-16) and Aβ (1-40) antibodies to confirm the presence of amyloid plaques (green & red) in the cortex. These findings qualify the selected treatment protocol (50 μL antibody & 1 MHz pulsed FUS with 10 ms burst length and 1 % DF at 16 W for 100 s) as an efficient BBBD method for the delivery of the specific anti-Aβ antibody into the mouse brain. The repeatability of obtained results was investigated in ten mice, which all showed successful antibody entry and specific binding to plaques. Indicative brain sections from six mice are shown in Fig. 7 revealing co-localization of antibodies (white circles) in the cortex.

4 DISCUSSION

FUS in combination with MBs has been confirmed by numerous studies [15,38,39] as an effective method for overcoming the BBB to deliver exogenous therapeutic agents to the brain at present. AD is the most common cause of dementia [19] with Aβ immunotherapy belonging to the most promising therapeutics to alter its course [33]. Several antibodies such as Aducanumab and Lecanemab/BAN2401 were used for targeting Aβ at different epitopes (3-7 and 1-16, respectively) in order to promote amyloid plaque clearance [40]. However, drug efficacy is low as only 0.1% of antibodies can pass the BBB [41]. This study aimed to investigate whether FUS-mediated BBB opening with an optimized protocol can be used to safely and efficiently deliver a specific anti-Aβ antibody; Aβ (1-40) into the brain of 5XFAD AD mice using a custom-made FUS positioning device. The specific antibody is directed

against the amyloid peptides Aβ (1-40) that represent the most abundant Aβ isoform in the AD brain [33], thus promoting plaque clearance. Unfortunately, its entrance in the brain is prohibited by the BBB due to its large molecular weight (150 KDa).

To our knowledge, this is the second study to report the use of the anti-Aβ antibody Aβ (1-40). In fact, there is a previous study that examined the feasibility of delivering this antibody into 3 mice by FUS-mediated BBBD. Authors report a 3-fold increase in fluorescence intensity of the antibody staining in brain regions treated with MRgFUS (in comparison to non-sonicated regions), with the H&E staining revealing hemorrhage in the sonicated brain tissue [34]. We have verified these preliminary findings in a larger mice population (n=10) showing that FUS-mediated BBBD facilitates antibody penetration into the brain. In this study, non-sonicated mice showed zero fluorescence intensity indicating complete absence of the exogenous antibody in the examined brain tissue. It is worth mentioning that the absence of fluorescence intensity in the non-sonicated mice confirms that the anaesthetic (Avertin) used during the experimental procedure did not affect the BBB permeability, whereas other anaesthetics such as propofol affect BBB permeability [42]. Additionally, our current results go beyond previous findings further demonstrating that the use of an optimized protocol allows for efficient BBBD and delivery of the specific antibody without any tissue damage and probably the use of a smaller antibody dose (half compared to the dose used previously [34]). However, this requires further investigation.

The first experimental part was carried out in WT mice (n=32) and was devoted to selecting the acoustic power/pressure for optimized BBBD. Notably, at sufficiently high acoustic pressure, the administered MBs begin to oscillate stably causing transient increase of permeability in the targeted area while above a threshold of pressure inertial cavitation occurs where MBs collapse violently [11,12]. In the former case, the endothelial ligaments recover completely within a few hours post-sonication [13]. Inertial cavitation is responsible for the

majority of adverse effects observed with this strategy, such as micro-hemorrhages [12]. Therefore, the various acoustic pressure levels were tested both in terms of BBBD extent using the EB dye method and sonication-related tissue effects using H&E staining.

The EB dye technique allowed visual confirmation of BBBD with the naked eye directly after brain exposure and ease assessment of BBBD using a fluorescence microscope. A potential limitation of this methodology is that it does not provide any quantitative information on the magnitude of BBBD [43]. The FUS+MBs treated mice showed higher levels of EB dye in all examined brain areas, whereas for the control mouse (EB only) the dye remained in the extracellular matrix. The *in situ* peak pressure amplitude of 0.5 MPa (16 W acoustic power) applied at a frequency of 1 MHz in the presence of MBs (5 μL) was selected as offering safe and efficient BBBD and employed in follow-up studies involving the antibody. The results of H&E histology revealed no structural damage and no signs of hemorrhage in none of the sonicated hemispheres.

These results are consistent with what has been found in previous state-of-the-art studies. In fact, pressure levels of up to 0.5 MPa have been previously proposed by Hynynen et al. [13] as suitable for consistent and safe BBBD in rabbits, where the observed side effects were mostly limited to few tiny extravasations of red blood cells. Above that value and up to 1.4 MPa more severe effects such as hemorrhages and mild damage to the brain parenchyma were observed. Herein, none of the tested focal pressures ranging from 0.3 to 0.6 MPa (*in situ)* showed evidence of FUS-related effects on tissue integrity. The efficiency of the selected pressure level (0.5 MPa) to disrupt the BBB with negligible effects on brain tissue has been confirmed by other studies as well, with McDannold et al. [44,45] reporting an estimated minimum threshold of 0.36 MPa for BBB opening. When comparing results, it must be pointed out that similar pulsed FUS parameters (10 ms burst length at 1 Hz repetition frequency) were employed in these studies, but a quite smaller frequency of 0.7 MHz.

Transgenic mouse models of AD constitute the main research tool in such studies since they are inexpensive, reproducible, and exhibit abundant plaque load. Herein, 5XFAD mice were bred for the antibody study (n=21). This is an excellent model since it recapitulates major features of the AD amyloid pathology at a very early age with a rapid amyloid beta plaque formation and severe gliosis [46], [47]. This is advantageous compared to other mouse models of AD that develop the pathology at a slower rate [48], [49]. It should be though noted that the absence of tau pathology that is a hallmark of AD can be a limitation of this model. Given that the interplay of Aβ and tau plays a major role in the development and acceleration of the disease, the disease mechanisms are not fully demonstrated [50].

The combined treatment involved retro-orbital injection of 50 μL of Aβ (1-40) antibody (2.85 mg), which is half the amount used in a previous study [34], and 5 μL of MBs (1 x 10^6 MBs) followed by pulsed FUS (16 W) at 1 MHz. Retro-orbital injection was used as an alternative to tail vein intravenous administration. Based on the literature, there is no difference in the drug delivery, absorption or pharmacokinetic activity of therapeutic agents such as drugs or antibodies [51], [52]. Following FUS treatment, the mouse was left 4 hours before it was sacrificed, which is considered the reliable post-treatment time window during which the BBB remains open [53,54], to allow the maximum amount of antibody to enter and distributed in the brain. Immunohistochemistry analysis of brain tissue sections confirmed that the antibody cannot normally enter the brain parenchyma. Specifically, no fluorescent was observed in the microscope indicating absence of the antibody when administered alone owing to its prohibitively large molecular weight of 150 kDa. A single treatment with the selected sonication protocol (1 MHz pulsed FUS with 10 ms burst length, 1 % DF, 16 W power, and 100 s duration) allowed the injected Aβ (1-40) antibody to enter the brain. In merged images, co-localization the Aβ (1-40) and Aβ (1-16) antibodies confirmed the presence of cortical plaques, successful trans-BBB entry of the injected anti-Aβ antibody in the sonicated brain, as

well as the specificity of the Aβ (1-40) antibodies to bind to the amyloid plaques. The results showed excellent consistency and reproducibility of BBBD and FUS-mediated antibody delivery by single sonication in the treated hemispheres of all mice (n=10, FUS+MBs plus Ab group). It is expected that antibody binding to amyloid plaques will enhance their clearance from the brain by facilitating recognition and uptake by glial and peripheral immune cells, thus leading to reduction of amyloid (1-40) loading and subsequently inhibiting toxic oligomerization of Aβ [55].

This is a preliminary study that was focused on the feasibility of safely and efficiently delivering the Aβ (1-40) antibody into the mouse brain following BBB opening by FUS. Although the antibody was widely distributed through the sonicated brain and bound to Aβ plaques, it remains unclear to which degree the selected antibody amount promotes plaque clearance and positive cognitive effects nor whether the antibody amount can be further decreased. Accordingly, longer-term studies are required to assess the effects of the antibody and dose on suppressing AD pathology, which may require repeated treatments.

The positioning device employed in the study was proven an ergonomic tool for trans-cranial FUS applications in mice. The special design of the system allowed attaching the water-filled cone to the mouse head with visual confirmation of proper coupling following easy targeting with the assistance of the laser system. The suitability of the single element FUS transducer of 1 MHz for the particular application of transcranial BBBD in rodents was demonstrated, being in agreement with other field studies where 1 MHz burst FUS was predominantly selected for similar applications [14,56–58]. Since this was a feasibility study, we did not attempt targeting a specific brain region. A global targeting approach was instead used where the beam was focused in the center of the left hemisphere. The blue dyed area in the perfused brain slice of Fig. 4 covers almost the entire targeted hemisphere. This is reasonable since the beam of the selected transducer is wide with focal point dimensions (≈ 2.5 mm lateral diameter) comparable

with the hemisphere dimensions. Of course, the extend of BBBD and EB extravasation depend on multiple other factors, such as the applied pressure and burst duration [59], as well as the type and dose of MBs [60]. Notably, the connectivity of the brain and the changes in the local environment (e.g., blood flow) after the FUS treatment might also contribute to this phenomenon. Generally, as evidenced by the extend of EB dye extravasation, FUS of 1 MHz applied with the specific transducer and proposed sonication parameters affected almost the entire targeted hemisphere, also provided the small size of the mouse brain. Follow up studies may use ultrasonic sources with stronger focusing and account for such parameters to enable a more specific delivery of the antibody in brain regions of interest.

5 CONCLUSIONS

Overall, the study findings demonstrated that the Aβ (1-40) antibody that is normally hampered by the BBB can efficiently and safely enter the brain parenchyma and bind to Aβ plaques of the 5XFAD mouse model of AD by FUS+MBs-mediated BBB opening with the proposed optimized protocol. Follow-up studies will examine the effects of this antibody on Aβ clearance and plaque load reduction, as well as whether repeated treatments can impart significant positive effects on cognition. These results hold promise for the development of disease modifying therapies for AD patients via the non-invasive anti-Aβ antibody delivery in future clinical applications.

LIST OF FIGURE CAPTIONS

Fig. 1 a CAD drawing of the 1-DOF manual positoning device comprising a FUS transducer of 1 MHz with a mouse positioned on the dedicated platform, **b** Indicative photo from experiment.

Fig. 2 Protocol timeline for FUS-mediated Aβ (1-40) antibody delivery in 5XFAD mice.

Fig. 3 Fluorescence images (10x magnification) of unstained brain sections at the level of the lateral ventricles of mice injected with EB: **a** No FUS, **b** FUS at 6.5 W, **c** FUS at 9.7 W, **d** FUS at 13 W, **e** FUS at 16 W, and **f** FUS at 19.5 W (acoustic power).

Fig. 4 a FUS beam targeting centrally at the left hemisphere, **b** Freshly perfused excised mouse brain treated with the selected protocol (5 μL MBs and 16 W acoustic power), **c** brain section after fixation in OCT revealing the distribution pattern of EB extravasation, **d-e** Fluorescence images (5x magnification) of unstained brain sections at the level of the cortex taken from perfused mice injected with EB and 5 μL MBs followed by sonication at 16 W (EB + FUS^{+MB}) and injected with EB only (control).

Fig. 5 Representative photos (10x and 40x magnification) of H&E staining from mice treated with MBs-enhanced pulsed FUS at 16 W for two different brain areas; corpus callosum (CC) and inferior colliculus (IC).

Fig. 6 Immunohistochemistry analysis of brain tissue sections of 5xFAD mice. **a** Control staining; brain tissue without any injected antibody or FUS+MBs stained with Aβ (1-16) and Aβ (1-40) antibodies to confirm the presence of amyloid plaques (green & red) in the cortex. **b** Mouse injected with saline followed by FUS+MBs. **c** Mouse injected with the Aβ (1-40) antibody alone. **d** Mouse injected with 50 μL of Aβ (1-40) antibody followed by FUS+MBs. Amyloid plaques (green) were stained with Aβ (1-16)**.** The Aβ (1-40) antibody was stained red. Co-localization of antibodies (white circles) in the cortex of the FUS+MBs plus Ab group (MERGE) confirmed successful entry and binding of the Aβ (1-40) with amyloid plaques

(Sonication parameters: f = 1 MHz, burst length = 10 ms, DF = 1 %, acoustic power = 16 W, and sonication duration = 100 s).

Fig. 7 Immunohistochemistry analysis of brain tissue sections of 5XFAD mice injected with 50 μL of Aβ (1-40) and 5 μL MBs followed by pulsed FUS (f = 1 MHz, burst length = 10 ms, DF = 1 %, acoustic power = 16 W, and sonication duration = 100 s). Fluorescence images (20x magnification) from (6) different mice at the cortex level where plaques are stained green; Aβ (1-16) and the antibody red; Aβ (1-40). Co-localization of antibodies (white circles) in the cortex confirmed the successful entry and specific binding of the Aβ (1-40) antibody.

DECLARATIONS

CONFLICT OF INTERESTS:

All authors declare NO conflict of interest.

DATA AVAILABILITY:

All data generated or analysed in the present study are available from the corresponding author on reasonable request.

CODE AVAILABILITY:

Not applicable.

CONSENT TO PARTICIPATE:

Not applicable. The study does not include data on patients.

CONSENT FOR PUBLICATION:

Not applicable. The study does not include data on patients.

COMPLIANCE WITH ETHICAL STANDARDS:

All animal experiments have been approved by the authorities of Veterinary Services, Ministry of Agriculture, Cyprus under the study license (CY/EXP/PR.L05/2021).

REFERENCES

[1] Kadry H, Noorani B, Cucullo L. A blood–brain barrier overview on structure, function, impairment, and biomarkers of integrity. Fluids Barriers CNS 2020;17:1–24. https://doi.org/10.1186/s12987-020-00230-3.

[2] Pandit R, Chen L, Götz J. The blood-brain barrier: Physiology and strategies for drug delivery. Adv Drug Deliv Rev 2020;165–166:1–14. https://doi.org/10.1016/j.addr.2019.11.009.

[3] Ebrahimi Z, Talaei S, Aghamiri S, Goradel NH, Jafarpour A, Negahdari B. Overcoming the blood–brain barrier in neurodegenerative disorders and brain tumours. IET Nanobiotechnology 2020;14:441–8. https://doi.org/10.1049/iet-nbt.2019.0351.

[4] Harilal S, Jose J, Parambi DGT, Kumar R, Unnikrishnan MK, Uddin MS, et al. Revisiting the blood-brain barrier: A hard nut to crack in the transportation of drug molecules. Brain Res Bull 2020;160:121–40. https://doi.org/10.1016/j.brainresbull.2020.03.018.

[5] Karmur BS, Philteos J, Abbasian A, Zacharia BE, Lipsman N, Levin V, et al. Blood-Brain Barrier Disruption in Neuro-Oncology: Strategies, Failures, and Challenges to Overcome. Front Oncol 2020;10. https://doi.org/10.3389/fonc.2020.563840.

[6] Rodriguez A, Tatter SB, Debinski W. Neurosurgical techniques for disruption of the blood–brain barrier for glioblastoma treatment. Pharmaceutics 2015;7:175–87. https://doi.org/10.3390/pharmaceutics7030175.

[7] Mesiwala AH, Farrell L, Wenzel HJ, Silbergeld DL, Crum LA, Winn HR, et al. High-intensity focused ultrasound selectively disrupts the blood-brain barrier in vivo. Ultrasound Med Biol 2002;28:389–400. https://doi.org/10.1016/S0301-5629(01)00521-X.

[8] Yang Y, Zhang X, Ye D, Laforest R, Williamson J, Liu Y, et al. Cavitation dose painting for focused ultrasound-induced blood-brain barrier disruption. Sci Rep 2019;9:1–10. https://doi.org/10.1038/s41598-019-39090-9.

[9] Gosselet F, Loiola RA, Roig A, Rosell A, Culot M. Central nervous system delivery of molecules across the blood-brain barrier. Neurochem Int 2021;144:104952. https://doi.org/10.1016/j.neuint.2020.104952.

[10] Aryal M, Fischer K, Gentile C, Gitto S, Zhang YZ, McDannold N. Effects on P-glycoprotein expression after blood-brain barrier disruption using focused ultrasound and microbubbles. PLoS One 2017;12:1–15. https://doi.org/10.1371/journal.pone.0166061.

[11] Sheikov N, McDannold N, Vykhodtseva N, Jolesz F, Hynynen K. Cellular mechanisms of the blood-brain barrier opening induced by ultrasound in presence of microbubbles. Ultrasound Med Biol 2004;30:979–89. https://doi.org/10.1016/j.ultrasmedbio.2004.04.010.

[12] Wasielewska JM, White AR. "Focused Ultrasound-mediated Drug Delivery in Humans – a Path Towards Translation in Neurodegenerative Diseases." Pharm Res 2022;39:427–39. https://doi.org/10.1007/s11095-022-03185-2.

[13] Hynynen K, Mcdannold N, Sheikov NA, Jolesz FA, Vykhodtseva N. Local and reversible blood – brain barrier disruption by noninvasive focused ultrasound at frequencies suitable for trans-skull sonications. Neuroimage 2005;24:12–20. https://doi.org/10.1016/j.neuroimage.2004.06.046.

[14] Choi JJ, Wang S, Tung Y-S, Morrison B, Konofagou EE. Molecules of various pharmacologically-relevant sizes can cross the ultrasound-induced blood-brain barrier opening in vivo. Ultrasound Med Biol 2010;36:58–67.

https://doi.org/10.1016/j.ultrasmedbio.2009.08.006.

[15] Chen K, Wei K, Liu H. Theranostic Strategy of Focused Ultrasound Induced Blood-Brain Barrier Opening for CNS Disease Treatment. Front Pharmacol 2019;10. https://doi.org/10.3389/fphar.2019.00086.

[16] Ghali MGZ, Srinivasan VM, Kan P. Focused Ultrasonography-Mediated Blood-Brain Barrier Disruption in the Enhancement of Delivery of Brain Tumor Therapies. World Neurosurg 2019;131:65–75. https://doi.org/10.1016/j.wneu.2019.07.096.

[17] Fishman PS, Fischell JM. Focused Ultrasound Mediated Opening of the Blood-Brain Barrier for Neurodegenerative Diseases. Front Neurol 2021;12:1–5. https://doi.org/10.3389/fneur.2021.749047.

[18] Lin CY, Hsieh HY, Pitt WG, Huang CY, Tseng IC, Yeh CK, et al. Focused ultrasound-induced blood-brain barrier opening for non-viral, non-invasive, and targeted gene delivery. J Control Release 2015;212:1–9. https://doi.org/10.1016/j.jconrel.2015.06.010.

[19] Alzheimer's disease. Alzheimer's Dis Int n.d. https://www.alzint.org/about/dementia-facts-figures/types-of-dementia/alzheimers-disease/ (accessed January 16, 2023).

[20] Choi JJ, Wang S, Brown TR, Small SA, Duff KEK, Konofagou EE. Noninvasive and Transient Blood-Brain Barrier Opening in the Hippocampus of Alzheimer ' s Double Transgenic Mice Using Focused Ultrasound. Ultrason Imaging 2008;30:189–200.

[21] Jordão JF, Thévenot E, Markham-Coultes K, Scarcelli T, Weng Y-Q, Xhima K, et al. Amyloid-β plaque reduction, endogenous antibody delivery and glial activation by brain-targeted, transcranial focused ultrasound. Exp Neurol 2013;248:16–29. https://doi.org/10.1016/j.expneurol.2013.05.008.

[22] Shen Y, Hua L, Yeh C, Shen L, Ying M, Zhang Z. Ultrasound with microbubbles

improves memory, ameliorates pathology and modulates hippocampal proteomic changes in a triple transgenic mouse model of Alzheimer' s disease. Theranostics 2020;10:11794–819. https://doi.org/10.7150/thno.44152.

[23] Poon CT, Shah K, Lin C, Tse R, Kim KK, Mooney S, et al. Time course of focused ultrasound effects on β-amyloid plaque pathology in the TgCRND8 mouse model of Alzheimer's disease. Sci Rep 2018;8:1–11. https://doi.org/10.1038/s41598-018-32250-3.

[24] Hsu PH, Lin YT, Chung YH, Lin KJ, Yang LY, Yen TC, et al. Focused Ultrasound-Induced Blood-Brain Barrier Opening Enhances GSK-3 Inhibitor Delivery for Amyloid-Beta Plaque Reduction. Sci Rep 2018;8:1–9. https://doi.org/10.1038/s41598-018-31071-8.

[25] Frost JL, Liu B, Rahfeld J-U, Kleinschmidt M, O'Nuallaina B, Le KX, et al. An anti-pyroglutamate-3 Aβ vaccine reduces plaques and improves cognition in APPswe/PS1ΔE9 mice. Neurobiol Aging 2015;36:3187–99. https://doi.org/10.1016/j.neurobiolaging.2015.08.021.

[26] Xhima K, Markham-Coultes K, Hahn Kofoed R, Saragovi HU, Hynynen K, Aubert I. Ultrasound delivery of a TrkA agonist confers neuroprotection to Alzheimer-associated pathologies. Brain 2022;145:2806–22. https://doi.org/10.1093/brain/awab460.

[27] Jordão JF, Ayala-Grosso CA, Markham K, Huang Y, Chopra R, McLaurin JA, et al. Antibodies targeted to the brain with image-guided focused ultrasound reduces amyloid-β plaque load in the TgCRND8 mouse model of Alzheimer's disease. PLoS One 2010;5:4–11. https://doi.org/10.1371/journal.pone.0010549.

[28] Bathini P, Sun T, Schenk M, Schilling S, Mcdannold NJ, Lemere CA. Acute Effects of Focused Ultrasound-Induced Blood-Brain Barrier Opening on Anti-Pyroglu3 Abeta

Antibody Delivery and Immune Responses. Biomolecules 2022;12:951. https://doi.org/10.3390/biom12070951.

[29] Sun T, Shi Q, Zhang Y, Power C, Hoesch C, Antonelli S, et al. Focused ultrasound with anti-pGlu3 Aβ enhances efficacy in Alzheimer's disease-like mice via recruitment of peripheral immune cells. J Control Release 2021;336:443–56. https://doi.org/10.1016/j.jconrel.2021.06.037.

[30] Bajracharya R, Cruz E, Götz J, Nisbet RM. Ultrasound-mediated delivery of novel tau-specific monoclonal antibody enhances brain uptake but not therapeutic efficacy. J Control Release 2022;349:634–48. https://doi.org/10.1016/j.jconrel.2022.07.026.

[31] Leinenga G, Koh WK, Götz J. A comparative study of the effects of Aducanumab and scanning ultrasound on amyloid plaques and behavior in the APP23 mouse model of Alzheimer disease. Alzheimer's Res Ther 2021;13:1–14. https://doi.org/10.1186/s13195-021-00809-4.

[32] Safety and Feasibility of Exablate Blood-Brain Barrier Disruption for Mild Cognitive Impairment or Mild Alzheimer's Disease Undergoing Aduhelm Therapy. Clin Identifier NCT05469009 n.d. https://beta.clinicaltrials.gov/study/NCT05469009 (accessed January 10, 2023).

[33] Fu HJ, Liu B, Frost JL, Lemere CA. Amyloid-β Immunotherapy for Alzheimer's Disease. CNS Neurol Disord Drug Targets 2010;9:197–206. https://doi.org/10.2174/187152710791012017.

[34] Raymond SB, Treat LH, Dewey JD, Mcdannold NJ, Hynynen K, Bacskai BJ. Ultrasound Enhanced Delivery of Molecular Imaging and Therapeutic Agents in Alzheimer ' s Disease Mouse Models. PLoS One 2008;3:1–7. https://doi.org/10.1371/journal.pone.0002175.

[35] Antoniou A, Giannakou M, Georgiou E, Kleopa KA, Damianou C. Robotic device for transcranial focussed ultrasound applications in small animal models. Int J Med Robot Comput Assist Surg 2022:1–11. https://doi.org/10.1002/rcs.2447.

[36] Madsen EL, Dong F, Frank GR, Garra BS, Wear KA, Wilson T, et al. Interlaboratory Comparison of Ultrasonic Backscatter, Attenuation, and Speed Measurements. J Ultrasound Med 1999;18:615–31. https://doi.org/10.7863/jum.1999.18.9.615.

[37] Todd N, Zhang Y, Arcaro M, Becerra L, Borsook D, Livingstone M, et al. Focused Ultrasound Induced Opening of the Blood-Brain Barrier Disrupts Inter-Hemispheric Resting State Functional Connectivity in the Rat Brain. Neuroimage 2018;178:414–422. https://doi.org/10.1016/j.neuroimage.2018.05.063.

[38] Burgess A, Kullervo HH. Drug delivery across the blood-brain barrier using focused ultrasound. Expert Opin Drug Deliv 2014;11:711–721. https://doi.org/10.1517/17425247.2014.897693.

[39] Gandhi K, Barzegar-Fallah A, Banstola A, Rizwan SB, Reynolds JNJ. Ultrasound-Mediated Blood–Brain Barrier Disruption for Drug Delivery: A Systematic Review of Protocols, Efficacy, and Safety Outcomes from Preclinical and Clinical Studies. Pharmaceutics 2022;14. https://doi.org/10.3390/pharmaceutics14040833.

[40] Plotkin SS, Cashman NR. Passive immunotherapies targeting Aβ and tau in Alzheimer's disease. Neurobiol Dis 2020;144. https://doi.org/10.1016/j.nbd.2020.105010.

[41] Lemere CA. Immunotherapy for Alzheimer's disease: Hoops and hurdles. Mol Neurodegener 2013;8:1–6. https://doi.org/10.1186/1750-1326-8-36.

[42] Hughes JM, Neese OR, Bieber DD, Lewis KA, Ahmadi LM, Parsons DW, et al. The Effects of Propofol on a Human in vitro Blood-Brain Barrier Model. Front Cell Neurosci 2022;16:1–13. https://doi.org/10.3389/fncel.2022.835649.

[43] Saunders NR, Dziegielewska KM, Møllgård K, Habgood MD. Markers for blood-brain barrier integrity: How appropriate is Evans blue in the twenty-first century and what are the alternatives? Front Neurosci 2015;9:1–16. https://doi.org/10.3389/fnins.2015.00385.

[44] McDannold N, Vykhodtseva N, Hynynen K. Use of ultrasound pulses combined with Definity for targeted blood-brain barrier disruption: a feasibility study. Ultrasound Med Biol 2007;33:584–90. https://doi.org/10.1016/j.ultrasmedbio.2006.10.004.

[45] McDannold N, Vykhodtseva N, Hynynen K. Effects of Acoustic Parameters and Ultrasound Contrast Agent Dose on Focused-Ultrasound Induced Blood-Brain Barrier Disruption. Ultrasound Med Biol 2008;34:930–7. https://doi.org/10.1016/j.ultrasmedbio.2007.11.009.

[46] Oakley H, Cole SL, Logan S, Maus E, Shao P, Craft J, et al. Intraneuronal β-amyloid aggregates, neurodegeneration, and neuron loss in transgenic mice with five familial Alzheimer's disease mutations: Potential factors in amyloid plaque formation. J Neurosci 2006;26:10129–40. https://doi.org/10.1523/JNEUROSCI.1202-06.2006.

[47] Angeli S, Kousiappa I, Stavrou M, Sargiannidou I, Georgiou E, Papacostas SS, et al. Altered Expression of Glial Gap Junction Proteins Cx43, Cx30, and Cx47 in the 5XFAD Model of Alzheimer's Disease. Front Neurosci 2020;14:1–20. https://doi.org/10.3389/fnins.2020.582934.

[48] Jankowsky JL, Fadale DJ, Anderson J, Xu GM, Gonzales V, Jenkins NA, et al. Mutant presenilins specifically elevate the levels of the 42 residue β-amyloid peptide in vivo: Evidence for augmentation of a 42-specific γ secretase. Hum Mol Genet 2004;13:159–70. https://doi.org/10.1093/hmg/ddh019.

[49] Radde R, Bolmont T, Kaeser SA, Coomaraswamy J, Lindau D, Stoltze L, et al. Aβ42-

driven cerebral amyloidosis in transgenic mice reveals early and robust pathology. EMBO Rep 2006;7:940–6. https://doi.org/10.1038/sj.embor.7400784.

[50] Claeysen S, Giannoni P, Ismeurt C. The 5xFAD mouse model of Alzheimer ' s disease. The Neuroscience of Dementia. Diagnosis Manag. Dement., vol. 1, Academic Press; 2020, p. 207–21. https://doi.org/10.1016/B978-0-12-815854-8.00013-6f.

[51] Schoch A, Thorey IS, Engert J, Winter G, Emrich T. Comparison of the lateral tail vein and the retro-orbital venous sinus routes of antibody administration in pharmacokinetic studies. Lab Anim (NY) 2014;43:95–9. https://doi.org/10.1038/laban.481.

[52] Steel CD, Stephens AL, Hahto SM, Singletary SJ. Comparison of the lateral tail vein and the retro-orbital venous sinus as routes of intravenous drug delivery in a transgenic mouse model. Lab Anim (NY) 2008;37. https://doi.org/10.1038/laban0108-26.

[53] Sheikov N, McDannold N, Sharma S, Hynynen K. Effect of focused ultrasound applied with an ultrasound contrast agent on the tight junctional integrity of the brain microvascular endothelium. Ultrasound Med Biol 2008;34:1093–1104. https://doi.org/10.1016/j.ultrasmedbio.2007.12.015.

[54] Downs ME, Buch A, Sierra C, Karakatsani ME, Chen S, Konofagou EE, et al. Long-term safety of repeated blood-brain barrier opening via focused ultrasound with microbubbles in non-human primates performing a cognitive task. PLoS One 2015;10:1–26. https://doi.org/10.1371/journal.pone.0125911.

[55] Suzuki K, Iwata A, Iwatsubo T. The past, present, and future of disease-modifying therapies for Alzheimer's disease. Proc Japan Acad Ser B Phys Biol Sci 2017;93:757–71. https://doi.org/10.2183/pjab.93.048.

[56] Choi JJ, Pernot M, Small SA, Konofagou EE. Noninvasive, transcranial and localized opening of the blood-brain barrier using focused ultrasound in mice. Ultrasound Med

Biol 2007;33:95–104. https://doi.org/10.1016/j.ultrasmedbio.2006.07.018.

[57] Choi JJ, Selert K, Gao Z, Samiotaki G, Baseri B, Konofagou EE. Noninvasive and Localized Blood—Brain Barrier Disruption using Focused Ultrasound can be Achieved at Short Pulse Lengths and Low Pulse Repetition Frequencies. J Cereb Blood Flow Metab 2011;31:725–37. https://doi.org/10.1038/jcbfm.2010.155.

[58] Wang S, Samiotaki G, Olumolade O, Feshitan JA, Konofagou EE. Microbubble type and distribution dependence of focused ultrasound-induced blood-brain barrier opening. Ultrasound Med Biol 2014;40:130–7. https://doi.org/10.1016/j.ultrasmedbio.2013.09.015.

[59] Shin J, Kong C, Cho JS, Lee J, Koh CS, Yoon MS, et al. Focused ultrasound-mediated noninvasive blood-brain barrier modulation: Preclinical examination of efficacy and safety in various sonication parameters. Neurosurg Focus 2018;44:1–10. https://doi.org/10.3171/2017.11.FOCUS17627.

[60] Song KH, Fan AC, Hinkle JJ, Newman J, Borden MA, Harvey BK. Microbubble gas volume: A unifying dose parameter in blood-brain barrier opening by focused ultrasound. Theranostics 2017;7:144–52. https://doi.org/10.7150/thno.15987.

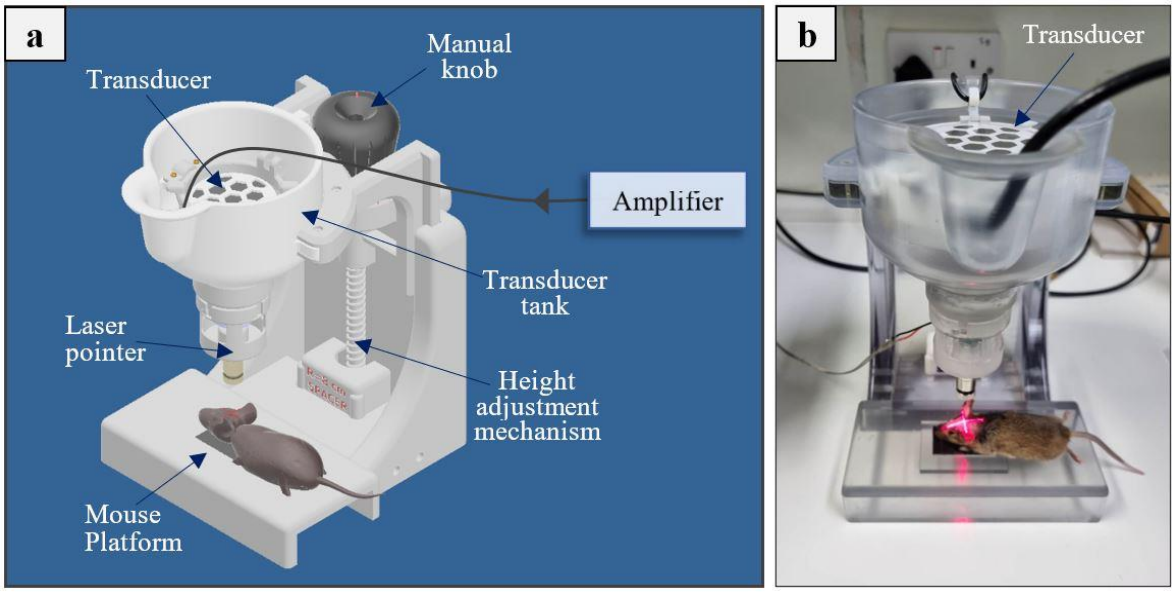
a
Transducer
Manual knob
Amplifier
Transducer tank
Laser pointer
Height adjustment mechanism
Mouse Platform
b
Transducer

Figure 1

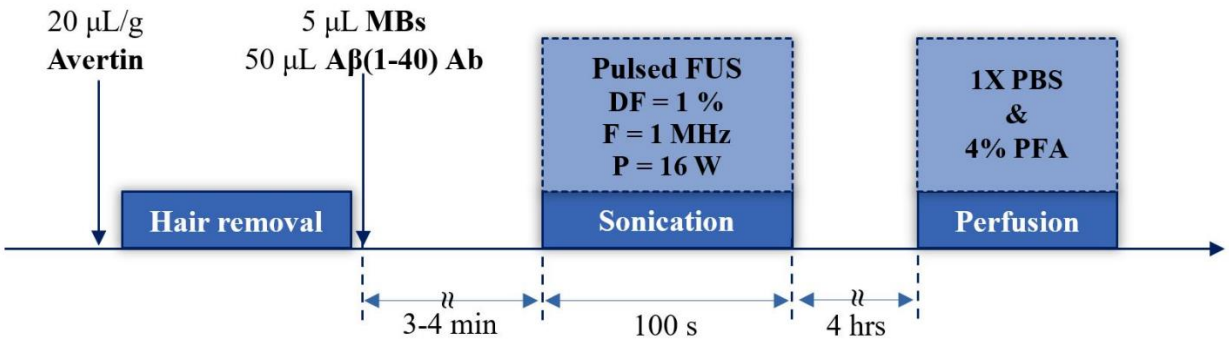
20 µL/g
Avertin
5 µL MBs
50 µL Aβ(1-40) Ab
Pulsed FUS
DF = 1 %
F = 1 MHz
P = 16 W
1X PBS
&
4% PFA
Hair removal
Sonication
Perfusion
3-4 min
100 s
4 hrs

Figure 2

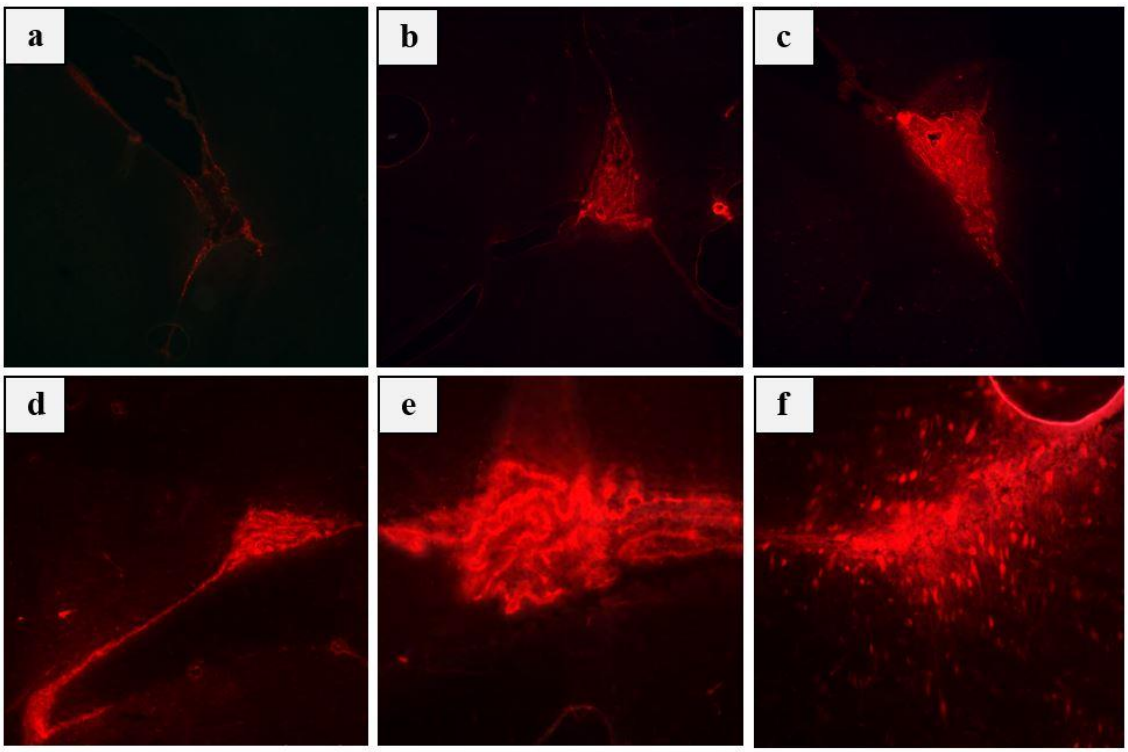

Figure 3

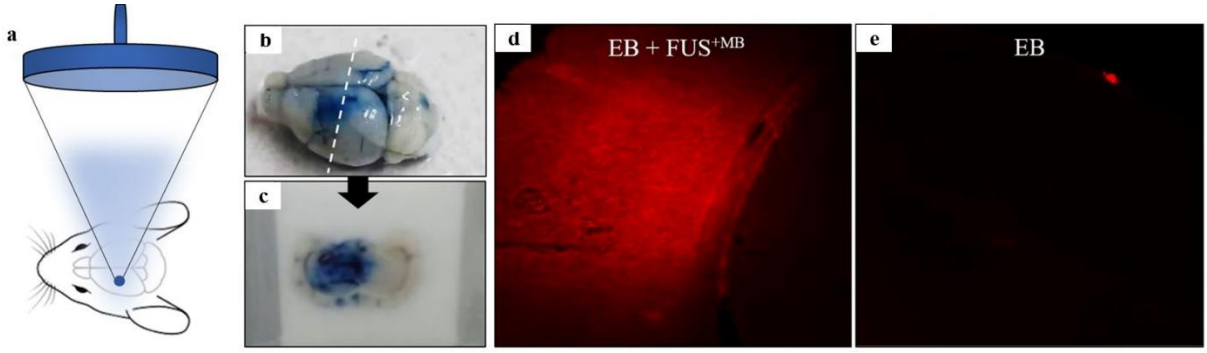

Figure 4

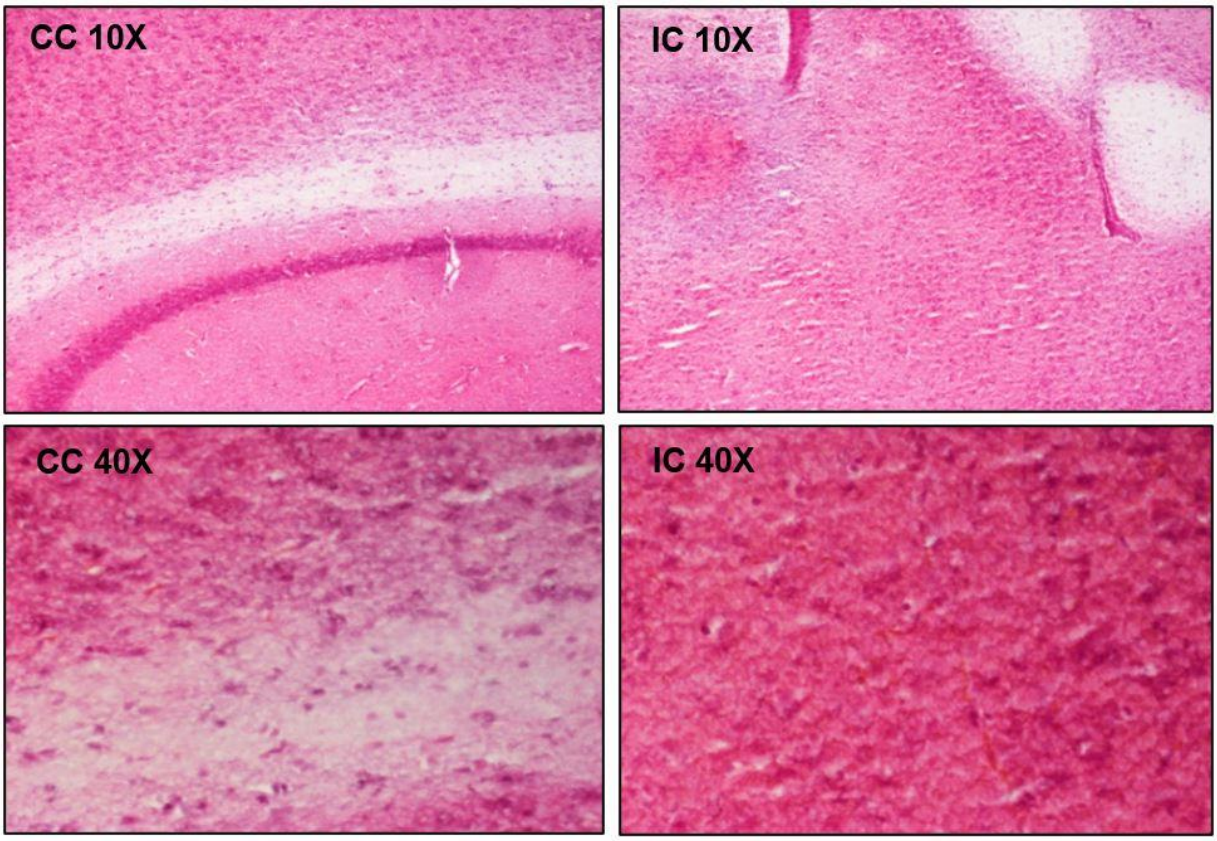

Figure 5

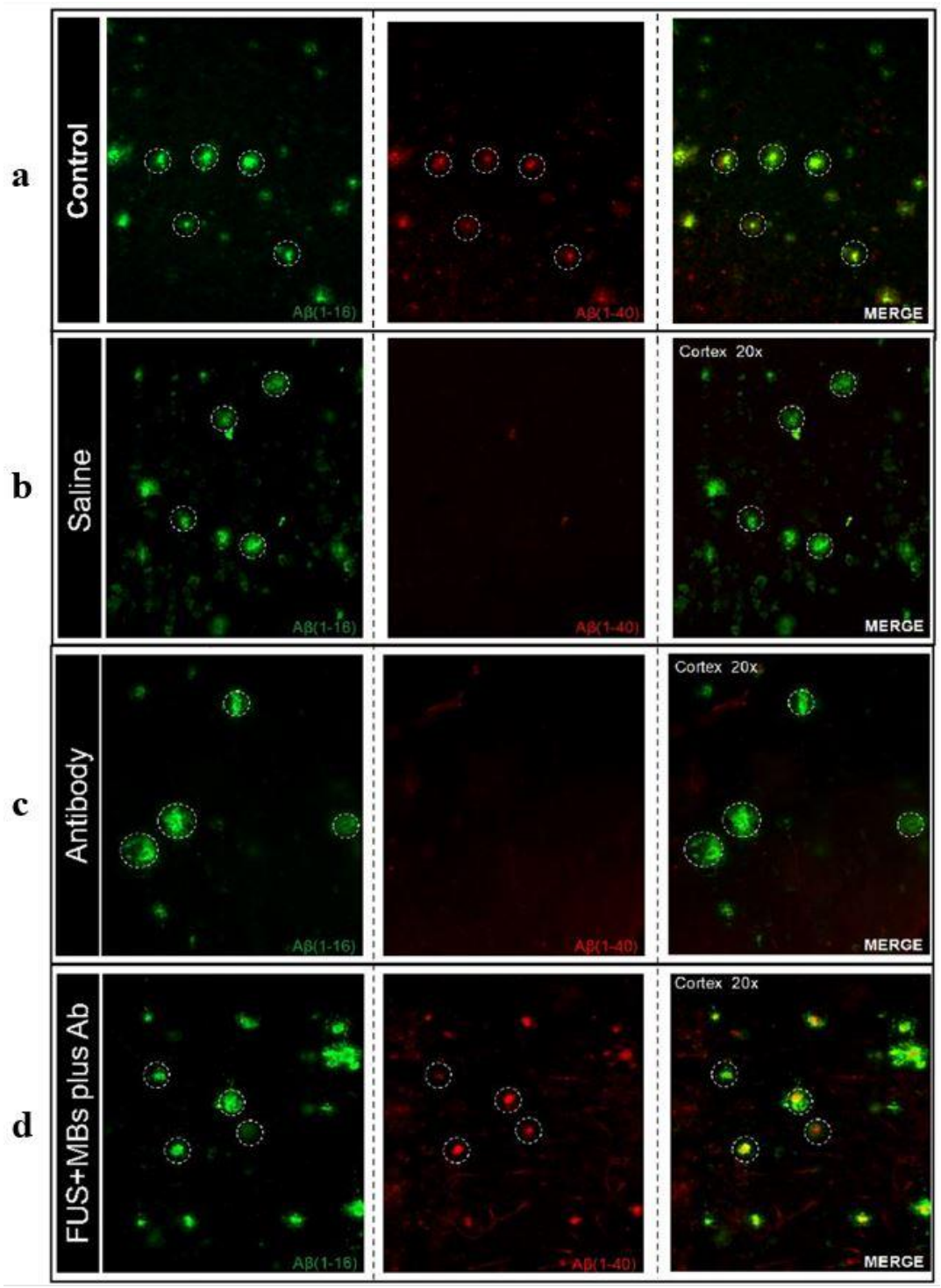
a
Control
Aβ(1-16)
Aβ(1-40)
MERGE
b
Saline
Aβ(1-16)
Aβ(1-40)
Cortex 20x
MERGE
c
Antibody
Aβ(1-16)
Aβ(1-40)
Cortex 20x
MERGE
d
FUS+MBs plus Ab
Aβ(1-16)
Aβ(1-40)
Cortex 20x
MERGE

Figure 6

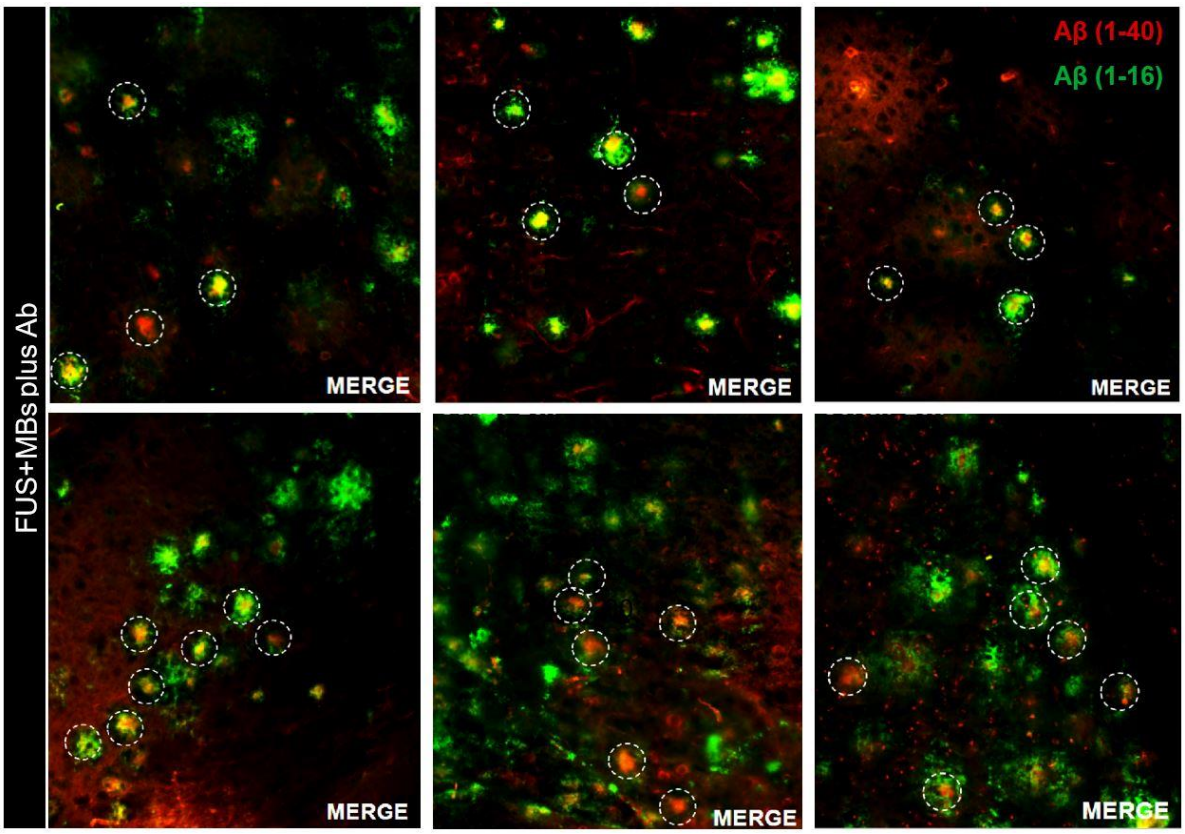
FUS+MBs plus Ab
MERGE
MERGE
Aβ (1-40)
Aβ (1-16)
MERGE
MERGE
MERGE
MERGE

Figure 7

Focused ultrasound heating in brain tissue/skull phantoms with 1-MHz single-element transducer

ABSTRACT

Purpose: The study aims to provide insights on the practicality of using single-element transducers for transcranial Focused Ultrasound (tFUS) thermal applications.

Methods: FUS sonications were performed through skull phantoms embedding agar-based tissue mimicking gels using a 1-MHz single-element spherically focused transducer. The skull phantoms were 3D printed with Acrylonitrile Butadiene Styrene (ABS) and Resin thermoplastics having the exact skull bone geometry of a healthy volunteer. The temperature field distribution during and after heating was monitored in a 3T Magnetic Resonance Imaging (MRI) scanner using MR thermometry. The effect of the skull's thickness on intracranial heating was investigated.

Results: A single FUS sonication at focal acoustic intensities close to 1580 W/cm^2 for 60 s in free field heated up the agar phantom to ablative temperatures reaching about 90 ˚C (baseline of 37 ºC). The ABS skull strongly blocked the ultrasonic waves, resulting in zero temperature increase within the phantom. Considerable heating was achieved through the Resin skull, but it remained at hyperthermia levels. Conversely, tFUS through a 1-mm Resin skull showed enhanced ultrasonic penetration and heating, with the focal temperature reaching 70 ˚C.

Conclusions: The ABS skull demonstrated poorer performance in terms of tFUS compared to the Resin skull owing to its higher ultrasonic attenuation and porosity. The thin Resin phantom of 1 mm thickness provided an efficient acoustic window for delivering tFUS and heating up deep phantom areas. The results of such studies could be particularly useful for accelerating the establishment of a wider range of tFUS applications.

KEYWORDS: focused ultrasound; phantom; MR thermometry; skull; single-element; transducer

1. INTRODUCTION

Transcranial focused ultrasound (tFUS) constitutes an evolving modality for non-invasive brain applications, including the treatment of neurodegenerative disorders such as Parkinson's disease and essential tremor [1], the temporal disruption of the blood-brain barrier (BBB) to deliver therapeutic agents [2], as well as the stimulation of brain tissue [3]. The widespread use of tFUS has been limited for a long period of time by the challenge of accurately delivering the acoustic waves in the brain through the complex skull structure. This issue has been addressed through the development of the phased array technology, which has been a significant milestone in the process of translating tFUS applications from benchtop to bedside [4]. Another key milestone in this process was the introduction of Magnetic Resonance Imaging (MRI)-based thermometry, which allowed for precisely monitoring the FUS-induced thermal effects intra-procedurally and treating deep Central Nervous System (CNS) tissue without threatening adjacent and intervening tissues [5].

Despite the limitations of single-element transducers in terms of beam steering, they remain a valuable tool for neurotherapeutics. In recent years, low intensity tFUS has received significant attention due to its potential as a non-invasive modality for neuromodulation [6]. Successful brain stimulation by delivering low-intensity pulsed ultrasound with single-element transducers has been demonstrated in small animals [7–9], non-human primates [10], and humans [11,12]. Single-element transducers were also proven efficient for BBB disruption (BBBD) in several animal models, including mice [13,14] and rabbits [15], using microbubbles-enhanced pulsed FUS at frequencies of 1.5 MHz and 0.7 MHz, respectively. Lower frequencies close to 0.5 MHz were employed for successful BBBD in non-human primates [16–18] to compensate for the increased ultrasonic scattering occurring within their complex skull structure. However, the complex subject-dependent skull geometry makes it difficult to predict the amount of transmitted energy and the exact brain region affected by

single-element emissions, thereby raising numerous concerns regarding clinical safety.

Image-guided numerical simulations can be used to predict ultrasonic propagation through the skull and simulate the intracranial field, thus being a valuable tool for correcting the focal point shifting and compensating for energy losses [19–22]. Such simulations are typically based on image data from computed tomography (CT) or MRI, from which the skull geometry is extracted. Yoon et al. [19] have proposed a finite-difference time domain-based simulation method employing a multi-resolution approach to model the trans-skull propagation of ultrasonic waves from single-element transducers. Performance evaluation in a sheep skull model suggests that the method can provide on-site feedback on the location, shape, and pressure profile of the focus to the user. This information is possible to allow for adjusting the transducer's location so that the desired pressure levels are achieved at the targeted tissue with sufficient precision. A similar simulation platform was employed by Deffieux et al. [21] in an effort to examine the focalization ability of single-element transducers operating at a low frequency range of 0.3 to 1 MHz through both primate and human skulls in the context of FUS-mediated BBBD. In another study [20], the wave propagation by single-element emissions and the resultant intracranial energy distribution were numerically investigated in a realistic multi-tissue model of the human head to assess the feasibility of low-intensity FUS neuromodulation of the hippocampus. ~~It~~ However, it should be noted that simulation-based guidance of tFUS may demand intensive computational resources to enable timely on-site feedback to the user.

Hydrophone-based experimental and numerical measurements were combined by Chen et al. [23], who examined the transmission of FUS from single-element transducers with frequencies of up to 1.5 MHz through human skulls. Interestingly, an exponential reduction in the transmission efficiency occurred with increasing ultrasonic frequency. An innovative virtual brain projection method has been recently proposed as another ergonomic tool for testing the behavior of tFUS beams of single-element transducers and identifying factors that

may impact the effectiveness of tFUS therapy in the treatment of neurological conditions [24]. It is also worth mentioning that recently the 3D printing technology was employed in the creation of customized patient-specific holographic acoustic lenses (i.e., 3D printed plastic lenses featuring textured surfaces) to counteract the beam aberration effects induced by the varying skull thickness [25,26]. Dedicated algorithms and simulation techniques can be used to design the digital model of the lens with the desired textured surface. This method was found to increase the energy accumulation within the targeted region by ten-fold [25], thus holding promise for tFUS thermal therapy using single-element transducers.

Recently, systems incorporating single-element transducers have been proposed for FUS-mediated BBBD under stereotactic targeting and real-time passive cavitation monitoring with the aim of enabling MRI-independent treatment sessions [27,28]. Pouliopoulos et al. [27] presented a neuronavigation-guided system featuring a 0.25 MHz single-element transducer. Simulation studies and hydrophone-based experiments involving a human skull fragment were performed to assess the transducer's focusing properties. As expected, the insertion of the skull fragment in the beam path resulted in considerable focal shifting and a pressure attenuation of about 45%. A similar approach was followed by Marquet et al. [28], who report successful BBBD of deep subcortical structures in monkeys with a 0.5 MHz transducer. The ultrasonic amplitude of emitted waves was increased based on pressure measurements taken in vitro to compensate for attenuation losses through the scalp and brain [28].

Tissue-mimicking phantoms have been a valuable tool in the early-stage assessment of FUS systems and emerging applications. Soft tissue is typically mimicked by a gel phantom, with agar- and PAA- based gels being widely employed for thermal studies with FUS mainly due to their ability to withstand ablative temperatures and replicate the most critical properties of biological tissues [29]. Regarding hard tissue, thermoplastic polymers have been selected for developing skull mimics by molding into dedicated patient-specific skull molds [30,31]. The

3D printing technology has emerged as a beneficial manufacturing method with the ability to develop more complex geometries with higher precision and detail compared to molding-based manufacturing [32–34]. In this regard, accurate geometric reconstruction of the skull bone is essential for replicating the defocusing effects caused by the variable thickness and complex structure of the cranium accurately. Accordingly, in the context of examining the feasibility of delivering FUS transcranially, experiments were carried out in both simplistic and more-advanced geometrically-accurate skull models using both thermocouple and MR thermometry measurements [32,33]. The general conclusion reached is that the skull phantoms decrease the temperatures recorded in free field substantially since the beam loses its focusing ability.

Given the recent scientific interest in transcranial FUS therapeutics using single-element transducers and the effort to establish techniques for overcoming their trans-skull steering inability, we herein present our findings on the feasibility of delivering FUS in a realistic brain tissue/skull phantom using a 1-MHz single-element spherically focused transducer. FUS sonications were performed through 3D-printed geometrically-accurate skull phantoms filled with an agar-based gel mimicking the brain tissue without any means of defocusing corrections. The temperature evolution and thermal field distribution during and after heating were monitored using MR thermometry. Skull phantoms made of two different thermoplastic materials were employed to assess the effect of ultrasonic attenuation on the thermal effects achieved within the soft tissue phantom. Furthermore, the study examined the feasibility of efficiently delivering FUS to heat up the phantom material through a 1-mm skull mimic. This technique is proposed as a potential novel approach to treat unresectable (i.e., multiple, recurrent, deep-seated, etc.) brain tumors by temporarily replacing the skull with a thin biocompatible insert to enable sufficient penetration and heating at ablative temperatures. Through these experiments, the study aims to provide insights on the practicality of using

single-element transducers for tFUS in the context of thermal therapy, also given that so far, ultrasonic transmission has been mostly assessed by numerical simulations.

2. MATERIALS AND METHODS

2.1 Construction of brain tissue/skull phantoms

Two-compartment skull phantoms were manufactured by rapid prototyping. The skull bone model was extracted by segmentation on CT head scan images of an anonymized female volunteer. A circular piece of the temporal-parietal skull region was isolated, resulting in a two-compartment skull model. The skull model was 3D-printed using two common thermoplastic materials; Acrylonitrile Butadiene Styrene (ABS, Stratasys) and Resin (Stratasys), on the F270 and Object30 Prime 3D printers of Stratasys (Minnesota, USA), respectively. Following further processing and smoothing on the dedicated software of each printer, the phantoms were manufactured with 100% infill. The circular insert had a diameter of 60 mm and an average thickness of about 6 mm.

Another thinner skull mimic was created to account for the effect of the skull thickness on ultrasonic transmission. Specifically, the stereolithography (STL) format of the circular skull insert was processed to adjust its thickness to 1 mm through its entire surface. The thin skull mimic was 3D-printed with Resin (Stratasys) material only. The rationale behind investigating the use of a 1-mm skull insert is that by temporarily removing a small skull part and replacing it with a thin biocompatible skull insert, the FUS ablation of unresectable brain tumors by single-element emissions could be feasible. Accordingly, the benefits of single-element transducers in terms of simplicity and cost-effective over phased array transducers could be exploited through this approach.

The brain tissue was mimicked by an agar-based gel containing a 6 % weight per volume (w/v) agar (Merck KGaA, EMD Millipore Corporation, Darmstadt, Germany) and 4 % w/v silicon dioxide (Sigma-Aldrich, St. Louis, Missouri, United States). The concentration of these

inclusions was proven to impart the desired phantom characteristics for the specific application of thermal FUS studies, including acoustical, thermal, and MRI properties comparable to human tissues [35–37]. The ultrasonic attenuation coefficient of this phantom was previously estimated at 1.10 ± 0.09 dB/cm-MHz [35]. The process for creating the gel phantom, as previously outlined by Drakos et al. [38], involved dissolving the agar and silicon dioxide powders in water. The agar solution was poured into the skull phantom and allowed to solidify, resulting in the final phantom shown in Fig. 1A. As shown in Fig. 1B, the circular skull insert can be easily removed to expose the brain-tissue phantom. Fig. 1C compares the 1-mm Resin insert with that of varying thickness.

2.2 CT imaging of the skull phantoms

Before proceeding to FUS experiments, it was considered essential to investigate the existence of air pores within the phantoms, which may be introduced during 3D printing and affect the propagation of ultrasonic waves considerably. Therefore, the radiographic behavior of the ABS and Resin skull mimics was investigated. CT imaging was performed with a General Electric (GE) CT scanner (Optima 580 RT, GE Medical Systems, Wisconsin, United States) using a tube voltage of 120 kV, a tube current of 410 mA, and a slice thickness of 1.25 mm to examine if there were any voids within the Resin and ABS samples.

2.3 FUS sonications in the phantom

FUS sonications were performed in the developed phantom with and without the circular skull insert (Fig. 1) in a 3T MRI scanner (Magnetom Vida, Siemens Healthineers, Erlangen, Germany). The FUS transducer employed in the study was made of a spherically focused single-element piezoelectric (Piezohannas, Wuhan, China) with an operating frequency (f) of 1.1 MHz, a diameter (D) of 50 mm, a radius of curvature (R) of 100 mm, and an acoustic efficiency of 30 %. The element was hosted in a dedicated MRI-compatible plastic housing. The transducer was supplied by an RF amplifier (AG1016, AG Series Amplifier, T & C Power

Conversion, Inc., Rochester, USA) located outside of the MRI room through MR shieled cables.

The experimental setup, as arranged on the MRI table, can be seen in Fig. 2. The brain tissue/skull phantom was submerged in a water tank filled with degassed and deionized water. The FUS transducer was attached to a specially designed 3D-printed holder facing toward the movable part of the phantom (circular insert). The transducer holder was attached on the top edges of the tank. The holder was able to be moved enabling adjustment of the distance between the transducer and phantom. For image acquisition, a multichannel body coil (Body18, Siemens Healthineers) was fixed on a dedicated support structure above the phantom. Caution was given not to include the transducer within the coil's detection area to avoid interference and signal loss [39].

For all reported experiments, the distance between the transducer and phantom was adjusted so that the focal depth is 40 mm. Continuous FUS was applied at acoustic power of 90 W for 60 s. The corresponding focal intensity was calculated as the acoustic power value divided by the beam area where the ultrasound energy is concentrated (i.e., cross-sectional area at the focal point; πr^2), equaling to 1583 W/cm^2. Notably, the focal beam diameter is typically calculated by the structural characteristics of the transducer, as $\frac{\lambda R}{D}$, where λ is the wavelength (defined by the operating frequency and speed of sound in the medium). The temperature evolution during sonication and having a 60-s cooling time was monitored using MR thermometry. The proton resonance frequency shift (PRFS) method [5] was used for calculating the temperature changes in a Region of Interest (ROI) set within the phantom. This technique correlates the PRF change occurring during changes in the subject's temperature with the observed differences in phase between an initial image obtained at a baseline temperature (φ_0) and subsequent images obtained at various time spots (φ) during and after sonication. These phase differences ($\varphi - \varphi_0$) can be converted into temperature changes (ΔT) as follows [5]:

$$\Delta T = \frac{\varphi - \varphi_0}{\gamma \, \alpha \, B_0 \, TE} \quad [1]$$

where α is the PRF change coefficient, γ is the gyromagnetic ratio, B_0 is the magnetic field strength (3T), and TE is the echo time. The magnitude of α was set at 0.0094 ppm/ºC [40,41].

The temperature changes in the ROI were calculated based on a pixel-by-pixel analysis of the phase differences. Coronal and axial thermal maps were derived from 2D Fast Low Angle Shot (FLASH) images acquired with the following parameters: Repetition time (TR) = 25 ms, Echo time (TE) = 10 ms, Field of view (FOV) = 280×280 mm^2, slice thickness = 3 mm, Number of excitations (NEX) = 1, Flip angle (FA) = 30º, Echo train length (ETL) = 1, matrix size = 96 x 96, pixel bandwidth = 250 Hz/pixel, and acquisition time/slice = 2.4 s. Color maps were produced by color-coding the measured temperatures from the minimum to the maximum value from yellow to red.

3. RESULTS

Indicative CT images of the two skull mimics made of ABS and Resin are presented in Fig. 3, revealing the presence of some air-filled pores within the ABS sample. On the contrary, the Resin sample appears completely solid. This finding was useful in interpreting the results of the follow-up FUS experiments.

The results of FUS sonications are summarized in Table 1, along with the ultrasonic attenuation coefficients for the Resin and ABS thermoplastics, as measured using a common transmission-through immersion technique [42]. Note that a single 60-s sonication at acoustic power of 90 W, corresponding to a focal intensity of about 1583 W/cm^2, without any obstacle in the beam path (free field), as well as through the 1-mm Resin insert, heated up the agar-based material from room temperature up to ablative temperatures (> 60 ºC). In fact, sonication in free field resulted in a maximum recorded focal temperature of 93 ºC. Indicative thermal maps acquired at various time spots during and after heating without any obstacle intervening

in the beam path are shown in Fig. 4. The corresponding results for similar sonications through the ABS and Resin skulls (of varying thickness) are shown in Fig. 5. Note that the ultrasonic waves were strongly blocked by the ABS skull resulting in zero temperature increase within the phantom volume. Conversely, detachable heating was observed in the case of the Resin skull, with the baseline temperature of 37 ºC increasing to almost 47ºC at the focal area but remaining at hyperthermia levels. Note also that heating through the ABS sample resulted in a slight temperature rise of 1.8 ºC in the phantom adjacent to the skull mimic surface interfering with the beam, revealing a negligible heat accumulation in the region.

The use of a thin skull phantom of 1 mm thickness provided significantly better results in terms of trans-skull ultrasonic transmission and heating of the phantom material compared to the thick one. The temperature profile of Fig. 6A reveals a maximum focal temperature of 70 ºC, compared to that of 47 ºC achieved by sonication through the varying thickness Resin skull. Fig. 6B presents indicative thermal maps acquired in both axial and coronal planes, showing efficient beam penetration and heating of the phantom material at ablative temperatures.

4. DISCUSSION

In the current study, we examined the heating capabilities of a custom-made 1-MHz single-element spherically focused transducer through geometrically accurate skull phantoms embedding a brain-tissue mimicking material based on MR thermometry measurements. The study further provides insights on the feasibility of precisely delivering FUS through a skull mimic of 1-mm thickness as a potential method for the treatment of unresectable brain tumors. At the same time, the findings of such experiments play an essential role in the protocol optimization of MRI-compatible FUS robotic systems [43–54].

A single FUS sonication at focal acoustic intensities close to 1580 W/cm^2 for 60 s in free field heated up the agar phantom to ablative temperatures. Ablative temperatures were also produced in the case of the 1-mm Resin insert, which allowed efficient ultrasonic penetration

(Fig. 6). The focal temperature change was reduced to 60 % (ΔT = 33 ˚C) of that achieved without any obstacle in the beam path (ΔT = 55 ˚C). These findings are consistent with what has been observed in prior animal research, where tFUS at frequencies close to 1 MHz was established as an efficient modality for applications in small animal models, such as mice and rabbits [14,15], whose skull thickness is comparable to that of the thin Resin insert. In this regard, single-element transducers may also be effective for therapeutic applications in toddles through the temporal bone, which is in the order of 2 mm in thickness [55], thus potentially constituting an effective acoustic window.

On the contrary, in the presence of the varying thickness Resin insert the temperature change was decreased to about 18 % (ΔT ≈ 10 ˚C) of that achieved in free field, whereas no heating was detected in the phantom bulk during sonication through the ABS skull. Being consistent with prior research, these findings validate that single-element transducers are incapable of effectively directing the beam through the human cranium to cause thermal heating of brain tissue unless a thorough correction method is implemented.

The Resin and ABS phantoms showed a completely different response to FUS heating. Since the defocusing effects of the varying skull thickness are considered similar for the two phantoms, this difference can be attributed to the higher ultrasonic attenuation (Table 1) and porosity of the ABS material. In fact, investigation of the radiographic behavior of the two thermoplastic materials revealed air gaps within the ABS sample. The ABS phantom was manufactured using the Fused Deposition Modeling (FDM) method, which constitutes a thermal technique that naturally incorporates pores into the manufactured specimens, thus unavoidably enhancing ultrasonic attenuation within the phantom's interior.

There are several energy loss mechanisms affecting the ultrasonic propagation through the real skull. Intense reflections of the propagating waves occur at the interface between the skull bone and outside fluid [56,57]. Within the skull bone, the acoustic wave is strongly scattered

due to its interaction with the internal microstructure of the skull with conversions between longitudinal and shear modes taking place [56,57]. The bone also absorbs some of the wave energy, which it then transforms into heat. Despite the complexity of quantifying the energy loss induced by each individual attenuation mechanism, it has been shown that the primary causes of attenuation are reflection, scattering, and mode conversion, whereas absorption is responsible for only a small part of the total attenuation [56]. On the contrary, in soft tissues, the wave attenuation is mostly caused by the absorption and conversion of ultrasonic energy into heat. Accordingly, the skull-induced spreading and defocusing of the beam reduces the penetration depth and energy deposited in tissue significantly.

The current study did not investigate the individual energy loss mechanisms occurring during propagation of ultrasonic waves through the skull phantoms. This area of investigation could be the subject of a future study. However, the study did perform a qualitative evaluation on the effect of the varying skull thickness on ultrasonic transmission and intracranial energy distribution. Although both Resin skulls allowed for sufficient beam focusing within the phantom, FUS sonication through the thin skull insert generated significantly higher temperatures (50 %), heating up a larger phantom area. Furthermore, a reduction in the beam's penetration depth was observed in the presence of the varying thickness insert, confining the heating in a narrower and shallower area of the phantom. These observations can be attributed to the acoustic aberration induced by the varying skull thickness, causing considerable energy losses and shifting of the focal spot [27].

An important consideration related to the highly aberrating nature of the human skull is the potential for thermal injuries of the skull and adjacent healthy tissues [56,58]. The PRFS-based MR thermometry method employed in this study does not allow for measuring the skull heating directly [5]. This method relies on the detection of temperature-induced changes in the resonance frequency of water protons, and thus, a large number of protons is needed to create

strong MRI signal for high quality imaging and the production of thermal maps [5]. Similarly, temperature monitoring within the thermoplastic materials that do not contain sufficient water protons is not feasible. However, the specific thermometry method can be used for monitoring the heat accumulation adjacent to the skull to assess potential damage of brain tissue [59].

In this study, there was evidence of a slight heat accumulation around the ABS skull insert. Specifically, a marginal temperature change of 1.8 ˚C was produced close to the skull. In the real scenario, it is expected that the complex porous structure of the cranium will more strongly attenuate the acoustic waves, potentially confining them within the skull bone, thus raising the safety concern of unwanted skull heating [60]. In this regard, an apparent limitation of the proposed skull model is its solid infill, which makes it a very simplistic model in comparison to the real cranium consisting of both cortical and cancellous bone compartments. Notably, studies have showed that during trans-skull heating, active cooling of the skull surface is essential to protecting the bone and surrounding tissues from thermal damages [56]. The Insightec's Exablate Neuro; the only FDA-approved MRI-guided FUS device for brain applications, performs active cooling of the cranium and scalp by water circulation [61]. In addition, the transmission efficacy can be enhanced by selecting a proper transducer frequency, further contributing to the mitigation of such risks [23].

Phased array ultrasonic transducers are predominantly used in the context of clinical tFUS since they allow for targeting deep brain regions with the required precision to produce the desired therapeutic effects without harming healthy tissue, thus meeting the clinical requirements [62]. They also contribute towards delivering the ultrasonic energy over a large skull area, thus reducing the possibility for excessive heat accumulation in the skull [63]. However, it could be argued that their main limitation compared to single-element transducers is their increased complexity and expensiveness, as well as the need to use advanced signal processing algorithms to control the individual elements of the array [62].

The present findings provide initial evidence on the feasibility of the proposed approach of treating recurrent, multiple, or deep-seated brain tumors that cannot be removed surgically by FUS ablation through a 1-mm biocompatible skull insert. Temporal replacement of a small skull part with a 1-mm skull mimic is expected to allow the development of high temperatures of up to 90 ºC within the tumor and repeated therapies to be performed. This approach exploits the unique advantages of single-element transducers (less expensive, more ergonomic, etc.) over phased arrays, thus addressing the concerns regarding insufficient trans-skull ultrasonic penetration and focal temperature increase. These benefits come at the cost of performing a small craniotomy, which is still far less invasive compared to the standard surgical therapy. Remarkably, the highest temperatures achieved through intact skull with phased arrays have been so far limited to around 60 °C [64]. Overall, a more comprehensive preclinical experimentation is required to demonstrate reproducibility of these promising results and the clinical potential of the proposed approach.

In conclusion, a variety of tFUS applications has been successfully performed using single-element FUS transducers mostly in the preclinical setting. The wider adoption and clinical translation of this modality is limited by challenges related to inefficient trans-skull ultrasonic transmission and relevant safety concerns. Although further research is needed to fully exploit the potential of this modality, the preclinical investigation of transcranial ultrasonic propagation from single-element transducers was limited to numerical studies in the context of low intensity tFUS neuromodulation. Therefore, experimental studies involving anthropomorphic phantoms such as the current one could be a valuable tool for accelerating the establishment of a wider range of tFUS applications (including tFUS ablation) potentially working supplementary to numerical studies.

Table 1: The focal temperature change (ΔT) recorded in the phantom using acoustical power of 90 W for 60 s at a focal depth of 40 mm with no plastic, as well as with the ABS and RESIN skull mimics intervening the beam.

Skull phantom	Thickness (mm)	ΔT (ºC)	Ultrasonic attenuation (dB/cm)
NO	-	55	-
ABS	6 (average)	1.8	37.7 ± 1.8
Resin	6 (average)	9.7	8.4 ± 0.2
Resin thin	1	33	

FIGURE CAPTIONS

Fig. 1 (A) The two-compartment skull phantom filled with the tissue mimicking agar gel. **(B)** The skull phantom with the circular insert being removed from the lateral side exposing the agar-based brain tissue phantom. **(C)** Comparison between the 1-mm and varying thickness Resin inserts.

Fig. 2 Photo of the experimental setup for FUS sonications in the brain tissue/skull phantom as arranged on the MRI table of the 3T scanner, with the various components indicated.

Fig. 3 CT images of the Resin and ABS samples acquired with a tube voltage of 120 kV, current of 410 mA, and a slice thickness of 1.25 mm.

Fig. 4 Coronal thermal maps derived from FLASH images during sonication in the phantom at acoustic power of 90 W for 60 s at a focal depth of 40 mm, without any obstacle in the beam path.

Fig. 5 Coronal thermal maps derived from FLASH images during sonication at acoustic power of 90 W for 60 s at a focal depth of 40 mm through the ABS and Resin skull inserts.

Fig. 6 (A) Temperature increase versus time during phantom sonication throught the 1-mm Resin skull at acoustic power of 90 W for 60 s at a focal depth of 40 mm. **(B)** Indicative axial and coronal thermal maps acquired during sonication.

DECLARATIONS

CONFLICT OF INTERESTS:

Authors declare no conflict of interest.

DATA AVAILABILITY:

All data generated or analysed in the present study are available from the corresponding author on reasonable request.

CODE AVAILABILITY:

Not applicable.

CONSENT TO PARTICIPATE:

Not applicable. The study does not include data on patients.

CONSENT FOR PUBLICATION:

Not applicable. The study does not include data on patients.

COMPLIANCE WITH ETHICAL STANDARDS:

Not applicable. The study does not involve animals or human participants.

REFERENCES

[1] Nicodemus NE, Becerra S, Kuhn TP, Packham HR, Duncan J, Mahdavi K, et al. Focused transcranial ultrasound for treatment of neurodegenerative dementia. Alzheimer's Dement Transl Res Clin Interv 2019;5:374–81. https://doi.org/10.1016/j.trci.2019.06.007.

[2] Wasielewska JM, White AR. "Focused Ultrasound-mediated Drug Delivery in Humans – a Path Towards Translation in Neurodegenerative Diseases." Pharm Res 2022;39:427–39. https://doi.org/10.1007/s11095-022-03185-2.

[3] Zhang T, Pan N, Wang Y, Liu C, Hu S. Transcranial Focused Ultrasound Neuromodulation: A Review of the Excitatory and Inhibitory Effects on Brain Activity in Human and Animals. Front Hum Neurosci 2021;15:749162. https://doi.org/10.3389/fnhum.2021.749162.

[4] Hynynen K, Clement GT, McDannold N, Vykhodtseva N, King R, White PJ, et al. 500-Element ultrasound phased array system for noninvasive focal surgery of the brain: A preliminary rabbit study with ex vivo human skulls. Magn Reson Med 2004;52:100–7. https://doi.org/10.1002/mrm.20118.

[5] Rieke V, Pauly KB. MR Thermometry. J Magn Reson Imaging 2008;27:376–90. https://doi.org/10.1002/jmri.21265.MR.

[6] Arulpragasam AR, Wout-Frank M van 't, Barredo J, Faucher CR, Greenberg BD, Philip NS. Low Intensity Focused Ultrasound for Non-invasive and Reversible Deep Brain Neuromodulation—A Paradigm Shift in Psychiatric Research. Front Psychiatry 2022;13. https://doi.org/10.3389/fpsyt.2022.825802.

[7] Kima H, Chiu A, Lee SD, Fischer K, Yoo S-S. Focused Ultrasound-mediated Non-

invasive Brain Stimulation: Examination of Sonication Parameters. Brain Stimul 2014;7:748–56. https://doi.org/10.1016/j.brs.2014.06.011.

[8] Focused ultrasound modulates region-specific brain activity. Neuroimage 2011;56:1267–1275. https://doi.org/10.1016/j.neuroimage.2011.02.058.

[9] Kim H, Park MY, Lee SD, Lee W, Chiua A, Yoo S-S. Suppression of EEG visual-evoked potentials in rats via neuromodulatory focused ultrasound. Neuroreport 2015;26:211–5. https://doi.org/10.1097/WNR.0000000000000330.

[10] Wattiez N, Constans C, Deffieux T, Daye PM, Tanter M, Aubry J-F, et al. Transcranial ultrasonic stimulation modulates single-neuron discharge in macaques performing an antisaccade task. Brain Stimul 2017;10:1024–31. https://doi.org/10.1016/j.brs.2017.07.007.

[11] Lee W, Kim HC, Jung Y, Chung YA, Song IU, Lee JH, et al. Transcranial focused ultrasound stimulation of human primary visual cortex. Sci Rep 2016;6:1–12. https://doi.org/10.1038/srep34026.

[12] Lee W, Kim S, Kim B, Lee C, Chung YA, Kim L, et al. Non-invasive transmission of sensorimotor information in humans using an EEG/focused ultrasound brain-to-brain interface. PLoS One 2017;12:1–20. https://doi.org/10.1371/journal.pone.0178476.

[13] Choi JJ, Selert K, Gao Z, Samiotaki G, Baseri B, Konofagou EE. Noninvasive and Localized Blood—Brain Barrier Disruption using Focused Ultrasound can be Achieved at Short Pulse Lengths and Low Pulse Repetition Frequencies. J Cereb Blood Flow Metab 2011;31:725–37. https://doi.org/10.1038/jcbfm.2010.155.

[14] Wang S, Samiotaki G, Olumolade O, Feshitan JA, Konofagou EE. Microbubble type and distribution dependence of focused ultrasound-induced blood-brain barrier opening.

Ultrasound Med Biol 2014;40:130–7. https://doi.org/10.1016/j.ultrasmedbio.2013.09.015.

[15] Hynynen K, Mcdannold N, Sheikov NA, Jolesz FA, Vykhodtseva N. Local and reversible blood – brain barrier disruption by noninvasive focused ultrasound at frequencies suitable for trans-skull sonications. Neuroimage 2005;24:12–20. https://doi.org/10.1016/j.neuroimage.2004.06.046.

[16] Samiotaki G, Karakatsani ME, Buch A, Papadopoulos S, Wu SY, Jambawalikar S, et al. Pharmacokinetic analysis and drug delivery efficiency of the focused ultrasound-induced blood-brain barrier opening in non-human primates. Magn Reson Imaging 2017;37:273–81. https://doi.org/10.1016/j.mri.2016.11.023.

[17] Wu SY, Aurup C, Sanchez CS, Grondin J, Zheng W, Kamimura H, et al. Efficient blood-brain barrier opening in primates with neuronavigation-guided ultrasound and real-time acoustic mapping. Sci Rep 2018;8:1–11. https://doi.org/10.1038/s41598-018-25904-9.

[18] Karakatsani ME, Samiotaki G, Downs ME, Ferrera VP, Konofagou EE. Targeting Effects on the Volume of the Focused Ultrasound Induced Blood-Brain Barrier Opening in Non-Human Primates in vivo. IEEE Trans Ultrason Ferroelectr Freq Control 2017;64:798–810. https://doi.org/10.1109/TUFFC.

[19] Yoon K, Lee W, Croce P, Cammalleri A, Yoo S-S. Multi-resolution Simulation of Focused Ultrasound Propagation through Ovine Skull from a Single-element Transducer. Phys Med Biol 2019;63:105001. https://doi.org/10.1088/1361-6560/aabe37.

[20] Huang Y, Wen P, Song B, Li Y. Numerical investigation of the energy distribution of Low-intensity transcranial focused ultrasound neuromodulation for hippocampus. Ultrasonics 2022;124:106724. https://doi.org/10.1016/j.ultras.2022.106724.

[21] Deffieux T, Konofagou EE. Numerical study of a simple transcranial focused ultrasound system applied to blood-brain barrier opening. IEEE Trans Ultrason Ferroelectr Freq Control 2010;57:2637–53. https://doi.org/10.1109/TUFFC.2010.1738.

[22] Seo H, Huh H, Lee EH, Park J. Numerical Evaluation of the Effects of Transducer Displacement on Transcranial Focused Ultrasound in the Rat Brain. Brain Sci 2022;12:216. https://doi.org/10.3390/brainsci12020216.

[23] Chen M, Peng C, Wu H, Huang CC, Kim T, Traylor Z, et al. Numerical and experimental evaluation of low-intensity transcranial focused ultrasound wave propagation using human skulls for brain neuromodulation. Med Phys 2023;50:38–49. https://doi.org/10.1002/mp.16090.

[24] Brinker ST, Preiswerk F, McDannold NJ, Parker KL, Mariano TY. Virtual Brain Projection for Evaluating Trans-Skull Beam Behavior of Transcranial Ultrasound Devices. Ultrasound Med Biol 2019;45:1850–6. https://doi.org/10.1016/j.ultrasmedbio.2019.03.009.

[25] Maimbourg G, Houdouin A, Deffieux T, Tanter M. 3D-printed adaptive acoustic lens as a disruptive technology for transcranial ultrasound therapy using single-element transducers. Phys Med Biol 2018;63:1–14. https://doi.org/10.1088/1361-6560/aaa037

[26] Ferri M, Bravo JM, Redondo J, Sanchez-Perez JV. Enhanced Numerical Method for the Design of 3-D-Printed Holographic Acoustic Lenses for Aberration Correction of Single-Element Transcranial Focused Ultrasound. Ultrasound Med Biol 2019;45:867–84. https://doi.org/ 10.1016/j.ultrasmedbio.2018.10.022.

[27] Pouliopoulos AN, Wu SY, Burgess MT, Karakatsani ME, Kamimura HAS, Konofagou EE. A Clinical System for Non-invasive Blood–Brain Barrier Opening Using a Neuronavigation-Guided Single-Element Focused Ultrasound Transducer. Ultrasound

Med Biol 2020;46:73–89. https://doi.org/10.1016/j.ultrasmedbio.2019.09.010.

[28] Marquet F, Teichert T, Wu SY, Tung YS, Downs M, Wang S, et al. Real-time, transcranial monitoring of safe blood-brain barrier opening in non-human primates. PLoS One 2014;9:1–11. https://doi.org/10.1371/journal.pone.0084310.

[29] Antoniou A, Damianou C. MR relaxation properties of tissue-mimicking phantoms. Ultrasonics 2022;119. https://doi.org/10.1016/j.ultras.2021.106600.

[30] Mackle EC, Shapey J, Maneas E, Saeed SR, Bradford R, Ourselin S, et al. Patient-specific polyvinyl alcohol phantom fabrication with ultrasound and x-ray contrast for brain tumor surgery planning. J Vis Exp 2020:e61344. https://doi.org/10.3791/61344.

[31] Tan ETW, Ling JM, Dinesh SK. The feasibility of producing patient-specific acrylic cranioplasty implants with a low-cost 3D printer. J Neurosurg 2016;124:1531–7. https://doi.org/10.3171/2015.5.JNS15119

[32] Hadjisavvas V, Mylonas N, Ioannides K, Damianou C. An MR-compatible phantom for evaluating the propagation of high intensity focused ultrasound through the skull. AIP Conf Proc 2012;1481:119–24. https://doi.org/10.1063/1.4757321.

[33] Menikou G, Dadakova T, Pavlina M, Bock M, Damianou C. MRI compatible head phantom for ultrasound surgery. Ultrasonics 2015;57:144–52. https://doi.org/10.1016/j.ultras.2014.11.004.

[34] Menikou G, Yiannakou M, Yiallouras C, Ioannides C, Damianou C. MRI-compatible breast/rib phantom for evaluating ultrasonic thermal exposures. Int J Med Robot Comput Assist Surg 2018;14:1–12. https://doi.org/10.1002/rcs.1849.

[35] Drakos T, Antoniou A, Evripidou N, Alecou T, Giannakou M, Menikou G, et al. Ultrasonic Attenuation of an Agar, Silicon Dioxide, and Evaporated Milk Gel Phantom.

J Med Ultrasound 2021;29:239–49. https://doi.org/10.4103/JMU.JMU.

[36] Menikou G, Damianou C. Acoustic and thermal characterization of agar based phantoms used for evaluating focused ultrasound exposures. J Ther Ultrasound 2017;5. https://doi.org/10.1186/s40349-017-0093-z.

[37] Antoniou A, Georgiou L, Christodoulou T, Panayiotou N, Ioannides C, Zamboglou N, et al. MR relaxation times of agar-based tissue-mimicking phantoms. J Appl Clin Med Phys 2022:213533. https://doi.org/10.1002/acm2.13533.

[38] Drakos T, Giannakou M, Menikou G, Constantinides G, Damianou C. Characterization of a soft tissue-mimicking agar/wood powder material for MRgFUS applications. Ultrasonics 2021;113: 10635. https://doi.org/10.1016/j.ultras.2021.106357.

[39] Antoniou A, Georgiou L, Evripidou N, Ioannides C, Damianou C. Challenges regarding MR compatibility of an MRgFUS robotic system. J Magn Reson 2022;344:107317. https://doi.org/10.1016/j.jmr.2022.107317.

[40] Peters RD, Hinks RS, Henkelman RM. Heat-source orientation and geometry dependence in proton-resonance frequency shift magnetic resonance thermometry. Magn Reson Med 1999;41:909–18. https://doi.org/10.1002/(SICI)1522-2594(199905)41:5<909::AID-MRM9>3.0.CO;2-N.

[41] Bing C, Staruch R, Tillander M, Köhler MO, Mougenot C, Ylihautala M, et al. Drift correction for accurate PRF shift MR thermometry during mild hyperthermia treatments with MR-HIFU. Int J Hyperth 2017;32:673–87. https://doi.org/10.1080/02656736.2016.1179799.

[42] Antoniou A, Damianou C. Feasibility of ultrasonic heating through skull phantom using single-element transducer. J Med Ultrasound 2023.

https://doi.org/10.4103/jmu.jmu_3_23.

[43] Epaminonda E, Drakos T, Kalogirou C, Theodoulou M, Yiallouras C, Damianou C. MRI guided focused ultrasound robotic system for the treatment of gynaecological tumors. Int J Med Robot Comput Assist Surg 2016;12:46–52. https://doi.org/10.1002/rcs.1653.

[44] Yiannakou M, Menikou G, Yiallouras C, Ioannides C, Damianou C. MRI guided focused ultrasound robotic system for animal experiments. Int J Med Robot Comput Assist Surg 2017;13:e1804. https://doi.org/10.1002/rcs.1804.

[45] Menikou G, Yiallouras C, Yiannakou M, Damianou C. MRI-guided focused ultrasound robotic system for the treatment of bone cancer. Int J Med Robot Comput Assist Surg 2017;13:1–11. https://doi.org/10.1002/rcs.1753.

[46] Antoniou A, Giannakou M, Evripidou N, Evripidou G, Spanoudes K, Menikou G, et al. Robotic system for magnetic resonance guided focused ultrasound ablation of abdominal cancer. Int J Med Robot Comput Assist Surg 2021;17. https://doi.org/10.1002/rcs.2299.

[47] Drakos T, Giannakou M, Menikou G, Filippou A, Evripidou N, Spanoudes K, et al. MRI-Guided Focused Ultrasound Robotic System for Preclinical use. J Vet Med Anim Sci 2021;4:1–11.

[48] Damianou C, Giannakou M, Menikou G, Ioannou L. Magnetic resonance imaging-guided focused ultrasound robotic system with the subject placed in the prone position. Digit Med 2020;6:24–31. https://doi.org/10.4103/digm.digm_2_20.

[49] Antoniou A, Giannakou M, Evripidou N, Stratis S, Pichardo S, Damianou C. Robotic system for top to bottom MRgFUS therapy of multiple cancer types. Int J Med Robot Comput Assist Surg 2022. https://doi.org/10.1002/rcs.2364.

[50] Giannakou M, Antoniou A, Damianou C. Preclinical robotic device for magnetic resonance imaging guided focussed ultrasound. Int J Med Robot Comput Assist Surg 2023;19:e2466. https://doi.org/10.1002/rcs.2466.

[51] Antoniou A, Giannakou M, Georgiou E, Kleopa KA, Damianou C. Robotic device for transcranial focussed ultrasound applications in small animal models. Int J Med Robot Comput Assist Surg 2022:1–11. https://doi.org/10.1002/rcs.2447.

[52] Filippou A, Evripidou N, Damianou C. Robotic system for magnetic resonance imaging-guided focused ultrasound treatment of thyroid nodules. Int J Med Robot 2023. https://doi.org/10.1002/rcs.2525.

[53] Giannakou M, Drakos T, Menikou G, Evripidou N, Filippou A, Spanoudes K, et al. Magnetic resonance image-guided focused ultrasound robotic system for transrectal prostate cancer therapy. Int J Med Robot 2021;7:e2237. https://doi.org/10.1002/rcs.2237.

[54] Yiallouras C, Yiannakou M, Menikou G, Damianou C. A multipurpose positioning device for magnetic resonance imaging-guided focused ultrasound surgery. Digit Med 2017;3:138–44. https://doi.org/10.4103/digm.digm_33_17.

[55] Rahne T, Svensson S, Lagerkvist H, Holmberg M, Plontke SK, Wenzel C. Assessment of Temporal Bone Thickness for Implantation of a New Active Bone-Conduction Transducer. Otol Neurotol 2021;42:278–84. https://doi.org/10.1097/MAO.0000000000002919.

[56] Pinton G, Aubry J, Bossy E, Muller M, Pernot M. Attenuation, scattering ,and absorption of ultrasound in the skull bone 2012;39:299–307. https://doi.org/10.1118/1.3668316.

[57] Fry FJ, Barger JE. Acoustical properties of the human skull. J Acoust Soc Am

1978;63:1576–90. https://doi.org/10.1121/1.381852.

[58] Pichardo S, Sin VW, Hynynen K. Multi-frequency characterization of the speed of sound and attenuation coefficient for longitudinal transmission of freshly excised human skulls. Phys Med Biol 2011;56:219–50. https://doi.org/10.1088/0031-9155/56/1/014.

[59] McDannold N, King RL, Hynynen K. MRI monitoring of heating produced by ultrasound absorption in the skull: in vivo study in pigs. Magn Reson Med 2004;51:1061–5. https://doi.org/10.1002/mrm.20043.

[60] Chen M, Peng C, Kim T, Chhatbar P, Muller M, Feng W, et al. Biosafety of low-intensity pulsed transcranial focused ultrasound brain stimulation: a human skull study. Heal. Monit. Struct. Biol. Syst. XV, 2021, p. 34. https://doi.org/10.1117/12.2582487.

[61] Sheehan J, Monteith S, Wintermark M. Transcranial MR-Guided Focused Ultrasound: A Review of the Technology and Neuro Applications. AJR Am J Roentgenol 2015;205:150–9. https://doi.org/10.2214/AJR.14.13632.

[62] Hynynen K, Jones RM. Image-guided ultrasound phased arrays are a disruptive technology for non-invasive therapy. Phys Med Biol 2016;61:206–248. https://doi.org/10.1088/0031-9155/61/17/R206.

[63] Sun J, Hynynen K. The potential of transskull ultrasound therapy and surgery using the maximum available skull surface area. J Acoust Soc Am 1999;105:2519–27. https://doi.org/10.1121/1.426863.

[64] Wu P, Lin W, Li KH, Lai HC, Lee MT, Tsai KWK, et al. Focused Ultrasound Thalamotomy for the Treatment of Essential Tremor: A 2-Year Outcome Study of Chinese People. Front Aging Neurosci 2021;13:1–8. https://doi.org/10.3389/fnagi.2021.697029.

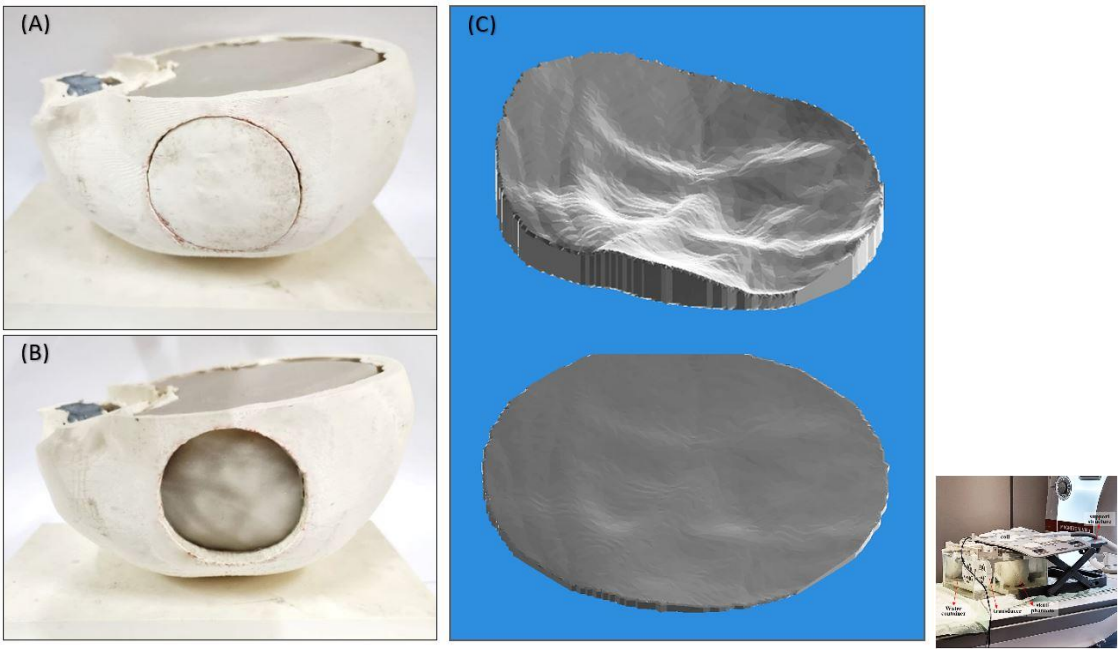

Figure 1

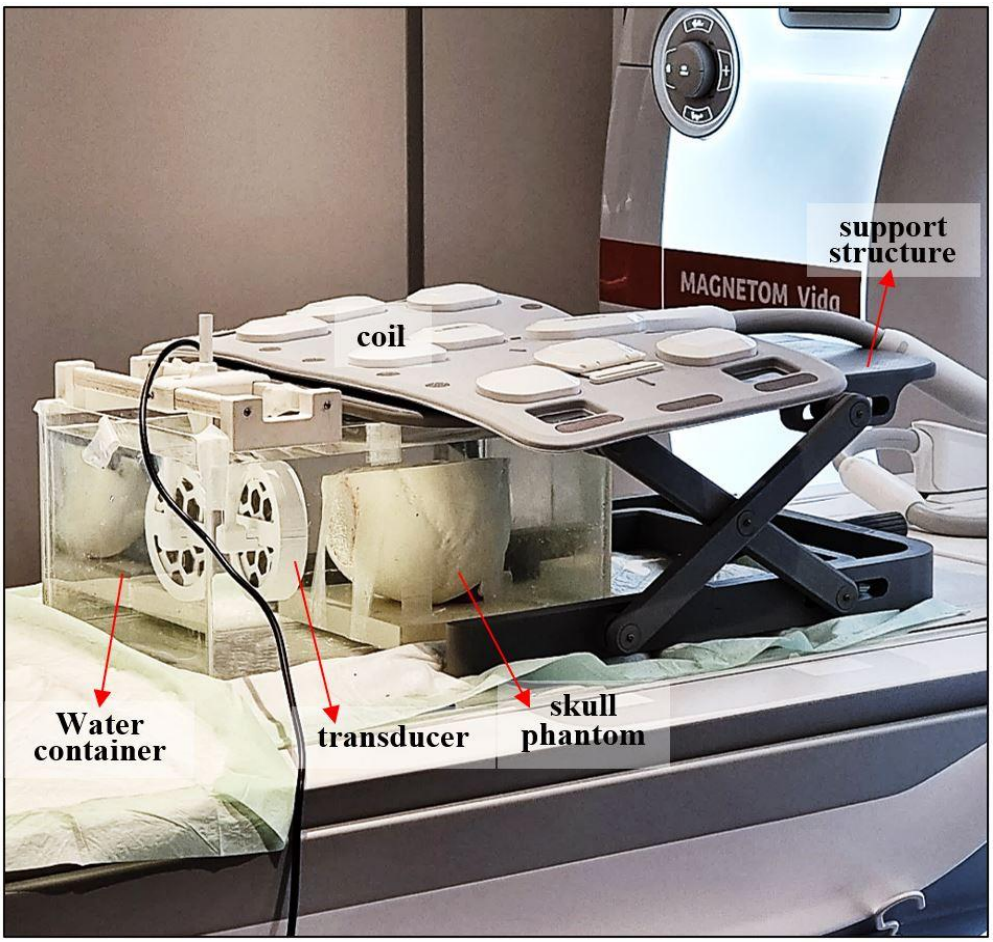
support
structure
MAGNETOM Vida
coil
Water
container
transducer
skull
phantom

Figure 2

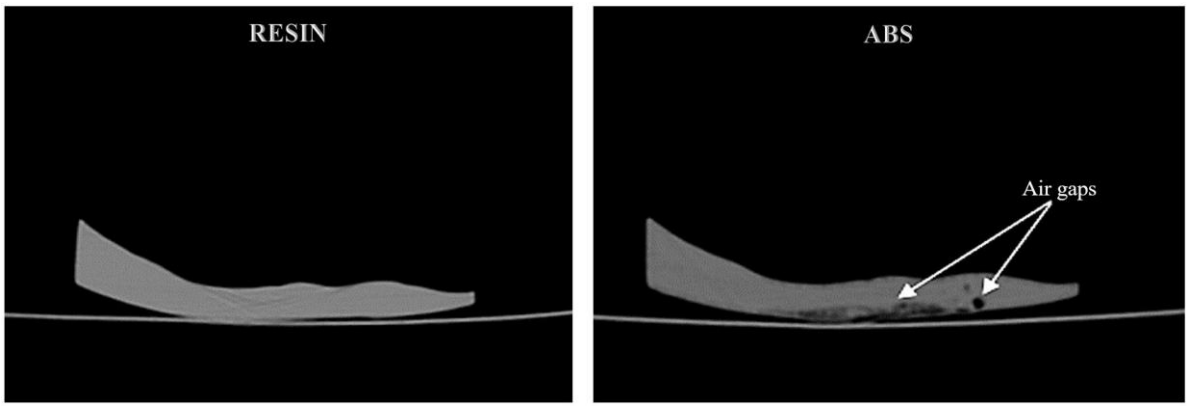

Figure 3

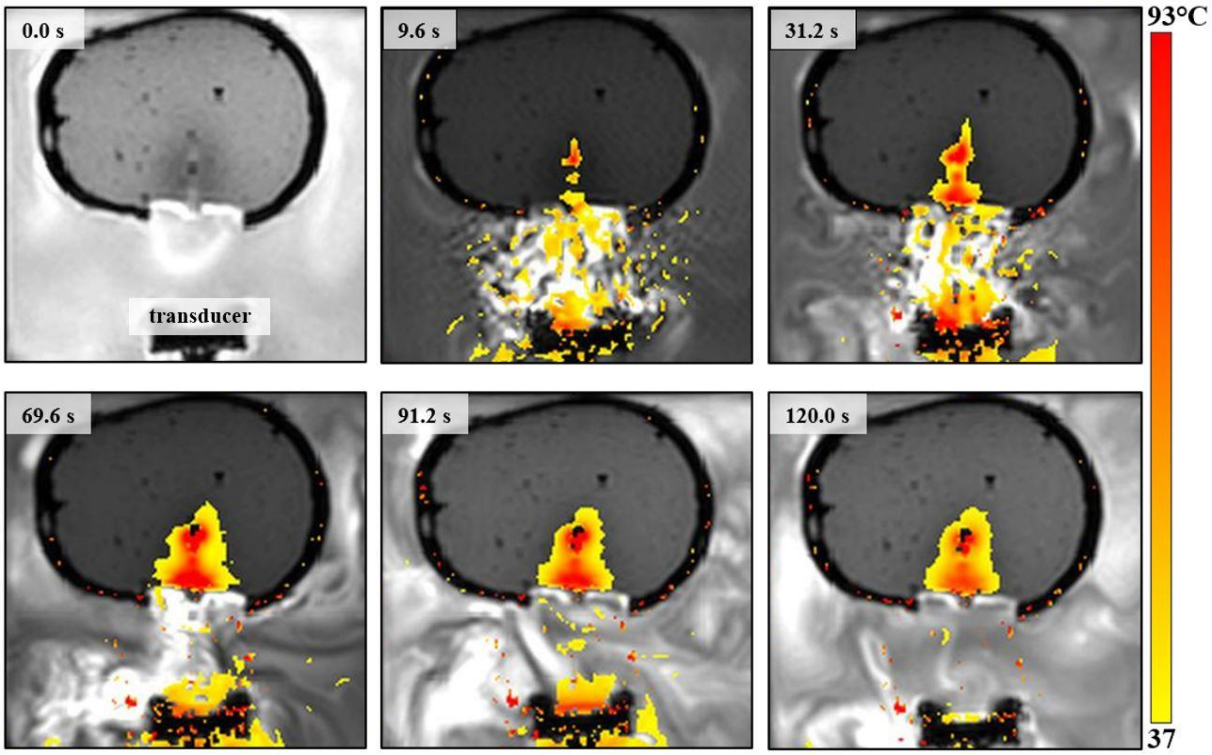

Figure 4

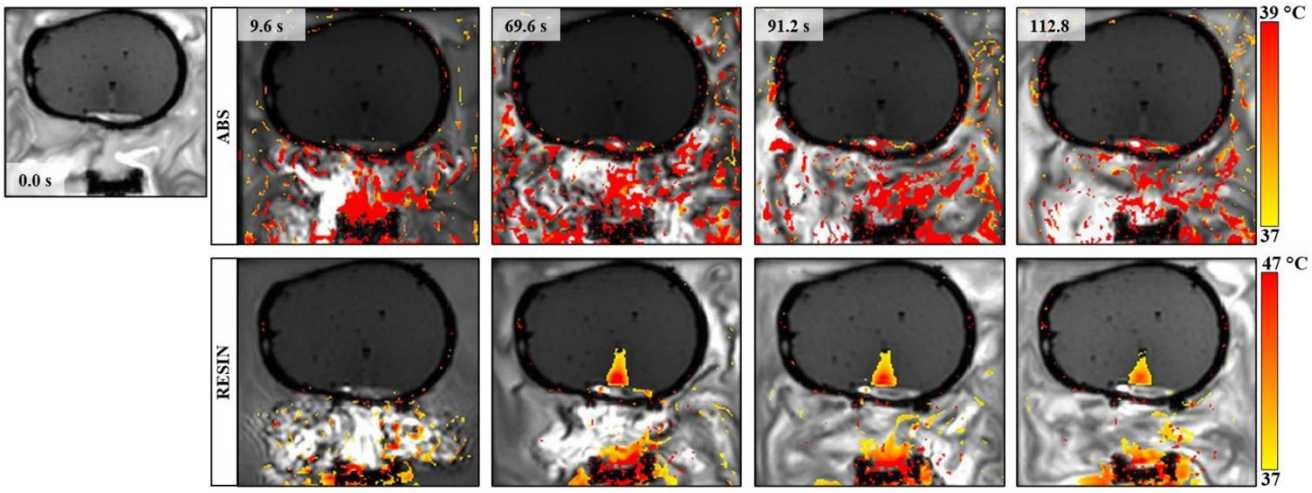

Figure 5

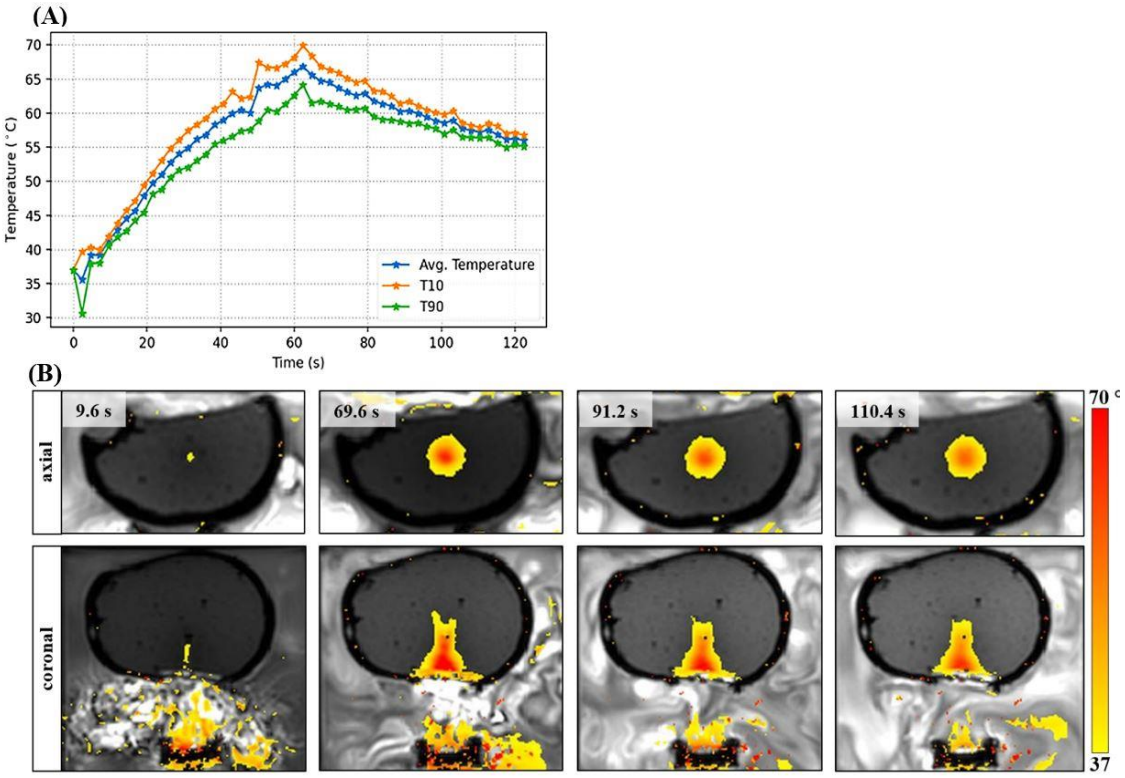
(A)
Temperature (°C)
Time (s)
Avg. Temperature
T10
T90
(B)
axial
coronal
9.6 s
69.6 s
91.2 s
110.4 s
70 °C
37

Figure 6

High Quality Agar and Polyacrylamide Tumour Mimicking Phantom Models for MR-guided Focused Ultrasound Applications

Panagiotis Sofokleous[1], Christakis Damianou[1]*.

[1]Department of Electrical Engineering, Computer Engineering, and Informatics, Cyprus University of Technology, Limassol, Cyprus.

*Corresponding author at: Department of Electrical Engineering, Computer Engineering, and Informatics, Cyprus University of Technology, 30 Archbishop Kyprianou Street, 3036 Limassol, Cyprus. Email: christakis.damianou@cut.ac.cy

ABSTRACT

Background: Tissue mimicking phantoms (TMPs) have been used extensively in clinical and non-clinical settings to simulate the thermal effects of focus ultrasound (FUS) technology in real tissue or organs. With recent technological developments in the FUS technology and its monitoring/guided techniques such as Ultrasound-guided FUS (USgFUS) and MR-guided FUS (MRgFUS) the need of TMPs are more important than ever to ensure the safety of the patients before being treated with FUS for a variety of diseases (e.g., cancer or neurological). The purpose of this study was to prepare a tumour mimicking phantom (TUMP) model that can simulate competently a tumour that is surrounded by healthy tissue.

Methods: The TUMP models were prepared by using polyacrylamide (PAA) and agar solutions enrich with MR contrast agents (silicon dioxide & glycerol), and the thermosensitive component bovine serum albumin (BSA) that can alter its physical properties once thermal change is detected, therefore offering real-time visualization of the applied FUS ablation in the TUMPs models. To establish if these TUMPs are good candidates to be used in thermoablation, their thermal properties were characterised with a custom-made FUS system in the lab and in an MRI setup with MR-thermometry. The BSA

protein's coagulation temperature was adjusted at 55°C by setting the pH of the PAA solution to 4.5, therefore simulating the necrosis temperature of tissue.

Results: The experiments carried out showed that the TUMP models prepared by PAA can change colour from transparent to cream white due to the BSA protein coagulation caused by the thermal stress applied. The TUMP models offered a good MRI contrast between the TMPs and the TUMPs including real-time visualisation of the ablation area due to the BSA protein coagulation. Also, the *T2*-weighted MR images obtained showed a significant change in *T2* when the BSA protein is thermally coagulated. MR thermometry maps demonstrated that the suggested TUMP models may successfully imitate a tumour that is present in soft tissue.

Conclusions: The TUMP models developed in this study have numerous uses in the testing and calibration of FUS equipment including the simulation and validation of thermal therapy treatment plans with FUS or MRgFUS in oncology applications.

KEYWORDS: Tumour, Phantom, Agar, Polyacrylamide, FUS, MRI

HIGHLIGHTS

- Tumour mimicking phantom (TUMP) models for FUS & MRgFUS application evaluation.
- Agar, Polyacrylamide and BSA protein are utilised to prepare the TUMP models.
- Monitoring of FUS thermal patterns in the TUMP models through MR thermometry.

1. INTRODUCTION

Image-guided thermal ablation technology has grown exponentially in the last decade as a minimally invasive therapy and is now frequently used to treat malignant or benign tumours in various tissues or organs [1-3]. MR-guided focused ultrasound (MRgFUS) technology is a representative example of an image-guided thermal ablation technique that is using focus ultrasound (FUS) under MR-guidance and has shown great promise in treating non-invasively many diseases such as cancer, neurological conditions, thrombolysis (clots formed by ischemic stroke) and palliative pain treatment caused by

cervical or bone cancer metastasis [4-6]. To specify, MRgFUS technology has been used successfully for the treatment of benign and malignant cancer tumours [7]: early stage prostate cancer [8], breast cancer [9], uterine fibroids [10], adenomyosis [11] and benign soft tissue carcinomas [12]; neurological diseases [13]: essential tremor [14], multiple sclerosis and Parkinson's disease associated tremor [15], etc. Other likely treatment contenders being investigated in ongoing clinical trials include brain, liver, kidney, pancreas & thyroid cancers [16], Alzheimer's disease and epilepsy [17] and other movement disorders [18]. INSIGHTEC is the only Company that has EU/CE and FDA approval for its MRgFUS technology (ExAblate Body & Neuro models) to be used in humans to treat benign prostate and breast tumours [19], uterine fibroids [20], adenomyosis [21] and essential tremor and tremors caused by Parkinson's disease [22].

Magnetic resonance imaging (MRI) is utilized in MRgFUS technology for target characterization, treatment planning and closed-loop control of the acoustic energy deposition delivered to the target by a single element ultrasonic transducer or a phase array transducer [23]. By combining the FUS and MRI technologies together as a single therapeutic system, enables the operator of the MRgFUS system to achieve high accuracy in terms of beam localisation & targeting while monitoring in real time the treatment process which results in the necrosis of the targeted tissue [24]. FUS can cause necrotic lesions in tumours located in deep-sited healthy tissue through thermal coagulation and cavitation disruption with minimal to no damage to the surrounding tissues [25].

To completely treat the targeted tissue volume during thermal ablation treatments while minimizing side effects to the patient, accurate control of the temperature magnitude and distribution of the ultrasonic energy being delivered to the target is essential [23]. Consequently, treatment planning is vital prior to the application of the ablative therapy, in calculating the sonication strength and duration required to produce the appropriate tissue necrosis in the desired tissue volume [4]. Unfortunately, accurately planning and monitoring the tissue heating through MR thermometry in the context of patient-specific and dynamic acoustic characteristics of tissues remains a problem in these type of thermal ablation procedures even today. Testing the MRgFUS technology on *ex-vivo* biological tissue

or organs like pig fat, beef liver or turkey breast, has numerous drawbacks that include high cost, lack of homogeneity, short shelf-life and their biohazardous nature. [26]. To overcome these issues, high quality tissue mimicking phantoms (TMPs) are being used for the preclinical development and testing of new FUS & MRgFUS therapeutic techniques [27, 28].

Therefore, TMPs have been employed to test and calibrate newly introduced FUS and MRgFUS systems in pre-clinical and clinical settings. TMPs are also employed in the pre-manufacturing of new ultrasound transducers and innovative FUS systems for therapy purposes [28, 29]. TMPs have the advantage of allowing for the construction of idealized tissue models with clearly specified acoustic characteristics, dimensions, and internal features, which simplifies and standardizes the treatment protocols & environment [30, 31]. TMPs can be engineered to mimic the biological components of interest and help simulate the absorption pattern of the ultrasonic energy delivered by the FUS technique to the targeted volume [32]. TMPs make it possible to conduct biomedical research in an ergonomic and cost-effective manner without the need for animal or human patients. TMPs have better availability and shelf-life than the *ex-vivo* models, great structural uniformity and quality assurance (QA); and can support the training of the operator while helping to optimize the necessary therapeutic MRgFUS protocols [33]. All these advantages can improve QA practices, efficiency, and safety in modern medical systems before and after they enter the market.

In recent years, researchers have used a variety of materials to fabricate TMPs that can simulate as close as possible the properties of the desired targeted biological tissue or organ. Some well-established materials used for producing these TMPs for imaging or thermal ablation purposes are agar [34-36], gelatin [37, 38], polyacrylamide (PAA) [39, 40], poly(vinyl alcohol) (PVA) [41, 42], polyvinyl chloride (PVC) [43, 44], silicone [45, 46], carrageenan [47, 48] and polysaccharide based materials (TX-150/TX-151) [27, 49]. Tissue substitutes used in thermal therapy systems (such as FUS and MRgFUS) must have acoustic properties that are similar to the biological tissue of interest. The most important acoustic characteristics of soft tissue that need to be imitated by TMPs are the compressional speed of sound, characteristic acoustic impedance, attenuation, backscattering coefficient and the non-linearity

parameter [30]. Also, to effectively mimic real tissue in MRgFUS applications, TMPs should be produced with precise *T1* and *T2* relaxation times [29]. Unlike in the case of a biological tissue, the thermally treated TMP material should experience a significant and irreversible change in MR characteristics (*T1* or *T2*) upon reaching a threshold temperature that allows thermal coagulation to take place and permit the MR monitoring of the coagulated volume [50]. Many different contrast agents (attenuation components) have been used over the years to successfully replicate some of the acoustical properties necessary for the MR imaging & monitoring of the treatment ablation process such as microbubbles [51] or nanobubbles [52], silicon dioxide [33], copper(II) sulphate ($CuSO_4$) [53], cellulose [54], etc. Egg whites [55], egg albumin [56], bovine serum albumin (BSA) [57] & thermochromatic inks [58] are also some materials used in TMPs to enhance the MRI contrast but at the same time permit through permanent coagulation or colour change the observation of the temperature distribution into the ablated volume. It should be noted than even though the monitoring of the temperature distribution in a TMPs or a biological volume can be achieved also with MR thermometry, not everyone has access to the advance technology required to do that [59].

Each one of the above-mentioned phantom engineering materials have their strengths and weaknesses in simulating perfectly a biological component on thermal ablation applications. For example, agar and carrageenan phantoms have good elastic and stability properties and can be shaped easily into any desired shape. However, gelatin and carrageenan phantoms are only advised to be used in hyperthermia applications because they are unable to endure the high FUS ablation temperatures [31]. PAA on the other hand, can withstand the high FUS ablation temperatures due to its high melting point, but the acrylamide required for the PAA phantom fabrication is highly neurotoxic so additional care must be taken during its preparation. Alternatively, agar phantoms don't have any toxicity problems and have been shown to be very promising for usage in MRgFUS technology [34]. It should be noted though that the PAA phantoms are safe for handling after the polymerisation process is completed and offer better optical transparency in comparison to agar ones, therefore allowing the direct observation of the coagulative lesions during the ablation process. PAA

and agar phantoms have shown that can mimic well many of the important thermal, acoustical and MR relaxation characteristics of different biological tissues or organs [29, 36].

Even though many biological mimicking phantoms have been introduced for use in thermal therapy applications, none of them fully satisfies all the criteria of an ideal tumour phantom. To add to that complexity of simulating a biological tissue or an organ with a TMPs, a limited number of them can be found in literature that can simulate a tumour model for thermal therapy experimentation with MRgFUS technology. After reviewing the available bibliography on TMPs, the materials of choice selected to overcome a variety of issues reported by other scientists are PAA & agar. Our purpose is to use PAA and agar materials with the appropriate MR contrast and heat-sensitive agents to engineer multi-modal TMPs that can simulate and monitor almost perfectly a tumour model. PAA material can be used to prepare a spherical tumour mimicking phantom (TUMP) with the appropriate agents that can simulate the malignant tissue. The spherical shape TUMP, can be then added into the centre of a secondary square shaped TMP, fabricated by either PAA or agar materials that can simulate the healthy tissue surrounding the TUMP. The PAA material was chosen to fabricate the TUMPs due to its high melting point, good mechanical strength and competence to fabricate high optical transparent TUMPs & TMPs at room temperature and at any desired shape [39]. BSA was selected as the heat-sensitive and MR contrast agent to simulate and monitor the thermal ablation of a malignant tissue, while simultaneously measuring the thermal dose applied to it through the FUS application [25]. Silicon dioxide and glycerol were also used as a contrast agent in both TUMPs (PAA & agar) to assist with the MR monitoring of the tumour model during thermal application [33]. Therefore, for this study we will prepare a TUMP model that will consist of 2 parts: a normal square TMP and a spherical TUMP that will be placed in the centre of the TMP. In a previous study [60], also published by the same team, a similar TUMP model was engineered where both parts of it (TMP and spherical TUMP) were fabricated with only agar material. In the spherical TUMP though, silicon dioxide was additionally added to provide the necessary contrast between the two types of phantoms during the MRI experiments. The novelty that the TUMP model described in this study has, is that the spherical TUMP merged in the

centre of a square TMP is fully transparent and is fabricated with PAA mixed with BSA protein that was adjusted to have specific thermosensitive properties (change colour due to coagulation after a critical temperature point is passed - e.g. 55°C) therefore giving the advantage to the user to track the ultrasonic ablation focusing area and the thermal changes in the TUMP model caused by the FUS application with 'naked eyes' without the necessity of using advance equipment and techniques such as MRI and MR-Thermometry.

2. MATERIALS & METHODOLOGY

2.1. General Methodology

Three cuboid shape 6x6x6cm phantoms were prepared consisting from a tissue mimicking base that integrated in their centre a 2 cm spherical shape TUMP. The phantom as a whole can mimic a TUMP model, where the tumour phantom is surrounded by the base TMP simulating the surrounding healthy tissue. The phantoms were fabricated in triplets by both PAA & Agar materials with the use of cuboid and spherical moulds. Firstly, the spherical TUMP was prepared and then placed in the centre of the cuboid mould by hanging horizontally by a thread. The tissue mimicking PAA or agar solution was then added in the cuboid mould, therefore surrounding the spherical PAA TUMP. Once the polymerisation phase was completed, by the addition of polymerisation initiators-activators for the PAA solutions, the TUMP models were ready for use and testing with FUS, MRgFUS and MR-thermometry technologies.

2.2. Preparation of TUMP models

2.2.1. Experiment 1 – Agar/PAA TUMP model with BSA protein

2.2.1.1. Methodology

The agar TMPs for **Experiment 1** were prepared based on the methodology and formulation followed by Anastasia, *et al.*, [31], Filippou & Damianou [61] and Menikou & Damianou [34] where in their experiments they used 6% (w/v) agar and 4% (w/v) silicon dioxide to prepare agar-based TMPs to measure their acoustic, scattering and thermal properties, including their MR relaxation times. The

preparation of the PAA *(acrylamide/bis-acrylamide)* TUMPs were prepared based on the methodology followed by Bu-Lin, *et al.* [40] and McDonald, *et al*. [50] where they used PAA solutions with BSA protein and adjusted pH (4.3-4.7) to prepare multi-modality TMP to monitor and visualise the temperature effect of the FUS ablation to the PAA mimicking phantoms due to the coagulation properties of the BSA protein emerged by a specific pH value and the thermal stress applied. The PAA formulation was also based on the research of Zhong, *et al.* [26] where they used silicon dioxide as an MR scatterer and BSA protein as a coagulation agent to monitor through MRI the FUS ablation the impact to the TMPs.

2.2.1.2. Preparation of the PAA polymerisation initiators-activators

L-ascorbic acid, iron(II) sulphate heptahydrate ($FeSO_4$) and hydrogen peroxide (H_2O_2) were used as catalysts to initiate the polymerisation of the PAA solutions. The reason the specific combination was chosen as a catalyst for the polymerisation of the PAA solutions is because citrate buffer was used in the mixture to lower the pH of the solution to approximately 4.5 and the above combination is more efficient and 'friendlier' with the citrate buffer than other existing ones (e.g. TEMED & APS) [50].

The polymerization of the PAA solution is initiated by the addition of 0.1g (0.001% w/v) of L-ascorbic acid, 0.25ml (0.0025% v/v) of 1% $FeSO_4$ (add 0.1g of $FeSO_4$ in 10ml of deionized water) and 0.3ml (0.0030% v/v) of 3.0% v/v H_2O_2 (dilute 1.0ml of 30% w/v stock H_2O_2 in 9.0ml of deionized water). The ascorbic acid is photosensitive; therefore, it must always be stored at a dark place. The prepared $FeSO_4$ solution should be kept at 4°C and the H_2O_2 solution must always be made fresh before each experiment as it degrades over time due to its weak peroxide bond into water and oxygen [50, 62].

2.2.1.3. Fabrication of spherical PAA TUMP.

Under a fume hood and in room temperature, a 0.2M citrate buffer solution was prepared with a pH of 4.5±0.1 by dissolving 2.09% (w/v) of citric acid monohydrate and 2.96% (w/v) of sodium citrate tribasic dihydrate in 100ml of deionized water. Sodium hydroxide (NaOH) or hydrochloric acid (HCL) were gradually added in the solution (while monitoring the solution with a pH meter), until it reaches the exact pH value of 4.5. BSA protein was then added to the citrate buffer solution at a concentration of 2% (w/v) and was stirred slowly until a homogeneous solution was formed. It is important to avoid

rapid mixing of the solution once the BSA protein is added to avoid any bubbles formation. Acrylamide (6.65 w/v) and N,N'-methylene-bis-acrylamide (0.35 w/v) were then added into the solution and stir gently until a clear and homogenous solution is achieved. Safety equipment must be always used during the handling and preparation of the PAA solution as it is neurotoxic before its polymerisation. After a clear PAA solution is achieved, 6% (v/v) of glycerol and 1.1% (w/v) silicon dioxide were added and the formed solution was top up with deionised water to the appropriate volume while stirring gently. Finally, the polymerisation initiators-activators were added to the PAA tumour solution: 0.3% (v/v) of 3% H_2O_2, 0.1% (w/v) L-ascorbic acid and 0.25% (v/v) of 1% $FeSO_4$ and transferred immediately the final solution into 20 ml syringes to load up the spherical 2 cm moulds (x3) before the polymerisation process is completed. The spherical moulds were filled through a 2 mm hole, each holding around 4.2 ml of PAA solution, and sealed with plasticine to prevent any unwanted leaks. A 10 cm thread with knots at each end was also placed in the centre of the spherical moulds before injecting them with the PAA solution. As the polymerisation process is exothermic, the spherical moulds loaded with PAA solution were immediately transferred into sealed freezer bags and placed to around 4°C for a minimum of 30 mins to avoid premature coagulation of the thermally sensitive BSA protein. The transparent spherical PAA TUMPs were then carefully removed from their moulds and placed in water-filled freezer bags (to prevent dehydration or swelling) until used. The TUMPs preparation took around 90 mins.

2.2.1.4. Fabrication of the TUMP model.

The Agar tissue mimicking solution that surrounds the TUMP was prepared by following a similar methodology as Filippou & Damianou [61]. Under a fume board, 800ml of distilled water were added into beaker and placed into a hot plate until it was heated to 50°C. Then, 48g of agar powder (6% w/v) was added slowly into the beaker and stirred with a magnetic stirrer for 5min. Finally, 32g of silica dioxide (4% w/v) were added into the agar solution and continue stirring for 15-20 mins until a temperature of 95°C was reached. The temperature was monitored constantly with an electronic thermometer with an accuracy of 0.1°C (Model: HH806AU, Omega Engineering, USA). The agar-silica

solution was left to cool down to around 45°C. While waiting for the agar-silica tissue solution to cool down, the previously prepared transparent spherical PAA TUMPs are removed from the water-filled freezer bag and placed in the centre of three 6x6x6cm cuboid moulds with the help of a 10 cm thread embedded in the centre of their spherical structure. The TUMP spheres are hold in place by the thread that was fixated at the side of the cuboid moulds with plasticine. Once the agar-silica tissue solution cools down to 45°C (to avoid coagulation of the BSA protein in the PAA TUMPs), it is poured slowly into the three cuboid moulds that hold 216 ml of solution each, then sealed and placed immediately at 4°C overnight. Finally, the Agar/PAA TUMP models are carefully removed from the cuboid moulds and are placed in freezing sealed bags at 4°C with deionised water until use. **Table 1** shows the transparent TUMP model formulation and **Figure 1** summarises the methodology followed to prepare it.

2.2.2. Experiment 2 – PAA/PAA TUMP model phantom with BSA protein

2.2.2.1. Methodology

For **Experiment 2**, the opaque agar TMP material that was used to fabricate the Agar/PAA TUMP models in **Experiment 1** is replaced with the transparent PAA material, while the TUMP formulation is kept the same. The PAA TMPs and TUMPs for Experiment 2 were prepared based on the same methodology followed in Experiment 1*,* and both were mixed with BSA protein to help monitor and visualise the temperature effect of the FUS ablation to the PAA TUMP models due to the coagulation properties of BSA protein emerged under the thermal stress applied*.* To fabricate the transparent and clear TUMP models, the concentration of the PAA solution and the BSA protein were selected to 7% (w/v) and 2% (w/v), respectively, similarly to Experiment 1. To fabricate the PAA TMPs surrounding the PAA TUMPs, the agar solution was replaced with a 7% (w/v) PAA solution concentration with the BSA protein concentration remaining at 2% (w/v). The 7% PAA tissue solution was prepared with the same methodology used for the fabrication of the 7% TUMPs. Additionally, the silicon dioxide was only added to the PAA TUMPs and not in the TMPs.

The tumour and tissue PAA solutions formulation used in Experiment 2 are shown in **Table 2**. The final 7% (w/v) PAA tissue solution was transferred into cuboids moulds, where transparent spherical PAA TUMPs were already placed in their centre with the help of a horizontal nylon thread that was fixed through the centre of the PAA TUMP. **Figure 2** shows the placement of the transparent PAA TUMP fixated in the square mould before pouring the agar or PAA tissue mimicking solutions, including rendered images of the opaque Agar/PAA and transparent PAA/PAA TUMP models.

2.3. Characterisation of the TUMP models

2.3.1. Density calculation of PAA TUMP by water displacement method

The water displacement method [34] was used to calculate the PAA TUMP density by immersing it in a known volume of water and measuring the difference in water level. Beforehand, the PAA phantom mass M (in grams - g) was measured in a high accuracy balance. Using the formula $V = V_f - V_i$ where V_f = final water volume and V_i = initial water volume, yields the volume V (in cm^3) of the PAA phantom submerged in water. Finally, to find the density D (in g/cm^3) of the PAA phantom submerge in water the formula D = M/V is used, where M (in g) is the mass of the phantom and V (in ml) is the water volume displacement (1 ml of water takes up 1 cm^3 of space). The experiment to measure the mass density of the PAA phantoms was repeated in triplicate. The density of the Agar phantom material is already measured by the team in previous studies [61].

2.3.2. Transmission through method for measuring acoustic attenuation coefficient.

To measure the acoustic attenuation coefficient of the PAA phantoms the same methodology as the research of *Menikou & Damianou* [28, 34] was followed, where two immersion planar transducer were used to measure it. One of the transducers was used to transmit the signal (operating at 4 MHz) and the other one was used to receive it. To ensure a consistent response, the two transducers run at the same central frequency and gain. A PAA phantom was fabricated with the same properties as in sections 2.2.1 and 2.2.2 by using a custom-made mould but with a size of 2.5x2.5x5.0cm (LxWxH). The PAA phantom was placed halfway between the two transducers, ideally outside of the transmitting transducer's far field, where the constructive interference of waves generated at the transducer's face

produces a uniform front that smoothly fades away with increasing distance. The experiment to measure the acoustic attenuation coefficient of the PAA phantoms was repeated 4 times. The agar's phantom acoustic attenuation coefficient was not measured for this experiment as it is already known by previous studies of the group [61].

2.3.3. FUS application – Demo of Necrosis

The FUS setup and parameters used to ablate the TUMP model were based on previous methodology carried out by Drakos, *et al.* [63]. An FUS transducer (MEDSONIC LTD, Limassol, Cyprus), with an operating frequency of 2.75 MHz, was used to sonicate the TUMPs and the experiment was repeated in duplicate to verify the FUS ablation in the preset focal point in the phantom (FUS Experimental parameters: Spatial Peak Temporal Average Intensity - I_{SPTA} = 0.042 W/cm^2, Electric Power = 200 W, Ablation Time: 60 s). The transducer, which is responsible for the thermal ablation in the spherical TUMP, is used to deliver the ultrasonic energy required to increase the temperature at a preset FUS focal point above 55°C which is in the range that causes tissue necrosis. The transducer operates at 2.75 MHz and has focal length of 6.5 cm and diameter of 4 cm. A 3D-printed (F270, Stratasys Ltd., Minnesota, USA) experimental setup was used to hold the transducer and the phantom stable at fixed positions (**Figure 3**). The whole setup was immersed in an acrylic water tank with a size of 23x15x18 cm (HxWxL). Degassed distilled water was included as a coupling media between the transducer and the phantom. The positioning device's arm held the transducer, which was submerged in the water tank to provide a good acoustical coupling with the phantom. The focal depth was set at 3 cm in the phantom.

The purpose of the experiment was to evaluate and visualise the temperature increase through FUS sonication in the Agar or PAA TUMP models containing a PAA tumour and assess if the BSA protein is coagulating due to the temperature risen above 55°C in the PAA TUMP, therefore changing colour from transparent to cream white.

2.3.4. MRgFUS application - MR Thermometry

An MRI-conditional FUS setup which can create controlled thermal lesions under MRI guidance previously developed by the team [36] was used to estimate the temperature elevation and pinpoint the thermal focal point in the Agar/PAA and PAA/PAA TUMP models produced by FUS sonication. The purpose of the experiment was to evaluate the temperature increase through sonication in the Agar or PAA TUMP models containing a PAA tumour while monitoring and evaluating the thermal process under a 3T MRI scanner.

Each of the TUMP models (Agar/PAA and PAA/PAA) were placed in the square phantom holder of the custom-made FUS setup that was set atop a specially designed plastic plate. The plate was then partially submerged in a tank of distilled water that had been degassed (coupling media between the transducer and the phantom). A 50 mm diameter with 100 mm radius of curvature spherically focused high intensity single element ultrasonic transducer (MEDSONIC LTD, Limassol, Cyprus) was submerged in the water tank beneath the phantom. The transducer was mounted on a piece of plastic that allowed for manual vertical and horizontal positioning. An RF generator (HP 33120A, Agilent technologies, Englewood, CO, USA) powered the transducer. A GPFLEX coil (GPFLEX, USA instruments, Cleveland, OH, USA) was wrapped around the TUMP models.

The parameters set for the Agar/PAA TUMP model experiment were as follow: Water tank with transducer parameters: Frequency=2.6MHz, Diameter=50mm, Radius of curvature=65mm, Efficiency=30%, Focal Depth=30 mm, sonication time: 30s-120s; Amplifier: AG1016 (AG Series Amplifier, T & C Power Conversion, Inc., Rochester, USA): I_{SPTA} = 0.058 W/cm^2, electric power: 250 W; acoustic power: 75W; Experimental set-up (see **Figure 4**): Water tank with transducer ID 57; MRI scanner: 3T (Healthineers, Siemens); Coil type: Body coil (Body_12_BM).

The experimental FUS setup described above was placed in the MRI's magnet isocentre to simultaneously measure the temperature change in the TUMP models using MR Thermometry. The PRF shift technique was used to measure the thermal changes in the phantoms [32, 64]. With this technique, the local temperature increase is connected to the accompanying phase shift of the MR signal. The transducer's position in relation to the TUMP phantom was finely adjusted using fast

gradient echo sequences (FGRE) by setting the following MRI parameters: echo time (TE) = 10 ms, repetition time (TR)= 25 ms, Flip angle (FA) = 30°, Receiving Bandwidth (BW) = 501 Hz, Acquisition Matrix = 96 x 96, Field of View (FOV) = 280x280x3 mm^3.

The TUMP models were treated also with an acoustic power of 60W (I_{SPTA} = 0.046 W/cm^2, electric power: 200W) for a duration of 30-120 s in both axial and coronal imaging plane to acquire the MR thermometry high-resolution images. Every 2.4 s seconds while the transducer was turned off, an image was obtained during sonication. The following MRI parameters were applied: Sequence = FLASH 2D, Coil type: Body_12_BM, TR = 25ms, TE = 10 ms, FA= 30°, acquisition matrix: 96 x 96, slice thickness: 3 mm, acquisition time/slice: 2.4 s, Echo train length: 1, Pixel BW: 501 Hz/pixel, FOV: 280x280x3 mm^3. Each thermometry image that was generated was analysed using specialized custom software created by the team (written in python) to provide the temperature shift measurements at various intervals.

3. RESULTS

3.1. General Discusion

The concentration of the PAA tumour solutions was selected to 7% (w/v) as it was previously proven that this specific concentration allows the PAA tissue phantoms to be clear and transparent, as the heat released into the PAA preparation solution, due to the exothermic polymerization reaction, is not enough to denature the BSA protein [57]. The concentration of BSA was set to 2% (w/v) as it was demonstrated from previous studies [40, 50] that at this concentration the coagulated lesions formed in the PAA phantoms during the FUS ablation offer good thermal visualization with the naked eye due to its transparent structure and also its distinguish contrast on the MR images between the coagulated and uncoagulated regions properties (coagulation of BSA protein results in *T2* relaxation time change) [40, 65].

The BSA protein coagulates at approximately 70°C, which is higher than the necrosis temperature of biological tissue (50-60°C), hence a citrate buffer (0.2M with pH=4.5) was used to lower the pH of the PAA solutions to 4.5 [40]. With this specific pH value, the BSA protein starts coagulating at around 55°C.

The specific citrate buffer concentration (see **Table 1 & 2**) was selected for this experiment not only because it can sustain constant pH (4.5) of the PAA solution as other ingredients are added, but also because it can offer the necessary electrical conductivity to the solution essential for FUS ablation [50]. The coagulation temperature of BSA protein was adjusted for the PAA TMPs and TUMPs to 55°C (pH=4.5) with the addition of an acid or a base, respectively; thus, safeguarding that the coagulation temperature of BSA is within the range of thermal injury to soft tissue of 50-60°C [62]. Silicon dioxide was also added in the tumour PAA solution as an MR attenuation agent to monitor through MRI the FUS ablation to the TUMP and distinguish it from the TMP [26]. To further enhanced the contrast of the phantoms in MR imaging, glycerol was also included into the PAA solutions and at the same time made the removal of the phantoms from their moulds easier. Glycerol is known to have a relatively long *T1* relaxation time, which can enhance the contrast in *T1*-weighted MR images.

3.2. Agar/PAA and PAA/PAA TUMP models

The cross-sections of the final Agar/PAA and PAA/PAA TUMP models fabricated are presented in **Figure 5**. The TUMP models were sliced in half carfeully with a sharp blade to identify if the PAA TUMP was in the centre of the TMP and if the BSA protein was not coagulated during the experimental preparation steps. **Figure 5** clearly shows that the PAA TUMP was entrapped in the centre of the TMP and the BSA protein didn't show any visible signs of coagulation.

3.3. Density and acoustic attenuation coefficient calculation of PAA tumour MP material.

The densities of the 6% (w/v) tissue agar and 7% (w/v) PAA tumour MPs used at the experiments were calculated at 1.060 ± 0.012 g/cm^3 and 1.076 ± 0.011 g/cm^3, respectively. The propagation speeds of the agar TMPs and PAA TUMPs measured at 2.7 MHz were 1537 ± 6 m/s and 1616 ± 7 m/s, respectively (see **Table 3**).

3.4. Creation of Necrosis

After thermal ablation, the PAA/PAA TUMP models were examined to identify if the ablation area was in the focal region set by the FUS parameters and if it could be visualised by the naked idea. The thermal effect was then evaluated by looking to see if the ablation region has covered a significant

part of the PAA TUMP. A hot water bath was also used to heat the PAA TUMPs (>55°C) to visualise if there were any colour differences between the heated and unheated samples. The PAA TUMP started coagulating once the water temperature was raised above 55°C (as intended) and fully coagulated at around 65°C (from transparent to cream white colour). **Figure 6a** shows the transparent PAA phantom fabricated for this study before the BSA coagulation process takes place and **Figure 6b** shows the same PAA phantom after heating it above 55°C in a water bath. **Figure 6c** shows the transparent PAA/PAA TUMP model after sonication, where it can be seen clearly the FUS focal point due to the coagulation of the BSA protein and the optical colour change from transparent to cream white, caused by the ablation applied to it.

3.5. MR Imaging & MR-Thermometry

The fabricated TUMP models were imaged in a 3 T Siemens MRI scanner to examine their MR properties depending on the effect of the various materials added in their composition. The TUMP models were positioned in the water tank incorporated in the custom-made FUS setup and were imaged with the MRI scanner with conventional T1W FSE and T2W FSE sequences. The transducer's parameters used were as follows: Frequency=2.6 MHz; Diameter=50 mm; Radius of curvature=65 mm; Efficiency=30%; Focal depth=30 mm. Additionaly, the MR-Thermometry PRF shift technique was used in both types of TUMP models to obtain high-resolution thermal images and the temperature evolution observed in a region of interest (ROI) set within the focal spot. The following MR parameters were used: Sequence = FLASH 2D, Coil type: Body_12_BM, TR = 25ms, TE = 10 ms, FA= 30°, acquisition matrix: 96 x 96, slice thickness: 3 mm, acquisition time/slice: 2.4 s, Echo train length: 1, Pixel BW: 501 Hz/pixel, FOV: 280x280x3 mm^3. The TUMP models (Agar/PAA and PAA/PAA) fabricated were treated with an electric power of 200W for a duration of 60 s in both axial and coronal imaging plane.

3.5.1. Agar/PAA TUMP model

The MRI images aquired by the T1W FSE and T2W FSE MRI sequences (the MR parameters used were stated above) for the opaque Agar/PAA TUMP model shown in **Figure 7**, clearly reveal the excellent contrast achieved between the TMPs and the TUMPs. This was due to the lowered MR relaxation

times of the PAA TUMPs achieved by the addition of silicon dioxide and glycerol. **Figure 7a & 7b** shows MR images obtained by using the T1W FSE sequence and **Figure 7c & 7d** the MR images obtained by using the T2W FSE sequence for the opaque Agar/PAA TUMP model.

Figure 8 shows coronal and axial thermal images obtained with MR Thermometry in the MRI scanner during the thermal ablation of the Agar/PAA TUMP model. The thermal images obtained and the temperature evolution observed in a region of interest (ROI) set within the focal spot, show that the focal point of FUS sonication was in the spherical PAA TUMP region as planned. **Figure 8a** & **8b** show thermal maps in coronal and axial plane, respectively, and depict the temperature evolution over time of the Agar/PAA TUMP model with sonication power of 200W for 60 s.

3.5.2. PAA/PAA TUMP model

The FUS application to the transparent PAA TUMP models show the successful coagulation of the BSA protein after the temperature exceeded 55°C in the transparent PAA TUMP that is surrounded by the transparent PAA TMP (**Figure 9**). This was also confirmed by the MR thermal images aqcuired by MR-thermometry in the 3 T Siemens MRI scanner.

Figure 10 shows coronal and axial thermal images obtained with MR Thermometry in the MRI scanner during the thermal ablation of the PAA/PAA TUMP model. The thermal images obtained and the temperature evolution observed in a region of interest (ROI) set within the focal spot, show that the focal point of FUS sonication was in the spherical PAA TUMP region as planned. **Figure 10a** and **Figure 10b** show thermal maps in coronal and axial plane, respectively, and depict the temperature evolution over time of the PAA/PAA TUMP model with sonication powers of 200W for 30 s (axial plane) and 250W for 120 s (coronal plane).

4. DISCUSSION

The study presented in this article aimed to fabricate and evaluate two types of TUMP models for use in the development and optimization of FUS & MRgFUS ablation treatments for different cancer types. The specific TUMP models were designed to have properties similar to spherical tumours surrounded

by healthy tissue and were fabricated by using agar and PAA materials. The PAA and Agar materials were favoured to make the TMPs and TUMPs with BSA protein because they are easy to prepare, they offer long-term stability, they can be fabricated to have a similar thermal conductivity to that of tissue and additionally the PAA TMPs and TUMPs can change from transparent to cream white when heated above 55°C. This specific temperature point of 55°C is important as it was reported by previous studies also working with the applications of high intensity FUS that a temperature above that point and held for 1 second or more can lead to coagulative necrosis and cell destruction [66, 67].

BSA protein was incorporated in the PAA TUMPs that were inserted in the centre of the TUMP models due to its thermosensitive coagulation properties. The BSA protein was used as the heat-sensitive indicator to assist the visual monitoring of the coagulation process taking place during thermal ablation, which was clearly shown by the experiments performed here. In both types of TUMPs models (with Agar or PAA) prepared here, silicon dioxide was added in the spherical PAA TUMPs as a contrast agent to aid in the MR monitoring of the TUMP model during thermal ablation and help disginguish the TMPs from the TUMPs. Glycerol was also added as a contrast agent in all the phantoms fabricated with PAA to further enchance the contrast in the MR images (due to *T1* relaxation time change).

To identify the creation of necrosis after FUS ablation in the spherical PAA TUMP incorporated in the TUMP models, the models were examined to ensure that the ablation area was in the focal region set by the FUS parameters and could be visualized by the naked eye. The experimental results showed the visible coagulation of the BSA protein from transparent to cream white in the PAA TUMP caused by the thermal stress applied to the focal point targeted with FUS ablation. In addition, a hot water bath was used to heat the PAA TUMPs to temperatures above 55°C, which caused the BSA protein to coagulate, leading to a change in color from transparent to cream white. The coagulation of the BSA protein also served as an indicator of the FUS focal point, which was clearly visible in the PAA/PAA TUMP model after FUS sonication.

The phantoms were also designed to be visible by MRI for real-time monitoring of the FUS ablation process, therefore the MR imaging features and thermochromic properties of the Agar/PAA & PAA/PAA TUMP models were examined. *T2*-weighted MR images were used to estimate the three-dimensional geometry of the heated volume since the TUMP models showed a significant change in *T2* when the BSA protein is thermally coagulated. MR thermometry maps demonstrated that the suggested TUMP models may successfully imitate a tumour that is present in soft tissue.

An ideal TUMP model for thermal ablation research must have the following requirements: a) the user should be able to replicate it in a short time and high consistency, b) it should be safe to be handled by the user, c) the operator should be able to add it into the FUS setup located in the MR scanner with ease, d) the phantom model should be thermochromic and therefore reveal the ablation region after thermal ablation and e) it should provide good MR contrast between the TMP and TUMP. All the requirements mentioned here are fullfilled by the TUMP models fabricated for this study. Furthermore, the TUMP models mentioned here are ideal to simulate a breast or a liver tumour, including many other types of deep tumours that their depth is no more than 6 cm as the transducer used in this study has a focal depth of 6.5 cm.

The Agar/PAA and PAA/PAA TUMP models studied here can be helpful models for determining the thermal patterns during FUS ablation application in oncology. The coagulation temperature of the transparent spherical PAA TUMPs can be easily adjusted by changing the pH of the PAA solution that is mixed with the thermosensitive BSA protein. By changing their composition while still keeping the appropriate pH to control the BSA coagulation temperature it is possible to modify their energy absorption properties to match the acoustical and optical absorption of a specific tumour type that is surrounded by a specific soft tissue. These TUMP models has numerous uses in the testing and calibration of FUS equipment, the validation of thermal therapy treatment plans in oncology with FUS or MRgFUS applications, including uses in the quality control and quality assurance assessments of FUS therapy systems.

5. TABLES

Table 1: F*ormulations used for the preparation of the Agar TMP (opaque) and the spherical PAA TUMP (transparent) with BSA protein. The TUMP is inserted in the centre of the TMP to give the final Agar/PAA TUMP model.*

			Tumour phantom*	***Tissue phantom***
#	**Materials**	**Product code****	**Quantity (%)**	**Quantity (%)**
1	Deionized water	-	90.00 (v/v)	100.00 (v/v)
2	Citric acid monohydrous	1.00244.1000	2.09 (w/v)	-
3	Sodium citrate tribasic dehydrate	S4641	2.96 (w/v)	-
4	Bovine serum albumin (BSA)	A9647	2.00 (w/v)	-
5	Acrylamide	A8887	6.65 (w/v)	-
6	N, N-methylene-bis-acrylamide	M7256	0.35 (w/v)	-
7	Glycerol	G7757	6.0 (v/v)	-
	Agar	1.01614.1000	-	6.0 (w/v)
8	Silicon dioxide (Silica / SO_2)	83340	1.1 (w/v)	4.0 (w/v)
			Top up with deionized water to 0.1L	-
	Polymerization initiators/activators			
9	L-ascorbic acid	A5960	0.10 (w/v)	-
10	1% iron (II) sulfate heptahydrate ($FeSO_4$)	F7002	0.25 (v/v)	-
11	3% Hydrogen peroxide (H_2O_2)	1072090250	0.30 (v/v)	-

*Before adding the polymerisation agents, the pH of the PAA tumour solution is adjusted by monitoring it with a pH meter to 4.5 (55°C) by gradually adding NAOH or HCL.
**All the materials were purchased from Sigma Aldrich (Merck KGaA, Darmstadt, Germany).

Table 2: *Shows the formulations used for the preparation of the PAA TMP (transparent) and the spherical PAA TUMP (transparent), both incorporated with BSA protein. The TUMP is inserted in the centre of the TMP to give the final PAA/PAA TUMP model.*

			Tumour phantom*	***Tissue phantom***
#	**Materials**	**Product code****	**Quantity (%)**	**Quantity (%)**
1	Deionized water	-	90.00 (v/v)	90.00 (v/v)

2	Citric acid monohydrous	1.00244.1000	2.09 (w/v)	2.09 (w/v)
3	Sodium citrate tribasic dehydrate	S4641	2.96 (w/v)	2.96 (w/v)
4	Bovine serum albumin (BSA)	A9647	2.00 (w/v)	2.00 (w/v)
5	Acrylamide	A8887	6.65 (w/v)	6.65 (w/v)
6	N, N-methylene-bis-acrylamide	M7256	0.35 (w/v)	0.35 (w/v)
7	Glycerol	G7757	6.0 (v/v)	6.0 (v/v)
8	Silicon dioxide (Silica / SO_2)	83340	1.1 (w/v)	-
			Top up with deionized water to 0.1L	Top up with deionized water to 1L
	Polymerization initiators/activators			
9	L-ascorbic acid	A5960	0.10 (w/v)	0.10 (w/v)
10	1% iron (II) sulfate heptahydrate ($FeSO_4$)	F7002	0.25 (v/v)	0.25 (v/v)
11	3% Hydrogen peroxide (H_2O_2)	1072090250	0.30 (v/v)	0.30 (v/v)
*Before adding the polymerisation agents, the pH of the PAA tumour solution is adjusted by monitoring it with a pH meter to 4.5 (55°C) by gradually adding NAOH or HCL. **All the materials were purchased from Sigma Aldrich (Merck KGaA, Darmstadt, Germany).				

Table 3: *Shows the densities and propagation speeds for the phantom types prepared.*

#	Phantom Material	Density	Propagation speed (2.7 MHz)
1	Agar (6% w/v)	1.060 ± 0.012 g/cm^3	1537 ± 6 m/s
2	PAA (7% w/v)	1.076 ± 0.011 g/cm^3	1616 ± 7 m/s

6. FIGURE LEGENDS

Figure 1: *Methodology followed in Experiment 1 showing the preparation of the transparent PAA TUMP and the opaque agar TMP, including the fabrication of the final Agar/PAA TUMP model with BSA protein.*

Figure 2: *Shows a) the placement of the spherical PAA TUMP in the acrylic mould before adding the TMP solution, b) a rendered cross-section image of the opaque Agar/PAA TUMP model and c) a rendered image of the transparent PAA/PAA TUMP model (rendered in OPENAI DALL-E online software).*

Figure 3: *Shows (a) a schematic of the FUS ablation to the PAA/PAA TUMP model and (b) the realistic custom-made FUS setup used for the thermal ablation.*

Figure 4: *Experimental setup inside the 3T MRI scanner with the FUS custom-made setup, in which the TUMP models were placed on the MRI table and a GPFLEX coil placed on top of it to take the MR images.*

Figure 5: *Shows photos of a) the opaque Agar/PAA TUMP model, b) the transparent PAA/PAA TUMP model and c) a cross section of Agar/PAA TUMP model and d) a cross section of PAA/PAA TUMP model.*

Figure 6: *Shows photos of a) the transparent PAA TUMP before heating it in a water bath, b) the coagulated PAA TUMP after immersing it in a water bath with temperature >55°C and c) the coagulated region in the centre of the PAA/PAA TUMP model after FUS ablation.*

Figure 7: *Shows MRI images of the opaque Agar/PAA TUMP model acquired by using (a) & (b) the T1W FSE sequence and (c) & (d) the T2W FSE sequence.*

Figure 8: *Shows MR-Thermometry images acquired for the opaque Agar/PAA TUMP model and the temperature evolution observed in a region of interest (ROI) set within the focal spot with a) a coronal thermal map with the sonication power set to 200W for 60 s & b) an axial thermal map with the sonication power set to 200W for 60 s. MR parameters used: Sequence = FLASH 2D, Coil type: Body_12_BM, TR = 25 ms, TE = 10 ms, FA= 30°, acquisition matrix: 96 x 96, slice thickness: 3 mm, acquisition time/slice: 2.4 s, Echo train length: 1, Pixel BW: 501 Hz/pixel, FOV: 280x280x3 mm^3.*

Figure 9: *Shows photos of a) the coagulation of the BSA protein from transparent to cream white in the PAA/PAA TUMP model formed by the thermal stress applied with FUS ablation and b) the coagulation of the BSA protein in the FUS focal spot located in the transparent TUMP fused in the centre of the also transparent PAA TMP material.*

Figure 10: *Shows MR-Thermometry images acquired for the transparent PAA/PAA TUMP model and the temperature evolution observed in a region of interest (ROI) set within the focal spot with a) a coronal thermal map with the sonication power set to 200W for 30 s and b) an axial thermal map with the sonication power set to 250W for 120 s. MR parameters used: Sequence = FLASH 2D, Coil type:*

Body_12_BM, TR = 25 ms, TE = 10 ms, FA= 30°, acquisition matrix: 96 x 96, slice thickness: 3 mm, acquisition time/slice: 2.4 s, Echo train length: 1, Pixel BW: 501 Hz/pixel, FOV: 280x280x3 mm^3.

7. CONFLICTS OF INTEREST STATEMENT

The authors declare that they have no known competing financial interests or personal relationships that could have appeared to influence the work reported in this paper.

8. ACKNOWLEDGMENTS

The project was funded by the Research and Innovation Foundation of Cyprus under the projects SOUNDPET (INTEGRATED/0918/0008) and FUSVET (SEED/1221/0080).

9. REFERENCES

1. Baek, J.H., et al., *Thermal ablation for benign thyroid nodules: radiofrequency and laser.* Korean Journal of Radiology, 2011. **12**(5): p. 525-540.
2. Rhim, H. and G.D. Dodd III, *Radiofrequency thermal ablation of liver tumors.* Journal of clinical ultrasound, 1999. **27**(5): p. 221-229.
3. Zhao, Z. and F. Wu, *Minimally-invasive thermal ablation of early-stage breast cancer: a systemic review.* European Journal of Surgical Oncology (EJSO), 2010. **36**(12): p. 1149-1155.
4. Johnson, S.L., et al., *Development and validation of a MRgHIFU non-invasive tissue acoustic property estimation technique.* International Journal of Hyperthermia, 2016. **32**(7): p. 723-734.

5. Furusawa, H., et al., *Magnetic resonance–guided focused ultrasound surgery of breast cancer: reliability and effectiveness.* Journal of the American College of Surgeons, 2006. **203**(1): p. 54-63.

6. Machtinger, R., et al., *MRgFUS for pain relief as palliative treatment in recurrent cervical carcinoma: a case report.* Gynecologic oncology, 2008. **108**(1): p. 241-243.

7. Hsiao, Y.-H., et al., *Clinical application of high-intensity focused ultrasound in cancer therapy.* Journal of cancer, 2016. **7**(3): p. 225.

8. Napoli, A., et al., *Real-time magnetic resonance–guided high-intensity focused ultrasound focal therapy for localised prostate cancer: preliminary experience.* European urology, 2013. **63**(2): p. 395-398.

9. Furusawa, H., et al., *The evolving non-surgical ablation of breast cancer: MR guided focused ultrasound (MRgFUS).* Breast cancer, 2007. **14**(1): p. 55-58.

10. Stewart, E.A., et al., *Clinical outcomes of focused ultrasound surgery for the treatment of uterine fibroids.* Fertility and sterility, 2006. **85**(1): p. 22-29.

11. Yoon, S.-W., et al., *Successful use of magnetic resonance–guided focused ultrasound surgery to relieve symptoms in a patient with symptomatic focal adenomyosis.* Fertility and Sterility, 2008. **90**(5): p. 2018. e13-2018. e15.

12. Ghanouni, P., et al., *MR guided focused ultrasound treatment of soft tissue tumors of the extremities—preliminary experience.* Journal of Therapeutic Ultrasound, 2015. **3**(1): p. 1-2.

13. Giammalva, G.R., et al., *Focused ultrasound in neuroscience. State of the art and future perspectives.* Brain sciences, 2021. **11**(1): p. 84.

14. Stavarache, M.A., J.L. Chazen, and M.G. Kaplitt, *Innovative applications of MR-guided focused ultrasound for neurological disorders.* World Neurosurgery, 2021. **145**: p. 581-589.

15. Máñez-Miró, J.U., et al., *Focused ultrasound thalamotomy for multiple sclerosis–associated tremor.* Multiple Sclerosis Journal, 2020. **26**(7): p. 855-858.

16. Yiallouras, C. and C. Damianou, *Review of MRI positioning devices for guiding focused ultrasound systems.* The International Journal of Medical Robotics and Computer Assisted Surgery, 2015. **11**(2): p. 247-255.

17. Jung, N.Y. and J.W. Chang, *Magnetic resonance-guided focused ultrasound in neurosurgery: taking lessons from the past to inform the future.* Journal of Korean medical science, 2018. **33**(44).

18. Davies, N., *The Future of Focused Ultrasound: Movement Disorders and Beyond.* NeurologyLive, 2019. **2**(4).

19. Al-Bataineh, O., J. Jenne, and P. Huber, *Clinical and future applications of high intensity focused ultrasound in cancer.* Cancer treatment reviews, 2012. **38**(5): p. 346-353.

20. Trumm, C.G., et al., *Magnetic resonance imaging–guided focused ultrasound treatment of symptomatic uterine fibroids: impact of technology advancement on ablation volumes in 115 patients.* Investigative Radiology, 2013. **48**(6): p. 359-365.

21. Rabinovici, J., et al., *Pregnancy and live birth after focused ultrasound surgery for symptomatic focal adenomyosis: a case report.* Human reproduction, 2006. **21**(5): p. 1255-1259.

22. Jones, R.M., et al., *Echo-Focusing in Transcranial Focused Ultrasound Thalamotomy for Essential Tremor: A Feasibility Study.* Movement Disorders, 2020. **35**(12): p. 2327-2333.

23. Schlesinger, D., et al., *MR-guided focused ultrasound surgery, present and future.* Medical physics, 2013. **40**(8): p. 080901.

24. Jolesz, F.A., *MRI-guided focused ultrasound surgery.* Annual review of medicine, 2009. **60**: p. 417.

25. King, R.L., et al., *Development and characterization of a tissue-mimicking material for high-intensity focused ultrasound.* IEEE transactions on ultrasonics, ferroelectrics, and frequency control, 2011. **58**(7): p. 1397-1405.

26. Zhong, X., et al., *A novel tissue-mimicking phantom for US/CT/MR-guided tumor puncture and thermal ablation.* International Journal of Hyperthermia, 2022. **39**(1): p. 557-563.

27. Dabbagh, A., et al., *Tissue-mimicking gel phantoms for thermal therapy studies.* Ultrasonic imaging, 2014. **36**(4): p. 291-316.

28. Menikou, G., et al., *MRI-compatible breast/rib phantom for evaluating ultrasonic thermal exposures.* The International Journal of Medical Robotics and Computer Assisted Surgery, 2018. **14**(1): p. e1849.

29. Antoniou, A. and C. Damianou, *MR relaxation properties of tissue-mimicking phantoms.* Ultrasonics, 2022. **119**: p. 106600.

30. Culjat, M.O., et al., *A review of tissue substitutes for ultrasound imaging.* Ultrasound in medicine & biology, 2010. **36**(6): p. 861-873.

31. Antoniou, A., et al., *MR relaxation times of agar-based tissue-mimicking phantoms.* Journal of Applied Clinical Medical Physics, 2022. **23**(5): p. e13533.

32. Menikou, G., et al., *MRI compatible head phantom for ultrasound surgery.* Ultrasonics, 2015. **57**: p. 144-152.

33. Eranki, A., et al., *Tissue-mimicking thermochromic phantom for characterization of HIFU devices and applications.* International Journal of Hyperthermia, 2019. **36**(1): p. 517-528.

34. Menikou, G. and C. Damianou, *Acoustic and thermal characterization of agar based phantoms used for evaluating focused ultrasound exposures.* Journal of therapeutic ultrasound, 2017. **5**(1): p. 1-14.

35. Partanen, A., C. Mougenot, and T. Vaara. *Feasibility of agar-silica phantoms in quality assurance of MRgHIFU*. in *AIP Conference Proceedings*. 2009. American Institute of Physics.

36. Drakos, T., et al., *An improved method to estimate ultrasonic absorption in agar-based gel phantom using thermocouples and MR thermometry.* Ultrasonics, 2020. **103**: p. 106089.

37. Dunmire, B., et al., *Characterizing an agar/gelatin phantom for image guided dosing and feedback control of high-intensity focused ultrasound.* Ultrasound in medicine & biology, 2013. **39**(2): p. 300-311.

38. Farrer, A.I., et al., *Characterization and evaluation of tissue-mimicking gelatin phantoms for use with MRgFUS.* Journal of therapeutic ultrasound, 2015. **3**(1): p. 1-11.

39. Prokop, A.F., et al., *Polyacrylamide gel as an acoustic coupling medium for focused ultrasound therapy.* Ultrasound in medicine & biology, 2003. **29**(9): p. 1351-1358.

40. Bu-Lin, Z., et al., *A polyacrylamide gel phantom for radiofrequency ablation.* International journal of hyperthermia, 2008. **24**(7): p. 568-576.

41. Surry, K., et al., *Poly (vinyl alcohol) cryogel phantoms for use in ultrasound and MR imaging.* Physics in Medicine & Biology, 2004. **49**(24): p. 5529.

42. Ambrogio, S., et al., *A polyvinyl alcohol-based thermochromic material for ultrasound therapy phantoms.* Ultrasound in Medicine & Biology, 2020. **46**(11): p. 3135-3144.

43. Maggi, L., et al. *Ultrasonic Attenuation and Speed in phantoms made of PVCP and Evaluation of acoustic and thermal properties of ultrasonic phantoms made of polyvinyl chloride-plastisol (PVCP)*. in *IWBBIO*. 2013.

44. Li, W., et al., *Polyvinyl chloride as a multimodal tissue-mimicking material with tuned mechanical and medical imaging properties.* Medical Physics, 2016. **43**(10): p. 5577-5592.

45. Ayers, F., et al. *Fabrication and characterization of silicone-based tissue phantoms with tunable optical properties in the visible and near infrared domain*. in *Design and Performance Validation of Phantoms Used in Conjunction with Optical Measurements of Tissue*. 2008. SPIE.

46. Ustbas, B., et al., *Silicone-based composite materials simulate breast tissue to be used as ultrasonography training phantoms.* Ultrasonics, 2018. **88**: p. 9-15.

47. Kim, J., et al., *Estimation of thermal distribution in tissue-mimicking phantom made of carrageenan gel.* Japanese Journal of Applied Physics, 2015. **54**(7S1): p. 07HF23.

48. Kuroda, M., et al., *Development of a new hybrid gel phantom using carrageenan and gellan gum for visualizing three-dimensional temperature distribution during hyperthermia and radiofrequency ablation.* International journal of oncology, 2005. **27**(1): p. 175-184.

49. Ito, K., et al., *Development and characteristics of a biological tissue-equivalent phantom for microwaves.* Electronics and Communications in Japan (Part I: Communications), 2001. **84**(4): p. 67-77.

50. McDonald, M., et al., *Multi-modality tissue-mimicking phantom for thermal therapy.* Physics in Medicine & Biology, 2004. **49**(13): p. 2767.

51. Huang, J., J.S. Xu, and R.X. Xu, *Heat-sensitive microbubbles for intraoperative assessment of cancer ablation margins.* Biomaterials, 2010. **31**(6): p. 1278-1286.

52. Xu, R.X., S.P. Povoski, and E.W. Martin, *Targeted delivery of microbubbles and nanobubbles for image-guided thermal ablation therapy of tumors.* Expert Review of Medical Devices, 2010. **7**(3): p. 303-306.

53. Chen, S.J.S., et al., *An anthropomorphic polyvinyl alcohol brain phantom based on Colin27 for use in multimodal imaging.* Medical Physics, 2012. **39**(1): p. 554-561.

54. Braunstein, L., et al., *Characterization of Acoustic, Cavitation, and Thermal Properties of Poly (vinyl alcohol) Hydrogels for Use as Therapeutic Ultrasound Tissue Mimics.* Ultrasound in Medicine & Biology, 2022. **48**(6): p. 1095-1109.

55. Takegami, K., et al., *Polyacrylamide gel containing egg white as new model for irradiation experiments using focused ultrasound.* Ultrasound in medicine & biology, 2004. **30**(10): p. 1419-1422.

56. Zhou, T., et al., *Phantom for Microwave Device Testing.* 2010.

57. Lafon, C., et al. *Development and characterization of an innovative synthetic tissue-mimicking material for high intensity focused ultrasound (HIFU) exposures*. in *2001 IEEE Ultrasonics Symposium. Proceedings. An International Symposium (Cat. No. 01CH37263)*. 2001. IEEE.

58. Zhou, Y., et al., *A thermochromic tissue-mimicking phantom model for verification of ablation plans in thermal ablation.* Annals of Translational Medicine, 2021. **9**(4).

59. Zhu, M., Z. Sun, and C.K. Ng, *Image-guided thermal ablation with MR-based thermometry.* Quantitative Imaging in Medicine and Surgery, 2017. **7**(3): p. 356.

60. Antoniou, A., et al., *Tumor phantom model for MRI-guided focused ultrasound ablation studies.* Med Phys, 2023.

61. Filippou, A. and C. Damianou, *Evaluation of ultrasonic scattering in agar-based phantoms using 3D printed scattering molds.* Journal of Ultrasound, 2022: p. 1-13.

62. Datla, N.V., et al., *Polyacrylamide phantom for self-actuating needle–tissue interaction studies.* Medical Engineering & Physics, 2014. **36**(1): p. 140-145.

63. Drakos, T., et al., *Ultrasonic attenuation of an agar, silicon dioxide, and evaporated milk gel phantom.* Journal of Medical Ultrasound, 2021. **29**(4): p. 239.

64. Rieke, V., *MR thermometry.* Interventional Magnetic Resonance Imaging, 2011: p. 271-288.

65. Zhong, X., Y. Cao, and P. Zhou, *Thermochromic Tissue-Mimicking Phantoms for Thermal Ablation Based on Polyacrylamide Gel.* Ultrasound in Medicine & Biology, 2022.

66. ter, H., et al., *High intensity focused ultrasound: Physical principles and devices.* International Journal of Hyperthermia, 2007. **23**(2): p. 89-104.

67. Dewhirst, M.W., et al., *Basic principles of thermal dosimetry and thermal thresholds for tissue damage from hyperthermia.* International journal of hyperthermia, 2003. **19**(3): p. 267-294.

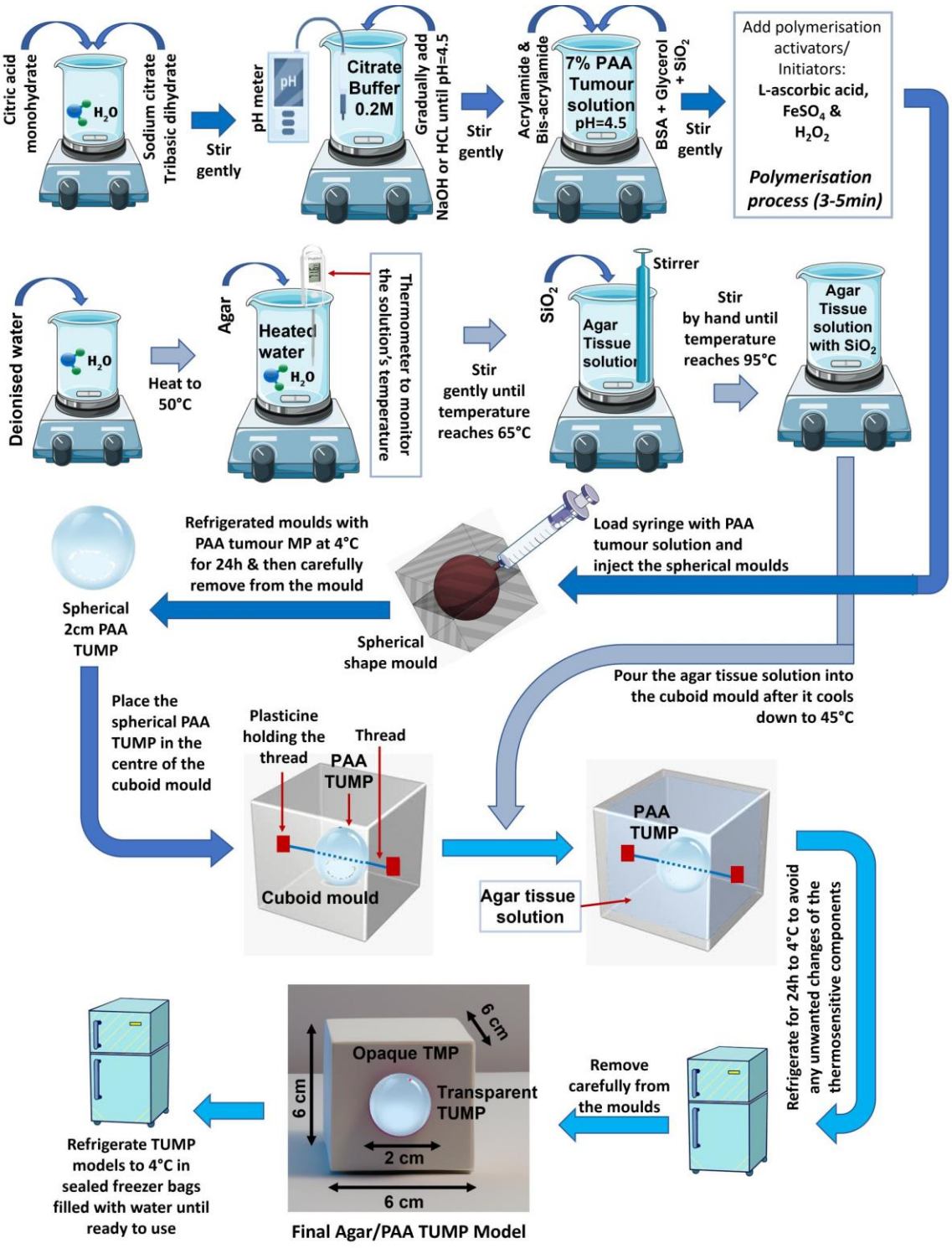
Citric acid monohydrate
Sodium citrate Tribasic dihydrate
H_2O
Stir gently
pH meter
Citrate Buffer 0.2M
Gradually add NaOH or HCL until pH=4.5
Stir gently
Acrylamide & Bis-acrylamide
7% PAA Tumour solution pH=4.5
BSA + Glycerol + SiO_2
Stir gently
Add polymerisation activators/ Initiators: L-ascorbic acid, $FeSO_4$ & H_2O_2
Polymerisation process (3-5min)
Deionised water
Heat to 50°C
Agar
Heated water
Thermometer to monitor the solution's temperature
Stir gently until temperature reaches 65°C
SiO_2
Agar Tissue solution
Stirrer
Stir by hand until temperature reaches 95°C
Agar Tissue solution with SiO_2
Load syringe with PAA tumour solution and inject the spherical moulds
Refrigerated moulds with PAA tumour MP at 4°C for 24h & then carefully remove from the mould
Spherical 2cm PAA TUMP
Spherical shape mould
Pour the agar tissue solution into the cuboid mould after it cools down to 45°C
Place the spherical PAA TUMP in the centre of the cuboid mould
Plasticine holding the thread
Thread
PAA TUMP
Cuboid mould
Agar tissue solution
PAA TUMP
Refrigerate for 24h to 4°C to avoid any unwanted changes of the thermosensitive components
Remove carefully from the moulds
Opaque TMP
Transparent TUMP
6 cm
6 cm
2 cm
6 cm
Refrigerate TUMP models to 4°C in sealed freezer bags filled with water until ready to use
Final Agar/PAA TUMP Model

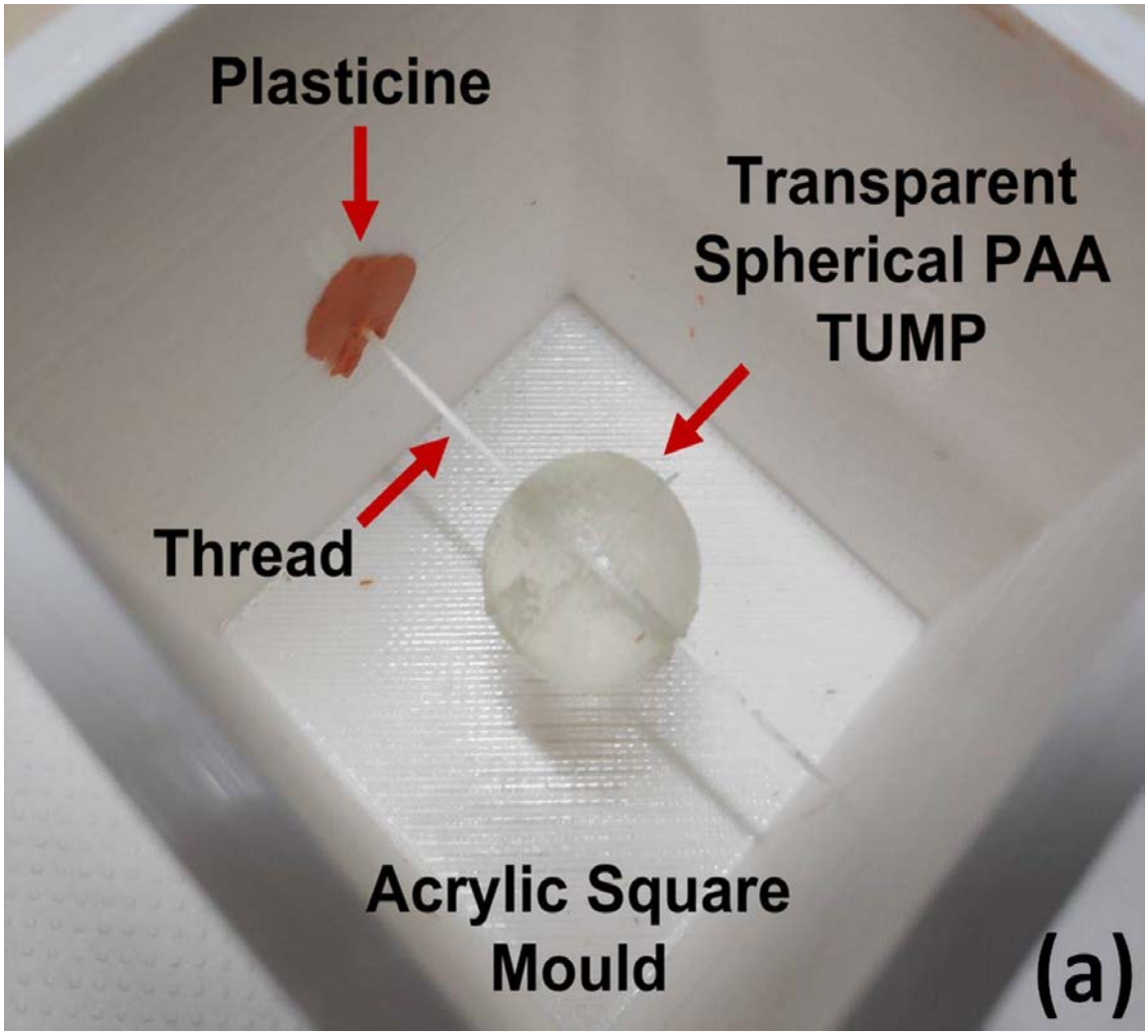
Plasticine
Transparent
Spherical PAA
TUMP
Thread
Acrylic Square
Mould
(a)

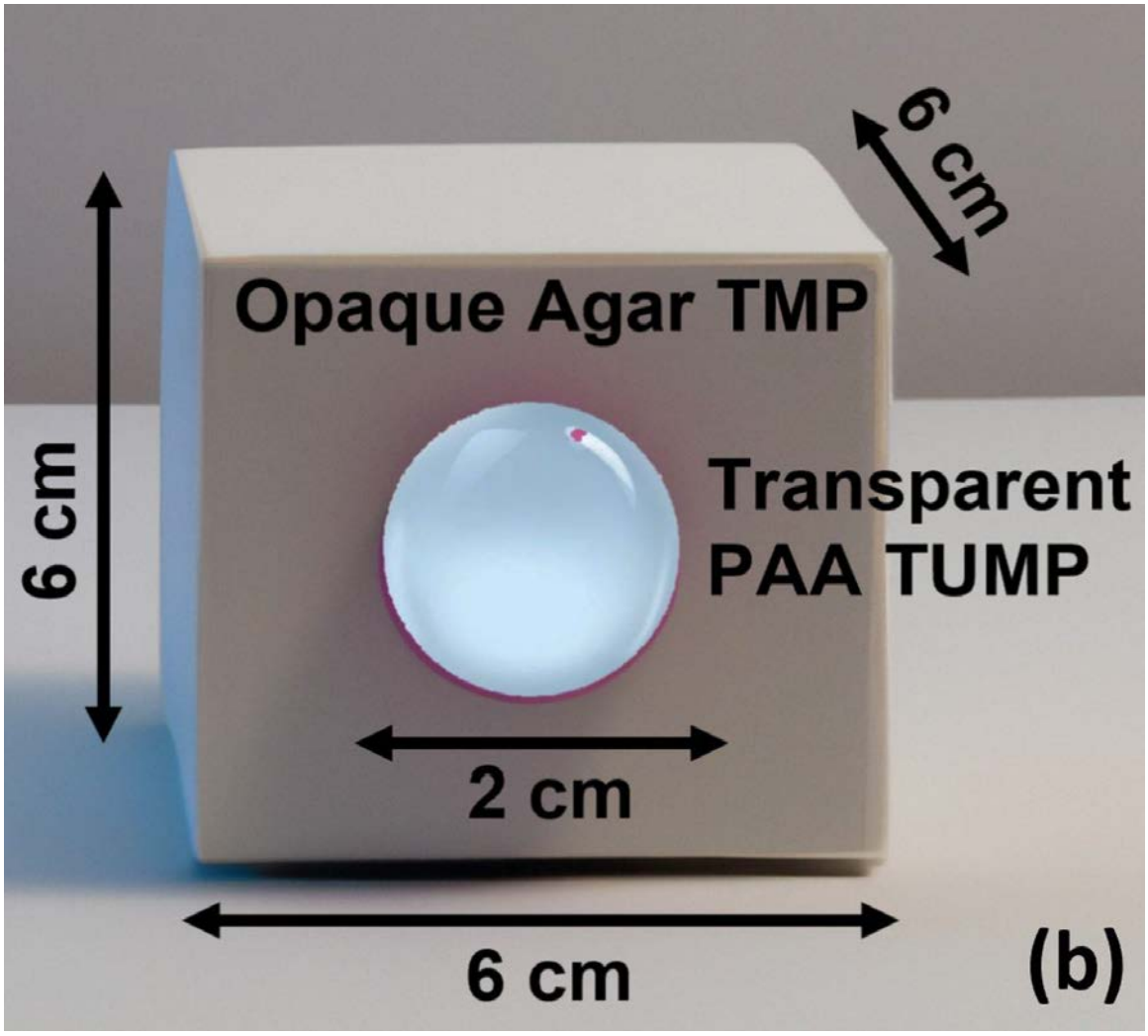
6 cm
Opaque Agar TMP
6 cm
Transparent
PAA TUMP
2 cm
6 cm
(b)

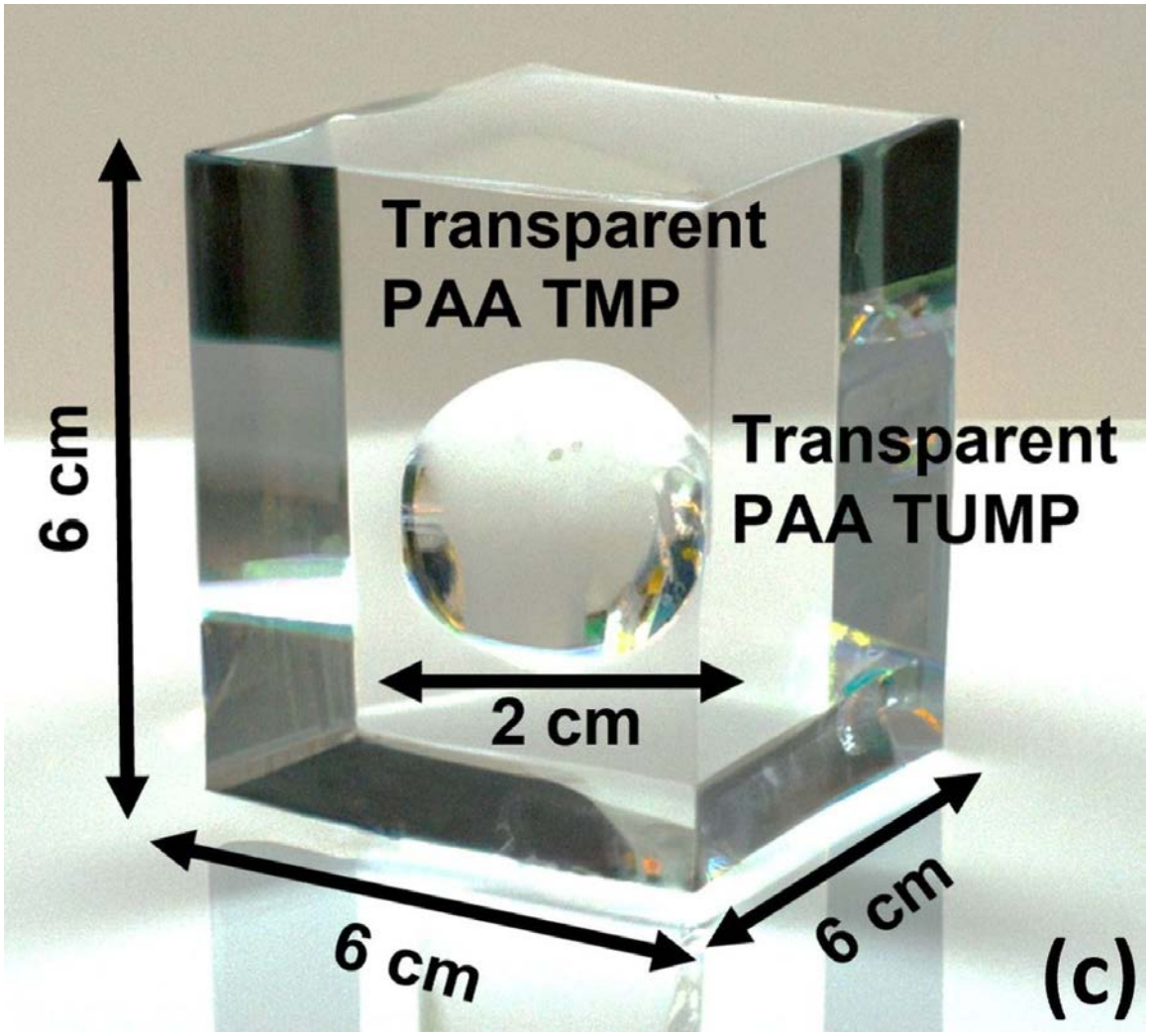
Transparent
PAA TMP
Transparent
PAA TUMP
6 cm
2 cm
6 cm
6 cm
(c)

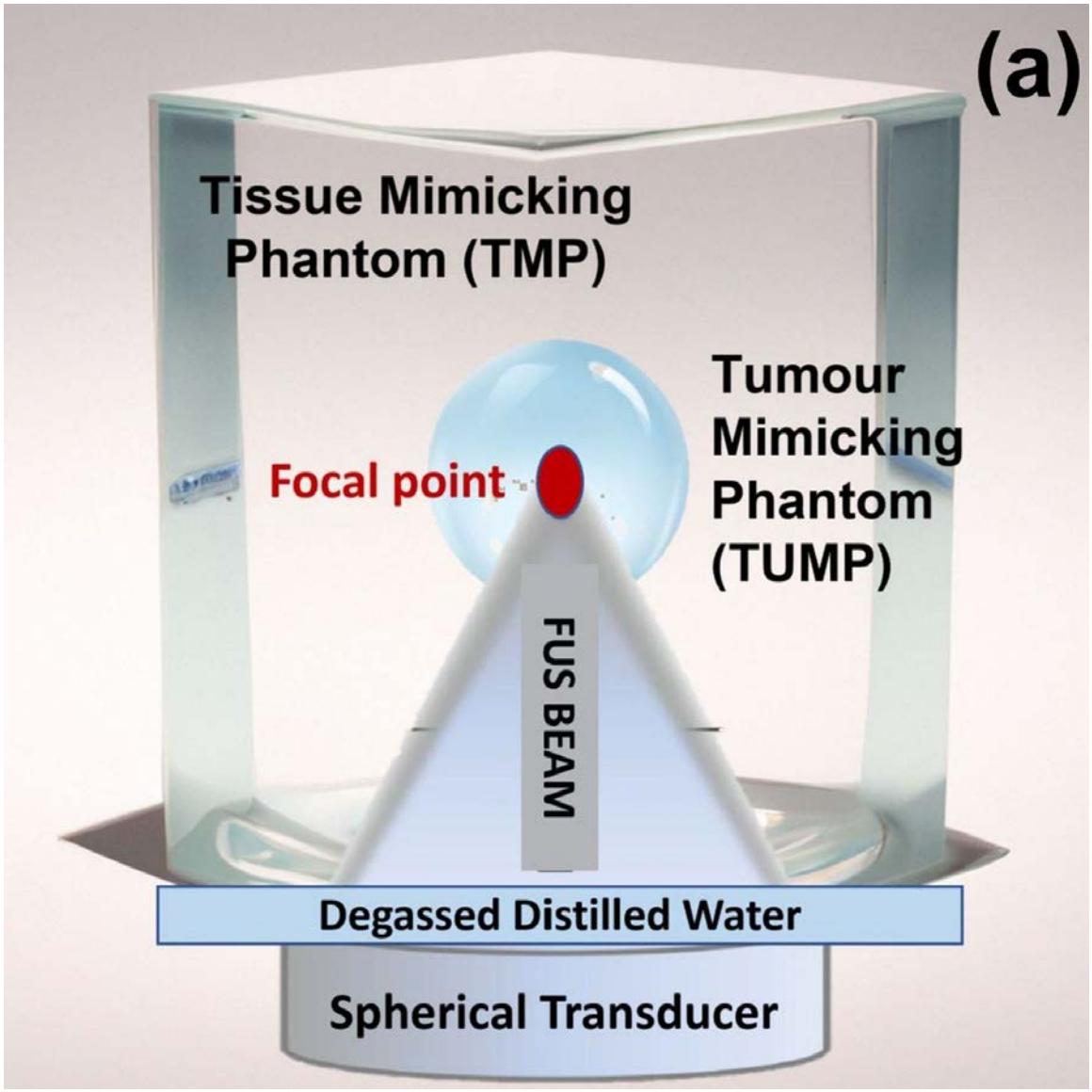
(a)
Tissue Mimicking Phantom (TMP)
Tumour Mimicking Phantom (TUMP)
Focal point
FUS BEAM
Degassed Distilled Water
Spherical Transducer

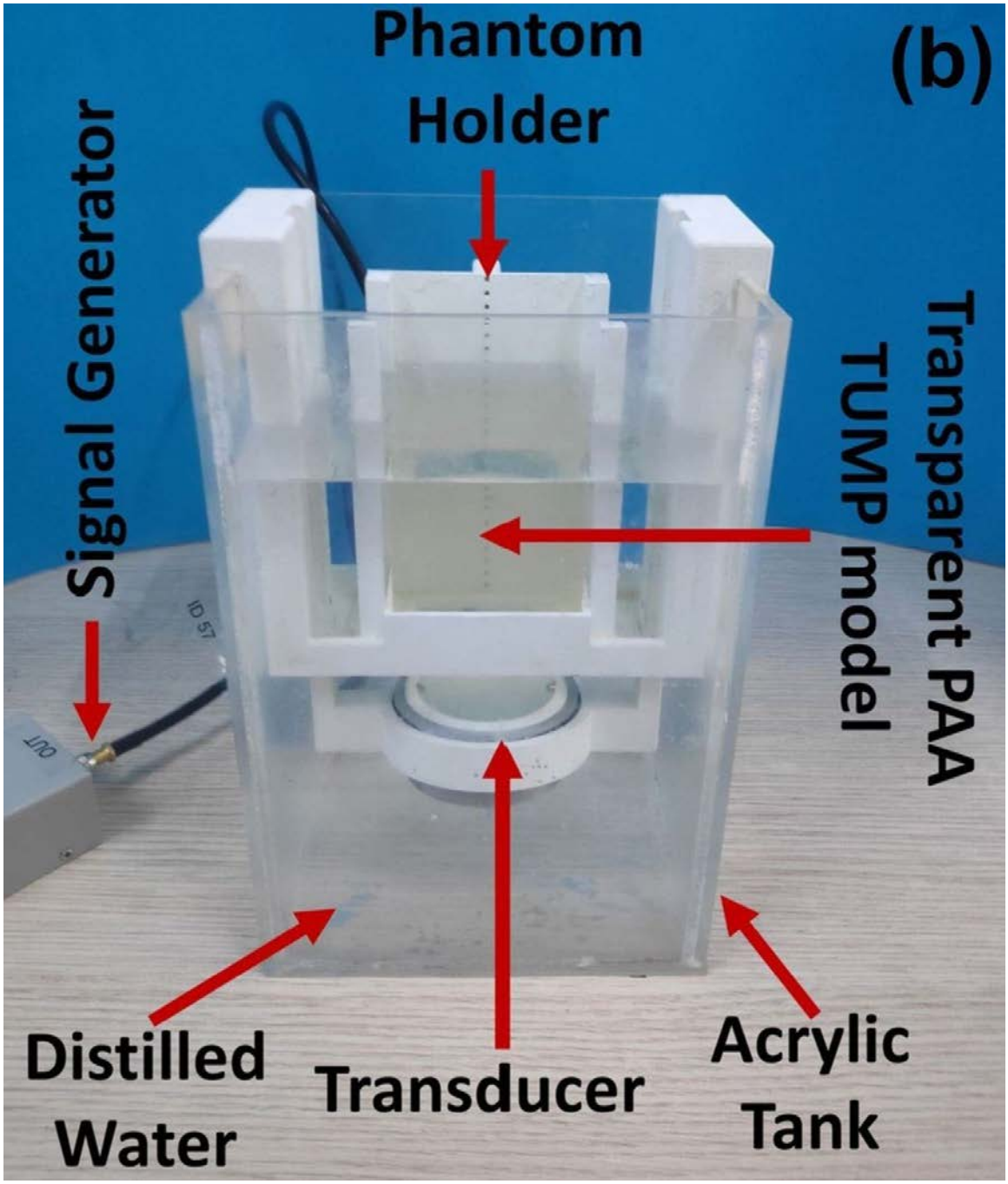
(b)
Phantom Holder
Signal Generator
Transparent PAA TUMP model
Distilled Water
Transducer
Acrylic Tank

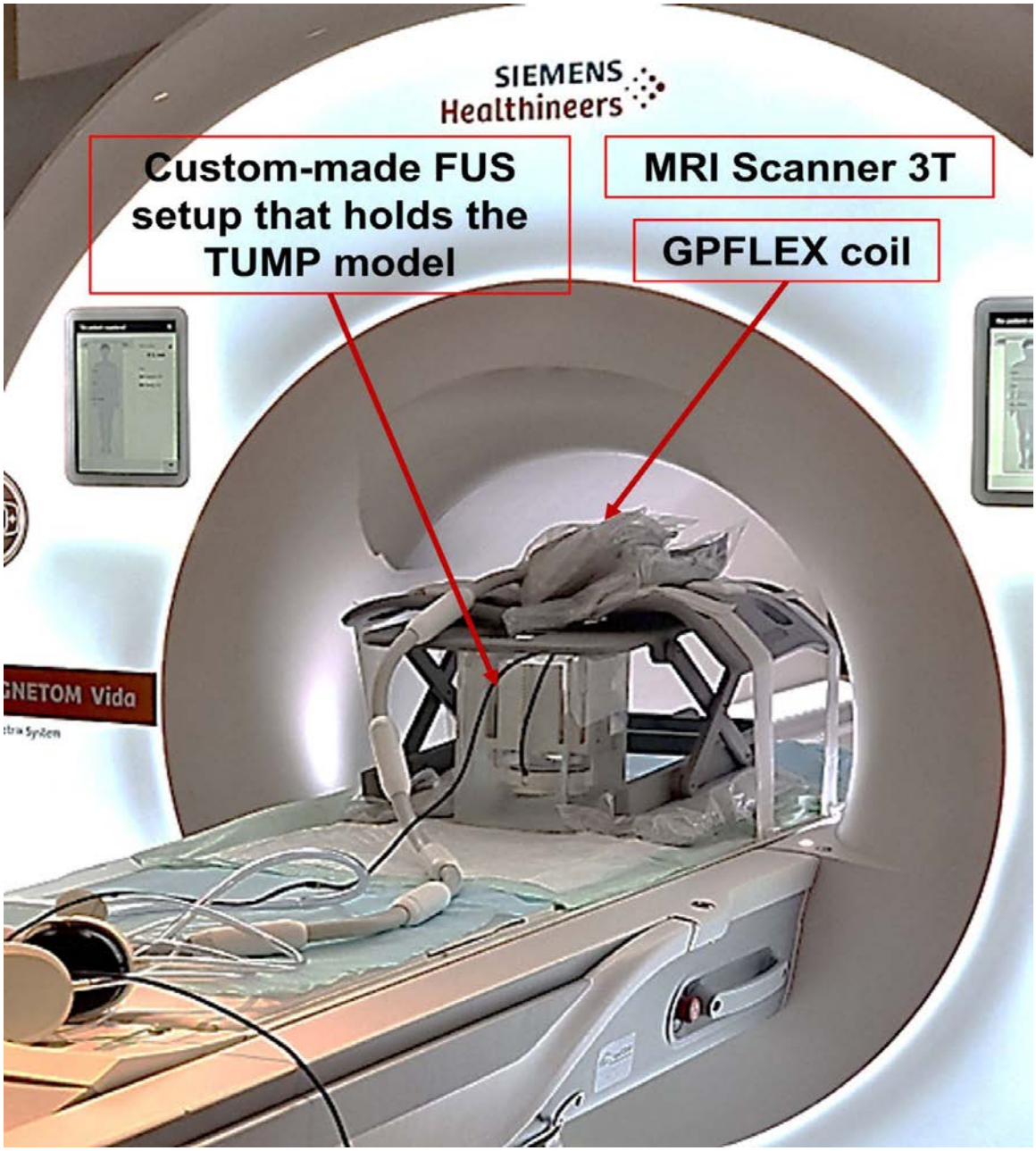
SIEMENS
Healthineers
Custom-made FUS setup that holds the TUMP model
MRI Scanner 3T
GPFLEX coil
GNETOM Vida

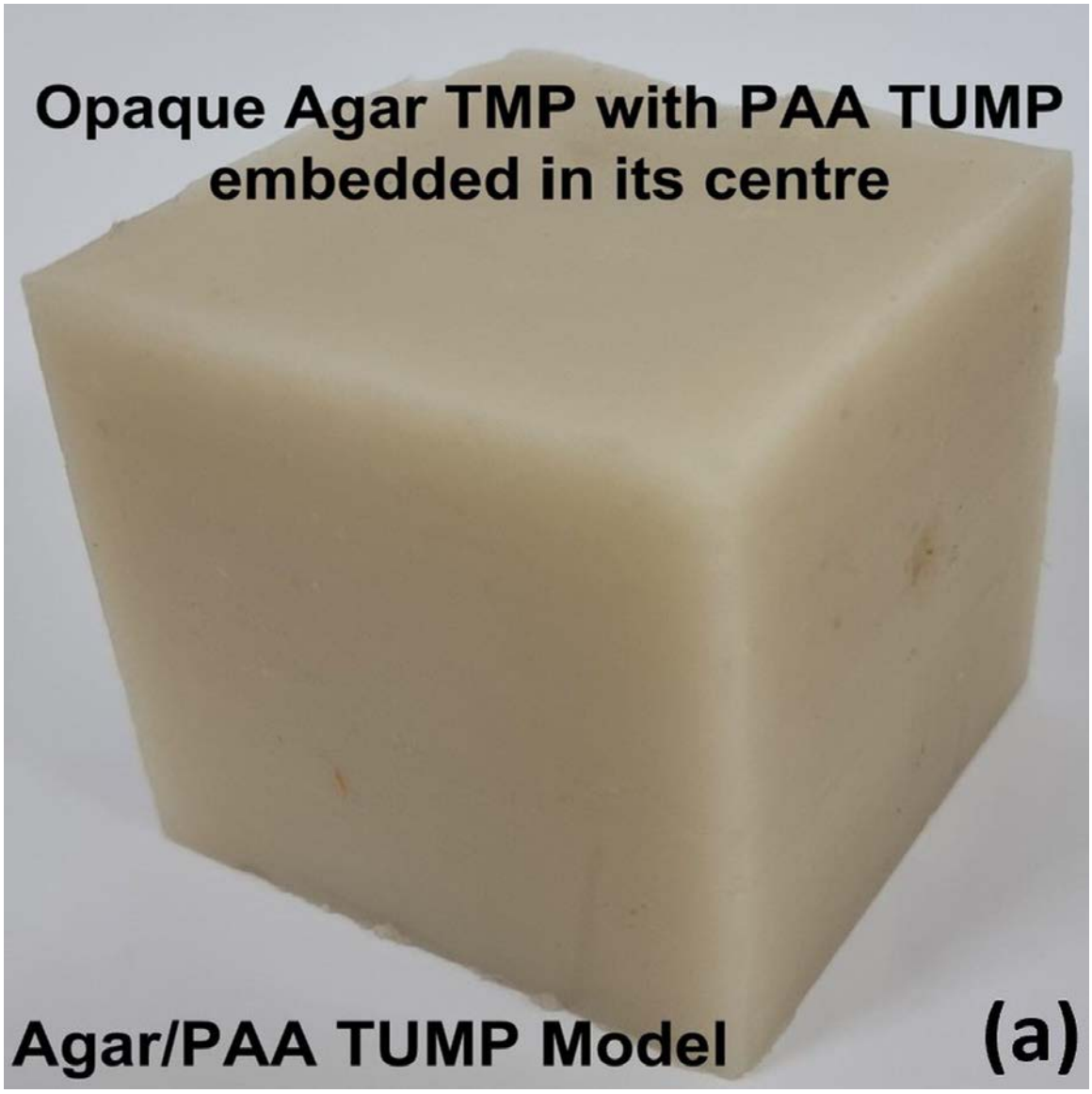
Opaque Agar TMP with PAA TUMP
embedded in its centre
Agar/PAA TUMP Model
(a)

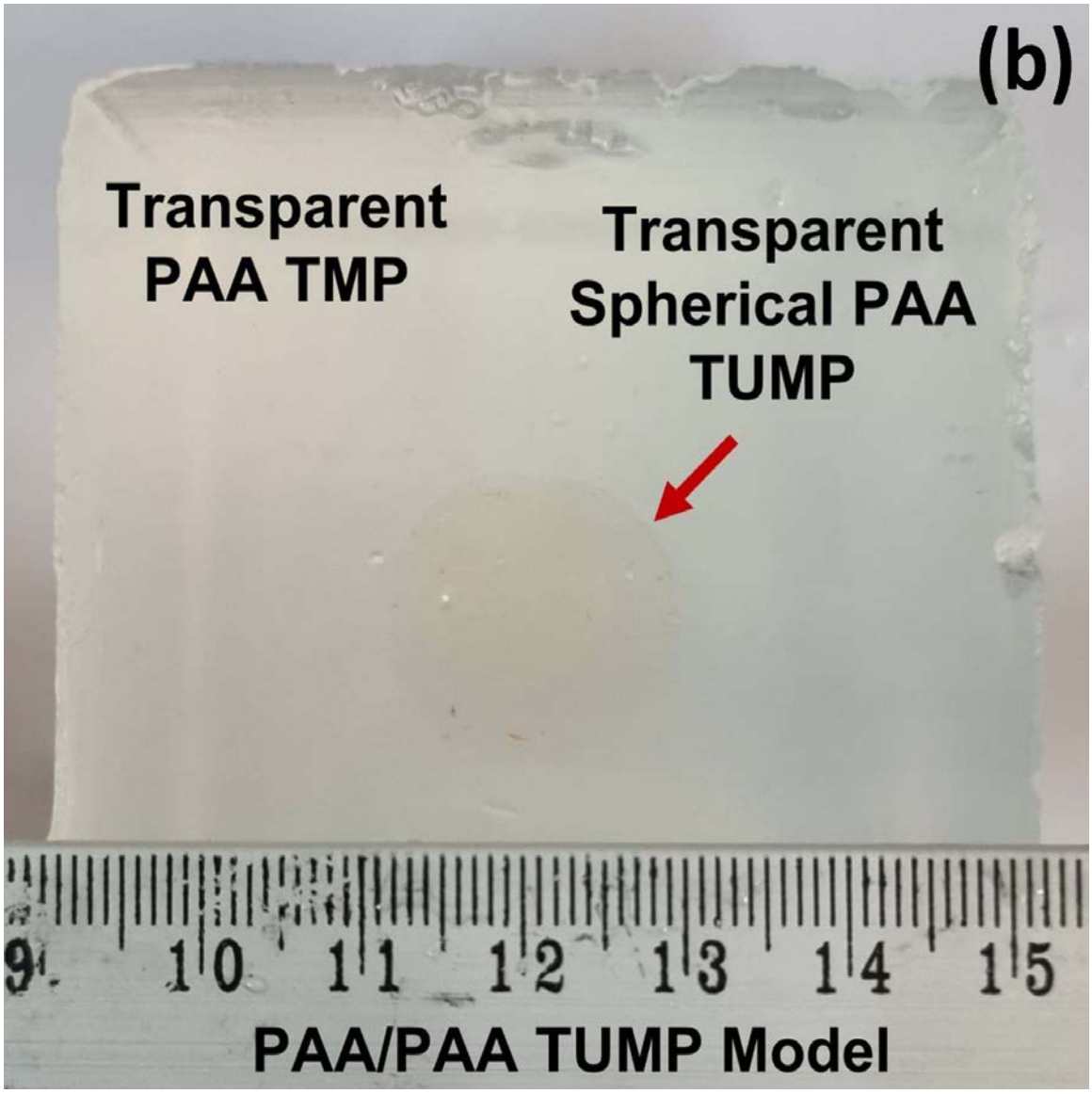
(b)
Transparent
PAA TMP
Transparent
Spherical PAA
TUMP
9
10
11
12
13
14
15
PAA/PAA TUMP Model

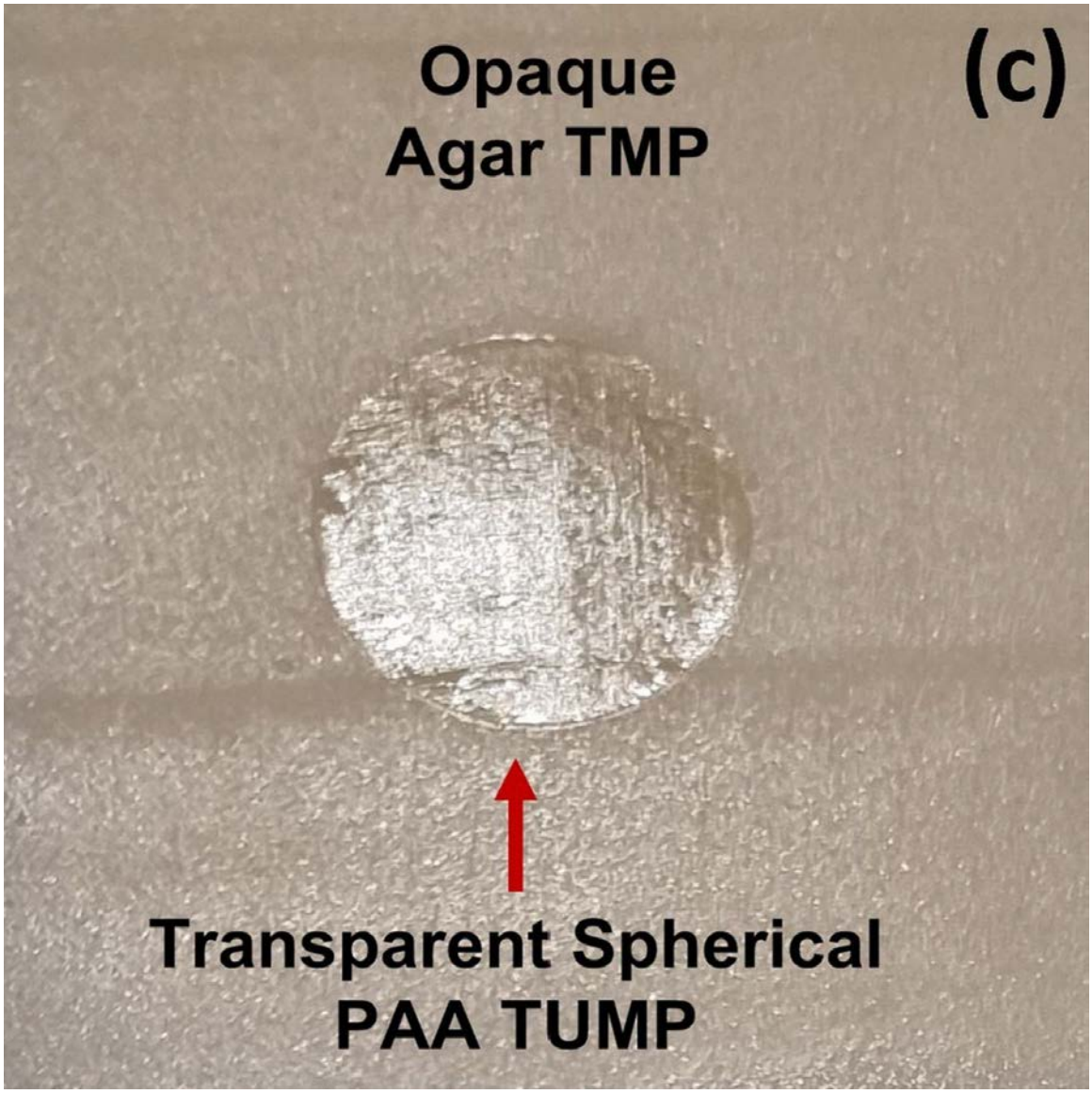
Opaque
Agar TMP
(c)
Transparent Spherical
PAA TUMP

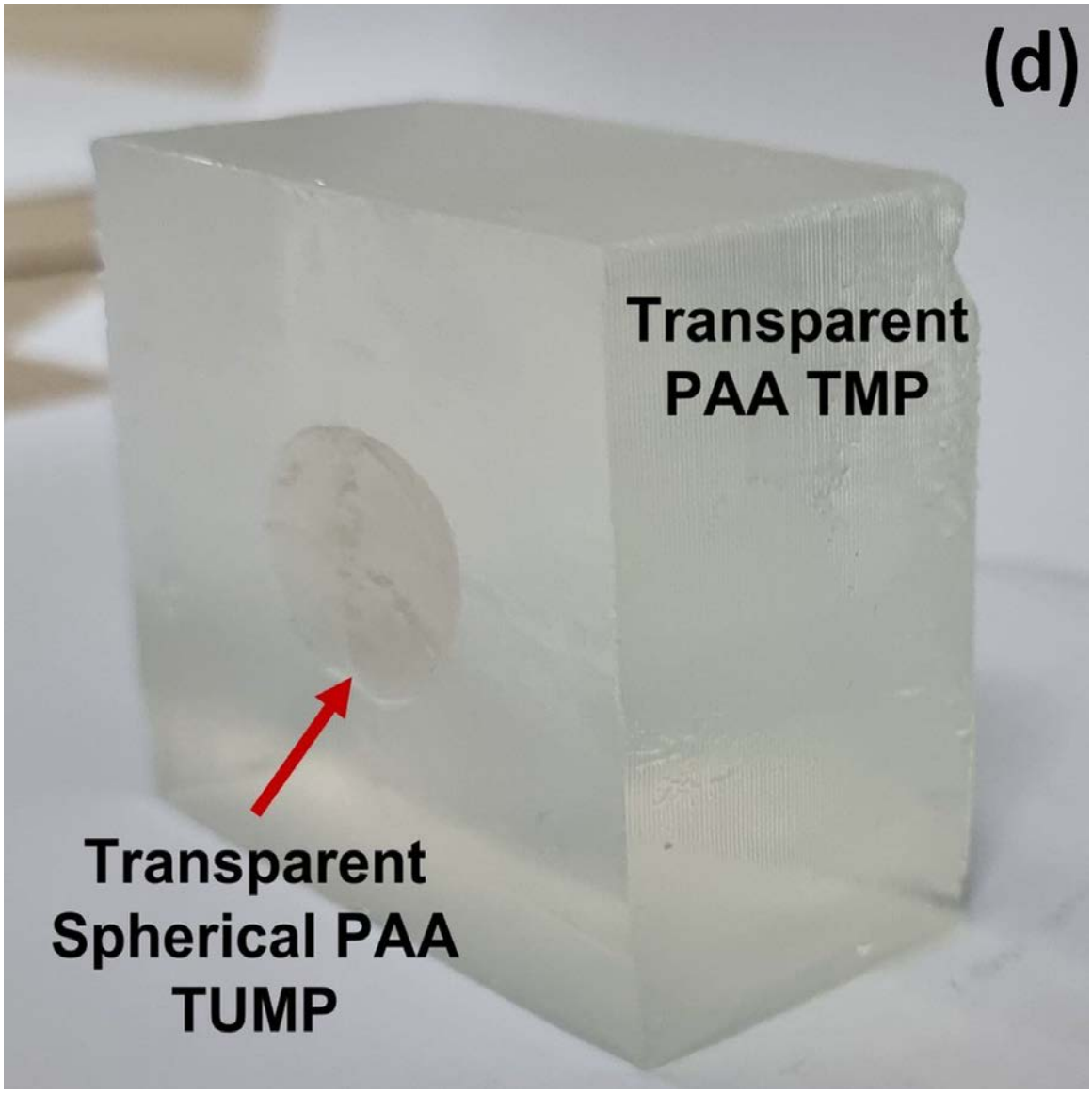
(d)
Transparent
PAA TMP
Transparent
Spherical PAA
TUMP

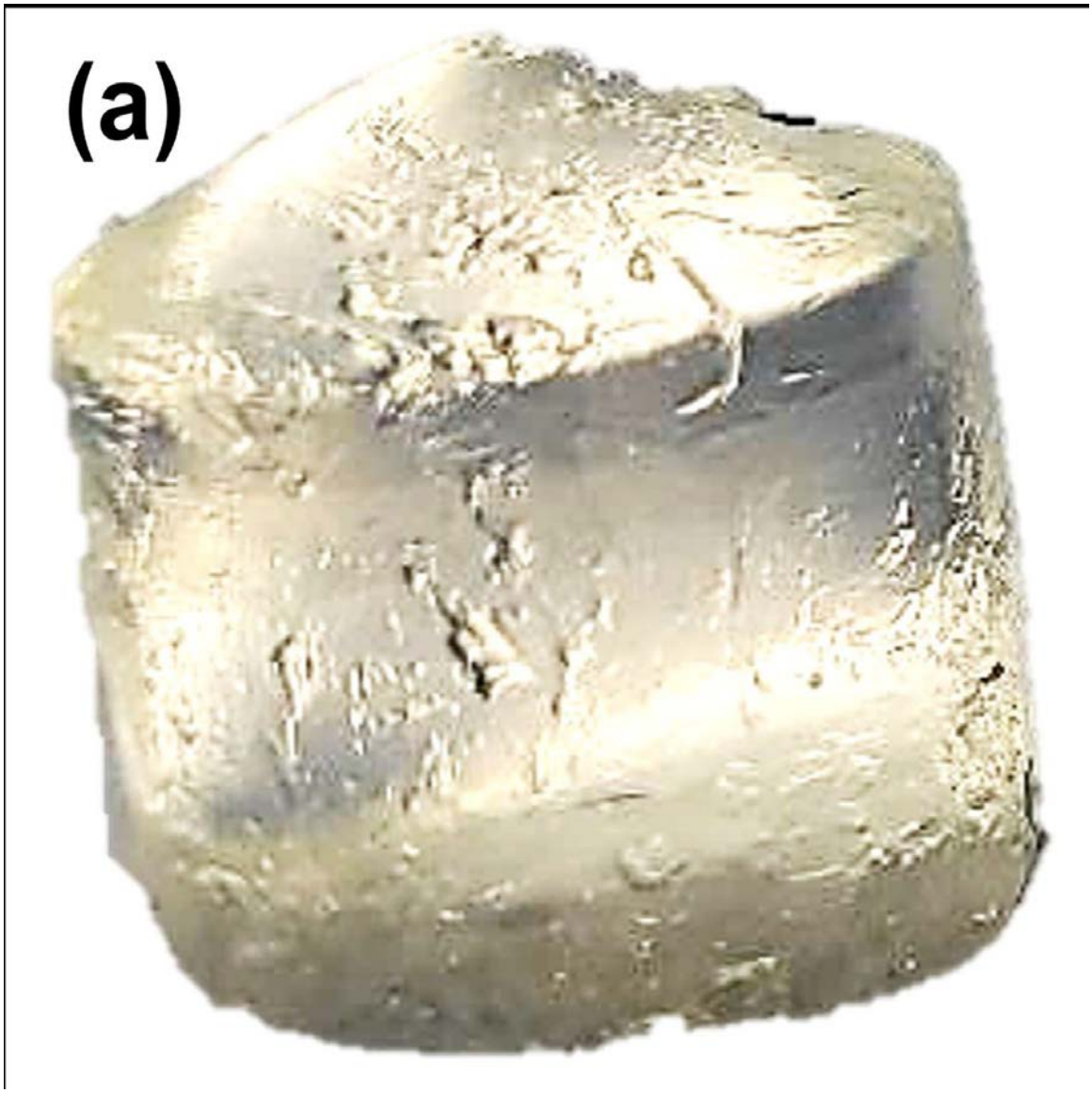
(a)

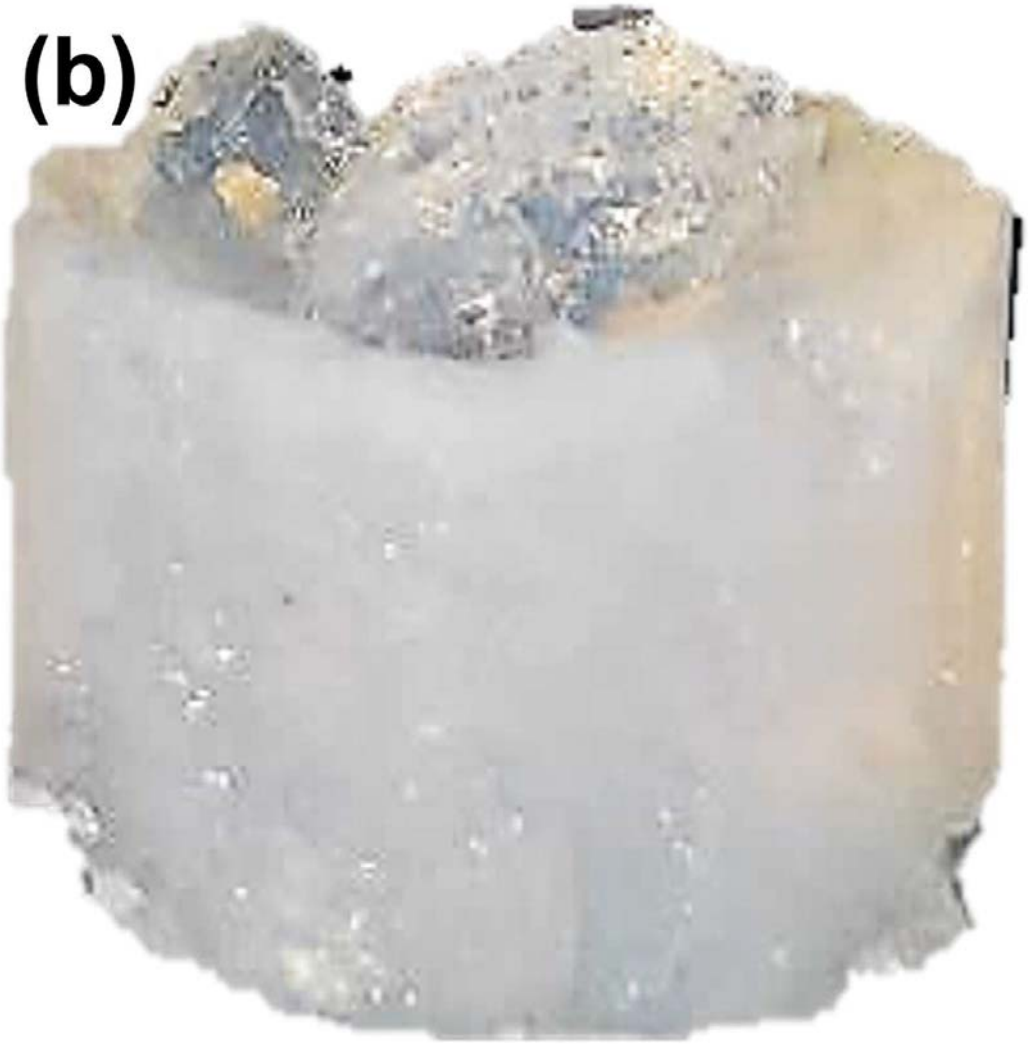
(b)

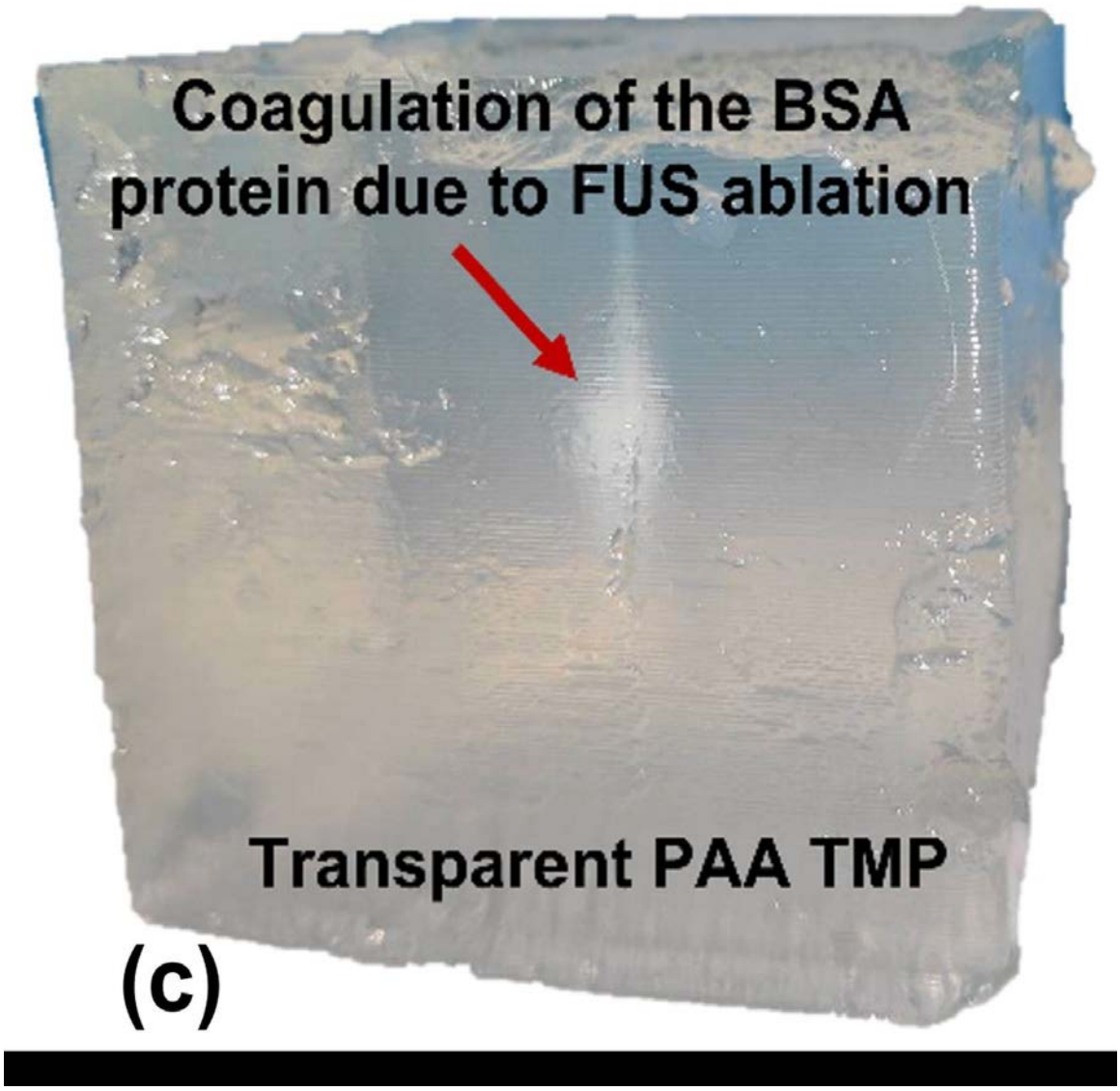
Coagulation of the BSA protein due to FUS ablation
Transparent PAA TMP
(c)

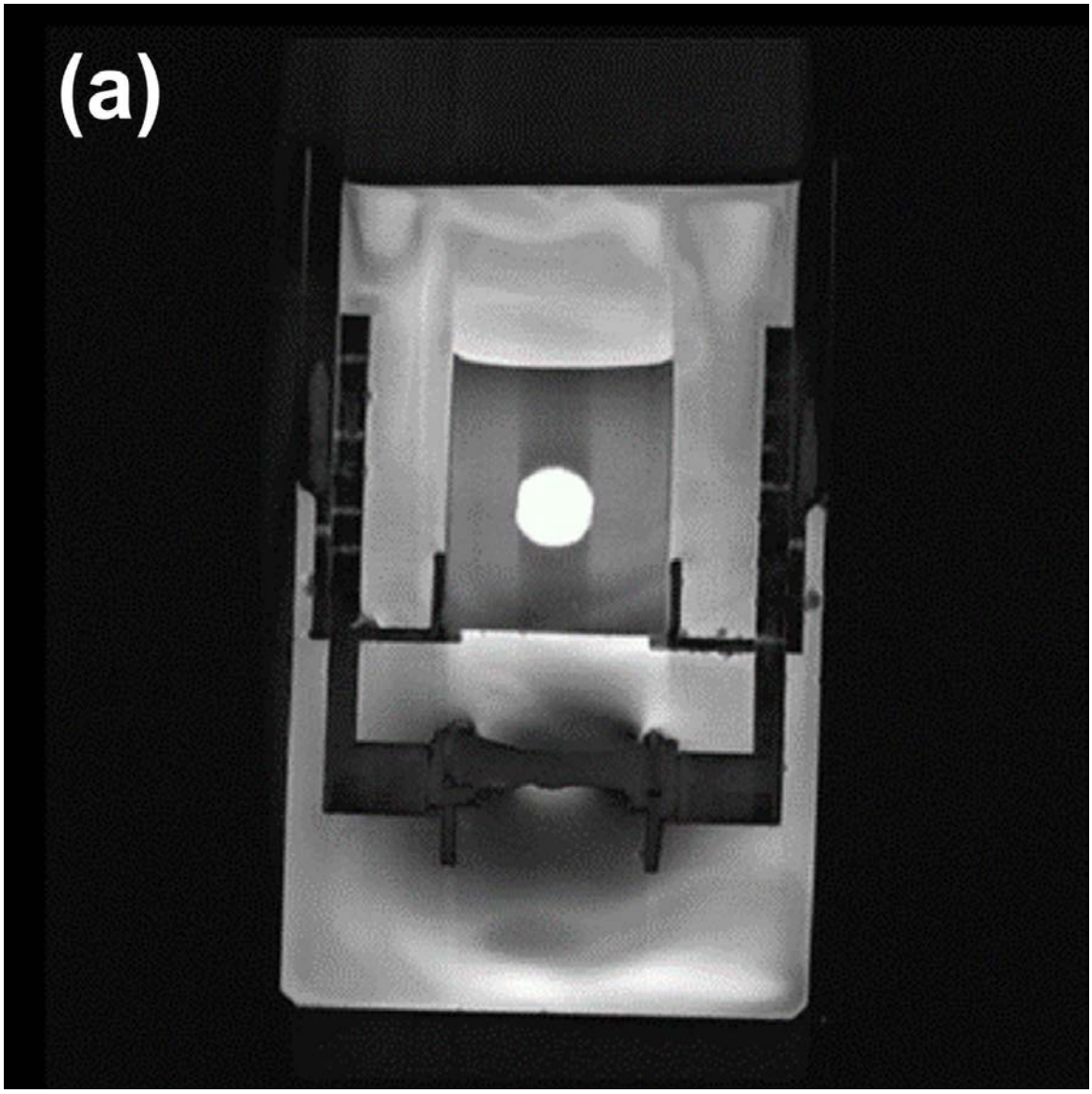
(a)

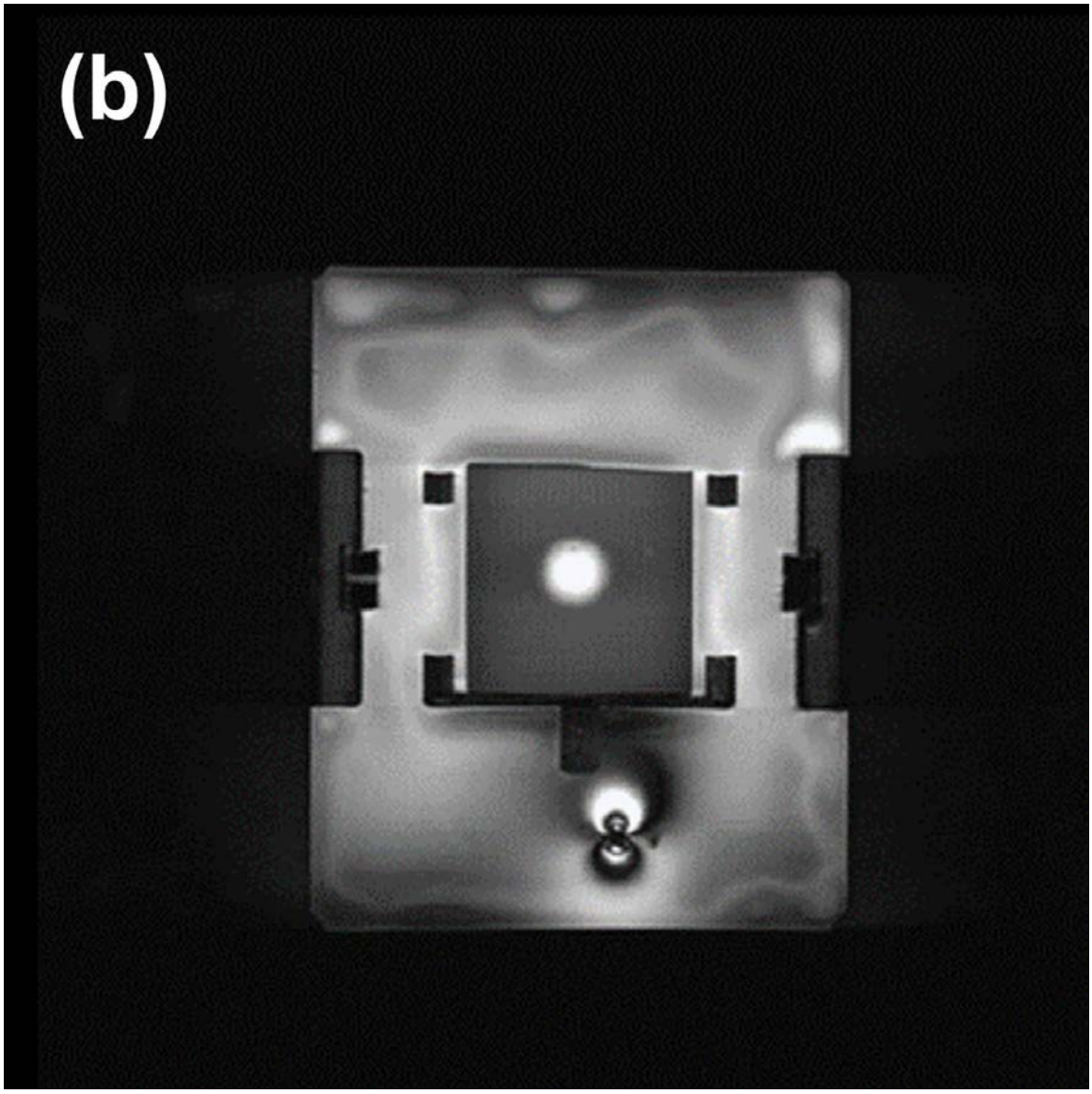
(b)

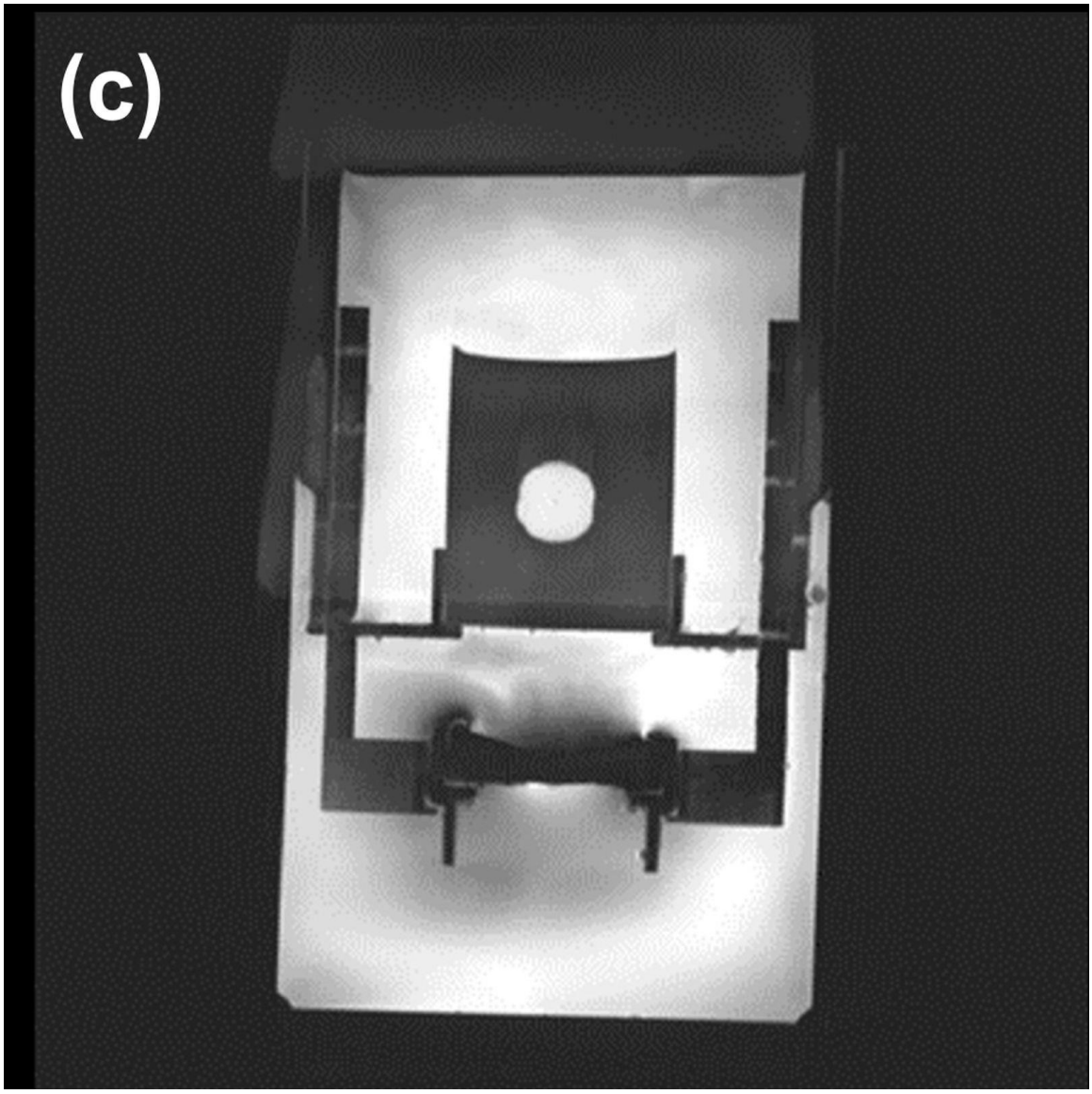
(c)

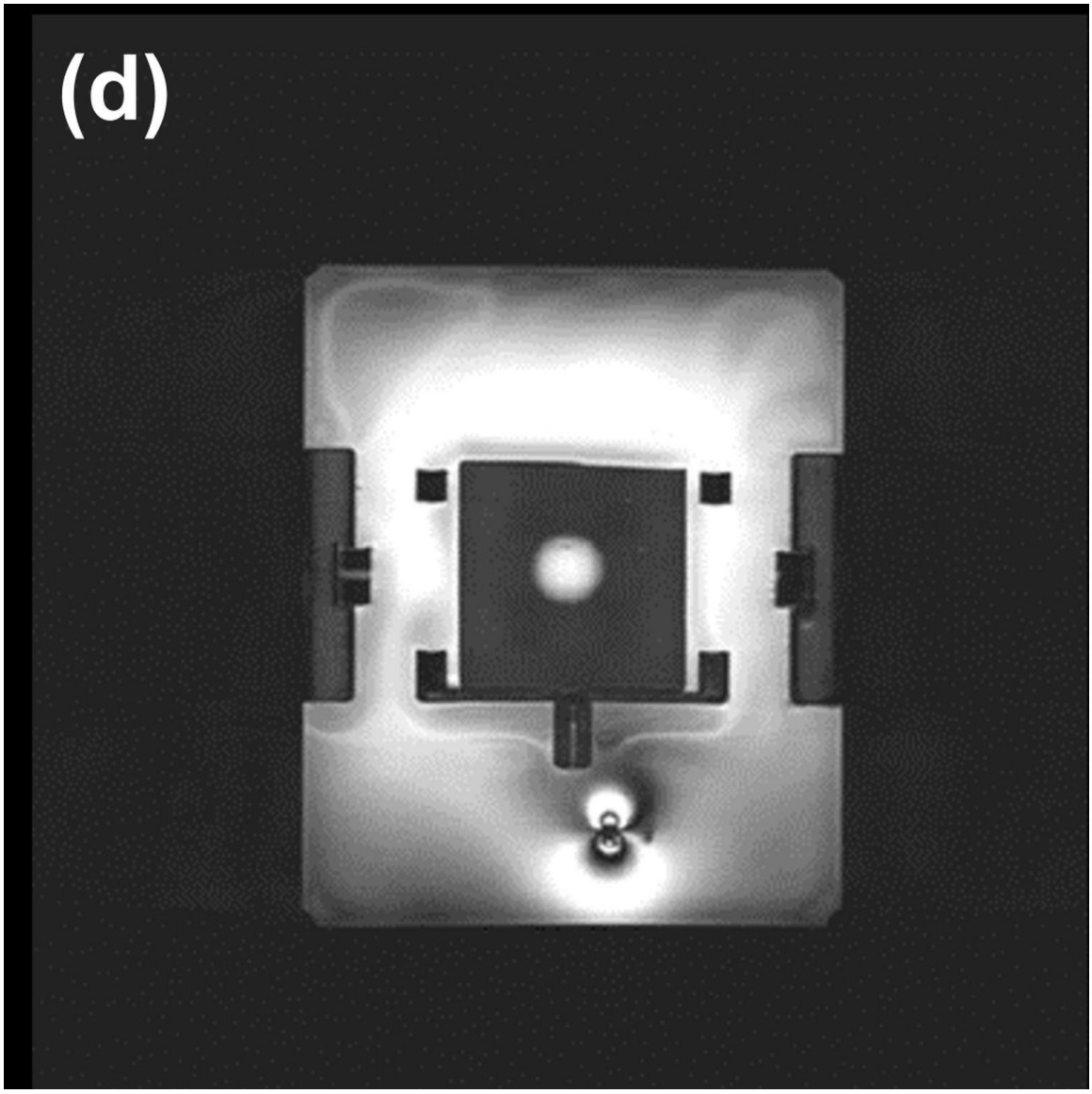
(d)

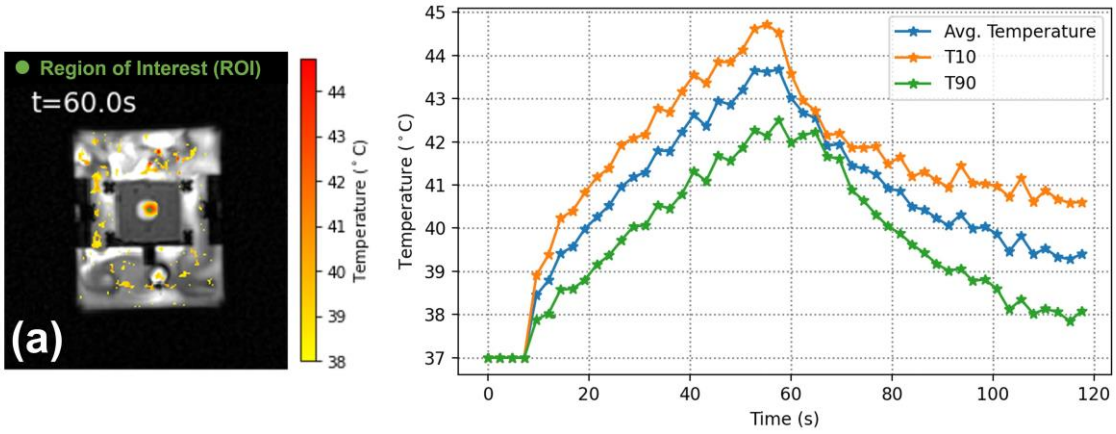
Region of Interest (ROI)
t=60.0s
(a)
Temperature (°C)
44
43
42
41
40
39
38
Avg. Temperature
T10
T90
Temperature (°C)
Time (s)
45
44
43
42
41
40
39
38
37
0
20
40
60
80
100
120

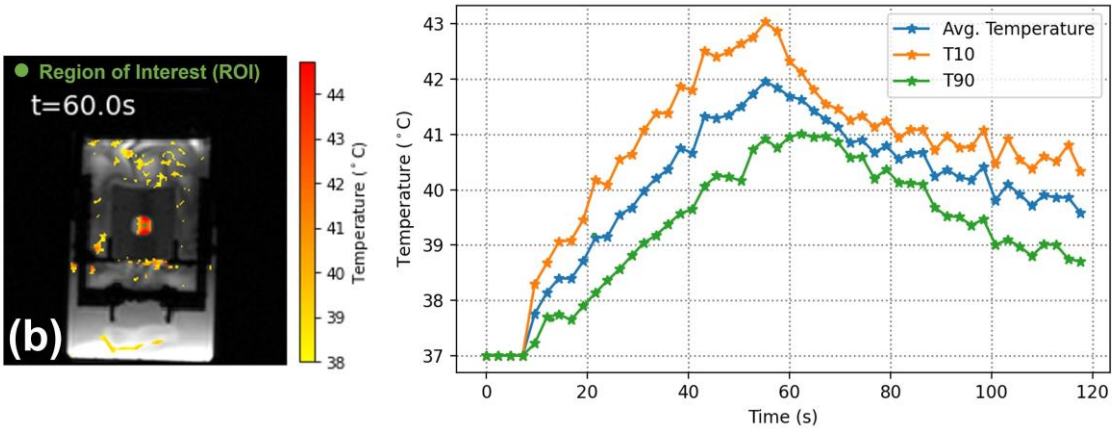
Region of Interest (ROI)
t=60.0s
(b)
Temperature (˚C)
44
43
42
41
40
39
38
Avg. Temperature
T10
T90
Temperature (˚C)
Time (s)
0
20
40
60
80
100
120
37
38
39
40
41
42
43

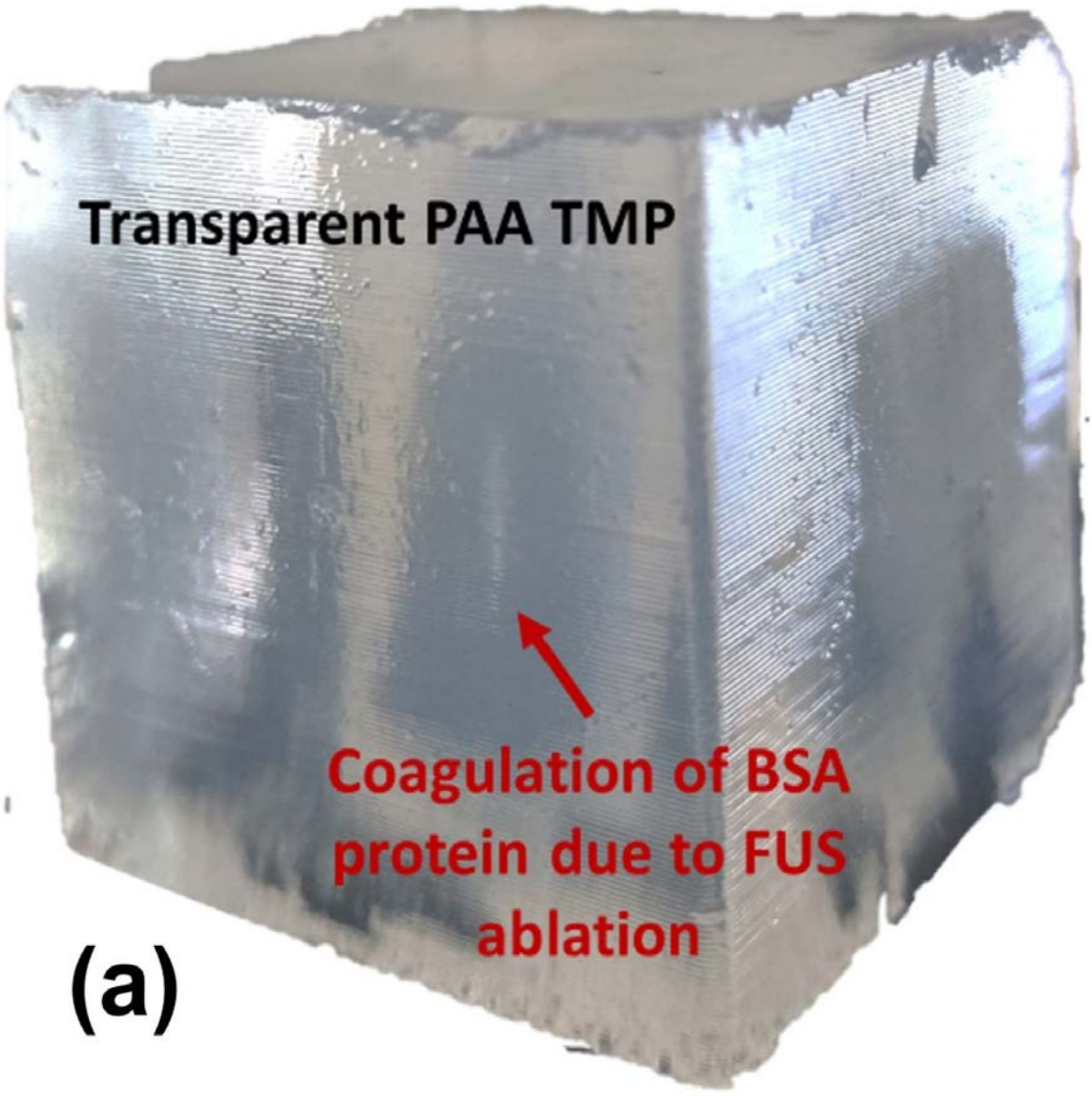
Transparent PAA TMP
Coagulation of BSA protein due to FUS ablation
(a)

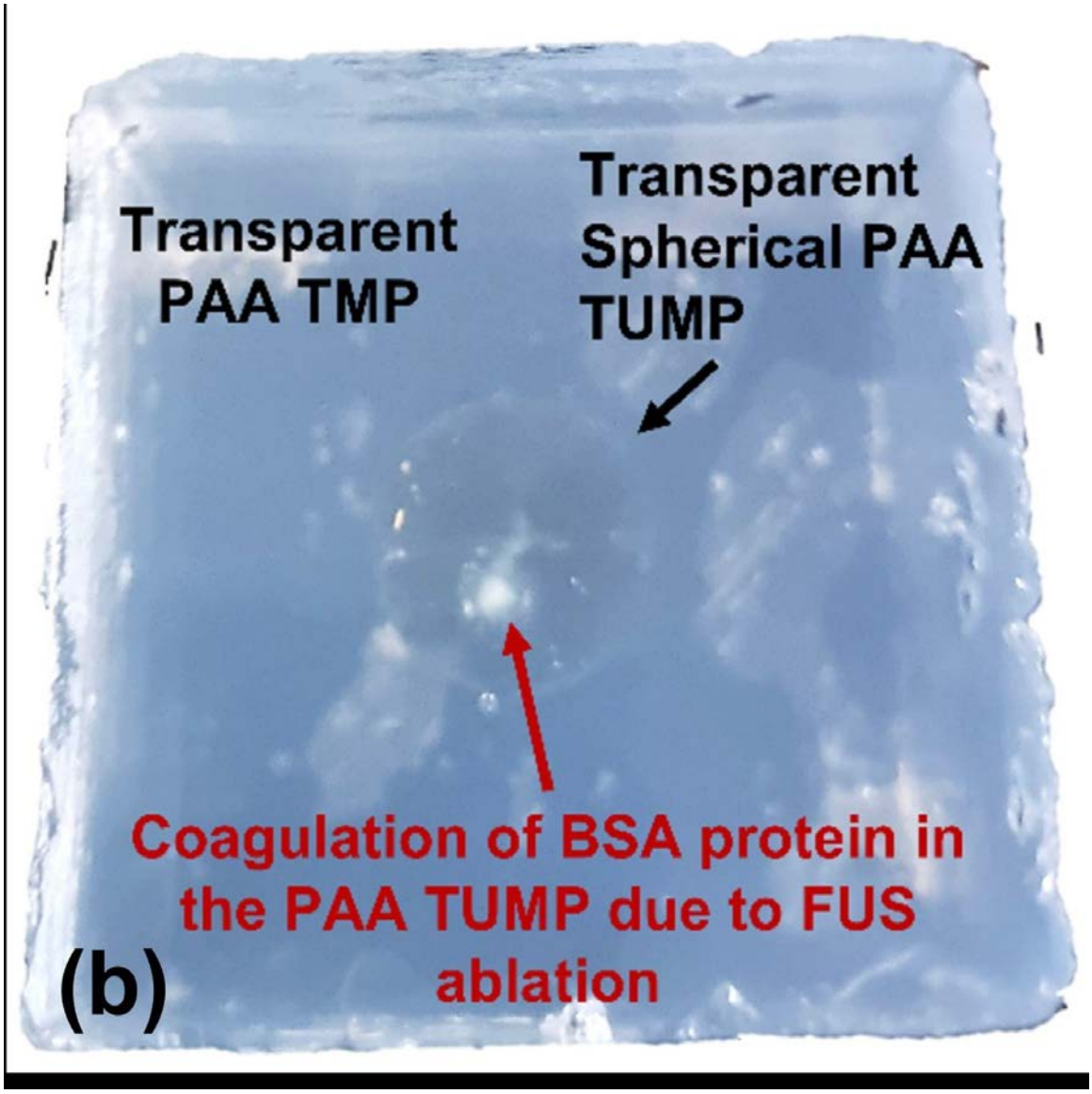
Transparent
PAA TMP
Transparent
Spherical PAA
TUMP
Coagulation of BSA protein in
the PAA TUMP due to FUS
ablation
(b)

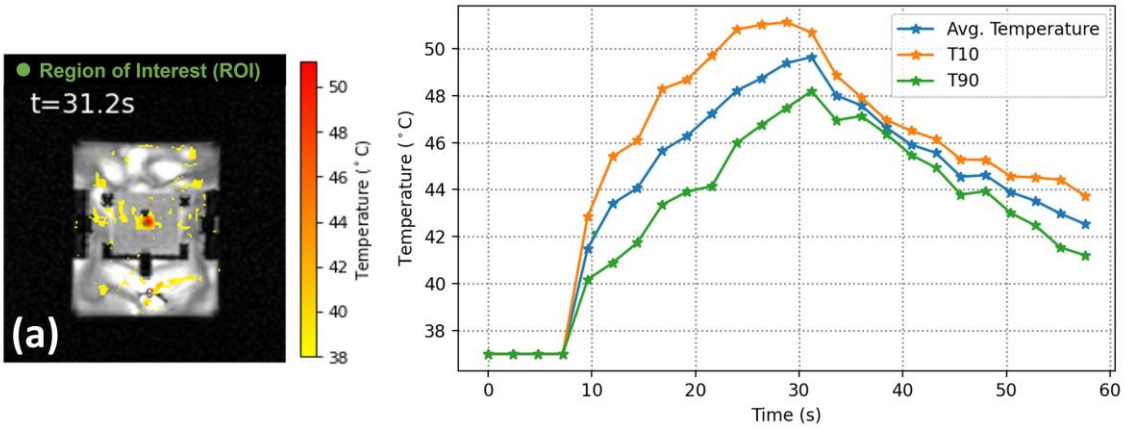
Region of Interest (ROI)
t=31.2s
(a)
50
48
46
44
42
40
38
Temperature (˚C)
Avg. Temperature
T10
T90
Temperature (˚C)
Time (s)
0
10
20
30
40
50
60

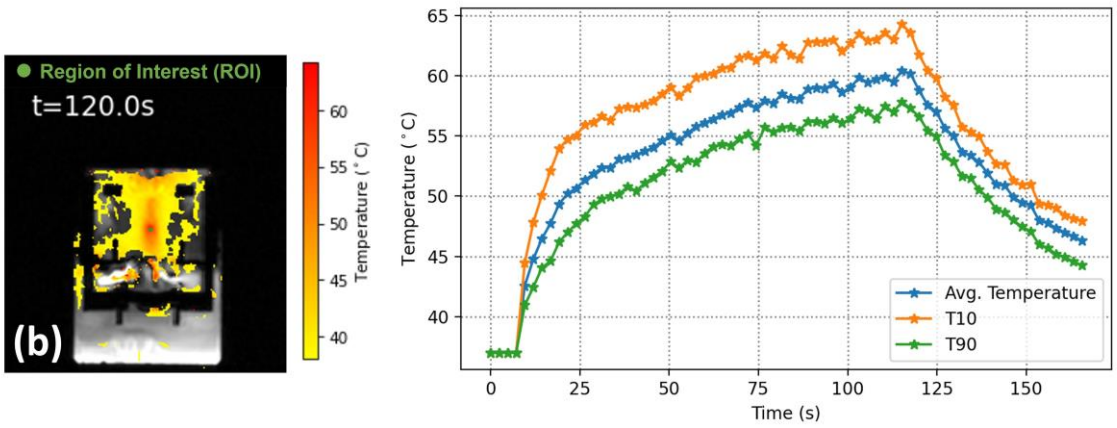
Region of Interest (ROI)
t=120.0s
(b)
60
55
50
45
40
Temperature (°C)
65
60
55
50
45
40
Temperature (°C)
0
25
50
75
100
125
150
Time (s)
Avg. Temperature
T10
T90

Robotic device for Magnetic Resonance Imaging guided Focused Ultrasound treatment of abdominal targets

Antria Filippou[a], Marinos Giannakou[b], Nikolas Evripidou[a], Andreas Georgiou[a], Anastasia Nikolaou[a], Christakis Damianou[a*]

[a] Cyprus University of Technology, Department of Electrical Engineering, Computer Engineering, and Informatics, Limassol, Cyprus.
[b]R&D, MEDSONIC LTD., Limassol, Cyprus.

***For correspondence contact:**
Christakis Damianou,
Cyprus University of Technology,
Electrical Engineering Department,
Cyprus University of Technology,
30 Archbishop Kyprianou Str.,
3036 Limassol,
CYPRUS
Email: christakis.damianou@cut.ac.cy
Tel.: 0035725002039
Fax: 0035725002849

MANUSCRIPT TYPE: Original Article
FUNDING: Funded by Research and Innovation Foundation of Cyprus
WORD COUNT: , **FIGURES:**

ABSTRACT

Background: An advanced robotic system intended for Magnetic Resonance guided Focused Ultrasound (MRgFUS) treatment of abdominal targets was manufactured based on clinical needs.

Methods: The system features motion in 4 degrees of freedom that manoeuvre a 2.75 MHz concave transducer inside a hermetically sealed enclosure that can be accommodated on the table of Magnetic Resonance Imaging (MRI) scanners interfacing with the prone positioned patient.

Results: The developed system was successfully assessed for its MRI compatibility in terms of Signal to Noise Ratio (SNR) changes, while *ex-vivo* ablation studies were executed in both laboratory and MRI environments to assess the system's thermal heating abilities. Excellent robotic motion accuracy was evidenced from sonications on plastic films. Well-formed discrete and overlapping lesions were successfully created on excised tissue following robotic motion along grid trajectories. MR thermometry demonstrated the transducer's efficacy in producing ablative temperatures that inflicted tissue necrosis evidenced with MR imaging.

Conclusions: The proposed MRgFUS system was proven efficient through *ex-vivo* feasibility studies with future *in-vivo* evaluation required for clinical adaptation offering MRgFUS treatment of abdominal targets.

KEYWORDS: abdominal; liver; kidney; pancreas; robotic; ultrasound; MRI

1. INTRODUCTION

High predominance of cancer in the abdominal area is observed annually[1], with liver[2], kidney[3], and pancreatic tumours[4] being one of the most prevailing cancer types globally, simultaneously reporting with a poor prognosis[1] and an excessive record of mortality rates[2–4]. Conventional surgical treatments[5,6] and minimally invasive ablative therapeutic techniques[7,8] are only applicable to selected cases and induce several adverse effects[5,6], with alternative treatments highly coveted. Over the past years, high intensity focused ultrasound (HIFU) is progressively gaining traction and clinical approval as an efficient alternative non-invasive treatment modality for several diseases, mainly in the oncological sector[9]. HIFU is employed extracorporeally, percutaneously focusing ultrasonic energy to the targeted tissue with a millimeter precision, where at the focus, energy absorption produces temperature increases higher than 60 ºC, leading to coagulative necrosis of the tissue cells[9].

HIFU was initially exploited preclinically for abdominal organ ablation, specifically liver and kidney tissues, in the late 1970s[10], and has thenceforth been abundantly investigated for its efficacy in ablating abdominal tumours in a range of preclinical[11–13] and clinical trials[14–16]. Particularly, clinical employment of HIFU with concurrent ultrasound guidance (US) used as a treatment monitoring modality for the management of liver cancer has reported to achieve effective tumour necrosis along with improved symptoms[14,17], with analogous results reported for similar employment of the technique for the treatment of kidney cancer[15,18]. Contrary, US-guided HIFU for pancreatic cancer management has only been shown to achieve considerable pain palliation and alleviation of symptoms due to the advanced stage of the disease[16,19,20]. Nevertheless, promising trials resulted in clinical adaptation of US-guided HIFU for the management of abdominal cancer, with three commercial US-guided systems, the JC-HIFU (Chongqing HAIFU Medical Technology, Chongqing, China)[19,21], the FEP-BY02 (Yuande Bio-Medical Engineering, Beijing, China)[16,22], and the HIFUNIT-9000 (Shanghai A&S Sci-

Tech, Shanghai, China)[23,24] regulatory approved for clinical management of abdominal tumours.

The advent of Magnetic Resonance Imaging (MRI) resulted in its employment as a guidance and control modality for HIFU procedures since the 1990s[25]. The excellent tissue contrast and high image resolution provided by MRI[26] as well as its ability to provide noninvasive monitoring of thermal heating during the procedures through the use of Magnetic Resonance (MR) thermometry[27] offered remarkable advancements of the HIFU technology and contributed to the wide clinical adaptation of MRI guided focused ultrasound (MRgFUS) systems. The ExAblate (Insightec, Haifa, Israel) and the Sonalleve (Profound Medical, Toronto, Canada) systems are probably the two most renowned commercial MRgFUS systems clinically applied for the treatment of uterine fibroids and alleviation of bone metastases-induced pain[28]. Both systems employ phased array transducers with all components embedded into a dedicated MRI-HIFU table for treatment[29]. Notably, not only are none of the commercial MRgFUS systems approved for treatment of abdominal tumours, but also studies reporting clinical employment of MRgFUS for abdominal tumour treatment are scarce. Specifically, in 2006, the first employment of MRgFUS for ablation of liver tumours was reported in a case study executed with the ExAblate system (Insightec) under respiratory monitoring, wherein targeting was performed in a liver section that spared the ribs, indicating the efficacy of the system but the necessary development of techniques that account for rib heating and organ motion before clinically envisaged[30]. Similarly, a clinical study[31] was later executed in three patients for MRgFUS treatment of one liver and two pancreatic tumours using the ExAblate system (Insightec) following controlled breathing. Complete ablation of the liver tumour, and up to 85 % ablation of the pancreatic tumours were evidenced on contrast-enhanced MRI images acquired directly post-treatment, with concurrent significant pain palliation achieved in the pancreatic cancer patients, revealing the efficacy of the system for treatment of abdominal

tumours, however with the integration of a motion control system necessary for future clinical establishment[31].

Due to the inherent advantages of HIFU over mainstay treatments, attempts are undertaken for the development of systems integrated with advanced features. Sakuma et al.[32] developed one of the first custom robotic systems for HIFU liver ablation that incorporated a ring HIFU transducer concentrically combined with a US imaging probe for 3D monitoring, which was navigated with 3 degrees of freedom (DOF) by a system of stepping motors having a reported motion accuracy of 3 mm. Around the same time, three focused transducers were linearly introduced on a custom robotic manipulator offering translational and rotational motion to the multiple transducer alignment and individual rotation of each transducer to achieve coincident focusing on a single point, resulting in a US-guided prototype for HIFU treatment of liver tumours[33]. Later, to account for manual transducer motion, use of step motors was reported for a 3D positioning device guiding a single-element HIFU transducer in vertical, horizontal, and rotational directions intended for treatment of kidney tumours[34]. The positioning device was integrated with a treatment planning software to achieve optimal tumour coverage and was proven accurate in prompt positioning and efficient in HIFU targeting through *ex-vivo* experiments, however with additions such as a matching layer, a patient supporting structure, possible design modifications, and integration of a US imaging transducer for monitoring, required before advancing to a clinical system[34].

A preclinical system offering robotically-assisted US-guided HIFU treatment of abdominal targets was developed in the study by Chanel et al.[35], compensating for respiration-induced motion in real-time, wherein an imaging and a therapeutic ultrasonic transducers were concentrically integrated as an end-effector to a 6 DOF robotic arm. Motion correction was performed according to speckles visible on US images, adjusting in real-time the position of the concentric transducer, with feasibility studies on moving excised chicken tissue resulting

in 80 % improved formation of lesions[35]. Notably, in an attempt to enhance existing HIFU systems, an advanced US-guided HIFU robotic system, the FUTURA platform, was developed in the framework of a research project, to offer noninvasive treatment of moving abdominal organs, specifically kidney[36,37], however also having use in other applications[37]. The system comprises two separate therapeutic and monitoring robotic arm applicators, each offering motion in 6 DOF, with a 16-channel phased array transducer mounted on the therapeutic unit and extracorporeally coupled to the abdomen, and the monitoring unit equipped with two US imaging transducers for therapy monitoring and organ tracking[37]. The FUTURA platform has been proven highly accurate through *in-vitro*[37] and *ex-vivo* experiments[38], however its *in-vivo* efficacy is yet to be assessed.

Exploitation of the superior features of MRI is imperative for amplifying HIFU treatments and offering enhanced safety[39], thus effective research is ongoing for the lookout of advanced MRgFUS robotic systems for abdominal tumours. The introduction of rapid prototyping aided the development of a range of custom MRgFUS robotic systems intended for liver, kidney, and pancreatic tumour ablations[40–45]. In 2007, one of the earliest 3D printed MRgFUS robotic positioners with an adaptable transducer coupling method able to ablate various organs, including the abdominal area, was reported, featuring piezoelectrically driven motion of the transducer in 3 DOF established through a series of neoprene belts[40], with *ex-vivo*[40], and *in-vivo* rabbit liver feasibility experiments[46] indicating the efficacy of the system[40]. Subsequent systems that were specifically proposed for abdominal organs[41] or could be applied to such targets[42,43], employed a series of jackscrew mechanisms to initiate motion in various piezoelectrically driven translational[43] or translational and rotational directions[41,42]. Initial configurations of these systems for abdominal targeting proposed a supine patient positioning on the MRI table with the device superiorly attached on the MRI bore[43], with subsequent systems easily mounted on the table with the patient in the prone position[41,42]. Lately, a compact

MRgFUS system was reported that provided increased space for prone patient positioning within the bore by employing three similar transducers incorporated at dissimilar heights within the robotic system, thus sparing the need for vertical transducer translation[41]. The system was proven capable of accurate abdominal ablation through *in-vivo* rabbit feasibility experiments, however with further design optimisations required for clinical adaptation[41]. Interestingly, a system enabling robotically assisted transducer positioning in 4 DOF (3 translational, and 1 rotational) and mountable to the MRI table through a C-shaped gantry was reported for superior to inferior MRgFUS treatment of a range of oncological diseases, including abdominal targets[44]. Notably, the system was designed based on clinical requirements, with acoustic coupling with the supine placed patient achieved with a water-filled cone sited to the targeted area through the positioning mechanisms and with *ex-vivo* experiments indicating the efficacy of the system[44]. Recently, a custom 3D-printed MRgFUS robotic platform was developed to be integrated within the MRI-HIFU table of commercial MRgFUS systems offering hydraulically actuated mechanical motion in 5 DOF to the phased array transducer so as to increase the available workspace and achieve accurate targeting of tumours in the abdominal area[45]. *In-silico* evaluation experiments proved accurate targeting of liver tumours, thus indicating the potential employment of the platform for the treatment of abdominopelvic tumours, combining mechanical and electronic steering of the annular transducer[45].

Herein, an MRgFUS robotic system designed for treatment of abdominal tumours is described. The proposed system can be easily integrated on the table of clinical MRI scanners with the patient in the prone position above the acoustic window for targeted treatment. Contrary to the commercial[16,19,21–24] or preclinical[32–37] US-guided systems, employment of MRI monitoring by the proposed system optimises treatment safety by enabling monitoring of the temperature evolution using MR thermometry tools. The developed robotic system offers computer-controlled motion to a single element focused transducer in 4 DOF, namely three

linear and one angular stages. Compared to previously proposed MRgFUS systems manufactured with rapid prototyping[40–44], the proposed device is characterised by advanced features and functionalities. Specifically, the proposed system incorporates novel piezoelectrically driven positioning mechanisms that improve the robustness and accuracy of robotic motion. Moreover, a pair of optical encoders was integrated on each positioning stage ensuring high accuracy of motion. More importantly, the device was designed based on clinical needs offering a proper and sufficient motion range for human applications. Furthermore, contrary to previous work[44], the positioning mechanisms of the proposed system are integrated in an enclosure that enhances safety and which was appropriately designed to provide a hermetic sealing to the water container wherein the transducer is actuated, thus avoiding water volume displacement observed in other proposed systems[41].

2. MATERIALS AND METHODS

2.1 Description of the design and principle of motion of the robotic system

The robotic system was designed featuring motion in 4 DOF utilising a computer aided design (CAD) software (Inventor, Autodesk, San Rafael, California, USA). The robotic system was manufactured by fused modelling additive manufacturing and thermoplastic Acrylonitrile Styrene Acrylate (ASA) material utilising an industrial rapid prototyping system (F270, Stratasys, Minnesota, USA). The produced plastic parts were assembled using non-ferromagnetic components like brass screws and brass rods to ensure suitable operation within MRI environments. The 4 DOF positioning mechanisms of the robotic system provide PC-controlled motion in three linear (X, Y, and Z) and one angular (Θ) stages. The X-stage offers forward and reverse motion, the Y-stage provides left and right motion, while the Z-stage moves in up and down directions with available motion ranges of 94 mm, 127 mm, and 47 mm, respectively. The Θ-stage offers rotational motion to the transducer relative to the X-stage, having an available motion range of 120^{o} (60^{o} in bilateral directions). Motion in each stage is

actuated by non-magnetic piezoelectric motors (USR60-S3N, Shinsei Kogyo Corp., Tokyo, Japan) with a pair of MRI-compatible linear (EM1-0-500-I, US Digital Corporation, Vancouver, USA) or angular (EM1-2-2500-I, US Digital Corporation) optical encoders utilised to ensure the linear and angular motion accuracy, respectively.

2.1.1 X-stage

Figure 1 shows the motion principle of the X-stage. The X-motor is rigidly secured on the rear end of the X-frame cover via brass screws. The shaft of the X-motor, through the X-frame cover, attaches to a spur gear existing within the X-frame. The spur gear is in turn bilaterally coupled to an identical pair of gear and pinion gear mechanisms. The single spur and the two pinion gear mechanisms were specifically designed with an identical size. Consequently, the rotational motion of the X-motor shaft is transferred to the spur gear, and through the gear mechanisms unaffectedly transmitted to the pinion gears, resulting in equal rotation of each of the pinion gears with rotation of the spur gear. The rotational motion of the pinion gears is transferred to the two X-jackscrews that have been individually rigidly mounted on each pinion gear through hexagonal couplings (not visible in Figure 1). Gear and jackscrew retainers are employed to provide a rigid support to the gear and jackscrew mechanisms on the rear of the X-frame, allowing unrestricted rotation whilst preventing inadvertent lateral displacement of the assembly. Notably, the X-brass shafts are securely attached to the X-frame acting as linear motion guides of the X-plate. To ensure stable and smooth motion of the X-plate along the X-brass shafts, the X-brass shafts are tightly connected with the double-sided X-frame supporting structures, while two X-brass shaft supporting structures (one for each X-brass shaft) are employed to secure each of the X-brass shafts to the X-frame supporting structures and in turn to the mechanism enclosure, providing stability of the X-brass shafts during robotic motion. Accordingly, the X-plate bilaterally couples to the two X-jackscrews through internally designed thread guides (not perceptible in Figure 1), while concurrently

being coupled to the X-brass shafts via internal cylindrical brass shaft guides (also not visible in Figure 1) with mounted ring-shaped brass shaft guides at the ends, allowing a tight connection with the X-brass shafts offering stability during motion. Consequently, the internal X-jackscrew thread guides convert the rotation of the X-motor shaft, and ultimately the angular displacement of the pinion gears and the X-jackscrews, to a smooth linear forward and reverse motion of the X-plate along the two X-brass shafts. Remarkably, for one complete rotation (360^{o}) of the X-motor shaft a 14.4 mm displacement of the X-plate is achieved. Notably, the pair of X-encoders were bilaterally installed on either sides of the X-plate (one encoder for each side) ensuring the motion accuracy of the X-plate. The X-housing switch mounted on the rear end of the X-frame identifies the initial point of the X-stage motion, with the X-housing switch stopper that is positioned on the X-plate acting as the triggering button of the X-housing switch.

2.1.2 Y-stage

Figure 2 shows the assembly and motion principle of the Y-stage. The Y-stage is connected to the X-stage through the two Y-brass shafts. The two Y-brass shafts are attached and secured to the X-plate through special tight couplings resulting in stable forward and reverse displacement of the Y-stage relative to the motion of the X-stage. The motion principle of the Y-stage is different compared to the X-stage. The Y-motor is rigidly attached to the Y-plate that is in turn connected at both ends, through inner couplings, with the two Y-brass shafts. The shaft of the Y-motor is connected to a gear mechanism assembly situated at the bottom of the Y-plate, with a cover at the lowest part employed to secure and protect the gear mechanism. The gear mechanism transfers the rotational motion of the Y-motor shaft to the outer gear of the assembly that is in turn connected to the Y-rack forming a rack and pinion actuator. In this sense, the rotational motion of the Y-motor shaft is translated to linear motion of the Y-plate along the Y-rack. Similar to the secure connection of the Y-brass shafts with the

X-plate, the Y-rack is secured at both ends on the inner sides of the X-plate, achieving rigidity during motion and ensuring a smooth displacement of the Y-stage according to the motion of the X-stage. The firm connection of the Y-brass shafts and the Y-rack with the Y-plate ensure the simultaneous linear motion of the Y-plate along the Y-rack and its linear left or right sliding along the Y-brass shafts, resulting in a sturdy displacement of 25.43 mm for one complete rotation of the Y-motor shaft. High motion accuracy of the Y-plate is achieved with the pair of Y-encoders coupled together on the upper end of the Y-motor. The Y-encoder cover is employed to rigidly attach and secure the Y-encoders on top of the Y-motor, while the Y-housing switch that identifies the initial position of the Y-stage is attached on the outer left side of the Y-plate and is triggered upon interfacing with the inner side of the X-plate.

2.1.3 Z-stage

Accordingly, Figure 3 shows the motion principle of the Z-stage. Notably, the anterior part of the Y-plate was designed to accommodate the positioning mechanisms of the Z-stage. Specifically, three Z-brass shafts (two anterior and one posterior) indicating the motion frame of the Z-stage were vertically accommodated and secured to the Y-plate using stiff couplings, integrating the Y and Z stages, ultimately achieving connection of the X and Z stages. Consequently, stable linear motion of the Z-stage is achieved according to the individual linear motions of the Y and X stages. The Z-stage employs a jackscrew mechanism to achieve vertical linear motion. Specifically, the Z-motor is located on the upper part of the Y-plate and is rigidly connected to the Z-jackscrew, achieving rotation of the Z-jackscrew according to the rotation of the Z-motor shaft. The Z-plate attaches through couplings to the three Z-brass shafts and the Z-jackscrew. In fact, coupling of the Z-plate with the Z-jackscrew is achieved through thread guides that were appropriately designed on the inner surface of the Z-plate. Therefore, the Z-plate thread guides convert the rotational motion of the Z-motor and the Z-jackscrew to linear motion of the Z-plate in the vertical direction. Concurrent and secure coupling of the Z-plate

with the three Z-brass shafts results in vertical sliding of the Z-plate along the Z-brass shafts. Remarkably, the triangular configuration of the three Z-brass shafts, with two shafts accommodated on the anterior part of the Y-plate and one shaft integrated on the posterior side, was chosen to enhance the stability of the Z-stage, offering rigidity during motion. Accordingly, a pair of Z-encoders is employed to ensure the motion accuracy of the Z-plate, with one encoder installed on each side of the Z-plate. Moreover, similarly to the X and Y stages, a Z-housing switch was coupled on the posterior upper inner part of the Y-plate indicating the initial point of the Z-stage motion. The Z-housing switch stopper was designed into the upper posterior part of the Z-plate acting as a triggering button of the Z-housing switch upon interfacing.

2.1.4 Θ-stage

Remarkably, the mechanisms of the Θ-stage are mounted on the space specifically designed on the anterior section of the Z-plate. Figure 4 shows the assembly of the positioning mechanisms of the Θ-stage. Specifically, the rear end of the Θ-motor is securely attached on the Θ-stage coupling integrated on the Z-plate. Moreover, the Θ-stage coupling allows tight enclosure of the Θ-motor, thus achieving a fixed and stable connection of the Θ and Z stages. Additionally, as a result of the advanced rigid connections between the aforementioned stages (X, Y, and Z), the assembly of all four positioning stages is achieved. The Θ-stage coupling attaches and secures with brass screws to the planetary gear mechanism frame. The Θ-motor shaft attaches, through appropriate connections allowed on the mechanism frame, to the planetary gear mechanism that achieves the angular motion of the Θ-stage and ultimately the rotation of the transducer. Specifically, the shaft of the Θ-motor is mounted on the sun gear section of the planetary gear mechanism where the rotary motion of the Θ-motor shaft forces identical rotation of the sun gear that is then equivalently transferred to the double-stage planetary gears of the planetary gear mechanism assembly and ultimately results in rotation of

the ring gear. The planetary gear mechanism frame encloses and secures the planetary gear mechanism, while the two Θ-brass shafts are employed as rotation axes of each of the double-stage planetary gears to enhance the stability of the planetary mechanism assembly. The ring gear of the planetary assembly extends and attaches to the transducer shaft with several brass screws employed to secure the connection, achieving linear arrangement of the transducer shaft ensuring unaffected transfer of the rotation of the ring gear to the transducer shaft. The front end of the transducer shaft connects to the transducer holder via couplings and secures with brass screws offering a stable alignment of the transducer with the four positioning mechanisms. The angular motion accuracy of the Θ-stage is achieved with the dual Θ-encoders which are integrated behind the planetary gear mechanism frame and secured with the Θ-encoders frame.

2.1.5 Entire positioning device

Remarkably, the positioning mechanisms were accommodated in a mechanism enclosure as shown in Figure 5A. Specifically, the X-frame and the X-frame supporting structures (where all four stages are attached to through advanced connections) are attached and secured to the lower part of the mechanism enclosure offering rigidity of the four positioning mechanisms during robotic operation. Notably, the mechanism enclosure consists of two independent sections, namely the main mechanism enclosure and the mechanism enclosure extension that was designed to adequately cover the motion range of the X-axis. Moreover, this configuration enables easy disassembly of the robotic device and replacement of the enclosure in the extreme case of damage. Remarkably, the ASA mechanism enclosure extension was specifically constructed with special hollow spaces to enable the lateral integration of three coupling brass shafts that achieve a rigid connection of the mechanism enclosure with the water container. The transducer shaft extends the transducer holder from the positioning mechanisms to the water container, achieving a coupling medium for optimal

ultrasonic beam transmission. An in-house developed flexible silicone bellow is employed to isolate and secure the positioning mechanisms from the water container, while simultaneously allowing the unrestricted displacement of the transducer shaft during robotic movement. Impressively, the water container was appropriately developed to enable creation of an ideal vacuum environment that maintains a constant water level within the container throughout robotic motion. Specifically, degassed water is poured in the water reservoirs with flexible polyvinyl chloride (PVC) tubes allowed through special inlets connecting the water container with the water reservoir. The PVC tubes pass from the water reservoirs through the mechanism enclosure, where via special outlets integrated at the rear-end of the mechanism enclosure can be connected to a pump. An ABS cover was manufactured and placed on top of the water container as shown in Figure 5B. The water container cover avoids water spillage, while it tightly attaches and hermetically seals with the lower water container and reservoirs. In this regard, the water container cover is irremovable, achieving a vacuum sealing. To achieve a proper transmission of the ultrasonic energy to the targeted anatomy, an acoustic window was allowed on the water container cover, with a 0.2 mm thin silicone membrane (Silex Limited, Hampshire, UK) securely enclosed within the respective housing, hermetically covering the acoustic window, and maintaining the required vacuum sealing of the water container. Degassed water can be inserted in the water reservoirs through the two water inlet valve caps integrated on the water container cover, and by employing the PVC tubes and the pump system, the water container can be properly filled. Remarkably, depending on the water level within the container, the installed PVC tube acts either as a water inlet or an air extract that removes any air remaining under the membrane, thus achieving unrestricted transmission of acoustic energy. Moreover, as shown in Figure 5B, the mechanism enclosure is also protected on top with a rigid cover that seals the robotic mechanisms from the patient.

The manufactured robotic device is shown in Figure 5C and Figure 5D. The final system is a compact device with exterior dimensions of 900 mm length, 350 mm width and 135 mm height. Additionally, the robotic system is effortlessly transportable since it weighs approximately 14 kg. The compact design of the robotic system enables its accommodation on the patient table of clinical MRI scanners as shown in Figure 6. The robotic device is appropriately incorporated within a 135 mm thick mattress that is sited on the MRI table to cover the system and simultaneously facilitate comfortable placement of the patient. The patient is positioned on the mattress in a prone position with the abdominal area positioned on the acoustic window of the robotic device for targeted treatment of the abdominal organ of interest. Ultrasound gel can be employed between the abdominal area and the silicone membrane of the acoustic window offering appropriate acoustic coupling for treatment.

2.2 HIFU apparatus

The HIFU therapeutic transducer manoeuvred by the robotic system was manufactured in-house employing only non-magnetic materials. A single focused piezoceramic element (Hubei Hannas Tech Co., Hubei, Wuhan, China) was chosen with appropriate structural characteristics following simulation studies that revealed the optimal features for sufficient tissue targeting. In this manner, a piezoceramic element operating at a frequency of 2.75 MHz, with a diameter of 50 mm and a geometric focus of 65 mm was enclosed in a custom 3D-printed (F270, Stratasys) ASA ring case. The in-house transducer is activated by an RF amplifier (AG1016, T&C Power Conversion, Rochester, New York, USA) achieving an efficiency of 30 %.

2.3 HIFU and robot control software

The robotic device and the HIFU set-up are remotely controlled with a custom in-house software developed in C# (Visual Studio, Microsoft Corporation, Washington, USA). Algorithms allow control of the robotic motion in the four positioning stages (X, Y, Z, and Θ)

and specify the transducer's trajectory in various patterns (grid or irregular) through proper selection of the motion operation parameters (i.e., pattern, grid size, spatial step and delay between sonications), with the respective commands sent to an electronic driving system manufactured in-house. Additionally, through proper commands, the housing switches incorporated in the three linear positioning stages (X, Y, and Z) register the initial position of the robotic system on each axis relative to the respective axis motion range, thus providing increased safety during robotic operation. Concerning control of the HIFU set-up and the ultrasonic exposures, relevant commands enable selection of the transducer's operating frequency, choice between pulse or continuous exposure mode, and specification of the applied power and sonication time. Furthermore, the control software can communicate with MRI scanners allowing transfer of MRI images, enabling treatment planning and ablation monitoring through MR thermometry.

2.3 Assessment of the performance of the robotic system

2.3.1 MRI compatibility

The MRI compatibility of the developed robotic system and the manufactured transducer was evaluated within a clinical 3 T MRI scanner (Magnetom Vida, Siemens Healthineers, Erlangen, Germany). Specifically, the assembled robotic system was accommodated on the table of the MRI scanner with a piece of freshly excised pork loin tissue mounted on the acoustic window. A 12-channel body coil (BioMatrix Body 12, Siemens Healthineers) was accommodated on the upper surface of the excised tissue using a custom-made rigid ASA supporting structure. MRI compatibility assessment was executed by evaluating the impact of various activation configurations on the Signal to Noise Ratio (SNR).

The excised pork tissue was sequentially imaged for a series of independent states of the robotic system and the ultrasonic transducer using a 2D Fast Low Angle Shot (FLASH) sequence with the following parameters: Repetition time (TR) = 25 ms, Echo time (TE) = 10

ms, Field of view (FOV) = 280×280 mm^2, Slice thickness = 10 mm, Acquisition matrix = 96×96, Number of excitations (NEX) = 1, Flip angle = 30°, and Pixel bandwidth = 240 kHz/pixel. Specifically, for the robotic system, excised tissue images were individually acquired with the positioning device solely sited on the MRI table and the motion and RF cables disconnected (regarded as a reference condition), with the motion cables connected, as well as upon electronic system activation. Regarding transducer compatibility, FLASH image acquisition was executed under a reference state (cables disconnected), with the RF cables connected, activation of the RF amplifier and no power applied, as well as upon transducer activation at acoustical powers of 30 W and 60 W. SNR calculations were individually executed for the FLASH images of the excised tissue by setting single region of interests (ROI) within the tissue and air background and substituting average signal intensities (SI) and standard deviations (σ) into the following equation:

$$SNR = {SI_{tissue}}/{\sigma_{air\ background}} \quad (1)$$

2.3.2 Motion accuracy

Initially, low power benchtop sonications were executed on thin (0.7 mm thickness) plastic films (Fortus FDM400mc print plate, Stratasys) to visually examine the accuracy of robotic motion following previously reported evaluation methods[47]. Thin plastic films have emerged as a simple and cost-effective method for evaluating the robotic motion accuracy of MRgFUS systems[47] since when exposed to proper amounts of ultrasonic energy during ablations they deform, with white lesions locally induced at the sonication site[47,48]. In this regard, the plastic films were accommodated on the acoustic window of the robotic system, at a distance of 65 mm from the ultrasonic transducer. It is worth stating that lesion formation on plastic films resulting ultrasonic exposures is attributed to ultrasonic reflection effects observed between the plastic film and the air interface, with proper levels of the water coupling medium critical for lesioning. Consequently, for the benchtop film ablations, the silicone membrane of

the acoustic window was removed, and the thin plastic films were accommodated on the acoustic window, with their rear end directly interfacing with the degassed water of the water container. Robotic motion of the ultrasonic transducer in grid trajectories was commanded by the in-house control software. Varied spatial steps were utilised to examine the ability of the positioning mechanisms to accurately cover large square sonication areas. Consequently, initially a 10 × 10 grid with a 5 mm step was commanded with each point automatically visited by the transducer and exposed to an acoustic power of 9 W for a sonication time of 1 s. Thereafter, an identical 10 × 10 grid operation was commanded with a smaller step of 3 mm with the same acoustical power of 9 W applied for a slightly increased sonication time of 3 s to control the diameter of the formed lesions. In both grid operations a 30 s time delay was employed between sequential sonications.

2.3.3 MRI *ex-vivo* tissue ablations

Initially, the heating abilities of the robotic system were assessed through a series of high-power sonications executed on freshly excised pork tissue within the clinical 3 T MRI scanner (Magnetom Vida, Siemens Healthineers). The robotic system was accommodated on the MRI table with a piece of excised pork tissue accommodated on the silicone membrane of the acoustic window, on top of the transducer, while ultrasound gel was employed between the membrane and excised tissue interface to accomplish acoustic coupling and achieve proper transmission of ultrasonic energy for ablations. The robotic system was interfaced, through the MRI penetration panel, with the control systems and software that were accommodated within the MRI control room. An 8 × 8 grid operation with a 10 mm spatial step was commanded using the software and each point of the grid trajectory was sonicated by applying an acoustical power of 75 W for a sonication time of 40 s at a focal depth of 25 mm. A time delay of 60 s was employed between adjacent sonications. The grid operation was automatically executed, while the evolution of temperature during sonications was monitored with MR thermometry.

MR thermometry temperature estimations were based on the proton resonance frequency (PRF) shift method[27]. The PRF technique is based on temperature-dependent changes observed in the resonance frequency of water protons during thermal heating of tissue that unavoidably induce a phase difference between acquired MR images[27]. Specifically, the shift between phases of a reference image acquired at a known temperature prior to thermal exposure $\varphi(T_o)$ and an image obtained at a specific time during thermal heating $\varphi(T)$ can be translated to the tissue temperature change ΔT as follows:

$$\Delta T = \frac{\varphi(T)-\varphi(T_o)}{\gamma.\alpha.B_o.TE} \quad (2)$$

where γ is the gyromagnetic ratio, α is the PRF change tissue coefficient (-0.01ppm/^{o}C), B_o is the local magnetic field strength and TE is the echo time.

During sonications, MR images of the excised tissue were acquired using the 12-channel body coil (BioMatrix Body 12, Siemens Healthineers) and the 2D FLASH sequence with identical acquisition parameters as employed for imaging for MRI compatibility purposes (Section 2.3.1). FLASH images acquired during the grid ablations were incorporated and processed by the control software using PRF-based MR thermometry. Specifically, the relevant temperature evolution during each exposure was derived at a specific ROI within the excised tissue and extracted as a timeseries temperature graph, while thermal maps were additionally extracted at specific temporal resolutions. Temperature elevations were colour-coded on the thermal maps and were overlapped with the corresponding magnitude FLASH scans, allowing for controlled exposures. Accordingly, a T2-Weighted Fast Spin Echo (T2-W FSE) scan of the excised tissue was executed with specific parameters (TR = 2500 ms, TE = 48 ms, FOV = 260×260 mm^2, Slice thickness = 10 mm, Acquisition matrix = 256×260, NEX = 1, Flip angle = 180^o, and Pixel bandwidth = 50 kHz/pixel) after execution of the grid operation to obtain a high-resolution image of the ablated area.

2.3.4 Benchtop *ex-vivo* tissue ablations

Thereafter, a series of benchtop feasibility studies were executed on freshly excised tissue to further examine the effectiveness of the system in successfully inducing distinct lesions during high-power sonications. In this manner, a piece of excised pork tissue was positioned on the acoustic window in an identical manner as the MRI ablations configuration (i.e., on the silicone membrane with ultrasound gel employed as coupling medium). Motion of the transducer was commanded through the in-house control software along predefined grid trajectories with varying spatial steps to examine the ability of the transducer in forming delineated thermal discrete and overlapping lesions. In this manner, an 8 × 8 grid with a 10 mm spatial step and a larger 10 × 10 grid with a 3 mm spatial step were selected. Both grid operations were automatically executed, with each predefined grid point that was visited by the transducer sonicated using an acoustic power of 60 W for a sonication time of 20 s. The two grid ablations were performed by applying a time delay of 60 s between consecutive sonications, while they were executed at a focal depth of 10 mm.

3. RESULTS

3.1 Assessment of the performance of the robotic system

3.1.1 MRI compatibility

Figures 7A, 7B and 7C show the coronal FLASH images of the excised tissue identically acquired during the various activation configurations of the robotic system (cables not connected, cables connected, and electronic system activation) for MRI compatibility purposes. Figure 7D shows a bar chart of the corresponding SNR calculations derived from the relevant FLASH images of the excised tissue for each tested activation state of the robotic system. Similarly, Figure 8A to Figure 8E show the series of FLASH images of the excised tissue correspondingly acquired during the numerous activation states of the developed transducer for assessing its MRI compatibility, while Figure 8F shows the SNR calculations respectively executed for each individual transducer activation state (reference state, RF cables

connected, amplifier activation, transducer activation at acoustic power of 30 W, and transducer activation at acoustic power of 60 W).

3.1.2 Motion accuracy

Benchtop ablations on plastic films executed in grid operations utilising low sonication protocols (acoustic power of 9 W for sonication times of 1 s or 3 s) provided visual evaluation of the robotic motion accuracy. Sonications of the plastic film in a 10 × 10 grid with a 5 mm step resulted in the formation of well-defined discrete lesions as shown in Figure 9A. The lesions were formed with an identical diameter of 2 mm at equally distant locations indicating the motion accuracy of the robotic system. Accordingly, identical application of acoustic power of 9 W for a longer sonication time of 3 s in the same 10 × 10 grid with a smaller spatial step of 3 mm resulted in the formation of overlapping lesions on the plastic film as shown in Figure 9B. The well-defined area of overlapping lesions was formed in a square area with an approximate size of 30 × 30 mm^2.

3.1.3 MRI *ex-vivo* tissue ablations

MR thermometry temperature estimations and thermal maps of the sonications (acoustic power of 75 W for a 40 s sonication time) executed in a grid trajectory (8 × 8) using a 10 mm spatial step were extracted at a temporal resolution of 2.4 s throughout the grid operation. Figure 10A shows a typical colour-coded thermal maps produced towards the end of the sonication at the first grid point on a coronal imaging plane (plane perpendicular to the ultrasonic beam transmission). Temperature elevations (from a baseline temperature of 37 ^oC) of approximately 30.6 ^oC were produced at the ROI set at the focal point within the excised tissue as indicated from the timeseries temperature graph shown in Figure 10B. Figure 11 shows the coronal T2-W FSE image of the excised tissue acquired post-ablations, assessing the extent of lesion formation on the excised tissue. Circular hypointense areas on the T2-W FSE image indicated the formation of discrete lesions along a square grid. After exposures, the

excised tissue was horizontally sliced at a 10 mm depth from the sonicated surface, revealing the formation of 59 discrete circular lesions as shown in Figure 12A. Appropriately, the tissue was vertically cut revealing the length of the distinguished induced lesions as indicatively shown in Figure 12B. The 59 discrete lesions were formed with an average diameter of 4.65 ± 1.72 mm and a mean length of 12.01 ± 4.03 mm.

3.1.4 Benchtop *ex-vivo* tissue ablations

Numerous benchtop sonications were executed on freshly excised tissue in different grid operations using a varied spatial step by applying a constant sonication protocol (acoustic power of 60 W for 20 s sonication time). Initially, ultrasonic exposure of the tissue following an 8 × 8 grid operation with a 10 mm step successfully induced 64 discrete lesions on the excised tissue. The tissue, after exposures, was sliced at a depth of 10 mm (equivalent to the focal depth of the sonications) on a plane perpendicular to the propagation of the ultrasonic beam, revealing 64 well-formed discrete circular lesions as shown in Figure 13A. Appropriately, the excised tissue was further sliced on a vertical plane (plane parallel to the ultrasonic beam propagation) to demonstrate the length with which the 64 lesions were formed, as shown in Figure 13B. The discrete lesions were formed with an average diameter of 7 mm and an average length of 22 mm as measured with a digital caliper. Identical application of the ultrasonic protocol (acoustic power of 60 W for 20 s sonication time) with a 10 × 10 grid operation and a smaller spatial step of 3 mm commanded, resulted in the formation of a well-demarcated area of overlapping lesions as shown in Figure 14. After exposures, the tissue was horizontally sliced at a depth of 10 mm from the sonicated surface, to reveal an almost square area of overlapping lesions, while it was also vertically cut (on a plane parallel to the ultrasonic beam propagation) revealing the length of the overlapping lesions. The area of overlapping lesions was formed with an approximate size of 40 × 40 mm^2 and a length of about 23 mm.

4. DISCUSSION

In the present study, an MRgFUS robotic system was developed to provide non-invasive targeted treatment of abdominal tumours present in organs such as the liver, kidney, and pancreas. The robotic device is transportable and easily accommodated on the table of conventional clinical MRI scanners with a prone patient positioning on the MRI table above the system, resulting in a targeted bottom to top treatment. The device features a 4 DOF positioning mechanism dedicated to navigating a custom single-element focused transducer operating at a central frequency of 2.75 MHz along the targeted area. Specifically, the transducer can be manoeuvred in three linear (X, Y, and Z) and one angular (Θ) stages. Notably, the angular stage integrated in the robotic system allows easy angular manoeuvrability of the transducer, enabling transmission of ultrasonic beam in several angles, thus sparing obstacles (i.e., rib cage), avoiding sensitive areas, and eluding the sonication of bones. Motion in the four positioning stages of the system is initiated using non-magnetic piezoelectric motors that have been popular in the manufacturing of MRgFUS systems[40–44,49–52].

The proposed robotic system was manufactured with a complex, yet ergonomic design, that integrates years of experience in the development of MRgFUS robotic devices[40–44,49–52], culminating in an advanced system that has been specifically designed for human applications according to clinical standards. Specifically, linear motion in the X, Y and Z stages is accomplished through a series of gear and either rack or jackscrew mechanisms that translate the rotational motion of the ultrasonic motors to linear motion of the attached plates. Remarkably, linear motion of the attached plates is executed along coupled solid brass shafts, rather than lengthways the jackscrew mechanisms, achieving a smooth and stable motion. Additionally, a minimum of two motion guides (three for the Z axis), were integrated on each stage increasing the rigidity of the positioning device and providing proper and strong alignment to the positioning mechanisms, achieving excellent motion accuracy along the defined trajectories. Accordingly, double brass shafts were employed to achieve a stable and

accurate rotation of the transducer shaft. In this regard, a pair of optical encoders were also installed on each linear or angular stage precisely providing feedback on the position of each axis during operation, thus ensuring a highly accurate motion. Furthermore, housing switches were incorporated on the motion origin points of each of the three linear stages providing precise initial point position indications, forcing automatic deactivation of robotic motion upon reach of the origin points, thereby achieving increased safety during operation.

Advantageously, the robotic device was designed with a motion range suitable for human applications and sufficient for ablation of abdominal targets. Simultaneously, the robotic device was specifically designed to maintain a constant water volume within the container during robotic motion, given that the bellow sealing that has been previously employed for mechanical part isolation[41] results in water volume changes. In this regard, the water container was sealed with a bellow and was specially designed with an appropriate configuration of various reservoirs, water inlets, and airtight enclosures to achieve a hermetic environment that prevents water-level variation during robotic operation. Consequently, a proper coupling with the targeted area is continuously achieved during treatment, ensuring efficient transmission of acoustic energy.

Considering employment of MRI guidance with the proposed system, the herein device was manufactured by incorporating only non-magnetic materials to enable suitable operation within clinical MRI environments. In this manner, MRI compatibility evaluation was executed to assess the effect of various activation conditions of the robotic system and the transducer on the MR image quality that was mainly evaluated in terms of SNR changes. A sufficiently high SNR (270) was calculated during sole accommodation of the robotic system on the table of the MRI scanner, enabling the acquisition of high-resolution FLASH images and suggesting the suitability of the raw materials (ASA thermoplastic, brass shafts, and brass screws) that were employed for system manufacturing with the strong magnetic field of the scanner. Remarkably,

approximately a 30 % increase in the SNR (350) from the reference state (270) was observed upon connection of the system with the motion cables, with a decrease, of the order of 20 %, in the SNR (287) observed upon further activation of the electronic driving system. Consequently, SNR values were minimally affected, while no artefacts were detected on the acquired FLASH images, suggesting minimal interference of the system's electronics with the high-field MRI scanner and an insignificant effect of electronics' activation on image quality. Correspondingly, noticeable SNR reductions from the reference state (270) were noticed upon connection and activation of the RF amplifier and ultrasonic transducer. Specifically, approximately a 25 % SNR reduction was observed upon amplifier activation, while a 1.6-fold decrease in SNR from the corresponding reference state was noticed upon transducer activation at an acoustic power of 30 W. Remarkably, a 2.25-fold SNR decrease from the reference condition was observed upon activation of the transducer at a 2.5-fold higher acoustic power (60 W). Nevertheless, the FLASH images acquired for the various RF activation states were of high quality despite SNR reductions, with no visual artefacts, and with the focal spot clearly detectable during transducer activation. Acquired images and concurrent SNR calculations indicated a minimal effect of the different activation states of the system on image quality, thus revealing its MRI compatibility and allowing the employment of MR thermometry monitoring tools. However, despite proper functioning within the high-field scanner and minimal effect on image quality and ultimately on MR thermometry monitoring, the system should be classified as MRI-conditional following the American Society for Testing and Materials standards[53].

Thereafter, the motion accuracy of the developed system was assessed following a simple visual method previously described for motion evaluation of MRgFUS robotic systems[47]. Specifically, a series of low power (acoustic power of 9 W) sonications were executed on thin plastic films with motion of the transducer commanded along predefined constant grid trajectories (10 × 10). Appropriate selection of the spatial grid step resulted in the

formation of white discrete or overlapping lesions on the plastic films post-ablations, thus visually demonstrating the excellent motion accuracy of the robotic system. Specifically, discrete lesions induced after application of the predetermined sonication protocol (acoustic power of 9 W for 1 s) were arranged at equally spaced locations along the plastic film with distances between the centres of successive lesions approximately identical to the commanded spatial grid step (5 mm), thus visually demonstrating the excellent motion accuracy of the robotic system. Overlapping lesions formed on the plastic film after execution of the same grid operation using a smaller spatial step (3 mm) and identical application of acoustic power for a 3-fold increased sonication time were arranged over a well-defined almost square area, thus further evidencing the extreme degree of motion accuracy of the developed positioning mechanisms.

The system was then evaluated for its thermal heating performance and its ability to induce coagulative lesions efficiently and controllably through a series of benchtop and MRI *ex-vivo* feasibility studies. Specifically, high-power sonications were executed following robotic motion over prearranged patterns utilising the grid operation of the developed control software. The heating abilities of the system were initially demonstrated through the MRI *ex-vivo* ablations and were validated using MR imaging and thermometry, while proper operation of the system within the MRI scanner for treatment execution was evidenced. Thermal maps were efficiently generated at specific temporal resolutions throughout the grid operation indicating the effectiveness of the system in inducing temperature evolutions adequate for tissue ablation. Post-ablation MR imaging with a high-resolution T2-W FSE sequence allowed assessment of the extent of tissue ablation prior to tissue dissection, with the formed lesions visually imaged as small circular hypointense areas in an array pattern. Tissue dissection revealed successful formation of equally spaced discrete thermal lesions around the targeted focal depth of 25 mm. Nevertheless, a variability in diameter and length was observed among

the formed lesions with necrosis not visible in 5 sonication sites (out of a total of 64). This could be attributed to the presence of air bubbles in the tissue or tissue inhomogeneities and fat fibres along the propagation of the ultrasonic beam which induce attenuation, thus affecting successful tissue ablation.

The heating abilities of the system were further demonstrated through the benchtop ablations that were performed following constant ultrasonic protocols with discrete and overlapping lesions successfully induced on excised pork tissue by properly commanding the spatial step between sequential grid sonications. The formed lesions demonstrated the ability of the system to produce ablative areas in grid patterns, while also indicating that the system achieves proper acoustic coupling between the airtight water container and the mounted excised tissue target. Notably, the discrete lesions were steadily formed on the tissue at approximately equally spaced locations with a small inherent variability in their diameter and length, thus demonstrating the tremendously accurate motion of the developed robotic system and the ability of the transducer to deliver consistent amounts of acoustic energy. Remarkably, the overlapping lesions induced on excised tissue after application of an identical sonication protocol were formed with an almost uniform length to the discrete lesions (accounting for standard measurement error) further proving the system's ability in controllably inducing necrosis.

MRI guidance is universally considered a superior method for monitoring HIFU procedures compared to US-guidance, since tissue ablation is executed with an increased safety attributed to the highly detailed anatomical tissue imaging and the non-invasive temperature monitoring that offer a higher ablation precision. In this manner, the MRgFUS system proposed herein exploits the advanced features of MRI guidance thus being superior to the commercial[16,19,21–24] or other preclinical systems[32–37] that employ US guidance. Furthermore, the current system is characterised by a simplistic design compared to commercial MRgFUS

systems[29] with its compact enclosure dimensions offering the advantages of portability as well as cost-effectiveness in terms of employment of a single-element transducer rather than a phased-array.

Remarkably, the current device is characterised by advanced features relative to previous custom-made MRgFUS systems that were either proposed[41,44] or could be potentially employed[40,42,43] for ablation of abdominal targets. Specifically, initial systems[40–43] mainly provided feasibility proof that was critical for development of the proposed prototype. Advantageously, the system incorporates novel positioning mechanisms that offer a rigid, smooth, and highly accurate motion, mainly attributed to the employment of brass shafts, double-motion guides, and paired encoders on each stage. Moreover, advances were also incorporated in the design of the water container that offers an airtight sealing to the enclosed water volume, thus addressing water displacement issues, while concurrently offering protection from water leakage during the procedure. More importantly, the proposed system was developed for clinical applications, having a proper and adequate motion range for human targets. Additionally, compared to a previously reported MRgFUS system that was also manufactured based on clinical needs for multiple applications including abdominal targets[44], the current system inherently provides superior functionalities in terms of increased motion range and higher motion accuracy due to the employment of double encoders. Moreover, the previously reported device achieved acoustic coupling through a water-filled cone that extracorporeally couples to the targeted area of interest[44]. This configuration results in a fixed focal depth within the body, with coupling gel pads, or alterations to the transducer element necessary to achieve ablation at different depths. Contrary, the Z-stage of the herein system enables easy alteration of the targeting depth of the transducer within the tissue, while all positioning mechanisms are integrated in an enclosure that advantageously provides increased

safety compared to the previously proposed configuration[44] wherein the mechanical components were proximal to the patient.

Concluding, *ex-vivo* feasibility studies corroborated the safety and efficacy of the system presented in this work in terms of MRI compatibility and thermal heating abilities adequate for inducing ablative temperatures and inflicting necrosis. Advantageously, the proposed system was designed based on clinical standards and requirements, enabling a smooth future clinical adaptation for non-invasive MRgFUS treatment of liver, kidney, and pancreatic tumours. Nevertheless, further *in-vivo* preclinical, and clinical evaluation is required to assess the performance and efficacy of the system for the proposed application, acquiring necessary evidence for clinical employment. Remarkably, the proposed system could also be applied to other abdominal or pelvic targets such as uterine fibroids.

ACKNOWLEDGMENTS

The study has been co-funded by the European Structural & Investment Funds (ESIF) and the Republic of Cyprus through the Research and Innovation Foundation (RIF) under the projects SOUNDPET (INTEGRATED/0918/0008).

CONFLICT OF INTERESTS

Antria Filippou declares no conflict of interests.

Marinos Giannakou declares no conflict of interests.

Nikolas Evripidou declares no conflict of interests.

Andreas Georgiou declares no conflict of interests.

Anastasia Nikolaou declares no conflict of interests.

Christakis Damianou declares no conflict of interests.

PRIOR OR DUPLICATE PUBLICATION

Not applicable.

ETHICS APPROVAL DECLARATION

Not applicable.

LIST OF FIGURE CAPTIONS

Figure 1: CAD drawing of the X-axis. A) Rear view, and B) Front view.

Figure 2: CAD drawing of the Y-axis. A) Front view, and B) Transparent front view.

Figure 3: CAD drawing of the Z-axis. A) Front view, and B) Rear view.

Figure 4: CAD drawing of the Θ-axis. A) Front view, and B) Transparent front view.

Figure 5: CAD drawing of the robotic system showing A) Assembly of parts within the enclosures, and B) Front view of the assembled robotic device, and Photos of the manufactured robotic system in C) Front view, and D) Rear view.

Figure 6: CAD drawing showing accommodation of the robotic device within the MRI scanner with the patient in a prone position.

Figure 7: Coronal 2D FLASH images of the excised tissue acquired with the A) Cables disconnected (reference), B) Motion cables connected, and C) Electronic system activated, and D) Bar chart of SNR calculations of the excised tissue FLASH images acquired at different activation configurations of the robotic system.

Figure 8: Coronal 2D FLASH images of the excised tissue acquired at different activation states of the transducer. A) Reference state, B) RF cables connected, C) Amplifier activated, and transducer activated at acoustic power of D) 30 W for 30 s, and E) 60 W for 30 s, and F) Bar chart of SNR calculations of the excised tissue FLASH images acquired at different activation configurations of the ultrasonic transducer.

Figure 9: A) Discrete lesions formed on plastic film after sonications in a 10 × 10 grid with a 5 mm step and time delay of 30 s using acoustic power of 9 W for a sonication time of 1 s, and B) Overlapping lesions formed on plastic film after sonications in a 10 × 10 grid with a 3 mm step and time delay of 30 s using acoustic power of 9 W for a sonication time of 3 s.

Figure 10: A) Coronal colour-coded thermal maps acquired towards the end of sonications (acoustic power of 75 W for 40 s at a 25 mm focal depth) at the first point of a grid operation (8 × 8 with a 10 mm spatial step) executed on excised pork tissue, and B) Timeseries temperature increase graph of the sonications.

Figure 11: Coronal T2-W FSE image of freshly excised pork tissue acquired after sonications in an 8 × 8 grid with a 10 mm spatial step using an acoustic power of 75 W for a sonication time of 40 s at 25 mm focal depth. Yellow square area indicates the tissue ablation extent.

Figure 12: Discrete lesions induced on excised pork tissue after sonications in an 8 × 8 grid with a 10 mm step and time delay of 60 s using acoustic power of 75 W for a sonication time of 40 s at 25 mm focal depth. A) Slice of the tissue at 10 mm revealing lesions formed on a plane perpendicular to the beam, and B) Indicative lesions formed on a plane parallel to the beam.

Figure 13: Discrete lesions induced on excised pork tissue after sonications in an 8 × 8 grid with a 10 mm step and time delay of 60 s using acoustic power of 60 W for a sonication time of 20 s at 10 mm focal depth. A) Slice of the tissue at 10 mm and its mirror (from right to left)

showing lesions on a plane perpendicular to the beam, and B) Lesions formed on a plane parallel to the beam.

Figure 14: Overlapping lesions induced on excised pork tissue after sonications in a 10 × 10 grid with a 3 mm step and time delay of 60 s using acoustic power of 60 W for a sonication time of 20 s at 10 mm focal depth. A) Slice of the tissue at 10 mm and its mirror (from right to left) showing lesions on a plane perpendicular to the beam, and B) Lesions formed on a plane parallel to the beam.

REFERENCES:

1. Mattiuzzi C, Lippi G. Current cancer epidemiology. *J Epidemiol Glob Health*. 2019;9(4):217-222. doi:10.2991/jegh.k.191008.001
2. Globocan Observatory 2020, International Agency for Research on Cancer (IARC), World Health Organization (WHO). Liver Cancer. Source: Globocan 2020. World Heal Organ Int Agency Res Cancer. Published 2020. Accessed February 1, 2023. https://gco.iarc.fr/today/data/factsheets/cancers/11-Liver-fact-sheet.pdf
3. Globocan Observatory 2020, International Agency for Research on Cancer (IARC), World Health Organization (WHO). Kidney Cancer. Source: Globocan 2020. World Heal Organ Int Agency Res Cancer. Published 2020. Accessed February 1, 2023. https://gco.iarc.fr/today/data/factsheets/cancers/29-Kidney-fact-sheet.pdf
4. Globocan Observatory 2020, International Agency for Research on Cancer (IARC), World Health Organization (WHO). Pancreas Cancer. Source: Globocan 2020. World Heal Organ Int Agency Res Cancer. Published 2020. Accessed February 1, 2023. https://gco.iarc.fr/today/data/factsheets/cancers/13-Pancreas-fact-sheet.pdf

5. Delis SG, Dervenis C. Selection criteria for liver resection in patients with hepatocellular carcinoma and chronic liver disease. *World J Gastroenterol*. 2008;14(22):3452-3460. doi:10.3748/wjg.14.3452

6. Griffin JF, Poruk KE, Wolfgang CL. Pancreatic cancer surgery: Past, present, and future. *Chinese Journal of Cancer Research*. 2015;27(4):332-348. doi:10.3978/j.issn.1000-9604.2015.06.07

7. Friedman M, Mikityansky I, Kam A, et al. Radiofrequency Ablation of Cancer. *Cardiovasc Intervent Radiol*. 2004;27(5):427-434. doi:10.1007/s00270-004-0062-0

8. Dick EA, Taylor-Robinson SD, Thomas HC, Gedroyc WMW. Ablative therapy for liver tumours. *Gut*. 2002;50(5):733-739. doi:10.1136/gut.50.5.733

9. Izadifar Z, Izadifar Z, Chapman D, Babyn P. An Introduction to High Intensity Focused Ultrasound: Systematic Review on Principles, Devices, and Clinical Applications. *J Clin Med*. 2020;9(2):460. doi:10.3390/jcm9020460

10. Frizzell LA, Linke CA, Carstensen EL, Fridd CW. Thresholds for Focal Ultrasonic Lesions in Rabbit Kidney, Liver, and Testicle. *IEEE Trans Biomed Eng*. 1977;BME-24(4):393-396. doi:10.1109/TBME.1977.326151

11. Kopelman D, Inbar Y, Hanannel A, et al. Magnetic resonance-guided focused ultrasound surgery (MRgFUS): Ablation of liver tissue in a porcine model. *Eur J Radiol*. 2006;59(2):157-162. doi:10.1016/j.ejrad.2006.04.008

12. Watkin NA, Morris SB, Rivens IH, ter Haar GR. High-intensity focused ultrasound ablation of the kidney in a large animal model. *J Endourol*. 1997;11(3):191-196. doi:10.1089/end.1997.11.191

13. Jiang L, Hu B, Guo Q, Chen L. Treatment of pancreatic cancer in a nude mouse model using high-intensity focused ultrasound. *Exp Ther Med*. 2013;5(1):39-44. doi:10.3892/etm.2012.744

14. Li CX, Xu GL, Jiang ZY, et al. Analysis of clinical effect of high-intensity focused ultrasound on liver cancer. *World J Gastroenterol*. 2004;10(15):2201-2204. doi:10.3748/wjg.v10.i15.2201

15. Marberger M, Schatzl G, Cranston D, Kennedy JE. Extracorporeal ablation of renal tumours with high-intensity focused ultrasound. *BJU International, Supplement*. 2005;95(2):52-55. doi:10.1111/j.1464-410x.2005.05200.x

16. Sofuni A, Moriyasu F, Sano T, et al. Safety trial of high-intensity focused ultrasound therapy for pancreatic cancer. *World J Gastroenterol*. 2014;20(28):9570-9577. doi:10.3748/wjg.v20.i28.9570

17. Xu G, Luo G, He L, et al. Follow-up of high-intensity focused ultrasound treatment for patients with hepatocellular carcinoma. *Ultrasound Med Biol*. 2011;37(12):1993-1999. doi:10.1016/j.ultrasmedbio.2011.08.011

18. Wu F, Wang ZB, Chen WZ, Bai J, Zhu H, Qiao TY. Preliminary experience using high intensity focused ultrasound for the treatment of patients with advanced stage renal malignancy. *Journal of Urology*. 2003;170(6 I):2237-2240. doi:10.1097/01.ju.0000097123.34790.70

19. Strunk HM, Henseler J, Rauch M, et al. Clinical Use of High-Intensity Focused Ultrasound (HIFU) for Tumor and Pain Reduction in Advanced Pancreatic Cancer. *RoFo Fortschritte auf dem Gebiet der Rontgenstrahlen und der Bildgebenden Verfahren*. 2016;188(7):662-670. doi:10.1055/s-0042-105517

20. Xie B, Ling J, Zhang W, Huang X, Zhen J, Huang Y. The efficacy of high-intensity focused ultrasound (HIFU) in advanced pancreatic cancer. *Chinese Journal of Clinical Oncology*. 2008;5(3):183-186. doi:10.1007/s11805-008-0183-3

21. Kennedy JE, Wu F, ter Haar GR, et al. High-intensity focused ultrasound for the treatment of liver tumours. *Ultrasonics*. 2004;42(1-9):931-935. doi:10.1016/j.ultras.2004.01.089

22. Sofuni A, Asai Y, Tsuchiya T, et al. Novel therapeutic method for unresectable pancreatic cancer—the impact of the long-term research in therapeutic effect of high-intensity focused ultrasound (Hifu) therapy. *Current Oncology*. 2021;28(6):4845-4861. doi:10.3390/curroncol28060409

23. Zhao H, Yang G, Wang D, et al. Concurrent gemcitabine and high-intensity focused ultrasound therapy in patients with locally advanced pancreatic cancer. *Anticancer Drugs*. 2010;21(4):447-452. doi:10.1097/CAD.0b013e32833641a7

24. Ji Y, Zhu J, Zhu L, Zhu Y, Zhao H. High-Intensity Focused Ultrasound Ablation for Unresectable Primary and Metastatic Liver Cancer: Real-World Research in a Chinese Tertiary Center With 275 Cases. *Front Oncol*. 2020;10:519164. doi:10.3389/fonc.2020.519164

25. Hynynen K, Darkazanli A, Unger E, Schenck JF. MRI-guided noninvasive ultrasound surgery. *Med Phys*. 1993;20(1):107-115. doi:10.1118/1.597093

26. Hernando CG, Esteban L, Cañas T, van den Brule E, Pastrana M. The role of magnetic resonance imaging in oncology. *Clinical and Translational Oncology*. 2010;12(9):606-613. doi:10.1007/s12094-010-0565-x

27. Rieke V, Pauly KB. MR Thermometry. *Journal of Magnetic Resonance Imaging*. 2008;27:376-390.

28. Siedek F, Yeo SY, Heijman E, et al. Magnetic Resonance-Guided High-Intensity Focused Ultrasound (MR-HIFU): Technical Background and Overview of Current Clinical Applications (Part 1). *RoFo Fortschritte auf dem Gebiet der Rontgenstrahlen und der Bildgebenden Verfahren*. 2019;191(6):522-530. doi:10.1055/a-0817-5645

29. Payne A, Chopra R, Ellens N, et al. AAPM Task Group 241: A medical physicist's guide to MRI-guided focused ultrasound body systems. *Med Phys*. 2021;48(9):e772-e806. doi:10.1002/mp.15076

30. Okada A, Murakami T, Mikami K, et al. A case of hepatocellular carcinoma treated by MR-guided focused ultrasound ablation with respiratory gating. *Magnetic Resonance in Medical Sciences*. 2006;5(3):167-171. doi:10.2463/mrms.5.167

31. Anzidei M, Napoli A, Sandolo F, et al. Magnetic resonance-guided focused ultrasound ablation in abdominal moving organs: a feasibility study in selected cases of pancreatic and liver cancer. *Cardiovasc Intervent Radiol*. 2014;37(6):1611-1617. doi:10.1007/s00270-014-0861-x

32. Sakuma I, Takai Y, Kobayashi E, Inada H, Fujimoto K, Asano T. Navigation of high intensity focused ultrasound applicator with an integrated three-dimensional ultrasound imaging system. In: *Lecture Notes in Computer Science (Including Subseries Lecture Notes in Artificial Intelligence and Lecture Notes in Bioinformatics)*. Vol 2489. ; 2002:133-139. doi:10.1007/3-540-45787-9_17

33. Pather S, Davies BL, Hibberd RD. The Development of a Robotic System for HIFU Surgery Applied to Liver Tumours. In: *Proceedings of the 7th International Conference on Control, Automation, Robotics and Vision, ICARCV 2002*. ; 2002. doi:10.1109/icarcv.2002.1238487

34. Lweesy K, Fraiwan L, Shatat A, Abdo G, Dawodiah A, Sameer M. Design and ex vivo kidney evaluation of a high-intensity focused ultrasound transducer and 3D positioner. *Med Biol Eng Comput*. 2010;48(3):269-276. doi:10.1007/s11517-009-0560-y

35. Chanel LA, Nageotte F, Vappou J, Luo J, Cuvillon L, de Mathelin M. Robotized High Intensity Focused Ultrasound (HIFU) system for treatment of mobile organs using motion tracking by ultrasound imaging: An in vitro study. In: *Proceedings of the Annual*

International Conference of the IEEE Engineering in Medicine and Biology Society, EMBS. Vol 2015-November. ; 2015:2571-2575. doi:10.1109/EMBC.2015.7318917

36. Cafarelli A, Mura M, Diodato A, et al. A computer-assisted robotic platform for Focused Ultrasound Surgery: Assessment of high intensity focused ultrasound delivery. In: *Proceedings of the Annual International Conference of the IEEE Engineering in Medicine and Biology Society, EMBS*. Vol 2015-November. ; 2015:1311-1314. doi:10.1109/EMBC.2015.7318609

37. Tognarelli S, Ciuti G, Diodato A, Cafarelli A, Menciassi A. Robotic Platform for High-Intensity Focused Ultrasound Surgery under Ultrasound Tracking: The FUTURA Platform. *J Med Robot Res*. 2017;2(3):1740010. doi:10.1142/S2424905X17400104

38. Diodato A, Schiappacasse A, Cafarelli A, Tognarelli S, Ciuti G, Menciassi A. Robotic-assisted Platform for USgFUS Treatment of Moving Organs. In: *10th Hamlyn Symposium on Medical Robotics 2017*. The Hamlyn Centre, Faculty of Engineering, Imperial College London; 2017:23-24. doi:10.31256/HSMR2017.12

39. Odéen H, Parker DL. Magnetic resonance thermometry and its biological applications – Physical principles and practical considerations. *Prog Nucl Magn Reson Spectrosc*. 2019;110:34-61. doi:10.1016/j.pnmrs.2019.01.003

40. Damianou C, Ioannides K, Milonas N. Positioning device for MRI-guided high intensity focused ultrasound system. *Int J Comput Assist Radiol Surg*. 2008;2(6):335-345. doi:10.1007/s11548-007-0145-x

41. Antoniou A, Giannakou M, Evripidou N, et al. Robotic system for magnetic resonance guided focused ultrasound ablation of abdominal cancer. *International Journal of Medical Robotics and Computer Assisted Surgery*. 2021;17(5):e2299. doi:10.1002/rcs.2299

42. Damianou C, Giannakou M, Menikou G, Ioannou L. Magnetic resonance imaging-guided focused ultrasound robotic system with the subject placed in the prone position. *Digit Med*. 2020;6(1). doi:10.4103/digm.digm_2_20

43. Yiallouras C, Yiannakou M, Menikou G, Damianou C. A multipurpose positioning device for magnetic resonance imaging-guided focused ultrasound surgery. *Digit Med*. 2017;3(3). doi:10.4103/digm.digm_33_17

44. Antoniou A, Giannakou M, Evripidou N, Stratis S, Pichardo S, Damianou C. Robotic system for top to bottom MRgFUS therapy of multiple cancer types. *International Journal of Medical Robotics and Computer Assisted Surgery*. 2022;18(2):e2364. doi:10.1002/rcs.2364

45. Dai J, He Z, Fang G, et al. A Robotic Platform to Navigate MRI-guided Focused Ultrasound System. *IEEE Robot Autom Lett*. 2021;6(3):5137-5144. doi:10.1109/LRA.2021.3068953

46. Damianou C, Ioannides K, Mylonas N, Hadjisavas V, Couppis A, Iosif D. Liver ablation using a high intensity focused ultrasound system and MRI guidance. In: *Final Program and Abstract Book - 9th International Conference on Information Technology and Applications in Biomedicine, ITAB 2009*. ; 2009. doi:10.1109/ITAB.2009.5394418

47. Antoniou A, Drakos T, Giannakou M, et al. Simple methods to test the accuracy of MRgFUS robotic systems. *International Journal of Medical Robotics and Computer Assisted Surgery*. 2021;17(4). doi:10.1002/rcs.2287

48. Antoniou A, Georgiou A, Evripidou N, Damianou C. Full coverage path planning algorithm for MRgFUS therapy. *International Journal of Medical Robotics and Computer Assisted Surgery*. Published online 2022. doi:10.1002/rcs.2389

49. Epaminonda E, Drakos T, Kalogirou C, Theodoulou M, Yiallouras C, Damianou C. MRI guided focused ultrasound robotic system for the treatment of gynaecological tumors.

International Journal of Medical Robotics and Computer Assisted Surgery. 2016;12(1). doi:10.1002/rcs.1653

50. Menikou G, Yiallouras C, Yiannakou M, Damianou C. MRI-guided focused ultrasound robotic system for the treatment of bone cancer. *International Journal of Medical Robotics and Computer Assisted Surgery*. 2017;13(1). doi:10.1002/rcs.1753
51. Yiannakou M, Menikou G, Yiallouras C, Ioannides C, Damianou C. MRI guided focused ultrasound robotic system for animal experiments. *International Journal of Medical Robotics and Computer Assisted Surgery*. 2017;13(4). doi:10.1002/rcs.1804
52. Giannakou M, Drakos T, Menikou G, et al. Magnetic resonance image–guided focused ultrasound robotic system for transrectal prostate cancer therapy. *International Journal of Medical Robotics and Computer Assisted Surgery*. 2021;17(3). doi:10.1002/rcs.2237
53. Schaefers G. Testing MR safety and compatibility. In: *IEEE Engineering in Medicine and Biology Magazine*. Vol 27. ; 2008. doi:10.1109/EMB.2007.910267

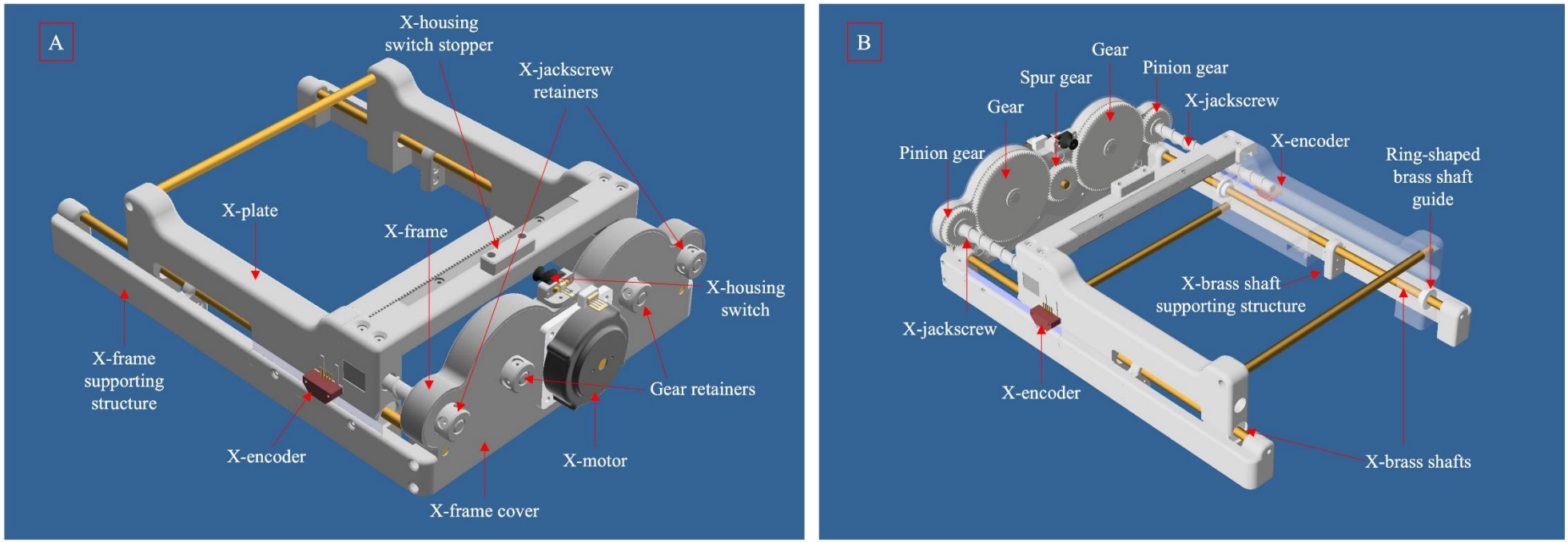
A
X-housing switch stopper
X-jackscrew retainers
X-plate
X-frame
X-housing switch
X-frame supporting structure
Gear retainers
X-encoder
X-motor
X-frame cover
B
Gear
Spur gear
Pinion gear
Gear
X-jackscrew
Pinion gear
X-encoder
Ring-shaped brass shaft guide
X-brass shaft supporting structure
X-jackscrew
X-encoder
X-brass shafts

Figure 1

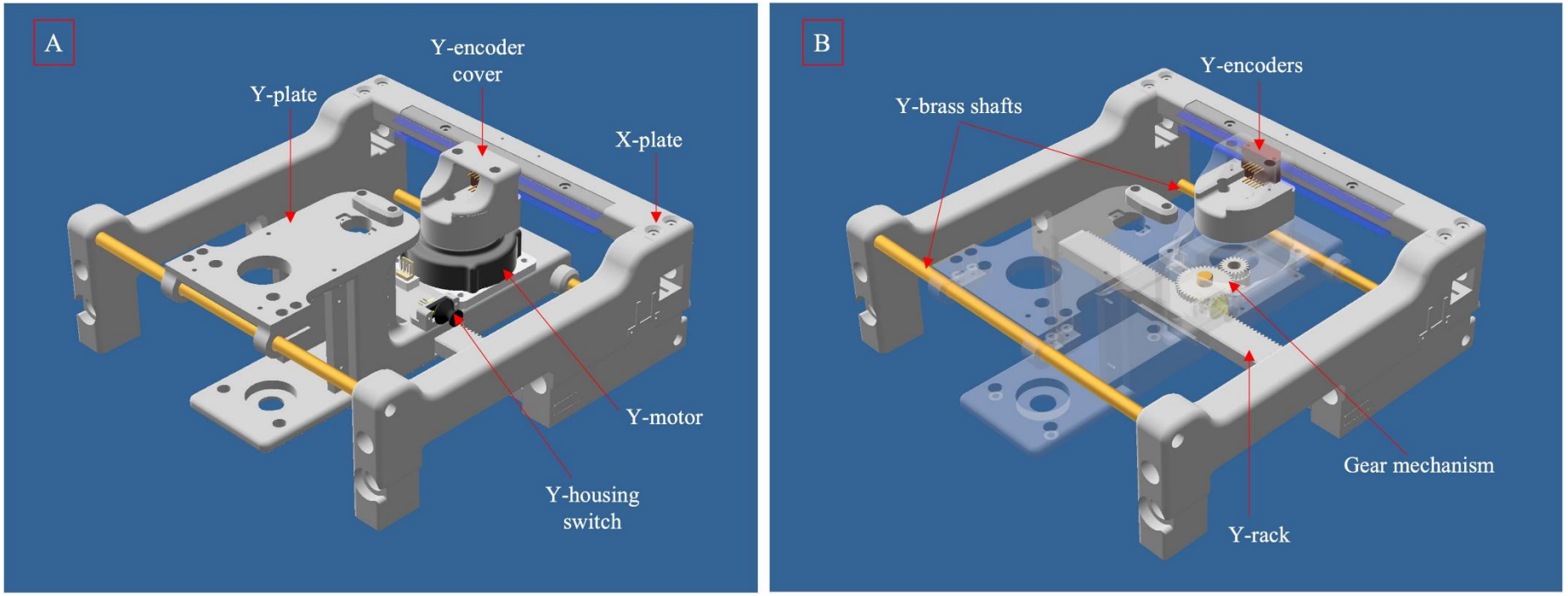
A
Y-encoder cover
Y-plate
X-plate
Y-motor
Y-housing switch
B
Y-encoders
Y-brass shafts
Gear mechanism
Y-rack

Figure 2

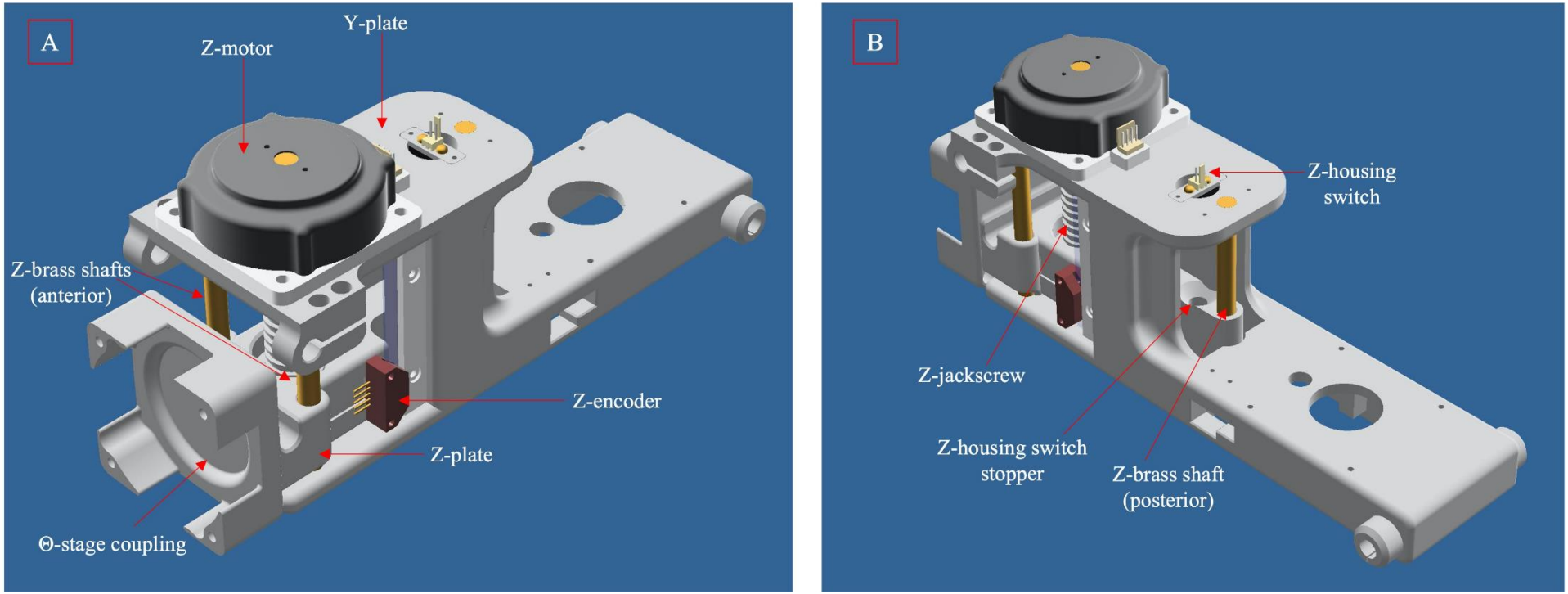
A
Y-plate
Z-motor
Z-brass shafts
(anterior)
Z-encoder
Z-plate
Θ-stage coupling
B
Z-housing
switch
Z-jackscrew
Z-housing switch
stopper
Z-brass shaft
(posterior)

Figure 3

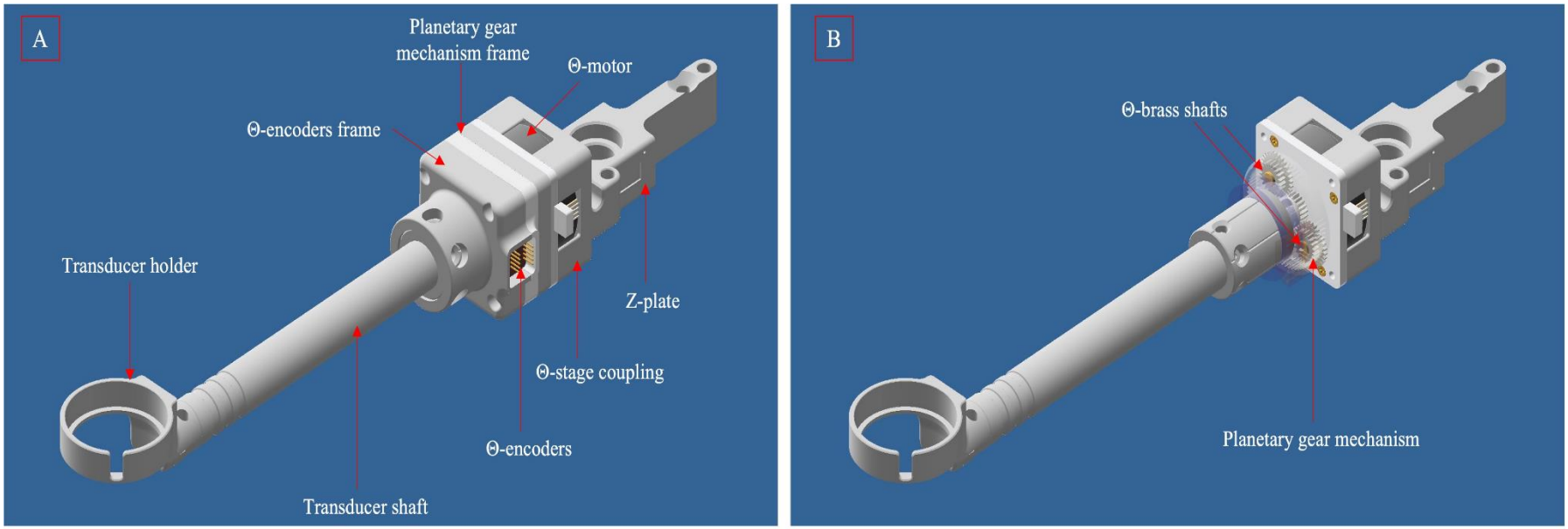
A
Planetary gear mechanism frame
Θ-motor
Θ-encoders frame
Transducer holder
Z-plate
Θ-stage coupling
Θ-encoders
Transducer shaft
B
Θ-brass shafts
Planetary gear mechanism

Figure 4

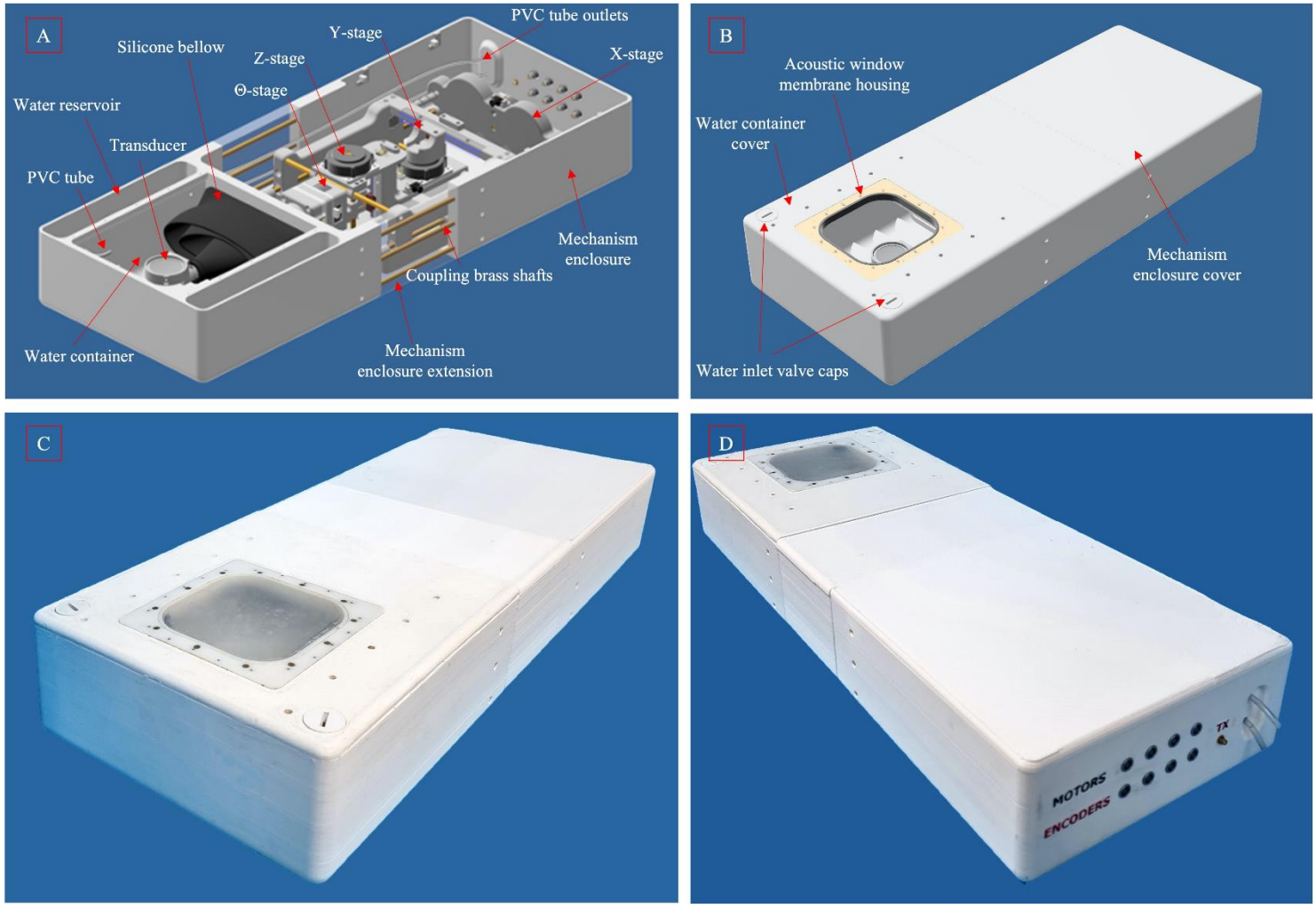
A
Silicone bellow
Y-stage
PVC tube outlets
Z-stage
X-stage
Θ-stage
Water reservoir
Transducer
PVC tube
Mechanism
enclosure
Coupling brass shafts
Water container
Mechanism
enclosure extension
B
Acoustic window
membrane housing
Water container
cover
Mechanism
enclosure cover
Water inlet valve caps
C
D
MOTORS
ENCODERS
TX

Figure 5

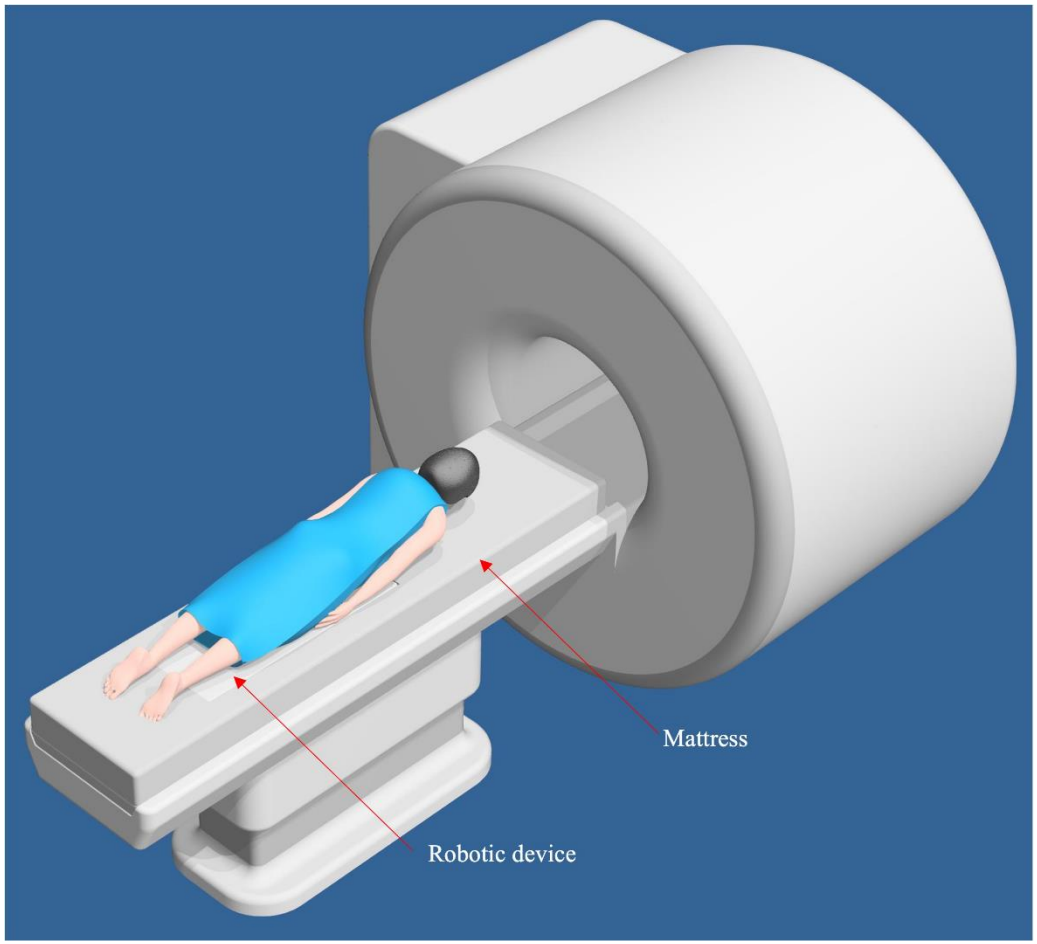

Figure 6

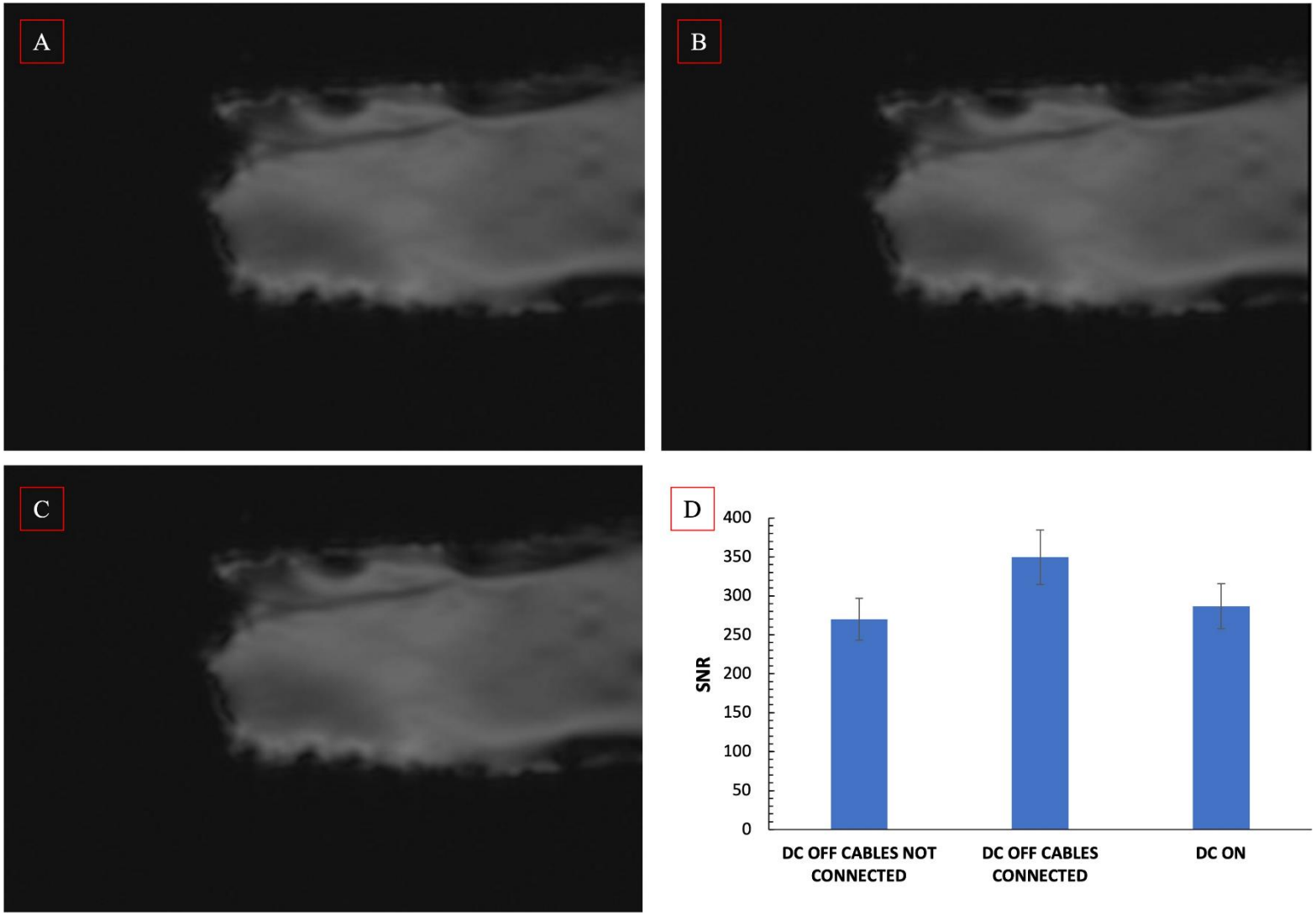
A
B
C
D
400
350
300
250
200
150
100
50
0
SNR
DC OFF CABLES NOT CONNECTED
DC OFF CABLES CONNECTED
DC ON

Figure 7

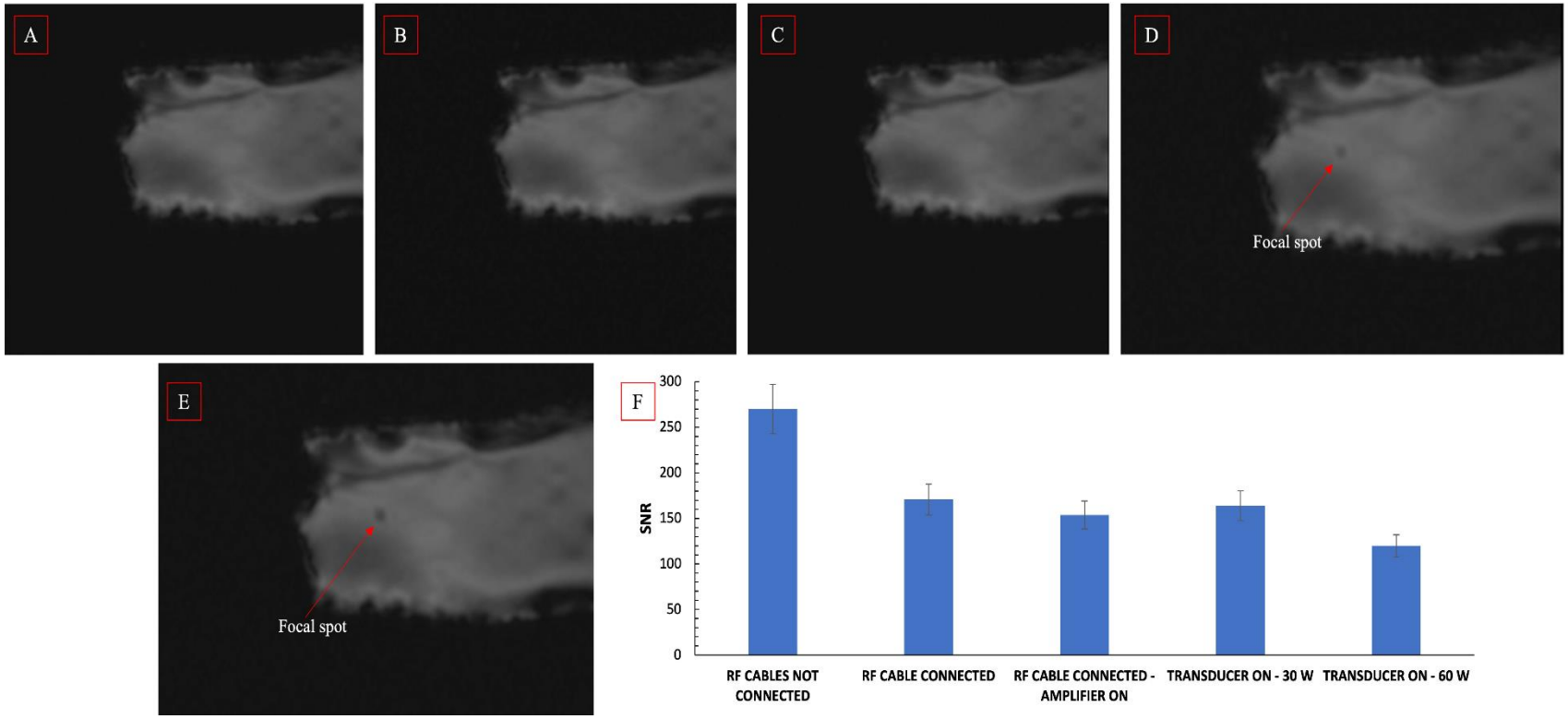
A
B
C
D
Focal spot
E
Focal spot
F
SNR
300
250
200
150
100
50
0
RF CABLES NOT CONNECTED
RF CABLE CONNECTED
RF CABLE CONNECTED - AMPLIFIER ON
TRANSDUCER ON - 30 W
TRANSDUCER ON - 60 W

Figure 8

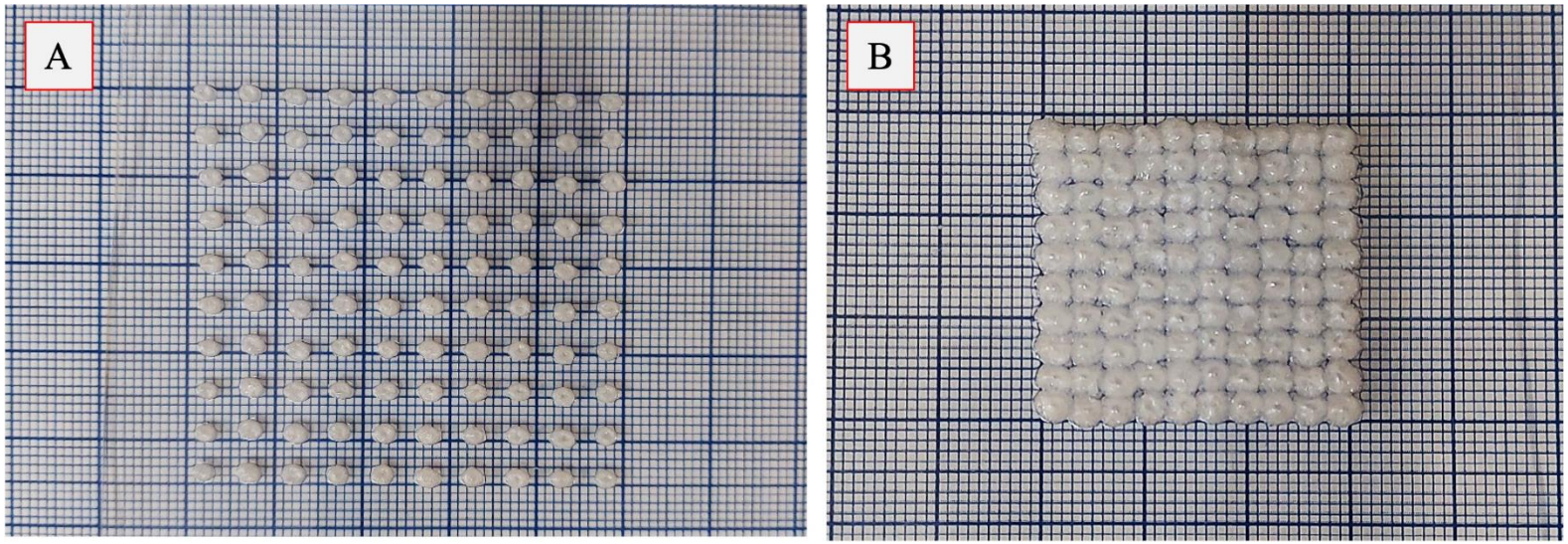

Figure 9

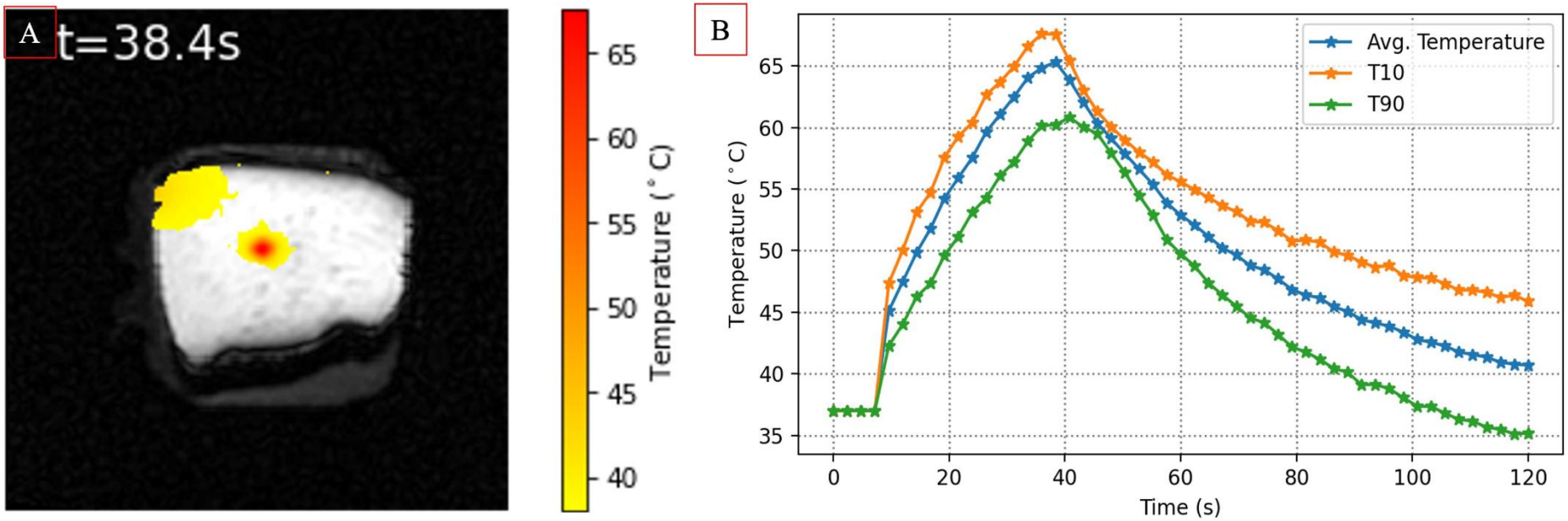
A
t=38.4s
65
60
55
50
45
40
Temperature (˚C)
B
Avg. Temperature
T10
T90
Temperature (˚C)
65
60
55
50
45
40
35
0
20
40
60
80
100
120
Time (s)

Figure 10

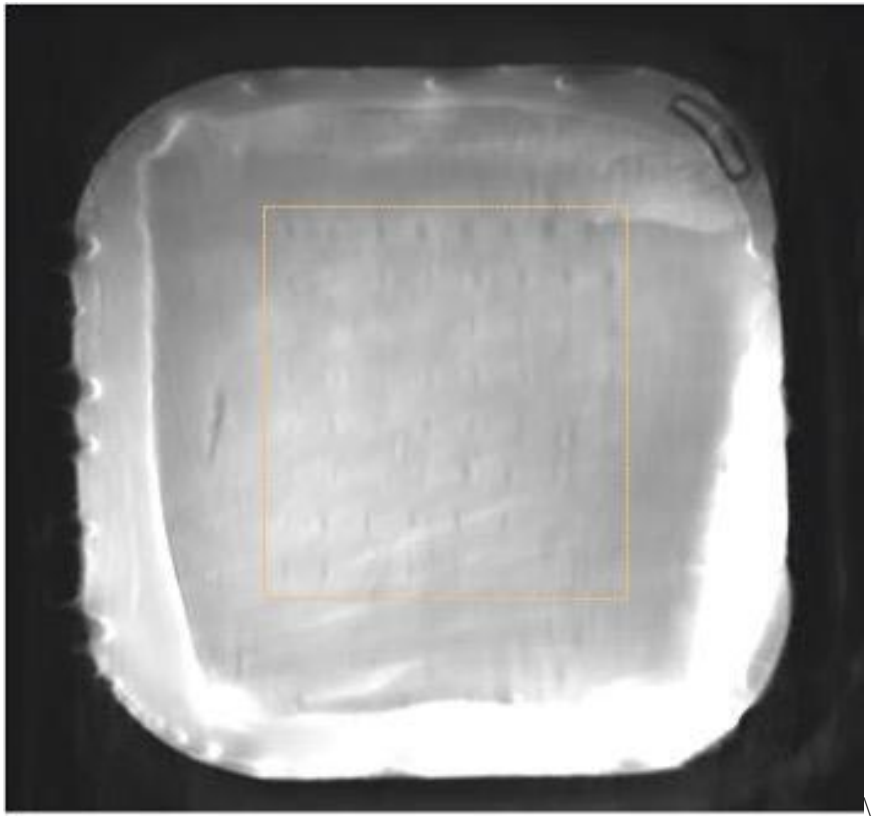

Figure 11

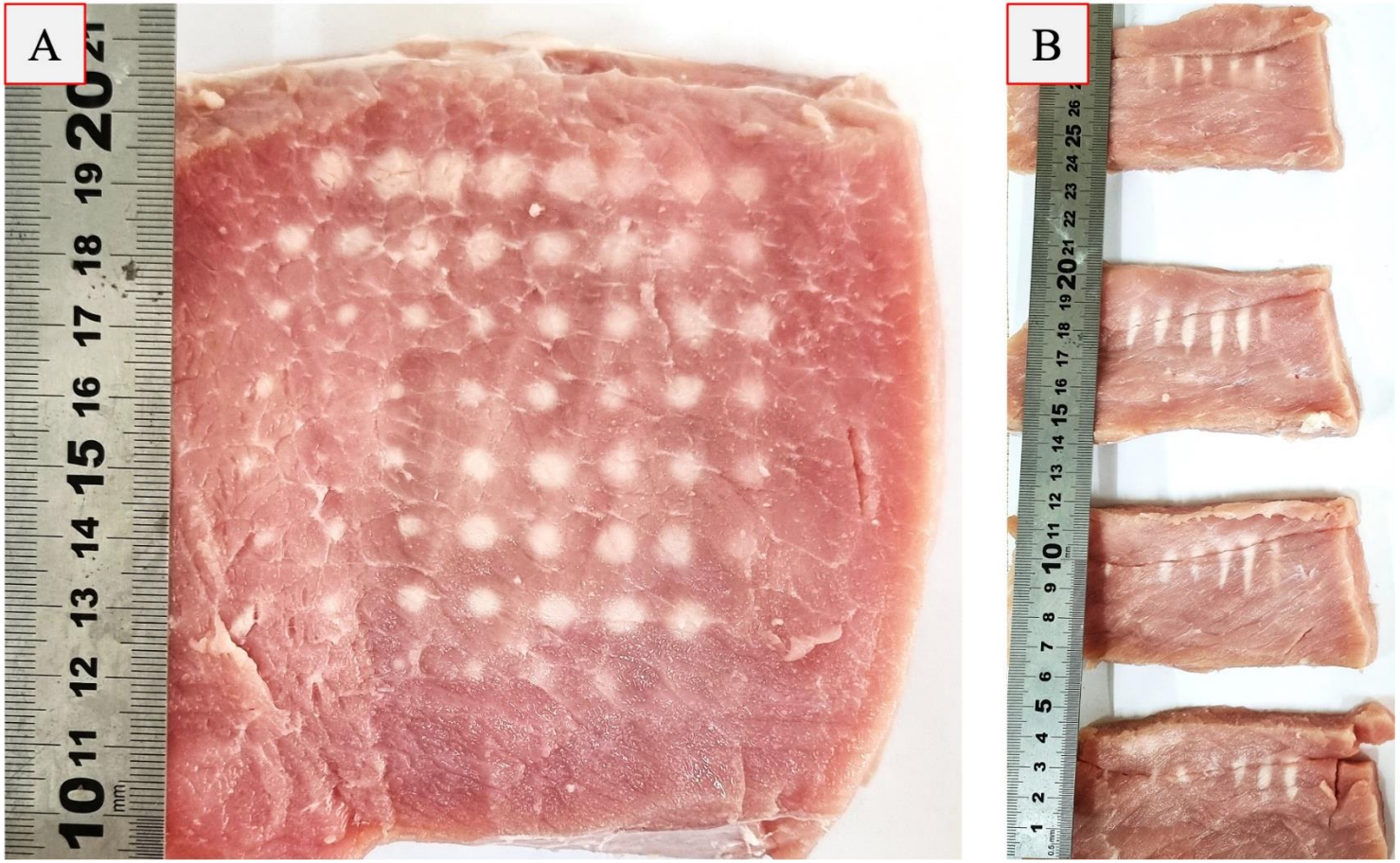

Figure 12

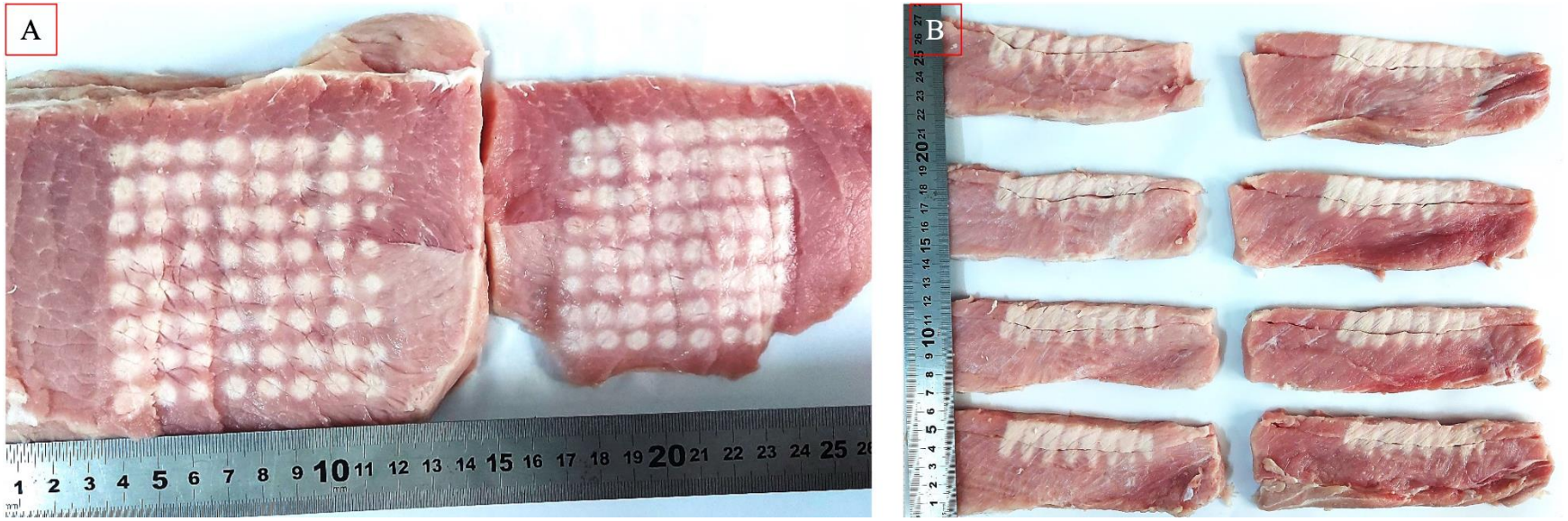

Figure 13

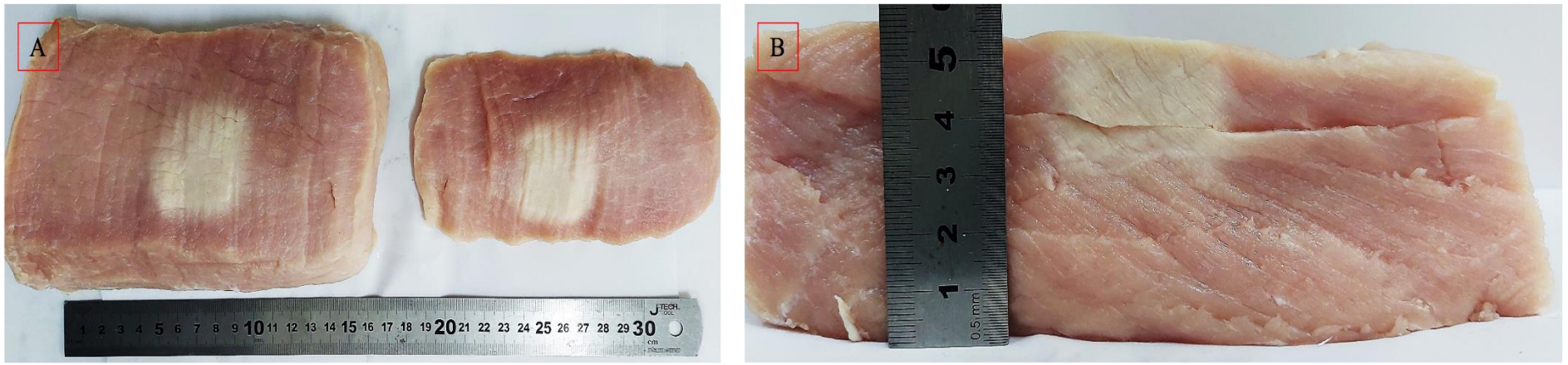

Figure 14